M.A.R.S: the charge ratio of muons in the range 20-500 geV/c in the vertical direction

C. J. Hume

How to cite:

Hume, C. J. (1974) M.A.R.S: the charge ratio of muons in the range 20-500 geV/c in the vertical direction. Doctoral thesis, Durham University.

M.A.R.S. - The Charge Ratio of Muons in the Range 20-500 GeV/c in the Vertical Direction

by

C J Hume, B.Sc.

A Thesis submitted to the University of
Durham in support of an application for
the Degree of Doctor of Philosophy

December 1974

ABSTRACT

The sea level muon charge ratio in the near vertical direction has been measured using the Durham spectrograph M.A.R.S. in the region 10 GeV/c to about 500 GeV/c.

A detailed description of the apparatus used in the experiment is given.

Based on approximately 1.3 x 10^6 particles the mean ratio, over the whole energy range is found to be 1.2850 ± 0.0023. This is consistent with previous measurements made with the same instrument and also with results of other workers. No evidence for pronounced maxima or minima in the ratio as a function of momentum is seen. There is however, some indication of a broad maximum in the ratio in the region 20-50 GeV/c followed by a somewhat lower ratio to about 200 GeV/c.

Using data from the intersecting storage rings experiment an attempt has been made to estimate the expected muon charge ratio at sea level. This estimated ratio is found to be higher than the observed value. The reasons for the discrepancy are thought to be a combination of inadequate pion production data and the effects of intra-nuclear cascading. Other possible causes - a breakdown in scaling and changes in the primary spectrum are also discussed.

PREFACE

The work presented in this thesis represents that carried out in the cosmic ray group of the Physics Department of the University of Durham during the period 1969-1973 while the author was a research student under the supervision of Dr M G Thompson and the period 1973-1974 while the author was a research assistant in the Department.

The M.A.R.S. spectrograph was in an advanced stage of construction when the author joined the group in 1969. Since then the author has played a part in the further construction and running of the instrument. Within this context he has been responsible for the construction, testing and operation of the instrument R.U.D.I. and for the analysis and interpretation of the gathered data. The work described in this thesis represents part of the first stage of the M.A.R.S. programme, the measurements having been made with the 'low momentum' system which will eventually be used as the momentum selector system for the 'high momentum' (up to 5000 GeV/c) measurements.

CONTENTS

CHAPTER 1 INTRODUCTION

CHAPTER 2 M.A.R.S.

CHAPTER 3 R.U.D.I.

CHAPTER 4 INSTRUMENTAL EFFECTS

CHAPTER 5 THE DATA

CHAPTER 1

Introduction

1.0 The Development of Cosmic Ray Studies

The study of cosmic rays has its origins in the investigations of ionization and electrical conduction in gases which were being made at the beginning of the century. During these investigations ionization was found to be present in closed vessels containing air. Rutherford found that the ionization could be reduced by surrounding the vessel with a lead shield; the remaining ionization he attributed to traces of radioactive material in the vessel walls. Just before World War I Hess, in Vienna and Kolhorster in Berlin made balloon ascents carrying sensitive electrometers with them. In September 1912 Hess reported that after an initial reduction in intensity he found the ionization to increase with altitude. He concluded that there was a penetrating radiation coming through the atmosphere from above (Hess, 1912). In 1918 Millikan began to study the ionization and its variation with height; he found a much weaker dependence than did Hess or Kolhorster and concluded in 1924 that there was no penetrating radiation. A year later Millikan and Cameron began a series of experiments to measure the ionization in snow fed lakes which were thought to be free from radioactive contamination. By reducing the background in this manner they obtained consistent results from two separate sites. They concluded that their results strongly indicated a radiation travelling downwards. At this time Millikan coined the name 'cosmic rays'.

Attention was now concentrated upon determining the nature of cosmic rays; they were initially assumed to be γ rays - the most penetrating form of radiation then known. At about this time (the late 1920's) two important instrumental advances were made. In 1929 Skobelzyn using a Wilson cloud chamber in a magnetic field to measure β particle energies found some extraneous tracks of particles of energy greater than 15 MeV. He also found, in a few of his photographs, cases of many simultaneous tracks crossing his chamber, these he called showers. Skobelzyn attributed the tracks to Compton recoil electrons secondary to the 'Hess ultra-γ radiation'. In the same year Bothe and Kolhorster used the recently invented Geiger-Muller tube to study cosmic rays. They found that when two such counters were placed one above the other, many simultaneous discharges occurred, indicating the passage of a charged particle through the pair. This was the first use of detectors 'in coincidence'.

Having found at least some charged cosmic rays Bothe and Kolhorster suggested that because of the geomagnetic field some variation in cosmic ray intensity with (geomagnetic) latitude might exist. Such observations had already been made by Clay in 1927 but it was not fully established until the international survey organized by Compton in 1932. A clear correlation between intensity and magnetic latitude was found. The latitude 'knee' - the latitude beyond which the increase of intensity with increasing latitude becomes less rapid - was also found. At this time it became clear that a large proportion of the rays were charged; the discovery in 1933 of the east-west effect indicated a predominance of positively charged particles. By 1933 the cosmic radiation in the lower atmosphere was known to consist of mainly positively charged particles with energies $\gtrsim 10^8$ eV; it was thought to be the secondary product of interactions between air nucleii and the primary cosmic radiation which was also composed of mainly positive particles and had energies $\gtrsim 3.10^{10}$ eV. From this time cosmic ray research expanded rapidly. The major research fields can be very roughly classified into five groups, each of which will be briefly described.

Studies of the Primary Cosmic Radiation - this is of interest because of the astrophysical information which may be gained and also because the high energy particles of which it is found to be composed can be used to derive information on nuclear interactions.

The primaries were found to be mainly protons by the balloon studies of Schein in the early 1940's. In 1947 other balloon experiments by Hereford showed the presence of nucleii of $Z \geqslant 2$ and in the following year Frier and her co-workers found nucleii of Z up to ~ 28. At the present time nucleii as heavy as uranium, or possibly heavier have been found. The main difference between the mass distribution of the primaries and that of the universal abundance is the considerable excess, in the former, of Li, Be and B. This is thought to be the result of the fragmentation of heavier nucleii in passing through the small amount of matter (~ 4 gms cm^{-2}) from their source to the vicinity of the Earth.

Early measurements of the primary energy spectrum utilised the latitude effect but balloons have also been used. In 1937 Bowen, Millikan and Neher flew up to 90,000 ft (~ 12 gms cm^{-2}) carrying ionization counters. Balloon-borne detectors remain one of the major sources of data on primary cosmic rays. Rocket-borne instruments have also made important contributions (notably the discovery of the Van Allen radiation belts). Satellite experiments have also been made but the results are still the subject of some discussion. Direct measurements of the primary spectrum have been confined to energies below a few thousand GeV for protons, to a much lower level of a few tens of GeV per nucleon for nucleii of $Z > 2$ and to an energy of about 500 GeV per nucleon for helium nucleii. Beyond about 3000 GeV indirect measurements of the spectrum must be made. For example, Brooke in 1964 used the measured muon sea level spectrum together with a model for high energy interactions to work back to the primary spectrum. Above about 10,000 GeV results from air shower studies have been used to obtain information on the primaries. Greisen (1965) summarised the then available data with the result shown in Fig 1.1. Below 3.10^{15} eV the integral intensity is $10^{-4}(10^{14}/E)^{1.6}$ sec^{-1} m^{-2} Sr^{-1} at which energy there is a dramatic change in slope the intensity thereafter being given by 2.10^{-10} $(10^{17}/E)^{2.2}$ sec^{-1} m^{-2} sr^{-1}: at about 3.10^{18} eV

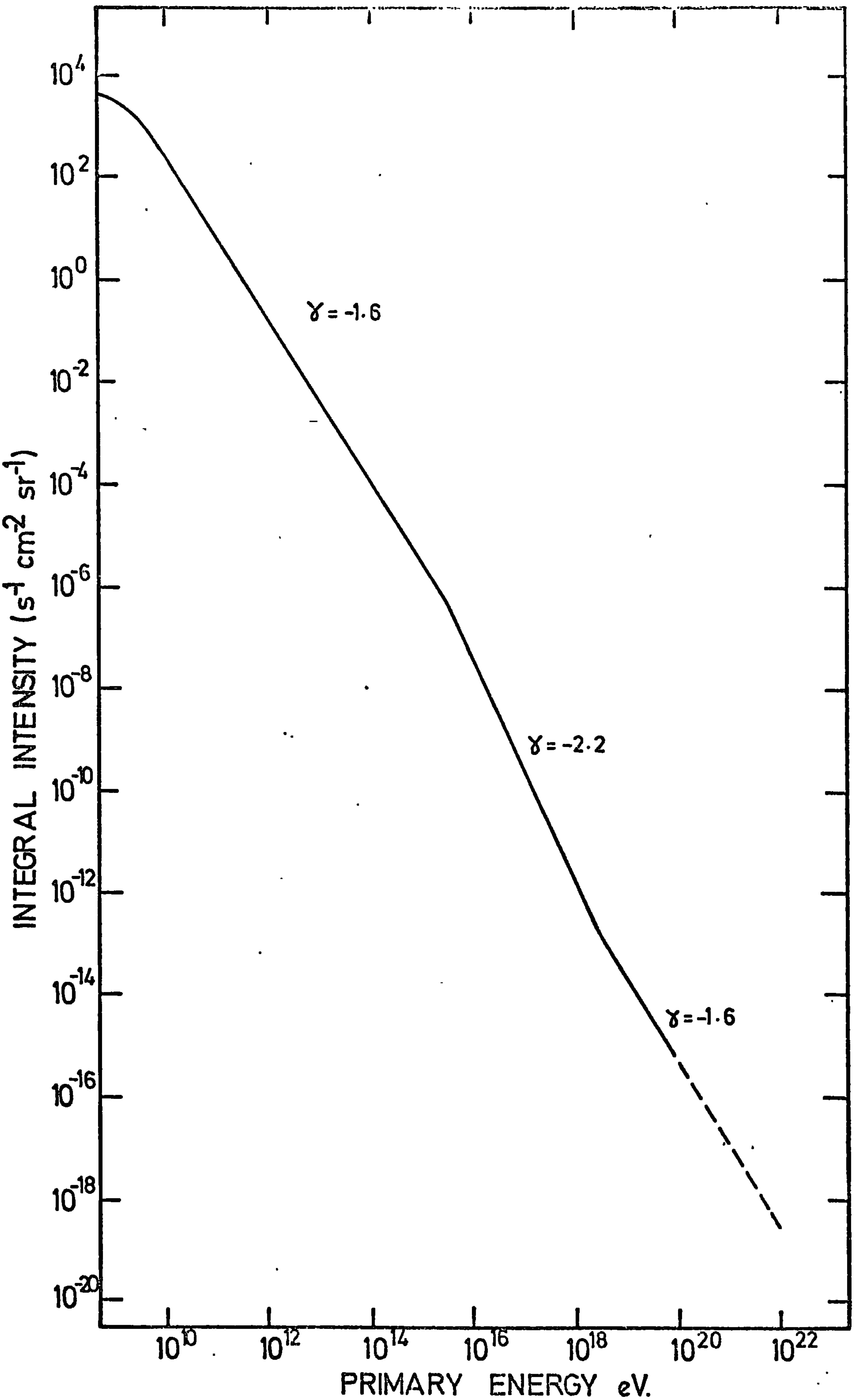

FIGURE: 1.1. THE INTEGRAL PRIMARY SPECTRUM.

the slope seems to revert to -1.6 but this remains a rather uncertain feature.

Other primary particles which have been found are electrons, X rays and γ rays. The former were first found by Earl in 1961 and further studies showed that the ratio of the numbers of positrons to electrons is less than unity and the combined flux is about 1% of the proton flux. Primary γ rays (energy $\gtrsim$ 100 MeV) were found by Clark in 1968 while lower energy X rays were found by Giacconi in 1962.

The question of the origin of the primary particles is still unsolved (apart from the low energy particles occasionally received from the sun). The first serious work on a possible acceleration mechanism was by Swann in 1933 who proposed betatron acceleration in the varying magnetic field which may exist around stars. A major advance was made by Fermi in 1949 when he considered the collision of charged particles with a moving magnetic field (such as contained in randomly moving clouds of gas). Following more detailed experimental observations Fermi modified his mechanism to involve the magnetic fields in the spiral arms of the galaxy. Ginzberg in 1953 suggested that conditions for Fermi acceleration would be favourable in disturbed regions such as supernova remnants (e.g. the Crab nebula). Other suggestions as to possible sources have been ordinary novae, pulsars and quasars. It is unknown whether the majority of particles arise from within the galaxy or are of extragalactic origin. Measurements of the arrival directions of the primaries have given no indication of any preferred directions. The change in slope of the primary spectrum (Fig. 1.1) at about 3.10^{15} eV is thought to be due to the inability of the galactic magnetic field to contain the particles. The flattening of the spectrum beyond about 3.10^{18} eV has been suggested as evidence of an extragalactic component. However, this flattening is not confirmed by experiment; a number of particles of energy believed to be greater than 10^{20} eV have been detected (although the energies are subject to some degree of uncertainty). The recent discovery of the $3^{o}K$ background radiation has led to the possibility of a steepening of the spectrum at around 10^{18} eV caused by the removal of higher energy protons in interactions with the low energy photons. At these high primary energies measurements are most often made with large air shower arrays.

Studies of Air Showers Air showers were first discovered by Bothe in 1937 when he obtained coincident pulses from counters up to 40 cm apart. Using better resolution counters Auger, Maze and Grivet-Meyer found coincidences up to 300 m apart. As the known total flux of particles could not contain so many independent particle pairs to generate the observed coincidence rate it was clear that a large shower of particles was involved. By adding a third and fourth counter to his experiment Auger, in 1939, showed that there were $\sim 10^{6}$ particles in the larger showers. Auger was also the first to realize the high energies of the primaries responsible for the showers. This discovery extended the energy scale of known radiations by an even greater factor than did the original discovery of cosmic rays. The calculations of Auger treated the shower as a multiplicative electron-photon cascade initiated by an electron or positron at the top of the atmosphere. Further experimental work indicated that some regenerating component was preventing the shower being attenuated as rapidly as predicted by theory. Realization that the shower initiating particles were the - mainly protonic - primary cosmic rays came from the emulsion experiment of Kaplon, Peters and Bradt in 1949. These authors also gave evidence for the existence of a neutral meson decaying into γ rays (which could then decay into electron pairs and provide the required regenerating mechanism).

The construction of large arrays of detectors to measure the flux of large showers began in about 1953 with the detection of showers caused by primaries of energy $\sim 10^{17}$ eV. The next generation of detectors cover areas of about 10 Km^2 and should detect primaries of $\sim 10^{20}$ eV. Between 10 and 15 events of energy $\geqslant 5.10^{19}$ eV have so far been recorded by various arrays. The energies of such particles are commonly estimated by comparing experimental data with the results of computer simulations of showers. Various shower models have been constructed and the interpretation of the highest energy experimental data is an active field of work.

In addition to measurements of the primary spectrum, showers also give information on high energy interactions.

High Energy Interactions   Studies of particle interactions and the discovery of new particles were amongst the most active research fields just before and just after the Second World War. Following the cloud chamber work of Skobelzyn in 1929 other groups began observations and found their photographs to show equal numbers of positive and negative particles. The former were assumed to be protons but were found to be insufficiently ionizing. In 1932 Anderson came to the conclusion that the particles were positive electrons. In 1937 range momentum measurements made by several independent groups pointed to the existence of a particle of mass $\sim$ 200 Me. Now called the muon, the particle was at first thought to be that which had been predicted by Yukawa in 1935; however it was found to interact only weakly whereas Yukawa's particle was of a strongly interacting type. The discovery of the latter had to await the refinement of the emulsion technique. Lattes, Muirhead, Occhialini and Powell in 1947, studying emulsion plates exposed at mountain altitudes found tracks they deduced to be those of the decay of one meson into a lighter one which they identified as the muon. The parent particle later identified as Yukawa's, they called a pion. Over the next few years, using cloud chambers and emulsion plates, cosmic ray experiments found several new particles - the K mesons (1947-8), the Λ hyperon (1951), the Ξ hyperon and the Σ hyperon (1953). No other particles have been found since this time but searches are still being made, in particular for quarks and W-particles and others such as magnetic monopoles and tachyons.

As particle accelerators of ever increasing energy have become available the role of cosmic rays has shifted to the study of interactions at even higher energies. Cosmic rays are the only source of particles of energies greatly in excess of those of the CERN ISR experiment and it is this fact that to some extent compensates for the often poor and rather qualitative results obtained from cosmic ray measurements. Interest in the ultra-high energy field has been stimulated by the theoretical ideas of, in particular, Feynman (1969) and Benecke et al (1969). The technique generally adopted in these studies is to form a simple model of a nuclear interaction (derived by extrapolation from the lower energy region) and then to perform various calculations using the model and then to compare with experiment. The deviations of the observations from prediction are then used as a basis for modifying the model. The experimental data are usually air shower measurements or the sea level spectra of various particles such as muons, protons or pions.

<u>Cosmic Rays at Ground Level</u> The primary nucleons incident on the top of the atmosphere have an interaction length of approximately 80 gms cm^{-2} and the probability of their arriving at ground level without interacting is less than 10^{-5}. Their interactions produce many types of secondaries. At the ground the great majority of particles are made up of muons, electrons, pions, protons and neutrons. The most numerous types are the first two; low energy muons and electrons form the soft component of the radiation while the hard component (defined by Greisen in 1942 to be the particles capable of traversing 10 cm of Pb) is mainly composed of muons. There are two main reasons for interest in ground level muons. Firstly the interactions of the muons can be studied in local detectors with the object of examining the character of the muon itself (attempting to distinguish it from a mere heavy electron).

Secondly, comparison can be made with calculations based upon various models of high energy collisions in the search for information on these collisions at very high energies. Particularly for the second reason the muon charge ratio, in addition to the energy spectrum is of some importance. Comparisons of muon spectra above and below ground relate to electro-magnetic processes and, by way of neutrinos, to weak interactions.

Pions are generated both in the first collision of the primary particle with an air nucleus and in the successive interactions of the products of that first collision with other air nucleii. Measurements of the pion spectrum are of nuclear physical interest.

In the interaction of nucleons with air nucleii one of the secondary particles is found to have a much higher energy ($\sim 50\%$ of the incident energy) than the other secondaries. This 'leading particle' is a nucleon and is considered to be the surviving incident nucleon. The probability of the leading particle being a neutron when the primary is a proton, and vice-versa, has been found to be such that at ground level the proton and neutron spectra are similar (except at low energies where the effect of ionization loss on the proton spectrum becomes important). Here again, measurement of these spectra is of use in determining some average characteristics of the nuclear collision.

Neutrinos were first postulated by Pauli in 1930 and the electron-neutrino was detected in 1953 by Reines and Cowan; later experiments demonstrated the existence of a second type of particle - the muon neutrino. The flux of cosmic ray muon neutrinos has two main components, the atmospheric neutrinos and the extraterrestrial neutrinos. The former arise from the decay of pions, kaons and muons while the latter are thought to come from interactions between the primary cosmic rays and the interstellar or intergalactic gas; some may also be produced in stellar interiors. The total cross section for interactions between energetic neutrinos and nucleons is a few times 10^{-38} cm^2. - on this scale the diameter of the earth is $\sim 10^{-4}$ interaction lengths. Detection is thus difficult and detectors are usually deep underground to reduce the cosmic ray background. The results of such experiments have enabled a lower limit of ~ 2 GeV/c^2 to be placed on the mass of the intermediate boson; they also show signs of a slowing at about 100 GeV of the rate of increase of interaction cross section with energy. The ratio of extraterrestrial to atmospheric neutrinos has been found to have an upper limit of 1.0 and a study of arrival directions has given no evidence for localized sources. Considering electron neutrinos these also have two major components - the same as muon neutrinos - and there is also a rather smaller component in the decay of radioactive material in the earth's crust. No electron neutrinos from either of the two main sources have been detected with certainty. The extra-terrestrial component should be mainly from the sun and it is solar neutrinos which have become the subject of much study.

Solar Cosmic Rays Between 1911 and 1913 Hess made a number of day and night balloon flights to determine whether the penetrating radiation came from the sun. Thereafter, many further attempts were made with ground based instruments to detect solar effects. The first report of a very small variation with local solar time was made by Hoffman and Lindholm in 1928. An important development was made in 1936 by Forbush with the establishment of a network of reliable continuously recording ionization chambers. The results from these instruments showed many types of cycle to be present in cosmic ray intensity variations. Theoretical descriptions of these effects made a major advance with the introduction of the concept of the solar wind (by Chapman and Ferraro in 1931) and most of the intensity variations can be at least approximately described in terms of the wind and its associated magnetic field. Very detailed studies of solar effects are being vigorously pursued.

A particularly important aspect of solar cosmic radiation is the study of solar neutrinos. It is generally believed that the energy of the sun is generated by nuclear fusion in the process of which electron-neutrinos are produced. As the expected energy spectrum of these particles depends upon solar parameters such as the constitution, density and temperature of the core, the measurement of this flux is helpful in establishing the values of the parameters. The main experiment to detect solar neutrinos, that of Davis, has so far failed to detect any flux above the background noise due to cosmic ray muons and atmospheric neutrinos. This has created some astrophysical controversey.

1.1. M.A.R.S.

M.A.R.S. - the magnetic automated research spectrograph at the University of Durham is one of the new generation of spectrographs possessing a high maximum detectable momentum (m.d.m). The main purpose of the instrument is the study of the muon energy spectrum and charge ratio.

The muon spectrum has most commonly been investigated by measuring the deflection of the muon in a magnetic field and relating this deflection to the particle's momentum. In the earlier spectrographs Geiger counters were used both as the triggering elements and for measuring the particle deflection. Subsequent spectrographs incorporated additional detectors, often flash tubes, to extend the range of particle momenta which could be measured. More recently, scintillation counters have been used as triggering elements and spark chambers have been used as the track defining elements. Spectrographs have used either air gap magnets or solid iron magnets (in which the muons traverse the magnetized iron). The latter generally have the higher m.d.m. but suffer from worse scattering problems. M.A.R.S. incorporates four large magnet blocks; the trajectory defining elements are trays of neon flash tubes located at the top and bottom of the instrument and also in the gaps between magnet blocks. Large area scintillation counters are the trigger detectors. The m.d.m. is about 6000 GeV/c. A multi-layer instrument has been chosen because of the need to allow for the increasing probability of burst production by the muon with increasing muon energy. Said (1966) gives the probability of a muon of 1000 GeV leaving a thick steel absorber being accompanied by a large burst as 16%. The four magnet blocks of M.A.R.S. are an attempt to ensure that most of the muons traversing the instrument will give enough accurately locatable points on their trajectories to enable a successful determination of their momenta.

1.2. The Present Work

During various stages of the construction of M.A.R.S. since its commencement in 1968 several experiments using the apparatus as it stood at that time have been performed. Details of most of these experiments and of M.A.R.S. itself are given in the next chapter.

The data reported in this thesis have been gathered in one of the longer term experiments performed during completion of the spectrograph.

Measurements of the muon charge ratio have been made over an energy range of approximately 10 GeV to 500 GeV.

CHAPTER 2

M.A.R.S.

2.0 Introduction

In this chapter an outline of the M.A.R.S. project is given in order that the parts of the project described in greater detail in later chapters may be seen in perspective.

2.1 The Trajectory of Muons in a Magnetic Field

A particle of charge ze and mass m moving with a velocity v in a magnetic field B is subjected to a force F given by

$$F = Bvze$$

in a direction perpendicular to v, thus causing the particle to move in a circle of radius r given by

$$F = mv^2/r$$

ie $r = mv/Bze = P/Bze$ where P is the momentum of the particle. The momentum of a muon in a known magnetic field may thus be found if the radius of curvature of the trajectory can be measured.

The inclusion of energy loss as the particle progresses changes the track from a circular to a spiral form. The energy loss of a particle moving a certain distance is much higher for a solid iron magnet type of spectrograph than for the air gap type. A further amplification is the effect of elastic scattering of the particle as it passes through the instrument - again this is most important in solid iron spectrographs. Yet another complication present in the latter is the effect of interactions in the iron - particularly near the bottom of the magnet - producing large bursts of electrons which can saturate the trajectory defining detectors. In an effort to minimise this problem M.A.R.S. - a solid iron magnet type of spectograph - has been built in layers. This ensures that enough accurately located points on the muon tracks can be obtained to enable their momenta to be determined.

2.2 M.A.R.S. - A General Description

The basis of the M.A.R.S. project is the large electro-magnet which has been built in the Sir James Knott Laboratory. The magnet consists of 4 separate iron blocks (Fig 2.1); in the gaps between blocks, above the top block and below the bottom block are placed trays of flash-tubes.

Using the tubes to locate the track of a particle traversing the whole magnet, the deflection of the particle - its direction and magnitude-can be measured. By combining this deflection with a knowledge of the value of the magnetic field within the blocks the momentum and charge of the particle may be calculated as previously described.

The most common method used by previous workers to record the discharged flash-tubes has been to photograph the trays; this involves tedious, time-consuming scanning of the resulting film. For the M.A.R.S spectrograph however, a new technique involving digitisation of the neon flash-tubes has been developed. The data from some of the flash-tube trays of the spectrograph are stored directly in a computer which is also used to calculate the momentum and charge of the particle. Another feature of the M.A.R.S. experiment is the use of a 'momentum selector' to reduce the number of low energy particles stored in the computer.

2.3 M.A.R.S. - Details

2.3.1. The Magnet The four magnet blocks are each composed of 78 iron plates (fig 2.2a). The coils on each block are wound as shown in Fig.2.2b. One side of the spectrograph has been designated the red side, the other side is the blue side. A detailed front view of M.A.R.S. is shown in Fig 2.3. The coils wound around each block are composed of 92 turns of 4 SWG copper wire. Two power supplies, each providing 50A at 120v are used to energise the magnet coils. One energises the blocks A and C and the other energises blocks B and D. Normally the magnetic fields in the blocks are parallel to each other but may be arranged to give other configurations. The connections between power supplies and

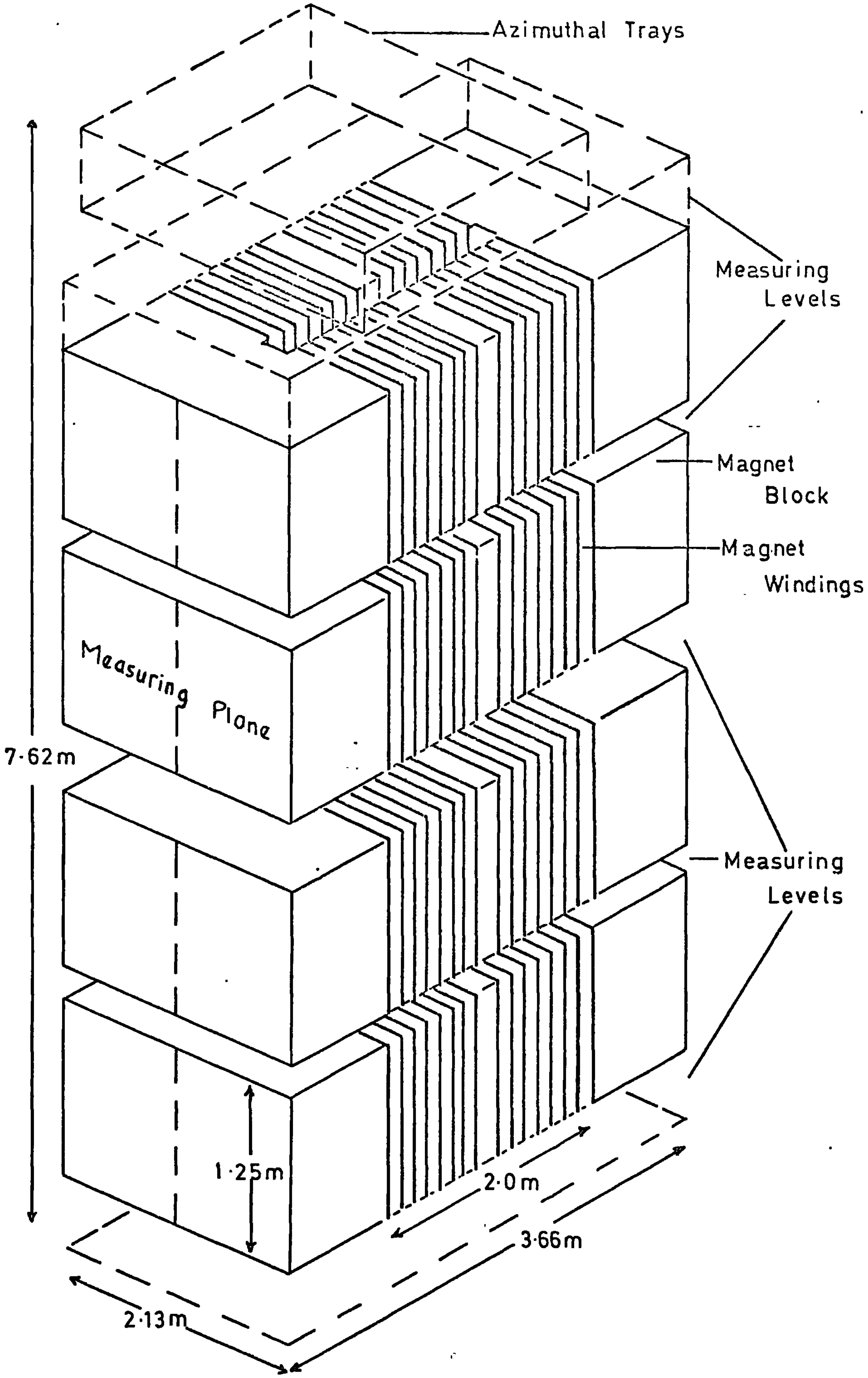

FIGURE. 2.1. THE GENERAL FEATURES OF MARS

NOT TO SCALE

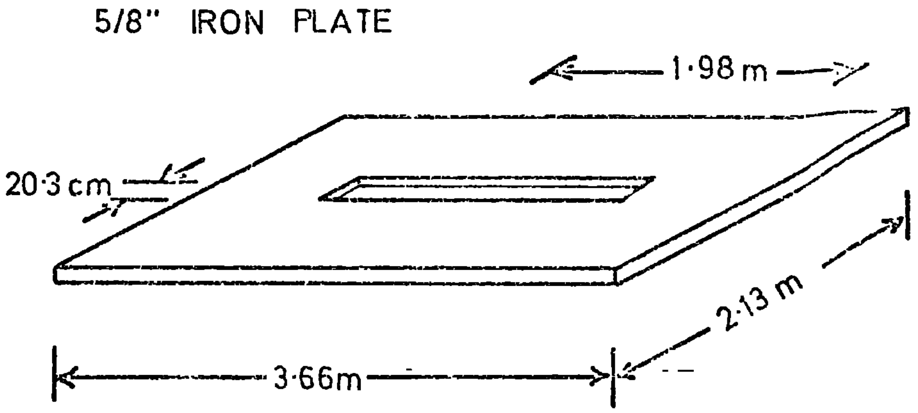

(a) MAGNET PLATE

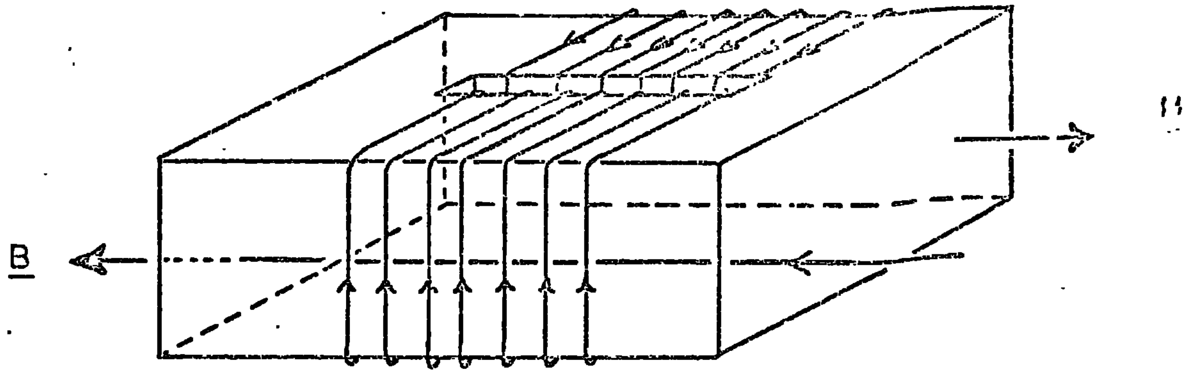

(b) MAGNET BLOCK

FIGURE: 2.2.

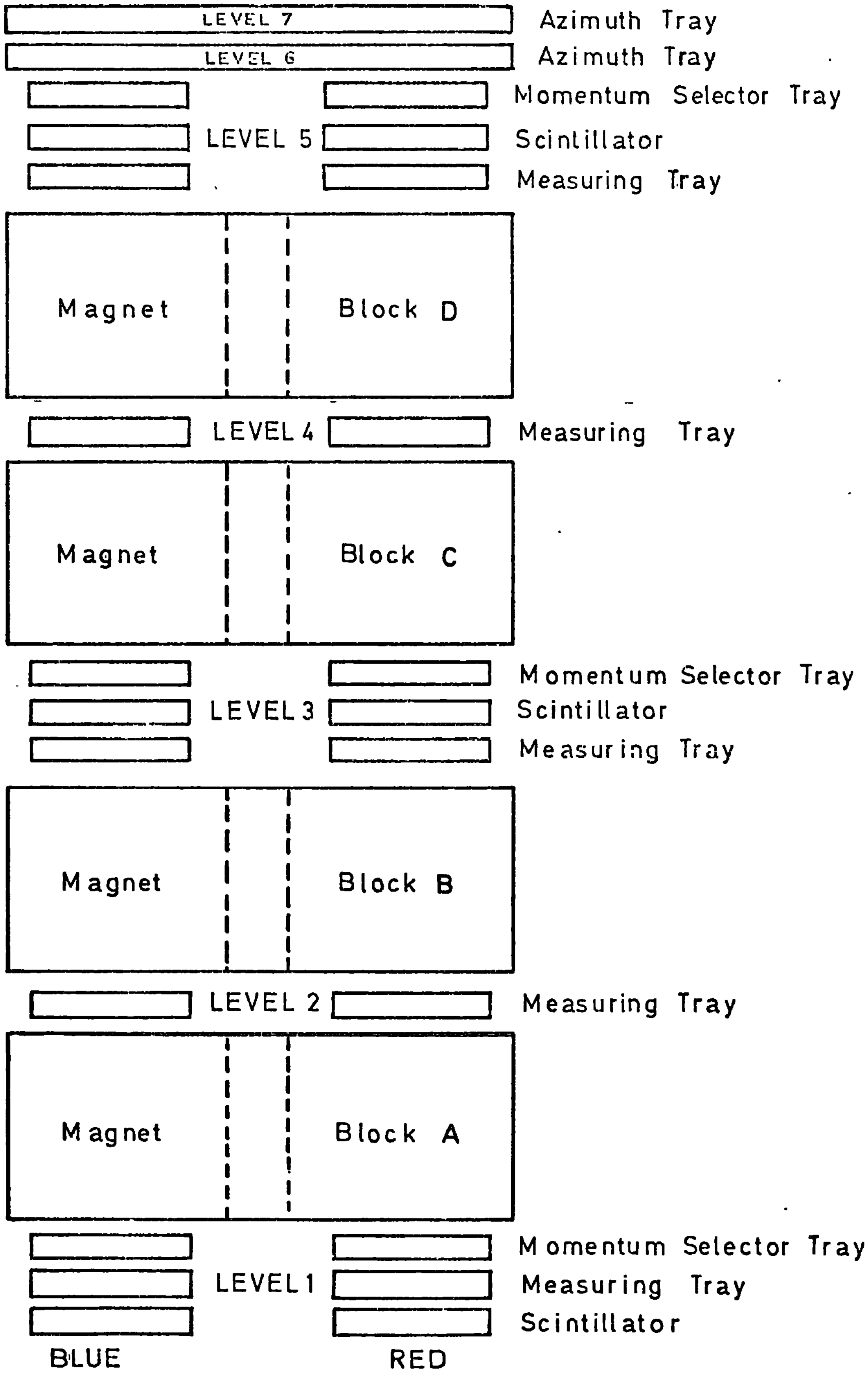

FIGURE: 2.3. M.A.R.S. FRONT VIEW

coils are readily accessible so that the energising coils can, if required, be connected in series, hence reducing the magnetizing current and consequently the magnetic field in the blocks.

With a current of 50A flowing through the coils of each block search coils indicate a magnetic field in the iron of 16.3 ± 0.1 kg. The hysterisis loop of a block shows the iron to be well saturated for this current - fig.2.4 (The uniformity in the field is given in Fig.2.5 and it is seen that the variation of the field over the sensitive volume of a block is ± 4%.

<u>2.3.2. The Triggering System</u> To detect the passage of a particle through a side of the spectrograph scintillation counters are placed at the top middle and bottom of the magnet (Fig.2.3). Each counter contains a slab of plastic scintillator (Ne102A) of size 133 cm x 75 cm x 2.5 cm. Each block of scintillator is viewed by four 53-AVP photomultipliers - 2 at each end. The outputs from diagonally opposite pairs of photomultipliers are passively summed and the resulting pulses amplified (Fig.2.6). These two resulting pulses are fed, separately, into discriminators. The outputs of the discriminators are taken to the input of a 2-fold coincidence circuit. An output pulse from this circuit is taken to mean that a particle has passed through the scintillation counter (although a very small fraction of the pulses is due to coincidences between the random noise pulses of each photomultiplier). The 2-fold coincidence pulses from each of the three scintillation counters on one side of the spectrograph pass to a 3-fold coincidence circuit, which detects the traversal of particles through one side of the spectrograph.

<u>2.3.3. The Acceptance of the Spectrograph</u> To determine the muon spectrum incident upon the spectrograph the acceptance - the 'collecting power' - of the instrument must be known. The minimum requirement for a muon to be detected is that it must traverse each of the three scintillation counters. The acceptance of the instrument under this

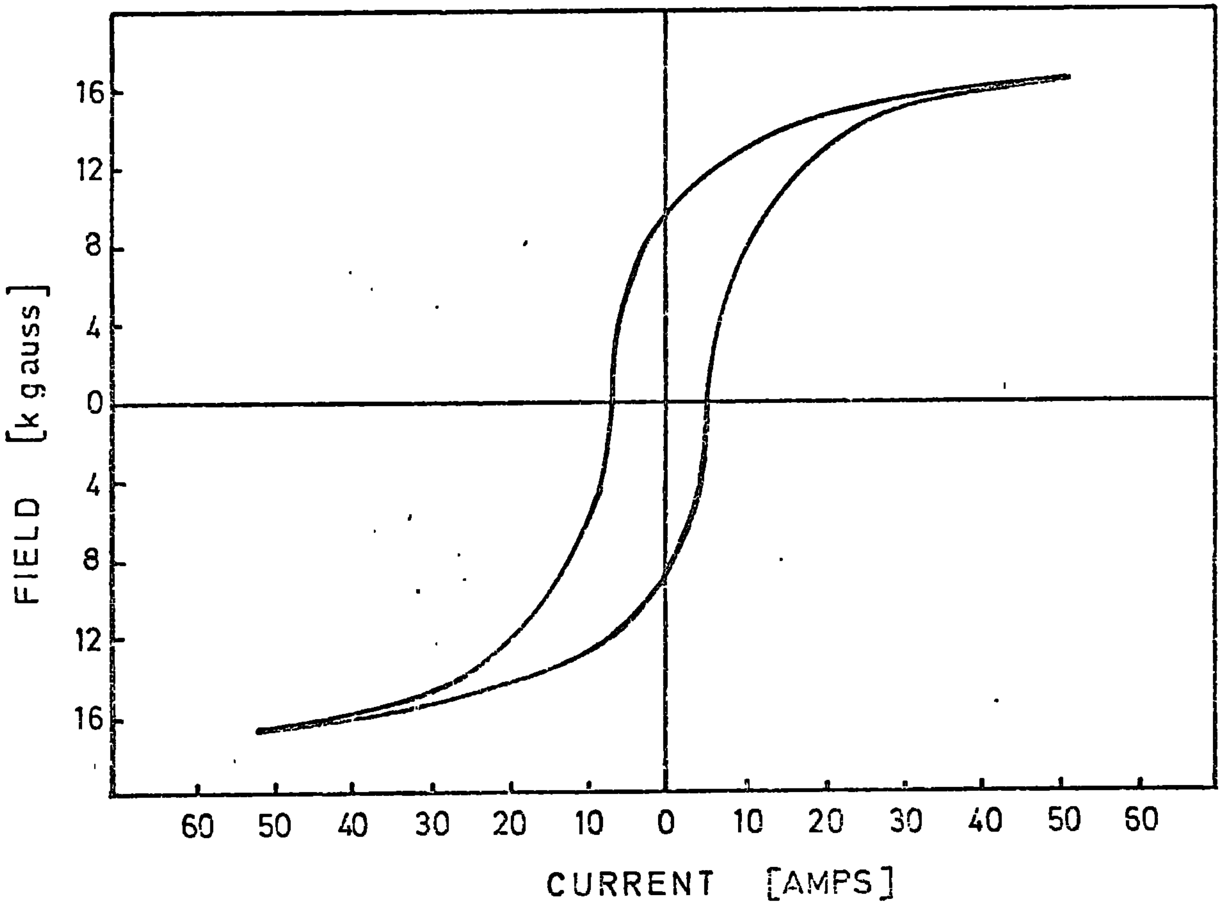

FIGURE: 2.4 HYSTERISIS LOOP OF A MAGNET BLOCK

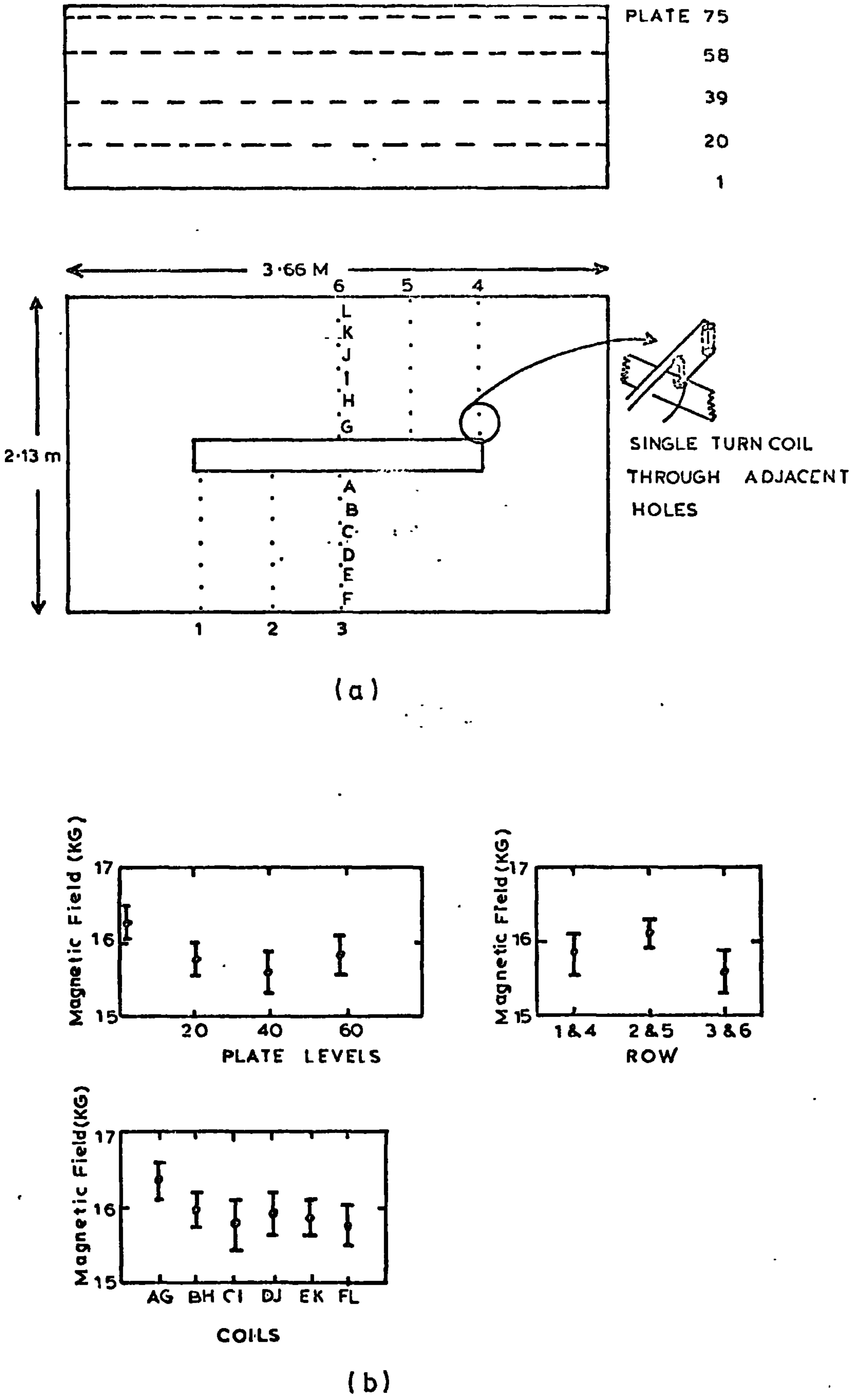
PLATE 75
58
39
20
1
3·66 M
2·13 m
6 5 4
L K J I H G
A B C D E F
1 2 3
SINGLE TURN COIL THROUGH ADJACENT HOLES
(a)
Magnetic Field (KG)
17
16
15
20 40 60
PLATE LEVELS
1&4 2&5 3&6
ROW
AG BH CI DJ EK FL
COILS
(b)

FIGURE: 2·5

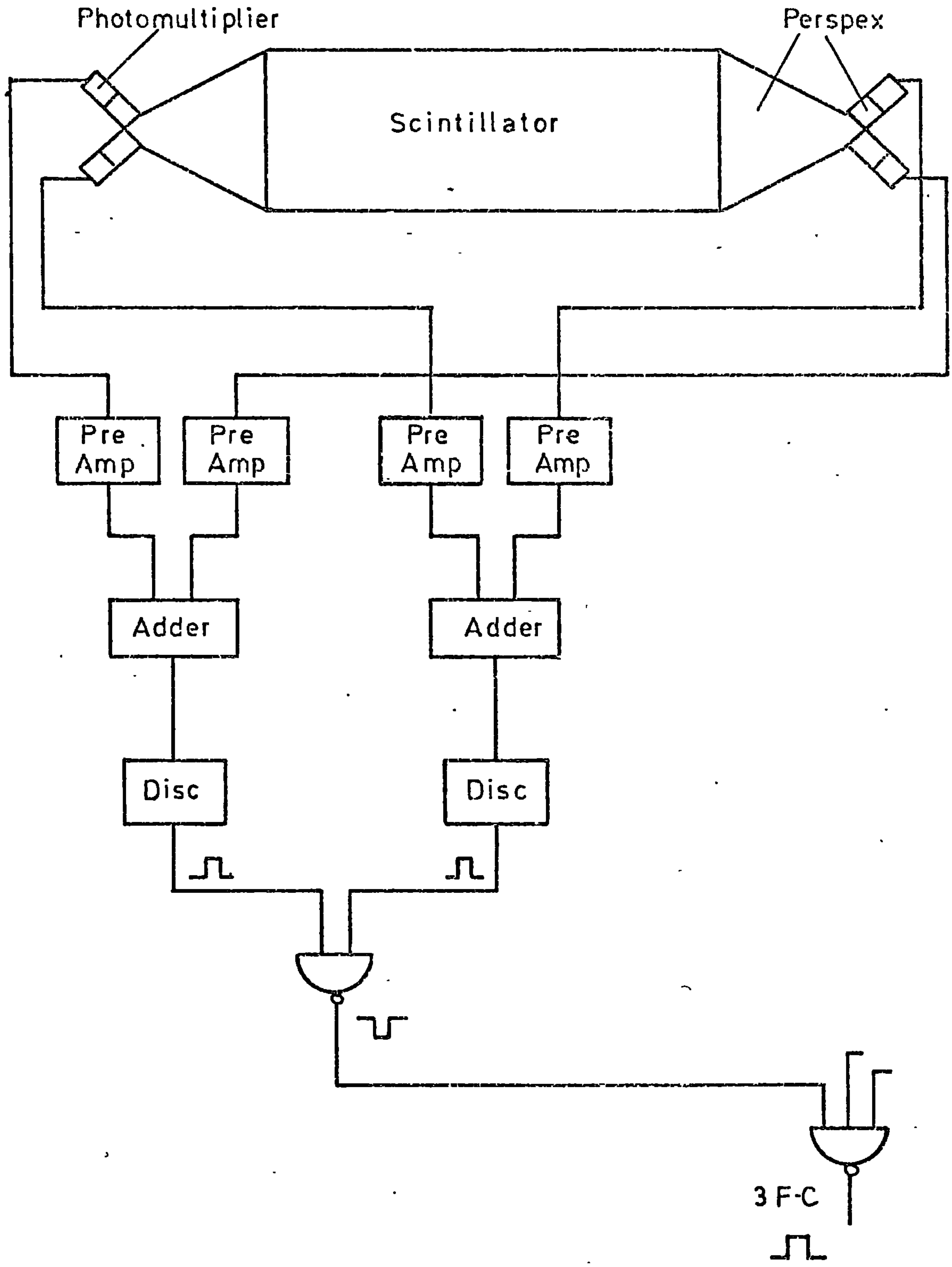

FIGURE: 2·6 SCINTILLATOR ELECTRONICS

condition, as a function of momentum, is shown in figure 2.7. Further details of the acceptance are given in chapter 4.

2.3.4. The Pulsing System A high voltage pulse is applied to the flash-tube trays in the spectrograph within 2 μs of a particle having been detected (by the scintillation counters) using a spark gap and 1 lumped constant delay line (Fig 2.8). The spark gap is triggered by discharging with a thyristor, a small capacitor (0.05 μf charged to 400v) through a pulse transformer. The output of the transformer is applied to the trigger electrode of the spark gap. To minimise the required trigger voltage a barium titanate ($BaTiO_3$) collar insulates the trigger electrode from the (earthed) spark gap electrode. The small trigger spark produced between trigger electrode and earthed electrode of the main spark gap initiates the spark discharge of the main gap and results in the production of a high voltage pulse across the matching resistors.

Delay lines have been constructed using 2500 pf, 20 K.V. D.C. capacitors and, for the inductors, 22 turns of 18 SWG copper wire wound on a wooden former of diameter 3.0 cm. A negative square pulse of width 2 Td (where Td is the propagation time of the delay line) and height Vs/2 (where Vs is the spark gap supply voltage, is generated. The pulse height is Vs/2 for R matched to the line ie R=Zc where Zc is the characteristic impedance of the line; otherwise the pulse height differs slightly from this value. Each flash tube tray is connected across a separate resistor R and is a capacitive load C_T . One spark gap is used to pulse several trays, hence there are several delay lines and their associated resistors connected to that spark gap. The spark gap, delay lines and terminating resistors are housed in an earthed aluminium box. Co-axial cables are used to transmit the high voltage pulses to the flash tube trays, this minimises electrical pick up problems.

In one side of the spectrograph two types of flash tubes are used

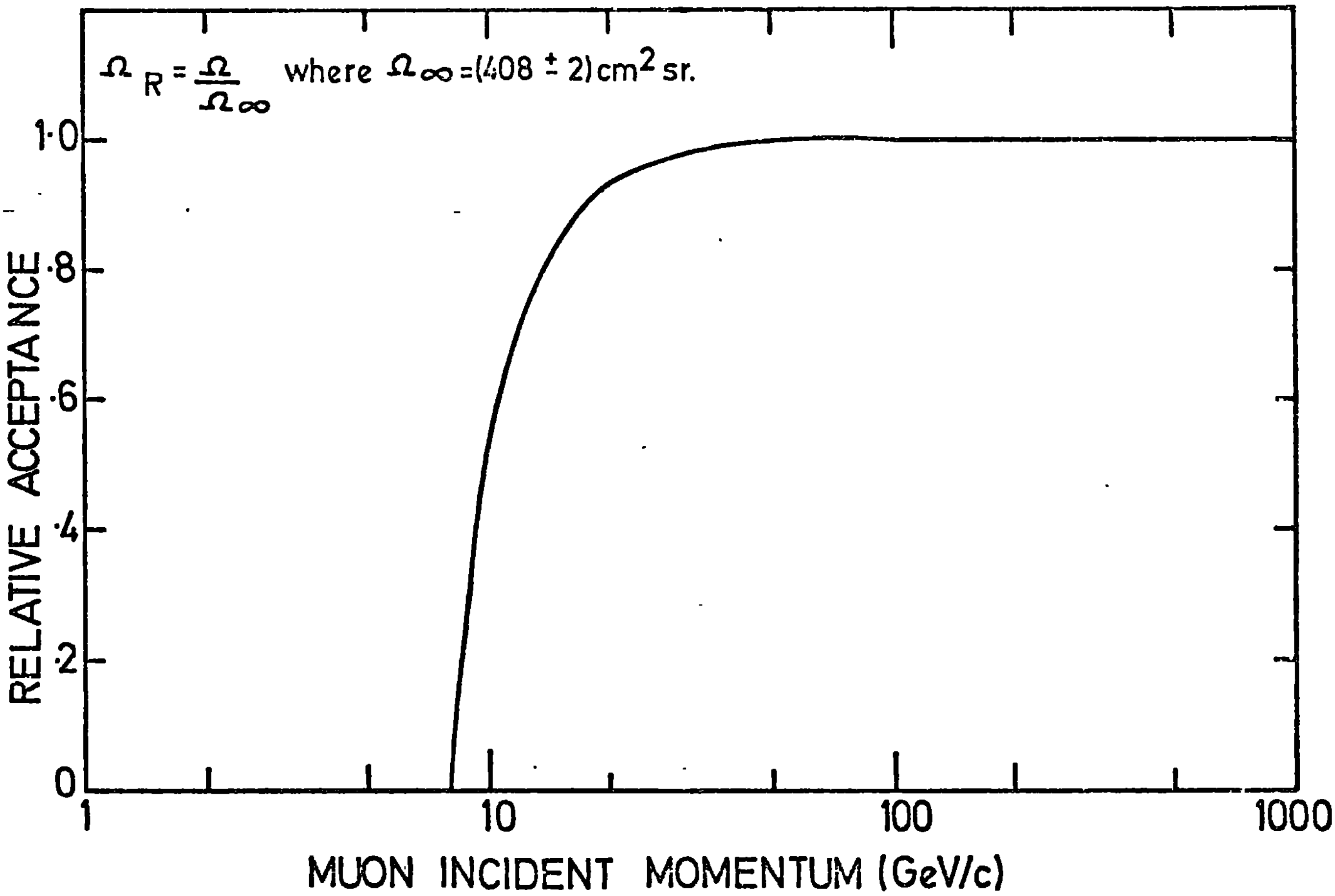

FIGURE: 2·7. THE OVERALL ACCEPTANCE (RELATIVE TO 408 cm^2 sr).

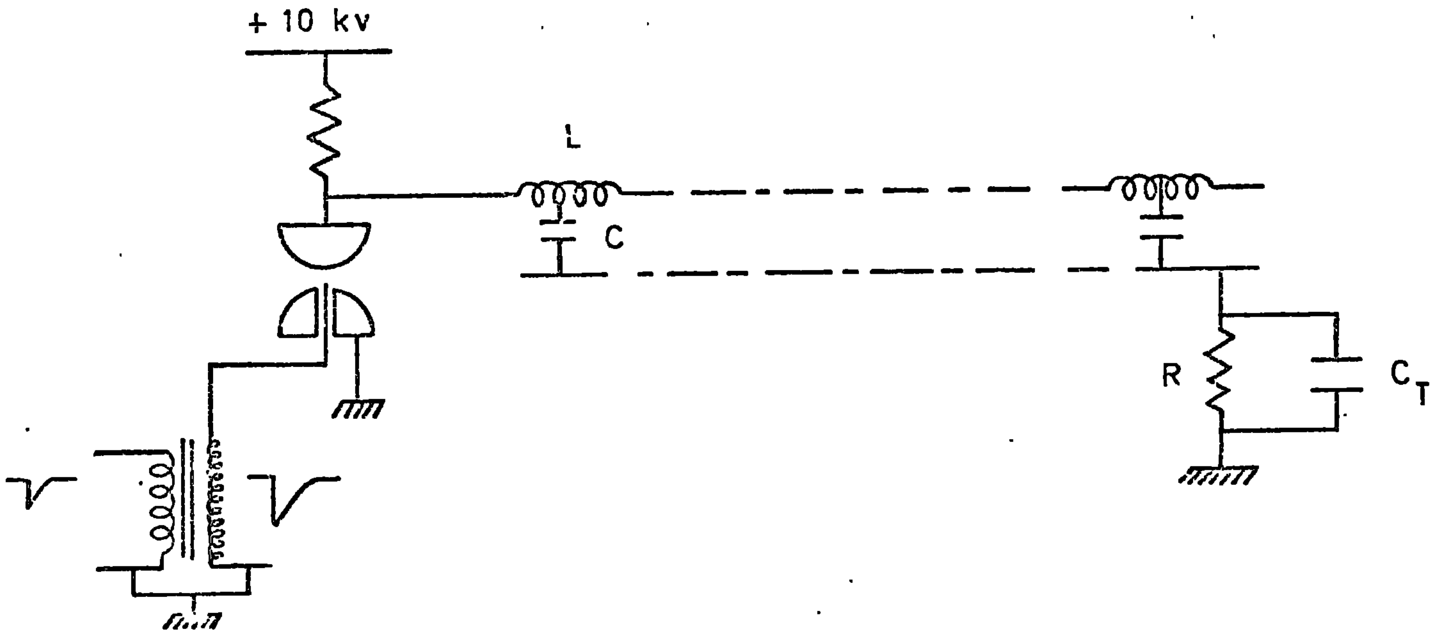

FIGURE: 2·8 GENERATION OF HIGH VOLTAGE PULSE large diameter (1.53 cm internal diameter filled with commercial Ne at 0.8 atmospheres) and small diameter (0.55 cm internal dia. and 2.4 atmospheres). For reasons given later in the chapter the trays of large diameter tubes (each containing 204 tubes in 4 layers) are known as momentum selector trays while the trays of small diameter tubes (each containing 712 tubes in 8 layers) are known as measuring trays. One spark gap is used to pulse the three momentum selector trays and a second gap to pulse the fine measuring trays. The 2 types of tray are pulsed via delay lines of differing characteristics:-

	Zc(Ω)	Pulse width (μs) (No trays)	G (μf)
Measuring Tray	22	1.5	.028
Mom-sel Tray	47	3.0	.005

Optimum flash tube efficiency has been obtained by measuring the layer efficiency of the trays as a function of applied pulse height. The important parameters of the pulsing system for M.A.R.S are:

	R (Ω)	Pulse Ht (kv)	Peak Fld across Tray (kv cm^{-1})	S.G.Supply (kv)
Meas. Tray	22	6	7.5	13
Mom.Sel.Tray	47	4.5	2.6	10

<u>2.3.5. The Principle of Digitisation</u> It was realized in the design stages of M.A.R.S. that, because of the high acceptance, photographic recording of the flash tube data was not practical - the scanning of the resulting large quantities of film would be impossible. Several attempts have already been made to find non-photographic methods (e.g. Bacon and Nash (1965), Reines (1967)),

During an investigation of this type it was found that a voltage pulse across a resistor held some distance from the tube was generated when the tube discharged. Using the arrangement of Fig 2.9a pulses on the metal probe were viewed on an oscilloscope.

The dependence of the digitisation pulse shape on l, d, t, l_2 and R was studied and indicated a weak dependence of pulse height on l and d and a stronger dependence on t and l_2. Variation of R had a large effect on both the height and length of the pulse. Having investigated the properties of a single tube the next step was to study an array of tubes. It was found that to reduce the electrical pick up from both the high voltage pulse and from any adjacent discharging tubes the probes had to be enclosed in a screen - Figure 2.9b.

The results of both sets of investigations showed that the probe should be as near the flash tube as possible in order to maximise the signal to noise ratio; the value of R can be adjusted to give the required pulse length while the pulse height can be selected by tapping off the required height from R. Similar results were obtained using small diameter flash tubes. These studies showed that an array of probes could be used to detect discharged flash tubes and that the resulting 'digitisation' pulses from the probes could be tailored to match any following circuitry. This is the basis of the digitisation system used by M.A.R.S.

2.3.6. The Momentum Selector System The purpose of the momentum selector system is to select particles of 'high' momentum ($\gtrsim$ 250 GeV/c) The system consists of the momentum selector flash-tube trays (3 in each side of the spectrograph), probes to provide digitisation pulses and electronic circuitry to fix the point across the width of the tray, where the particle traversed the tray. Further electronic equipment using the information on the particle positions from each of the 3 levels in the spectrograph to determine whether or not the particle was of high momentum, completes the system. If a high momentum event is indicated the system initiates the storing of data from the trays of tubes designated 'measuring trays' in the computer.

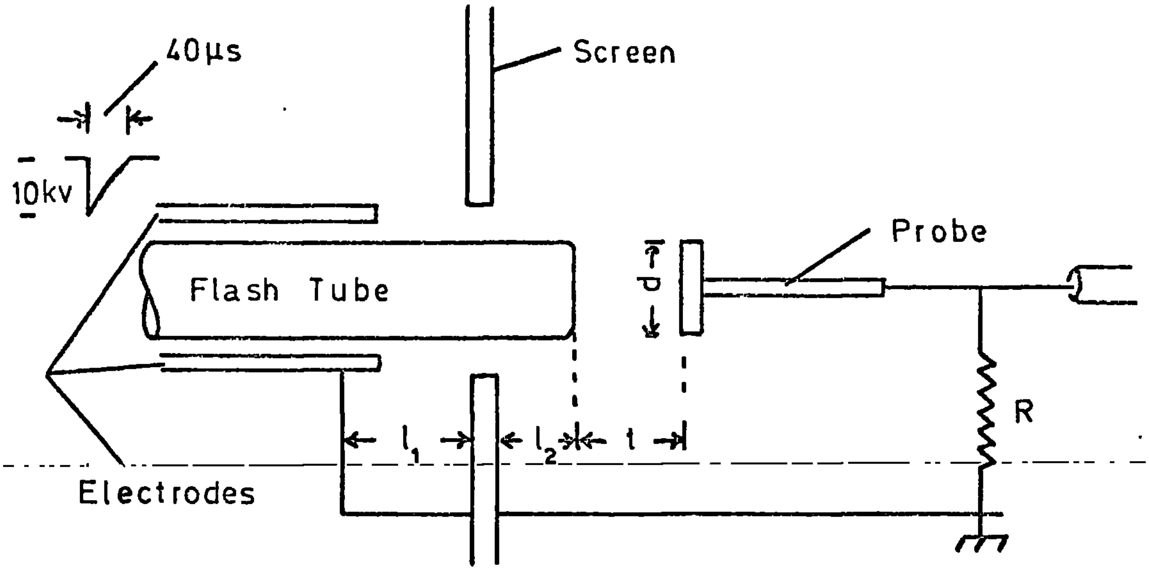

(a)

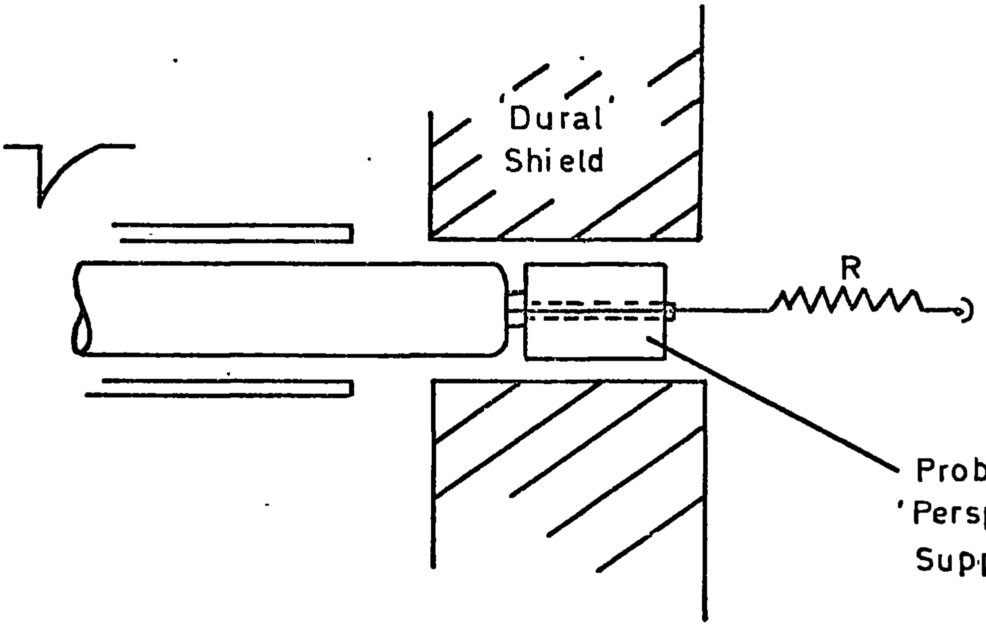

(b)

FIGURE: 2·9 DIGITISATION STUDIES

The initial location of the particle in a momentum tray to within 2.5 mm of the true position is performed by considering which tubes of the momentum selector trays have discharged. The output of each probe of a tray is fed to a memory circuit (based on integrated circuit logic function blocks) known as a latch. An interrogation pulse applied at the same instant to all the latches causes pulses to be given out by those associated with a discharged tube. By taking suitable coincidence and anti-coincidence arrangements of these pulses the width of a tray front is effectively divided up into 152 cells each of width 5mm and the particle track is assigned to one of these cells. Having performed this assignation at each of the 3 momentum selector trays the remaining part of the momentum selector system decides whether the particle was of high momentum.

The information on which cells have been traversed is transferred to the momentum selector shift register unit, a unit containing three 152-bit shift registers - one register per tray and one bit per cell. Loading of the registers is complete within 3 us of applying the interrogation pulse. Figure 2.10a shows the registers in schematic form where it can be seen that registers A and C are each extended by the addition of another 76 bits. A high momentum event can be defined initially as one whose track is a straight line. The momentum selector shift register unit scans the data from the 3 trays (which is now held in the 3 shift registers) for such straight lines. The scanning process is described below.

Bit 76 of shift register (written SR, in future) B is connected to 151 3-1/P coincidence gates. Adjacent cells of level A are OR-ed together in groups of 3 starting with group [0,1,2] (where 0 is in fact a dummy input since cell 0 does not exist) and then group [1,2,3] etc., finishing with group [150,151,152]. The 151 outputs from this OR-ing process are taken to the inputs of the 3-fold coincidence gates.

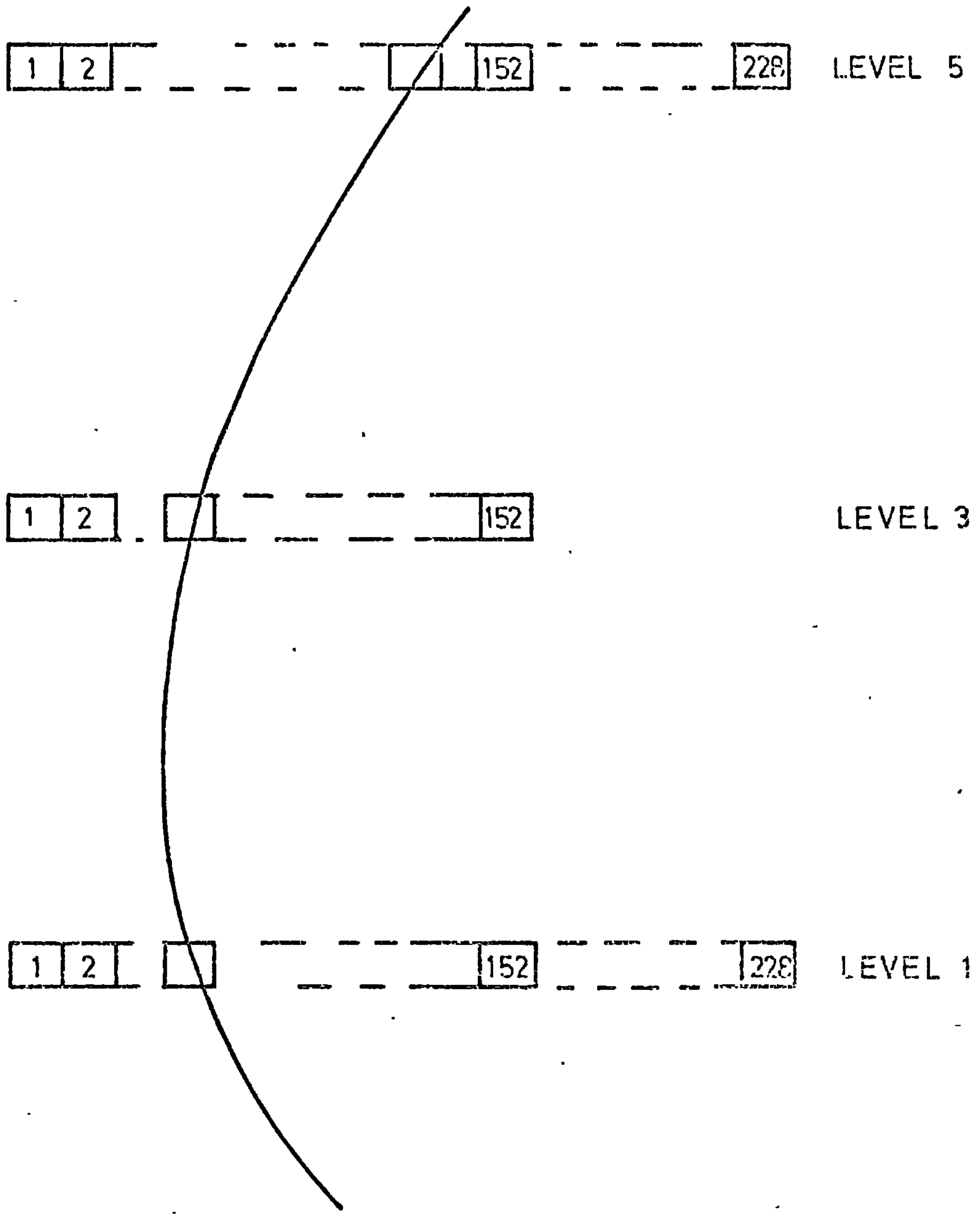

(a)

FIGURE : 2·10 MOMENTUM SELECTOR SHIFT REGISTERS

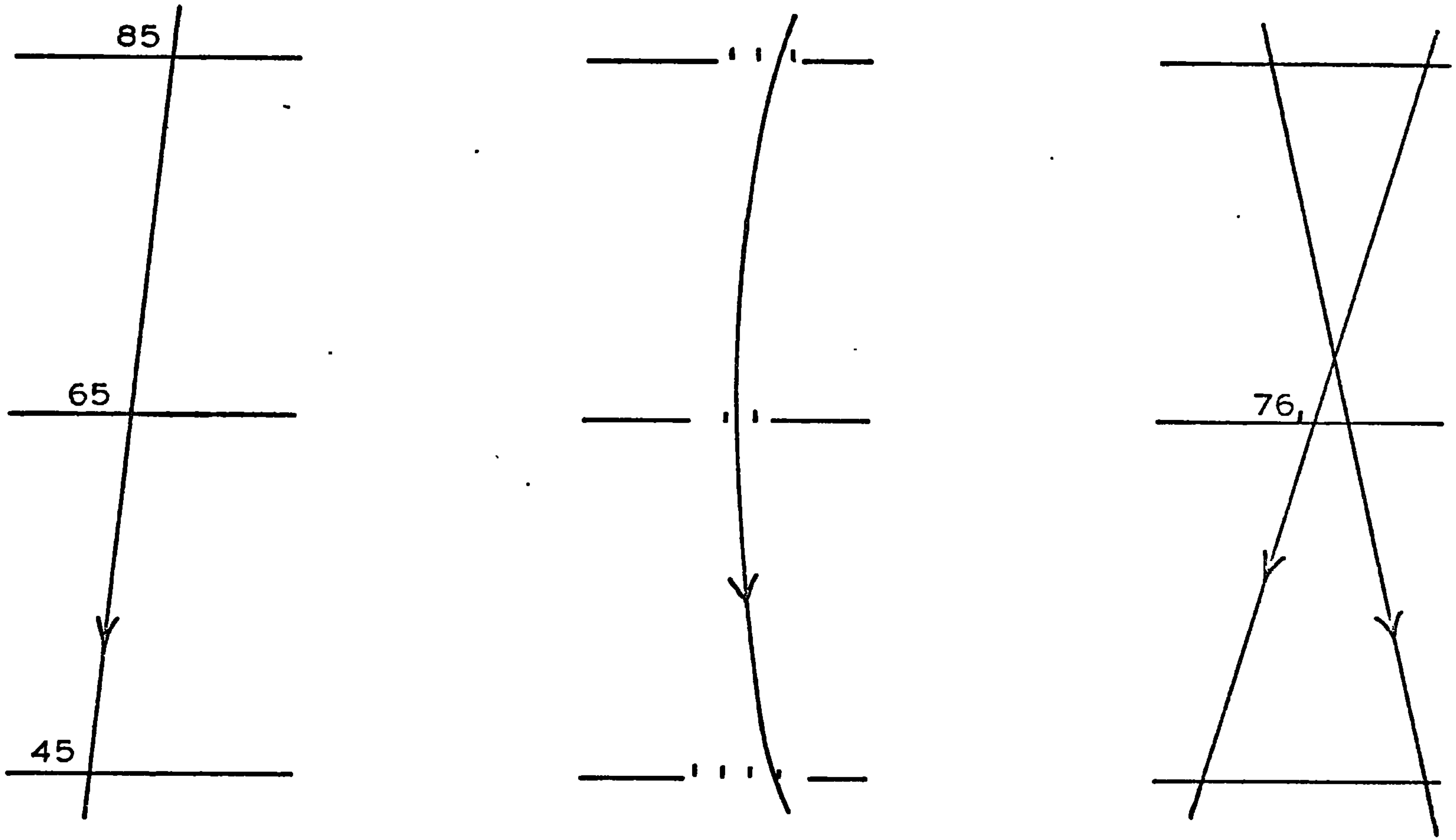

(b) (c) (d)

FIGURE :2·10

Level C is treated identically except the results of the OR functions are allocated to the 3-fold gates in the reverse order to that of level A. Thus the complete inputs of the first 2 and last 2 3-fold gates are:

INPUT	GATE 1	GATE 2	3, 4 149	GATE 150	GATE 151
1	SR B76	SR B76		SR B76	SR B76
2	[A(0) + A(1) + A(2)]	[A(1) + A(2) + A(3)]		[A(149) + A(150) + A(151)]	[A(150) + A(151) + A(152)]
3	[C(150) + C(151) + C(152)]	[C(149) + C(150) + C(151)]		[C(1) + C(2) + C(3)]	[C(0) + C(1) + C(2)]

The symbol + indicates the 'OR' function

The output of the threefold coincidence gate changes only when all 3 inputs are in the same state. Some 3 μs after loading of the shift registers a train of clock pulses (frequency 925 KHz) is applied to the 3 shift registers causing the contents of each bit to shift to the right.

Now consider Fig 2.10b which shows the cells set off by a straight track. After 11 clock pulses the output of SRB76 will change from its reset state, logical '0', to logical '1'. The outputs of the 2 OR gates with inputs A(95), A(96), A(97) and C(55), C(56), C(57) will change - also to '1' states. Thus the threefold coincidence gate having as its inputs:

1 SR B76
2 [A(95)+A(96)+A(97)]
3 [C(55)+C(56)+C(57)]

will indicate a coincidence - the output changes state. Thus the change in state of the output indicates a straight line track - a high momentum event.

It will be seen that if the particle had passed through cells 95 or 97 in level A or through cells 55 or 57 in level C the result would be the same - a high momentum event would be indicated. This property has been deliberately built into the system (by use of the OR function on the 3 adjacent cells) in an attempt to minimise the effect of incorrect cell allocation. The particle may be misallocated to a cell on either side of its true cell and still be detected as a high momentum event. By doing this, any bias due to mis-allocation introduced into the measured high energy muon spectrum will be small, and can be further reduced by subsequent correction factors. As can be seen from fig 2.10c, in the extreme case a low energy particle suffering a '2 cell' deflection may be classed as a straight track event.

For the tracks shown in fig 2.10d the method described above would fail because the particle passed to the right of SR B76. This is overcome by building an identical system to that described above but using bit 152 of SR B in place of bit 76, in the set of threefold coincidence gates. The reason for the extension of shift registers A and C can now be seen -- to accommodate shift register bits initally loaded into SRA or SRC between bits 76-152 on subsequent shifting of the bits to the right.

<u>2.3.7 High Momentum Events</u> When a high momentum event has been detected storage of the measuring tray data commences. The data from the trays, consisting of the column numbers of the discharged tubes and the patterns of discharged tubes in those columns is fed, along with other subsidiary data such as event number, time, date, magnetic field direction and atmospheric pressure, into a 1024 byte (1 byte = 8 bits) core store. The store can hold all the data from one event. After assembly of the data in the core store is completed the computer is interrupted and the data transferred to it. In addition to handling M.A.R.S. data the computer is also used for on-line control of bubble chamber film analysis and this can mean that transferrence may not be immediate; the maximum delay however is only 2 secs. The data is initially held in the store of the computer but when 4 or 5 events have accumulated it is written onto a magnetic disc. When film analysis is in progress the data is only stored but when film analysis has ceased for

the night an alternative programme operates to analyse the events stored in the previous period of film analysis and at the same time to continue storage of more M.A.R.S. data.

As mentioned previously the most common method of recording flash tube data is by photography and subsequent scanning of the film. The programmes to analyse the M.A.R.S. data have had to express the actions of the film scanner in a logical form.

The aim of the first part of the programme is to obtain an initial estimate of the trajectory of the particle. The data from individual trays is first divided into groups of discharged tubes. An initial scan of the data is made to eliminate spuriously flashing tubes, spurious triggers of the spectrograph and multiple (> 2 muons) tracks. Bursts in a tray are defined as a group of 10 or more discharged tubes and are not used in further calculations but a check is later made to ensure that the final calculated particle trajectory passes within the burst region. Having thus decided which groups may be used for track defining purposes each group is split into sub-groups and attempts made to fit a line through the discharged tubes of the sub-groups.

Although it is not possible to define the point at which a particle passed through a given discharged tube the path of the particle may still be accurately located by considering the discharged tubes in various layers of the tray. For each subgroup a line is fitted to the flashed tubes. This line is then modified by considering the particle to have passed through gaps between tubes in those layers with no discharged tubes in them. By moving this second line about its calculated position until it violates the given data, approximate limits to the channel through which the particle passed are found. If however it is not possible to fit a line without contradicting the given data then it is assumed that some incorrect information is present. This may be due to either a tube inefficiency - ie. a tube should have flashed but did not - or to knock-on electrons causing a tube some distance from the main track to discharge. The fitting routine includes various options by which it can turn tubes off or put tubes on until a fit is obtained. Eleven options are available and are tried in a fixed order. The first option to give a fit is accepted as that giving the true track in the tray. This procedure is repeated for each sub group in a tray and that giving the highest probability track - defined by which option has been called - is used in later calculations. The procedure is repeated for each tray and hence an initial estimate of the channel, in each measuring tray, through which the particle passed.

Using the mid point of each channel at the central horizontal plane of each measuring tray as the co-ordinate of the trajectory a parabola is fitted to the trajectory. The least squares method is used.

The derived parabola is now used to define the angle of the track at each measuring level. If the angle is incompatible with the flash tube data in a tray the remaining track fitting options are tried and other subgroups examined until compatability is achieved. In most cases these considerations result in narrower channel widths for the possible track, also the mid-point of the new channel does not necessarily coincide with that of the original channel, With the data from the new channels a new parabola is fitted. At this stage any bursts in the trays are checked to ensure they lie on the track.

The coefficients of the terms in the equation of the fitted parabola enable the momentum of the particle to be found.

The results of this analysis are stored back among the basic data for the event. The time taken for the analysis of each event depends upon what options need to be tried but the average time is about 40 secs.

The standard deviation of the distribution of cell widths is found to be 0,29 mm which is in agreement with an estimate made in M.A.R.S. I (Ayre et al (1972a,b) of 0.30 mm. For the latter value an m.d.m of 5800 GeV/c is obtained for a fit which is able to utilise the data from all 5 measuring trays. The m.d.m is dependent upon which trays yield usable data the worst case is found to be when only trays 1, 2, 3 or 3, 4, 5 yield good data - the m.d.m. is then approx 1300 GeV/c.

2.3.8 'Low' Momentum Events Up to now no mention has been made of those particles which do not give a straight line track. Information on the trajectories of these particles is available in the shift registers of the momentum selector shift register unit. Because of the high acceptance of M.A.R.S. the rate of these particles is high and the opportunity of a very accurate measurement of the spectrum and charge ratio at momenta below a few hundred GeV/c presents itself. To this end a device, known as RUDI has been constructed to measure the deflection of particles using the information present in the shift registers. The results from RUDI cover the range $20 \lesssim P_\mu \lesssim 700$ GeV/c. At the highest energies RUDI and the computer analysed events overlap and will provide useful checks on the validity of the data.

2.3.9. Results from M.A.R.S. Construction of the magnet blocks began in 1968 and approximately one year later the spectrograph was operated using the conventional photographic method of recording the flash-tube information. The results of this preliminary experiment were presented in 1971 (Ayre et al (1971, 1971a, 1971b). By August 1971 the trays of large diameter flash tubes were in place in the blue side of the spectrograph and digitised information on particle tracks was obtained by RUDI. Preliminary measurements of the muon charge ratio were made (Ayre et al (1972)) along with investigations of the interactions of cosmic ray muons (Grupen et al (1972)). Since then further results on the muon spectrum, the muon charge ratio and the absolute intensity of the muon beam have been made (Ayre et al (1973a, 1973b).

2.4 Summary

This chapter has outlined the spectrograph and its operation. The data reported in this thesis have been [illegible] chapter is devoted to a detailed discussion of this instrument.

CHAPTER 3

R.U.D.I.

3.0 Introduction

This chapter describes firstly, the manner in which a particle traversing the spectrograph is allocated to a cell in a momentum - selector tray and secondly, the instrument - R.U.D.I - which utilises the data from the 3 momentum trays on one side of the spectrograph to derive the sign and momentum of the particle.

3.1 The Momentum Selector Trays

The framework of a momentum selector tray is made up of 1" x $\frac{1}{2}$" bright steel bar and has an overall size of 283 cm x 84 cm x 12.7 cm (fig 3.1a). Seven struts across the width of the tray keep the sides parallel. At each end of the tray a 1/8" brass plate is mounted. Each plate has 155 holes in each of which a flash-tube is located. The brass plates are 197 cm apart and the average length of the flash-tubes is about 220 cm. The 4 layers of tubes are interspersed with 5 aluminium plate electrodes (each 270 cm x 83 cm) held in 'Tufnol' supports mounted on the frame. The 2 outer plates and the centre plate are at earth potential while the high voltage pulse is applied to the remaining 2 plates.

Onto the front brass plate is attached a 3.8 cm thick Dural block with matching holes for the flash-tubes, this is the digitisation shield. The flash-tubes penetrate 1.0 cm into the block (fig 3.1b); the remaining 2.8 cm is taken up with a perspex cylinder held in place by an 'Araldite' adhesive. Through the centre of the cylinder passes a 6 BA screw with its head touching the flash-tube. This is the digitisation probe.

Since the brass plates are the means by which the tubes are located both with respect to one another and with respect to the tray framework as a whole, extreme care was taken in their machining.

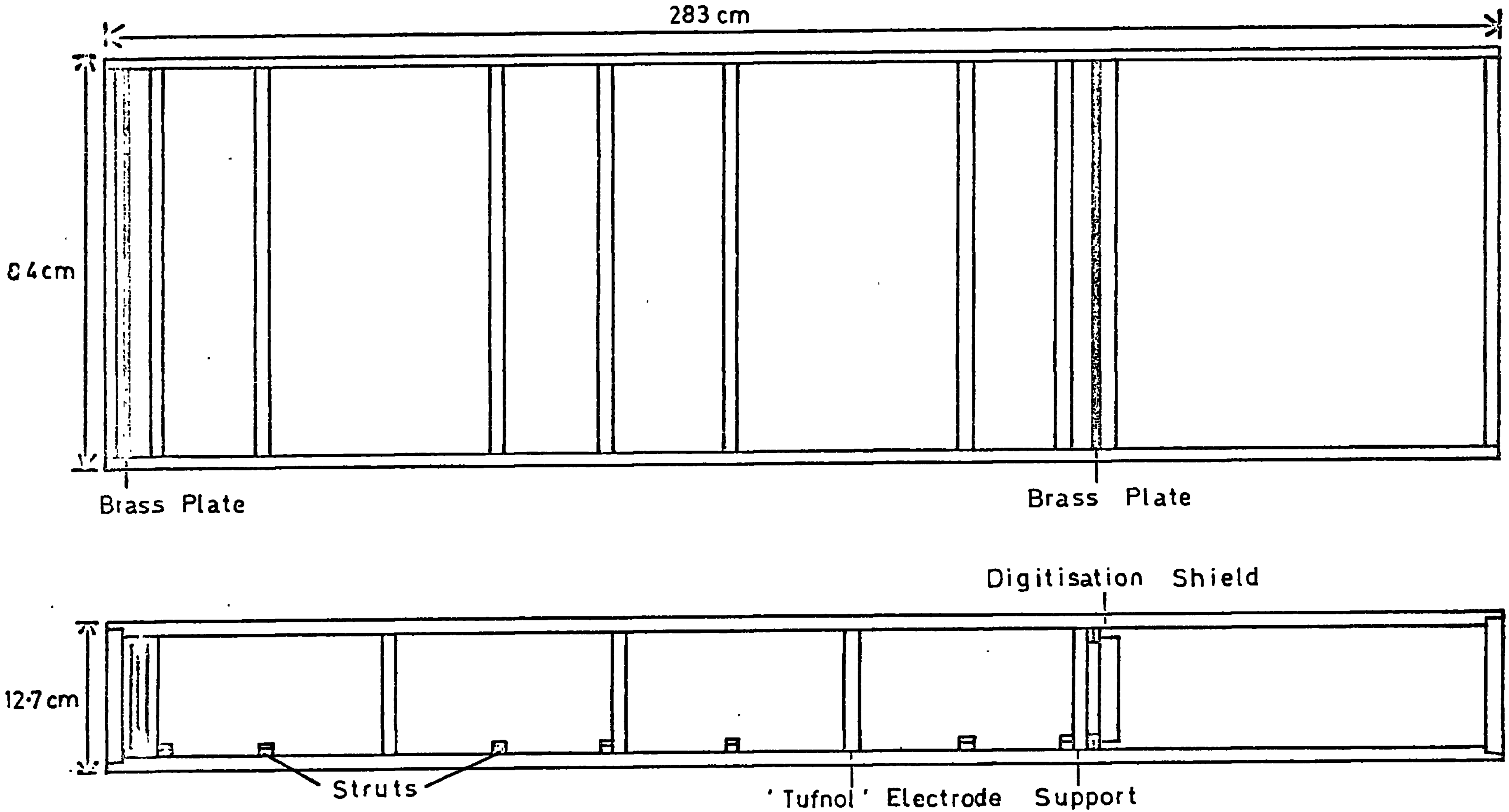

FIGURE 3.1a PLAN AND SIDE ELEVATION OF MOMENTUM SELECTOR TRAY

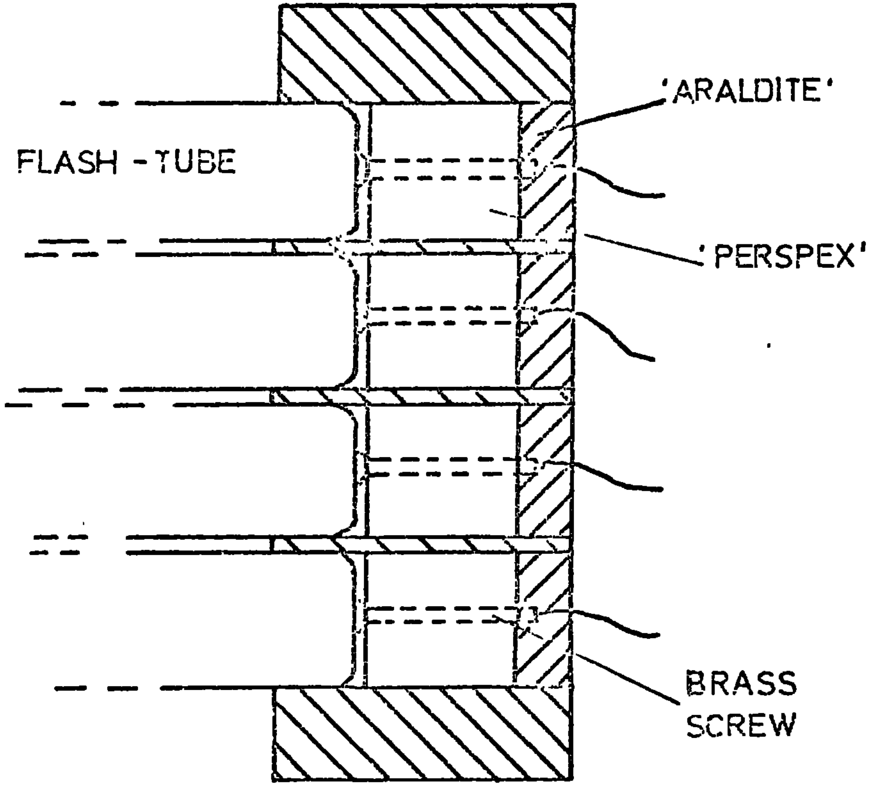

FIG. 3·1b. PROBE ASSEMBLY

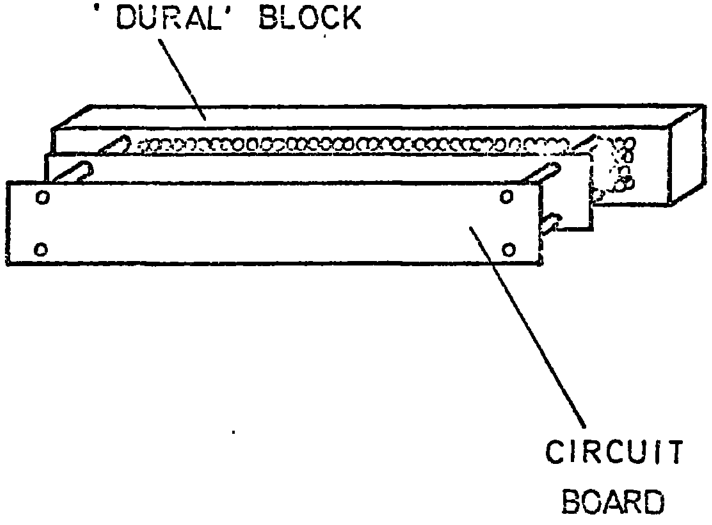

FIG. 3·1c. CIRCUIT BOARD ON TRAY FRONT

A connection is made from the end of the digitisation probe to the first of 2 layers of circuit board that are mounted on the dural block - fig 3.1c. The first layer holds the resistors R described in 2.4.5 and which in this case have a value of 2.7 kΩ. Connections from the resistors are taken to the memory latches on the next layer of circuit board. Above this layer of circuit board; supported on a steel and 'Perspex' framework which in turn is mounted on the dural block, are boards of i/c blocks forming the cell allocation circuitry.

3.2 The Digitisation Electronics

3.2.1 The Memories As stated in the previous section, the digitisatio pulses from the flash tubes are detected by a brass screw and then fed to latches. Each latch is a memory circuit whose output must be gated. In the initial (reset) condition the output is a logical 1 state; if the associated flash tube discharges then point X (fig.3.2) changes to a logical 0. To obtain a pulse at the output of the memory circuit a gating pulse must be applied to all the latches as shown in fig. 3.2. The outputs of the latches are taken to the cell allocation circuitry.

3.2.2. The tray fronts A scale diagram of a momentum selector tray front is shown in fig 3.3. Also shown are the 5 mm cells to which a particle traversing the tray is allocated. By examining the combination of tubes which have discharged it is possible to allocate the position of the particle to one of the cells. Since the spectrograph will accept 'high' momentum particles (400 GeV/c)within 7° of the vertical the cell allocation circuitry was designed to correctly allocate particle tracks within this angular range. For example, discharge of tubes 7, 27, 37 indicates that the particle traversed cell 9; discharge of tubes 17, 37 indicates cell 10. However, for some combinations the particle could have passed through either of 2 adjacent cells:

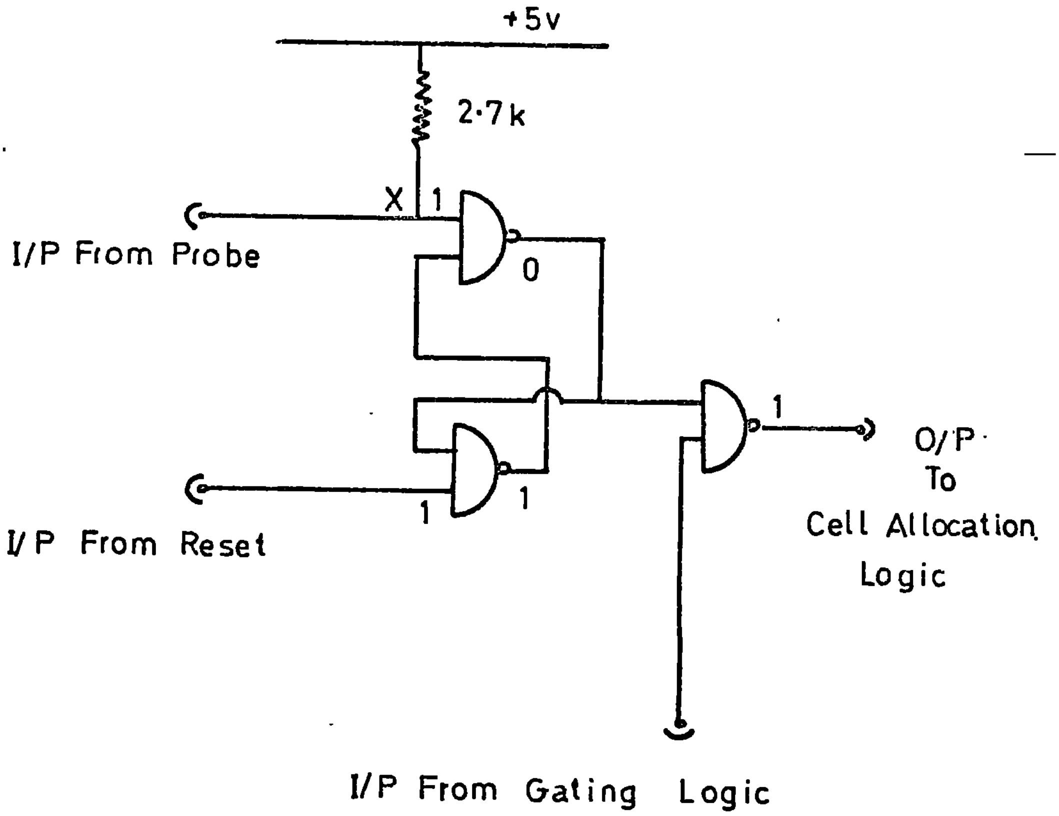

FIGURE: 3·2. ELECTRONIC MEMORY AND GATING SYSTEM USED WITH EACH PROBE.

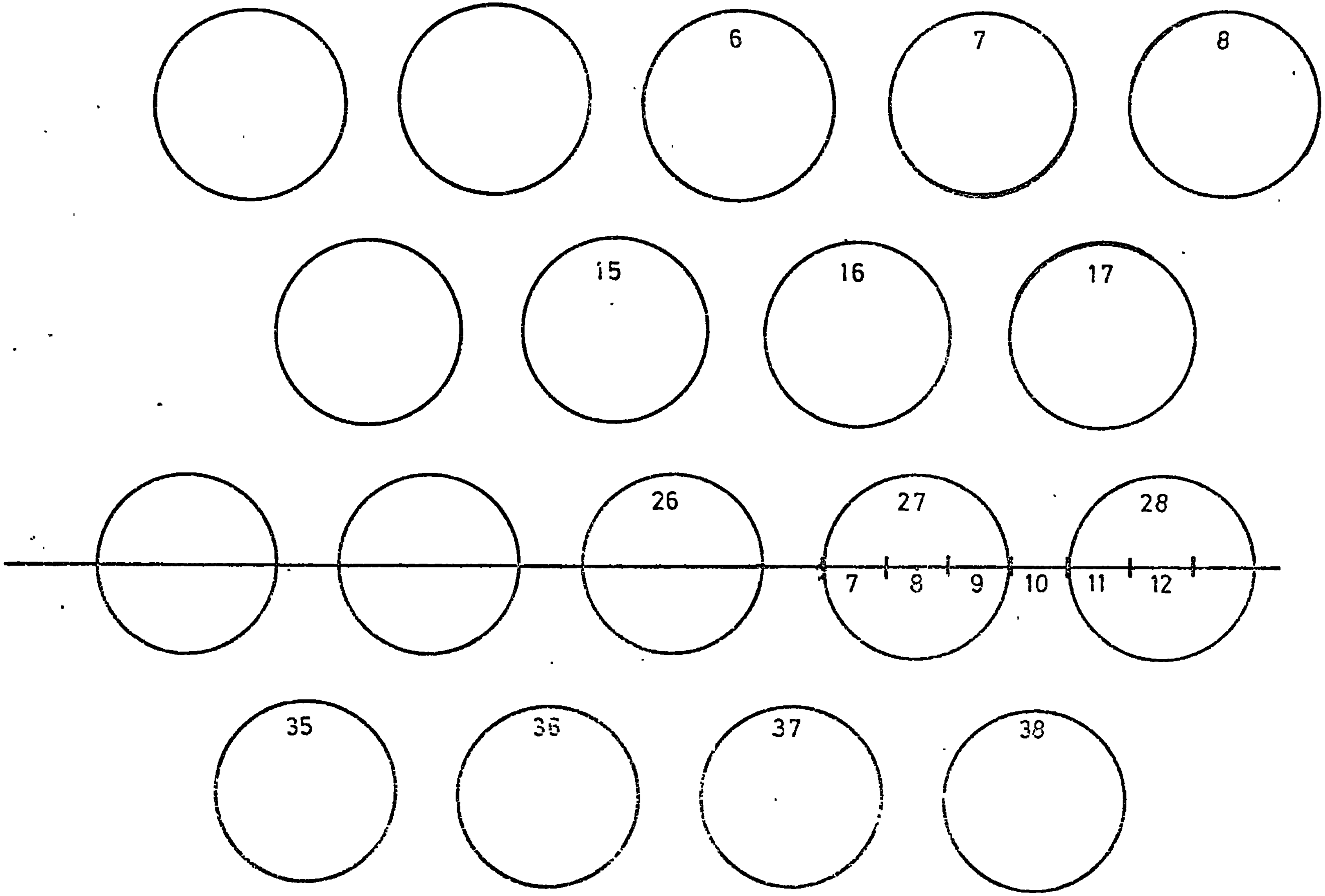

FIGURE 3.3. MOMENTUM SELECTOR TRAY FRONT

(i) the combination 7, 27 can be allocated to cells 8 or 9
(ii) " " 7,16,27,37 " " " " 8 or 9
(iii) " " 3,7,12,16 " " " " 7 or 8

This ambiguity was reduced somewhat by calculating, geometrically, the probabilities of a particle passing through each of the cells and then allocating the particular flash tube combination to the cell having the highest probability. In particular for case (iii) - cell 7 had the higher probability (~0.6). The remaining cases were found to have an equal probability of passing through either possible cell. The 2 cells in question are the same for each flash tube combination so one combination was allocated to one cell and the other combination to the remaining cell. After applying these corrections the flash tube combinations and their derived cells are as shown in table 3.1.

FLASH TUBE COMBINATION	Cell No.
16, 27/7, 16, 27/7, 16, 27,37/16, 27, 37/	8
7, 27/7, 17, 27, 37/7, 27, 37/	9
17, 37/7, 37/7, 17, 37	10
8, 17, 28, 37/17, 28, 37/7, 17, 28, 37/7, 17, 28/	11
17, 28/8, 17, 28/8, 17, 28, 38/17, 28, 38/	12
8, 28/8, 18, 28, 37/8, 28, 38/	13

The Flash Tube Combinations

Table 3.1

As can be seen from table 3.1 the flash tube combinations are repeated every 4 cells; this being the spacing of the tubes. The efficiency with which cells are correctly determined is discussed later (Chapter 4). Having decided upon the cell allocation the logic circuitry required to achieve this allocation will now be described.

3.2.3. The Cell Allocation Electronics An important factor in designing the circuitry was that only one cell should be indicated by the traversing particle. The restriction is necessary to allow R.U.D.I to determine a unique momentum and sign of the particle.

To reduce the amount of circuitry required on the tray fronts, the flash tubes of row 1 are used only when absolutely necessary. For example, combination 7, 17, 27, 37 (cell 9) is still correctly allocated if tube 7 is ignored, similarly for combination 8, 17, 28 (cell 12) flash tube 8 may be ignored. The modified set of combinations is shown in table 3.2.

FLASH TUBE COMBINATION	Cell No.
(7), 16, 27/(7), 16, 27, 37/	8
7, 27/(7), 17, 27, 37/7, 27, 37/	9
(7), 17, 37/7, 37/	10
8, 17, 28, 37/(7), 17, 28, 37/7, 17, 28	11
(8), 17, 28/(8), 17, 28, 38/	12
8, 28/(8), 18, 28, 38/8, 28, 38	13

( ) Denotes a flash-tube which is not used in coincidence with the other flash-tubes in the combination.

The Flash Tube Combinations Using Row 1 Only When Necessary

Table 3.2

Using row 1 in this manner means the effective measuring level is close to the mid-point of the remaining 3 rows; for this reason the measuring level is taken as lying exactly on the centre line of row 3.

Because of the requirement that only one cell should be indicated in each tray simply feeding the memory (latch) outputs to coincidence gates is not sufficient as can be seen in the following example. In the case of this method the discharge of tubes 17, 28, 37 would indicate, in addition to the true cell (11), cells 10 (from tube combination 17, 37) and 12 (combination 17, 28). Thus some form of vetoing the additional cells is required. However, not all of the combinations of tubes form part of some larger combination and need not be vetoed. The combinations requiring veto logic are listed in table 3.3

FLASH TUBE COMBINATION REQUIRING VETO	FLASH TUBE COMBINATIONS PRODUCING VETO
7, 27 (Cell 9)	7, 16, 27, 36 (Cell 7) (7), 16, 27 (Cell 8) (7), 16, 27, 37 (Cell 8)
7, 27, 37 (Cell 9)	(7), 16, 27, 37 (Cell 8)
7, 37 (Cell 10)	(7), 17, 27, 37 (Cell 9) 7, 27, 37 (Cell 9) (7), 17, 28, 37 (Cell 11)
17, 37 (Cell 10)	(7), 17, 27, 37 (Cell 9) 8, 17, 28, 37 (Cell 11) (7), 17, 28, 37 (Cell 11)
17, 28 (Cell 12)	7, 17, 28 (Cell 11) (7), 17, 28, 37 (Cell 11) 8, 17, 28, 37 (Cell 11)

The Veto Requirements Over a Tube Spacing

Table 3.3

The logic diagram of the cell allocation circuitry - coincidence gates and veto logic - is shown in fig 3.4. The circuit may be divided into 3 stages as shown. Upon application of the gating pulse the output pulses of those latches associated with discharged tubes are inverted and fed into the first stage which is an array of gates to find initially which cell(s) possibly contain the particle track. As described above, tubes 17, 28, 37 would indicate cells 10, 11, 12. Those outputs of the first stage which may require veto-ing are taken to the second stage; the remaining outputs are taken directly to the third stage. The second stage consists of an array of inverting delays, monostables and coincidence gates. Considering again tubes 17, 28, 37 - cells 10 and 12 are to be vetoed. This is achieved by taking the pulses after being delayed and inverted by the elements D from those gates performing the

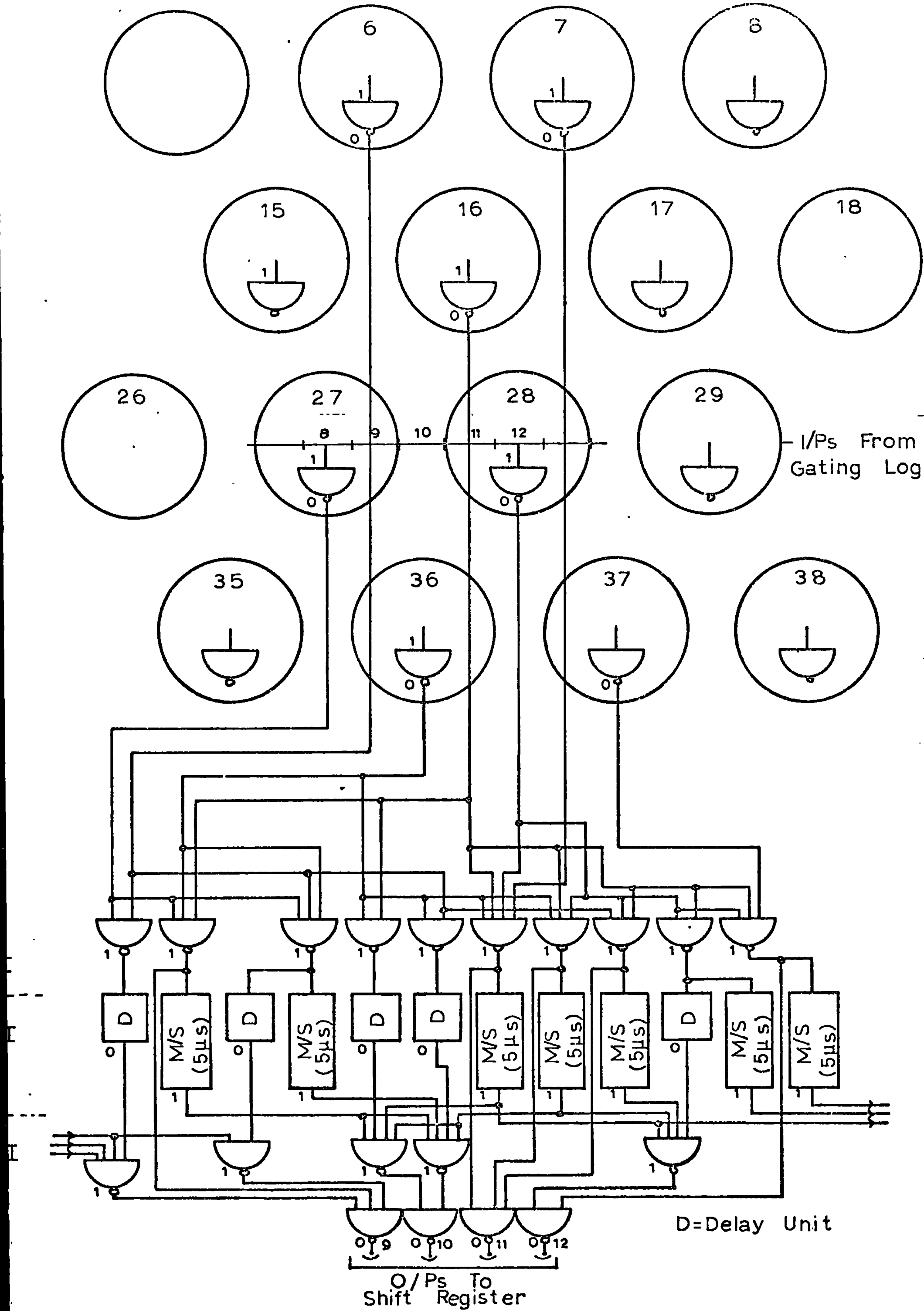
6
7
8
15
16
17
18
26
27
28
29
35
36
37
38
8
9
10
11
12
I/Ps From Gating Log
D
M/S (5µs)
D=Delay Unit
9
10
11
12
O/Ps To Shift Register

FIGURE: 3.4.

functions (17, 37) and (17, 28) to the coincidence gates where a coincidence with any possible veto pulse is sought. The veto pulses are derived via the monostables (M/S) from other flash tube combinations containing tubes 17, 37 or 17, 28. These are, from table 3.2:

combination	/17, 37/	combination	/17, 28/
17, 27, 37	Cell 9	17, 28, 37	Cell 11
17, 28, 37	Cell 11	7, 17, 28	Cell 11
8, 17, 28, 37	Cell 11	8, 17, 28, 37	Cell 11

and can be seen on the logic diagram. For the example under consideratio a veto pulse is obtained from the combination 17, 28, 37. The veto pulses are 5 µs negative pulses. The delay units D give positive pulses of length 0.15 µs, delayed by 0.85 µs from the leading, negative, edge of the input pulse. The delay units were incorporated into the circuit as a precaution against any unwanted delay in the veto circuit which could allow pulses to indicate incorrect cells. Since the veto pulses arrive before the delayed pulses the outputs of those gates receiving veto pulses are held in the logical 1 state - the quiescent state. If no veto pulse is received then the gate output is a negative pulse of length 0.15 µs. The outputs of these gates, together with the outputs of those gates of stage 1 having no veto requirements, are taken to the final stage of the circuit. The latter consists of 4 coincidence gates, the output of each corresponding to a cell. A negative pulse received at any of the inputs indicates the traversed cell and at the output of the relevant gate a positive pulse is produced.

The outputs of the 152 gates across the tray front are taken to the momentum selector shift register unit situated some distance from the spectrograph described in Chapter 2. The output of each cell is used to set an element of a 152-bit shift register. Some time after this loading of the shift registers all 3 registers (one register for each momentum tray) are clocked at 980 kHz. In the reset condition the shift register elements are all in a logical 1 state; the pulse from an indicated cell flips the relevant element to a logical 0. This element gives a negative pulse when clocked off the end of the shift register and it is upon detection of this pulse that the operation of R.U.D.I. is based.

3.3 R.U.D.I.

3.3.1 Introduction The Restricted Use Digital Instrument - R.U.D.I - is the instrument used to calculate the sign and momentum of triggering muons and also to give some measure of their zenith angle. The calculation of these quantities is based on the generation of 2 numbers.

3.3.2 Determination of the Muon Deflection The 2 numbers mentioned above are produced by 2 scalers counting the clock pulses of the momentum selector shift registers. Figure 3.5 shows the circuit diagrammatically - shift registers A, B, C represent the momentum selector trays at the top, middle and bottom of the magnet. The first scaler, scaler AB, is controlled by the negative pulses, denoting the traversed cells, from the shift registers A and B; the second scaler is controlled by the pulses from shift registers B and C. A pulse from shift register A (SRA) starts scaler AB counting. Upon reception of a pulse from SRB, the counting in scaler AB stops, and counting in scaler BC commences. Counting in BC continues until stopped by a pulse from SRC. The order of arrival of the pulses is not important and thus scaler AB may be started by a pulse from either of SRA or SRB and correspondingly stopped by pulses from SRB or SRA. The number in scaler AB is a measure of incoming zenith angle of the particle trajectory and the deflection suffered by the particle in traversing the upper half of the magnet; the number in scaler BC is a measure of the zenith angle and the deflection suffered in the lower half of the magnet, given in units of cell width (0.5 cm).

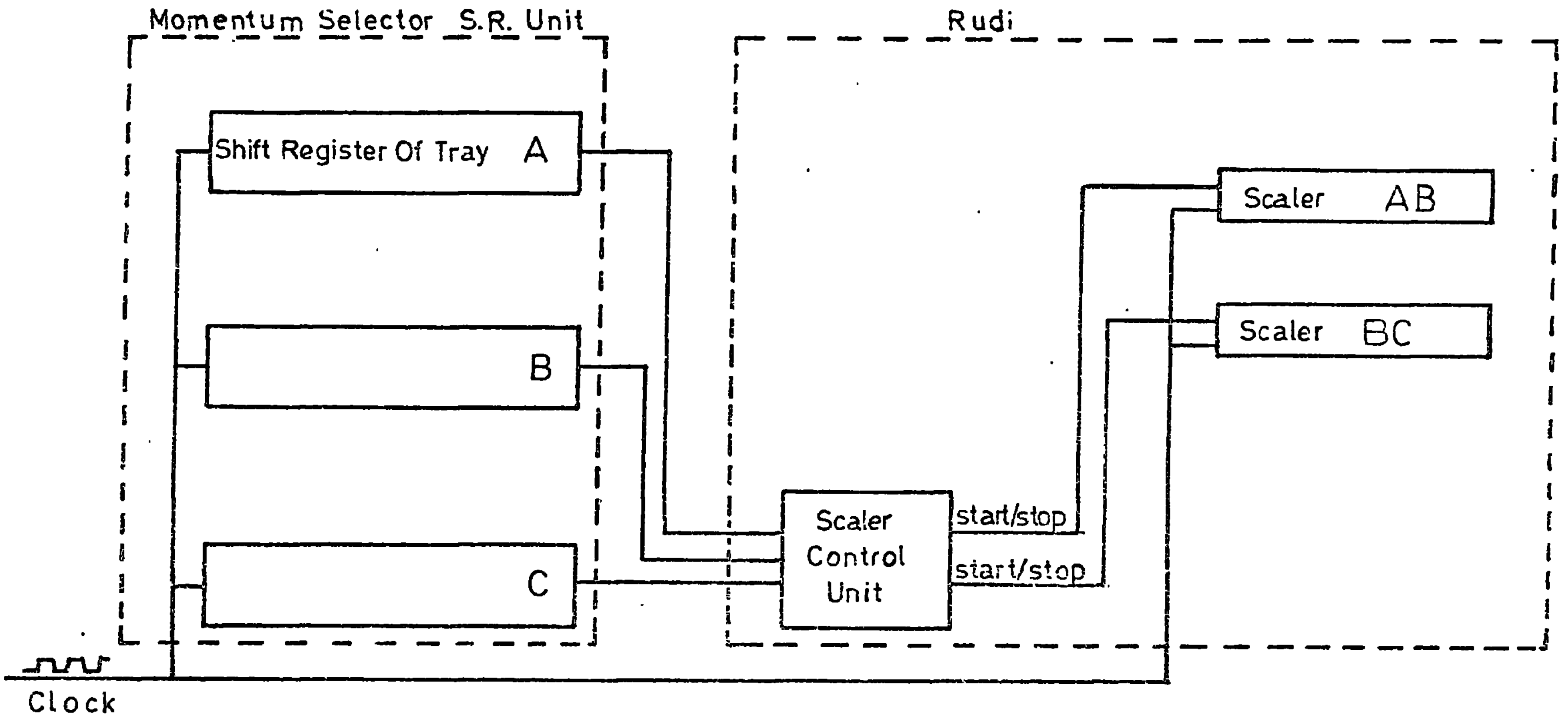

FIGURE: 3.5 CONTROL OF SHIFT REGISTERS AB AND BC.

The deflection of a traversing particle is defined as the distance shown in Fig 3.6; the relation between Δ and the momentum of the particle is derived in the next chapter -

$$p\Delta \sim 400$$

where p is the momentum in GeV/c and

Δ is the deflection in cms.

Figure 3.7a shows a particle traversing the spectrograph and the resulting shift register and scaler readings. In this case Δ is obtained by subtracting the two scaler readings:

$$\begin{aligned}\Delta &= \text{scaler AB count} - \text{scaler BC count}\\ &= 45-12\\ &= 33 \text{ cell widths} = 33 \times 0.5 \text{ cm} = 16.5 \text{ cms.}\end{aligned}$$

In fact, a small correction to Δ is necessary because the second momentum selector tray is not exactly midway between the outer trays. This correction is not incorporated in R.U.D.I but is applied at a later stage in the treatment of the data. Fig 3.7b shows a particle of opposite sign to 3.7a. In this case, Δ is obtained by adding the scaler counts:

$$\begin{aligned}\Delta &= 45 + 72\\ &= 117 \text{ cell widths} = 58.5 \text{ cms}\end{aligned}$$

The decision to add or subtract the scaler counts is made in R.U.D.I.

The data from R.U.D.I. are accumulated in the memory of a 400 channel pulse height analyser (PHA). Because of the limited number of channels not all deflections can be allocated to individual channels. Thus, all deflections greater than 22 cell widths are stored in a single channel; deflections of 22 or less are stored in separate channels. This is shown diagrammatically in Fig 3.8. In this way all deflections are stored in 24 channels and so a total of 16 such deflection spectra, separated by a spare channel, can be stored. The spare channel should

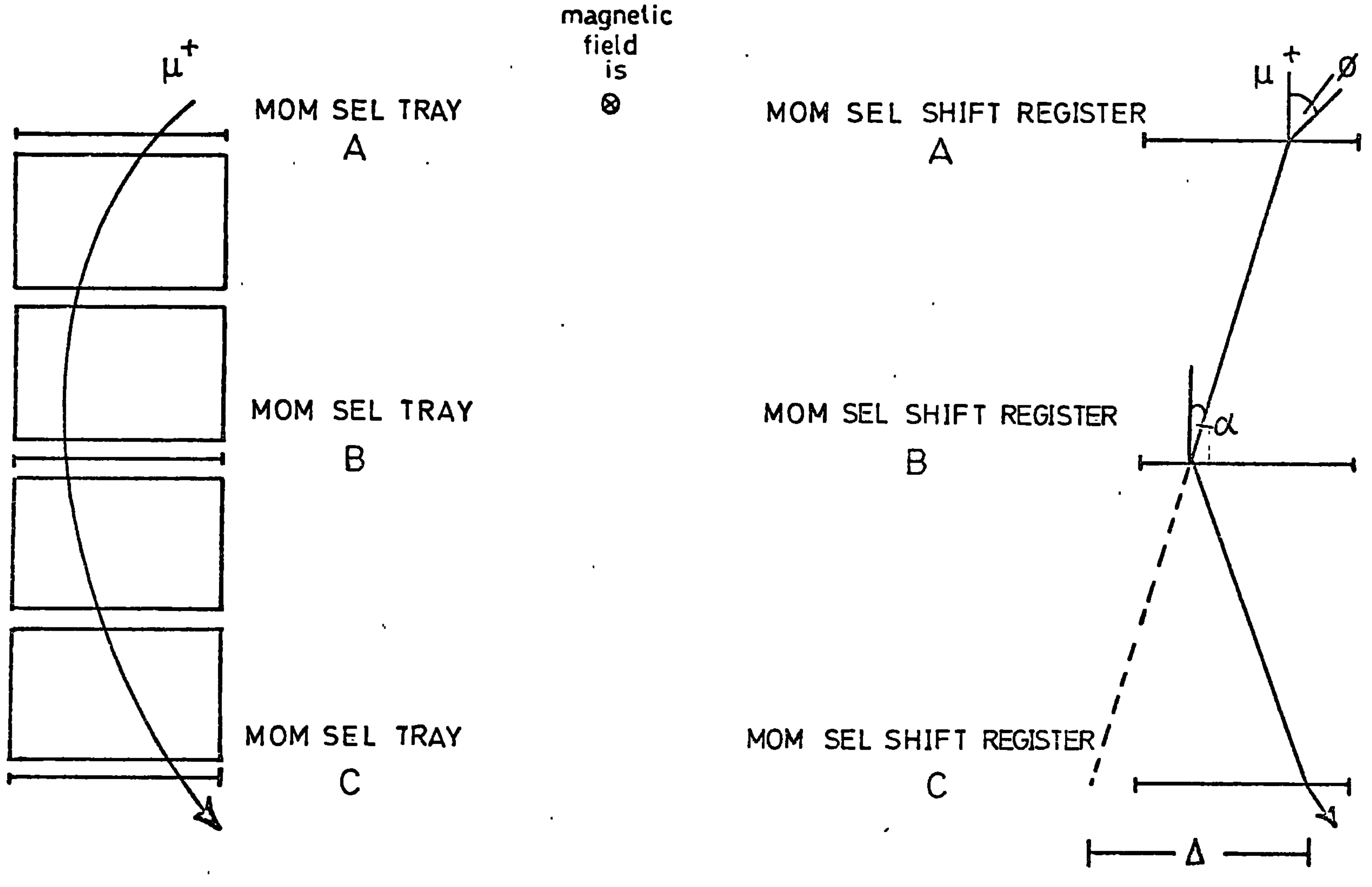

FIGURE:3.6. DEFINITION OF Δ

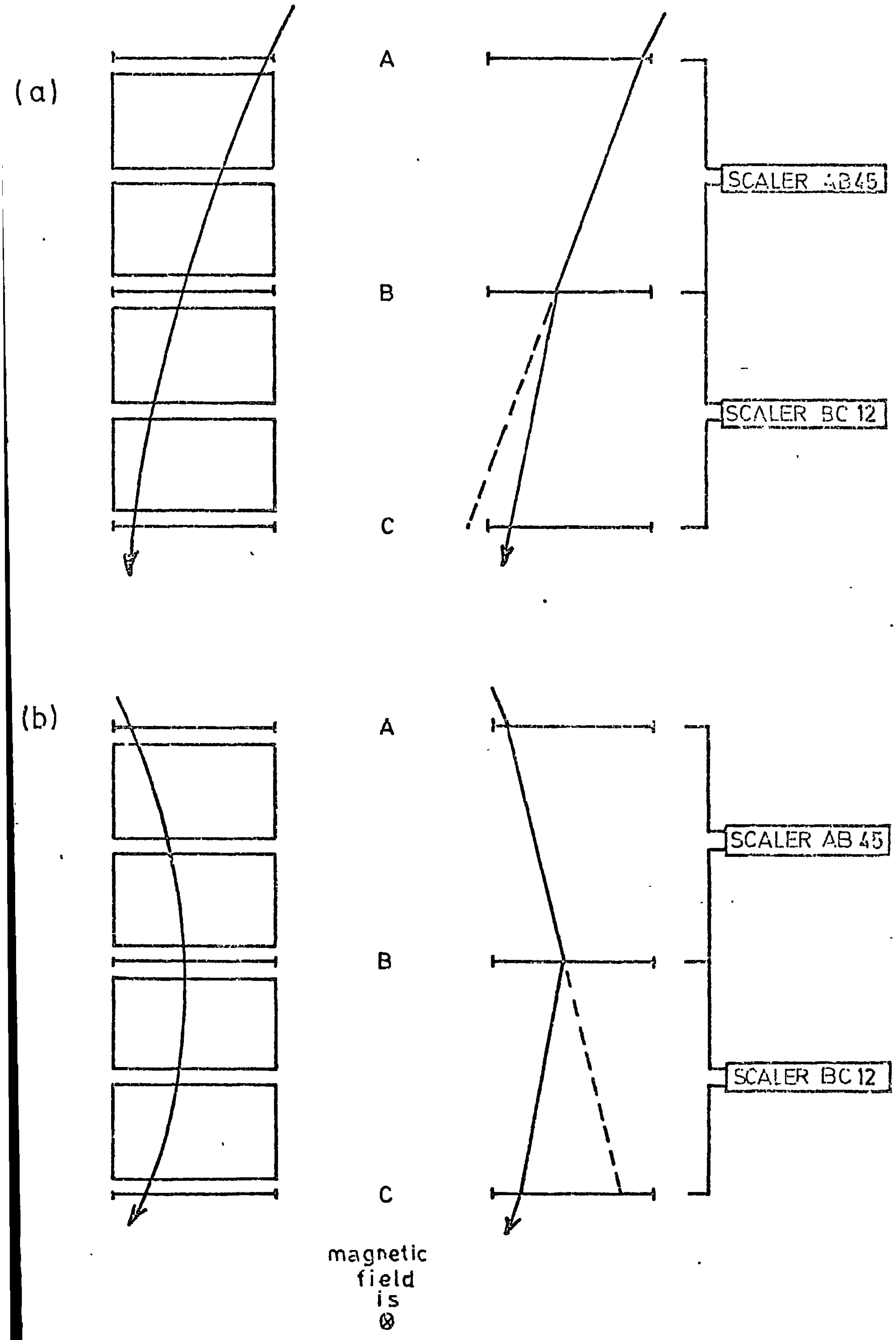

FIGURE 3·7. CALCULATION OF Δ

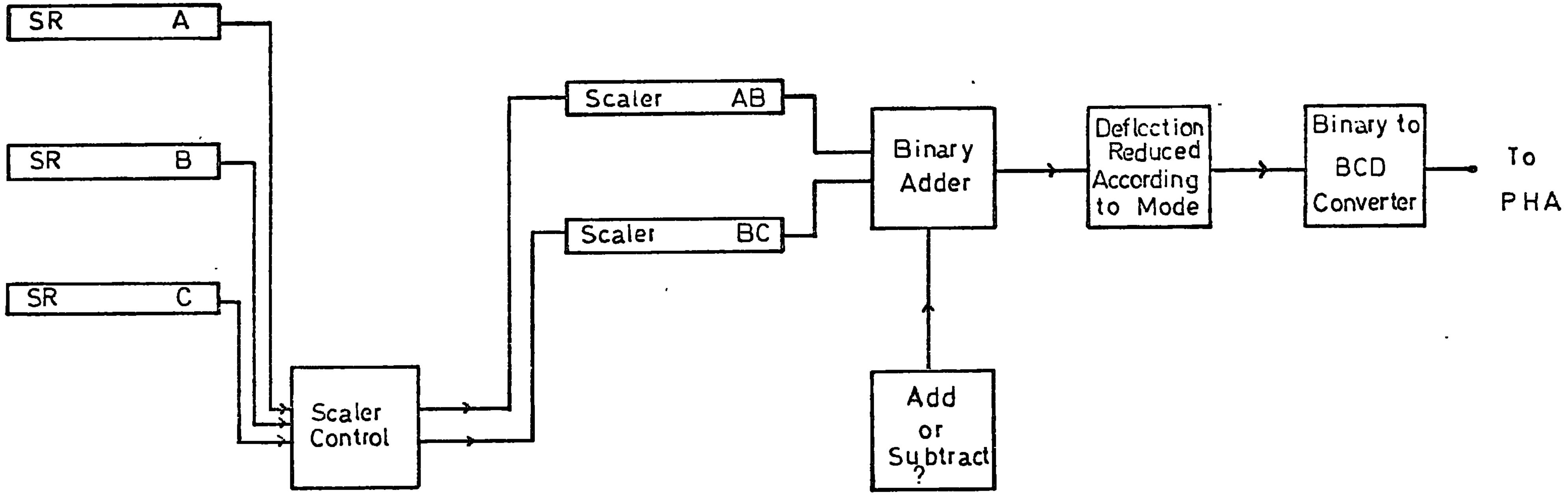

FIGURE: 3.8. GENERATION AND REDUCTION OF DEFLECTION remain empty and serves as a useful check on the functioning of R.U.D.I. Of the sixteen spectra, 8 contain data from positive muons and the remaining 8, data on negative muons. The 8 spectra of a given sign are classed according to the approximate zenith angle of the muons.

The range of R.U.D.I. can be extended by manipulating the output of the binary adder before it is taken to the circuit responsible for dealing with deflections of 23 cells. The output of the adder is in binary format of 8 bits. If the binary 1 output is ignored and the remaining outputs designated 1, 2, ... 64 then any original output has been halved and truncated. Thus, a deflection of 22 cells is classed as a deflection of 11 cells; a deflection of 23 cells is also classed as one of 11 cells. The new cells are thus 1 cm wide whereas the original cells were 0.5 cm wide. The greatest deflection, in this alternative mode, which is not put in the integral channel is 45 cells (of 0.5 cm width), this is recorded as 22 cells (of 1 cm width) and is a particle of lower momentum than a normal mode 22 cell deflection. In this new mode of operation - '1 cm cell operation' - the mean momentum of each cell is approximately halved and the range of R.U.D.I. thus extended at a cost of a loss of momentum resolution. This modification is indicated in Fig 3.8.

To determine whether the scaler readings are to be added or subtracted it is necessary to consider all of the possible types of particle trajectory. These are shown in Figs 3.9 a and b, for the case of a 'positive' magnetic field i.e. one directed into the plane of the page. The arrival order written under each diagram is simply the order in which the negative pulses from the momentum selector shift registers are fed to R.U.D.I. From fig 3.9a it can be seen that to obtain Δ the following rule can be used:

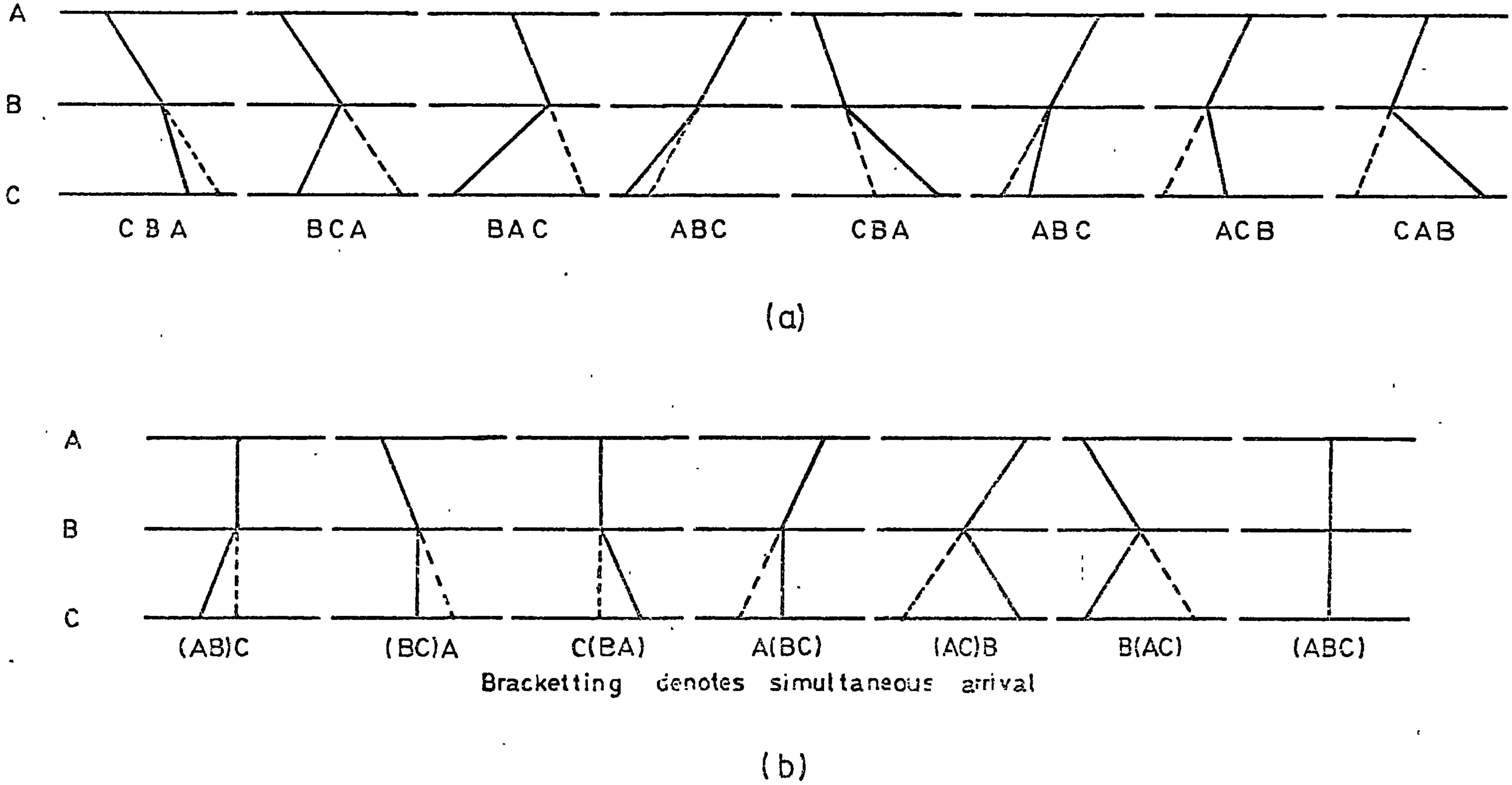

FIGURE:3.9 TRAJECTORY COMBINATIONS

If B arrives first or last then Δ is the sum of the scaler counts ie BA + CB. If B arrives second then Δ is the difference of the scaler counts ie CB-BA.

Some complication to this rule may arise due to pairs of A and B or B and C arriving simultaneously. These cases are shown in fig 3.9b. In these cases any inherent delay in applying control pulses to the scaler could result in a scaler being started by a slightly delayed pulse and then counting continually as the only pulse which could stop it has previously been applied. This problem is overcome by delaying the pulse from B by a useful amount but an amount which is negligible with respect to the clock pulse duty cycle (a delay of 0.1 us is used in practice). The simultaneous arrival of A, C is covered by the fact that B correspondingly arrives either first or last; this fact also deals with the case of a vertical trade. These last 2 cases are also shown in fig 3.9.

Including the need to determine the arrival order the system is now as shown in fig. 3.10.

3.3.3. Determination of the Muon Sign. The sign of the muon is derived initially by assuming the magnetic field to be in a particular direction - the positive direction.

Referring again to figs 3.9 a and b consider the events with arrival orders BCA, BAC, (AB)C, (CB)A, B(AC) and those with arrival orders ACB, CAB, C(AB), (AC)B, A(BC). For these cases the sign of the muon is unambiguous, that of the first group is negative, that of the second is positive. The case of (ABC) is that of a particle passing vertically through the spectrograph and suffering a deflection less than 1 cell width (the corresponding particle momentum is $\gtrsim$ 800 GeV/c) and thus cannot be assigned a meaningful sign. It is arbitrarily defined as a negative muon and is put into the first group of events above.

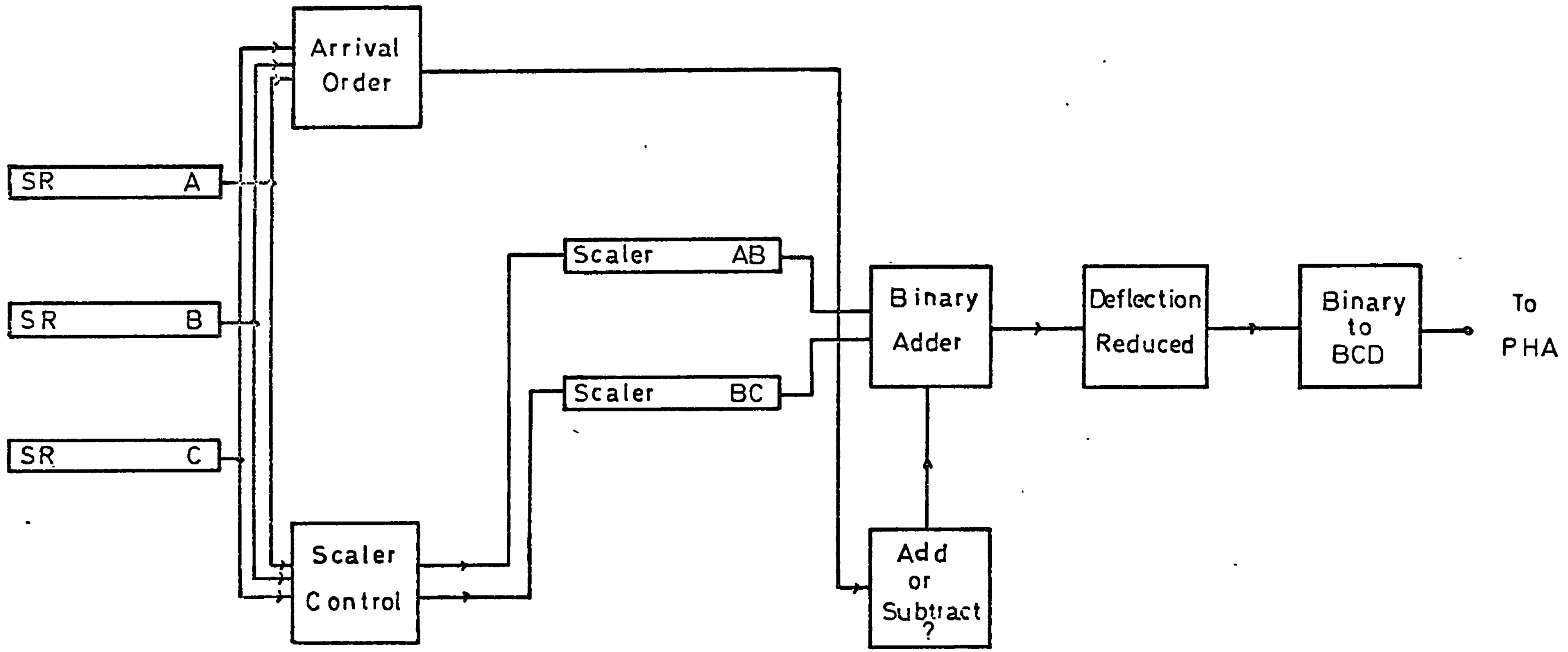

FIGURE: 3.10 GENERATION AND REDUCTION OF DEFLECTION INCLUDING ARRIVAL ORDER

For the arrival orders ABC, CBA the muon sign is not obvious. In these cases the procedure is as follows. From the rule derived in the previous section the scaler counts AB and BC must be subtracted. The circuits of R.U.D.I. are such that the subtraction performed is (BC-AB) as distinct from (AB-BC). This is done by taking the complement of AB (i.e. $\overline{\text{AB}}$) and adding it to BC:

(1) If BC$>$AB the subtraction involves carrying 1 from the end of the 9-bit binary adder to the beginning (i.e. from binary position 256 to position 1). For example, consider AB=4 BC=6.

AB = 000000100 ($\overline{\text{AB}}$ = 111111011)

BC = 000000110

```
then BC-AB is      000000110
                   111111011
                 ┌─000000001···:
                 └─1 ──>·······:
                   carry 1
```

when the carry 1 is added, the answer becomes

000000010 i.e. the correct answer:2.

(2) If BC$\leqslant$AB the subtraction does not involve a carry but to obtain the correct answer the result of the initial subtraction (BC-AB) must be complemented. For example, consider AB=4, BC=3.

```
then BC-AB is      000000011
                   111111011
                   111111110
```

This value is ($\overline{\text{true answer}}$), and must be complemented to give

000000001 i.e. the correct answer:1.

Now consider the arrival order CBA; if BC$>$AB the muon is positive. Thus the presence of logic states indicating

a) the arrival order CBA and,

b) the presence of a 'carry 1' logic state from the adder,

are used to specify the particle as positive.

For a negative muon BC $<$ AB and the presence of states indicating

a) the arrival order CBA and

b) the presence of no carry 1 from the adder are used to specify the particle as negative.

In the case of a high momentum ($\gtrsim$ 800 GeV/c) particle having a deflection less than 1 cell the designation of sign becomes arbitrary. Since no 'carry 1' state is produced when AB = BC the procedure just described defines a CBA high momentum event as negative.

Now consider the arrival order ABC; if $AB > BC$ the muon is positive and the presence of logic states indicating

a) the arrival order ABC and

b) the presence of no 'carry 1' from the adder are used to specify the sign as such.

For a negative muon $AB < BC$ and the presence of states indicating

a) the arrival order ABC and

b) the presence of a 'carry 1' from the adder specify the particle as negative.

In the case of a high momentum ($\gtrsim$ 800 GeV/c) particle the sign is again arbitrary. From the procedure just described an ABC high momentum particle is defined as positive.

Until now the muon sign has been determined by assuming a positive field. Information as to the true direction is now inserted. If the field is positive or zero, the sign remains unchanged; if the field is negative the sign is reversed.

A schematic diagram of the circuit used to determine the deflection and sign of the muon is given in fig 3.11. It now remains to obtain a measure of the zenith angle.

<u>3.3.4. Determination of the Muon Zenith Angle.</u> R.U.D.I. is unable to measure the true zenith angle of the muon. The angle which is measured is the angle α of fig 3.6. From a knowledge of the momentum of the particle the relation between α and the true zenith angle ϕ may be

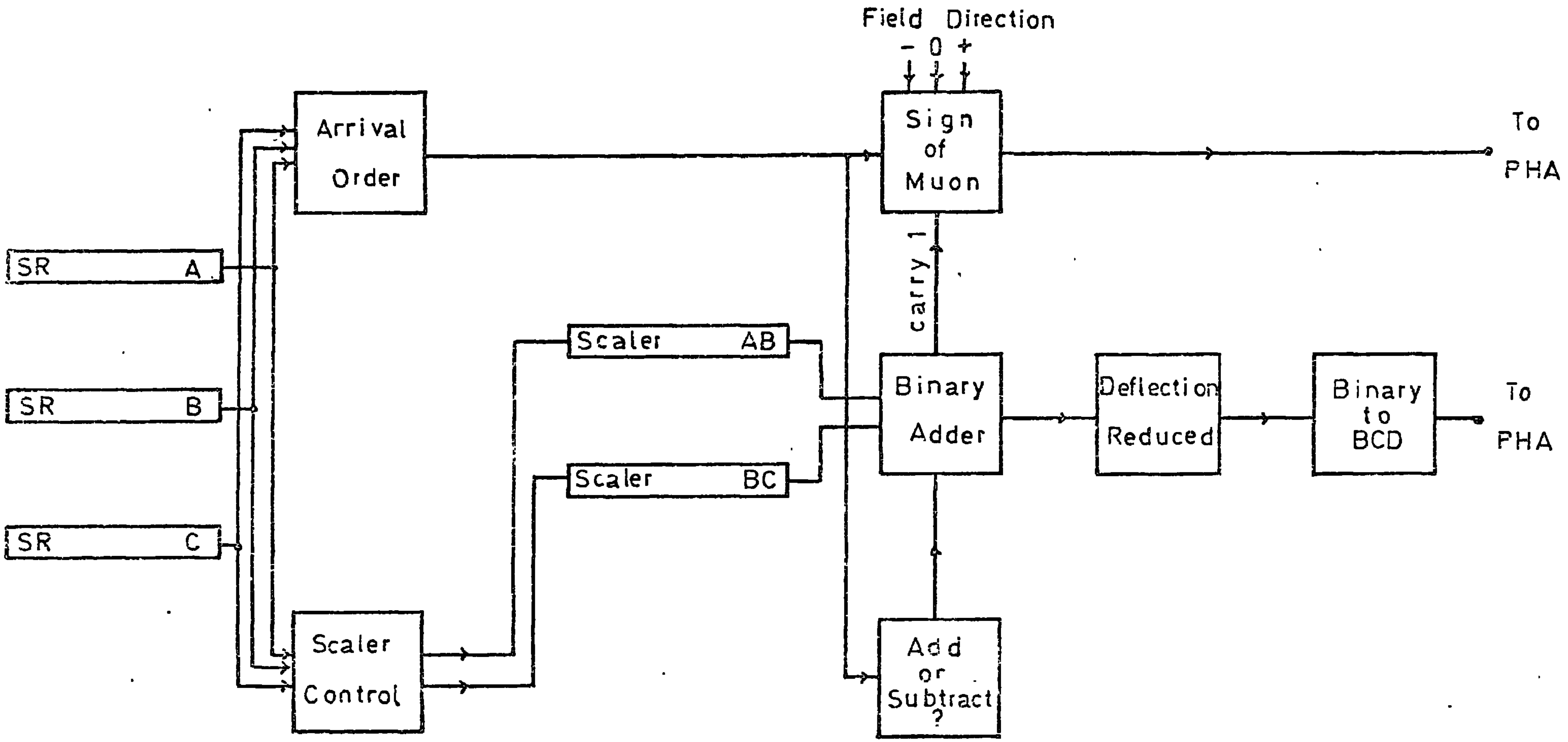

FIGURE: 3.11 DETERMINATION OF SIGN AND DEFLECTION calculated - Chapter 4.

The arrival direction - East or West - is found by considering the arrival order of pulses from levels A and B. If the particle traverses the RED side of the spectrograph then:

if A follows B then the direction is West,
if A precedes B " " " " East

Since for both sides of the spectrograph the momentum selector shift registers are shifted towards the centre of the magnet the above directions must be reversed for a particle traversing the BLUE sides of the spectrograph. Thus the side of the magnet traversed must be identified and fed to R.U.D.I.

The angle α is grouped into 4 ranges of scaler AB count as shown:

GROUP	a	b	c	d
SCALER AB COUNT	$AB < 16$	$16 \leqslant AB < 32$	$32 \leqslant AB < 48$	$AB \geqslant 48$
EQUIVALENT ANGLE α	$\alpha < 1.43^{\circ}$	$1.43^{\circ} \leqslant \alpha < 2.87^{\circ}$	$2.87^{\circ} \leqslant \alpha < 4.37^{\circ}$	$\alpha \geqslant 4.37^{\circ}$

A schematic diagram of the circuit so far is shown in fig 3.12.

3.3.5. The Final Output of R.U.D.I. In the last 3 sections the muons have been grouped into:

a) 2 classes according to sign: + or -
b) 2 classes according to arrival direction: E or W
c) 4 classes according to the angle α.

Thus there are 16 spectra to be stored in the 400 channels of the PHA - 25 channels/spectrum. Each spectrum contains deflections 0,1,2, ...21,22, (23 or more) cell widths; the remaining 25th channel is empty.

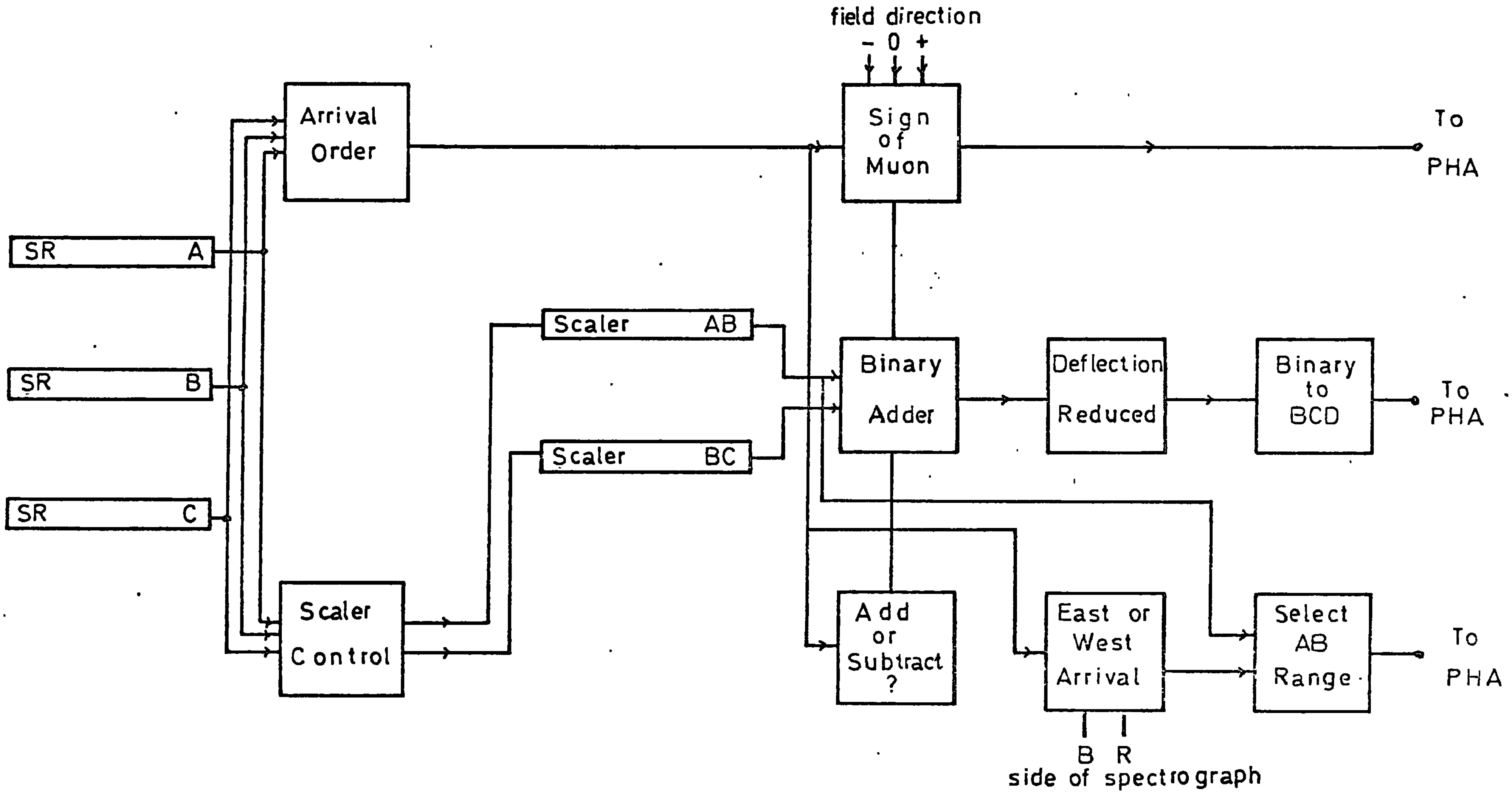

FIGURE: 3.12. DETERMINATION OF SIGN, DEFLECTION AND ARRIVAL DIRECTION

Each of the spectra is given an identifier of the form (n x 25 + 1) where n = 0,1,2, ...14,15. These numbers in terms of sign, arrival direction and range of are as below.

	$AB < 16$	$32 > AB \geq 16$	$48 > AB \geq 32$	$AB \geq 48$
u-W	001	026	051	076
u-E	101	126	151	176
u+W	201	226	251	276
u+E	301	326	351	376

For a particular event the deflection of the muon and the identifier of the spectrum to which it belongs are added. The result is the address of a channel in the store of the PHA and the contents of that channel are, provided the event satisfies certain criteria to be described, incremented by one.

The address sent to the PHA is in binary coded decimal (BCD). The logic levels of R.U.D.I. and the PHA are different and the address must pass through the 'logic level change' circuit. The relevant logic levels are given below. Those of the PHA have been specified by Nuclear Chicago Ltd, the manufacturers of the PHA; those of R.U.D.I. are the DTL logic levels

	Logical 1	Logical 0
R,U,D,I.	+2.2v or more +	+.8v or less +
PHA	-6v or more neg.	0.5v or more +

The address and muon sign are displayed on the front panel of R.U.D.I. This introduces the need for a memory circuit and, since the address display is in decimal form, a BCD to Decimal conversion circuit. Also displayed is the deflection of the particle before reduction. This display is in binary form and no memory is required since the display is reset only by the next event.

A schematic diagram of the circuit so far is shown in Fig. 3.13.

3.3.6. The Functioning of R.U.D.I. In addition to producing an address for the PHA, a pulse - the 'store' pulse - must be generated to increment the contents of that address by 1. The store pulse is produced by R.U.D.I. and is transmitted to the PHA only if certain conditions are satisifed, if they are not, then the address contents are not incremented and the event is thus not stored.

It was mentioned in 3.2.3. that 1, and only 1, traversed cell must be indicated at each of the 3 levels. The reason for this is now obvious - more than 1 cell at any of the levels would start or stop the scalers AB and BC in positions having no relation to the deflection of the particle. A circuit is included in R.U.D.I. to prevent the storage of such events. This is shown schematically in Fig.3.14. Two tests are made; one ensures that the number of cells indicated at each level is 0 or 1, the second ensures that the No. of cells is 1 or more. The results of the tests are combined so that only if both are satisfied is a pulse - the 'arithmetic' pulse - transmitted to the adder to initiate addition or subtraction.

In order to be stored, an event must satisfy a further 3 checks in addition to that above. These checks are made on logic states generated by R.U.D.I. They test that:

(i) the add or subtract instruction sent to the adder is unambiguous i.e. the instruction is either add or subtract, not both, not neither.

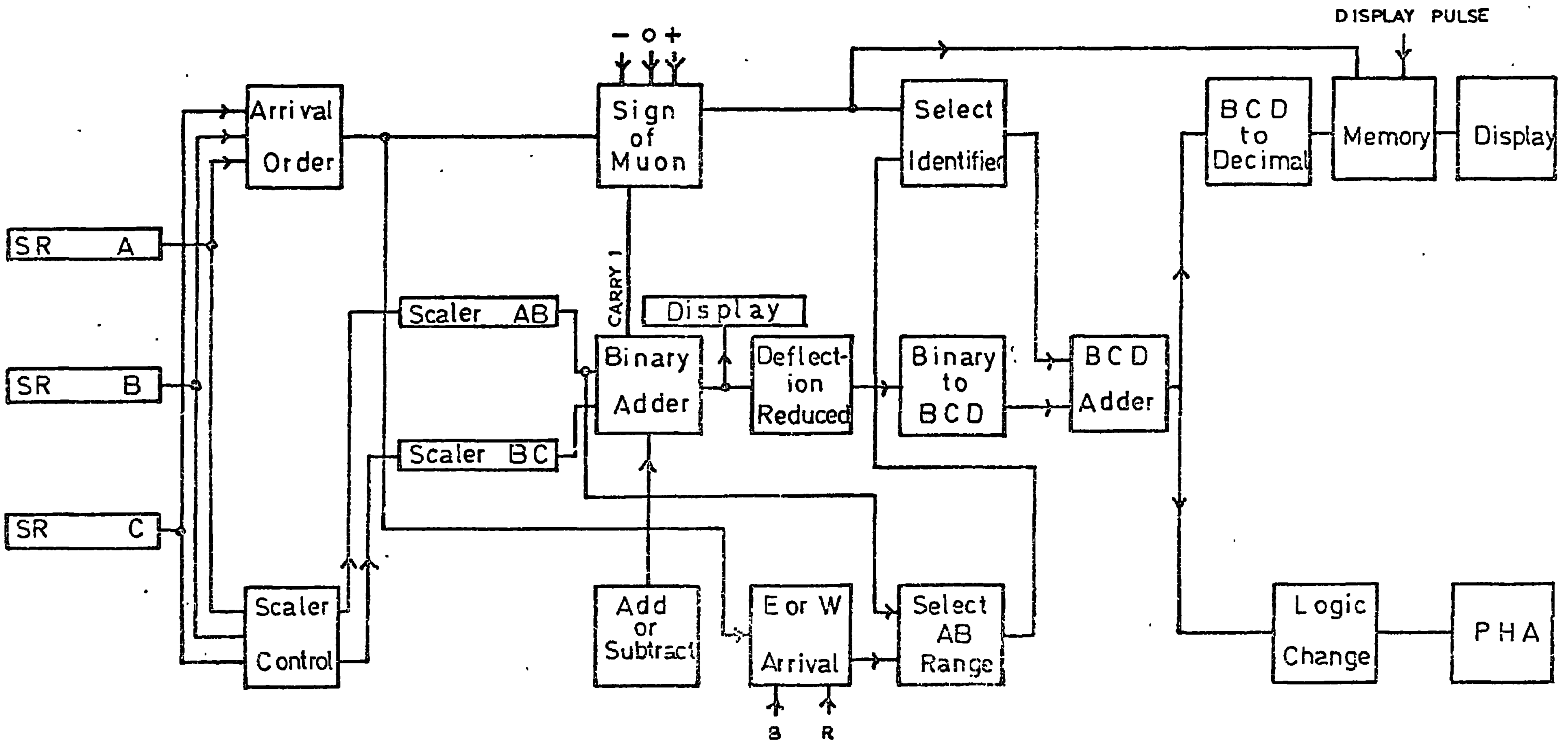

FIGURE 3·13. OVERALL SYSTEM FOR GENERATING PHA ADDRESS

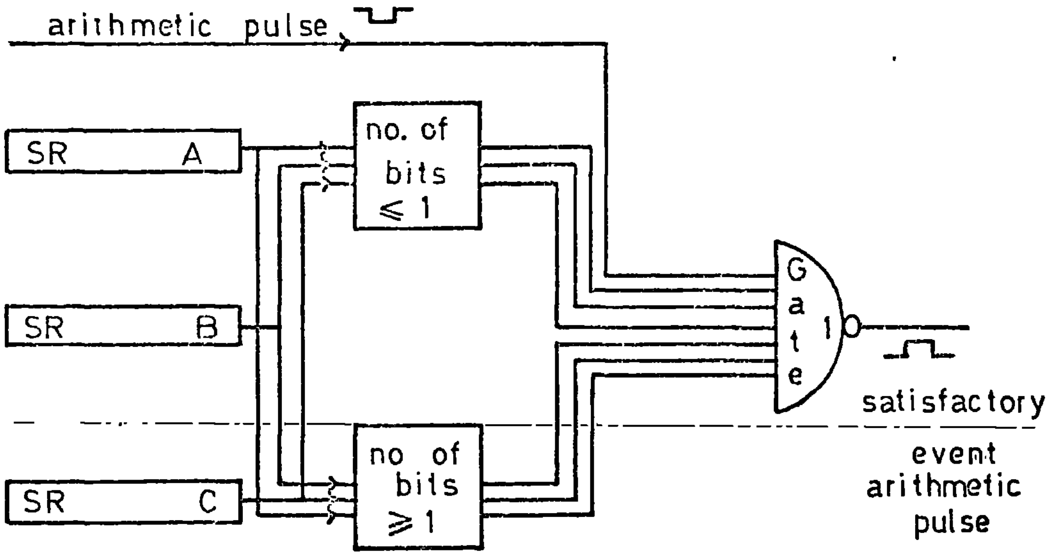

FIGURE: 3·14. SINGLE CELL CHECK

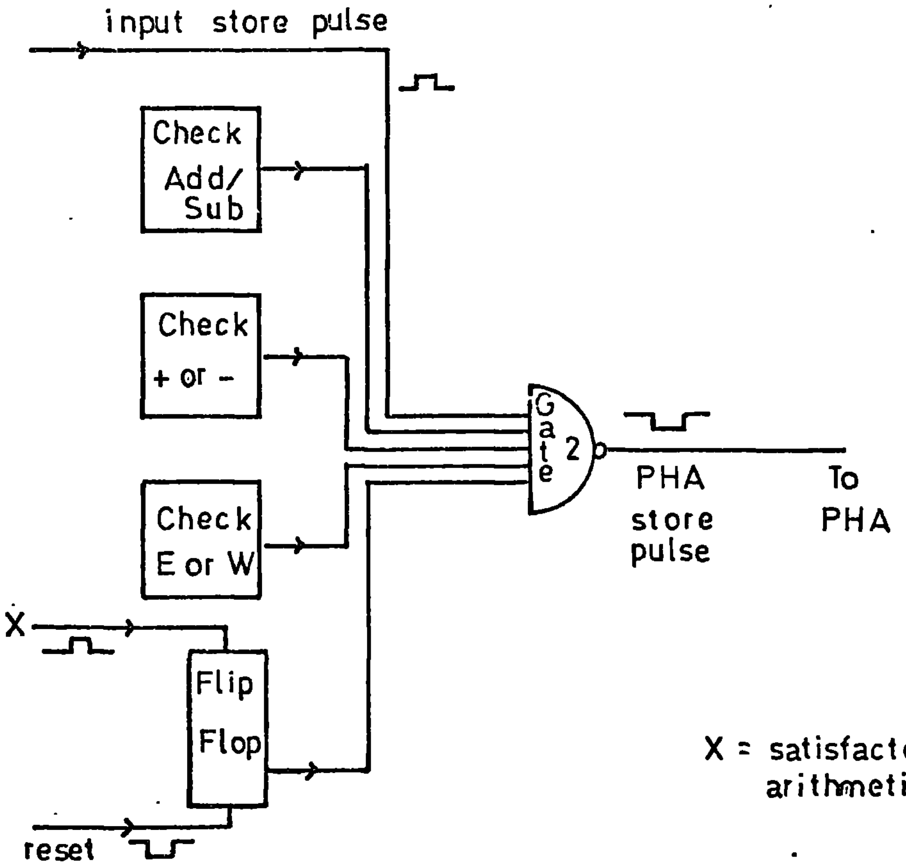

X = satisfactory event arithmetic pulse

FIGURE: 3·15. UNAMBIGUOUS INSTRUCTION CHECK

(ii) the generated muon sign is unambiguous i.e. it is either positive or negative, not both, not neither.

(iii) the East or West arrival direction generated is unambiguous i.e. either East or West, not both, not neither.

Only when an event has satisifed the four conditions will it be stored in the PHA. The circuit is illustrated in Fig. 3.15.

In addition to these pulses from the momentum-selector shift registers another 3 pulse trains are required to control the timing of R.U.D.I., these are:

(i) the clock pulses used to clock the shift registers. These pulses are shaped by R.U.D.I. before being fed to the various circuits.

(ii) an initial reset pulse. The BLUE side 3-fold coincidence pulse is used to reset initially R.U.D.I. after a particle has traversed the spectrograph but before data is received from the shift registers.

(iii) the 'C90' pulse. This pulse triggers 3 monostables, one to produce the 'arithmetic' pulse which is input at gate 1 of Fig. 3.14; another to produce the 'display' pulse which updates the memory of the PHA address display and the last to produce the original store pulse which must pass through gate 2 of Fig. 3.15. The C90 pulse originates within the momentum selector circuitry and is fed to R.U.D.I. simply for convenience. After a 750 μs delay it triggers the aforementioned monostables.

The timing sequence of R.U.D.I. and the spectrograph as a whole is shown in Fig. 3.16.

An example of a deflection spectrum produced by R.U.D.I. and stored in the PHA is given in Figure 3.17. Most of the channels showing data are the category 23 type channels, the data in the remaining channels are too few to be seen on the vertical scale used. On the

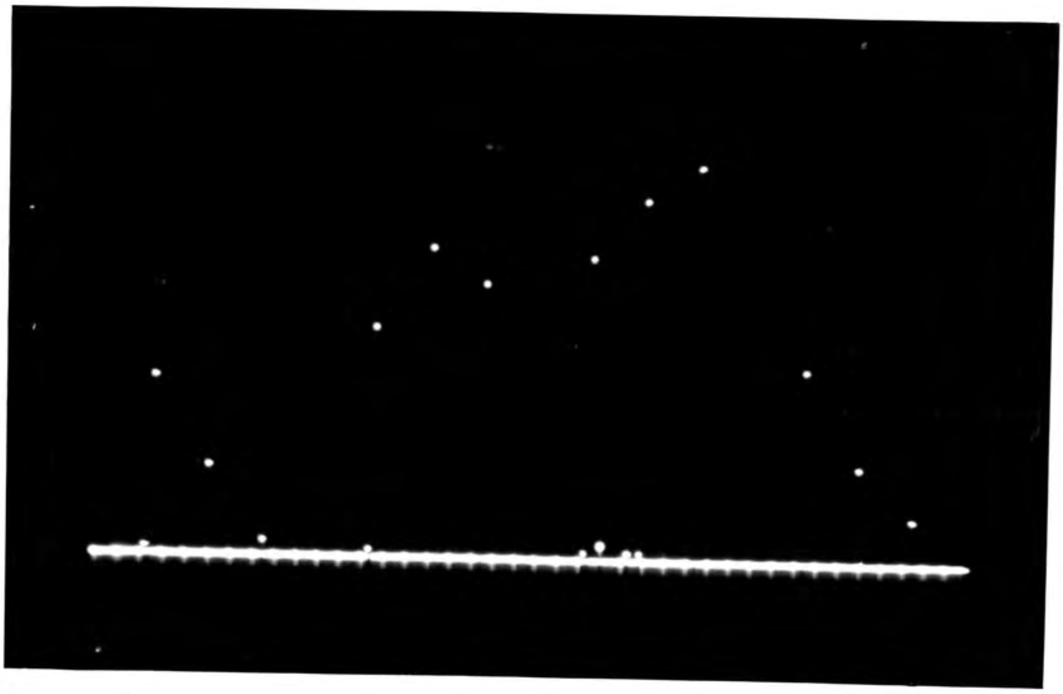

FIGURE 3.17

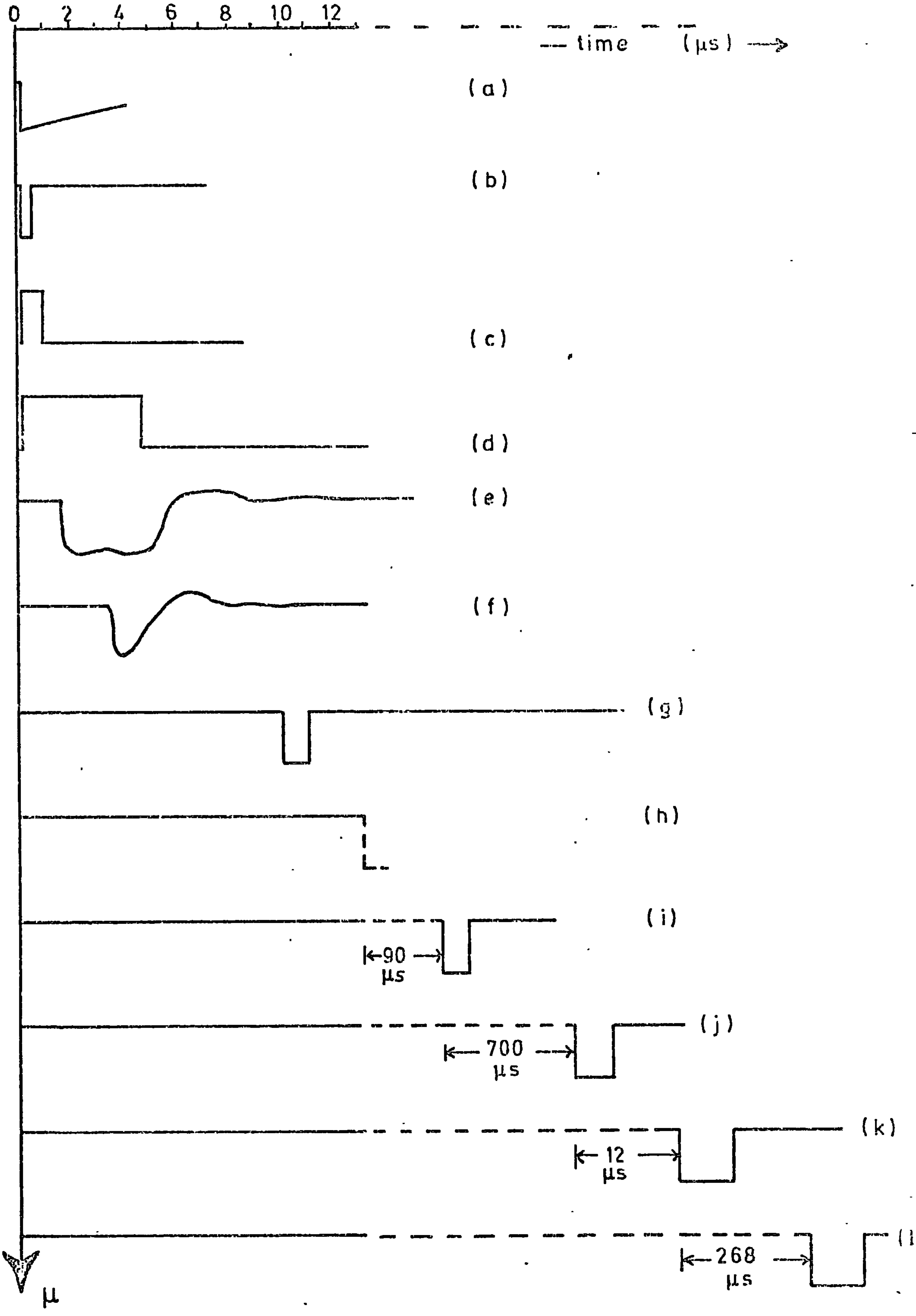

FIGURE:3·16. RUDI TIMING DIAGRAM

horizontal scale the small vertical lines are at 10 channel intervals. Channels 1-100 and 101-200 contain negative particles from the west and east respectively; channels 201-300 and 301-400 contain positive particles from the west and east respectively. This spectrum was collected with a positive magnetic field. It can be seen that the predominantly accepted arrival direction is east for the negative particles and west for positive particles. This demonstrates the higher acceptance for these directions with a positive magnetic field; reversing the field changes the predominant directions.

3.3.7. The Construction of R.U.D.I. All of the logic circuitry of R.U.D.I. has been constructed from DTL logic blocks. The logic level change circuit, the PHA address display driving circuits and the store pulse finally fed to the PHA are discreet transistor circuits. Logic diagrams and circuit diagrams, together with a description of the working of each board are given in Appendix 2.

The final logic diagram of R.U.D.I. is shown in Fig. 3.18.

3.3.8. Operating R.U.D.I. During data collection, R.U.D.I. is tested approximately once per week. To facilitate testing, an instrument - the R.U.D.I. Test Instrument - has been constructed. The logic diagram, circuit diagram and operation of the instrument are described in Appendix 3. The instrument simulates the outputs of the momentum selector shift register units; by selecting various cell combinations the working of R.U.D.I. can be checked.

While it is operating, the performance of R.U.D.I. is continually monitored. The monitoring instrument counts the number of triggers of the spectrograph and the number of times the shift registers are clocked all the way across the 152 cells. These 2 numbers should be equal but in practice it has been found that due to malfunctions of the shift-registers discrepancies can arise. Sets of data in which such discrepancies occur are rejected. The instrument also counts the number of events which have at least 1 cell set in each of the shift registers.

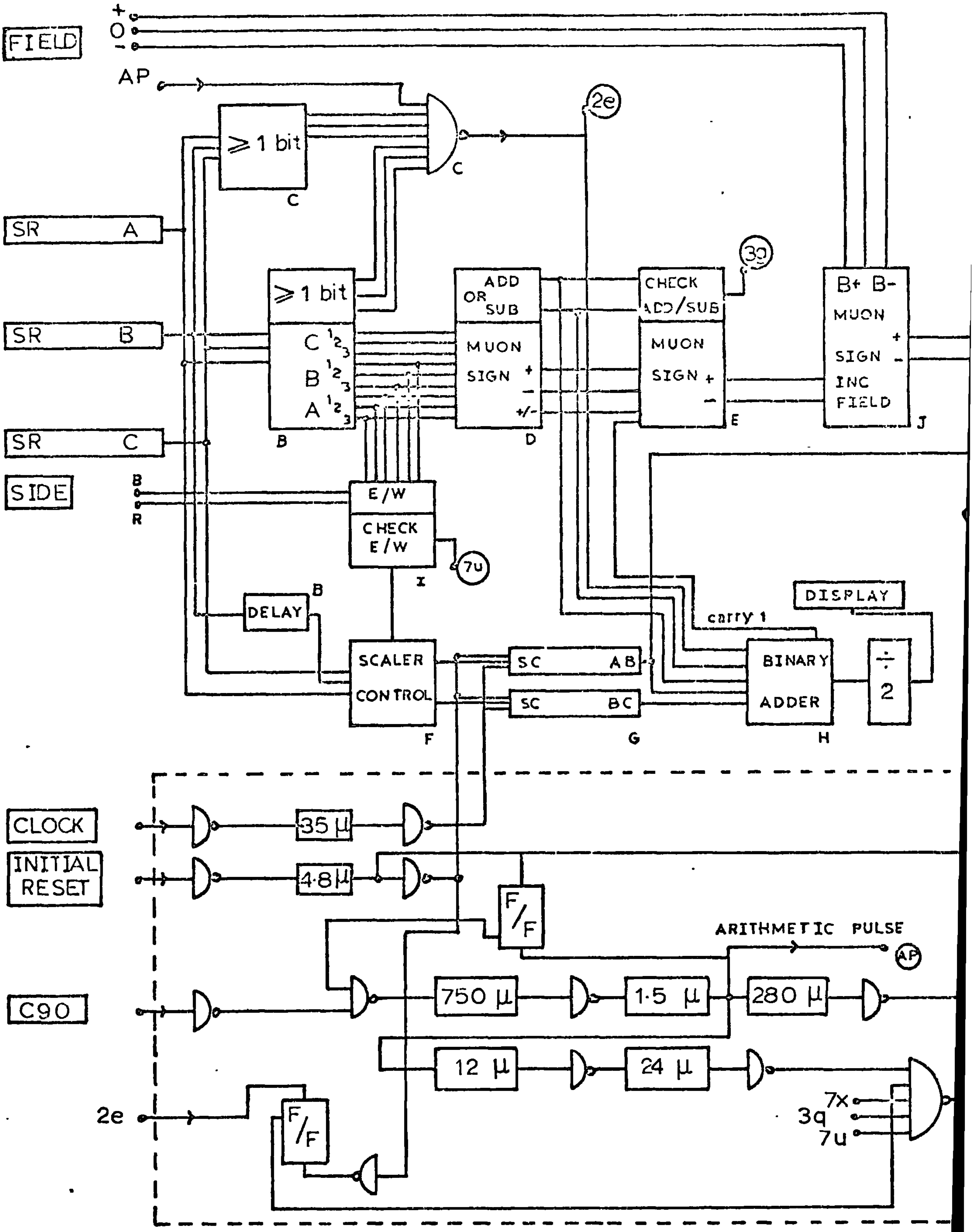

FIGURE 3.18. RUDI

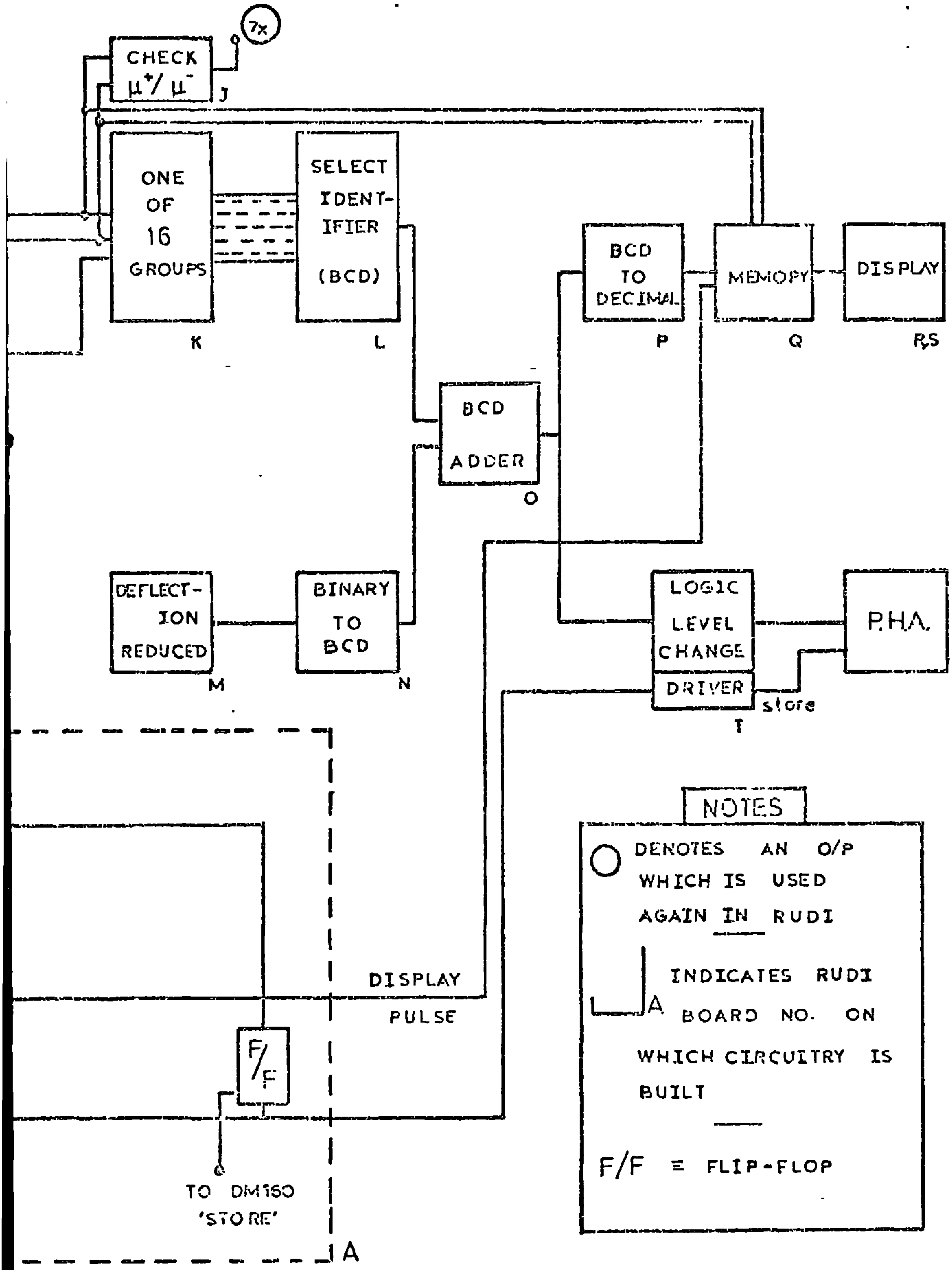

NOTES

○ DENOTES AN O/P WHICH IS USED AGAIN IN RUDI

A INDICATES RUDI BOARD NO. ON WHICH CIRCUITRY IS BUILT

F/F ≡ FLIP-FLOP

This is useful as described in Chapter 4.

Another instrument has been constructed to count the number of cells indicated at a given level. Ideally the number of cells should always be 1 but a number of zero's and two's are also found; the rare events showing 3 or more cells are also recorded. This device is also able to detect which cell is indicated at a given level for a particular event. The results obtained from this instrument are given in Chapter 4 and a circuit diagram is given in Appendix 4.

It has been found that fluctuations in the current of the PHA core store can lead to counts not being stored for some addresses. An instrument has been built to test the PHA by sequentially generating each address and incrementing the contents by one and then repeating the cycle. Any fault in storage can then be seen from the PHA display.

Data is gathered by R.U.D.I. in a series of 'Runs'. Each run lasts about 15 hrs and collects about 5000 events. At the end of a run the contents of the PHA memory are printed out. This output is checked to ensure that the number of events stored in the PHA agrees with the number of store pulses transmitted to the PHA. The output is then transferred onto punched cards and analysed by computer. The print out from the computer displays the results of the run grouped into the various spectra and also a number of rates and charge ratios. The data from several series of runs of the spectrograph and studies of various bias effects in them are described in the next chapter.

CHAPTER 4

Instrumental Effects

4.0 Introduction

This chapter describes various instrumental effects of the spectrograph and the momentum selector celling system.

4.1 Acceptance Effects

For a particle of infinite momentum the overall acceptance of the spectrograph has been found using the method of Lovati et al (1954). Taking the zenith angle dependence of the muon beam to follow a $\cos^n\theta$ law, where θ is the zenith angle, these authors show the acceptance of the arrangement of Fig 4.1 to be given by:

$$A_n \quad \int_0^{\tan^{-1}2Y/Z} \cos^{n+1}\theta_o \, d\theta_o \int_{-Y}^{Y-Z\tan\theta_o} dy \int_{-X}^{X} dx \int_{\psi_1}^{\psi_2} \cos^{n+2}\psi \, d\psi$$

For M.A.R.S., concerned with momenta $\gtrsim$ 7 GeV it is adequate to take $n = 0$ (Fowler and Wolfendale (1961), Coates (1967). The first three integrals of the above expression have been evaluated for a number of values of n, giving the following results:

$$A_0 = \int_0^{\tan^{-1}2Y/Z} 2\left[A\tan^{-1}A - \ln(1+A^2)^{1/2} + \ln\sec\tan^{-1}A\right]\left[2Y - Z\tan\theta\right]d\theta \qquad (A = 2X\cos\theta/Z)$$

$$A_1 = \int_0^{\tan^{-1}2Y/Z} 2\cos\theta\left[2\sec\tan^{-1}A - \cos\tan^{-1}A - 1\right]\left[2Y - Z\tan\theta\right]2/3\, Z\, d\theta$$

$$A_2 = \int_0^{\tan^{-1}2Y/Z} 2\cos^2\theta\left[\sin^2(\tan^{-1}A)\right]\left[2Y - Z\tan\theta\right]Z/4\, d\theta + \int_0^{\tan^{-1}2Y/Z}(\partial A_0/\partial\theta)\,3/4\cos^2\theta\, d\theta$$

$$A_3 = \int_0^{\tan^{-1}2Y/Z} 2\cos^3\theta\left[\sec\tan^{-1}A - 1\right]\left[2Y - Z\tan\theta\right]2/5\, Z\, d\theta + \int_0^{\tan^{-1}2Y/Z}(\partial A_1/\partial\theta)\,4/5\cos^2\theta\, d\theta$$

$$A_4 = \int_0^{\tan^{-1}2Y/Z} 2\cos^4\theta\left[1 - \cos\tan^{-1}A\right]\left[2Y - Z\tan\theta\right]Z/12\, d\theta + \int_0^{\tan^{-1}2Y/Z}(\partial A_2/\partial\theta)\,5/6\cos^2\theta\, d\theta$$

Taking Z to represent the distance between the centres of the outer two scintillators of the spectrograph the values $A_0 - A_4$ are respectively 406.0, 403.5, 401.2, 398.8 and 396.5. The acceptance is rather insensitive to n, there being a change of ~ 2% in going from n = 0 to

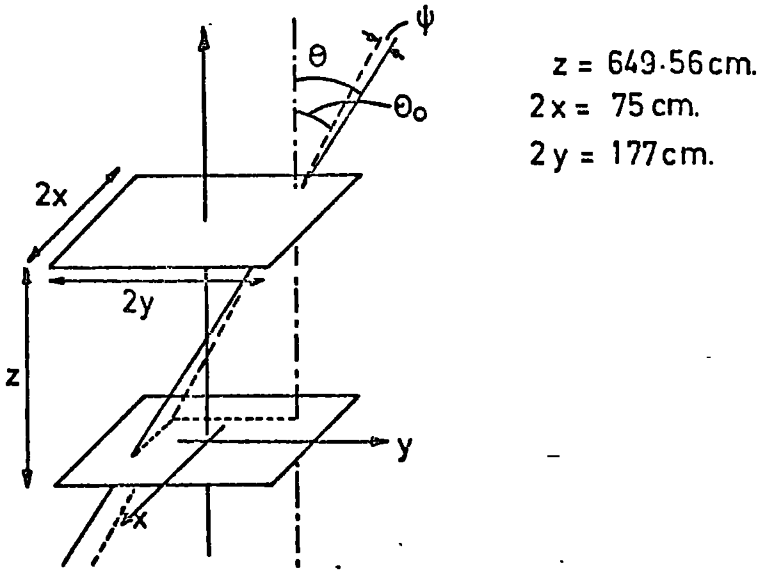

FIGURE: 4·1. THE ARRANGEMENT OF LOVATI et al (1954)

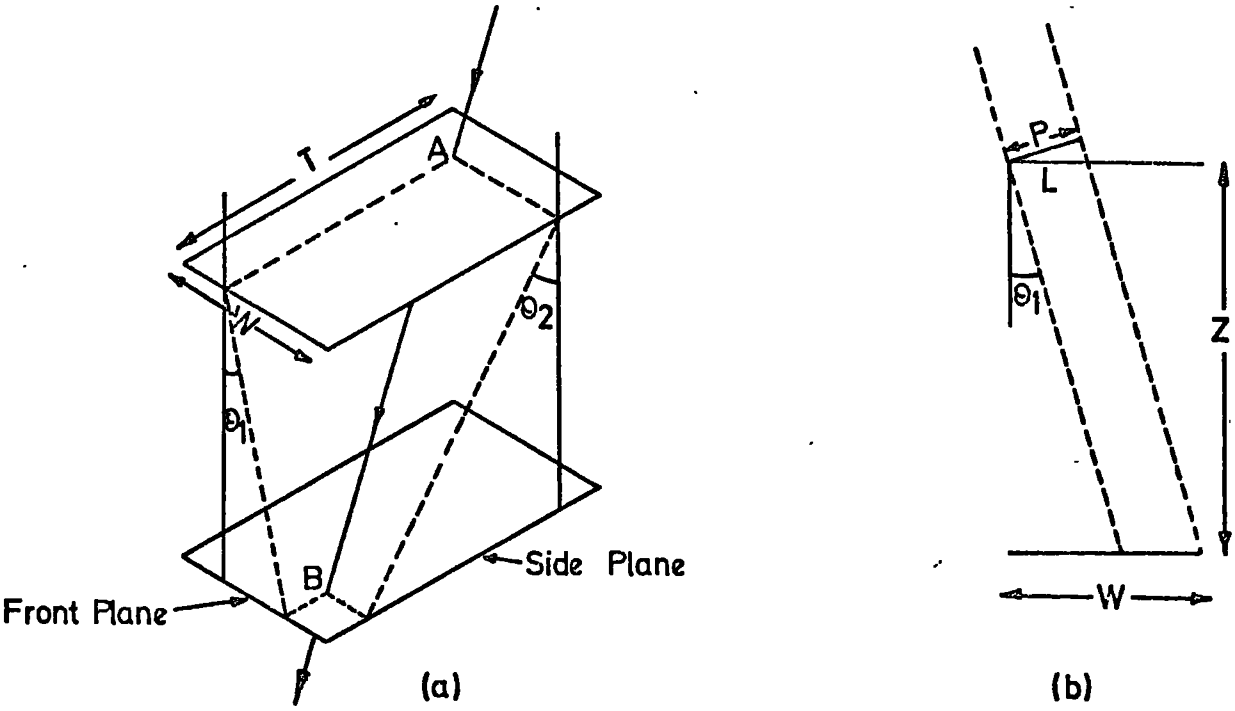

(a) (b)

FIGURE: 4 · 2. PROJECTED ANGLES.

$n=4$,

To obtain the acceptance for finite momenta, the paths of particles through the spectrograph have been simulated in a computer programme. Figure 4.2a shows schematically the path of a particle through the spectrograph; the two planes represent the outer scinitillators. The two components of the muon track, one parallel to the magnetic field and one perpendicular to it, may be considered separately, The projection of the track onto the front plane is shown in figure 4.2b. The acceptance at angle θ_1, is represented by the distance P which by simple geometry is given by

$$P = W \operatorname{Cos} \theta_1 - Z \operatorname{Sin} \theta_1$$

The acceptance (A_1) in this plane is then:

$$A = 2\int_0^{\theta_{max}} (W \cos\theta_1 - Z \sin\theta_1)\, d\theta_1 \quad = 2\left[(Z^2+W^2)^{1/2} - Z\right]$$

where $\theta_{max} = \tan^{-1} (W/Z)$ for a particle of infinite momentum. The acceptance in the remaining plane is given by a similar expression with T replacing W. Since both planes are taken to be independent the total (three-dimensional) acceptance (A) is the product of the two-dimensional acceptances and thus:

$A = ((Z^2 + W^2)^{1/2} - Z) . ((Z^2 + T^2)^{1/2} - Z)$ for a particle of infinite momentum. This yields an acceptance identical to that calculated as previously described. For a particle of finite momentum some deflection occurs in the front plane (the plane perpendicular to the magnetic field) and the values of P as a function of θ are obtained from the computer model. The technique used to find P has been to select the momentum and incident angle of a particle and then find that length L along the top of the spectrograph over which the particle track will satisfy certain criteria. These latter were that the track should pass through all three scintillators and all three momentum selector trays and should also stay within the solid iron of the magnet blocks. The computer programme was written to consider only magnetic deflection - scattering was neglected. Energy loss in the iron was taken into account using the results of Sternheimer and Peierls (1971). Figures 4.3 and 4.4 show the variation of P(=LCos θ_1) with zenith angle for the two field configurations most often used in the experiment. The momentum variation of these roughly triangular shaped curves is rather better illustrated in Figures 4.5 and 4.6. Integrating over θ gives the front plane acceptance; the side plane acceptance is constant since no deflection occurs parallel to the magnetic field. The resulting variation of acceptance with momentum is given fig 4.7.

From curves such as those of figures 4.5 and 4.6 graphs showing the relation between incident momentum and the most probable zenith angle have been constructed. These are shown for various field configurations in figures 4.8, 4.10 and 4.12. The computer programme simulated the paths of positive particles. It is useful to note that because of the shape of the acceptance curves the most probable, the mean and the median angles are all similar. The most probable angle emerging from the bottom of the spectrograph (corresponding to the most probable zenith angle incident on the spectrograph) as a function of incident momentum is shown in fig 4.14. Only the most commonly used field configurations are given. To show more clearly the relation between top and bottom angles the most probable values are related in figures 4.15 and 4.16.

As mentioned in a previous chapter it is not possible, using R.U.D.I. to measure the zenith angle of a particle. The angular ranges into which particles are grouped are based upon the angle indicated by the scaler ab of R.U.D.I. The relation between the latter and the projected zenith angle (the zenith angle projected onto the front plane) is given, for the two commonly used field directions, in figures 4.17a, b. On the ordinate are shown the 4 angular ranges (the ranges a, b, c and d) into which the particles are automatically grouped. The end points of the lines are at the angles at which the acceptance has fallen to zero. The dashed line represents a particle

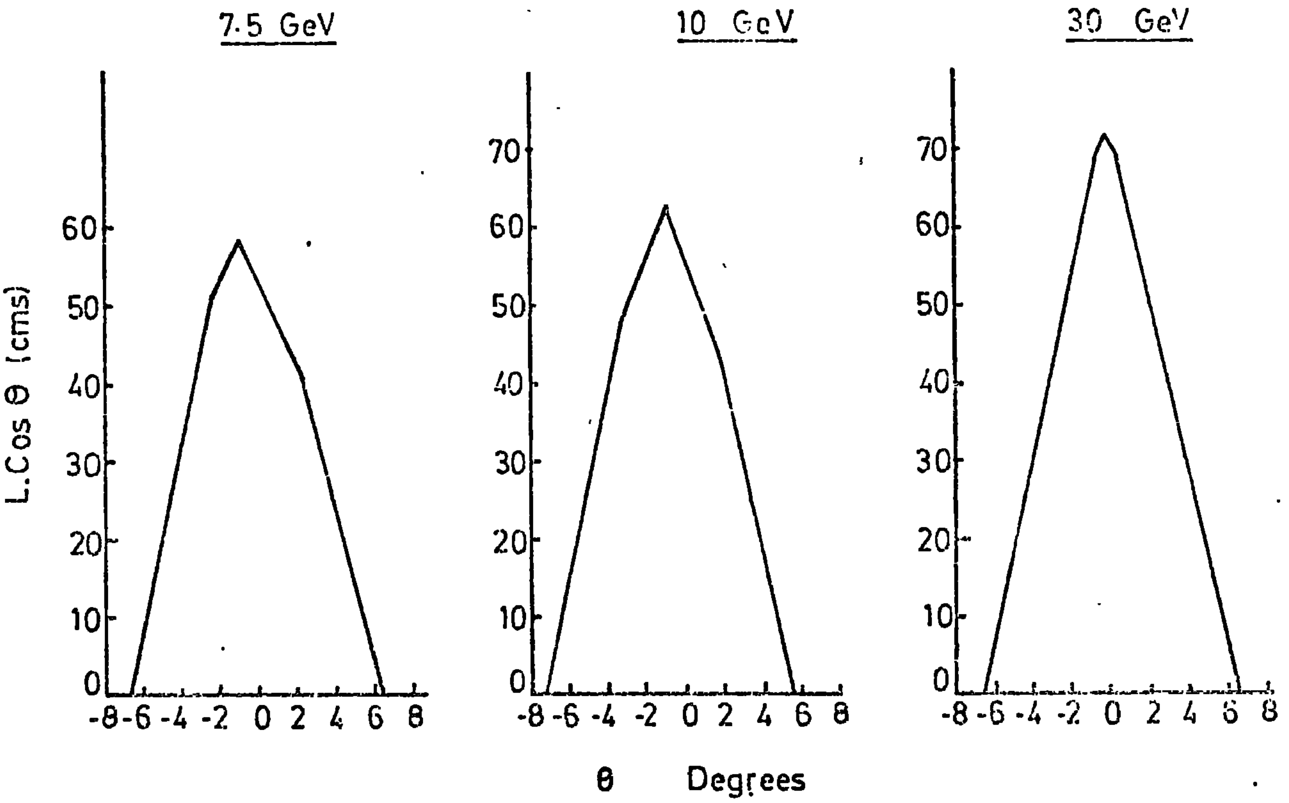

FIGURE: 4·3 CROSSED FIELD

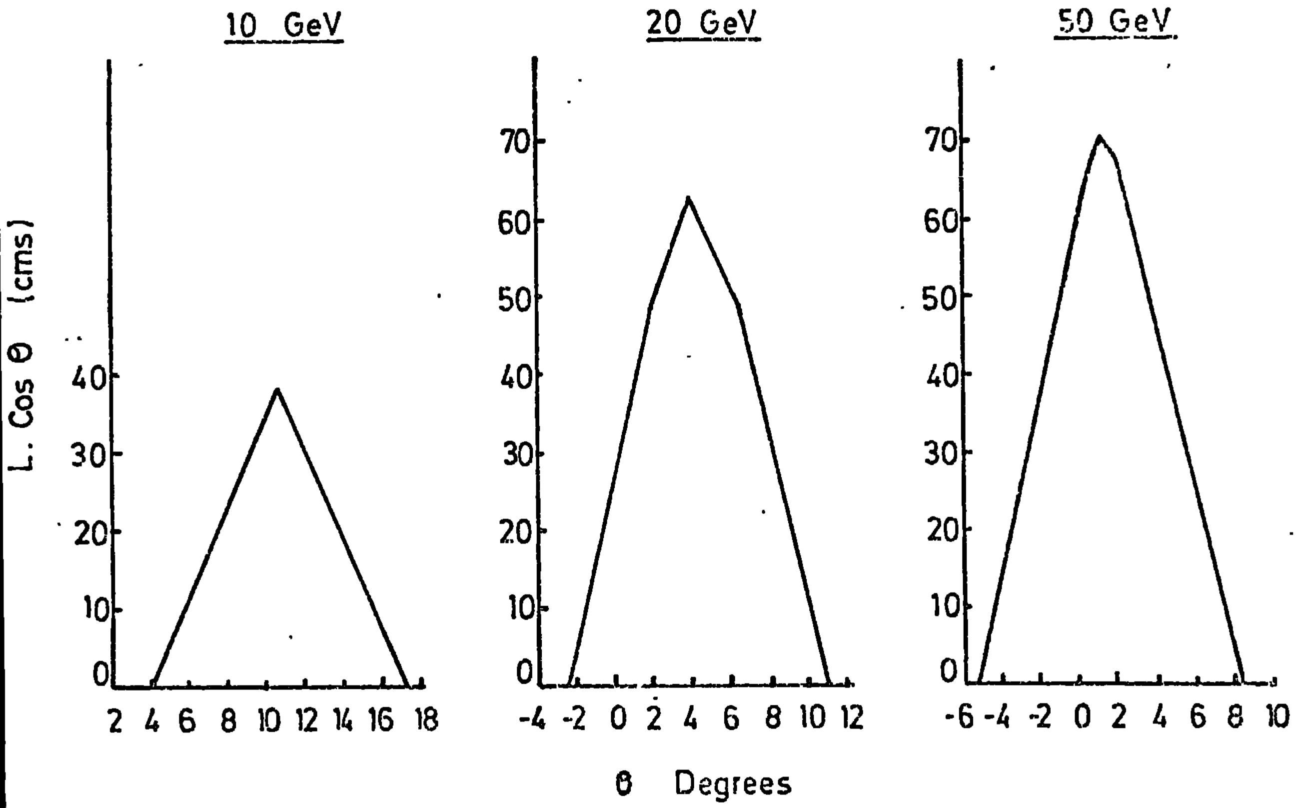

FIGURE: 4·4 NORMAL FIELD

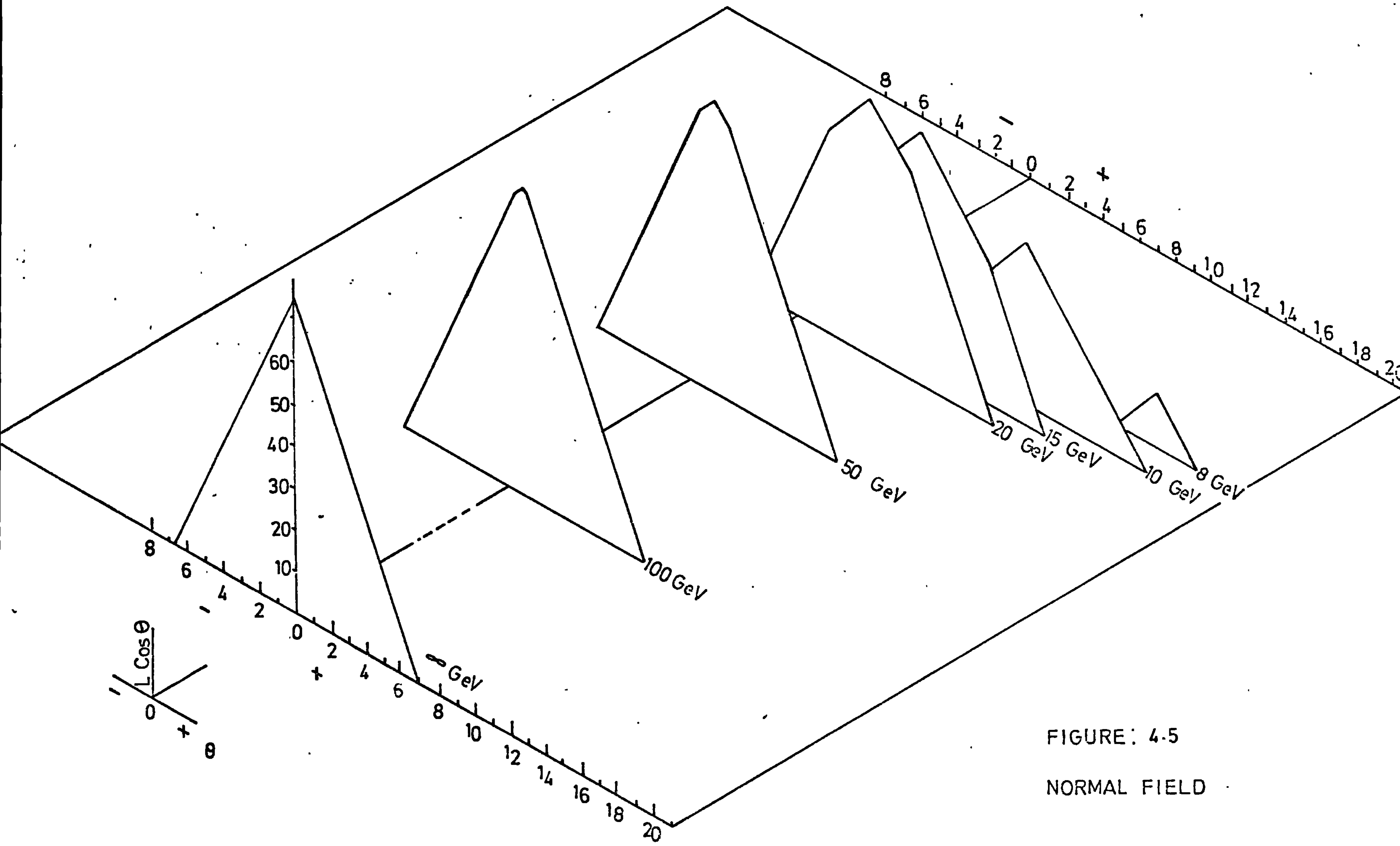

FIGURE: 4.5

NORMAL FIELD

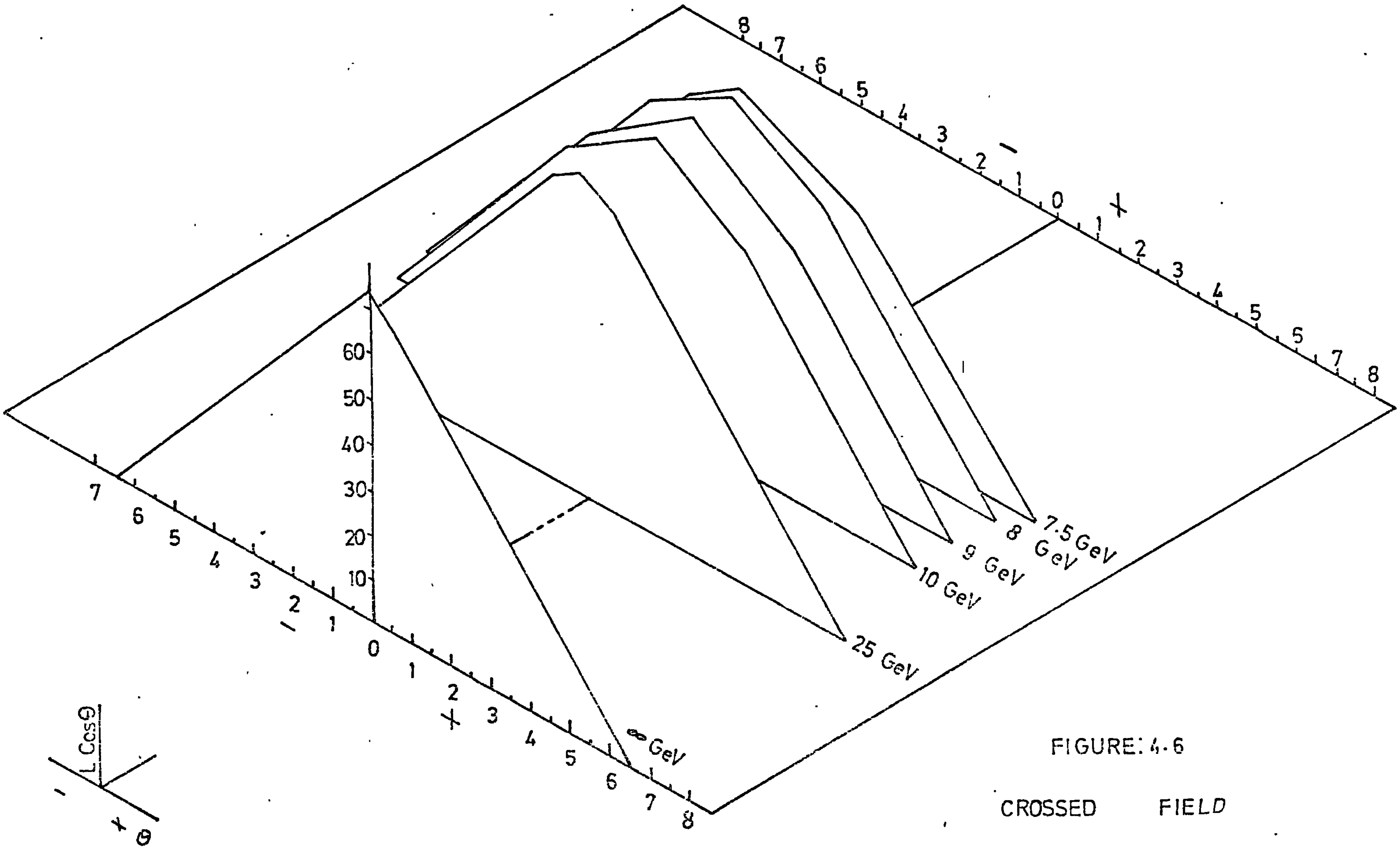

FIGURE: 4.6

CROSSED FIELD

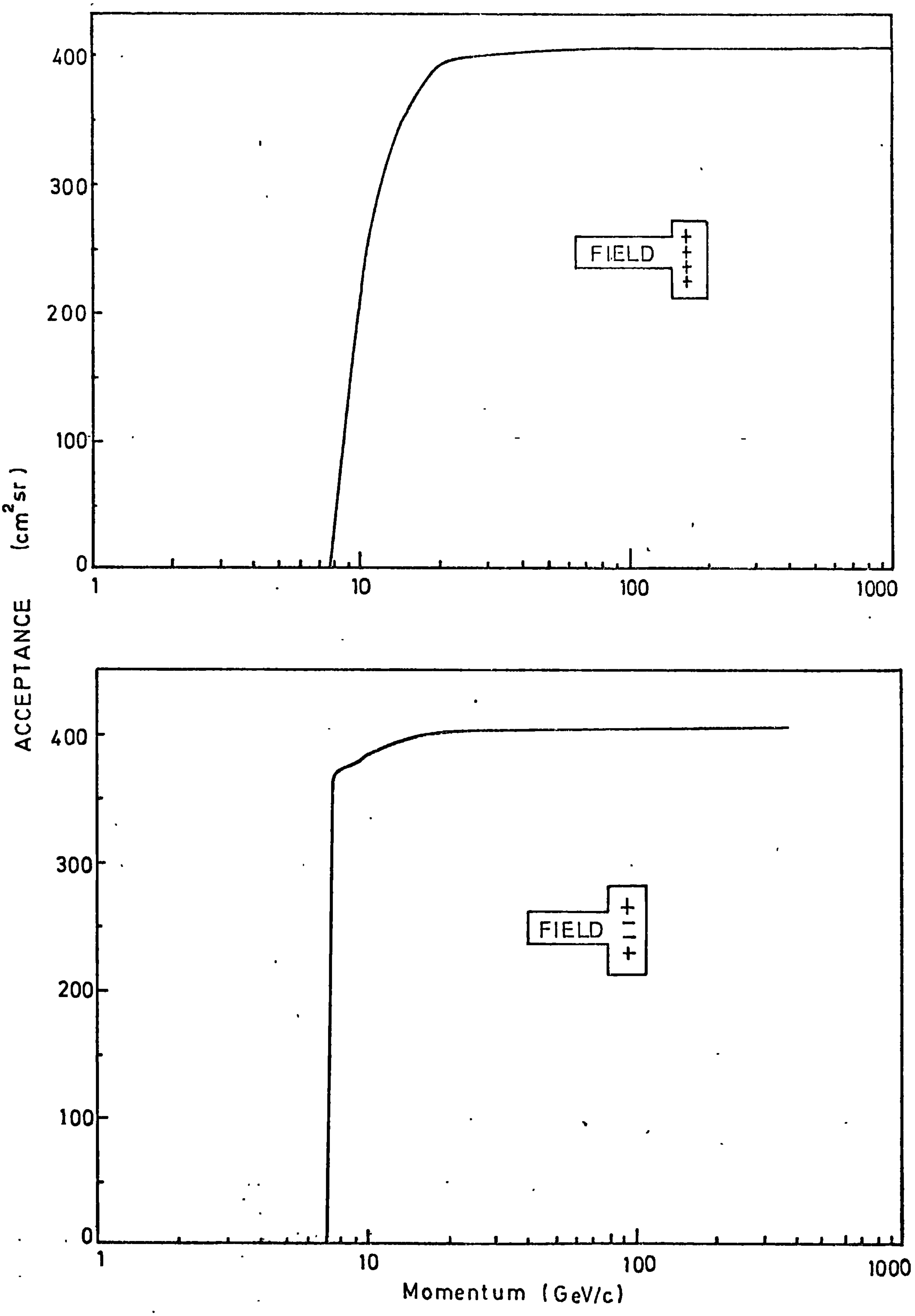

FIGURE:4·7 ACCEPTANCES

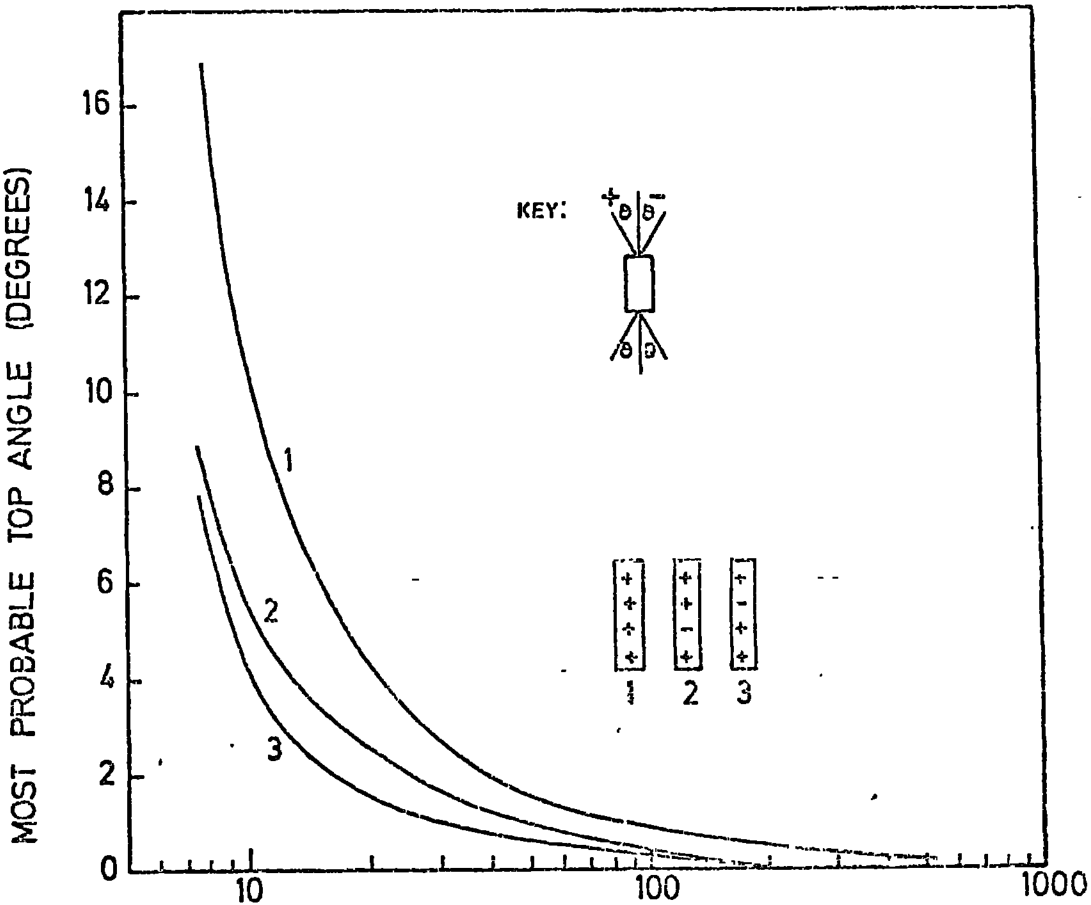

FIGURE:4·8.MOST PROBABLE ANGLE VERSUS MOMENTUM

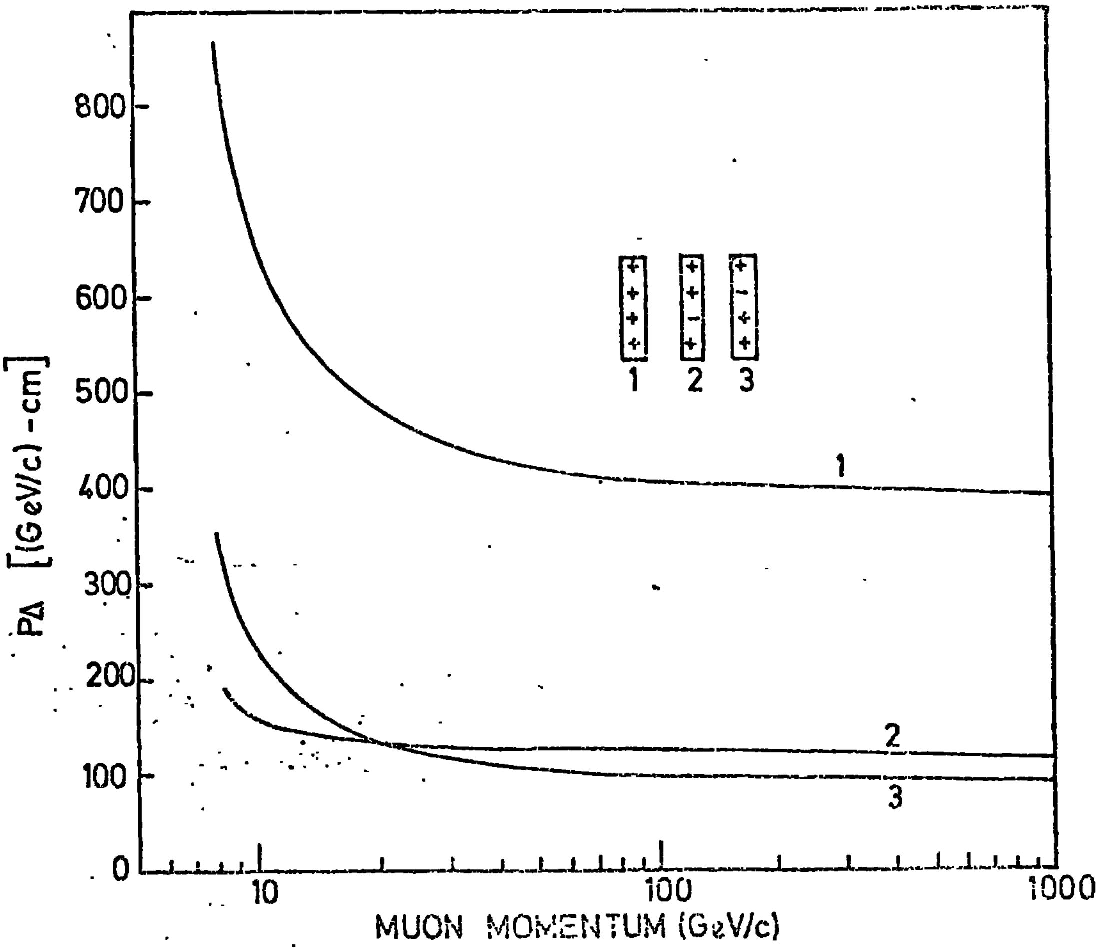

FIGURE:4·9 PΔ RELATION VERSUS MOMENTUM

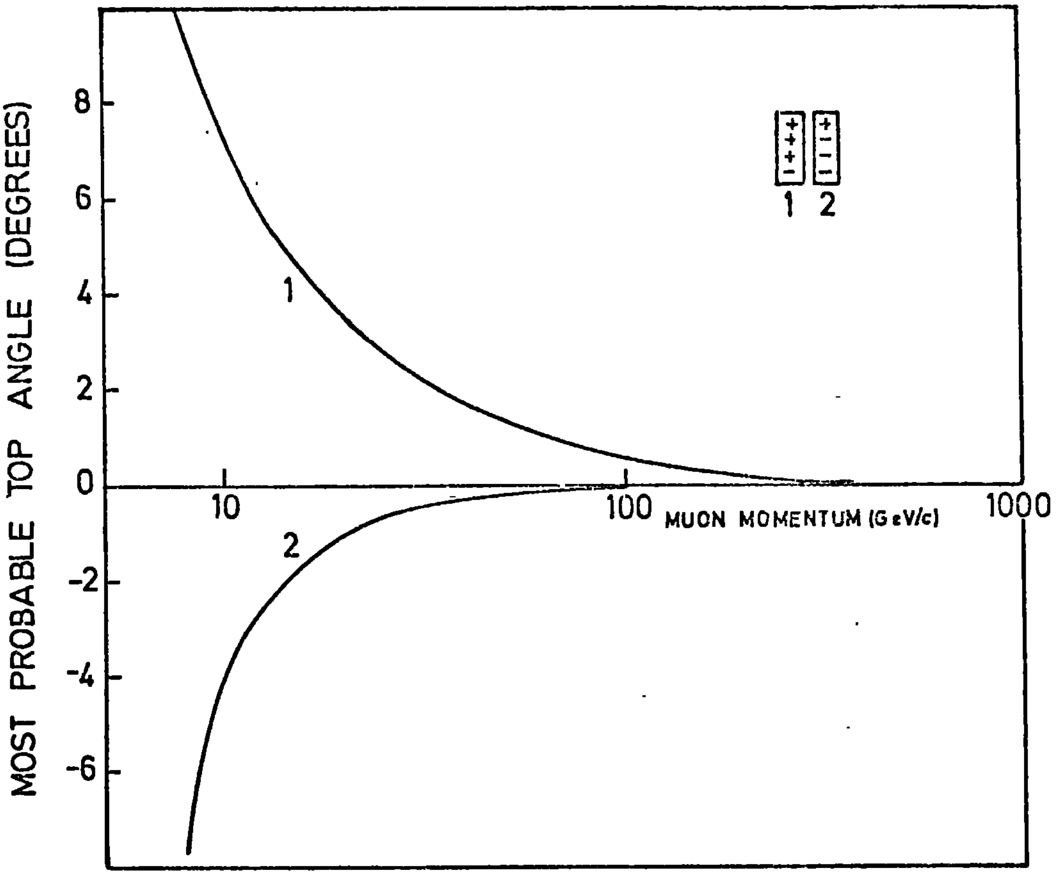

FIGURE: 4·10. MOST PROBABLE ANGLE VERSUS MOMENTUM

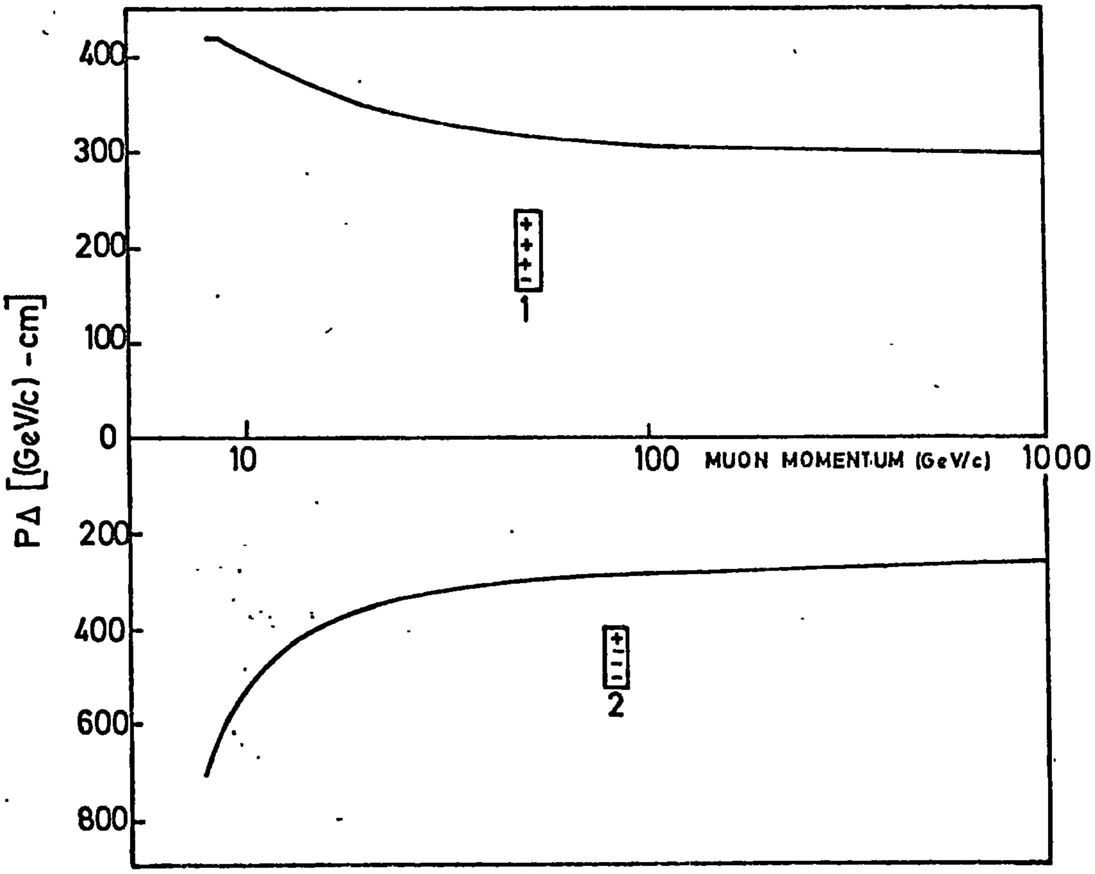

FIGURE: 4·11. PΔ RELATION VERSUS MOMENTUM

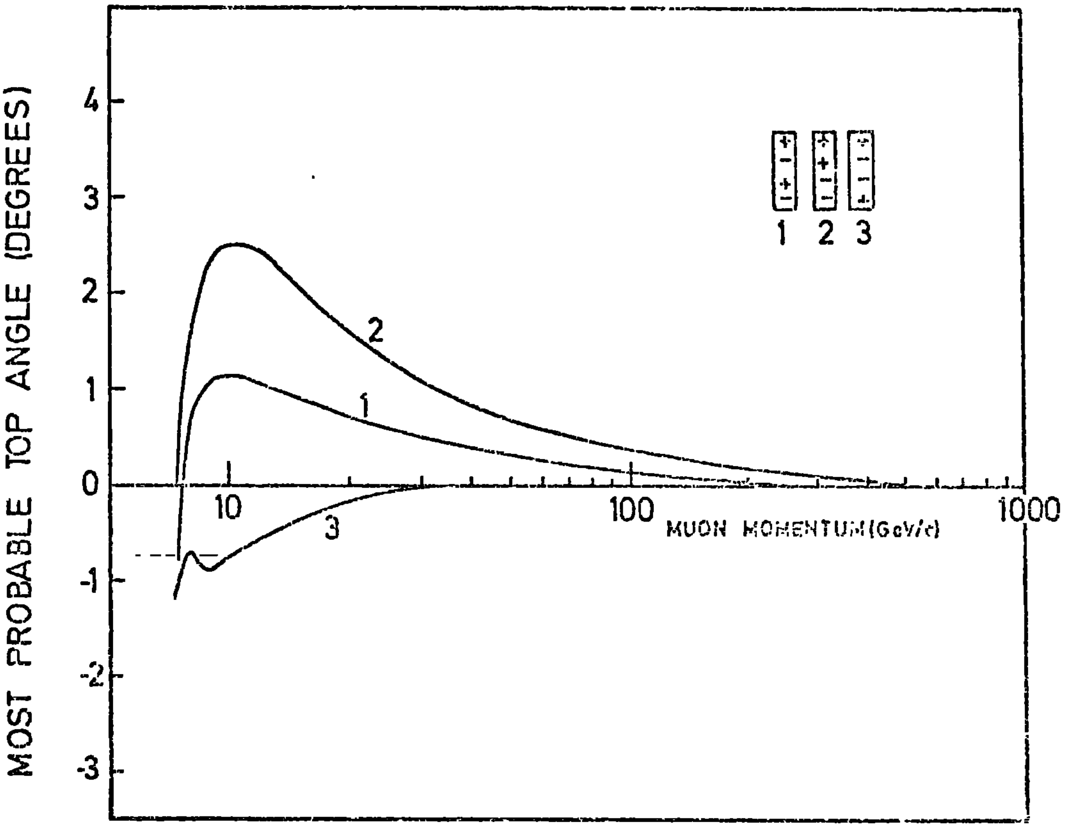

FIGURE: 4.12. MOST PROBABLE ANGLE VERSUS MOMENTUM

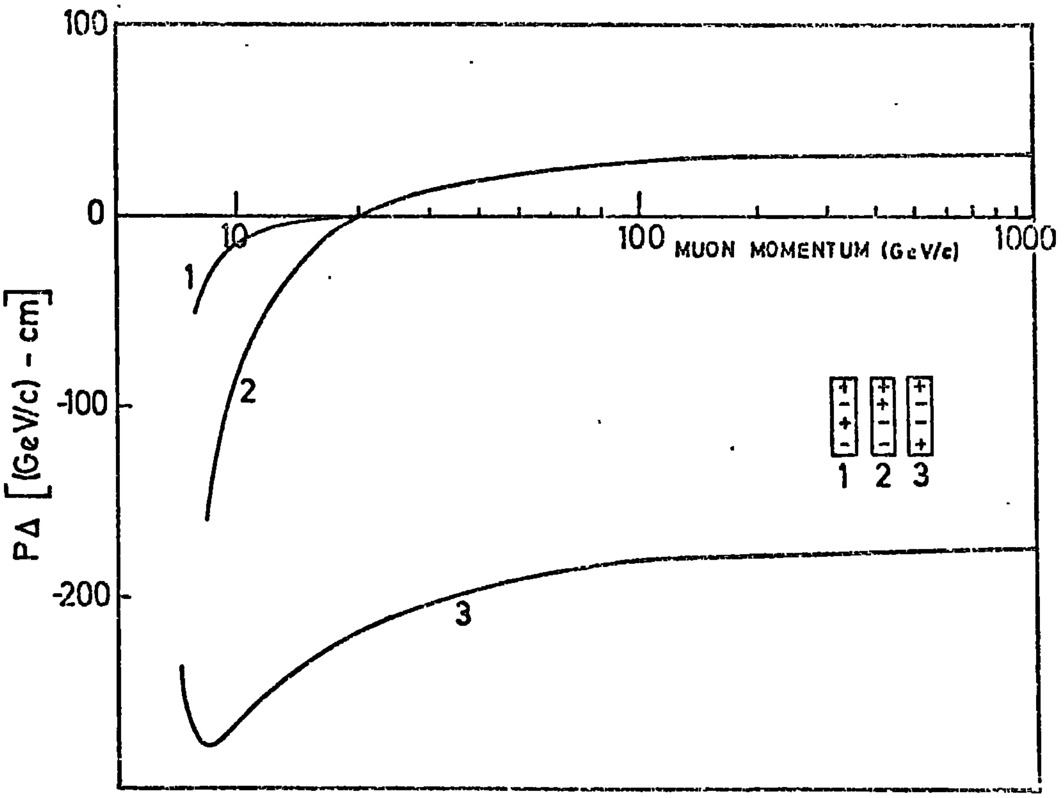

FIGURE: 4.13. PΔ RELATION VERSUS MOMENTUM

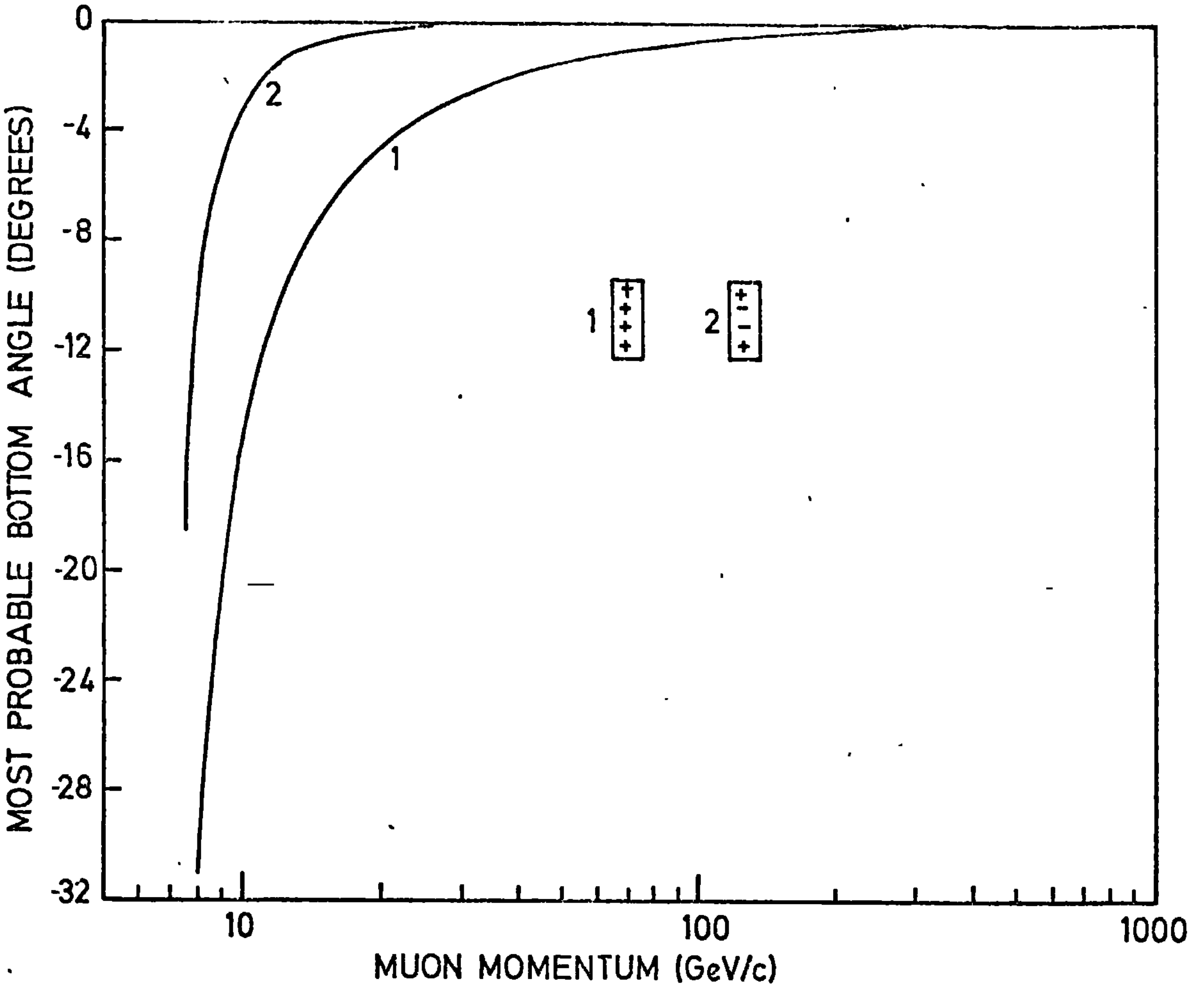

FIGURE: 4.14. MOST PROBABLE ANGLE VERSUS MOMENTUM

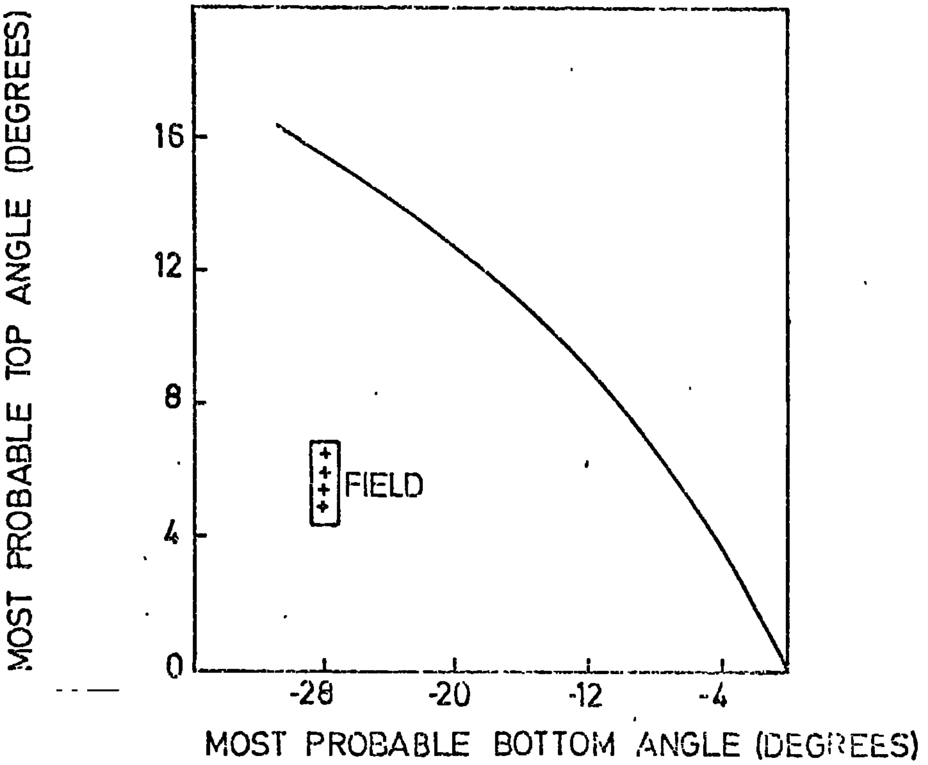

FIGURE 4·15. MOST PROBABLE ANGLES IN TOP & BOTTOM TRAYS

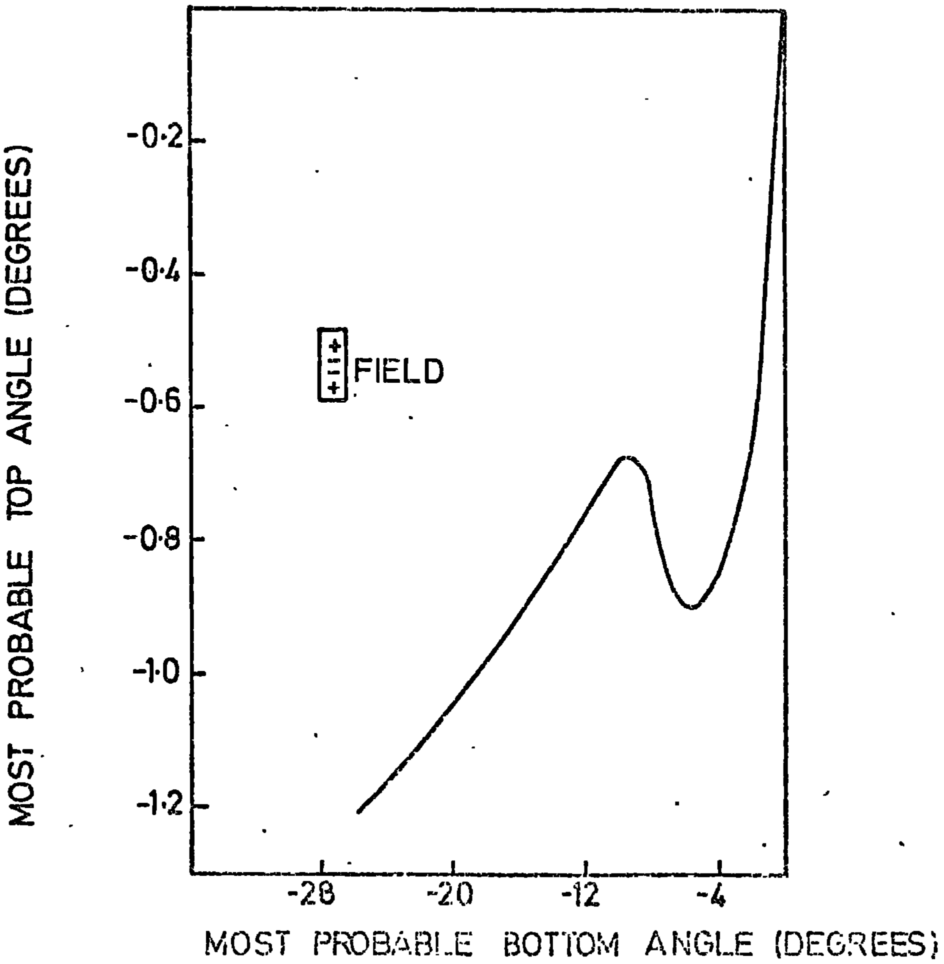

FIGURE 4·16. MOST PROBABLE ANGLES IN TOP & BOTTOM TRAYS

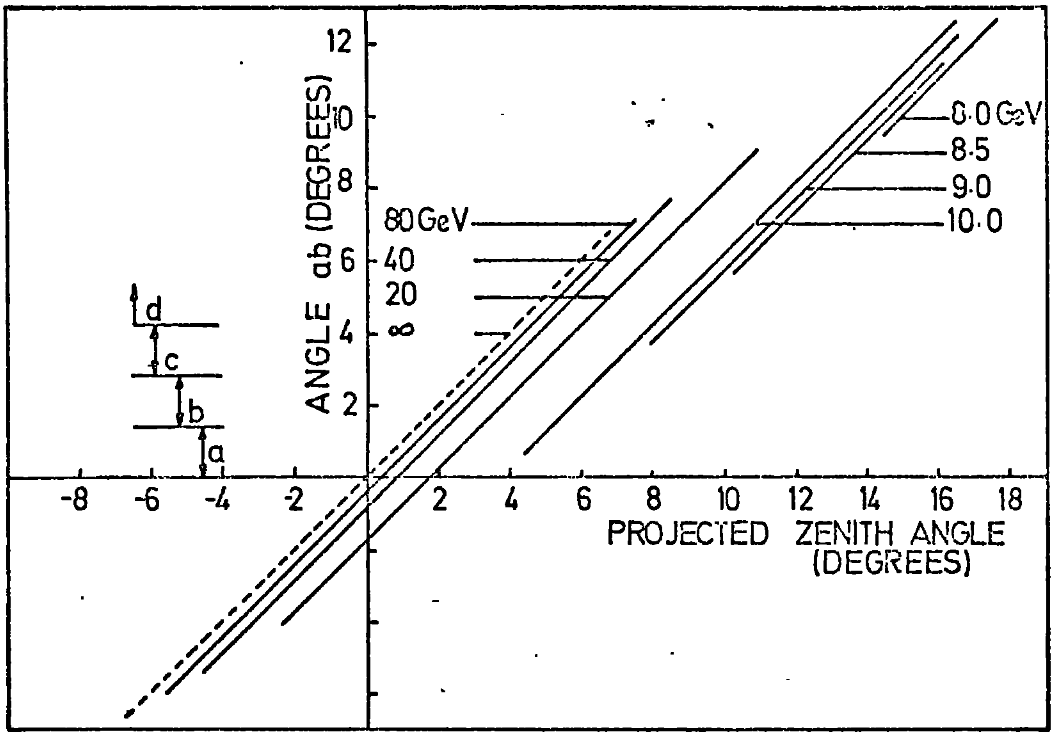

FIGURE: 4.17a. ZENITH ANGLES FOR CONVENTIONAL FIELD

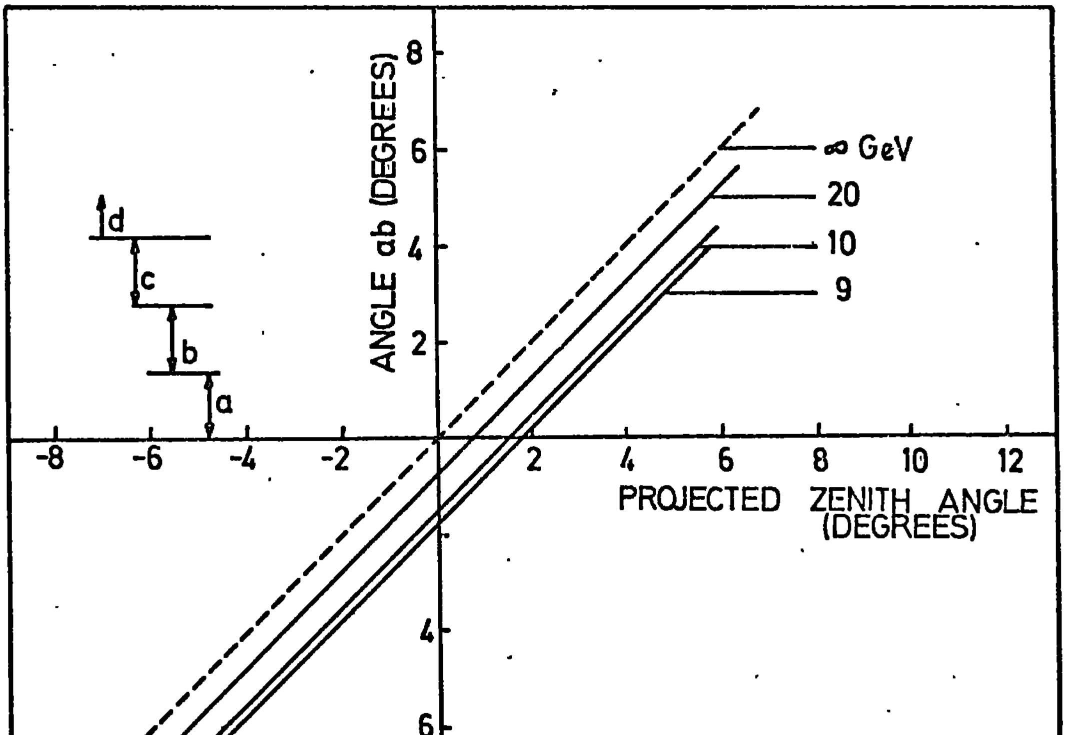

FIGURE: 4.17b. ZENITH ANGLES FOR CROSSED FIELD of infinite momentum.

The computer programme has also been used to derive the relation between momentum and deflection. The deflection (Δ) is given by

$$\Delta = x + Z - 2y + (1 - l_2/l_1)(y - x)$$

where x, y and Z are the track positions at the upper, middle and lower momentum trays respectively; and l_1 and l_2 are the lengths of the upper and lower arms of the spectrograph. By simulating the passage of particles of known momentum (P) incident at the appropriate most probable angle this deflection has been found and the product $P\Delta$ calculated. The values of $P\Delta$ as a function of P, for the various field combinations are plotted in figures 4.9, 4.11 and 4.13. For the conventional field the expression

$$(P - 4.02)\,\Delta = 384.9 \qquad [P \text{ in GeV/c}, \ \Delta \text{ in cms.}]$$

fits the illustrated curve to within about 2% over the momentum range 500 GeV/c to 20 GeV/c. For the crossed field the expression

$$(P - 3.38)\,\Delta = 176.6 \qquad [P \text{ in GeV/c}, \ \Delta \text{ in cms.}]$$

fits the curve to within about 2% over the momentum range 500 GeV/c to 10 GeV/c.

4.2 The Category Acceptance

By category acceptance is meant the range of deflections which are assigned to a given category. A muon track is assigned, by R.U.D.I. to a category nt defined by

$$n_t = na + nc - 2nb$$

where n represents the cell at the upper (a), middle (b) or lower (c) level to which the muon trajectory has been allocated by the momentum selector celling system. The cells are of width 0.5 cm. The category acceptance has been calculated using a method suggested by Nandi (1972, private communication).

Figure 4.18 shows a schematic diagram of the magnet blocks and momentum selector trays; it is seen that the trajectory positions (x) at levels 3 and 1 are

$$x_3 = x_5 - y_5 \tan \Psi + \delta_1 + \delta_2 + (y_5 - y_2)\Delta\Psi_1 + (y_5 - y_4)\Delta\Psi_2 \qquad \ldots .(4.1)$$

$$x_5 = x_5 - y_{10} \tan \Psi + \delta_1 + \delta_2 + \delta_3 + \delta_4 + (y_{10} - y_2)\Delta\Psi_1 + (y_{10} - y_4)\Delta\Psi_2 + (y_{10} - y_7)\Delta\Psi_3 + (y_{10} - y_9)\Delta\Psi_4 \qquad \ldots .(4.2)$$

From the work of Ashton and Wolfendale (1963) the various angular deflections ($\Delta\Psi$) and linear displacements (δ) are, in the general case, given by

$$\Delta\Psi(P, \alpha, l) = \frac{300B}{\alpha} \ln\left(1 - \alpha l/P\right)$$

and

$$\delta(P, \alpha l) = \frac{300Bl^2}{2P}\left[1 + \tfrac{1}{3}(\alpha l/P) + \tfrac{1}{6}(\alpha l/P)^2 + \tfrac{1}{10}(\alpha l/P)^3 + \cdots\cdots\right]$$

where P (ev) is the momentum of a particle entering a magnet block of length l (gms cm^{-2}); α is the mean energy loss per unit path length in the block (eV cm^{-1}) (assumed constant over the trajectory).

The method adopted is to specify the category number and then to consider a particle of fixed deflection (and hence known momentum using the results of section 4.1). To find the acceptance it is necessary to find the range of zenith angles within which the particle is allocated to the selected category. By specifying the discharged cells (C5 and C3 say) in the upper two momentum selector trays the range of projected zenith angles over which a particle passing through C5 and C3 may be incident is found from equation 4.1. (Defining C5 and C3 also fixes C1, the discharged cell at the lowest level). The range of zenith angles is found by considering particles incident at various positions in the top cell and constraining them to pass through the extremeties of the cell in the middle level. Plotting the maximum and minimum angles as a function of the incident position gives a closed

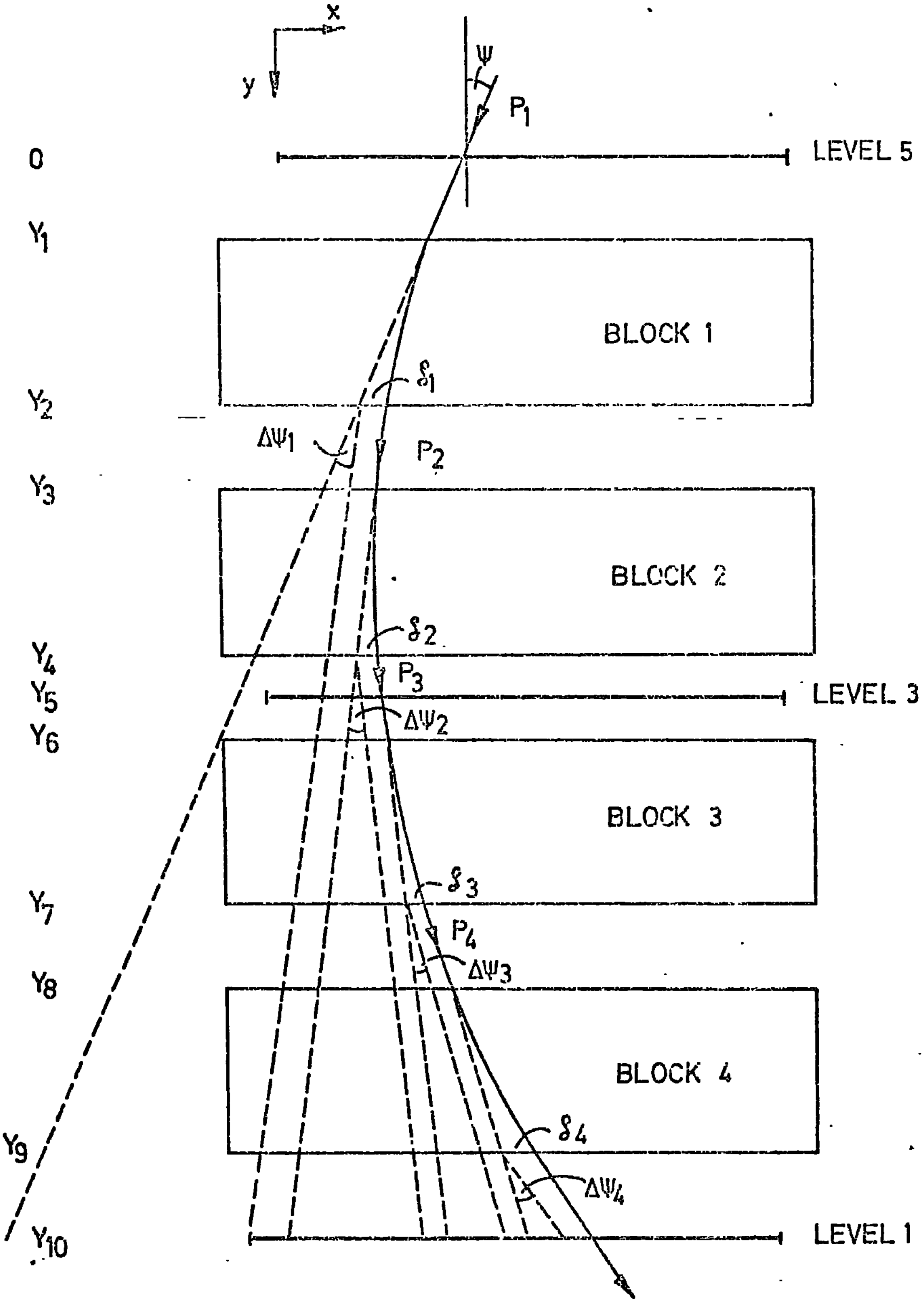

FIGURE: 4·18. MAGNET AND MOMENTUM SELECTOR TRAYS.

curve (a rectangle) whose area is proportional to the acceptance of the top two levels of the magnet. Using the now defined discharged cell in the lowest level an identical procedure using the outer two trays and equation 4.2 yields a second closed curve. The area common to the two closed curves is proportional to the acceptance of the spectrograph for the particle of the selected category number and deflection. This acceptance is then weighted by the the number of possible ways, the same category can be produced by trajectories parallel to the track specified by the positions C5, C3 and C1. The total acceptance for the configuration under consideration is thus produced. The process is repeated for all possible cell configurations leading to the required category. The resulting acceptances are then summed to give the total acceptance for the particular category and deflection.

For category 10 the results of these calculations are shown as the solid curve of figure 4.19. It is seen that the category, although nominally of width 0,5 cm does not have a square acceptance function but contains particles over an approximately 4 cm spread of deflection. The peak of the curve is not at 5.0 cm but is slightly shifted (by 0.07 cm) to a smaller deflection. The shapes of the acceptance curves for other categories are the same as that of category 10. The shifting of the peak from the value (category number + 2) however does increase with decreasing momentum (larger category number); for categories 20, 30 and 40 the shifts are respectively 0.12 cm, 0.16 cm and 0.17 cm. The shift is due to the spectrograph not being perfectly symmetrical.

The results of the above calculations have been checked by simulating, with a computer programme, the passage of particles through the spectrograph. The histogram of figure 4.19 shows the results and the agreement is thought to be adequate for the purposes of this work.

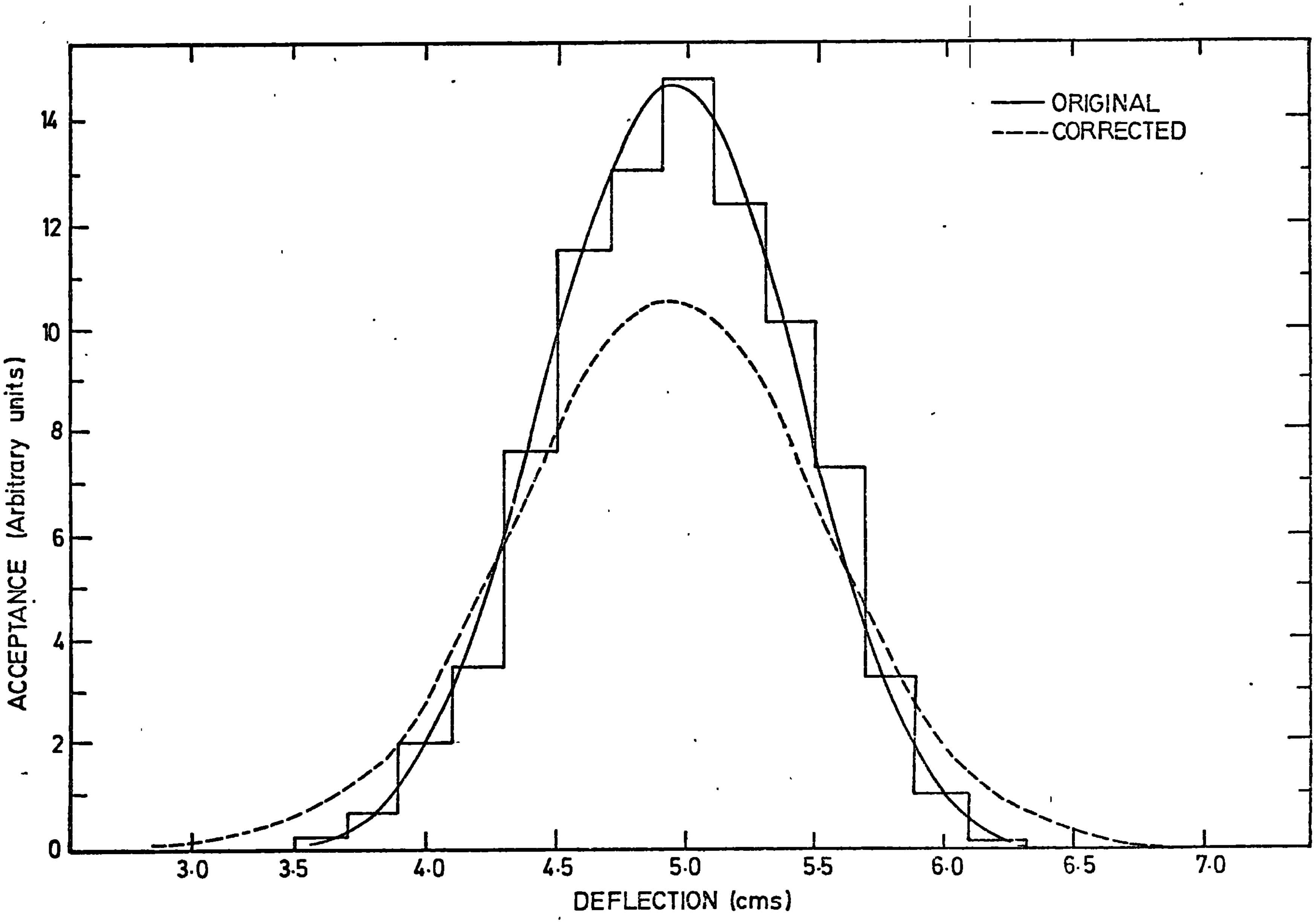

FIGURE: 4·19. ACCEPTANCE CURVE.

In figure 4.18 the conventional magnetic field has been assumed; when the crossed field configuration is considered the shapes of the acceptance curve are not found to be significantly different from that shown in figure 4.19.

Using the curve of figure 4.19, the previously described pΔ relation and the differential momentum spectrum of Allkofer et al (1971) the mean deflection and mean momentum of each 0,5 cm cell category has been found. This gives a mean momentum of category 0 of 680 GeV/c. Adding to the curve of figure 4.19 a curve of identical shape but with peak displaced by 0.5 cm gives the acceptance function for 1.0 cm cell operation. From the appropriate pΔ relations the mean momenta for the categories 0 under conventional and crossed field modes are 520 GeV/c and 200 GeV/c respectively. It should be noted that the acceptance curve of figure 4.19 is that which would be obtained under ideal conditions. There is however the possibility that a trajectory may be allocated to one or more wrong cells at each of the different levels; the reasons for such mis-allocations are:-

(a) The electronic logic performing the celling is not completely efficient. This effect is to some extent momentum dependent and is most serious at low momenta when particles pass through the instrument with large angles.

(b) The flash-tube efficiency is not unity

(c) Knock-on electrons produced in the glass walls of the flash tubes may cause either the wrong cell or in some cases, two cells to be discharged.

(d) Burst production near the bottom of an iron block may give rise to electrons discharging one or more cells.

The effect of (a) on the charge ratio is discussed in chapter 5 and calculations of the efficiency of the celling system are described in section 4.3. In this work no calculations of the effect on the acceptance curves of the above factors have been made. The dashed line of figure 4.19 shows the results of calculations performed by Whalley (1974) in which the effects of (a)-(c) were considered. The effect of (d) is momentum dependent but should be the same for both positive and negative muons and will not be considered further. The broadening of the acceptance function, as indicated by the dashed line, combined with the steepness of the muon differential spectrum causes the mean deflection within a category to increase. The mean momenta of categories 0 for Series 4, 5 and 6, Series-7 and Series 8 became 442 GeV/c, 376 GeV/c and 126 GeV/c respectively. Table 4.1 gives the mean momenta for the various experimental arrangements.

TABLE 4.1. Median Momenta

Category No.	Series 4,5,6 0.5 cm cell Normal Field	Series 7 1.0 cm cell Normal Field	Series 8 1.0 cm cell Crossed Field
0	442 GeV/c	376 GeV/c	126 GeV/c
1	358	236	81.0
2	274	160	68.3
3	214	118	54.7
4	177	93.0	43.5
5	145	76.6	36.8
6	128	65.3	31.8
7	112	57.0	27.8
8	98.3	50.7	25.3
9	88.3	45.8	22.8
10	80.0	41.7	21.1
11	73.7	38.3	19.5
12	67.9	35.3	18.2
13	63.0	33.1	17.0
14	58.9	31.0	16.1
15	55.2	20.3	15.3
16	52.1	27.7	14.5
17	49.3	26.3	13.9
18	47.1	25.1	13.3
19	44.8	24.1	12.8
20	43.8	23.1	12.3
21	40.8	22.1	11.9
22	39.3	21.3	11.5
23	13.9	12.4	9.7

4.3. The Celling System

The efficiency of the logic of the celling system has been found by simulating the logic in a computer programme and determining the response to particles passing through the system at various angles. If a single cell at each level is not allocated to a traversing particle, the event is rejected by R.U.D.I. The probability of a single cell being generated at a level is shown in figure 4.20.

4.4. Other Effects

a) The Number of Discharged Cells. Using the R.U.D.I. cell monitor (Appendix 4) the number of cells discharged at each level has been measured. The results are tabulated below:

mber of lls	% of events having the indicated number of discharged cells					
	Positive Field			Negative Field		
	Top Tray	Middle Tray	Lower Tray	Top Tray	Middle Tray	Lower Tray
	7.5 ± 0.5	3.0 ± 0.3	12.0 ± 0.8	7.5 ± 0.5	2.1 ± 0.3	11.6 ± 0.7
	84.4 1.6	88.0 0.5	77.0 0.5	84.1 1.5	88.1 0.5	78.6 1.5
	6.0 0.6	5.3 0.4	7.8 0.5	6.7 0.6	5.7 0.4	7.6 0.4
	0.7 0.2	1.3 0.2	1.7 0.3	1.0 0.2	1.4 0.3	1.2 0.3
	0.3 0.1	0.8 0.2	0.5 0.1	0.3 0.1	0.6 0.2	0.5 0.1
	0.9 0.2	0.6 0.2	0.7 0.2	1.5 0.2	0.6 0.2	0.7 0.2

) The Distribution of Discharged Cells Across a Tray. The cell monitor has also been used to find, at a given level of the spectrograph, which cell has been discharged. The cells have been considered in groups of four (equivalent to one flash tube spacing). There are 38 such groups across a tray but the last is neglected since it contains only 3 cells. Neglecting any extreme edge effects it would be expected that within a group the position of the cell containing the maximum number of measured events would be randomly distributed. The positions of the maximum cells have been plotted in figure 4.21. The two magnetic field directions have been considered separately and the upper graph in each

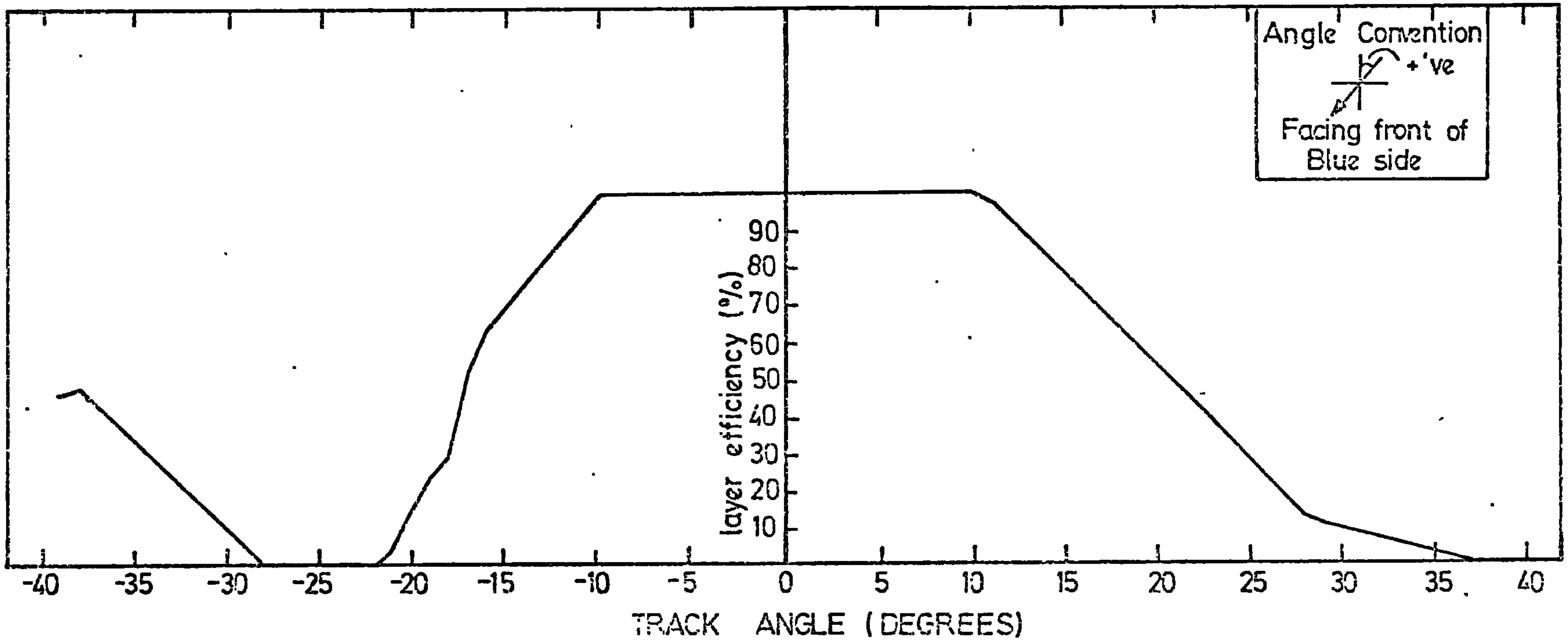

FIGURE: 4.20 CELLING EFFICIENCY

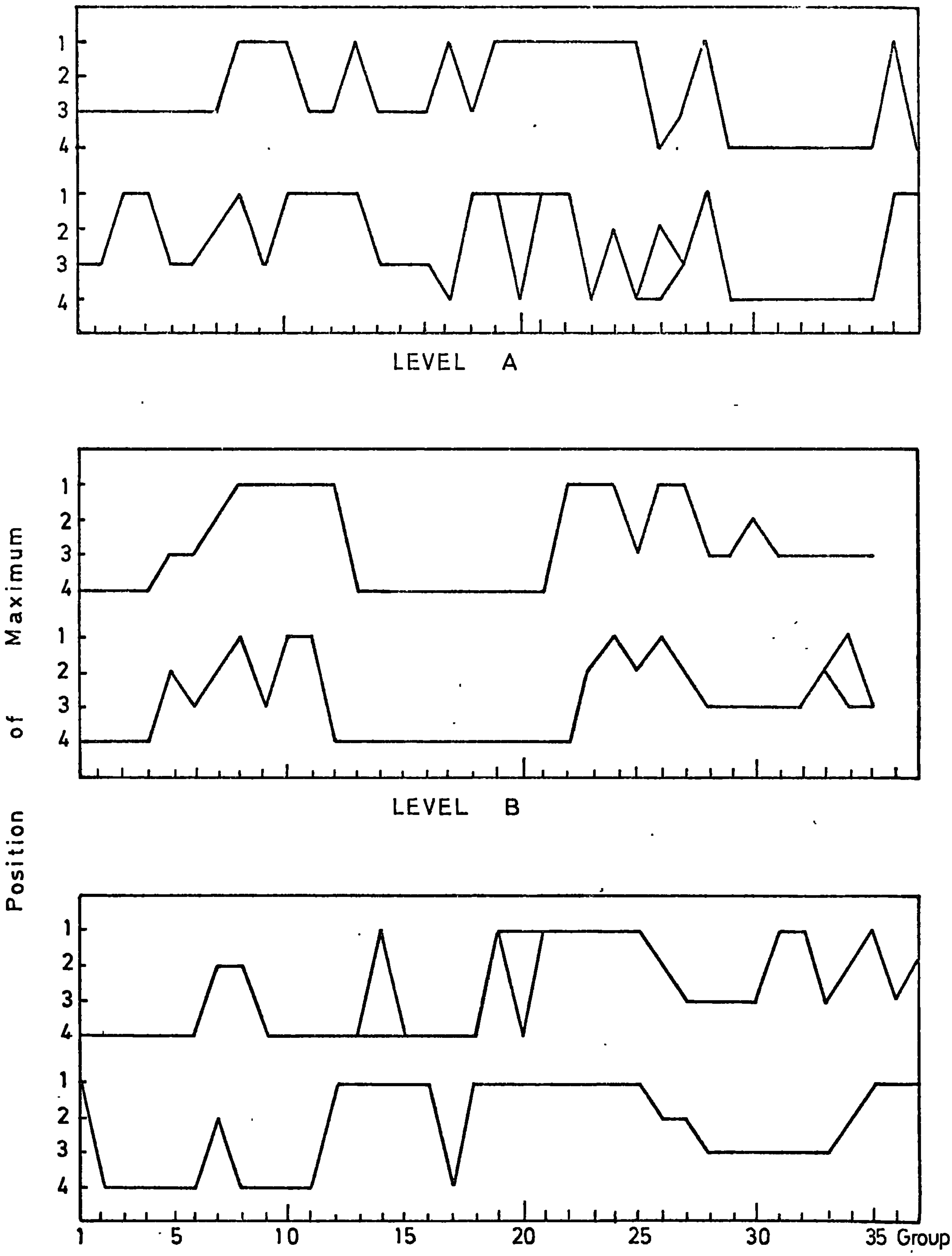

FIGURE: 4.21 MAXIMUM CELLS

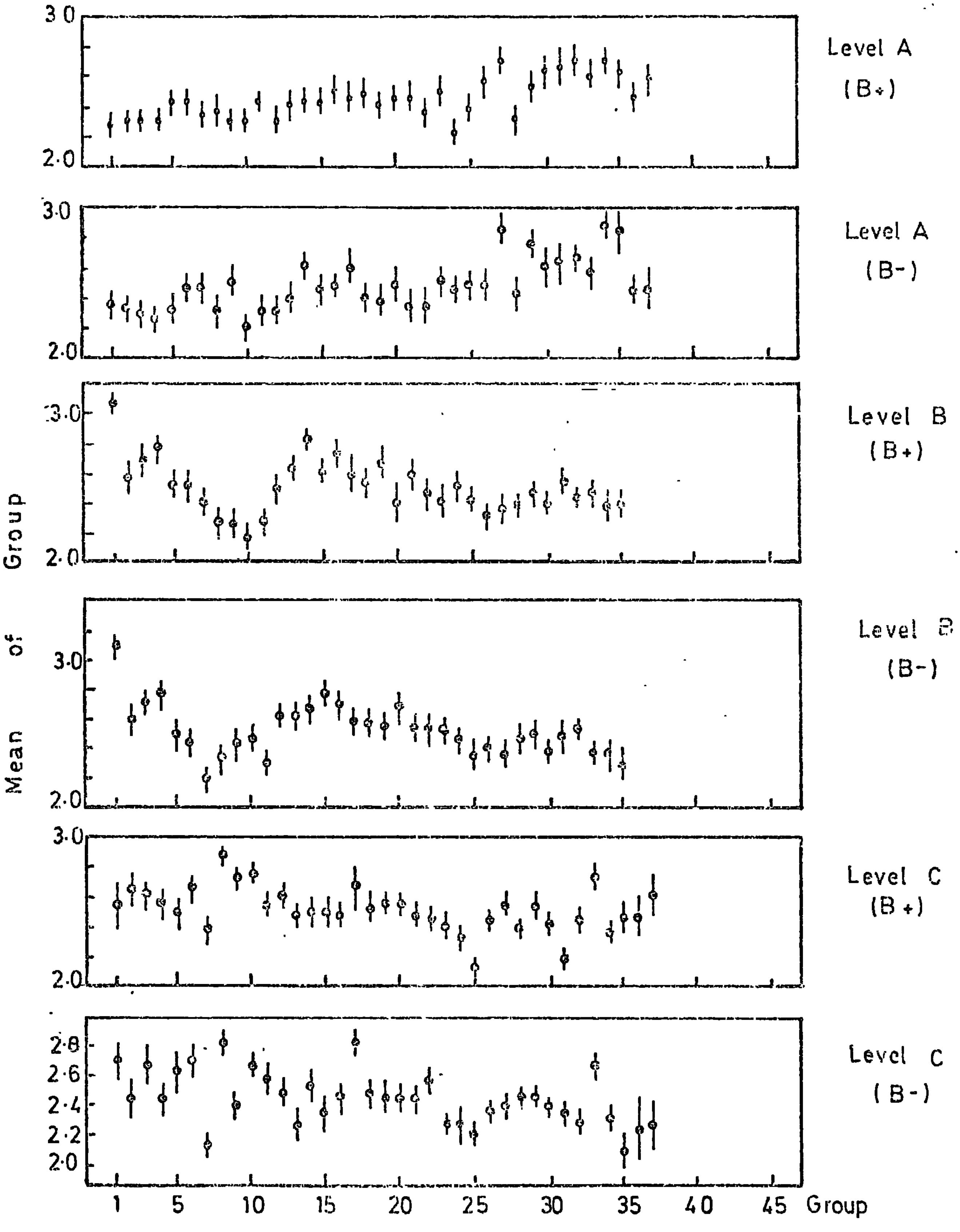

FIGURE 4.22 MEANS OF CELL GROUPS

case is for the positive magnetic field. It can be seen that, particularly for the lower two levels there are large sections of the tray where the maximum cell lies in the same position. In figure 4.20 some groups have a maximum cell appearing in two positions, this means that there were equal numbers in the two positions.

This effect is interesting but unexplained. The slow, systematic variation of the effect is shown in figure 4.22. In this case the distribution of events within a group has been treated as a histogram and it is the position of the mean that is plotted in figure 4.22. The error flags represent the standard error of the mean. If the distribution within a group were uniform the value of the mean would be 2.5. The deviations from this value are seen to be systematic and do not seem to depend on field direction. This latter point does not support the suggestion that the phenomenon is due to the effect of the magnetic field on the integrated circuit blocks.

These measurements have also been used to locate 'dead' cells i.e. cells which have never been discharged because of some fault in the circuitry.

c) Pairing of the Data This is mentioned in chapter 5 and illustrated in figure 5.9. The effect is unexplained.

CHAPTER 5

THE DATA

5.0 Introduction

This chapter contains a tabulation of the basic data obtained from R.U.D.I. The charge ratio data are examined for biases.

5.1 The Data

Data collection using R.U.D.I. was performed in a series of 'runs'; each run represents a period of continual operation of the spectrograph. A typical run commenced at 1800 hours and was terminated at 0900 hours the next day. In an attempt to minimise any bias effects due to assymetries in the magnetic field the direction of the magnetic field was reversed regularly. Some bias due to this cause was found.

Corresponding to particular modes of operation of R.U.D.I. and/or the spectrograph a number of runs have been grouped together to form a Series. At present (July 1973) 8 Series have been completed.

The results of Series 1, 2, 3 and 4 have been reported previously (Ayre et al (1972)). The results reported in this work are those of Series 4, 5, 6, 7 and 8 and have been reported by Ayre et al (1973a, 1973b). Since Series 4 forms only a small fraction of the later data the two sets may be considered independent.

Series 4, 5 and 6 were obtained under identical modes of operation (0.5 cm. cells and conventional magnetic field) and have been summed together. Series 7 data were obtained using 1.0 cm. cells and conventional magnetic field. Series 8 data were obtained using 1.0 cm. cells and 'crossed' magnetic fields (in which the field direction in the centre two blocks of the magnet was in the opposite direction to that of the outer two blocks).

The data are given in tables 5.1 - 5.3. Because of the above mentioned bias due to magnetic field direction the data have been presented separately for each direction. The apparent arrival direction is simply the East or West direction indicated by the discharged cells in the top two trays. In part (iii) of each table the bracketed values are those obtained after correcting for events in which the particle sign was wrongly determined. These bracketed values have been used in calculating the charge ratios and excesses.

In the remaining tables (5.4 - 5.6) the data summed over both field directions are given. The charge ratio and its error were calculated using the relation

$$R = N_+/N_- \pm R(1/N_+ + 1/N_-)^{\frac{1}{2}}$$

the charge excess (δ) and its error were found using the relation

$$\delta = (N_+ - N_-)/(N_+ + N_-) \pm (2/(N_+ + N_-)^2).(N_-N_+^2 + N_-^2N_+)^{\frac{1}{2}}$$

where N+ and N- refer to the numbers of positive and negative muons. The derivation of the errors of R and δ is discussed in Appendix 1.

The values of N+ and N- have been obtained by simply summing the data from both magnetic field directions. It can be shown however that the best estimate of R is obtained not by such a summation but by using the quantity $R = \sqrt{R_+ R_-}$ where R_+ and R_- are the charge ratios observed for positive and negative fields respectively. This is discussed in Appendix 1. In the case of the data in tables 5.1 - 5.3 this latter representation gives a value of R which is negligibly different (typically 0.3%) from that obtained by summation. Consequently the summation method has been used. The given values of δ have been calculated from the summations; in Appendix 1 it is shown that the best estimate of δ is indeed obtained by such a summation and not by the geometric mean as in the case of R.

5.2 Experimentally Observed Biases in the Charge Ratio

The most significant bias on the charge ratio measurements that has (so far) been detected is that of the effect of magnetic field direction. The measured ratios for the positive and negative field directions of each Series have been plotted in fig 5.1. The data have been summed over several cells as shown in order that the error bars may be a reasonable size. The most important feature of each of these graphs is the difference between the ratios of category 23 for the two field directions. For Series' 4, 5, 6 and Series 7 the negative field yields the higher ratio while the situation is reversed for Series 8. For Series' 4, 5, 6, Series 7 and Series 8 the separations are ± (4.7 ± 0.2)%, ± (5.9 ± 0.5)% and ± (2.1 ± 0.7)% from the mean ratio obtained by summing over both field directions.

The cause of this separation has been found by consideration of the angles made by the muon tracks in the momentum selector trays. Considering Series 4, 5, 6, figs 5.2 a, b show the charge ratios of those muons having similar trajectories through the magnet. For example a positive muon incident from a Westerly direction when the magnetic field is positive has a similar trajectory to a negative muon from the same direction when the magnetic field is in the negative direction; the numbers of these muons have been denoted by $\mu^+ WB^+$ and $\mu^- WB^-$ respectively. The same convention is used for other trajectories. In fig 5.2a two sets of ratios have been plotted. Account was taken of the fact that the data collection was not equally divided between positive and negative magnetic fields by using a normalization procedure. Before calculating the ratios plotted, the total number of particles gathered with a positive field was normalized to that gathered with a negative field. Compared to the ratio using the un-normalized data the change in the ratio is small(0.01 in the absolute value of the ratio). In fig 5.2a

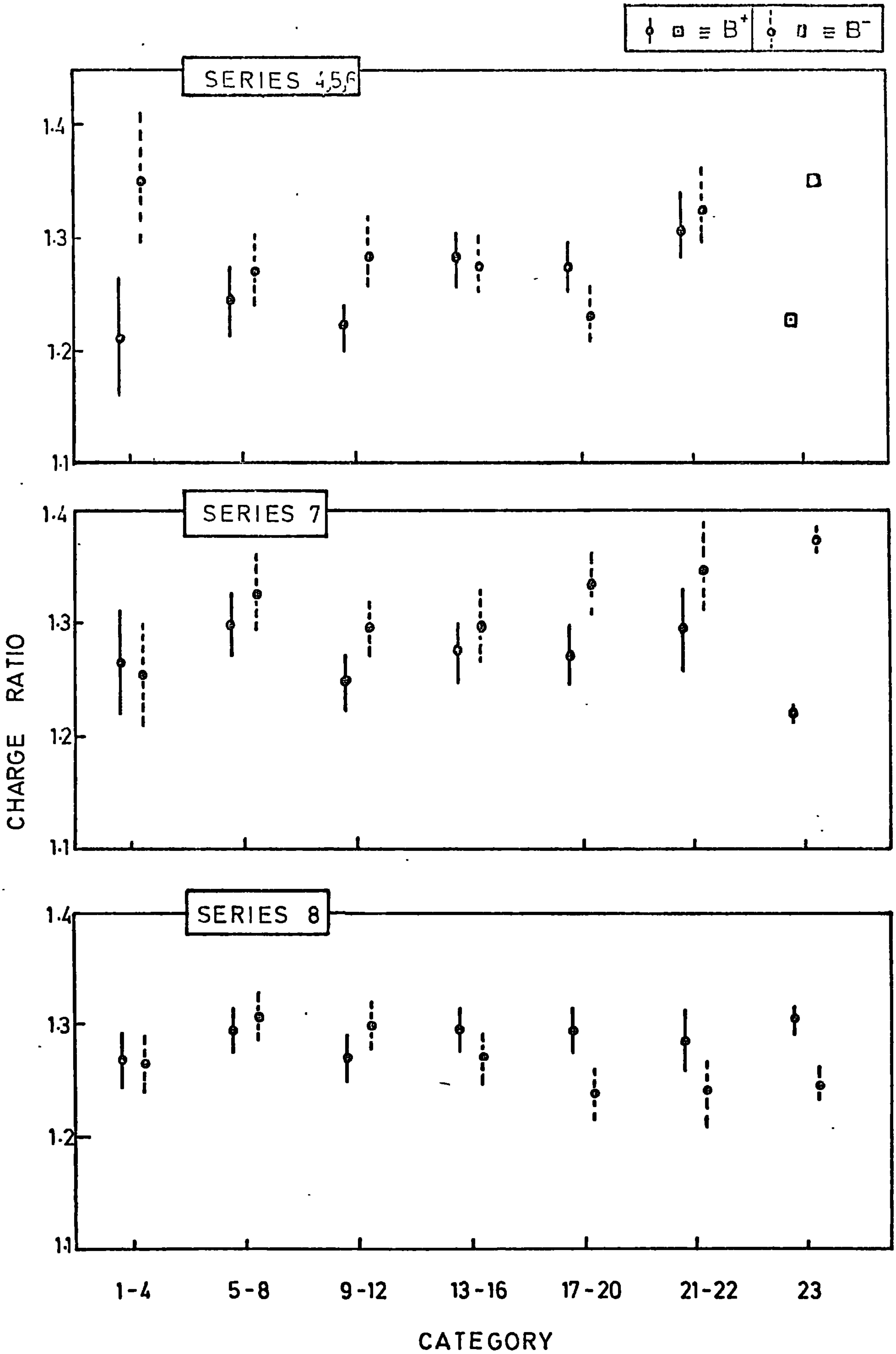

FIGURE:5·1. CHARGE RATIOS FOR B⁺ AND B⁻

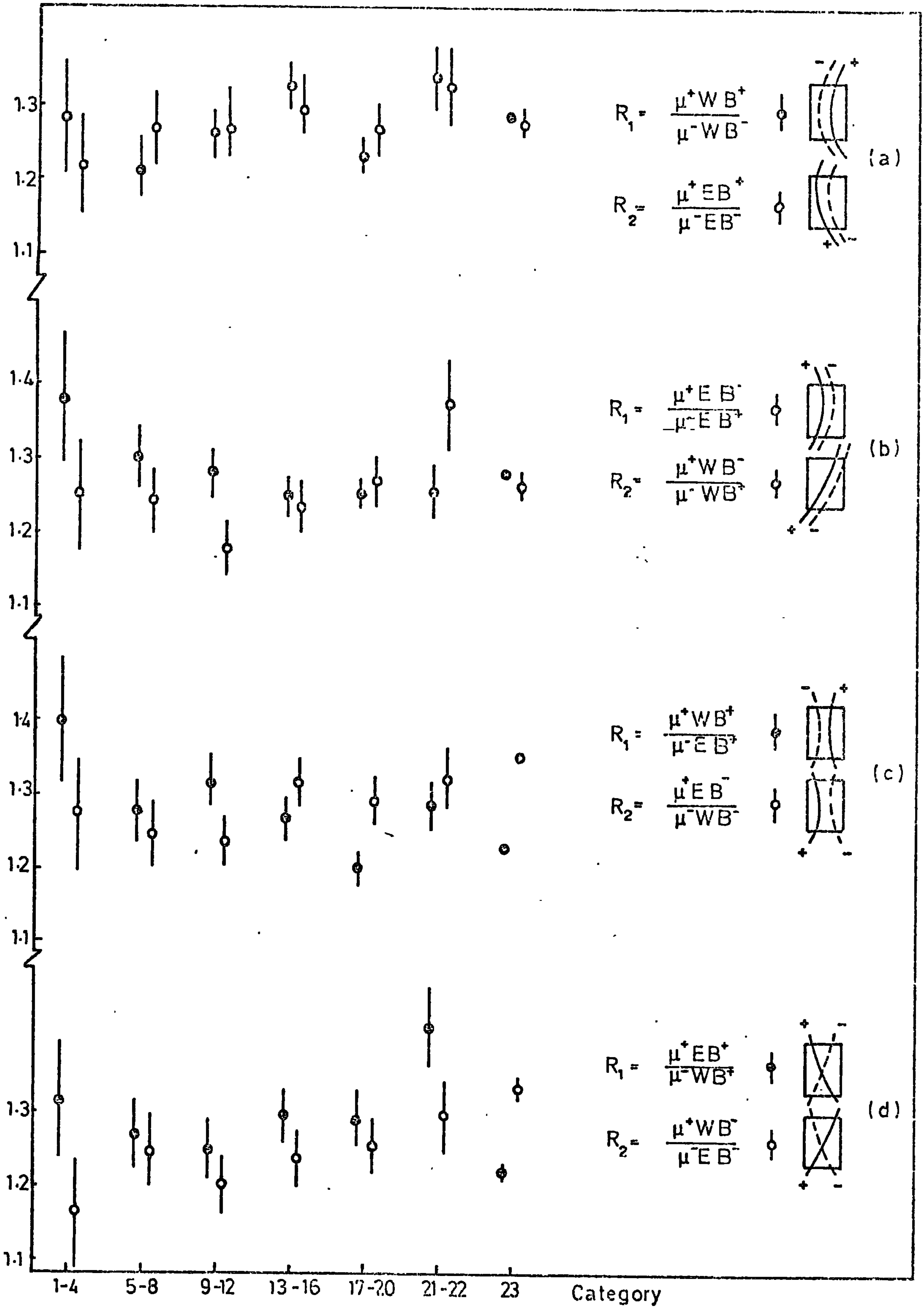

FIGURE 5.2. SERIES 4,5 & 6

the trajectories involved have the common feature that the angles in the bottom tray are, at least for those particles in category 23, predominantly positive. For higher momenta (lower category numbers) the contribution of non-positive angles in the lower tray to the ratio R_1 will increase. It can be seen from fig 5.2a that the ratios obtained by selecting similar trajectories are in good agreement and this also applies to fig 5.2b which shows the ratio for trajectories involving mainly negative angles in the bottom tray. Figures 5.2c, d show the ratios found with dissimilar trajectories. The large discrepancy observed between the category 23 ratios is due to the differing efficiencies of cell allocation for positive and negative angles.

As shown in Chapter 4 the probability of a single cell being allocated to a track is somewhat higher for positive angles (θ) such that $10^\circ < \theta \lesssim 30^\circ$. It has also been shown that the most probable angle (which is close to the median) is, in the bottom tray, $> 10^\circ$ for momenta $\lesssim$ 12 GeV/c. Hence for these momenta some difference in detection efficiency is to be expected.

Consider now the ratio R_1 of fig 5.2c. The positive particles are incident in the top tray at a positive angle and hence have a higher detection efficiency relative to the negative particles which are incident at negative angles. At the bottom tray the situation is reversed- the negative particle which is now moving at a positive angle has the higher detection efficiency. The overall efficiency of detection is taken as the product of the efficiencies at the top and bottom levels; the middle level will be neglected. As shown in Chapter 4 the median angle in the bottom tray is generally larger than that in the top and since the rate of fall of efficiency with angle is greater in the negative direction the overall efficiency is lower for the particle that moves at a negative angle in the lower tray - the positive particle in this case. The relative loss of positive particles results in a reduction in the charge ratio. For the ratio R_2 of Fig 5.2c identical reasoning leads to a loss of negative muons and an increase in the ratio. These features are shown by the data. Similar arguments may be used to explain the ratios of category 23 of fig 5.2d.

The data of Series 7 (plotted in figs 5.3 a-d) exhibits similar behaviour to that of Series 4, 5, 6. The major difference is that the splitting of the ratios of category 23 is rather larger. The median momentum of this category is lower than for Series 4, 5, 6 and since the difference between positive and negative particle detection efficiencies increases with increasing angles then a larger splitting would be expected.

A more quantitative estimate of this effect of differing efficiencies has been obtained for Series 4, 5, 6 and Series 7 as follows. For a fixed magnetic field direction (positive) the mean angles in the top and bottom trays, as a function of momentum, were found (by calculating the acceptance as a function of angle). These angles are denoted $\hat{\theta}_t$ and $\hat{\theta}_b$. Dependent upon the sign of muon the values of θ_t and θ_b may be positive or negative; for example in the case of a positive muon of energy say, 10 GeV, $\hat{\theta}_t$ and $\hat{\theta}_b$ are positive and negative respectively (assuming the same sign convention of Chapter 4). From the graph of detection efficiency as a function of angle (Chapter 4) the corresponding efficiencies were obtained and are plotted in figs 5.5 a, b. The probability of a single but incorrect cell being generated is rather small and has been neglected. Beyond about 15 GeV/c both $\hat{\theta}_t$ and $\hat{\theta}_b$ are less than 10° and the detection efficiency is unity. The overall detection efficiency is taken to be the product of the top and bottom tray efficiencies. In the case of the example above, the overall efficiency is the product of the top efficiency (θ_t positive) and the bottom efficiency (θ_b negative). The results for both types of muon are shown in fig 5.5c.

Using these efficiencies together with the 0.5 cm. cell acceptance curve for category 23, the overall acceptance of the spectrograph as a

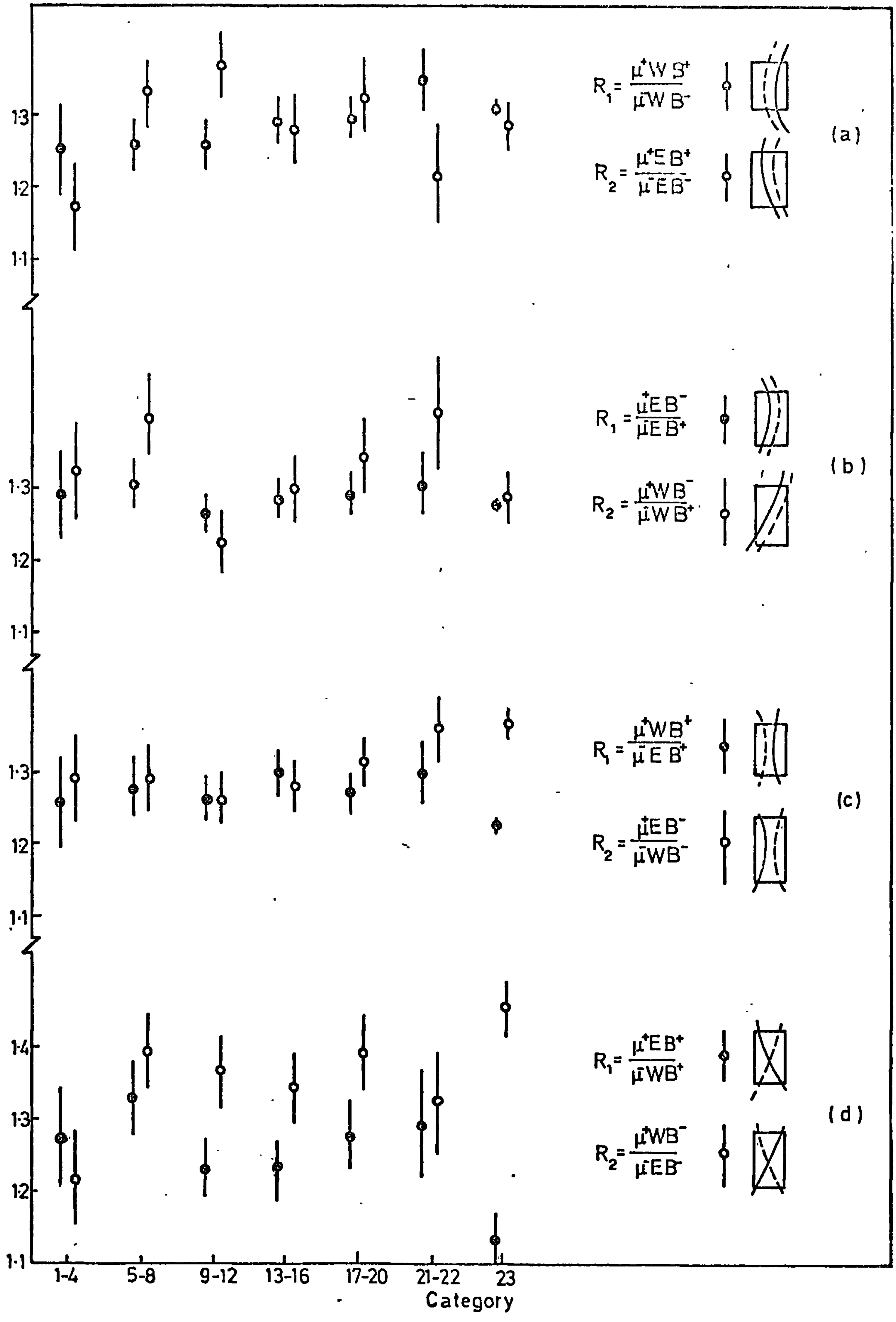

FIGURE: 5·3 SERIES 7

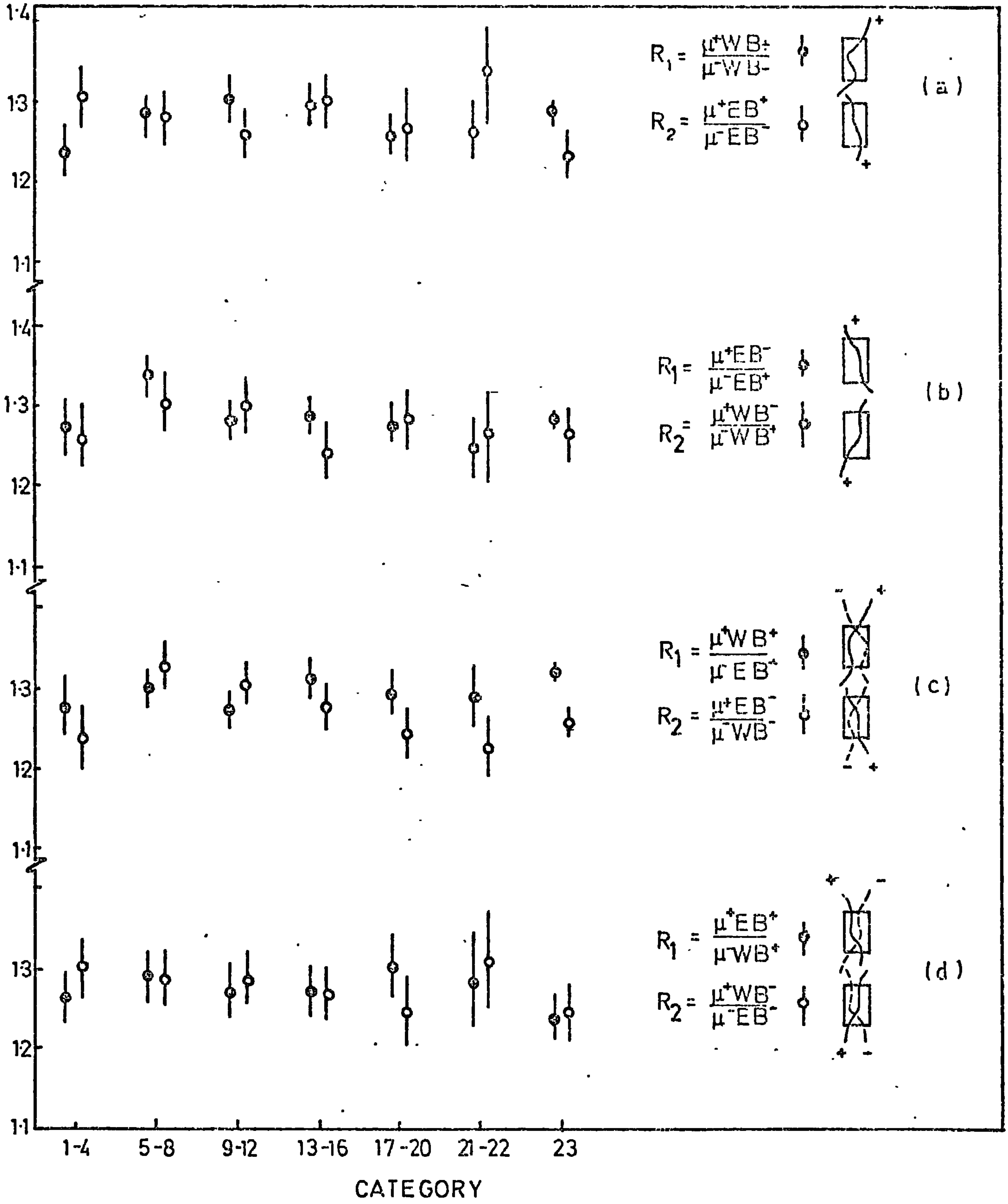

FIGURE: 5·4 SERIES 8

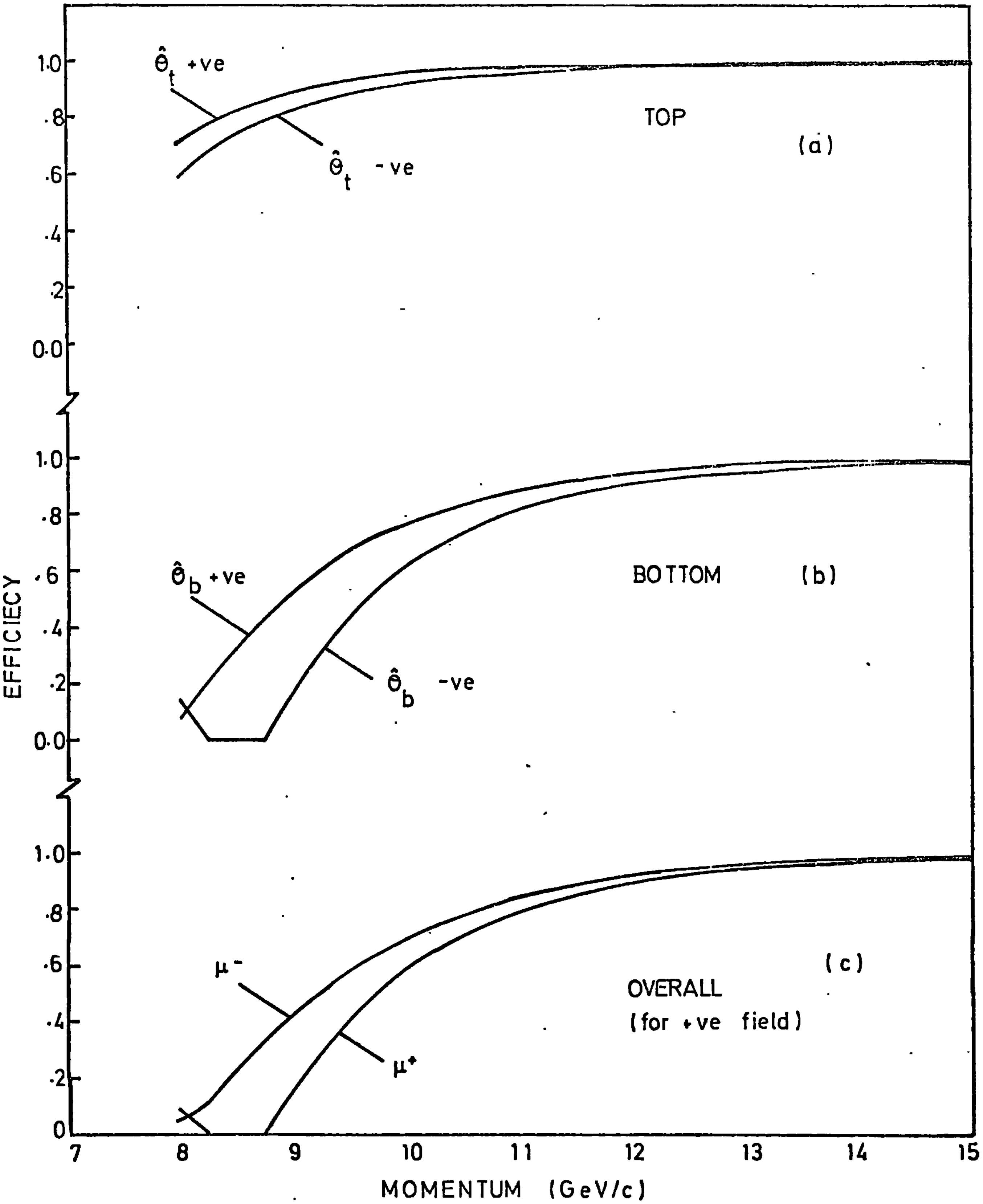

FIGURE:5.5. CONVENTIONAL FIELD EFFICIENCIES function of momentum and assuming an incident muon differential spectrum (Allkofer et al (1971)) the momentum distribution of particles in category 23 was calculated. A charge ratio of 1.0 was assumed. Integrating over momentum gives the ratio of each kind of particle to be μ^-/μ^+ = 1.043 thus indicating a reduction in the true charge ratio of 4.3%. Taking the true ratio as that obtained by summing the data over both field directions this figure is in good agreement with the observed (4.7 ± 0.2)%.

To obtain the equivalent figure for the Series 7 data the only change to the above procedure is the use of the 1 cm. cell acceptance for category 23. The results of this calculation indicate a reduction in the charge ratio of 5.9%. This is in excellent agreement with the observed value of (5.9 ± 0.5)%.

Turning now to Series 8, the charge ratios of category 23 are found to deviate by ± (2.1 ± 0.7)% from the mean. The rather small splitting is qualitatively understandable since with this magnetic field configuration the angles of particle tracks are not as extreme as in the conventional case. This leads to a higher overall detection efficiency for both signs of particles and consequently a closer approach to the true ratio. The splitting of this Series is in the opposite direction to that of the previous cases. It should be remembered however that the 'positive' and 'negative' momenclature describes the field direction in only the centre two magnet blocks.

Figures 5.4 a-d show the charge ratio for the various trajectories. Excluding category 23 the ratios for both similar (fig 5.4 a, b) and dissimilar (fig 5.4 c, d) trajectories are in good agreement; within the error bars there are no obvious systematic trends. In the case of category 23 the situation is less clear. Firstly, the splitting seen in fig 5.4 a is larger than that in 5.4 b and secondly fig 5.4 c shows a large splitting as may be expected but fig 5.4 d shows no such effect.

At present, neither of these details is understood but a possible explanation is that they are statistical fluctuations.

A descriptive explanation of the splitting shown in fig 5.4 c can be obtained by considering fig 5.6 in which some typical particle trajectories are shown. The diagrams are schematic only and represent the tracks of particles of momenta $\lesssim 8$ GeV/c. Figure 5.6 a shows the paths of those particles forming the ratio R_1 of fig 5.4 c. The large deflection suffered by the particle in the last magnet block is due to the fact that it has lost a large fraction of its energy in passing through the upper blocks. It can be seen that positive and negative particles emerge at positive and negative angles respectively and since the detection efficiency is highest at positive angles the resulting charge ratio R_1 is enhanced. Figure 5.6 b shows those tracks forming R_2 of fig 5.4 c. Here the situation is reversed and negative muons have the higher detection efficiency resulting in a depressed charge ratio.

A more qualitative measure of this effect has been made in a similar manner to that described previously. In this case the range of incident angles under consideration is within the range $\pm 10^\circ$ and the detection efficiencies are unity in the top level. In the bottom tray much larger angles are involved; the mean angles have been calculated and the corresponding efficiencies are plotted in fig 5.7. Beyond about 9 GeV/c there is no difference in the detection efficiencies of positive and negative muons. Using the same procedure as before the expected ratio of the numbers of particles of each kind was found to be 1.043 i.e. with the field direction shown ('positive') the enhancement of the true charge ratio is 4.3%. The agreement with the observed value of $(2.1 \pm 0.7)\%$ is not good and is unexplained; it is rather surprising in view of the results obtained with Series 4, 5, 6 and Series 7. This may be an indication of some effect which is, as yet, undetected. Since the difference between the observed and expected values is reasonably

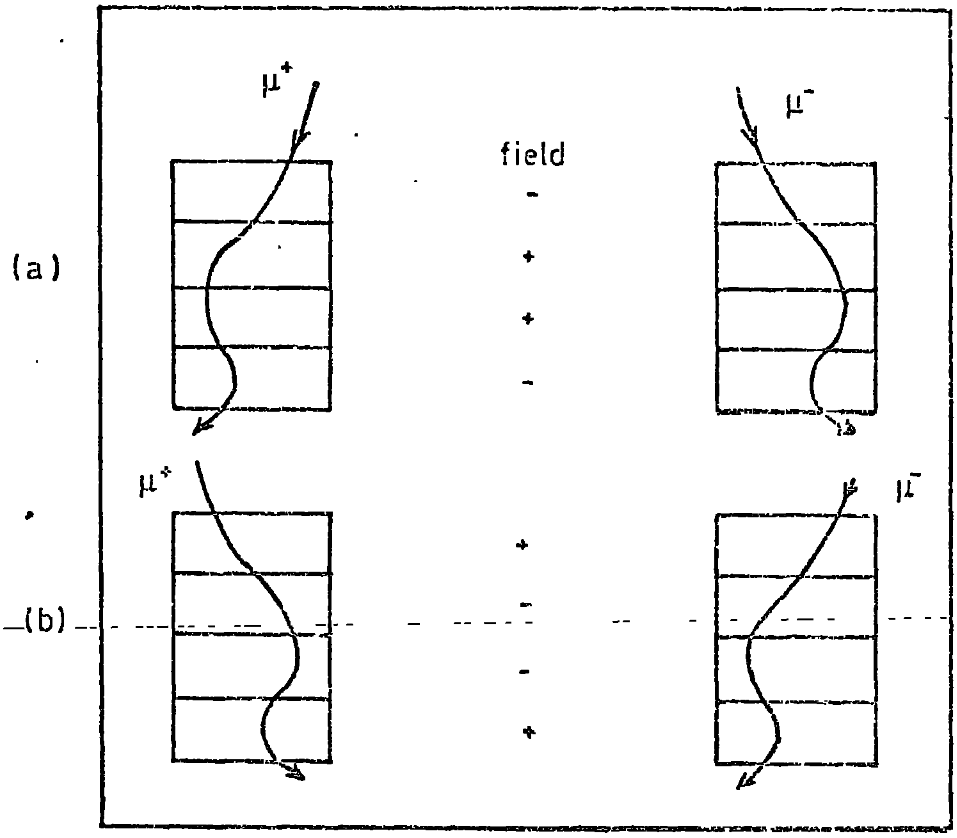

FIGURE:5·6. TYPICAL TRACKS

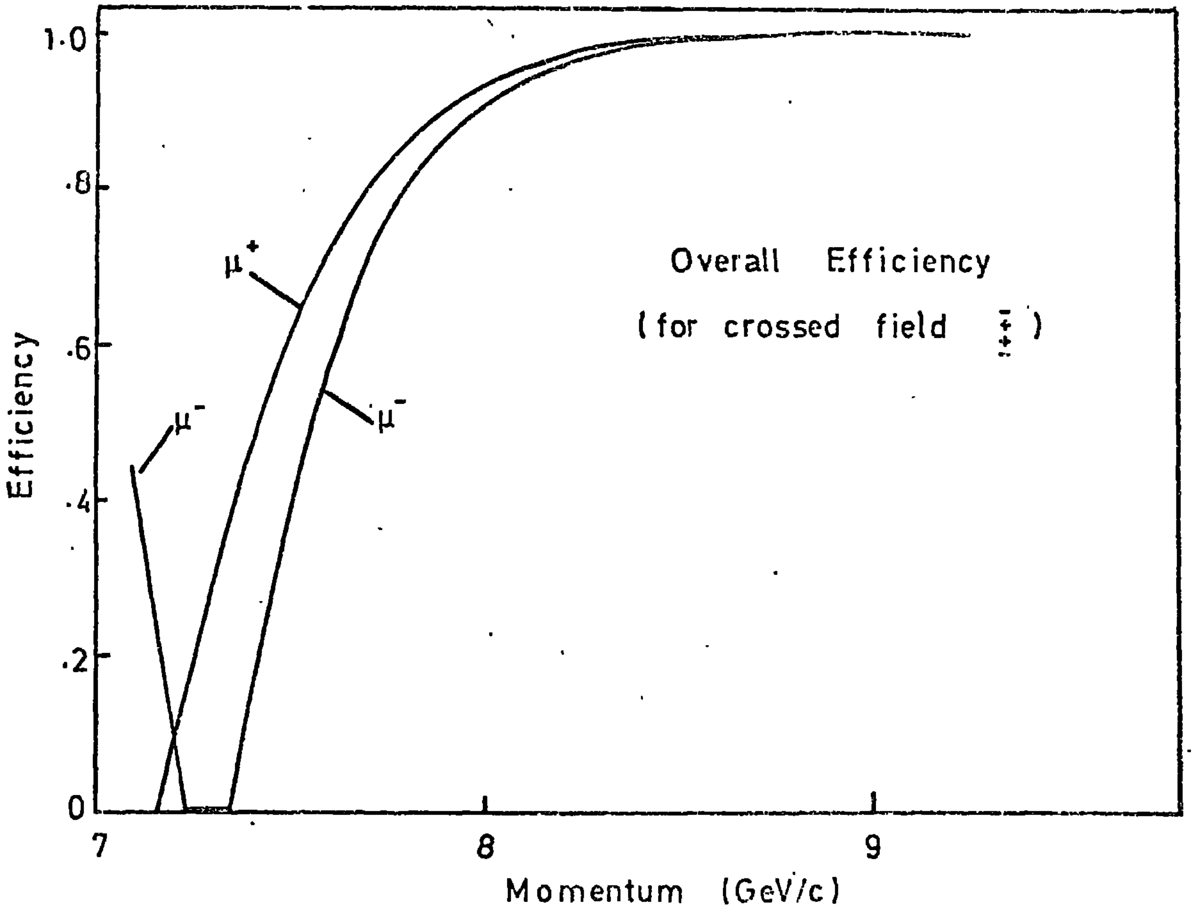

FIGURE:5·7. CROSSED FIELD EFFICIENCIES

small ($\sim 2\%$) and since the charge ratio in this category is not in serious conflict with that from the remainder of the data it is felt that there is justification for taking the result at its face value.

This concludes the description of the bias introduced due to different detection efficiencies of particles of different sign,

Another check for bias in the data has been made by examining the distributions of the observed ratios. For each series the distributions of R_{all} and R_{23} have been obtained; these are first, the overall charge ratio of a run and secondly the ratio found by considering only the data in categories 0-$\overline{22}$ inclusive. This latter is useful in that it does not include category 23 which, since it contains a large number of particles, heavily weights the overall ratio. To account for the different statistical weights of the measured ratios due to runs of different lengths the distribution of the quantity d, given by $d = (R_i - \overline{R})/\sigma_i$ where R_i and σ_i are the ratio and error of the i^{th} run and $\overline{R}$ is the mean for the series, is plotted. The results for Series 4, 5, 6 have been summed and are shown in Fig 5.8 a; the two field directions are presented separately. For Series 7 and Series 8 the results from the two field directions have been added to improve the statistics of the plots; they are given in Figs 5.8 b, c. The dashed lines represent Gaussian distributions and are the expected distributions when only random statistical errors are present. The error flags on the histograms are the Poissonian errors except where the number of runs is 10 in which case the Regener statistical limits have been used (Regener (1951)). Because of the size of those error bars the interpretation of the plots is rather difficult but there seem to be no gross errors in the data.

To test for the possibility of some progressively developing fault in the system causing the measured charge ratio to be a monotonic function of time a straight line was fitted to the results of each series expressed as a function of time. In all cases the slope of the line

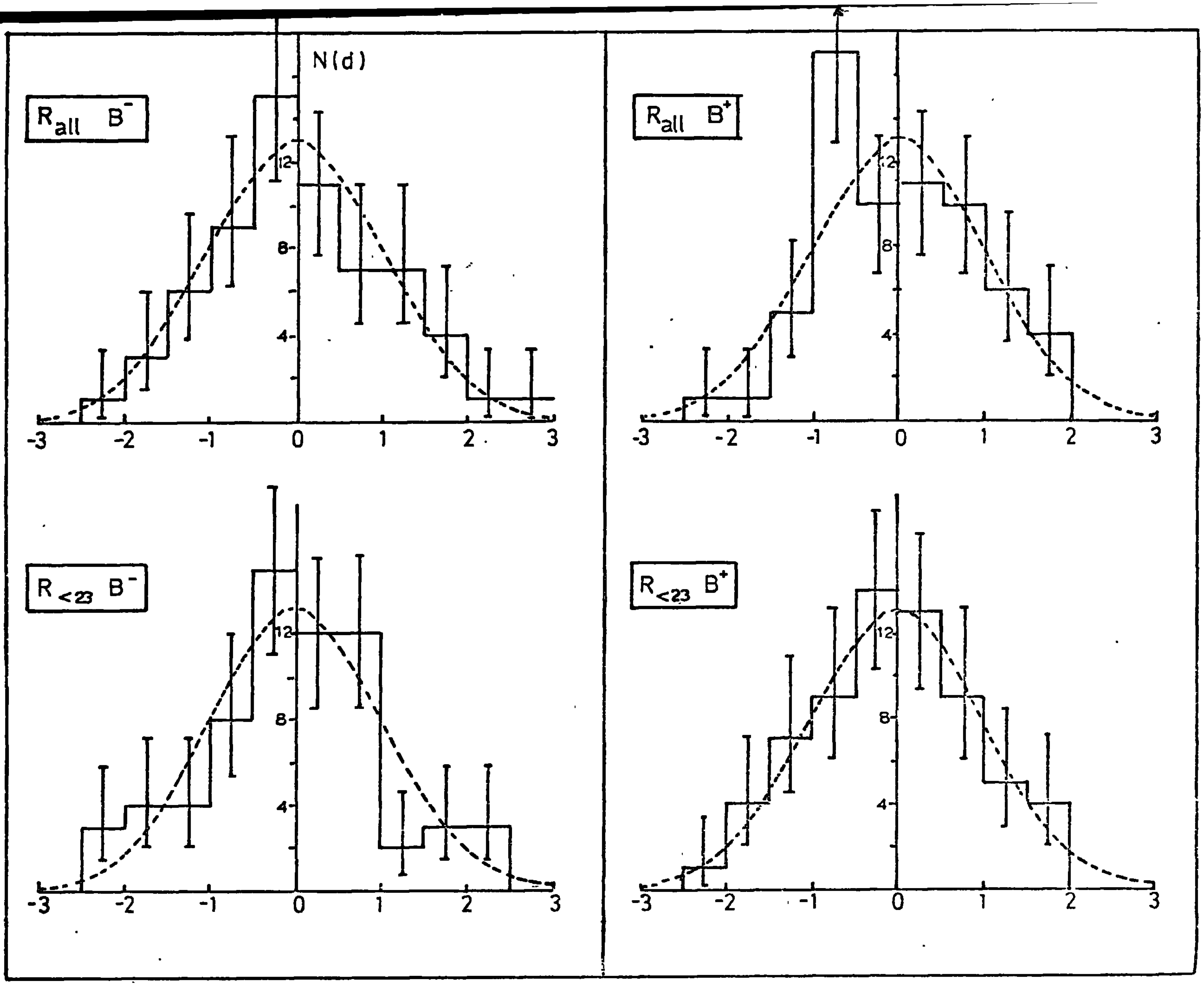

FIGURE:5·8a. SERIES 4, 5,& 6

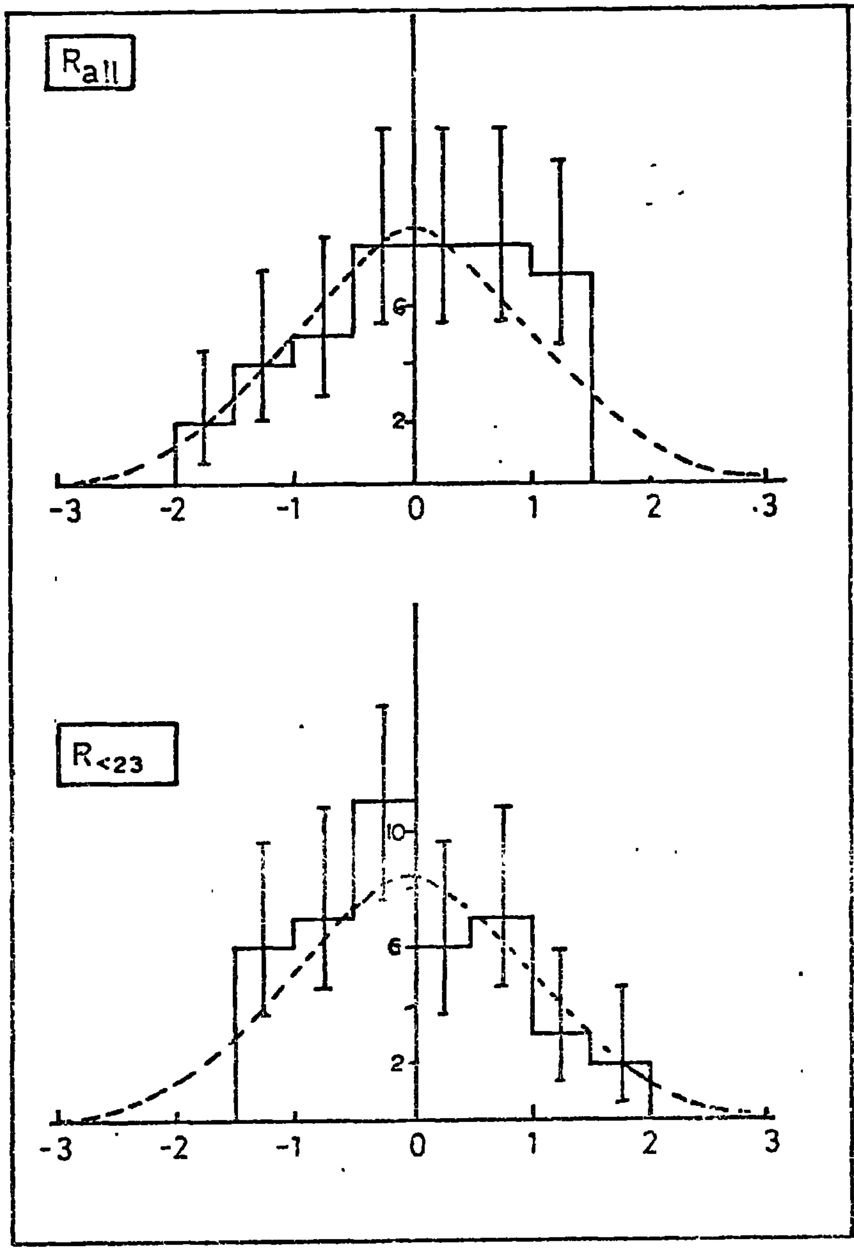

FIGURE:5.8b. SERIES 7

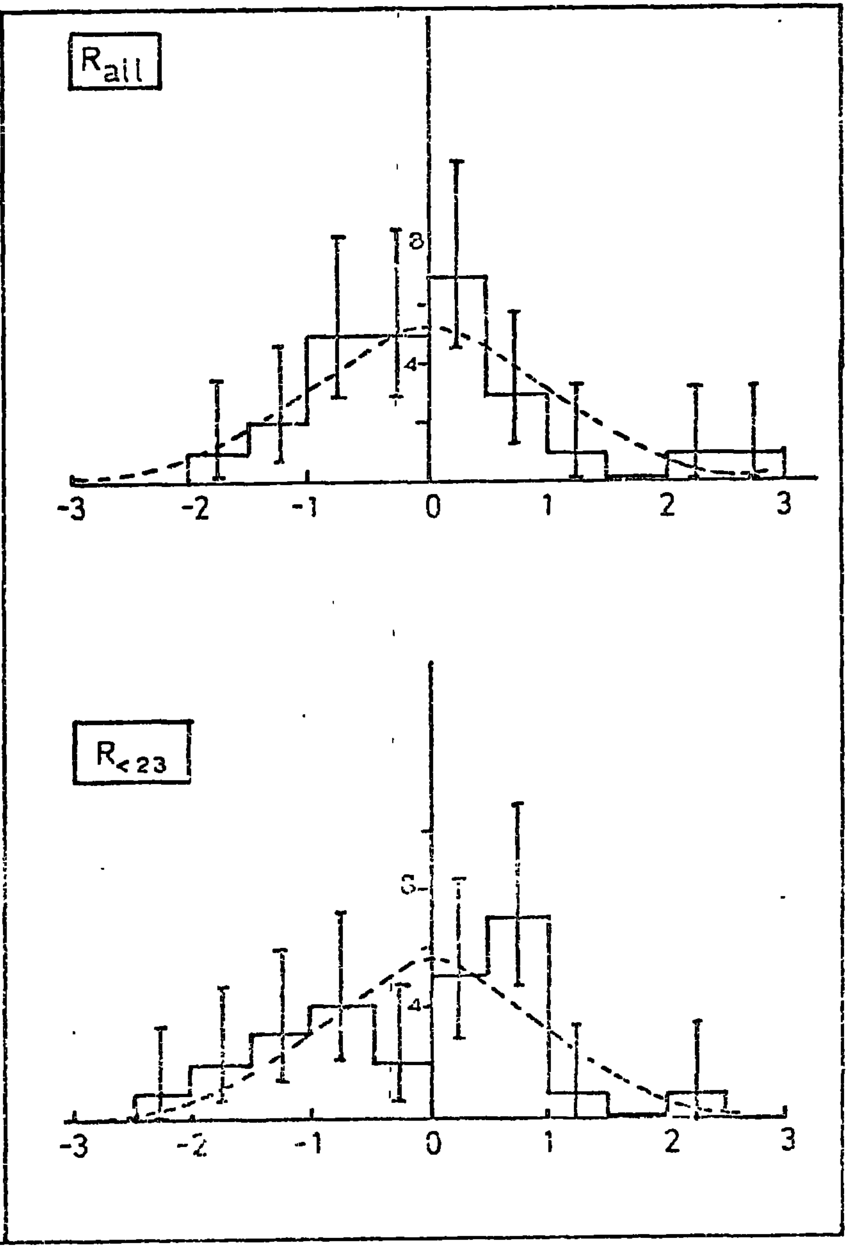

FIGURE:5.8c. SERIES 8

was found to be consistent with zero.

To allow for incorrect determination of the muon sign a correction has been applied. From the acceptance curves of categories 1 and 2 (as described in the previous chapter) the fraction of events which are mis-allocated are 9.1% and 1.7% respectively (for 0.5 cm. cell operation) and 0.6% for category 1 during 1.0 cm. cell operation. For higher category numbers the corrections are negligibly small or zero.

5.3 Biases in the Spectrum Measurements

Some bias has been found in the intensity measurements of Series 4, 5, 6. The deflection spectrum of this series is shown in fig 5.9; it can be seen that the results in categories 4 and 5, categories 6 and 7, etc up to categories 18 and 19 seem to be paired. No such effect is seen in the results of Series 7 (also shown in the figure) or of Series 8. Separating the spectrum of Series 4, 5, 6 into its positive and negative components shows the effect to be present in both and thus there is no effect on the measured charge ratio. Since the phenomenon is present only in the 0.5 cm. cell results, all spectrum measurements have been made using 1.0 cm. cells - the results of Series 7 and 8 were obtained in the 1.0 cm. cell mode and the results of Series 4, 5, 6 have been grouped into 1.0 cm. cells (when no pairing is evident).

Another form of bias peculiar to the data produced by R.U.D.I. is due to the fact that the instrument is capable of analysing only those events in which a single cell is discharged at each level. Extra cells can be discharged by the electrons of bursts produced near the bottom of magnet blocks. Since the probability of burst production is momentum dependent then so is the correction which must be applied. A similar bias occurs for accompanied muons. The distribution of the number of discharged cells in each level is given in Chapter 4.

A further bias (as yet unexplained) is indicated in the distribution of discharged cells across the momentum selector trays (Chapter 4).

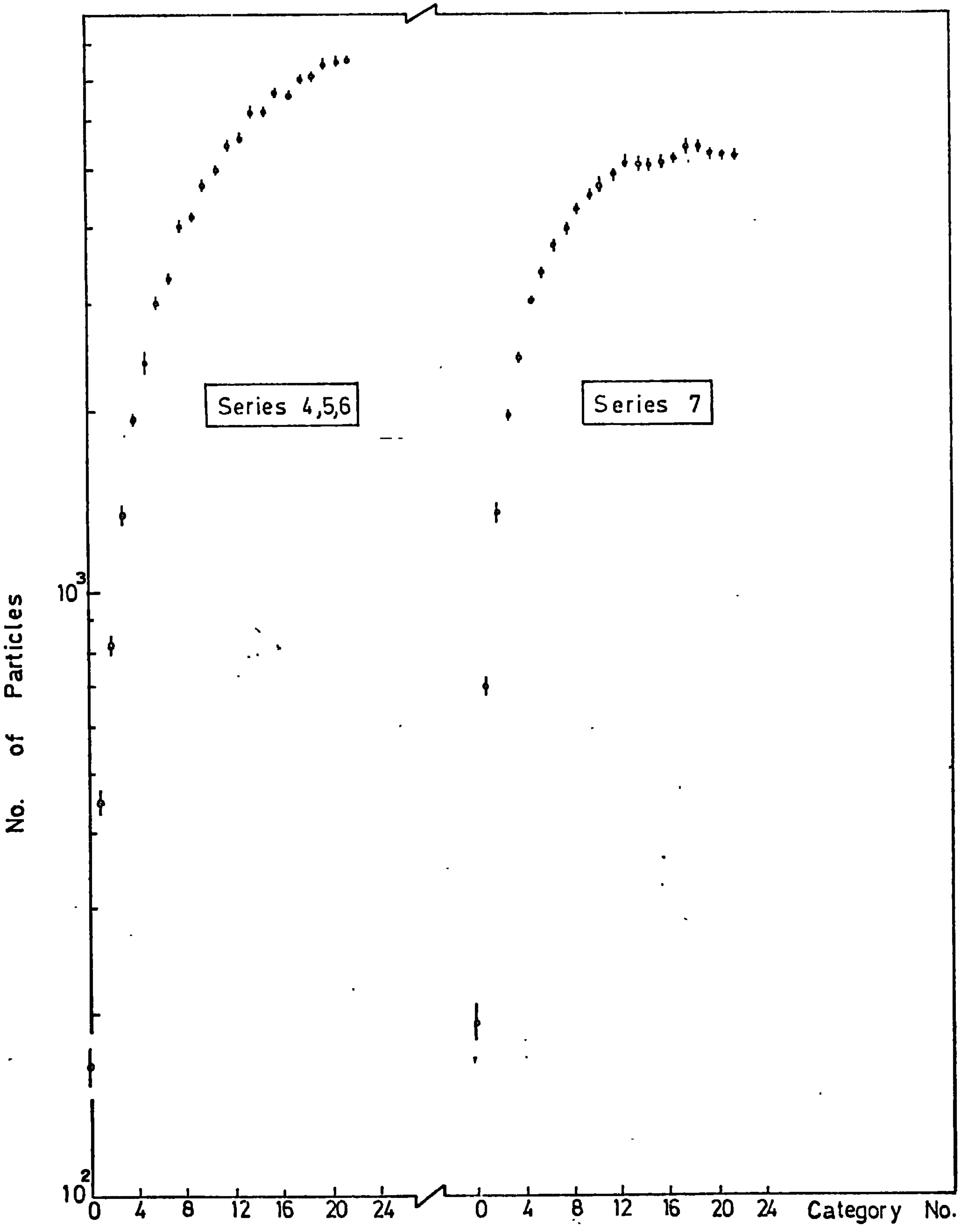

FIGURE.5.9. PAIRING OF DATA

In this thesis no spectrum measurements are described; detailed descriptions can be found in Ayre et al (1973b) and Whalley (1974).

5.4 Conclusion

The conclusion of this chapter is that as far as the charge ratio measurements are concerned the most obvious bias (that of magnetic field direction) is fairly well understood and its effect has been minimised by the frequent field reverals. The effect of other biases is small. The data are therefore thought to be reliable.

The charge ratio as a function of momentum for the various series' and for the sum of the series' are plotted in figs 5.10 - 5.13.

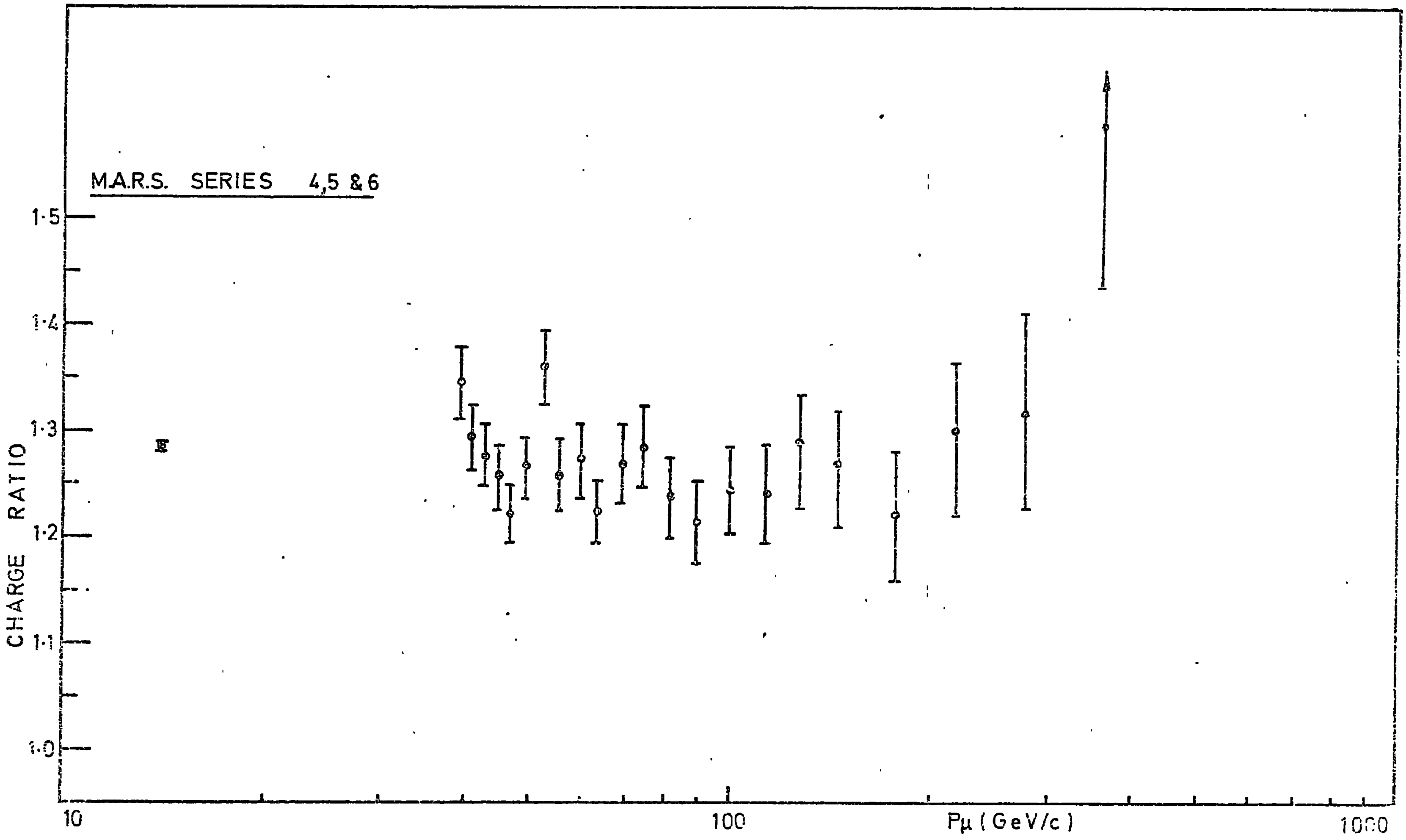
M.A.R.S. SERIES 4,5 & 6
CHARGE RATIO
1·5
1·4
1·3
1·2
1·1
1·0
10
100
1000
Pμ (GeV/c)

FIGURE: 5.10.

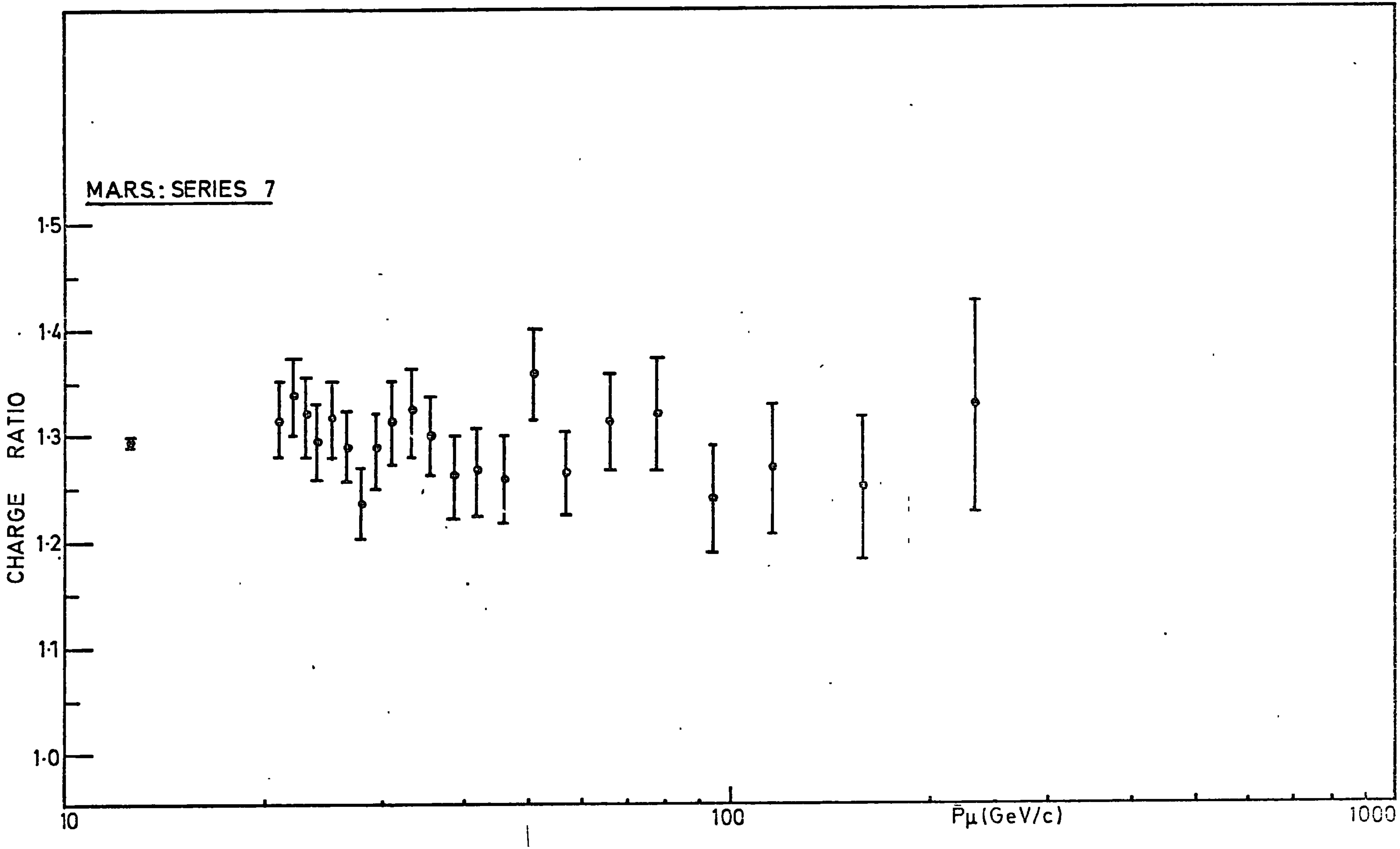

FIGURE: 5·11.

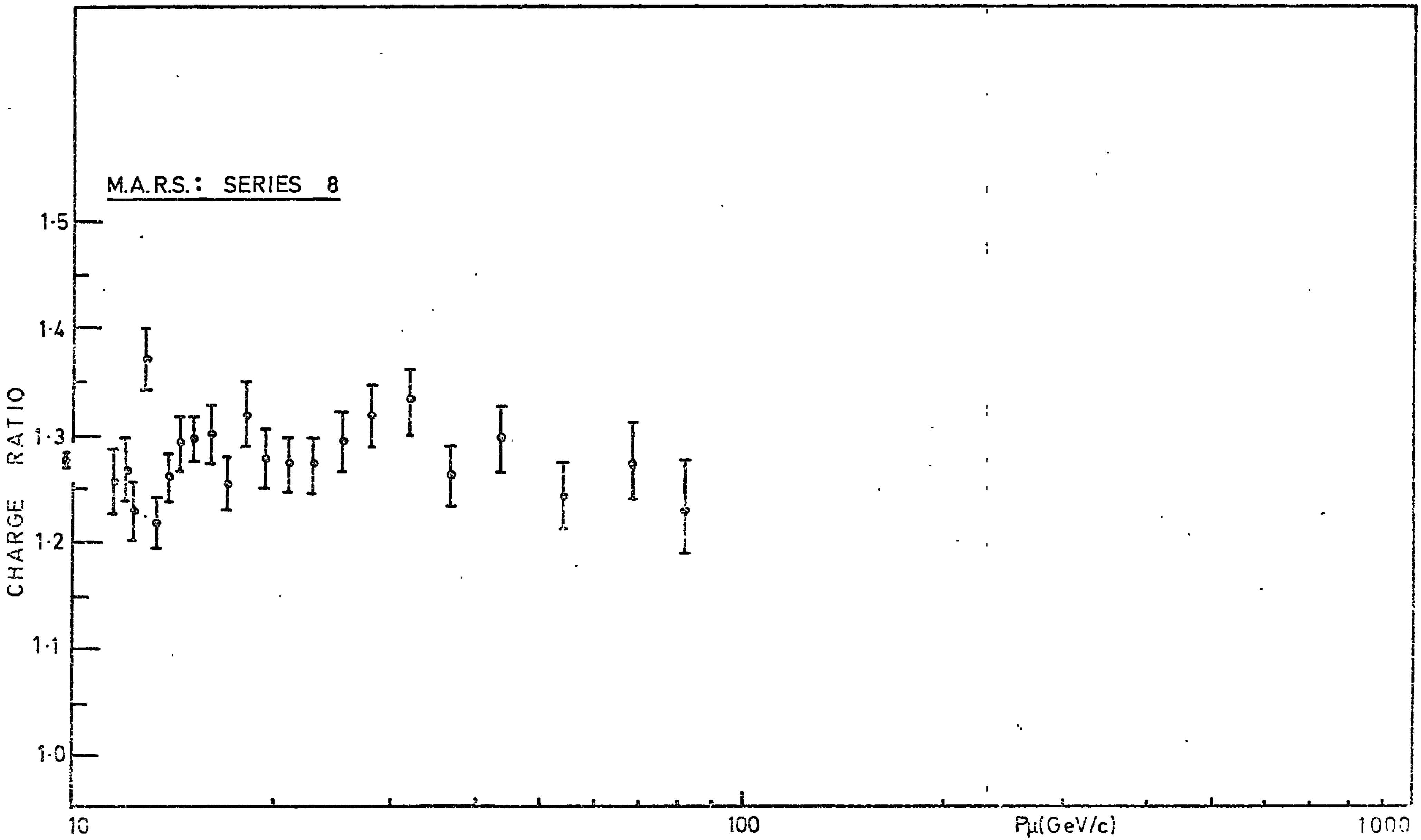

FIGURE: 5·12.

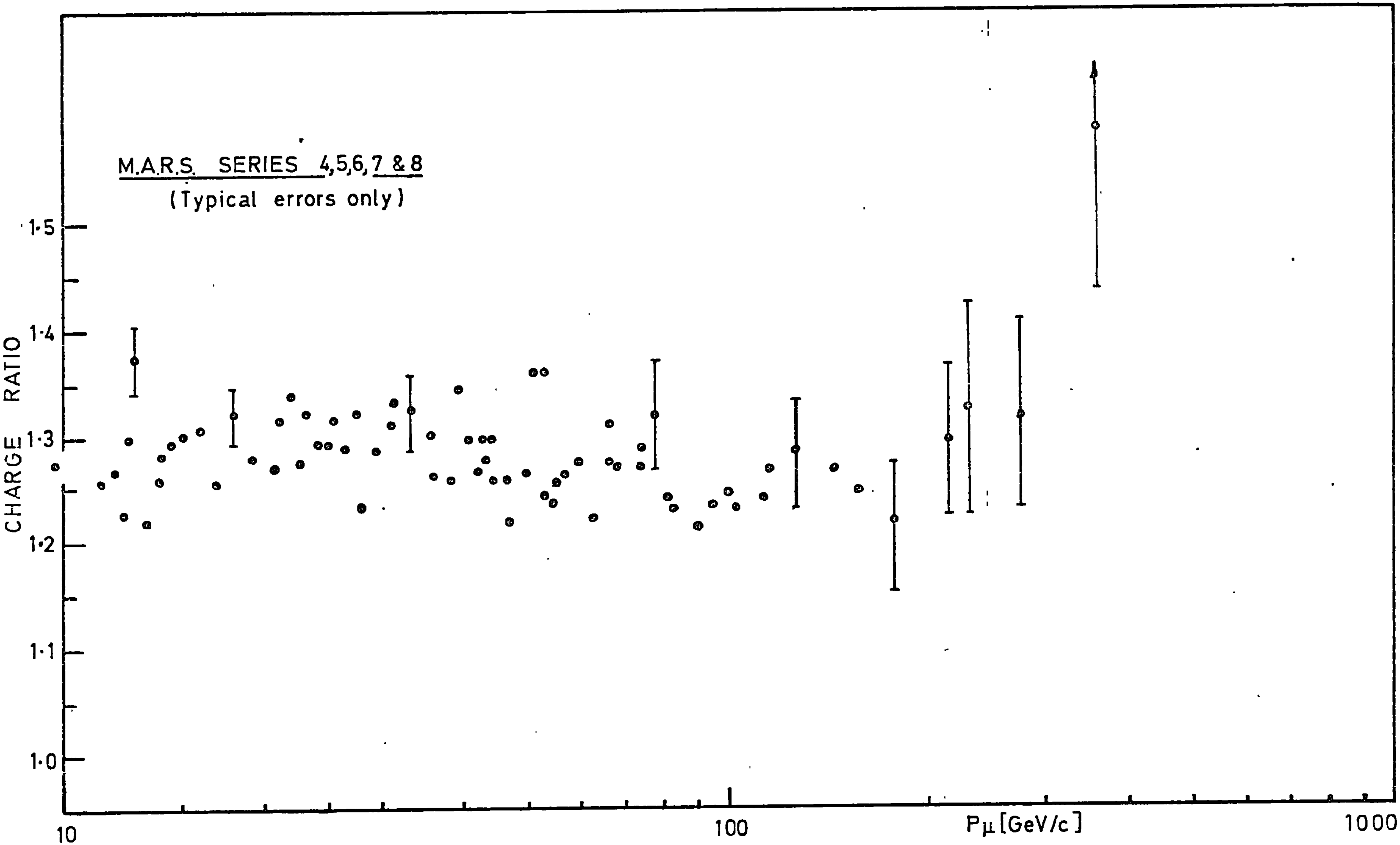
M.A.R.S. SERIES 4,5,6,7 & 8
(Typical errors only)
CHARGE RATIO
1·5
1·4
1·3
1·2
1·1
1·0
10
100
1000
Pμ [GeV/c]

FIGURE: 5·13.

Table 5.1 (Part (i))

SERIES 4, 5 and 6

Starting Date	13.5.72
Finishing Date	25.9.72
Cells	0.5 cm.
Magnet Configuration	conventional
Total Run Time	2458 h 20 m
Total Live Time	1157 h 6 m 3 s
Number of Spectrograph Triggers	1278411
Events accepted by R.U.D.I.	778978
Efficiency	0.61
Accepted Run Numbers (Positive Field)	195, 197, 199, 201, 203, 205, 207, 209, 211, 213, 215, 217, 219, 223, 227, 231, 233, 235, 237, 239, 241, 243, 245, 247, 249, 251, 253, 255, 257, 259, 261, 263, 265, 267, 273, 275, 279, 281, 283, 285, 287, 289, 291, 293, 297, 299, 301, 303, 305, 307, 309, 311.
Accepted Run Numbers (Negative Field)	196, 198, 200, 202, 204, 206, 208, 210, 212, 214, 216, 218, 222, 224, 226, 228, 230, 232, 234, 236, 238, 240, 242, 244, 246, 248, 250, 254, 256, 258, 260, 262, 264, 272, 274, 276, 278, 280, 282, 284, 288, 290, 292, 294, 295, 298, 300, 302, 304, 306, 308, 310.

In tables 5.1 - 5.3 the presented data are first classified according to apparent zenith angle and direction; they are then summed over apparent angles and then finally over both apparent directions. The directions and angles are only the apparent quantities since they have been calculated using the top two trays of the magnet.

TABLE 5.1 Part (iia) POSITIVE FIELD

PARTICLE:	NEGATIVE								POSITIVE							
APP. DIRECTION:	WEST				EAST				WEST				EAST			
APP. ANGLE:	a	b	c	d	a	b	c	d	a	b	c	d	a	b	c	d
CELL																
0	0	0	0	0	14	11	16	4	9	10	4	8	0	0	0	0
1	24	8	8	9	18	9	8	4	24	26	8	4	36	20	18	10
2	31	25	22	10	36	30	16	7	44	26	19	13	43	38	23	15
3	49	52	37	18	52	37	25	7	80	45	49	26	72	64	39	23
4	64	83	48	27	54	69	33	26	108	75	53	31	93	83	55	40
5	99	68	54	23	122	86	40	30	126	111	73	45	137	93	72	18
6	133	96	77	39	125	84	59	45	191	135	72	57	146	131	77	43
7	119	97	76	34	158	132	94	39	202	142	87	63	181	135	109	31
8	156	132	89	35	182	138	81	70	220	175	106	90	199	165	92	49
9	184	107	77	40	187	152	88	70	252	185	118	88	216	169	81	44
10	195	145	106	38	191	185	128	102	312	215	152	128	234	165	105	52
11	200	142	91	34	215	193	111	85	312	246	154	103	224	209	113	44
12	214	166	97	32	271	199	147	110	339	266	196	137	285	202	134	56
13	206	185	99	35	293	187	165	110	316	284	178	146	278	204	130	40
14	238	182	102	41	291	286	163	130	360	290	220	176	302	241	141	54
15	241	190	90	27	295	254	171	133	355	317	246	154	314	237	133	42
16	253	191	96	33	298	255	189	152	387	356	254	224	309	247	146	50
17	247	157	95	19	308	281	198	153	376	348	243	198	315	227	119	54
18	249	203	108	37	329	262	221	188	377	341	253	210	320	235	160	35
19	262	182	99	16	342	326	206	185	364	392	274	212	353	233	125	32
20	270	203	121	31	322	304	244	187	411	362	246	267	341	255	140	44
21	254	173	102	19	375	311	220	206	462	410	277	243	312	300	133	23
22	210	210	96	25	330	308	234	229	425	443	311	274	340	256	145	33
23	12372	6855	2189	202	19347	23338	24563	62740	23692	28693	30499	76657	15075	8377	2709	214
SUM =	16274	9353	3979	825	24176	27439	27420	65012	29754	33898	34092	79554	20130	12291	4999	1026

TABLE 5.1 (Part (iib)) NEGATIVE FIELD

PARTICLE:	NEGATIVE								POSITIVE							
APP. DIRECTION:	WEST				EAST				WEST				EAST			
APP. ANGLE:	a	b	c	d	a	b	c	d	a	b	c	d	a	b	c	d
CELL																
0	23	9	5	4	0	0	0	0	0	0	0	0	12	6	18	5
1	16	9	9	3	18	18	11	11	24	20	10	11	29	18	4	5
2	36	27	10	8	33	26	24	13	37	54	28	18	38	35	19	14
3	72	36	20	11	73	49	35	18	76	49	42	16	71	65	35	15
4	92	74	37	27	70	73	44	34	97	67	54	36	117	80	45	29
5	119	92	64	23	85	82	50	23	124	83	65	27	133	118	72	37
6	119	119	70	56	114	95	62	35	151	128	90	46	172	124	80	66
7	154	117	66	46	124	117	70	32	152	124	85	35	189	139	107	52
8	185	150	96	67	157	133	90	42	205	170	98	47	235	193	123	78
9	225	170	93	77	167	127	88	43	206	122	92	41	243	204	154	83
10	202	166	132	107	190	135	78	35	234	169	103	38	266	209	149	104
11	241	178	127	105	187	144	92	41	257	174	107	49	280	272	167	102
12	214	210	154	105	190	164	94	41	234	199	102	50	296	244	177	141
13	270	228	132	94	223	185	107	35	281	204	106	36	316	274	190	141
14	289	216	136	139	209	189	120	28	283	221	146	52	372	282	214	162
15	278	262	166	113	249	168	95	43	277	193	101	36	369	332	206	167
16	263	244	210	148	219	169	106	39	319	236	159	45	394	335	225	213
17	316	254	174	145	226	216	105	25	305	240	118	35	377	340	243	176
18	294	285	223	195	252	192	124	37	307	257	145	49	330	330	260	229
19	346	291	180	172	240	187	113	27	299	207	128	33	420	376	294	246
20	309	315	218	197	231	202	104	31	357	243	149	31	404	399	287	267
21	345	296	223	180	273	196	102	21	314	246	144	29	449	386	289	249
22	314	322	229	191	264	174	98	22	353	238	126	39	455	381	302	254
23	18154	22041	23247	59165	11643	6425	2157	206	15550	8591	2812	261	24273	29719	31519	80147
SUM =	22876	26111	26021	61379	15437	9466	3970	882	20447	12245	5015	1060	30290	34881	35179	82987

TABLE 5.1 (Part (iiia) POSITIVE FIELD

PARTICLE	NEGATIVE		POSITIVE			NEGATIVE	POSITIVE
APP. DIRECTION	WEST	EAST	WEST	EAST		WEST + EAST	WEST + EAST
CELL							
0	0	45	31	0		45	31
1	49	39	62	84		88(82)	146(152)
2	88	89	102	119		177(176)	221(222)
3	156	121	200	198		277	398
4	222	202	267	276		424	543
5	244	278	355	325		522	680
6	345	313	455	397		658	852
7	326	423	494	456		749	950
8	412	471	591	505		883	1096
9	408	497	643	510		905	1153
10	404	606	807	556		1010	1363
11	467	604	815	590		1071	1405
12	509	727	938	677		1236	1615
13	525	735	924	652		1260	1576
14	563	870	1046	738		1433	1784
15	548	854	1082	726		1402	1808
16	573	894	1221	752		1467	1973
17	518	940	1165	695		1458	1860
18	597	1000	1181	750		1597	1931
19	559	1059	1242	743		1618	1985
20	625	1057	1286	780		1682	2066
21	548	1112	1392	768		1660	2160
22	541	1101	1453	774		1642	2227
23	21618	129988	159546	26375		151606	185921
SUM =	30931.	144047	177293	38446		174978	215744

TABLE 5.1 (Part (iiib)) NEGATIVE FIELD

PARTICLE	NEGATIVE		POSITIVE			NEGATIVE	POSITIVE
APP. DIRECTION	WEST	EAST	WEST	EAST		WEST + EAST	WEST + EAST
CELL							
0	41	0	0	41		41	41
1	37	58	65	56		95(92)	121(124)
2	81	95	137	106		177(176)	243(244)
3	139	175	183	186		314	369
4	250	221	254	271		451	525
5	293	240	304	360		538	664
6	364	306	415	442		670	857
7	383	343	396	487		726	883
8	493	422	520	629		920	1149
9	565	425	461	689		990	1150
10	607	438	549	728		1045	1277
11	652	464	587	821		1116	1408
12	683	489	585	858		1172	1443
13	724	550	627	921		1274	1548
14	780	545	707	1030		1326	1737
15	819	555	612	1074		1374	1686
16	865	535	739	1167		1398	1926
17	889	573	698	1136		1462	1834
18	997	605	758	1219		1602	1977
19	989	567	667	1336		1556	2003
20	1039	563	780	1357		1607	2137
21	1044	592	733	1373		1636	2106
22	1056	558	756	1392		1614	2148
23	122607	20431	27214	165658		143038	192872
SUM =	136387	29755	38768	183337		166142	222104

Table 5.2 (Part (i))

SERIES 7

Starting Date	26. 9.72
Finishing Date	15.11.72
Cells	1.0 cm
Magnet Configuration	conventional
Total Run Time	740 h 2 m
Total Live Time	359 h 59 m 45 s
Number of Spectograph Triggers	490545
Events Accepted by R.U.D.I.	238831
Efficiency	0.49
Accepted Run Numbers (Positive Field)	313, 315, 317, 319, 321, 323, 325, 327, 329. 331, 333, 335, 337, 339, 341, 343, 345, 347, 349, 353.
Accepted Run Numbers (Negative Field)	312, 314, 316, 318, 320, 322, 324, 326, 328, 330, 332, 334, 336, 338, 340, 342, 344, 348, 352. 354, 355, 358

TABLE 5.2 (Part (iia)) POSITIVE FIELD

PARTICLE	NEGATIVE								POSITIVE							
APP. DIRECTION:	WEST				EAST				WEST				EAST			
APP. ANGLE:	a	b	c	d	a	b	c	d	a	b	c	d	a	b	c	d
CELL																
0	7	4	6	1	11	6	5	5	7	12	7	5	7	7	5	5
1	25	29	22	9	26	14	11	8	31	29	26	7	37	36	17	15
2	60	40	25	7	62	51	37	19	92	48	33	21	60	64	42	24
3	66	56	43	19	87	65	55	25	128	75	59	42	92	82	39	21
4	83	88	52	22	117	91	45	42	143	94	71	49	118	91	66	26
5	109	62	58	16	142	109	70	62	148	157	104	77	135	122	66	32
6	131	103	52	26	162	119	95	65	183	159	141	101	158	127	74	30
7	144	102	60	29	159	157	106	77	216	169	137	101	163	140	90	30
8	127	101	56	17	157	155	124	99	211	204	135	128	194	120	90	18
9	166	137	76	18	162	200	113	106	268	228	159	140	181	148	95	26
10	155	123	69	21	226	188	131	122	248	225	149	142	185	158	74	24
11	151	113	69	22	212	183	157	123	265	221	183	163	196	132	93	15
12	180	115	61	12	216	202	155	147	262	290	202	195	215	164	92	12
13	157	134	55	6	197	195	168	184	269	297	217	206	213	142	92	9
14	185	125	53	7	182	218	162	182	278	234	222	242	196	155	86	17
15	149	128	71	7	189	217	177	190	272	252	243	232	198	144	70	7
16	166	110	56	4	209	222	183	223	274	264	214	244	212	138	61	5
17	161	124	51	2	222	223	194	102	290	258	235	270	217	154	57	6
18	161	97	43	0	214	212	199	244	274	279	240	313	198	150	49	3
19	159	95	43	1	243	244	177	227	266	284	271	319	193	134	56	4
20	156	97	39	0	183	241	211	265	260	295	261	312	186	120	40	2
21	152	78	32	0	195	206	238	252	240	271	284	345	176	117	52	1
22	134	94	27	0	182	223	211	270	256	285	250	374	164	117	40	2
23	2045	835	117	0	3539	4566	5344	16681	4118	5675	6718	20533	2293	945	156	1
SUM=	5034	2990	1236	246	7289	8307	8358	19815	9003	10355	10561	24566	5987	3727	1602	335

TABLE 5.2 (Part (iib)) NEGATIVE FIELD

PARTICLE	NEGATIVE								POSITIVE							
APP. DIRECTION:	WEST				EAST				WEST				EAST			
APP. ANGLE:	a	b	c	d	a	b	c	d	a	b	c	d	a	b	c	d
CELL																
0	16	5	7	5	8	0	6	4	6	8	6	2	6	9	4	2
1	24	20	21	10	33	19	22	7	29	34	24	14	38	32	15	14
2	67	47	28	19	56	44	32	14	68	49	37	33	83	52	30	24
3	79	70	54	23	90	69	46	20	114	72	43	34	101	96	58	40
4	130	76	47	41	105	77	53	21	130	105	48	25	159	104	83	67
5	143	142	60	64	107	86	51	24	135	124	64	33	203	167	87	68
6	159	129	95	53	103	97	44	30	159	133	85	37	198	149	101	79
7	154	127	103	84	160	97	74	23	176	118	89	39	231	172	133	100
8	204	152	112	97	122	99	59	18	196	165	83	25	246	227	150	110
9	195	189	112	116	135	110	50	17	177	155	89	20	233	191	154	154
10	203	179	133	132	139	110	54	11	216	150	88	18	302	235	190	154
11	233	200	143	127	161	114	49	15	202	165	73	13	255	262	188	166
12	203	183	161	144	134	134	69	14	217	137	79	19	231	258	190	156
13	192	240	156	166	163	131	61	14	234	152	91	16	290	291	200	219
14	206	202	156	172	163	122	53	5	220	149	59	14	231	275	185	220
15	215	201	174	200	152	106	55	7	234	148	73	11	252	282	221	234
16	207	242	179	196	172	114	40	4	198	157	74	8	290	298	211	224
17	228	197	166	225	172	100	39	4	205	151	66	9	255	310	210	259
18	206	237	219	243	147	100	35	6	230	125	60	7	276	310	258	334
19	202	243	182	254	171	98	36	0	213	159	51	3	262	271	256	328
20	174	211	205	229	140	107	28	1	186	140	44	3	268	308	272	321
21	167	138	212	276	140	88	43	0	209	139	59	0	279	289	261	307
22	205	206	173	277	152	102	23	1	193	100	28	0	231	309	271	375
23	3175	4302	5027	15729	1785	727	135	3	2570	1117	174	2	4319	5953	6905	21425
SUM =	6998	7988	7925	18882	4730	2851	1157	264	6517	3952	1599	385	9323	10850	10613	25378

TABLE 5.2 (Part (iiia)) POSITIVE FIELD

PARTICLE	NEGATIVE		POSITIVE			NEGATIVE	POSITIVE
APP. DIRECTION	WEST	EAST	WEST	EAST		WEST + EAST	WEST + EAST
CELL							
0	18	27	31	24		45	55
1	85	59	93	105		144	198
2	132	169	194	190		301	384
3	184	232	304	234		416	538
4	250	295	357	301		545	658
5	245	383	486	355		628	841
6	312	441	589	389		753	978
7	335	499	623	423		834	1046
8	301	535	678	422		836	1100
9	397	581	795	450		978	1245
10	368	667	764	441		1035	1205
11	355	680	837	456		1035	1293
12	368	720	949	483		1088	1432
13	352	744	989	456		1096	1445
14	370	744	1026	454		1114	1480
15	355	768	999	419		1123	1418
16	336	837	996	416		1173	1412
17	338	821	1052	434		1159	1486
18	301	869	1106	400		1170	1506
19	298	891	1140	387		1189	1527
20	292	900	1128	348		1192	1476
21	262	891	1140	346		1153	1486
22	255	886	1165	323		1141	1488
23	2997	30130	37044	3395		33127	40439
SUM =	9506	43769	54485	11651		53275	66136

TABLE 3.2 (Part (iiib)) NEGATIVE FIELD

PARTICLE	NEGATIVE		POSITIVE			NEGATIVE	POSITIVE
APP. DIRECTION	WEST	EAST	WEST	EAST		WEST + EAST	WEST + EAST
CELL							
0	33	18	22	21		51	43
1	75	81	101	99		156	200
2	161	146	187	189		307	376
3	226	225	268	295		451	563
4	294	256	306	392		550	698
5	409	268	356	530		677	886
6	436	274	414	527		710	941
7	478	354	422	636		832	1058
8	565	298	474	733		863	1207
9	613	312	441	712		925	1153
10	647	334	472	881		981	1353
11	703	339	459	871		1042	1330
12	691	351	452	885		1042	1337
13	754	369	493	1000		1123	1493
14	736	344	442	961		1080	1403
15	790	320	464	989		1110	1453
16	824	330	437	1023		1154	1460
17	816	315	431	1034		1131	1465
18	905	288	422	1178		1193	1600
19	881	305	426	1117		1186	1543
20	819	276	373	1169		1095	1542
21	843	271	407	1136		1114	1543
22	861	278	321	1186		1139	1507
23	28233	2650	3863	38600		30883	42463
SUM =	41793	9002	12453	56164		50795	68617

Table 5.3 (Part (i))

SERIES 8

Starting Date	16.11.72
Finishing Date	2. 1.73
Cells	1.0 cm
Magnet Configuration	crossed
Total Run Time	636 h 26 m
Total Live Time	246 h 56 m 23 s
Number of Spectrograph Triggers	401110
Events Accepted by R.U.D.I.	276981
Efficiency	0.69
Accepted Run Numbers (Positive Field)	360, 364, 368, 370, 372, 374, 378, 380, 382, 384, 387, 389
Accepted Run Numbers (Negative Field)	361, 363, 369, 371, 373, 375, 377, 379, 381, 383, 385, 388, 390, 391

TABLE 5.3 (Part (iia)) POSITIVE FIELD

PARTICLE	NEGATIVE								POSITIVE							
APP. DIRECTION:	WEST				EAST				WEST				EAST			
APP. ANGLE:	a	b	c	d	a	b	c	d	a	b	c	d	a	b	c	d
CELL																
0	25	29	14	12	64	41	34	25	63	54	18	16	36	41	25	20
1	131	119	93	45	147	107	64	28	194	122	75	39	157	140	101	61
2	198	169	117	53	221	176	101	56	295	204	145	86	261	207	127	74
3	254	218	130	73	316	231	123	100	347	282	199	110	342	270	149	91
4	324	211	154	51	313	302	192	106	456	351	232	159	416	294	179	90
5	325	262	170	63	350	319	188	138	453	384	278	193	421	311	190	31
6	316	246	138	53	408	346	184	173	484	433	274	228	483	292	204	38
7	321	272	155	48	407	327	243	195	517	445	306	235	432	337	197	63
8	318	256	174	59	389	379	249	202	544	487	308	263	425	311	200	76
9	334	264	150	63	440	368	277	216	563	460	323	268	424	327	176	70
10	351	255	163	43	413	377	281	238	534	445	367	294	418	300	204	64
11	310	243	139	39	418	379	305	229	567	475	380	315	428	277	168	55
12	345	209	98	33	427	405	276	250	541	518	382	305	421	282	203	40
13	308	246	126	36	409	278	289	253	526	504	359	318	414	320	153	31
14	324	226	107	25	418	368	300	258	519	484	364	326	389	291	153	40
15	303	214	109	13	401	355	300	268	515	497	385	371	363	293	141	29
16	293	230	96	16	337	308	298	272	494	500	395	430	370	260	130	19
17	275	206	90	11	386	386	275	302	487	472	383	438	350	254	118	16
18	266	211	102	11	348	372	295	314	400	447	373	412	364	234	136	12
19	209	172	71	7	321	340	271	307	458	476	368	413	329	248	101	8
20	224	187	85	5	326	353	302	319	443	380	369	423	306	207	92	5
21	242	169	76	3	347	325	296	307	383	431	354	471	272	221	96	5
22	221	134	48	3	303	276	294	331	369	430	355	396	277	190	86	4
23	2271	1285	331	3	3316	3311	3614	6130	4301	4835	4773	8355	2788	1602	423	8
SUM =	8438	6035	2936	779	11258	11119	9051	11022	14453	14116	11766	14867	10886	7509	3757	1051

TABLE 5.3 (Part (iib)) NEGATIVE FIELD

PARTICLE	NEGATIVE								POSITIVE							
APP. DIRECTION:	WEST				EAST				WEST				EAST			
APP. ANGLE:	a	b	c	d	a	b	c	d	a	b	c	d	a	b	c	d
CELL																
0	63	38	27	13	28	35	13	9	37	36	29	13	70	46	26	21
1	137	86	60	53	135	117	89	32	175	143	87	53	175	130	87	40
2	226	165	121	72	188	190	110	62	275	208	152	68	282	207	151	95
3	306	219	148	106	258	191	134	60	317	249	176	92	374	281	170	112
4	346	262	204	130	280	215	137	55	367	304	186	72	413	348	241	151
5	392	286	199	144	305	242	169	81	393	322	180	97	477	361	275	165
6	397	344	220	159	361	231	142	58	415	335	218	81	544	419	317	222
7	386	347	247	175	319	274	144	56	429	341	200	87	544	456	333	240
8	415	335	270	185	354	255	157	46	400	335	207	64	539	466	330	276
9	419	372	248	220	338	262	132	44	427	364	164	64	559	462	324	299
10	416	383	283	235	324	235	152	49	430	345	197	59	586	489	311	280
11	423	400	267	222	345	258	134	28	412	336	175	52	549	477	354	275
12	410	339	276	234	321	253	124	40	429	262	164	32	519	507	376	347
13	436	415	273	253	313	224	120	29	373	307	176	30	489	496	335	328
14	436	392	242	246	288	218	128	31	378	263	151	35	553	492	370	395
15	395	384	282	291	283	222	105	26	385	274	145	24	477	509	336	367
16	340	386	289	296	282	194	103	23	344	259	127	15	480	463	358	376
17	335	409	315	313	265	230	90	18	338	230	140	17	442	478	385	376
18	367	391	289	322	268	201	85	9	283	248	106	17	447	455	351	409
19	325	350	288	328	253	173	83	7	346	224	110	4	434	479	400	407
20	337	347	284	315	260	173	57	4	330	207	98	11	379	423	341	383
21	338	299	274	350	225	137	62	8	300	202	104	6	366	424	348	404
22	292	337	258	361	203	151	68	2	266	157	83	3	384	392	342	399
23	3207	3783	3735	6411	2258	1326	315	2	2831	1629	390	2	4235	4797	4616	7807
SUM =	11144	11069	9099	11434	8459	6006	2853	779	10682	7580	3765	998	14317	14057	11483	14174

TABLE 5.3 (Part (iiia)) POSITIVE FIELD

PARTICLE	NEGATIVE		POSITIVE			NEGATIVE	POSITIVE
APP. DIRECTION	WEST	EAST	WEST	EAST		WEST + EAST	WEST + EAST
CELL							
0	80	164	151	122		244	273
1	328	346	430	459		734(753)	889(890)
2	542	554	731	669		1096	1400
3	675	770	938	852		1445	1790
4	740	913	1198	979		1653	2177
5	820	995	1308	1003		1815	2311
6	760	1111	1419	1067		1871	2486
7	796	1172	1503	1034		1968	2537
8	807	1219	1602	1012		2026	2614
9	811	1301	1614	997		2112	2611
10	812	1309	1640	986		2121	2626
11	731	1331	1737	928		2062	2665
12	685	1358	1746	946		2043	2692
13	716	1334	1707	923		2050	2630
14	683	1344	1695	873		2027	2568
15	639	1324	1768	822		1963	2590
16	635	1338	1819	779		1973	2598
17	582	1349	1780	738		1931	2518
18	590	1329	1632	746		1919	2378
19	459	1239	1715	686		1698	2401
20	501	1300	1615	610		1801	2225
21	490	1275	1639	594		1765	2233
22	406	1204	1550	557		1610	2107
23	3890	16871	22265	4821		20761	27086
SUM =	18238	42450	55202	23203		60688	78405

TABLE 5.3 (Part (iiib)) NEGATIVE FIELD

PARTICLE	NEGATIVE		POSITIVE			NEGATIVE	POSITIVE
APP. DIRECTION	WEST	EAST	WEST	EAST		WEST + EAST	WEST + EAST
CELL							
0	141	85	115	163		226	278
1	336	373	458	432		709(708)	890(891)
2	504	530	703	741		1034	1444
3	779	643	834	937		1422	1771
4	942	687	929	1153		1629	2082
5	1021	797	994	1278		1818	2272
6	1120	792	1049	1502		1912	2551
7	1155	792	1057	1573		1947	2630
8	1205	812	1006	1611		2017	2617
9	1259	776	1019	1644		2035	2663
10	1317	760	1031	1666		2077	2697
11	1312	765	975	1655		2077	2630
12	1259	738	897	1749		1997	2646
13	1377	686	886	1648		2063	2534
14	1316	665	827	1810		1981	2637
15	1352	641	828	1689		1993	2517
16	1311	602	745	1677		1913	2422
17	1372	603	725	1681		1975	2406
18	1369	563	654	1662		1932	2316
19	1291	516	684	1720		1807	2404
20	1283	494	646	1526		1777	2172
21	1261	432	612	1542		1693	2154
22	1248	424	509	1517		1672	2026
23	17135	3901	4852	21455		21037	26307
SUM =	42746	18097	23025	54031		60843	77056

Table 5.4

SERIES 4, 5, 6

Category No.	Momentum GeV/c			Charge Ratio			Charge Excess		
0	442	86	72						
1	358	174	276	1.586	±	0.154	0.227	±	0.046
2	274	352	466	1.316		0.093	0.137		0.035
3	214	591	767	1.298		0.071	0.129		0.027
4	177	875	1068	1.221		0.056	0.099		0.023
5	145	1060	1344	1.268		0.052	0.118		0.020
6	128	1328	1709	1.287		0.047	0.125		0.018
7	112	1475	1833	1.243		0.044	0.108		0.017
8	98.3	1803	2245	1.245		0.039	0.109		0.016
9	88.3	1895	2303	1.215		0.038	0.097		0.015
10	80.0	2135	2640	1.237		0.036	0.106		0.014
11	73.7	2187	2813	1.286		0.037	0.125		0.014
12	67.9	2408	3058	1.270		0.035	0.119		0.013
13	63.0	2554	3124	1.223		0.033	0.100		0.013
14	58.9	2759	3521	1.276		0.032	0.121		0.013
15	55.2	2776	3494	1.259		0.032	0.115		0.013
16	52.1	2865	3899	1.361		0.034	0.153		0.012
17	49.3	2920	3694	1.265		0.031	0.117		0.012
18	47.1	3199	3908	1.222		0.029	0.100		0.012
19	44.8	3174	3988	1.257		0.030	0.114		0.012
20	43.8	3289	4203	1.278		0.030	0.122		0.011
21	40.8	3296	4266	1.294		0.030	0.128		0.011
22	39.3	3256	4375	1.344		0.031	0.147		0.011
23	13.9	294644	378793	1.2856		0.0032	0.1250		0.0012

Table 5.5

SERIES 7

Category No.	Momentum GeV/c			Charge Ratio		Charge Excess	
0	376	96	98				
1	236	300	398	1.327	± 0.101	0.140	± 0.037
2	160	608	760	1.250	0.068	0.111	0.027
3	118	867	1101	1.270	0.058	0.119	0.022
4	93.0	1095	1356	1.238	0.050	0.106	0.020
5	76.6	1305	1727	1.323	0.049	0.139	0.018
6	65.3	1463	1919	1.312	0.046	0.135	0.017
7	57.0	1666	2104	1.263	0.041	0.116	0.016
8	50.7	1699	2307	1.358	0.043	0.152	0.016
9	45.8	1903	2398	1.260	0.039	0.115	0.015
10	41.7	2016	2558	1.269	0.038	0.118	0.015
11	38.3	2077	2623	1.263	0.037	0.116	0.014
12	35.3	2130	2769	1.300	0.038	0.130	0.014
13	33.1	2219	2938	1.324	0.037	0.139	0.014
14	31.0	2194	2883	1.314	0.037	0.136	0.014
15	29.3	2233	2871	1.286	0.036	0.125	0.014
16	27.7	2327	2872	1.234	0.034	0.105	0.014
17	26.3	2290	2951	1.289	0.036	0.126	0.014
18	25.1	2363	3106	1.314	0.036	0.136	0.013
19	24.1	2375	3070	1.293	0.035	0.128	0.013
20	23.1	2287	3018	1.320	0.037	0.138	0.014
21	22.1	2267	3029	1.336	0.037	0.144	0.014
22	21.3	2280	2995	1.314	0.037	0.136	0.014
23	12.4	64010	82902	1.2951	0.0068	0.1286	0.0026

TABLE 5.6

SERIES 8

ategory No.	Momentum GeV/c			Charge Ratio			Charge Excess		
0	126	470	551						
1	81.0	1441	1781	1.233	±	0.044	0.104	±	0.018
2	68.3	2230	2844	1.275		0.036	0.121		0.014
3	54.7	2867	3561	1.242		0.031	0.108		0.012
4	43.5	3282	4259	1.298		0.030	0.130		0.011
5	36.8	3633	4583	1.262		0.028	0.116		0.011
6	31.8	3783	5037	1.332		0.029	0.142		0.011
7	27.8	3915	5167	1.320		0.028	0.138		0.010
8	25.3	4043	5231	1.294		0.027	0.128		0.010
9	22.8	4147	5274	1.272		0.026	0.120		0.010
10	21.1	4198	5323	1.268		0.026	0.118		0.010
11	19.5	4139	5295	1.279		0.027	0.123		0.010
12	18.2	4040	5328	1.319		0.028	0.137		0.010
13	17.0	4113	5164	1.256		0.026	0.113		0.010
14	16.1	4008	5205	1.299		0.027	0.130		0.010
15	15.3	3956	5107	1.291		0.027	0.127		0.010
16	14.5	3886	5020	1.292		0.028	0.127		0.011
17	13.9	3906	4924	1.261		0.027	0.115		0.011
18	13.3	3851	4694	1.219		0.027	0.099		0.011
19	12.8	3505	4805	1.371		0.031	0.156		0.011
20	12.3	3578	4397	1.229		0.028	0.103		0.011
21	11.9	3458	4387	1.269		0.029	0.118		0.011
22	11.5	3282	4133	1.259		0.029	0.114		0.012
23	9.7	41798	53393	1.2774		0.0083	0.121		0.0032

CHAPTER 6

RESULTS OF OTHER WORKERS

6.0 Introduction

This chapter contains a summary of the results of a number of measurements of the muon charge ratio.

As mentioned in Chapter 1 the presence of an excess of positive particles in the sea level cosmic ray beam was first indicated by the discovery of the east-west effect in 1933. The early work of Blackett (1937), Jones (1939) and Hughes (1940) gave for the mean ratio of the numbers of positive and negative particles the value 1.225 ± 0.049 in the particle momentum range 0.4 - 20 GeV/c. The post war studies of Nereson (1948), Conversi (1949), Bassi et al (1949) and Brode (1949) found the ratio to be around 1.25. Since these times there have been many measurements of the charge ratio.

The experimental results summarized in this chapter have been divided into 2 classes - those measuring in the near-vertical direction and those measuring in the near-horizontal direction. The two sets of results are then combined by considering the charge ratio at the muon production energy.

6.1 The Near-Vertical Direction

Figures 6.1 and 6.2 show respectively the charge ratio and charge excess measured in the experiments reported by the following : Filosofo et al (1954), Moroney and Parry (1954), Pine et al (1959), Owen and Wilson (1951), Appleton et al (1971), Nandi and Sinha (1972), Hayman and Wolfendale

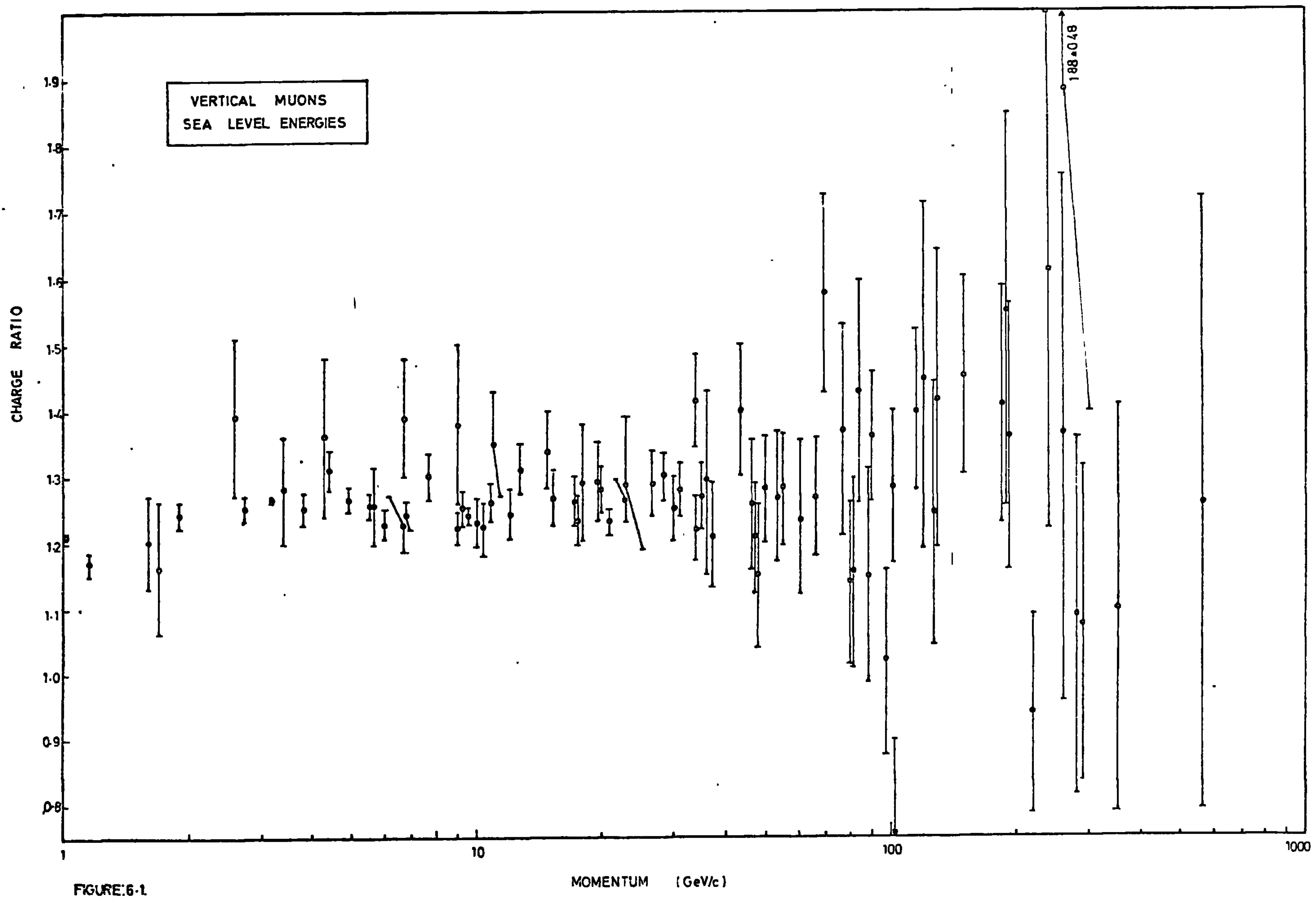
VERTICAL MUONS
SEA LEVEL ENERGIES
CHARGE RATIO
1.9
1.8
1.7
1.6
1.5
1.4
1.3
1.2
1.1
1.0
0.9
0.8
1.88±0.48
1
10
100
1000
MOMENTUM (GeV/c)

FIGURE 6.1

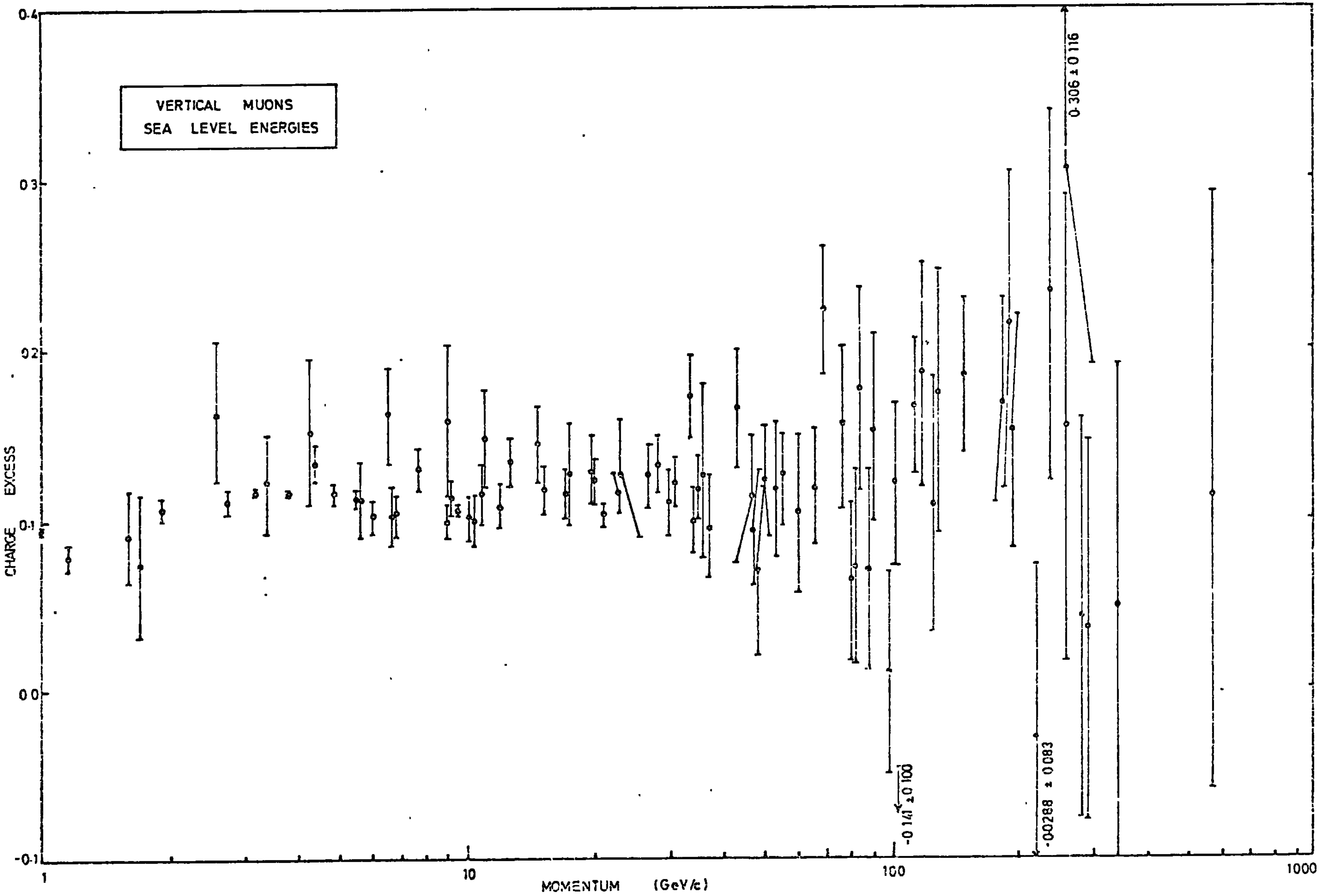
VERTICAL MUONS
SEA LEVEL ENERGIES
CHARGE EXCESS
0.4
0.3
0.2
0.1
0.0
-0.1
1
10
100
1000
MOMENTUM (GeV/c)
0.306 ± 0.116
-0.141 ± 0.100
-0.0288 ± 0.083

FIGURE: 6-2.

(1962), Holmes et al (1961), Aurela et al (1966) Allkofer et al (1969), Burnett et al (1973), Allkofer et al (1971).

To examine the degree of consistency between the various measurements the distributions of the parameters

$t = (R_i - \bar{R})/\sigma(R_i)$ and

$t' = (\delta_i - \bar{\delta})/\sigma(\delta_i)$ have been obtained.

$\bar{R}$ and $\bar{\delta}$ are the overall mean ratio and excess (respectively 1.2431 ± 0.0023 and 0.1084 ± 0.0009 in this case),

$\sigma(R_i)$ is the standard error of an individual measurement of the ratio (R_i),

$\sigma(\delta_i)$ is the standard error of an individual measurement of the charge excess (δ_i).

The resulting distributions are compared with Gaussian distributions in Fig. 6.3 - the dashed lines. There seem to be no serious deviations from the expected curves. This indicates little energy dependence of the quantities and also that the results of the experiments are consistent. The two extreme data points on either side of the appropriate histograms of Fig. 6.3 are from the same experiment - that of Filosofo et al (1954).

The data of Fig. 6.1 have been grouped and are plotted, along with the M.A.R.S. data (also grouped) of the previous chapter in Fig. 6.4. The results of Filosofo et al (1954) have been kept separate from the other results of Fig. 6.1 since they are of particularly high precision. The mean ratio from this experiment is 1.2401 ± 0.0026; the mean ratio from the

Non-Vertical Direction — Production Energies

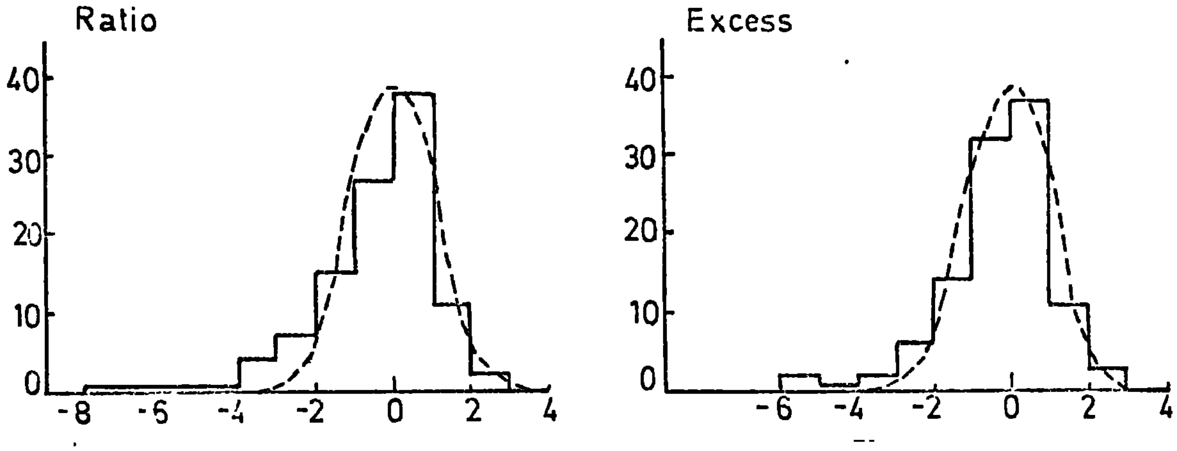

Non-Vertical Direction — Sea Level Energies

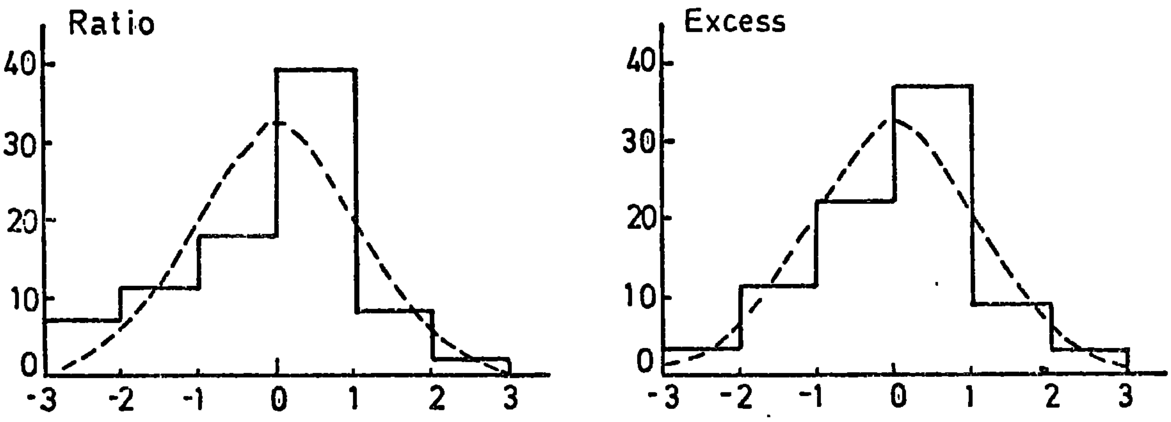

Vertical Direction — Sea Level Energies (Excluding MARS)

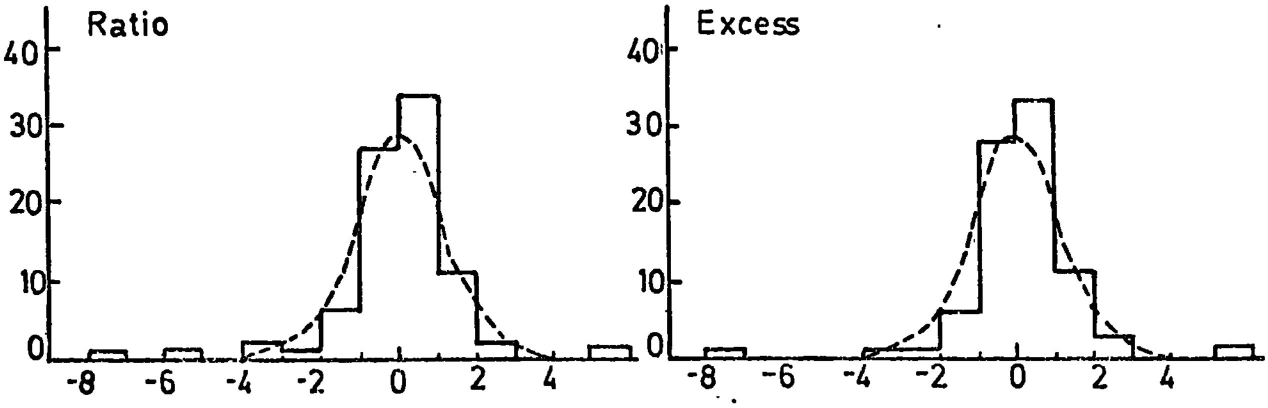

FIGURE 6.3. DISTRIBITION OF DEVIATIONS

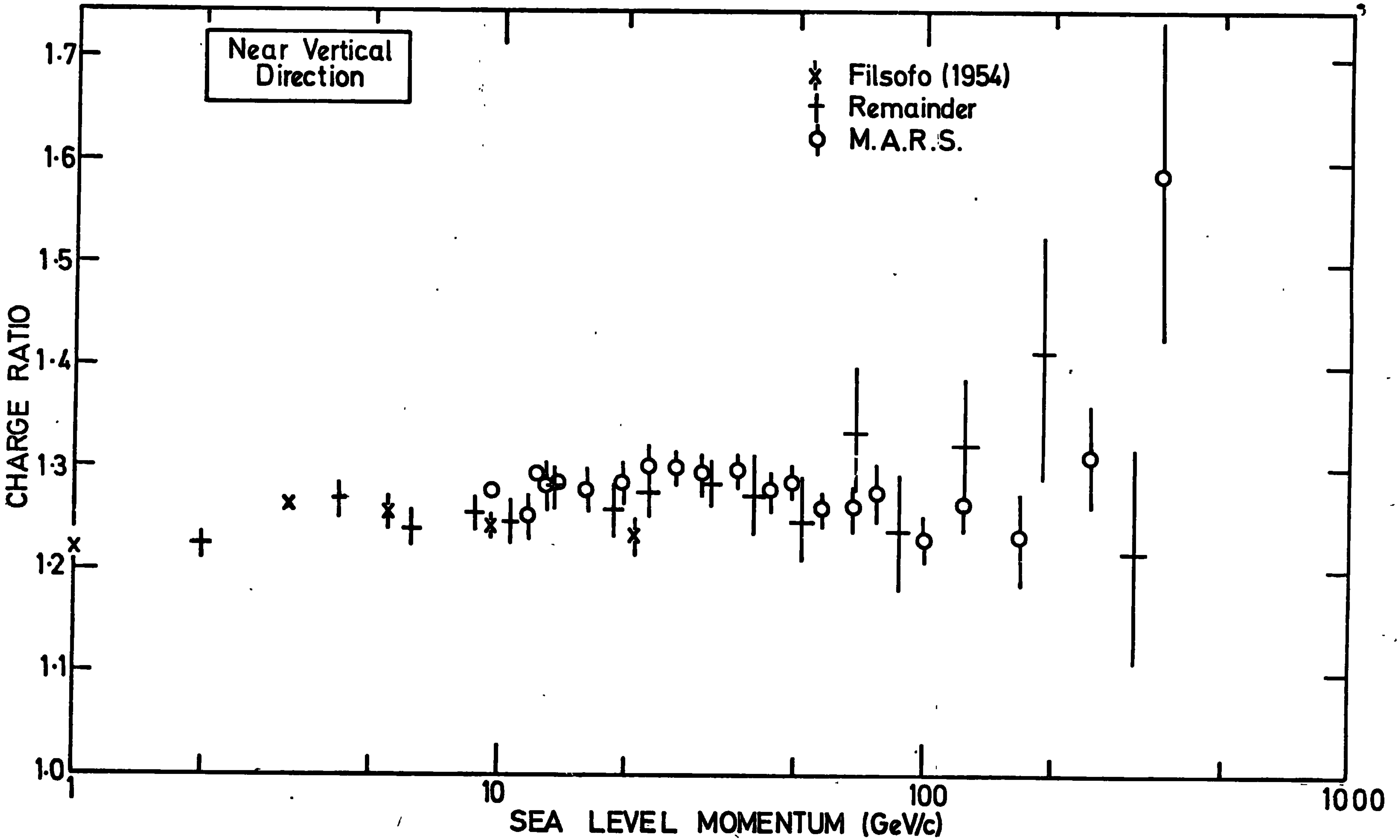
Near Vertical Direction
x Filsofo (1954)
+ Remainder
o M.A.R.S.
CHARGE RATIO
1·7
1·6
1·5
1·4
1·3
1·2
1·1
1·0
1
10
100
1000
SEA LEVEL MOMENTUM (GeV/c)

Figure 6·4

remaining experiments of Fig. 6.1 is 1.2540 ± 0.0051; combining the two groups gives a mean of 1.2431 ± 0.0023. The mean ratio of the M.A.R.S. data (which involve more particles than the combined data of Fig. 6.1) is 1.2850 ± 0.0023 and the distribution of t is well fitted by a Gaussian curve. This value is heavily weighted by the category 23 results at 9.7, 12.4 and 13.9 GeV/c. Excluding these results yields an overall mean of 1.2818 ± 0.0042, a ratio not significantly different from the original value. These values are consistent with other, independent sets of M.A.R.S. data i.e. those of Ayre et al (1971) (mean ratio 1.29 ± 0.03 for momenta greater than 10 GeV/c) and of Ayre et al (1972) (mean ratio 1.284 ± 0.004 for momenta greater than 10 GeV/c).

The difference from the M.A.R.S. result is 0.0449 ± 0.0034 which is (statistically) highly significant. This is mainly due to those few low charge ratios measured for momenta $\lesssim$ 3 GeV/c (Fig. 6.1). Considering only momenta $\gtrsim$ 9.7 GeV/c gives for Fig. 6.1 a mean ratio of 1.2635 ± 0.0075 leading to a deviation from the M.A.R.S. result of 0.0215 ± 0.0078. This is slightly less than three standard errors and its significance is uncertain. The value 1.2850 ± 0.0023 is in good agreement with the recent results obtained by Allkofer et al (1971) who found a mean of 1.29 ± 0.02 for momenta greater than 10 GeV/c and by Nandi and Sinha (1972) who found a mean of 1.28 ± 0.02 for momenta greater than about 5 GeV/c.

As mentioned above the lack of marked deviations from normality of the distribution of t indicates a lack of momentum dependence of the charge ratio. The grouped data of

Fig. 6.1 show little evidence for momentum dependence except at very low momenta ($\lesssim$ 3 GeV/c) where the ratio is rather low. Considering the M.A.R.S. data alone it can be seen that there is no confirmatory evidence for the sharp maxima and minima suggested by a number of workers. For example the results of Ayre et al (1971) indicated a minimum in the ratio at ~70 GeV/c, the results of Allkofer et al (1971) indicated a maximum in the same region and a minimum at ~100 GeV/c. A maximum at 25 GeV/c was observed by Tebb et al (1971). In the present M.A.R.S. data there does seem to be some suggestion of a broad maximum in the range 20-50 GeV/c followed by a somewhat lower ratio out to about 200 GeV/c. Grouping the data into different momentum bins does not change the overall pattern. Below 50 GeV/c the mean ratio is 1.2867 ± 0.0024; again below 50 GeV/c but neglecting the three heavily weighting points the mean is 1.2878 ± 0.0048 - not significantly different; above 50 GeV/c the mean is 1.2617 ± 0.0086.

The conclusion is that although the data are, as a whole, consistent with a constant charge ratio there is some slight indication of a slow variation with momentum. At momenta beyond 200 GeV/c no useful conclusions can be drawn but the ratio shows no tendency to fall to 1.0. This latter is supported by the high energy data of Ashley II et al (1973) which is shown later in this chapter.

6.2 The Near-Horizontal Direction

Interest in the muon beam at large zenith angles was initiated by the realization that although the integral muon intensity is much reduced by the increased depth of atmosphere, an increase in the intensity of particles above about 100 GeV/c could be expected. Thus the mean sea level energy of muons increases with increasing zenith angle and studies of high energy particles are more profitably carried out at these large angles.

Such measurements have the further significance that the particle beam should be an almost pure muon beam, strongly interacting particles having been absorbed by the large depth of atmosphere.

Figures 6.5 and 6.6 show the charge ratio and excess as a function of sea level momentum. Figures 6.7 and 6.8 show the same variable as a function of production momentum. All of these results have been obtained at zenith angles $\geq 75^{\circ}$ with the exception of Higgs (1973) in which the angle was 30°. In the first pair of graphs the results are those of the following : Kasha et al (1968), Alexander (1970), Kawaguchi et al (1966), Aurela et al (1966), Flint and Nash (1971), Ashton and Wolfendale (1963), Mackeown et al (1965), Kamiya et al (1971) and Higgs (1973). In the second pair of graphs the results are those of the following : Kawaguchi et al (1966), Aurela et al (1966), Flint and Nash (1971), Ashton and Wolfendale (1963), Mackeown et al (1965), Kamiya et al (1971), Higgs (1973), Burnett et al (1973), Ashley II et al (1973).

Distributions of t and t' have been obtained for the various cases and are shown in Fig. 6.3; as before, there seems to be no large deviations from normality.

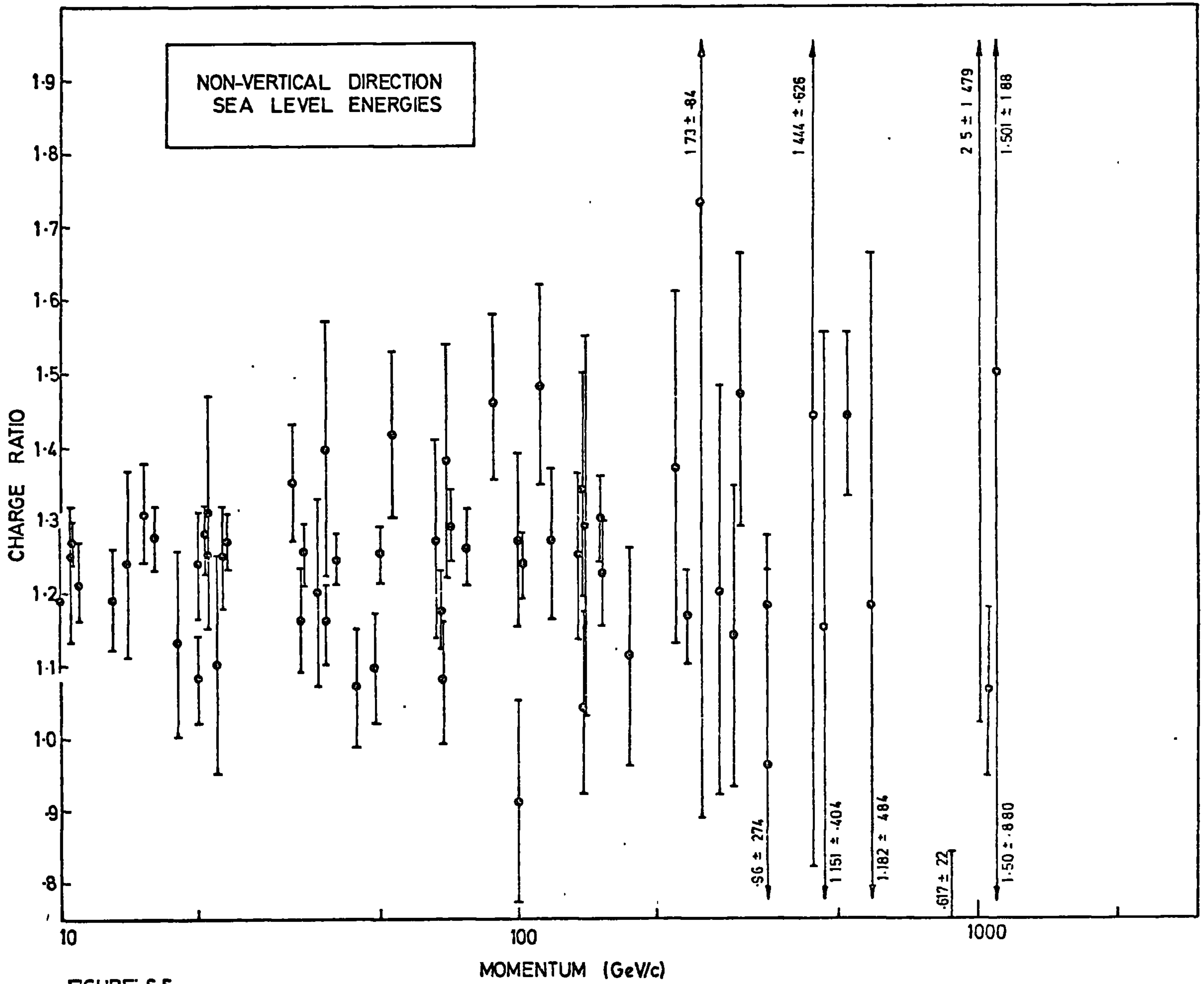
NON-VERTICAL DIRECTION
SEA LEVEL ENERGIES
CHARGE RATIO
1·9
1·8
1·7
1·6
1·5
1·4
1·3
1·2
1·1
1·0
·9
·8
10
100
1000
MOMENTUM (GeV/c)
1·73 ± ·84
1·444 ± ·626
2·5 ± 1·479
1·501 ± 1·88
·96 ± ·274
1·151 ± ·404
1·182 ± ·484
·617 ± ·22
1·50 ± ·880

FIGURE: 6.5.

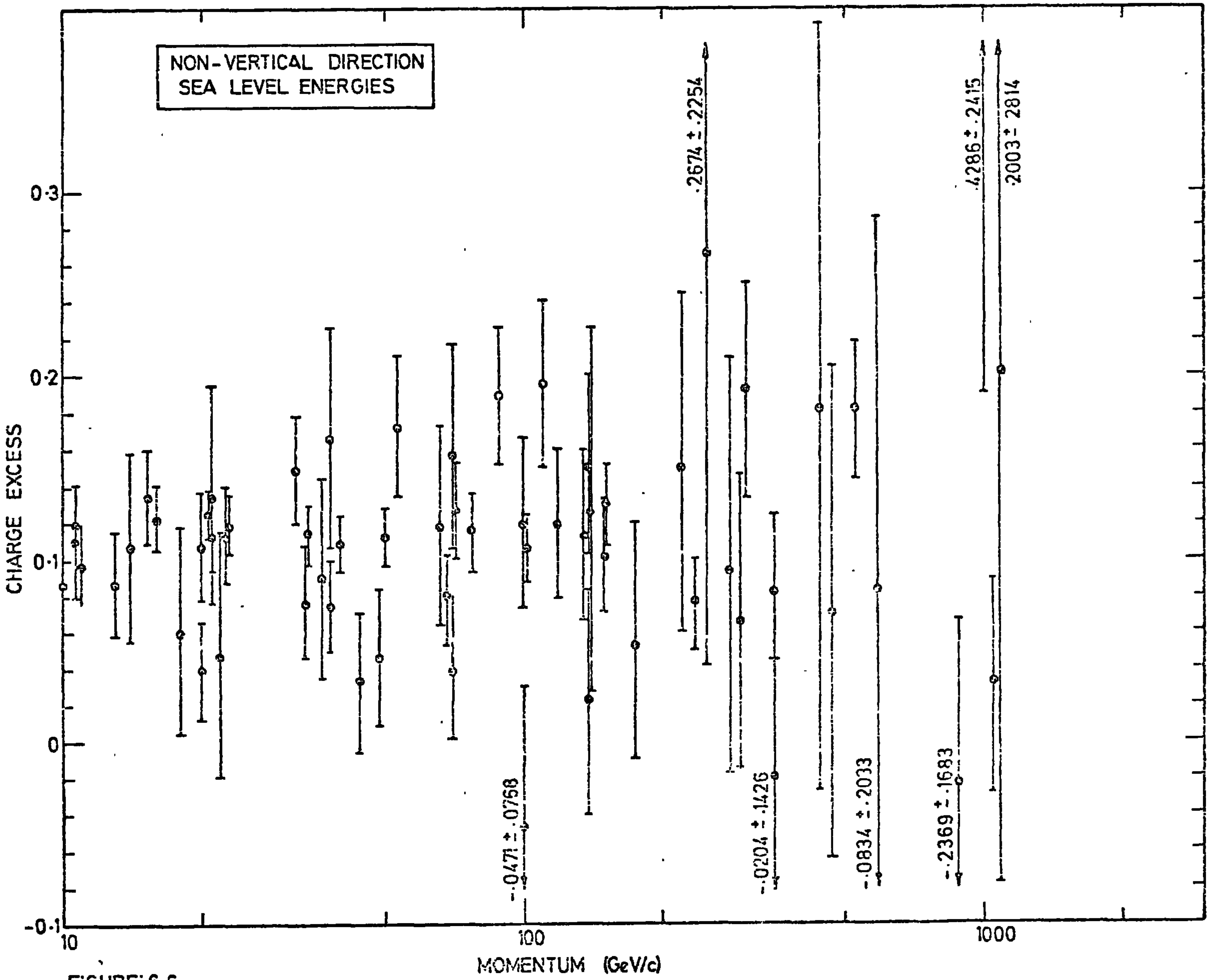
NON-VERTICAL DIRECTION
SEA LEVEL ENERGIES
CHARGE EXCESS
0·3
0·2
0·1
0
-0·1
10
100
1000
MOMENTUM (GeV/c)
·2674 ± ·2254
·4286 ± ·2415
·2003 ± ·2814
-·0471 ± ·0768
-·0204 ± ·1426
-·0834 ± ·2033
-·2369 ± ·1683

FIGURE: 6.6

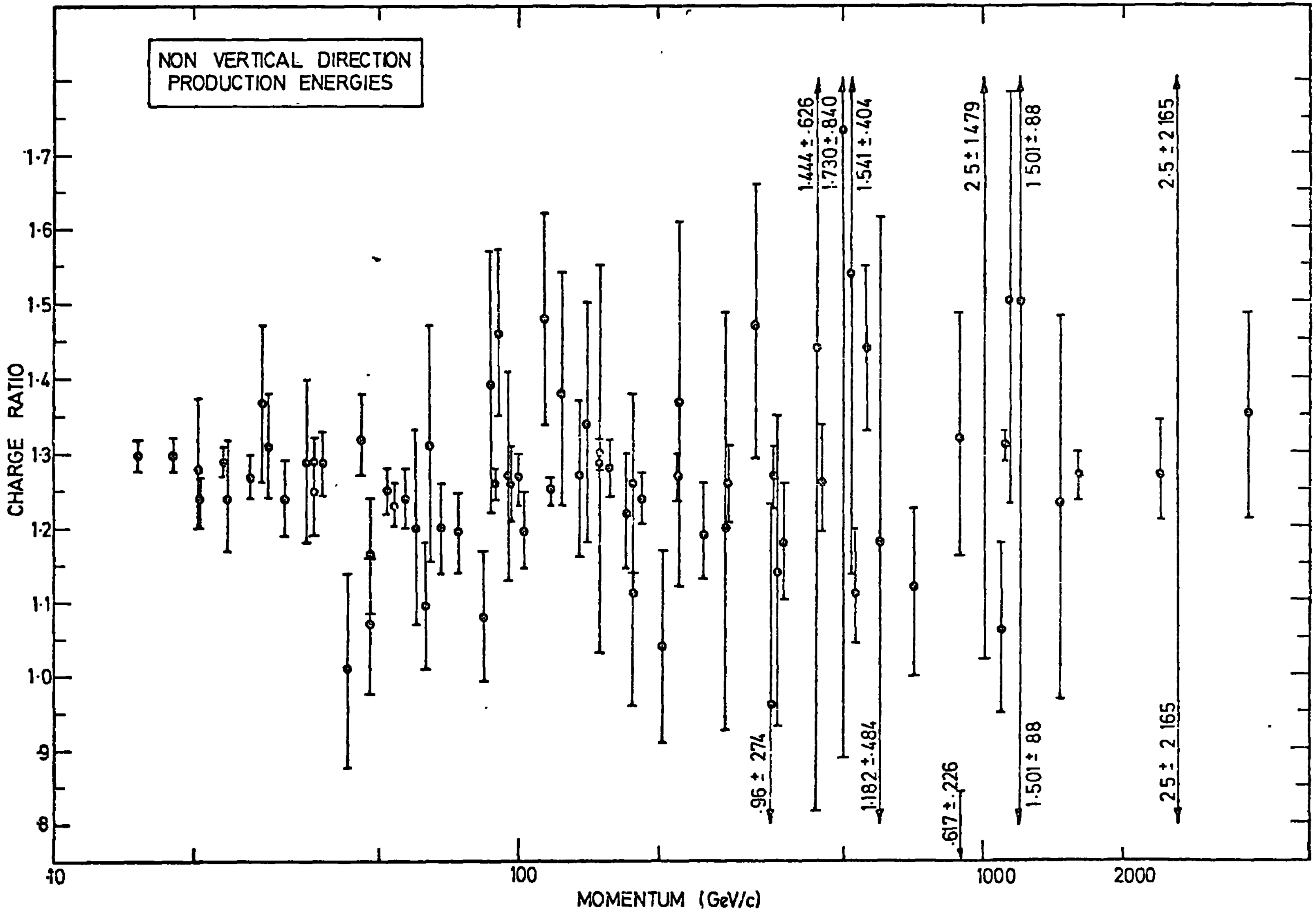NON VERTICAL DIRECTION
PRODUCTION ENERGIES
CHARGE RATIO
1·7
1·6
1·5
1·4
1·3
1·2
1·1
1·0
·9
·8
10
100
1000
2000
MOMENTUM (GeV/c)
1·444 ± ·626
1·730 ± ·840
1·541 ± ·404
2·5 ± 1·479
1·501 ± ·88
2·5 ± 2·165
·96 ± ·274
1·182 ± ·484
·617 ± ·226
1·501 ± ·88
2·5 ± 2·165

FIGURE: 6·7.

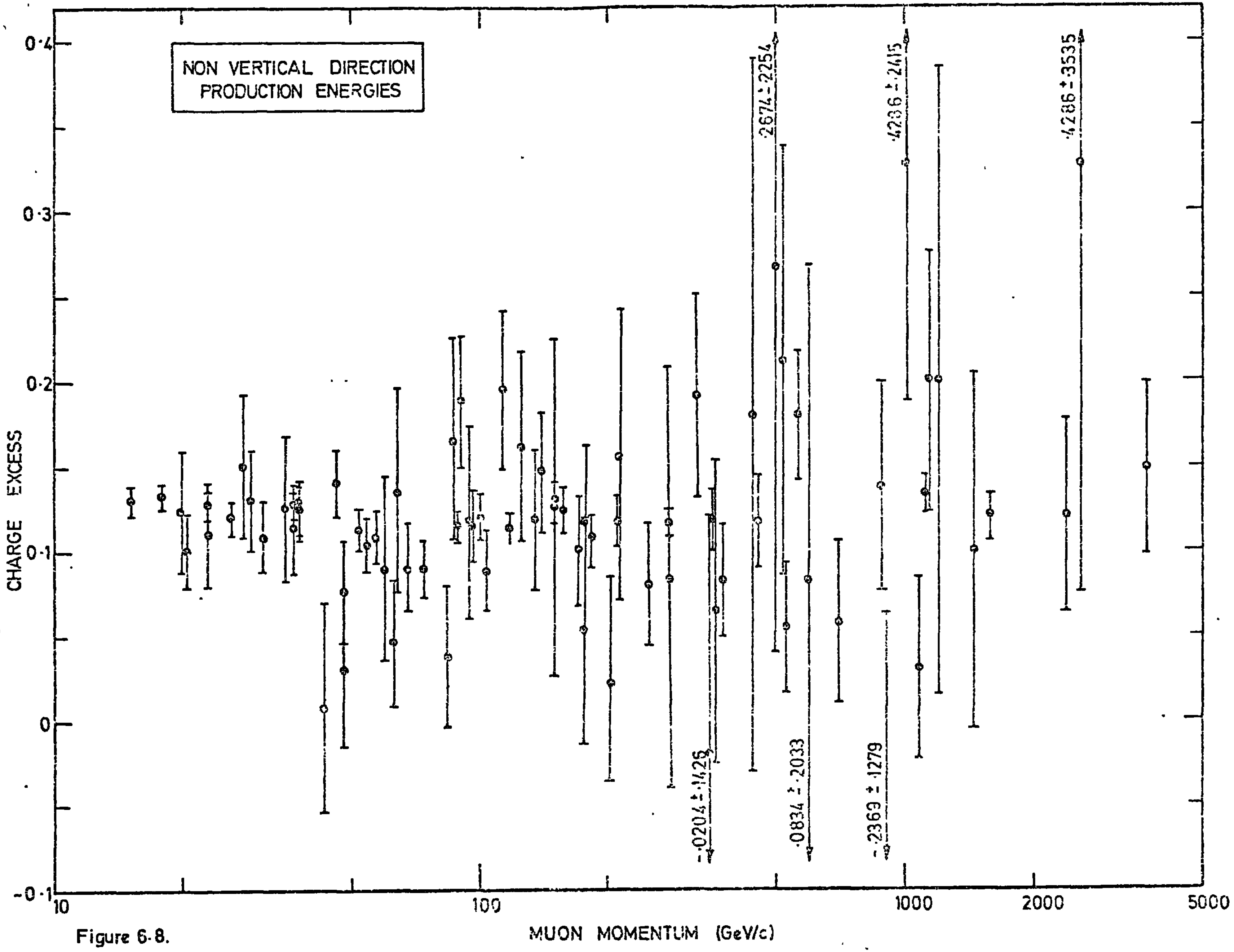
NON VERTICAL DIRECTION
PRODUCTION ENERGIES
CHARGE EXCESS
0·4
0·3
0·2
0·1
0
-0·1
10
100
1000
2000
5000
MUON MOMENTUM (GeV/c)
·2674 ± ·2254
·4286 ± ·2415
·4286 ± ·3535
-·0204 ± ·1425
·0834 ± ·2033
-·2369 ± ·1279

Figure 6·8.

Sea Level Momenta

The data of Figure 6.5 have been grouped and are shown in Figure 6.9. The results of Kamiya et al (1971) and Flint and Nash (1971) have been kept separate since they have a noticeably greater statistical significance than the remainder, at least up to momenta of ~100 GeV/c. At higher momenta the errors are large. The overall mean charge ratio of Kamiya et al (1971) is 1.259 ± 0.015; that of Flint and Nash (1971) is similar at 1.262 ± 0.016. The overall mean of the remaining data is rather lower at 1.222 ± 0.013. The last point plotted for this data has been obtained from experiments covering the wide energy range 600-2600 GeV. The low charge ratio may be due to the data having been collected near the m.d.m. of the individual experiments and for this reason the point should be treated with some reserve. Combining all three sets of data yields a mean ratio of 1.2449 ± 0.0085.

Figure 6.9 shows some very slight indications of a rather sharp dip in the ratio at ~60 GeV/c and of a broad peak in the ratio at ~ 20 GeV/c. A possible explanation of the latter, in terms of the production of (mainly positive) particles of high transverse momentum in the nuclear collisions generating the muon parents, has been put forward by Kelly et al (1968). However it can be seen that more accurate charge ratio data are required before a study of its momentum dependence is likely to be profitable.

Production Momenta

The data of Fig. 6.7 have been grouped as shown in Fig. 6.10. The results of the more precise experiments -

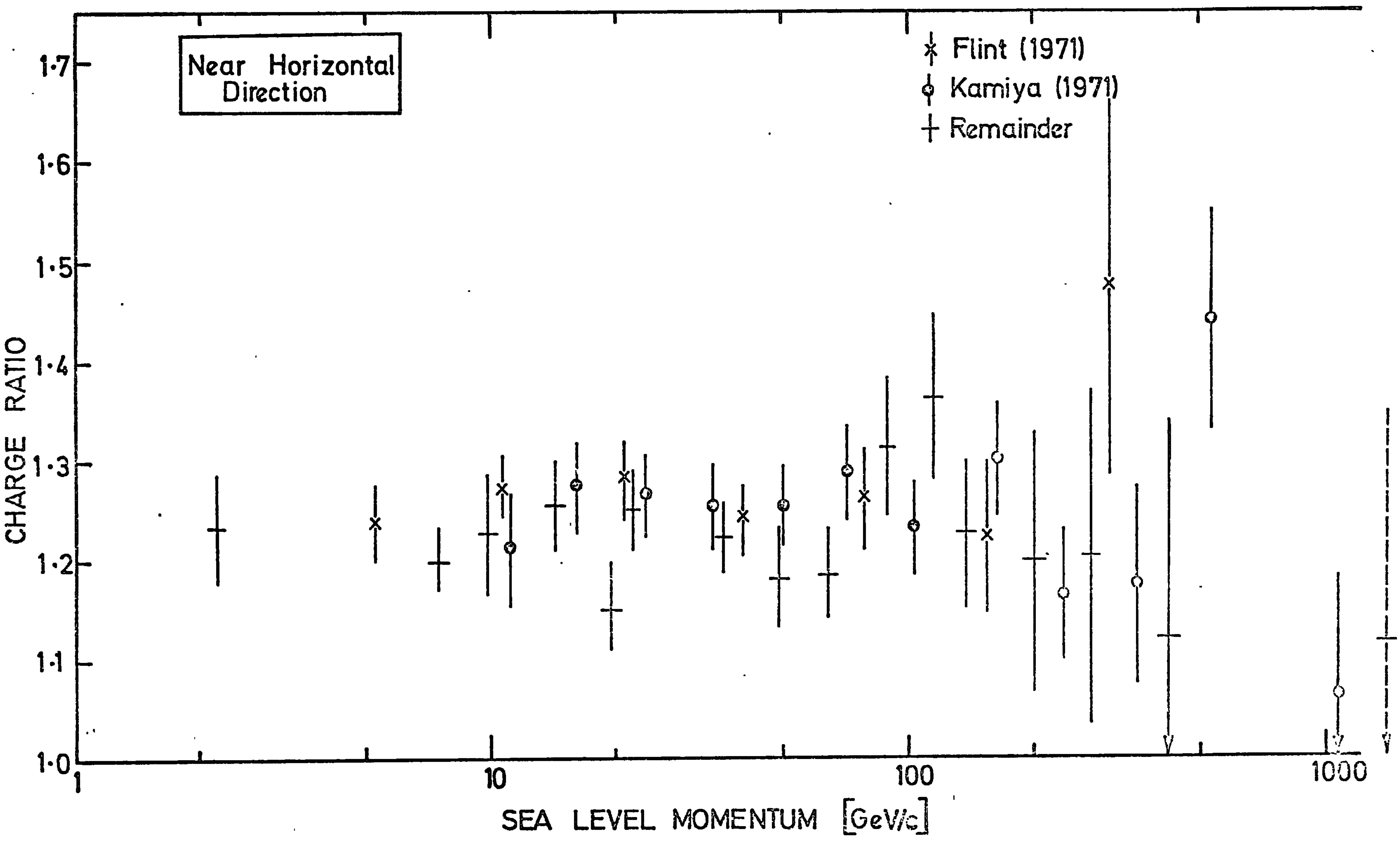
Near Horizontal Direction
Flint (1971)
Kamiya (1971)
Remainder
CHARGE RATIO
1·7
1·6
1·5
1·4
1·3
1·2
1·1
1·0
1
10
100
1000
SEA LEVEL MOMENTUM [GeV/c]

Figure 6.9

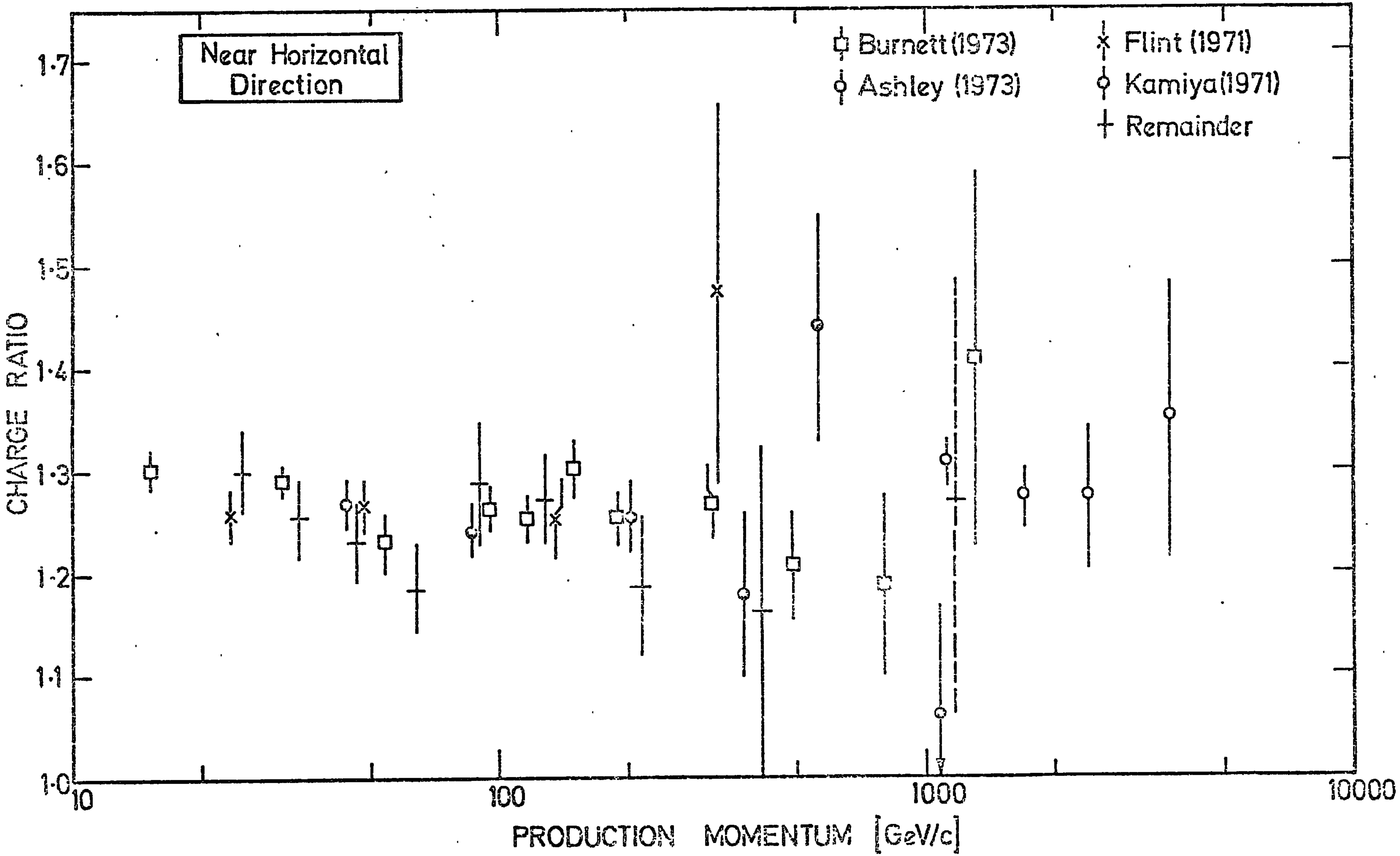
Near Horizontal Direction
Burnett (1973)
Ashley (1973)
Flint (1971)
Kamiya (1971)
Remainder
CHARGE RATIO
1·7
1·6
1·5
1·4
1·3
1·2
1·1
1·0
10
100
1000
10000
PRODUCTION MOMENTUM [GeV/c]

Figure 6.10

Flint and Nash (1971), Kamiya et al (1971), Burnett et al (1973) and Ashley II et al (1973) - have been kept separate. The latter are of particular importance since they extend to the highest energies and are reasonably precise. The data point shown dotted is a summary of the less precise experiments covering an energy range 500-2600 GeV.

The overall mean charge ratios of the four experiments above and of the remainder of the results of Fig. 6.7 are in reasonable agreement; they are respectively 1.263 ± 0.016, 1.255 ± 0.015, 1.2795 ± 0.0070, 1.298 ± 0.017 and 1.250 ± 0.018. Combining these gives a mean of 1.2738 ± 0.0053.

There are no strong indications of any momentum dependence of the charge ratio. The results of Ashley II (1973) do however, indicate that the ratio is not falling to unity.

6.3 Combination of the Data

The results shown in Figs. 6.1 and 6.7 may be combined if the former are expressed as a function of production momentum. This has been done simply by adding 2 GeV/c to the momenta of the data points of Fig. 6.1. For each of the two diagrams (6.1 and 6.7) the results have been grouped without discriminating between experiments of different precision; the last data point of Fig. 6.7 has been ignored because of its wide momentum range and poor statistical significance. The results are plotted in Fig. 6.11 along with the M.A.R.S. results.

The overall mean charge ratios for the near vertical sea level data, the non-vertical production data and the M.A.R.S.

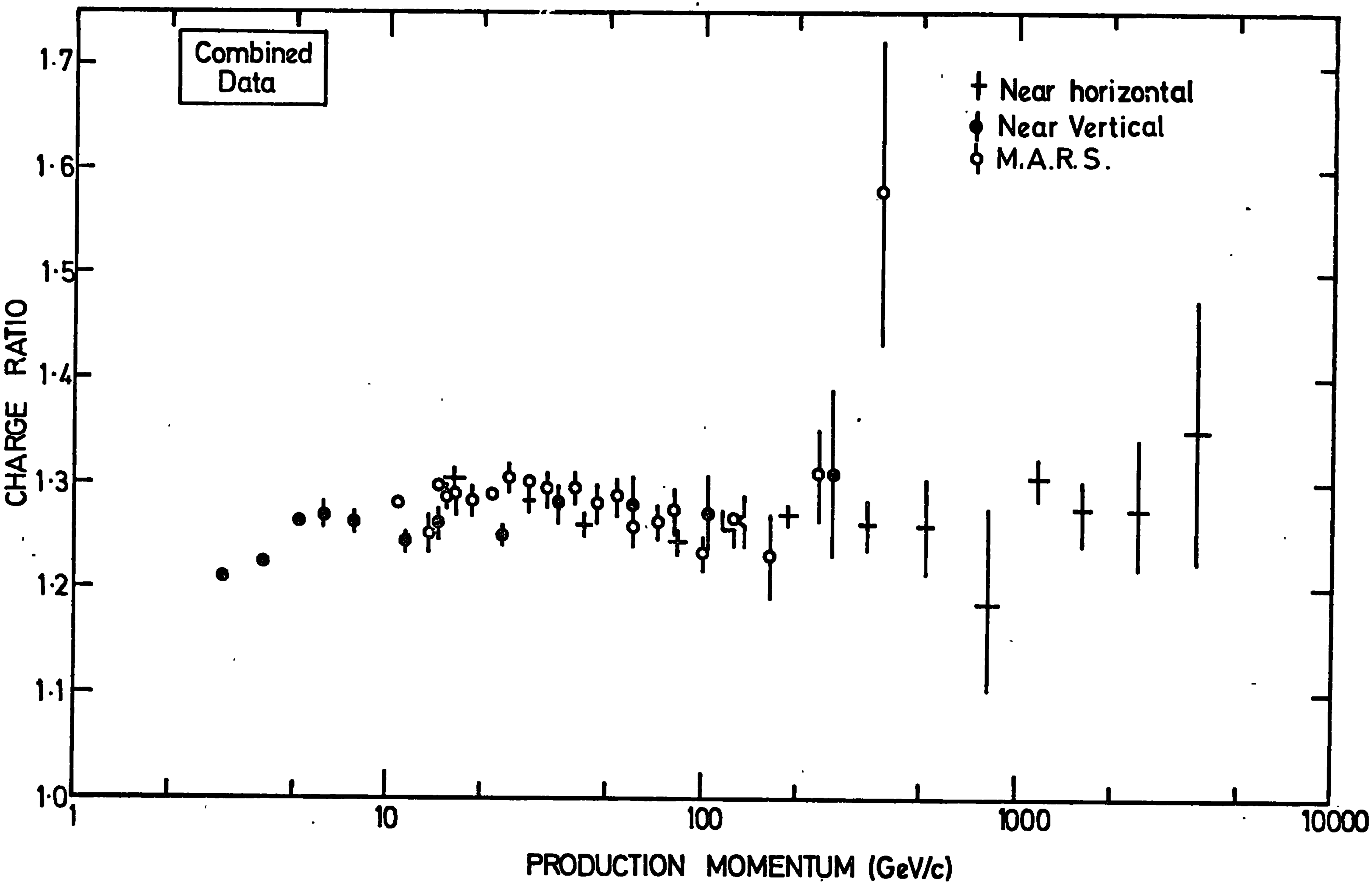
Combined Data
Near horizontal
Near Vertical
M.A.R.S.
CHARGE RATIO
1·7
1·6
1·5
1·4
1·3
1·2
1·1
1·0
1
10
100
1000
10000
PRODUCTION MOMENTUM (GeV/c)

Figure 6.11

data are, as already described 1.2431 ± 0.0023, 1.2738 ± 0.0053 and 1.2850 ± 0.0023 respectively. The total data give a mean of 1.2660 ± 0.0016; if results only at momenta $\geqslant$ 9.7 GeV/c are considered, the mean is 1.2818 ± 0.0020.

Comparing the near vertical data (excluding M.A.R.S. and results below 9.7 GeV/c) and the non vertical production data no obvious zenith angle dependence emerges. Also, the low energy points are best established in the near-vertical direction whilst the high energy region (beyond 200 GeV/c) is dependent upon studies at large zenith angles. The M.A.R.S. data show no systematic deviations from the other data sets. There is little evidence from Fig. 6.11 for any sharp maxima or minima.

CHAPTER 7

HIGH ENERGY INTERACTIONS

7.0 Introduction

The purpose of this chapter is to present a brief summary of the experimental features of high energy collisions which are most relevant to an attempt to predict the observed muon sea level charge ratio. The features summarized have mainly been derived from accelerator experiments in which N-N, and to a lesser extent meson-N collisions have been studied.

7.1 Accelerators

Until about 1968 the highest energy available from an accelerator was around 30 GeV and extensive studies of the particle production in N-N collisions (usually p-p collisions) yielded seven major results :-

(i) the average number of produced particles is small - much smaller than would be the case if most of the available energy were converted into particles. The average charged particle multiplicity is roughly proportional to $E_L^{\frac{1}{4}}$, where E_L is the laboratory energy of the projectile particle.

(ii) the transverse momentum (P_t) of all of the produced particles is small - the mean value being 0.3 - 0.4 GeV/c. The cross-section for particle production as a function of P_t falls rapidly with increasing P_t (an approximately exponential fall but recent results show a flattening).

(iii) the leading particle effect - the projectile and target particles tend to retain their identity in a collision.

This is shown in the Peyrou plots for various interactions as shown by, for example, Horn (1972). These same plots also show a cloud of pions centred on the origin i.e. near-zero longitudinal centre-of-mass (CM) momentum.

(iv) pionization - this is the name given to the above mentioned pion cloud. This phenomenon was first discussed by Pal and Peters (1964) in describing cosmic ray results. A rigorous definition of pionization is that 'pionization exists if, as the incoming energy tends to infinity the fraction of produced particles with energy less than some fixed quantity approaches a non-zero limit' (Chou and Yang, 1970).

(v) the existence of resonances - these are revealed by 'bumps' in the variation of cross section with energy; they are confined to projectile energies $E_L \lesssim 5$ GeV. They will not be considered further.

(vi) the majority (about 80%) of the produced particles are pions.

(vii) the total cross-section falls from almost 200 mb at 1 GeV to about 50 mb at 10 GeV and thereafter falls only slowly to 40 mb at 30 GeV (recent results indicate a rise at higher energies - this will be mentioned later).

Since 1970 data at energies $>$ 30 GeV has become available from :-

(a) the 70 GeV proton synchrotron at the I.H.E.P., Serpukhov, U.S.S.R.,

(b) the proton syndrotron at the N.A.L., Batavia, U.S.A. which operates in the range 200-500 GeV, and

(c) the intersecting storage ring (I.S.R.) facility at C.E.R.N, Geneva, in which p-p collisions at (equivalent) laboratory energies up to about 2000 GeV are studied, (Fig.7.1).

7.2 Theoretical Aspects

The theoretical treatment of multi-particle production has developed rapidly in the past few years. These studies have mainly involved the development of both basic hypotheses (which describe various aspects of high energy collisions in broad terms) and the more specific models (used to give detailed descriptions of many experimentally measured parameters).

In this work no attempt has been made to develop a model; it has been found adequate to consider only the basic hypotheses. Of these latter the most relevant are those due to Benecke et al (1969) and to Feynman (1969a,b). Detailed discussions of these ideas are given in many review articles (for example Horn (1972), Feinberg (1972)) and only a short description need be given here.

It is customary to use the variables x and y - the reduced longitudinal momentum and the longitudinal rapidity respectively.

The former has been defined by Feynman (1969b) as

$$x = 2P_L / \sqrt{s}$$

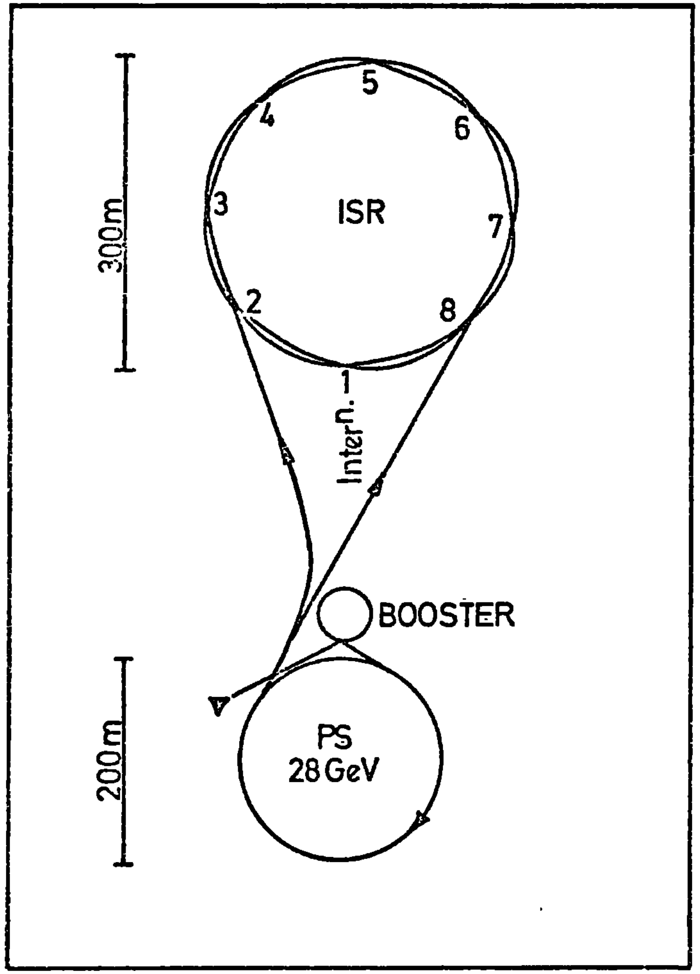

FIG. 7-1.

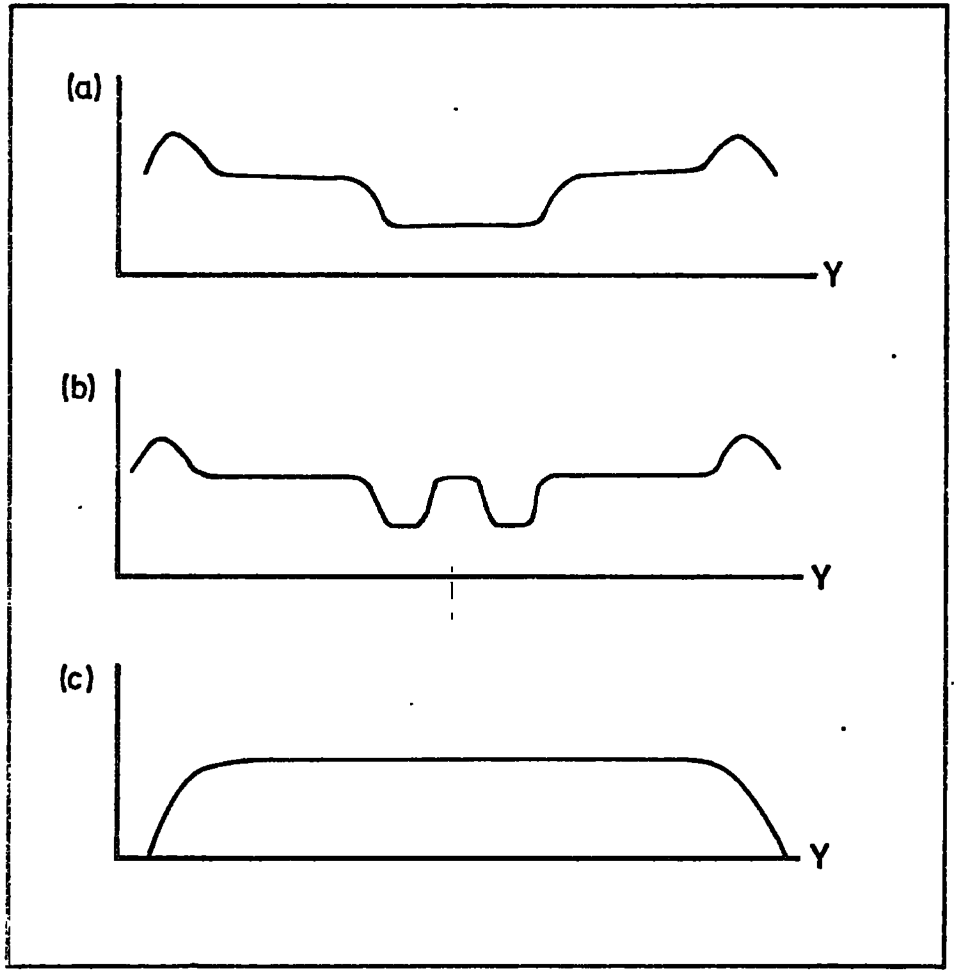

FIG. 7-2.

where P_L is the CM longitudinal momentum of the produced particle and $\sqrt{s}$ is the total energy of the colliding particle system. In most cases $\sqrt{s}/2$ is numerically close to the maximum kinematically allowed value of the cm momentum (P_{max}) of the particle, hence

$$x = P_L/P_{max}$$

The difference between P_{max} and $\sqrt{s}/2$ is important for low energy experiments - the discrepancy is about 5% at an incident laboratory energy of 20 GeV. In published comparisons of high (usually I.S.R.) and low energy data the value of P_{max} for the latter is usually found from the relation

$$P_{max} = \frac{1}{2\sqrt{s}} \left[(s - (m + m_x)^2)\ (s - (m - m_x)^2) \right]^{\frac{1}{2}}$$

where m is the mass of the particle under consideration and m_x is the minimum mass of those other particles which are produced in satisfying the conservation of charge, baryon number and strangeness. Thus when m is the mass of π^-, π^+, k^-, k^+, $\bar{p}$ or p then m_x is the mass of $2p + \pi^+$, $p + n$, $2p + k^+$, $\Lambda + p$, $3p$ or p respectively.

The longitudinal rapidity in the centre of mass system (yc) is defined by

$$yc = \frac{1}{2} \ln \left[(E + P \quad / (E - PL) \right]$$

where E is the cm energy of the particle. Taking the velocity of light as unity gives $yc = \frac{1}{2} \ln \left[(1 + \beta)/(1 - \beta) \right]$, where β is the longitudinal β value. Since yc is a monotonically increasing function of β (or velocity) the name rapidity has been coined. In the non - relativistic case the last expression reduces to β. Other, equivalent, expressions for yc are :-

$$yc = \tanh^{-1} (PL/E)$$

$$yc = \cosh^{-1} (E/\mu)$$

$$yc = \sinh^{-1} (PL/\mu)$$

where $\mu = (M^2 + P_t^{\,2})^{\frac{1}{2}}$, the so-called longitudinal mass and P_t is the cm transverse momentum.

Combining the last expression with the definition of x gives

$$yc = \sinh^{-1} \frac{x\sqrt{s}}{2u} = \ln \left(\frac{\sqrt{s}}{2\mu}\right) + \ln \left(x + (x^2 + 4\mu^2/s)^{\frac{1}{2}}\right)$$

and

$$x = \frac{2\mu}{\sqrt{s}} \sinh yc$$

Thus there is not a one-to-one relation between x and yc since the P_t - dependent longitudinal mass enters the expression.

Also $$dx = \frac{2E}{\sqrt{s}} dyc$$

and $$dyc = \frac{dx}{\{x^2 + 4\mu^2/s\}^{\frac{1}{2}}} = \frac{dPL}{E}$$

Since the denominator of the last expression is usually < 1 it can be seen that a plot using yc as a variable is expanded compared to one using x as the variable; the expansion increases as smaller x values are considered.

A useful feature of yc is the ease with which it is transferred from one reference frame to another. The laboratory energy (EL) of a particle in terms of its centre of mass energy (E) and longitudinal momentum (P) is

$$EL = \gamma(E + \beta P)$$

By expressing this in terms of the centre of mass rapidity yc and a new variable y defined by $y = \cosh^{-1} \gamma$ the previous equation becomes

EL = μ cosh (yc + y), where μ is the longitudinal mass. The quantity (yc + y) is known as the laboratory rapidity y_L. Since $dy_c = dy_L$ the transform leaves the shape of a function unchanged - it simply shifts the distribution by an amount $y = \cosh^{-1} \gamma$. Rapidity may also be related to a well known cosmic ray variable. If θ_c (θ_L) is the polar angle in the CM (LAB) system measured with respect to the incident particle direction then since $P_t = P_L \tan \theta_c$ and assuming $P_L^2 \gg P_t^2 \gg m^2$ the rapidity may be written

$$y = -\log (\tan \theta_c/2)$$

Substituting $\tan \theta_c/2 = \gamma \tan \theta_L$ where γ is the Lorentz factor of the CM system gives

$y = -\log (\tan \theta_L) - \log \gamma$ which is almost identical to the variable (λ) used in cosmic ray emulsion studies

$$\lambda = \log (\tan \theta_L).$$

Some care should be exercised in using this relation since the assumption used to derive it is often not fulfilled.

Experimental data on particle production are commonly presented in terms of an invariant production cross section defined as

$$F_o (PL, Pt, S) = E \frac{d^3\sigma}{d^3p}$$

where E is the cm energy of the particle. Averaging over the azimuth angle (Gellert, 1972) gives the useful relation

$$E\,\frac{d^3\sigma}{d^3p} = \frac{E}{2\pi P_t}\;\frac{d^2\sigma}{dP_L\,dP_t} = \frac{E}{PL^2}\;\frac{d^2\sigma}{dP_L\,d\Omega}$$

where Ω represents the solid angle.

The hypotheses which will be briefly described are the hypothesis of limiting fragmentation (referred to in future as HLF) of Benecke et al (1969) and the scaling hypothesis of Feynman (1969a,b). The former was suggested in an attempt to find a framework within which high energy hadron-hadron collisions could be described.

Stated succinctly the HLF asserts that in a collision between two hadrons such as when a beam of accelerated particles strikes a stationary target the projectile and target separately fragment. As the incident energy increases, the fragments from the target are supposed to approach a limiting distribution when viewed in the laboratory reference frame. Similarly the projectile fragments approach a limiting distribution when viewed in the projectile reference frame where the projectile is at rest. There may or may not be other kinds of particles emitted in the collision in addition to these two kinds of fragments. The intuitive picture on which the hypothesis was based is analagous to the optical model developed to treat high energy elastic scattering. The target is regarded as a droplet and serves as an absorbing and refractive medium through which an incoming particle propagates as a wave. In this picture the incoming particle viewed in the laboratory frame is Lorentz contracted into a thin disc. The target particle (for example a proton) has a geometrical extension of about 7.10^{-14} cm. Passage of the thin disc through the target takes place in about

2.10^{-24} sec and both target and projectile become excited in this time and this is assumed to be the cause of the breakup of the particles. The mechanism of excitation is not considered in detail by the authors but is thought to be similar to diffraction dissociation. As the incident energy increases the disc becomes more compressed but the authors assume this has no effect on the excitation of the particles. This assumption was based upon the experimentally observed constancy of the total and elastic cross sections in the range 15-30 GeV. The observation of an increasing total cross section at higher energies had not been made at the time the idea was formulated. However this does not seem to have invalidated the theory as the results of a recent experiment (Belletini et al, 1973) designed to test the HLF have shown. This experiment, performed with the I.S.R., compared the particle distributions in the fragmentation region of one beam (beam 1) which was fixed in momentum while varying the momentum of the other beam (beam 2), hence changing the available energy. Over the momentum range covered by beam 2 the total cross-section has been observed to rise by about 5%. The experiment showed that the angular distribution of particles in the hemisphere surrounding beam 1 downstream of the interaction point were independent of the momentum of beam 2. Experimental errors were around ± 2%. An important deviation from this independence was found for particles emitted at large angles ($\geqslant 45^{\circ}$ in the centre of mass). This has been attributed to 'spill over' of particles associated with beam 2 into the hemisphere of beam 1. However at smaller angles the conclusion is that the HLF is valid.

Of particular relevance to the interpretation of the muon charge ratio are the roles of pionisation and charge exchange within the framework of the HLF. The HLF is independent of the existence or non-existence of pionization. At high energies the authors of the HLF considered, as a separate hypothesis, that pionization was unlikely to occur (Yang, 1969) since this would imply that the colliding particles arrested one another with the subsequent evaporation of slow pions. Such a picture was thought to be inconsistent with the idea of two extended objects passing through one another and shattering in the process. Results from the I.S.R. have since shown however that the majority of pions are, in the centre of mass system, of low energy and are grouped around zero centre of mass momentum. Benecke (1971) shows the expected rapidity distribution for particle production according to the HLF (Fig. 7.2a); also given is the expected distribution (Fig. 7.2b) when a pionization component is added. This component was derived from the work of Cheng and Wu (1969). Another interpretation of the HLF as given by Morrison (1972) shows the expected rapidity distribution to be as in Fig. 7.2c. The previously mentioned 'spill-over' of particles from one hemisphere to another may be the result of some pionization type of mechanism. At infinite incident energy the spill over is expected to be zero i.e. all of the target fragments are contained in one hemisphere and all of the projectile fragments in the other. This means that at increasingly high energies the probability of charge exchange between the particles tends to zero.

In summary, the HLF can be said to provide a reasonable framework on which can be based some speculations on the behaviour of very high - higher than presently available with particle accelerators - energy collisions. The HLF has many features in common with the scaling hypothesis of Feynman.

The meaning of scaling in the context of the hypothesis is that when the differential cross-section for particle (e.g. pion) production is expressed in terms of appropriate parameters then the resulting function has the same form, independent (at high values of $\sqrt{s}$) of the available energy of the colliding system ($\sqrt{s}$). This function is known as the scaling function. The appropriate parameters, suggested by Feynman, were the CM transverse momentum (P_t) and the CM reduced longitudinal momentum (x). If the invariant cross section $Ed^3\sigma/d^3p$ (where E is the CM energy of the secondary particle) is written as

$$E\frac{d^3\sigma}{d^3p} \quad \left(= \frac{E}{2\pi Pt}\ \frac{d^2\sigma}{dPL\ dPt} \right) \quad = \quad f_o\ (x,\ P_t,\ s)$$

then according to the scaling hypothesis f_o depends (at high values of $\sqrt{s}$) only upon P_t and x, that is

$$f_o\ (x,\ Pt,\ s) \xrightarrow[s \to \infty]{} f_o\ (x,\ Pt)$$

(In fact this is not expected to hold for very small values of x ($x \lesssim 2/\sqrt{s}$) as will be mentioned later). The above representation is that used by, for example, Damgaard and Hansen (1972) and by Gellert (1973). A slightly different representation is used by, for example, Michejda (1971) :-

$$E\frac{d^2\sigma}{dPL\ dPt} = f\ (x,\ Pt,\ s)$$

and, according to scaling

$$f\ (x,\ Pt,\ s) \xrightarrow[s \to \infty]{} f\ (x,\ Pt)$$

The difference between these two formulations is the factor $2\pi Pt$. If particle ratios at fixed Pt are considered then it is unimportant but when particle multiplicities are concerned it must be taken into account.

The scaling concept arose from Feynman's introduction of the parton model to describe high energy collisions. It has been found from the results of deep inelastic e-p scattering experiments that a nucleon interacts with γ-quanta as an aggregate of point-like charged particles. In the Feynman approach, nucleons are taken to be composed of a cluster of such particles and it is these particles which have been named partons. A possible interpretation of partons is that they are quarks; this subject is discussed by, for example, Lipkin (1973).

Using a heuristic argument based upon a quantum field theory Feynman has indicated that the wave function describing the parton distributions in, say, a colliding proton-proton system could be expected to be, at 'high' incident energies, a function only of x and P_t.

To describe the interaction between the two nucleons by parton exchange Feynman considers that the interaction is mediated only by partons of very low momentum (in the CM system) - those of 'wee' momentum - defined as those with momentum less than 1 GeV/c i.e. those with $x \lesssim 1/\sqrt{s}/2$. This is thought reasonable since the probability of interaction is closely related to the probability that a parton in the right-moving cluster of the initial state can be 'mistakenly' considered as a parton belonging to the left-moving cluster. Such an amplitude is a maximum for the lowest momentum partons. Other features of particle interaction were obtained using an analagy with bremsstrahlung - this is described later.

Concerning the momentum distribution of the partons, Feynman, assuming a constant interaction cross section showed that partons of momenta other than wee should be distributed as dx/x while the wee parton distribution should be constant. This latter distribution applies from $x \sim 2/\sqrt{s}$ down to $x = 0$ - hence there is a dependence upon the available energy. Thus the statement that the wave function is dependent only upon x and Pt is not strictly true - it applies only to x not wee.

As mentioned above, Feynman attempted to obtain some details of particle production by likening such production to bremsstrahlung. In the study of electro-dynamics a sudden reversal of electric current is considered to induce bremsstrahlung; in a particle collision the reversal of some other current (such as that carried by the third component of isotopic spin) is assumed to induce bremsstrahlung production not of photons but of partons or other fundamental particles. Clusters of partons are identified as the produced particles observed in such a collision. The momentum distribution of these particles is shown to be dx/x for x not wee - this is the same as the distribution of the partons which formed the initial state of two nucleons and as an extension of this fact the more general rule, that the momentum distribution of the produced particles is qualitatively the same as that of the partons for all x values, is derived. Thus the distribution of produced particles (mainly pions) of non-wee momentum is expected to be of the form dx/x and independent of primary energy whereas in the wee region the distribution is constant. The width of the wee region is primary energy dependent and it is this feature which allows for the observed increase in multiplicity with increasing primary energy.

The total number of particles of a particular kind is the sum over the wee and non-wee regions. The former is, by the definition of wee momenta, independent of primary energy; the latter contribution is given by $c\int dx/x$ where c is some constant. The upper limit to the integral is unity and the lower limit is the wee-x value at which the dx/x formula fails i.e. $x = 2/\sqrt{s}$. Hence the number of produced particles varies with primary energy according to an expression of the form (constant + $c \ln(\sqrt{s})$). Using Regge theory, Feynman was able to obtain a rough estimate of C and the resulting expression fits the observations quite well. Taking the upper limit of the integral to be unity may however be incorrect since in the large x region ($x \gtrsim 0.5$, say) the dx/x parameterization could be expected to fail because if such a large amount of energy is taken from the primary particle by radiation of one particle then subsequent emissions would be affected. A more rapid decrease of the distribution at large x values is thus indicated but this is not expected to seriously alter the form of the multiplicity variation with primary energy.

The distribution whose shape is predicted by the Feynman approach is that of particles of a particular kind, independent of the emission of other particles. Such a distribution has been named an inclusive distribution. An exclusive distribution is one obtained in an experiment in which it is demanded that only certain specified particles of fixed P_t and x be found in the final state and no others. The former type of distribution (the inclusive) is experimentally the easiest and hence the most often measured.

The distribution of produced particles as a function of x and y_C as predicted by Feynman are shown in Fig. 7.3 a,b. From the rapidity distributions it can be seen that the Feynman approach and Morrison's (1972) interpretation of the HLF are in agreement.

Experimental evidence supporting scaling of some particle distributions from about 20 GeV up to I.S.R. energies has accumulated rapidly. Scaling of pion distributions for $P_t \lesssim$ 0.8 GeV/c and $x \gtrsim 0.2$ is generally accepted, for positive kaons a rather lower limit on P_t (about 0.4 GeV/c) is required while for negative kaons scaling does not work well. Anti-proton distributions are generally found to scale over the energy range covered by the I.S.R. but do not agree with the distributions obtained at lower energies. Proton distributions are thought to scale over I.S.R. energies.

More details of the distributions of the various particles are given in the next section.

7.3 Particle Spectra

In this section the experimentally observed high energy production spectra of various particles are summarized. Some low energy spectra are shown in Fig. 7.3c. Results on some other features of particle production are also described.

7.3.1 Charged Pions

To determine whether scaling may be applied to pion spectra the regions $x = o$ and $x > o$ will be considered separately.

At $x = o$ the results of two I.S.R. experiments and a

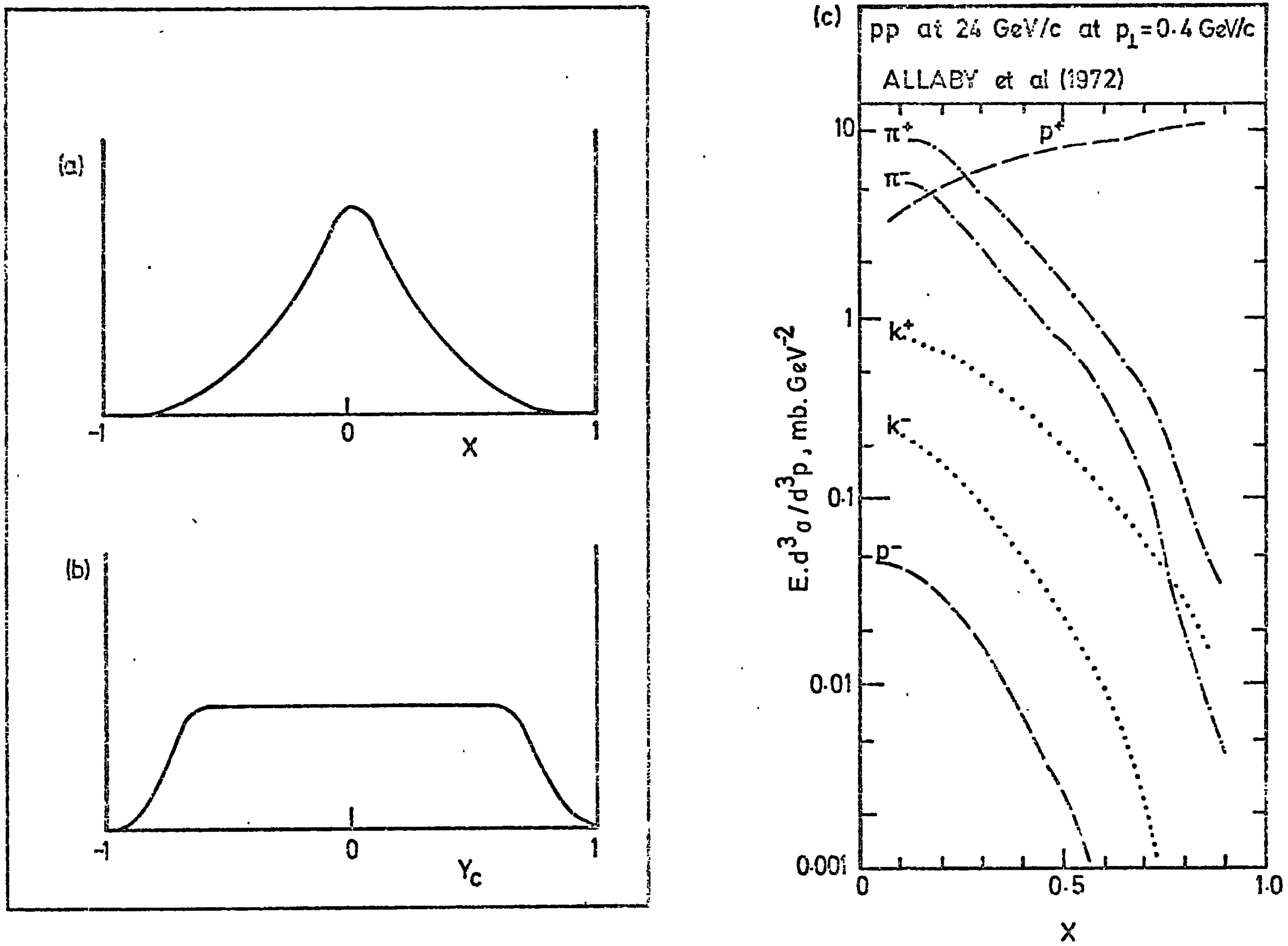
(a)
-1
0
1
X
(b)
-1
0
1
Y_c
(c)
pp at 24 GeV/c at $p_\perp = 0.4$ GeV/c
ALLABY et al (1972)
$E.d^3\sigma/d^3p$, mb. GeV^{-2}
10
1
0.1
0.01
0.001
π^+
π^-
p^+
k^+
k^-
p^-
0
0.5
1.0
X

FIG.7.3.

low energy experiment are plotted in Fig. 7.4. The lowest energy results are consistently below those of the higher energies and hence scaling cannot be applied to the low energy data.

Considering the two I.S.R. experiments separately the diagrams show, within the errors of about 10%, no obvious energy dependence of the cross section over the range of $\sqrt{s}$ of 30-53 GeV. This, however, is not the conclusion of Lillethun (1973) who, in describing the results of a later and more accurate experiment at $P_t = 0.4$ GeV/c shows that some energy dependence is present in the form $Ed^3\sigma/d^3p \propto S^{-\frac{1}{2}}$. The absolute values of the cross sections obtained in this latter experiment and in the two I.S.R. experiments plotted in Fig. 7.4 are all in disagreement. This is probably due to errors in the luminosity measurement. It can be seen from the diagram that, within the errors, the numbers of positive and negative pions, at each I.S.R. energy, are equal.

To explore a wider range of P_t the results of Lillethun et al (1972) have been used. These authors found that within their rather large errors of ± 15% scaling could be applied to the 30-50 GeV range and also to data at $\sqrt{s} = 23$ GeV. This latter contrasts with the results of Fig. 7.4 where a distinct rise in cross section over the range 23-30 GeV is seen. Lillethun et al (1972) also found the $\pi^{\pm}$ cross sections to be equal for the range $P_t = 0.2$ to 1.3 GeV/c; their data are given in Fig. 7.5 where the points plotted are alternately π^+ and π^-. Lillethun (1973) however shows that the results of a later, more precise experiment indicate a π^+/π^- ratio increasing from about 1.00 at $P_t = 0.1$ GeV/c to about 1.15 at $P_t = 1.0$ GeV/c.

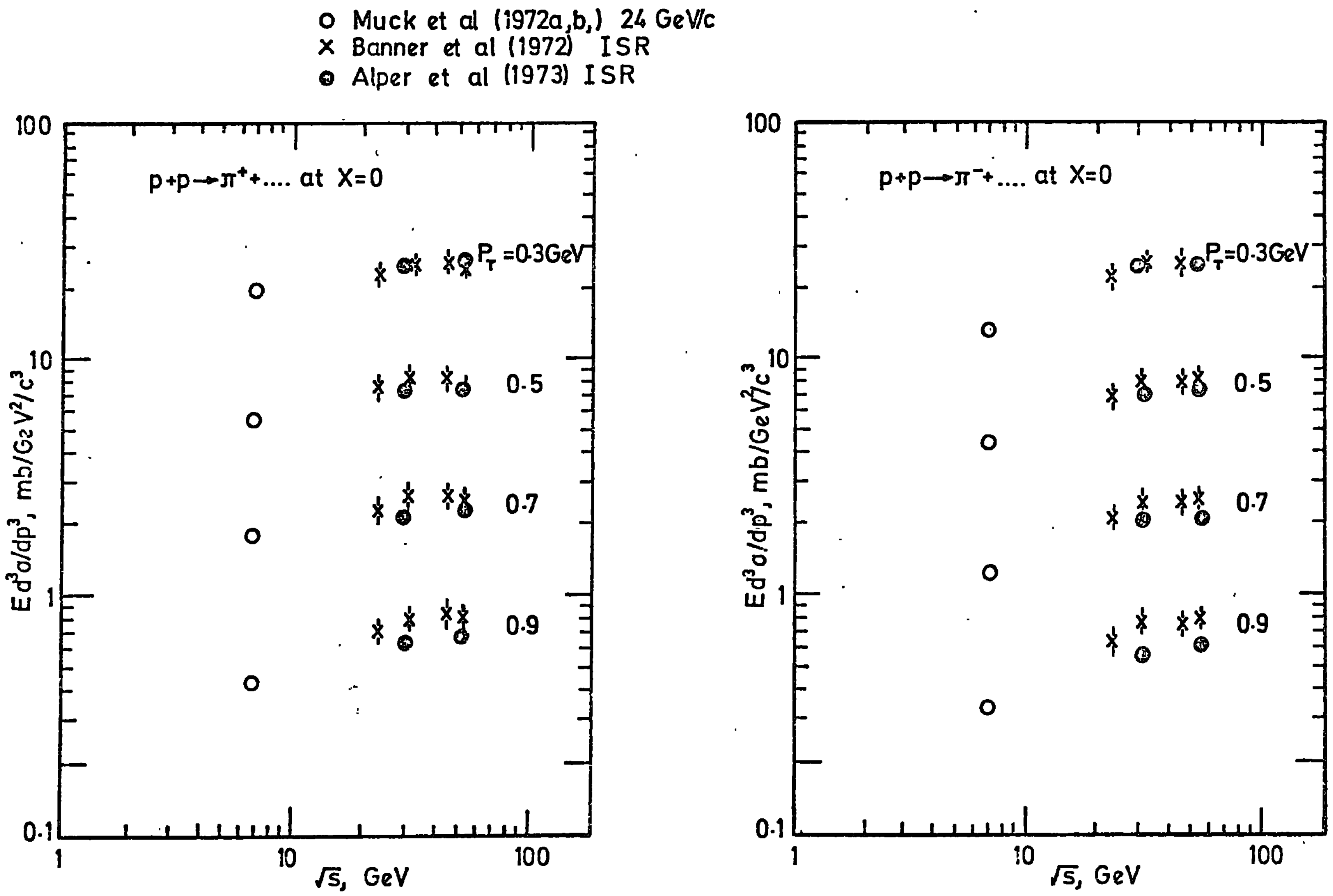

FIGURE: 7.4. PION PRODUCTION AS A FUNCTION OF INCIDENT ENERGY

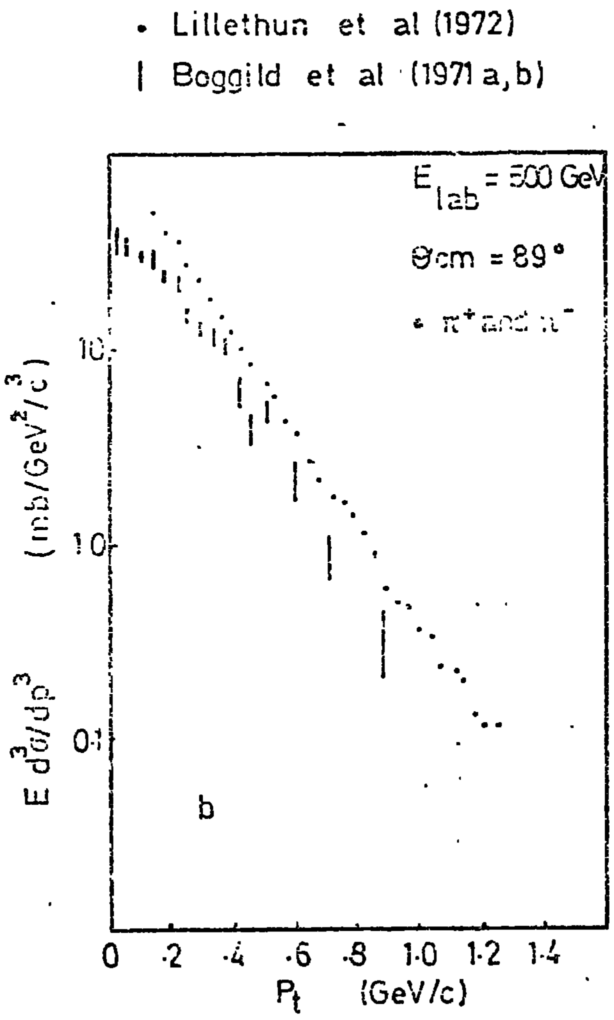

FIGURE:7.5.

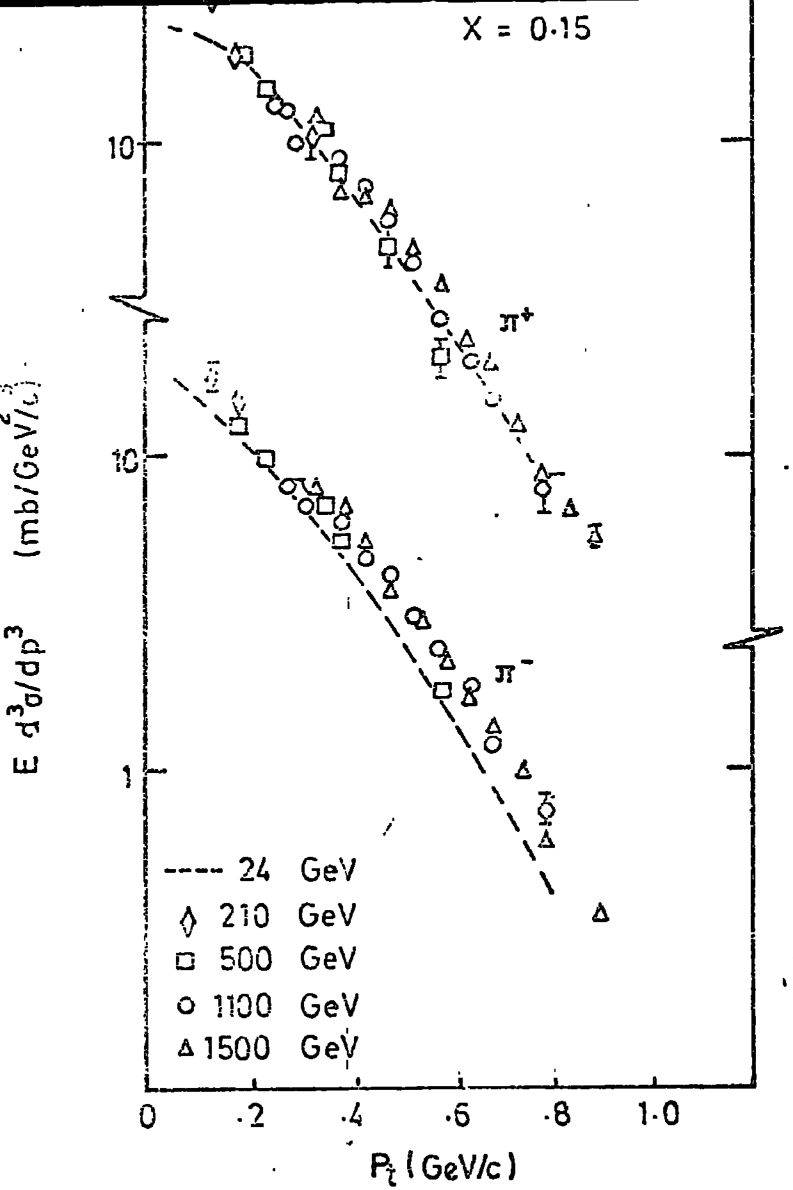

FIGURE:7.6.

Summarizing for $x = o$. The situation is rather unclear; early experiments indicated satisfactory scaling at least over the range 500-1500 GeV/c laboratory momentum and P_t = 0.3 to 0.9 GeV/c but a later experiment has shown some energy dependence. The comparison of several sets of independent data of precision at least equal to that reported by Lillethun (1973) should resolve the problem. Scaling of low energy results ($\sim$ 20 GeV laboratory momentum) is not valid.

To consider the applicability of scaling to $x > o$ the results of Antinucci et al (1973), for $x = 0.15$, may be considered (Fig. 7.6). These are the most accurate data available (as of May 1973). The errors are around ± 10% and according to the authors there is no systematic trend as a function of I.S.R. energy. (This presumably applies to the energy range 500-1500 GeV since there are very few data at 210 GeV). A similar conclusion is reached by Lillethun (1973) for a similar range of P_t values and x values between 0.15 and 0.8.

A comparison of I.S.R. data and lower energy data is given in Fig. 7.7. It can be seen that scaling is quite well satisfied for positive pions but less so for negative pions. This is also seen in Fig. 7.6 More recent and precise data reported by Lillethun indicates that scaling between low energies ($\sim$ 20 GeV) and the I.S.R. results occurs for $P_t \lesssim 0.8$ GeV/c and $0.15 \lesssim x \lesssim 0.8$. This behaviour contrasts with that at $x = o$.

By combining the results of a number of I.S.R. experiments the longitudinal momentum distribution of pions may be found; those due to Sens (1972) are shown in Fig. 7.8a,b.

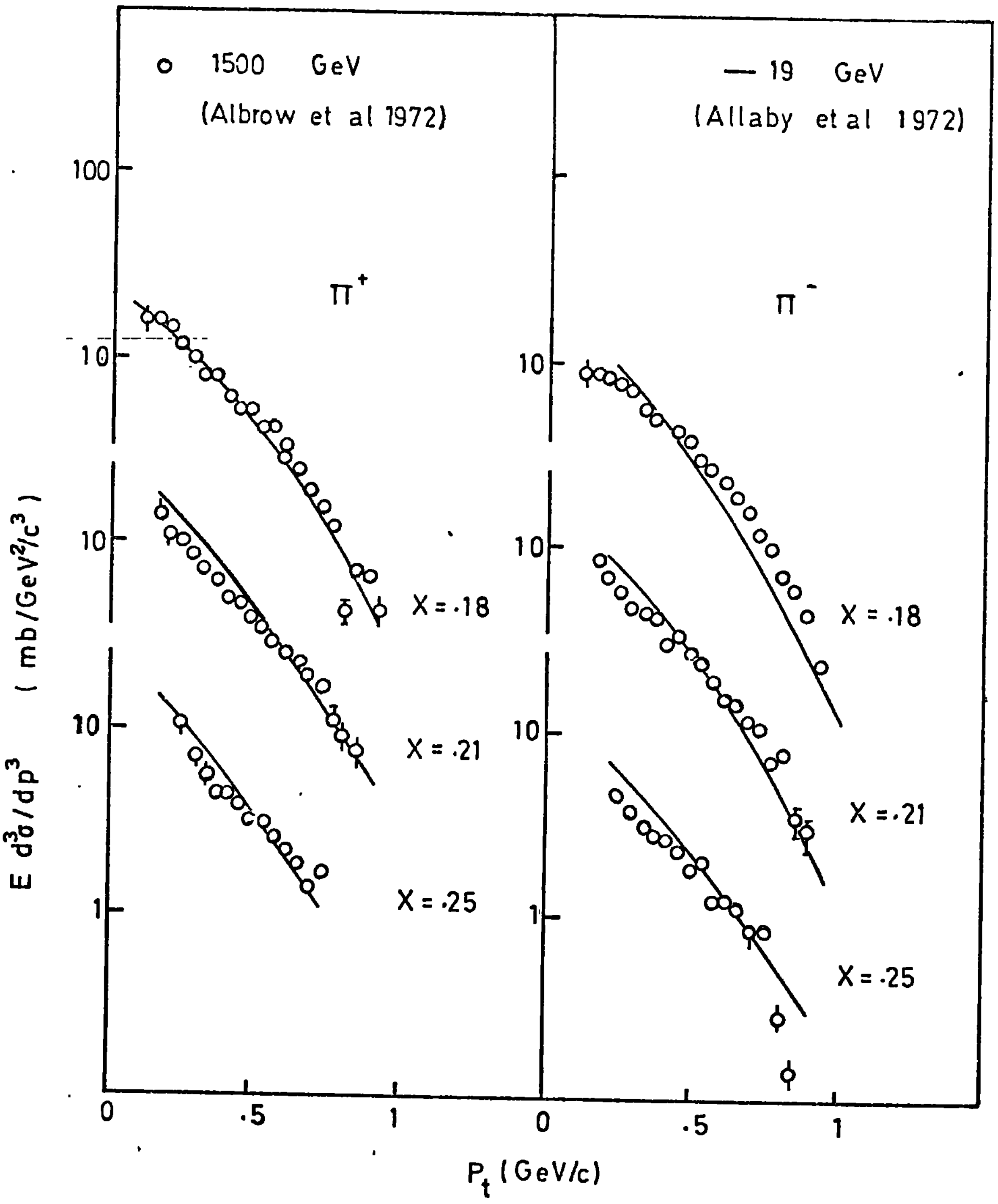

o 1500 GeV
(Albrow et al 1972)
— 19 GeV
(Allaby et al 1972)
π⁺
π⁻
100
10
10
10
1
10
10
10
1
X = ·18
X = ·21
X = ·25
X = ·18
X = ·21
X = ·25
E d³σ/dp³ (mb/GeV²/c³)
0
·5
1
0
·5
1
Pt (GeV/c)

FIGURE: 7·7.

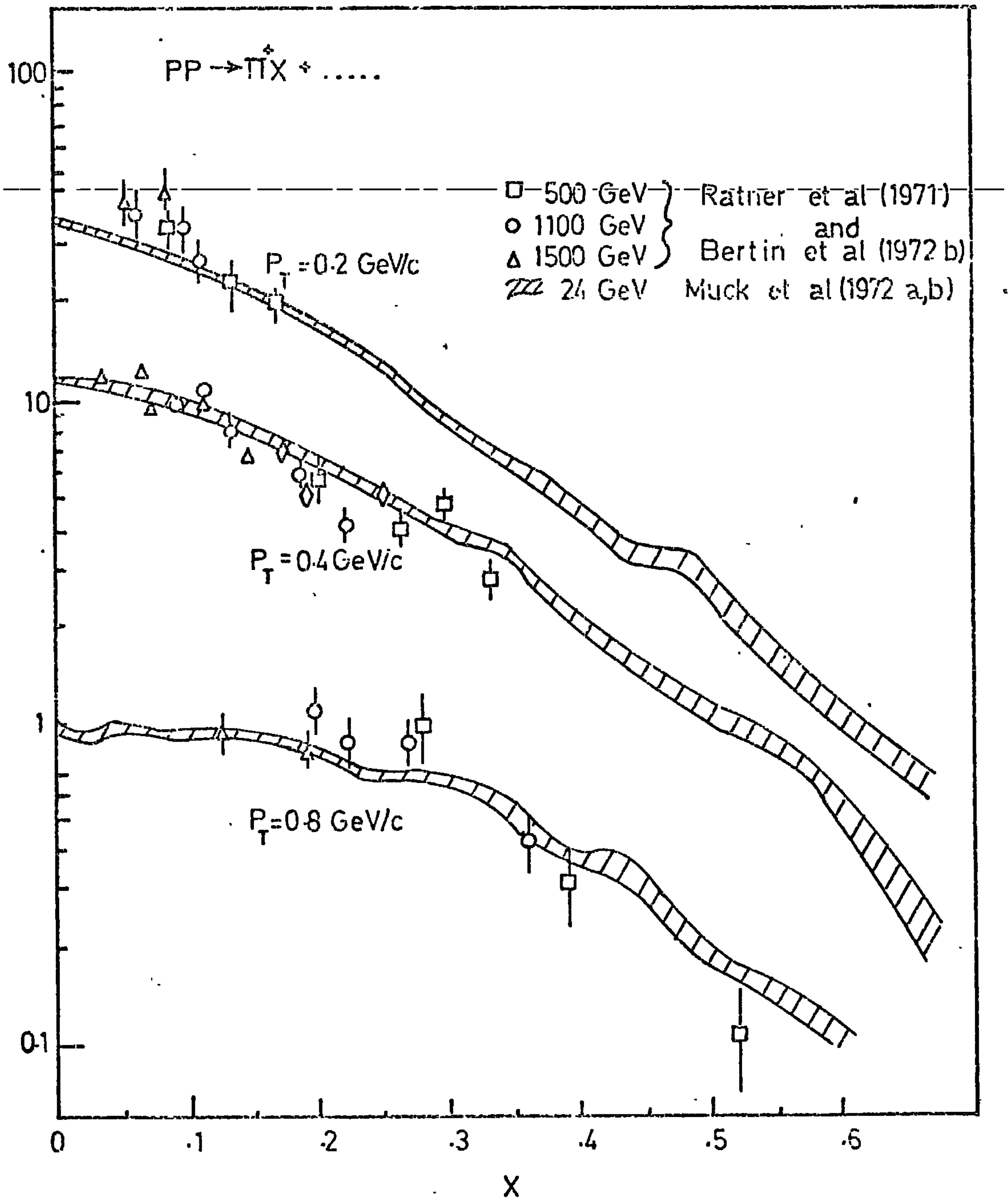
PP → π⁺X + ...
□ 500 GeV
○ 1100 GeV
Δ 1500 GeV
Ratner et al (1971) and Bertin et al (1972 b)
▨ 24 GeV Muck et al (1972 a,b)
P_T = 0.2 GeV/c
P_T = 0.4 GeV/c
P_T = 0.8 GeV/c
100
10
1
0.1
0
.1
.2
.3
.4
.5
.6
X

FIGURE: 7.8a.

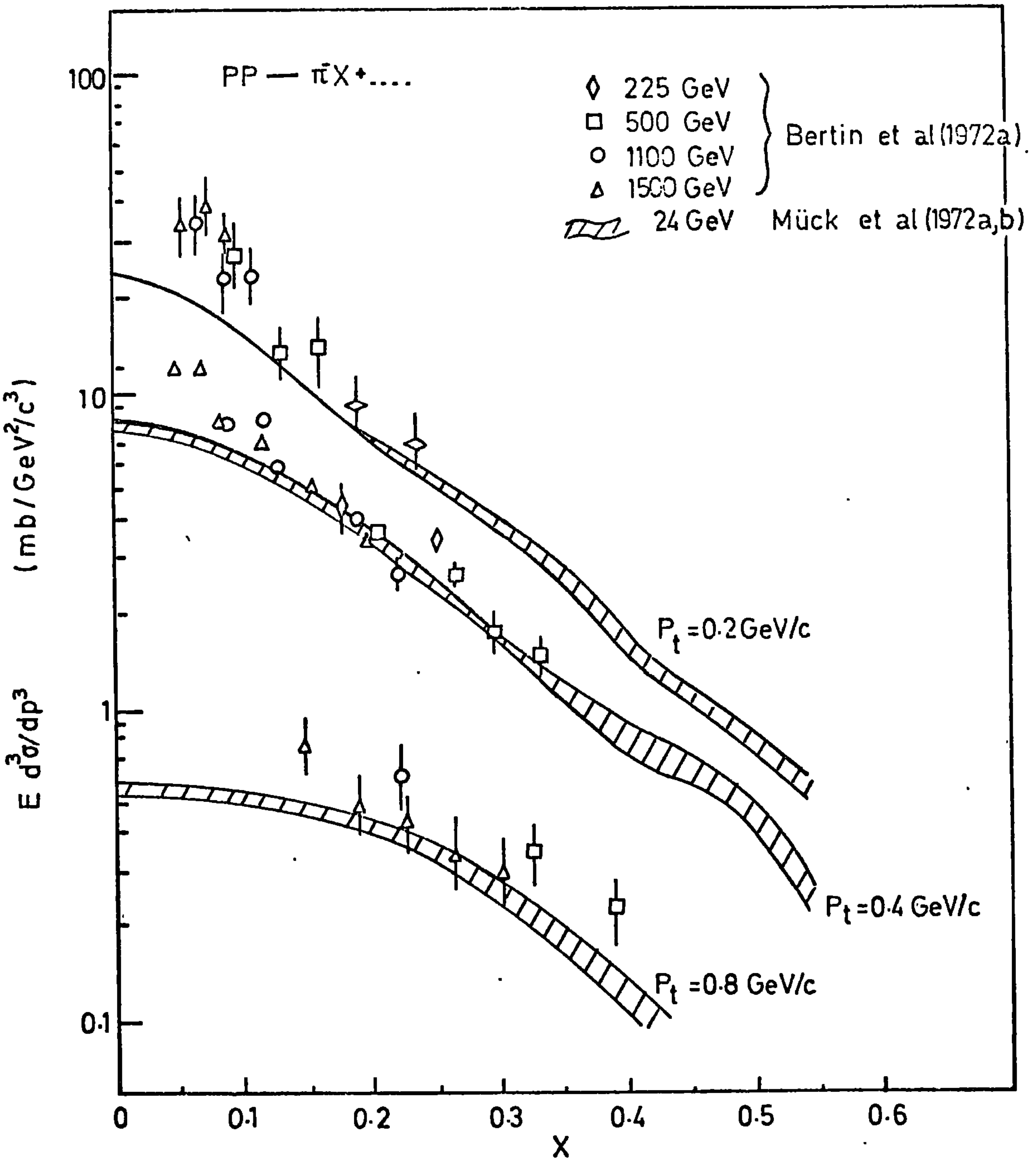
PP — π̄X+....
◊ 225 GeV
□ 500 GeV
○ 1100 GeV
△ 1500 GeV
Bertin et al (1972a)
24 GeV Mück et al (1972a,b)
P_t =0·2 GeV/c
P_t =0·4 GeV/c
P_t =0·8 GeV/c
E d³σ/dp³ (mb/GeV²/c³)
100
10
1
0·1
0
0·1
0·2
0·3
0·4
0·5
0·6
X

FIGURE: 7·8b.

Damgaard and Hansen (1972) have found equations giving a best fit to each set of data; the equations, for π^+ and π^- respectively are :-

$$E\, d^3\sigma/d^3p = 137 \exp(-2.25\, Pt) \exp(-6.93 \sqrt{x^2 + (0.57\, Pt)^2}\ )$$

and

$$E\, d^3\sigma/d^3p = 162 \exp(-6.2\, Pt) \exp(-17\sqrt{x^2 + 0.0001}\ ) \exp(14.5 x Pt^{\frac{1}{3}})$$

Typical transverse momentum distributions for a variety of x values are shown in Figs. 7.9 and 7.10. These data show an exponential dependence on P_t. A pure exponential of the form

$E\, d^3\sigma/d^3p = A_1 \exp(-B_1 P_t)$, where A_1 and B_1 are constants, has been fitted by Antinucci et al (1973). This fit was made over a range of incident energies and P_t values; details are given below.

Particle	Energy Range (GeV)	x	P_t Range (GeV/c)	B_1 $(\text{GeV}/c)^{-1}$	$\langle P_t \rangle$ (GeV/c)
+	110 - 1500 210 - 1500 500 - 1500	0.075 0.15 0.30	0.2 - 0.6 0.2 - 0.9 0.4 - 1.4	6.3 ± 0.3 5.4 ± 0.1 4.8 ± 0.2	0.32 0.37 0.42
-	1100 - 1500 210 - 1500 500 - 1500	0.075 0.15 0.30	0.2 - 0.6 0.2 - 0.9 0.4 - 1.4	6.0 ± 0.3 5.1 ± 0.1 4.8 ± 0.2	0.33 0.39 0.42

The values of the slope parameter B_1 are plotted in Fig. 7.11; since B_1 is a decreasing function of x then the mean transverse momentum, $\langle P_t \rangle$ ($= 2/B_1$) is an increasing function. The values of B_1 seem to be the same for π^+ and π^-.

a: Banner et al (1972)

b: Antinucci et al (1973)

c: Albrow et al (1972)

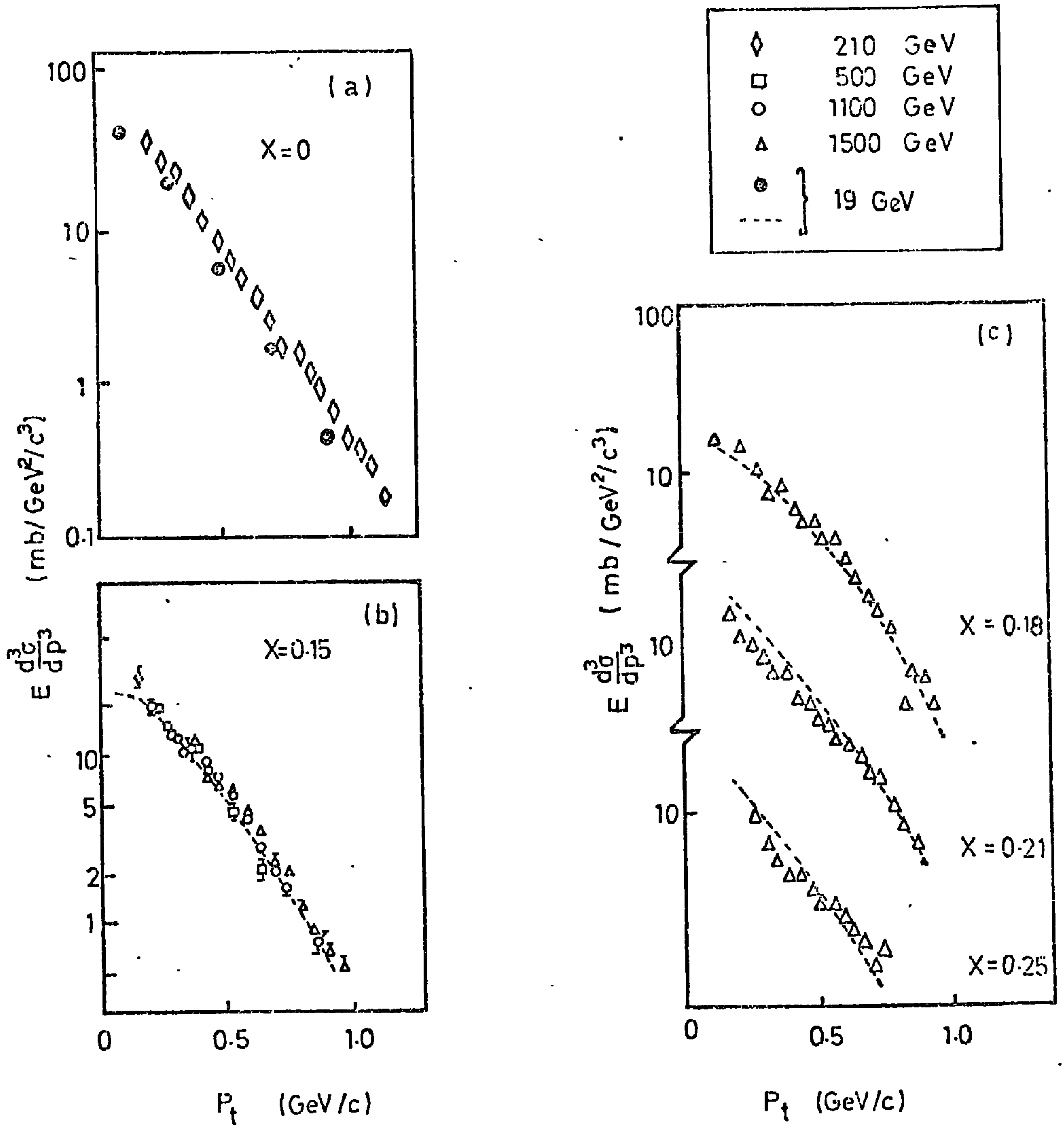

FIGURE: 7.9. TRANSVERSE MOMENTUM OF π^+

a: Banner et al (1972)

b: Antinucci et al (1973)

c: Albrow et al (1972)

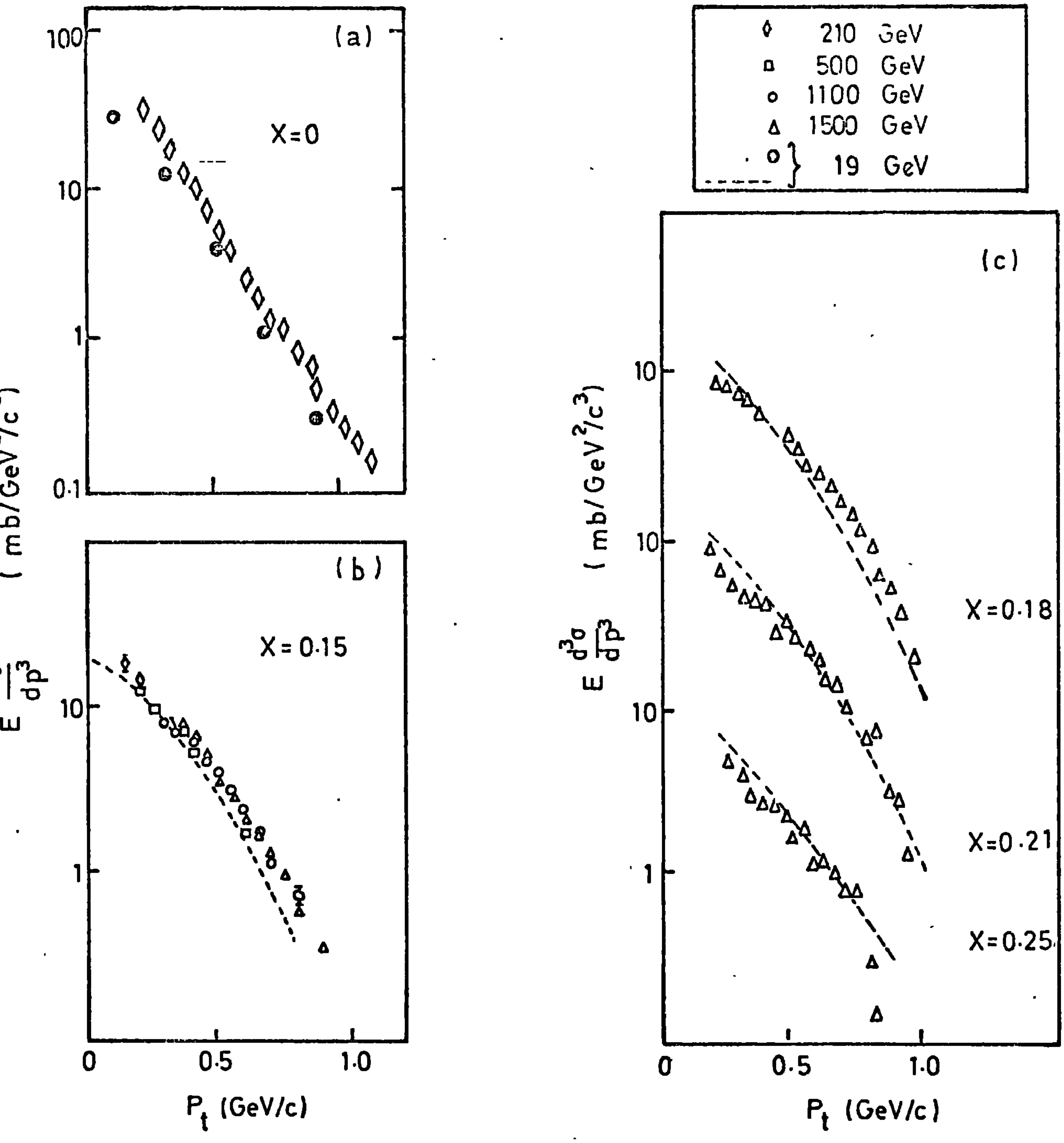

FIGURE:7.10. TRANSVERSE MOMENTUM OF π^-

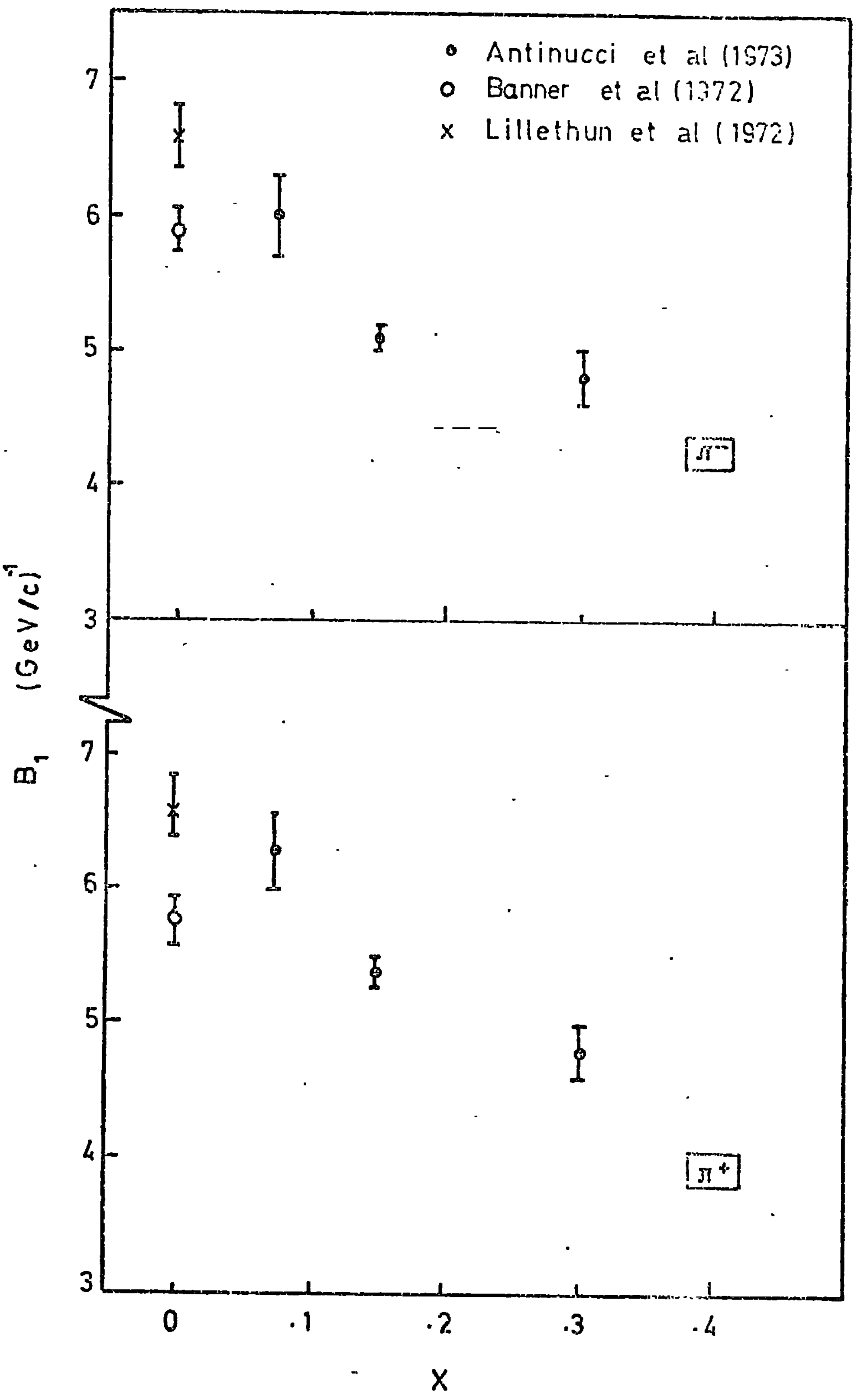

FIGURE 7.11. VARIATION OF B1

An experiment by Banner et al (1972) has yielded values of B_1 at $x = o$ and these are also shown in Fig. 7.11. These authors found the numbers of positive and negative ions to be equal - agreeing with the results of Lellethun (1972) also at $x = o$. The slope parameter of the latter experiment is plotted in Fig. 7.11 and is the slope derived by fitting an exponential curve to half the sum of the positive and negative pion data.

The two sets of results at $x = o$ are inconsistent. This is unfortunate since it becomes impossible to say whether the spectrum is flattening at small x values. There is no clear cause of the discrepancy; both sets of data are averages over the 210 - 1500 GeV energy range and over the P_t range 0.2 - 1.2 GeV/c. Because it is the slope of a distribution no normalisation (i.e. luminosity) problems arise. The situation is unresolved.

So far only the slope parameter has been discussed; values of A_1 are rarely given because of the difficulty of luminosity measurement. At $x = o$ values of A_1 are given by Banner (1972) and for the sake of completeness they are tabulated below. The given values of A_1 should be used with caution although the quoted errors do include estimates of systematic effects; the mean of the B_1 values given correspond to those plotted in Fig. 7.11.

ELAB (GeV)	210		500	
	π^+	π^-	π^+	π^-
A_1 (mb/GeV^2/c^3)	135 ± 7	132 ± 8	144 ± 9	149 ± 9
B_1 (GeV/c)$^{-1}$	5.86 ± 0.34	5.97 ± 0.35	5.80 ± 0.35	5.92 ± 0.36
				contd ..

ELAB (GeV)	1100		1500	
	π^+	π^-	π^+	π^-
A_1 (mb/GeV^2/c^3)	139 ± 9	145 ± 9	128 ± 8	137 ± 9
B_1 (GeV/c)$^{-1}$	5.72 ± 0.36	5.91 ± 0.37	5.65 ± 0.38	5.75 ± 0.36

An alternative to a pure exponential dependence has been proposed by Albrow et al (1972) whose data are plotted in Figs. 7.9c and 7.10c. A fit of the form

$E\, d^3\sigma/d^3p = A_2 \exp(-B_2 P_t^2)$ has been used. The data were collected at a single incident energy of 1500 GeV and the motivation for the type of fit used was the curvature exhibited by the data. The values of A_2 and B_2 are tabulated below and as before the results for A_2 should be used with care.

Particle	x	A_2 (mb/GeV^2/c^3)	B_2 (GeV/c)$^{-2}$
π^+	0.18 0.21 0.25	16.1 ± 1.1 12.9 ± 0.9 9.2 ± 0.8	4.27 ± 0.16 4.17 ± 0.19 3.80 ± 0.31
π^-	0.18 0.21 0.25	9.8 ± 0.3 7.6 ± 0.5 5.0 ± 0.4	3.92 ± 0.07 4.05 ± 0.15 3.74 ± 0.28

7.3.2 Charged Kaons

The kaon production cross-section is about a factor of ten smaller than that for pions and consequently the available data is less precise.

At $x = o$ and $P_t = 0.4$ GeV/c the results of Alper et al (1973) give the following values of the kaon invariant cross section

	1100 GeV C/Sect (mb/GeV^2/c^3)	1500 GeV
k^+	1.5 ± 0.3	1.5 ± 0.3
k^-	1.1 ± 0.1	1.3 ± 0.2

This is the best available data for $x = o$. The indication is that scaling is occurring over the given incident energy range; the mean k^+/k^- ratio assuming this to be true is 1.25 ± 0.21.

No low energy data at $x = o$ are available for comparison with the I.S.R. results.

Considering $x > o$ the results of Antinucci et al (1973) and Albrow et al (1972) are plotted in Figs. 7.12a, b and give some idea of the validity of scaling over the range 500-1500 GeV. There is a suggestion in the data that the cross sections at the highest energy are somewhat larger than those at lower energies; this is most marked for k^+. However, the report of Lillethun (1973) indicates that more accurate data show scaling to be occurring over the range 500-1500 GeV.

Figure 7.12 also shows some low energy results and scaling for k^+ can be seen to be fairly good but for k^- there is a great difference between the two sets of data. For both k^+ and k^- the approach to scaling decreases with increasing P_t. This is better exhibited in Fig. 7.13 where the longitudinal momentum distribution of charged kaons is

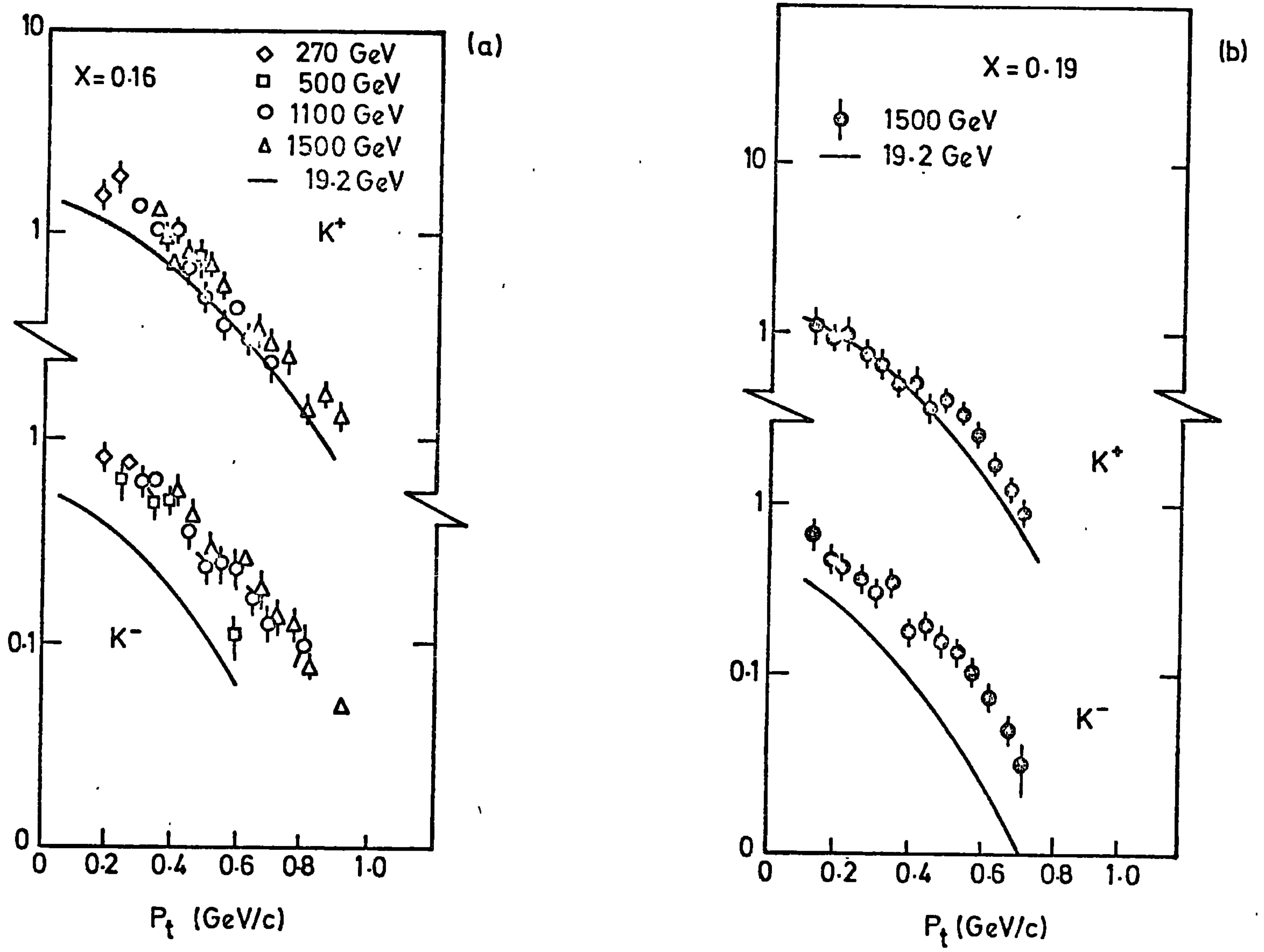
(a)
X=0·16
270 GeV
500 GeV
1100 GeV
1500 GeV
19·2 GeV
K⁺
K⁻
10
1
1
0·1
0
0
0·2
0·4
0·6
0·8
1·0
P_t (GeV/c)
(b)
X = 0·19
1500 GeV
19·2 GeV
K⁺
K⁻
10
1
1
0·1
0
0
0·2
0·4
0·6
0·8
1·0
P_t (GeV/c)

FIGURE: 7·12.

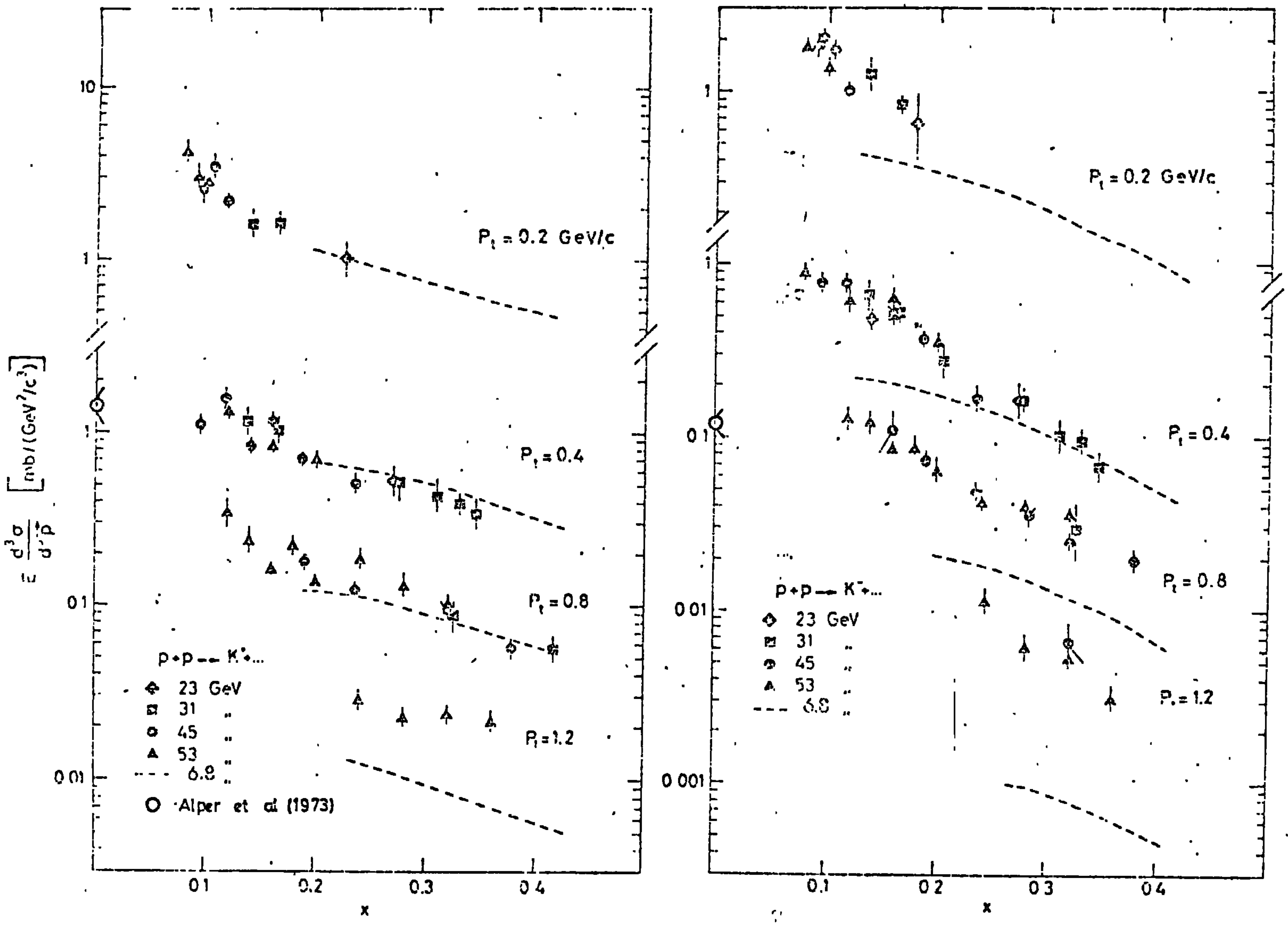
$E\frac{d^3\sigma}{d^3p}$ [mb/(GeV²/c³)]
10
1
0.1
0.01
0.001
0.1
0.2
0.3
0.4
x
P_t = 0.2 GeV/c
P_t = 0.4
P_t = 0.8
P_t = 1.2
p+p → K⁺+...
23 GeV
31 "
45 "
53 "
6.8 "
Alper et al (1973)
p+p → K⁻+...
23 GeV
31 "
45 "
53 "
6.8 "

FIGURE. 7.13.

plotted with P_t as a running parameter.

Considering transverse momentum distributions these are illustrated in Fig. 7.12. As in the case of charged pions, two representations of the distribution have been proposed. The data of Fig. 7.12a have been fitted with an exponential in P_t and the values of the slope parameter B_1 for k^+ and k^- respectively are 4.0 ± 0.2 $(GeV/c)^{-1}$ and 4.4 ± 0.2 $(GeV/c)^{-1}$. The results apply over the energy range 1100-1500 GeV, at $x = 0.16$ and for $0.2 \lesssim P_t \lesssim 0.9$. The data of Fig. 7.12b were obtained at 1500 GeV only, at $x = 0.19$ and over a similar P_t range to the above. The values of A_2 and B_2 the amplitude and slope parameters for k^+ are 1.11 ± 0.05 mb/GeV^2/c^3 and 2.75 ± 0.13 $(GeV/c)^{-2}$ respectively and for k^- are 0.56 ± 0.03 mb/GeV^2/c^3 and 3.09 ± 0.15 $(GeV/c)^{-2}$ respectively. The quoted errors include estimates of systematic effects.

7.3.3 Protons

From low energy accelerator (Fig. 7.3c) results it is seen that the proton spectrum is different in shape from that of the other particles; this feature is also present at I.S.R. energies.

For fixed values of P_t (0.4, 0.8 GeV/c) a survey of the available I.S.R. data on the longitudinal momentum spectrum of protons has yielded Fig. 7.14. The results of several different experiments are shown and there are significant differences in the absolute values of the cross sections. This is due to the difficulty in measuring the luminosity and makes intercomparisons difficult. However, the results of Albrow et al (1973),

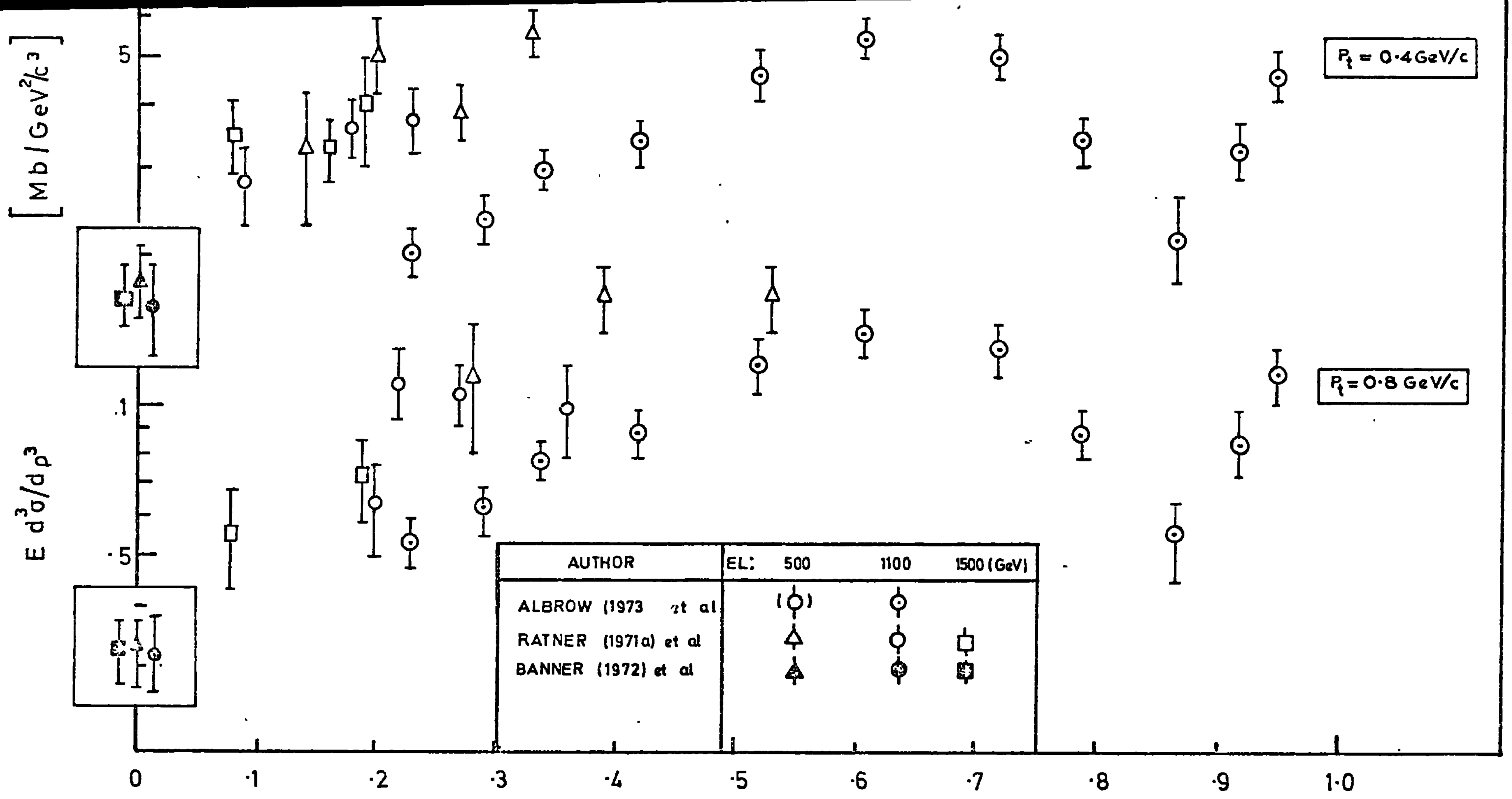

FIGURE: 7.14. PROTON LONGITUDINAL MOMENTUM DISTRIBUTION

Antinucci et al (1973) and the report of Lillethun (1973) indicate

(i) that for x between 0.0 and 0.3 and P_t between 0.1 and 1.0 GeV/c the low energy cross sections (laboratory energy $\sim$ 20 GeV) are greater than those at I.S.R. energies. The discrepancy is a factory of two at $x \sim 0.1$ and $P_t \sim 0.4$ GeV/c and decreases with increasing x.

(ii) that for $x \gtrsim 0.2$ scaling occurs over the I.S.R. energy range (210-1500 GeV laboratory energy).

The main features of the proton spectrum are its minimum at $x = o$ followed by a broad hump finishing in a valley at around $x = 0.9$ after which it rises steeply. This rise is due to a mixture of elastic and inelastic events. In Fig. 7.14 the elastic contribution has been subtracted and what remains is the effect of one of the incident protons becoming excited into an isobar and subsequently decaying.

Considering the distribution in transverse momentum, the I.S.R. results show that at fixed values of x the cross-section decreases exponentially with increasing P_t. Experimental data is usually fitted to one of two equations

$$E\, d^3\sigma/d^3p \propto \exp(-B_1 Pt) \quad \text{or} \quad E\, d^3\sigma/d^3p \propto \exp/-B_2 Pt^2).$$

The first representation has been used by Antinucci et al (1973) to fit the data shown in Fig. 7.15a. It is found that B_1 is a function of x and this is shown in Fig. 7.15b. The mean transverse momentum is thus a decreasing function of x as shown below.

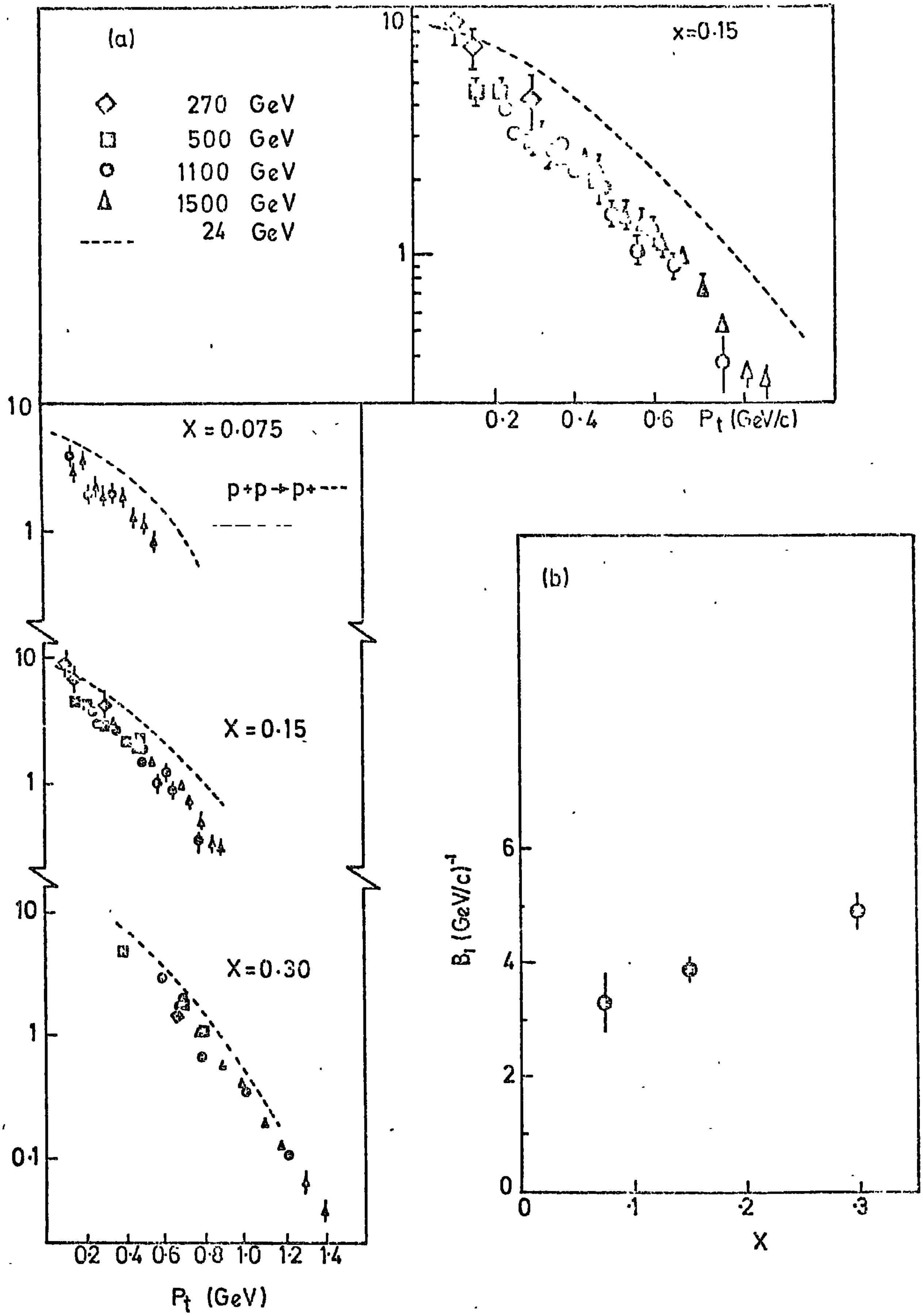

TRANSVERSE
MOMENTUM DISTRIBUTION

VARIATION OF B_1

FIGURE. 7.15.

Energy Range (GeV)	x	Pt Range (GeV/c)	B_1 $(GeV/c)^{-1}$	Pt $(GeV/c)^{-1}$
1100-1500	0.08	0.2 - 0.6	3.3 ± 0.5	610
500-1500	0.15	0.2 - 0.9	3.9 ± 0.2	510
500-1500	0.30	0.4 - 1.4	4.9 ± 0.3	410

The second representation has been used by Albrow et al (1972, 1973) and Ratner et al (1971a). Figures 7.16a,b show the results of these experiments plotted against P_t^2. In this case B_2 is constant over most of the x range ($0.2 < x < 0.9$). For $x > 0.9$ B_2 starts to rise as shown in Fig. 7.16c. The mean value of P_t is thus indepdent of x for $0.2 < x < 0.9$. Data for $x < 0.2$ is sparse but the preliminary results of Lillethun et al (1972) are shown as open triangles in Fig. 7.16b and refer to $x = 0.0$. The results obviously suffer from a normalisation problem but the general trend is similar to that at other values of x. No errors are given in the original source but are > 15%.

The variation of the cross section over the whole I.S.R. energy range is best seen from Fig. 7.15a (the inset reproduces the data for $x = 0.15$ on an expanded scale). Within the errors of 10-15% the distributions for energies $\geqslant$ 500 GeV coincide. There is some indication that the data at 270 GeV (at $x = 0.15$) are systematically higher than for other energies plotted.

Comparison of the I.S.R. P_t distributions with those at lower energy can be made in Fig. 7.15a. For the range of x values given, the lower energy results indicate the higher cross

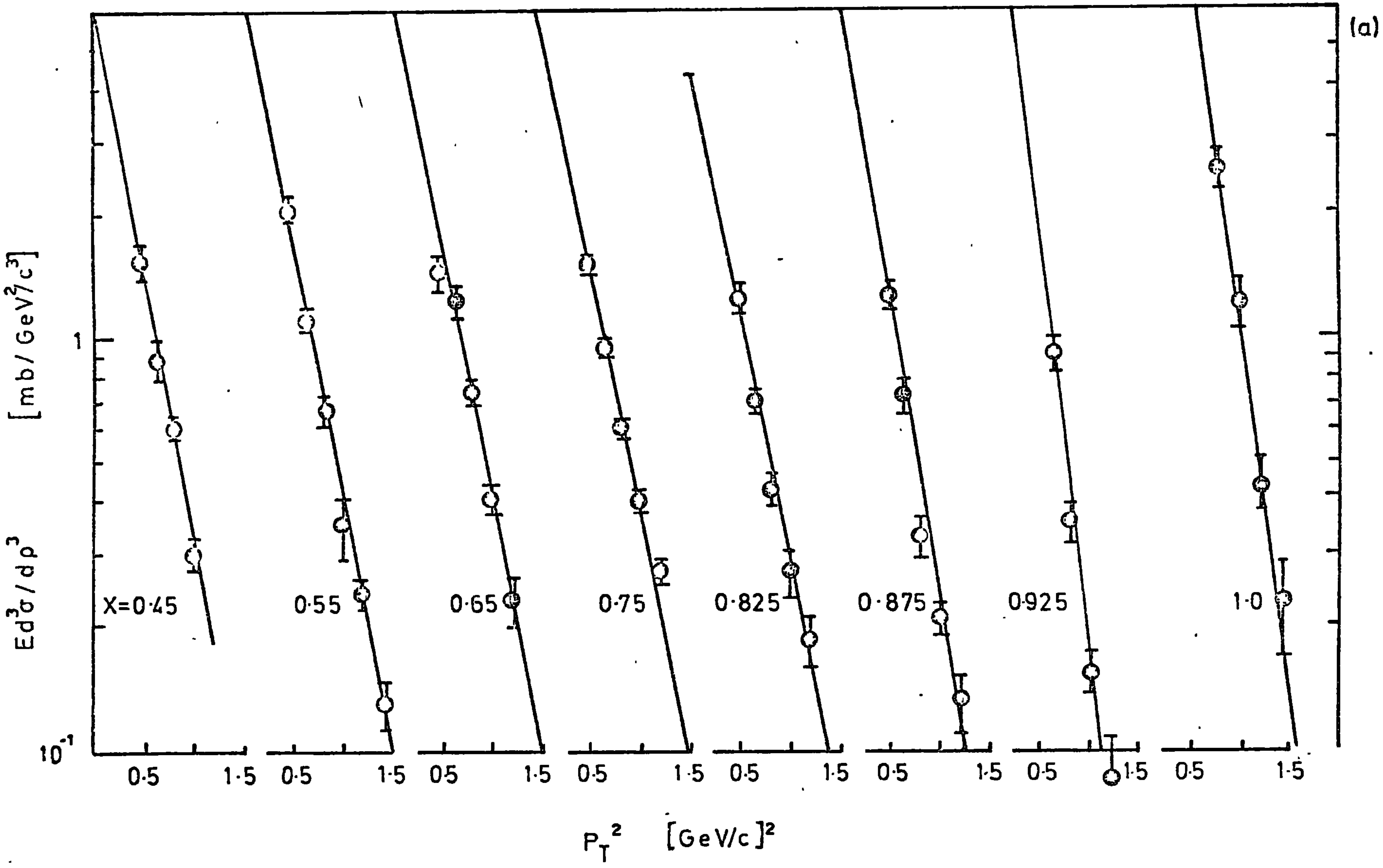

FIGURE:7.16 PT^2 DISTRIBUTION OF PROTONS AT E_L = 10·50 GeV

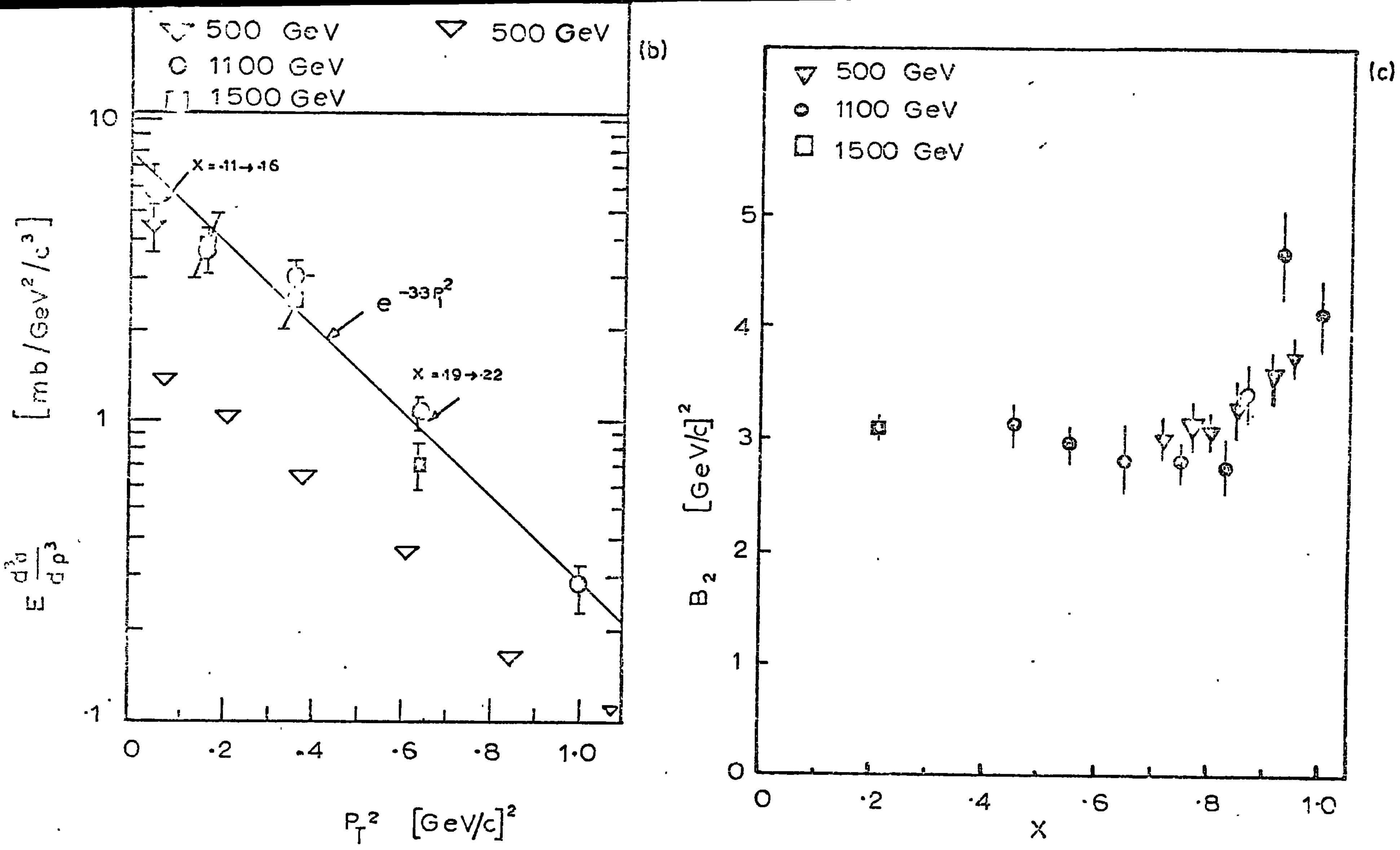

PT^2 DISTRIBUTION
FOR PROTONS

VARIATION OF B_2

FIGURE: 7.16

sections. The difference between high and low energy results decreases with increasing x and should reach zero around x = 0.5.

Turning now to anti-protons the longitudinal momentum distribution at P_t = 0.4 GeV/c is shown in Fig. 7.17a. The rather large error bars (which represent both statistical and systematic errors) make comment about scaling over the I.S.R. energy range difficult. More recent data from the same experiment Antinucci et al (1973a) does however give evidence of a cross section which is increasing with primary energy. Some of these results are shown, as a function of transverse momentum, in Fig. 7.17b where an increase by a factor of 2-3 over the energy range 500-1500 GeV can be seen. Considering Fig. 7.17a the low energy data (24 GeV) shows lower cross sections, the discrepancy is a factor of about ten at the lowest x values. Longitudinal spectra for values of P_t other than 0.4 GeV/c are given by Lillethun (1973) and show that the deviations from scaling between high and low energy increase as P_t and x are increased and reduced respectively. From Fig. 7.17a the low energy results are seen to flatten as x decreases; this contrasts with the I.S.R. data which maintain their exponential shape.

Transverse momentum distributions of the $\bar{p}$ have been fitted to an exponential in P_t by Antinucci et al (1973a) whose data is reproduced in Fig. 7.18a. The slope parameter, B_1 (of the fit $E\, d^3\sigma/d^3p \propto \exp(-B_1 P_t)$) is found to be a function of x (Fig. 7.18b). B_1 rises with increasing x and the mean transverse momentum ($\langle P_t \rangle = 2/B_1$) consequently decreases, in contrast with the behaviour of pions. The values of B_1 and $\langle P_t \rangle$ are listed below :-

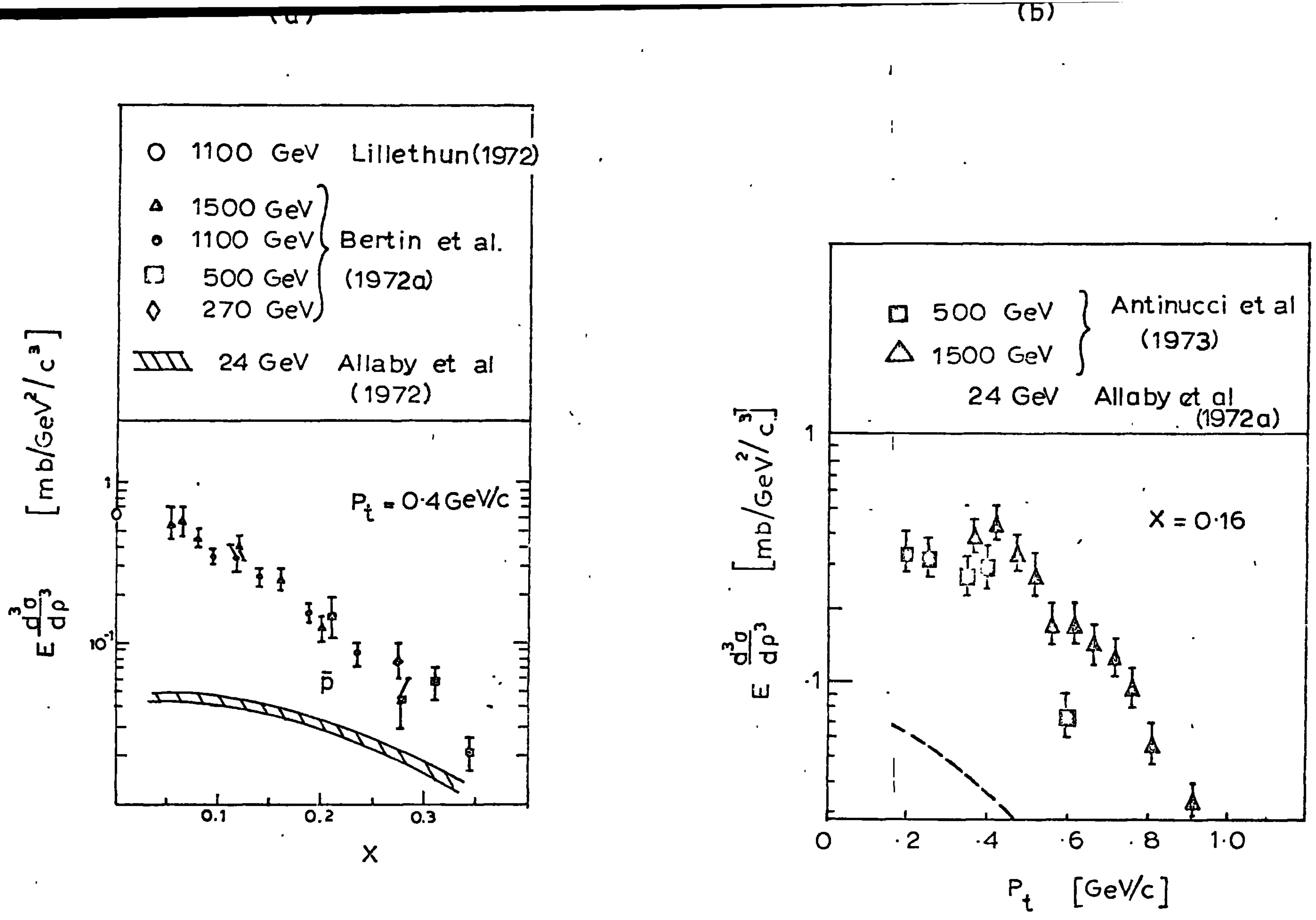

FIGURE: 7.17. ANTI-PROTON MOMENTUM DISTRIBUTIONS.

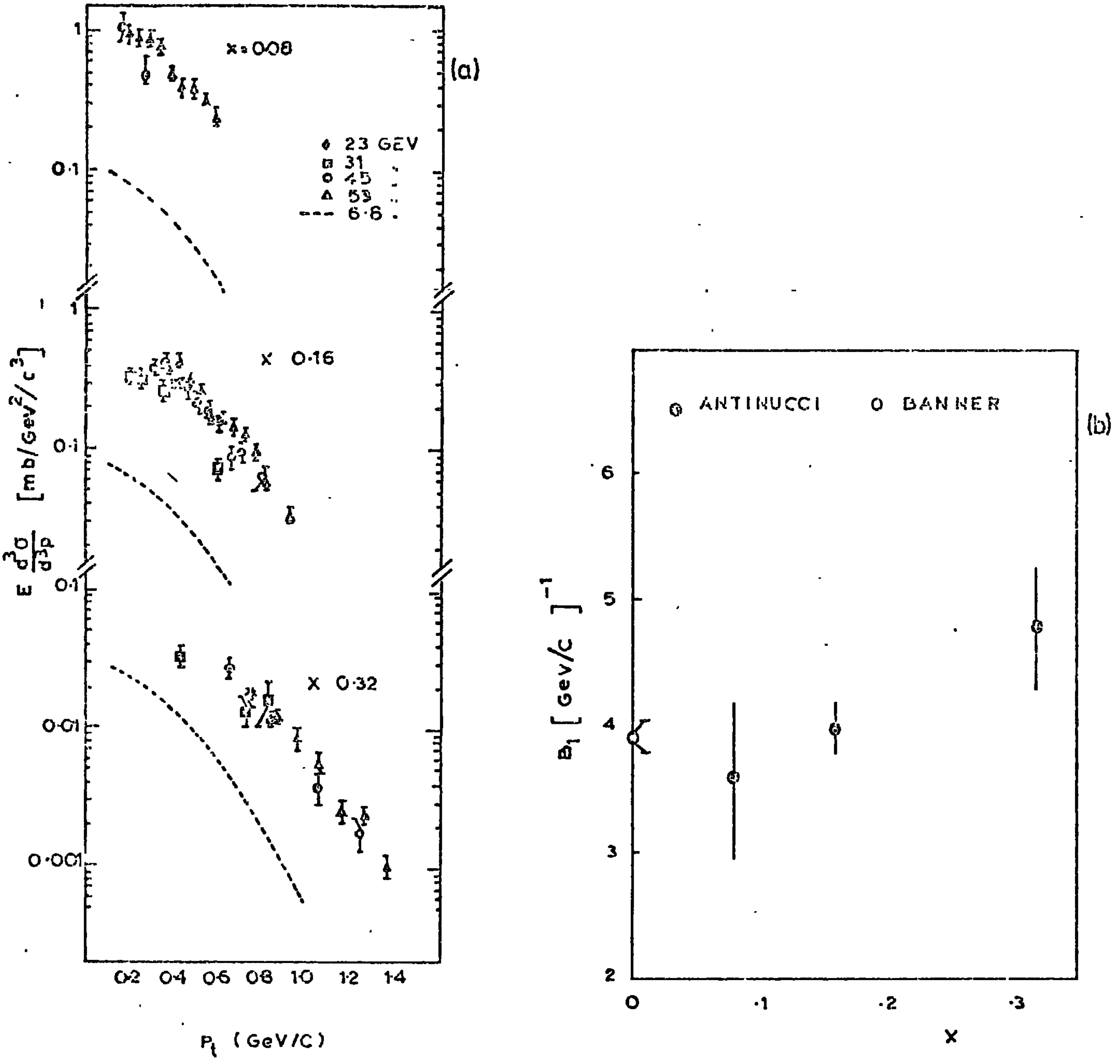

FIGURE 7.18. ANTI-PROTON TRANSVERSE MOMENTUM

Energy Range (GeV)	x	Pt Interval (GeV/c)	B_1 $(\text{GeV/c})^{-1}$	$\langle P_t \rangle$ (GeV/c)
1100-1500	0.08	0.2 - 0.6	3.6 ± 0.6	0.56
1100-1500	0.16	0.3 - 0.9	4.0 ± 0.2	0.50
1100-1500	0.32	0.6 - 1.4	4.8 ± 0.5	0.42

At x = 0.0 the distribution is similar to that at other x values as shown in Fig. 7.19 where the results of Lillethun et al (1972) (preliminary data) and Banner et al (1972) are plotted. The results of the latter are at either extreme of the normal I.S.R. operating range and clearly show the lack of scaling over the 210-1500 GeV range.

7.3.4 Particle Ratios

The pion charge ratio as a function of x has been derived using the equations of Damgaard and Hansen (1972) which fitted the experimental I.S.R. data shown in Fig. 7.8. The multiplicity of pions is given by

$$\langle n\pi^{\pm} \rangle = \frac{2}{\sigma_{inel}} \int_0^{\infty} \int_0^{1} \frac{2\pi \, Pt}{\left[x^2 + \frac{Pt^2 + M\pi^2}{P_{max}^2} \right]^{\frac{1}{2}}} \cdot E \frac{d^3\sigma}{d^3p} \, dx \, dP_t$$

where σ_{inel} is the inelastic pp cross section (taken to be 32 mb) and P_{max} is the centre of mass energy of the incident proton (taken to be 25 GeV, but the expression is insensitive to the value of P_{max}). After integrating over P_t the results for different regions of x are as below :-

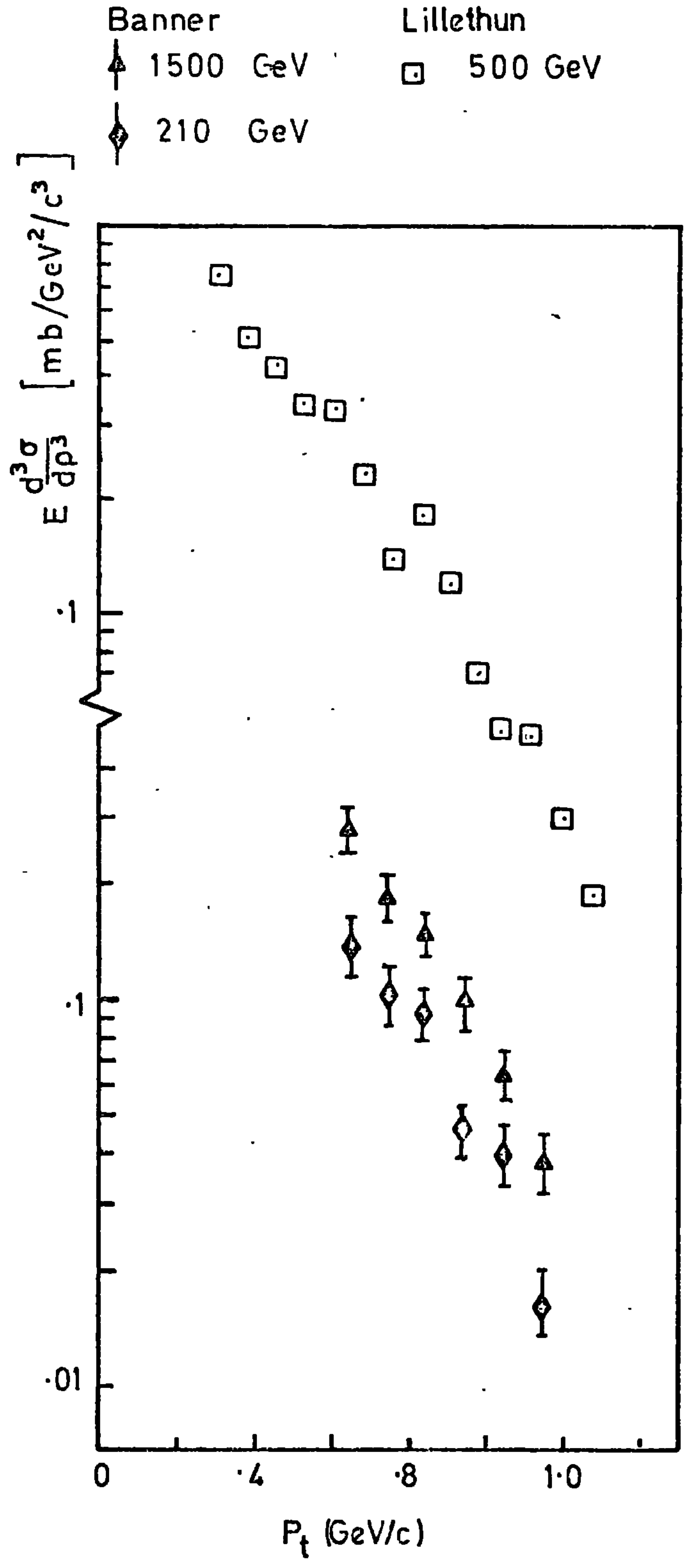
Banner
1500 GeV
210 GeV
Lillethun
500 GeV
$E\frac{d^3\sigma}{dp^3}$ [mb/GeV²/c³]
·1
·1
·01
0
·4
·8
1·0
P_t (GeV/c)

FIGURE. 7·19.

x	0.0-0.1	0.1-0.2	0.2-0.3	0.3-0.4	TOTAL
$\langle n\pi^-\rangle$	3.5	0.41	0.12	0.05	4.2
$\langle n\pi^+\rangle$	3.8	0.65	0.23	0.09	4.8
π^+/π^-	1.07	1.60	1.90	2.3	1.16

It is interesting to plot the integrand of the above expression on a linear scale as in Fig. 7.20. The majority of particles are in the region close to $x = 0$; in fact at $P_t = 0.4$ GeV/c about 70% of the pions are contained in the region $0 \leqslant x \leqslant 0.05$.

For transverse momenta of 0.2, 0.4 and 0.8 GeV/c the charge ratio over a number of regions of the x variable have been calculated and are given below :-

x Range	Transverse Momentum (GeV/c)		
	0.2	0.4	0.8
0.00 - 0.05	1.03	1.01	0.96
0.05 - 0.10	1.36	1.24	1.06
0.10 - 0.15	1.66	1.49	1.17
0.15 - 0.20	1.94	1.69	1.26
0.20 - 0.25	2.20	1.85	1.31
0.25 - 0.30	2.46	1.96	1.32
0.30 - 0.35	2.72	2.04	1.30
0.35 - 0.40	3.00	2.10	1.26

Turning now to experimentally measured particle ratios some of these obtained by Bertin et al (1972b) and a number of other experiments are shown in Figs. 7.21 and 7.22; these refer to Pt = 0.4 GeV/c. These experiments were specifically designed to measure particle ratios and it is best to use these results rather than those obtained by fitting equations to experimental data. The effect of uncertainties in the luminosity

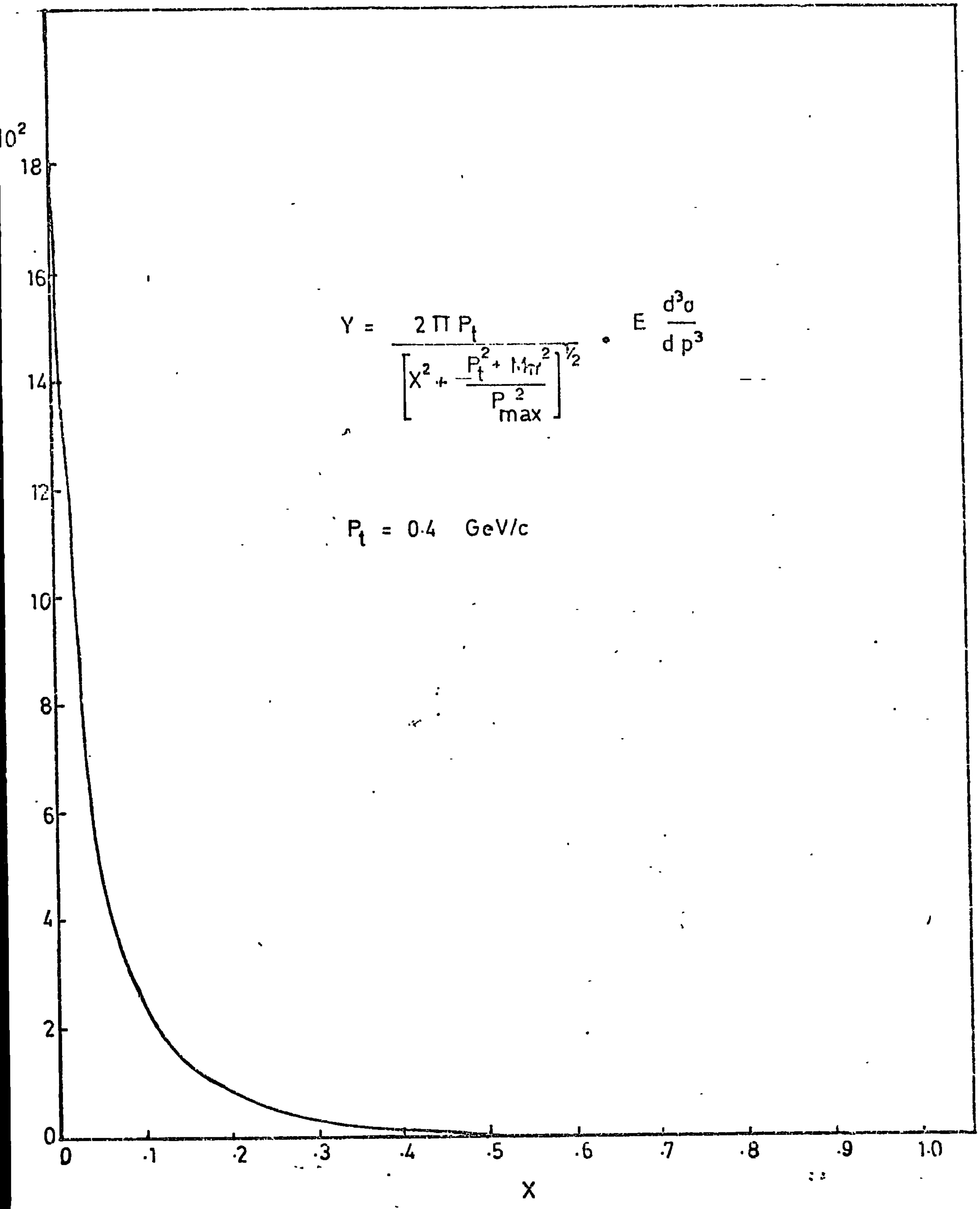$\times 10^2$
18
16
14
12
10
8
6
4
2
0
$Y = \frac{2\pi P_t}{\left[X^2 + \frac{P_t^2 + M_\pi^2}{P_{max}^2}\right]^{1/2}} \cdot E\,\frac{d^3\sigma}{dp^3}$
$P_t = 0{\cdot}4$ GeV/c
0
·1
·2
·3
·4
·5
·6
·7
·8
·9
1·0
X

FIGURE:7·20.

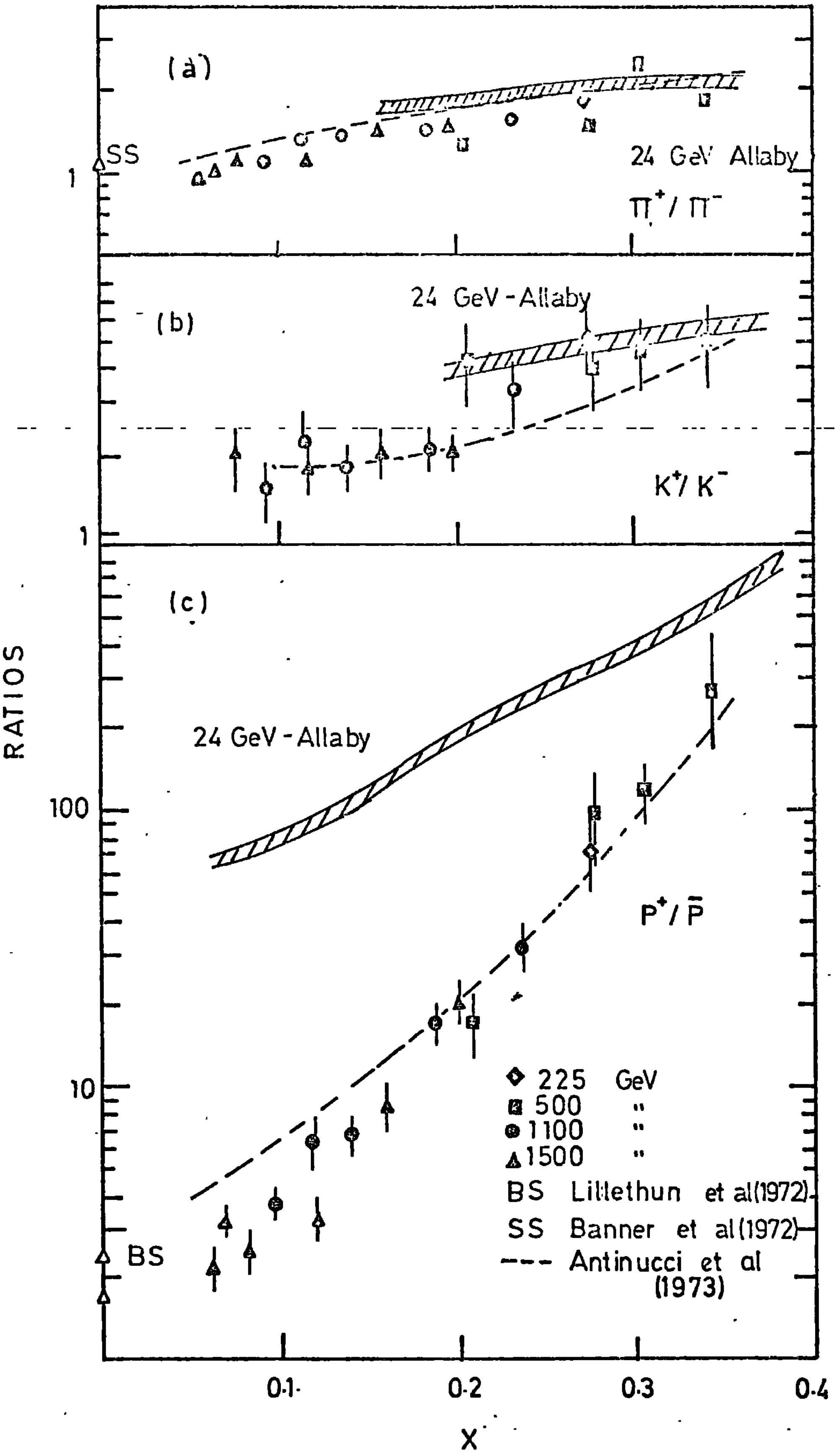
(a)
SS
1
24 GeV Allaby
π^+/π^-
(b)
24 GeV - Allaby
K^+/K^-
1
(c)
RATIOS
24 GeV - Allaby
100
$P^+/\bar{P}$
10
◇ 225 GeV
▣ 500 "
● 1100 "
▲ 1500 "
BS Lillethun et al (1972)
SS Banner et al (1972)
--- Antinucci et al (1973)
BS
0·1
0·2
0·3
0·4
X

FIGURE: 7·21.

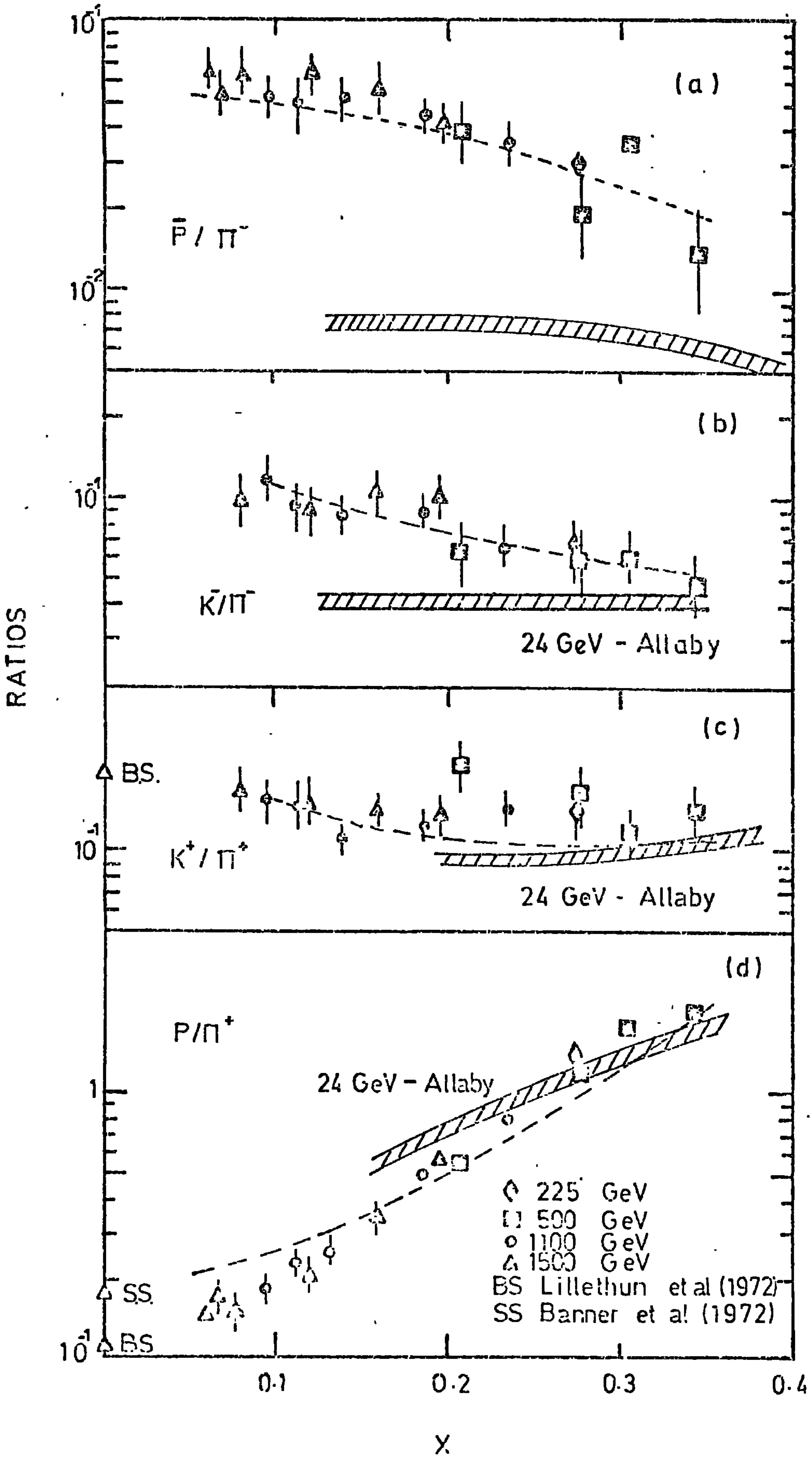
RATIOS
(a)
$\bar{P}/\pi^-$
10^{-1}
10^{-2}
(b)
K^-/π^-
10^{-1}
24 GeV - Allaby
(c)
K^+/π^+
10^{-1}
BS.
24 GeV - Allaby
(d)
P/π^+
1
24 GeV - Allaby
225 GeV
500 GeV
1100 GeV
1500 GeV
BS Lillethun et al (1972)
SS Banner et al (1972)
SS
BS
10^{-1}
0·1
0·2
0·3
0·4
X

FIGURE 7·22.

measurement is minimized by taking data for the particles during the same experimental run. Figure 7.21 shows the ratios of the invariant cross sections of particles to anti-particles (π^+/π^-, k^+/k^-, $p/\bar{p}$) as a function of x. Figure 7.22 shows the ratios of particles to pions of the same sign ($\bar{p}/\pi^-$, k^-/π^-, p/π^+, k^+/π^+). The main features of the results are :

(i) Within the experimental errors there is no obvious variation of the ratios with I.S.R. energy. This is true for all except the k^+/k^- ratio which exhibits a step function at $x = 0.2$; for smaller x values the data are from the 1100-1500 GeV incident energy range while for $x > 0.2$ most of the data refer to the 200-500 GeV energy range. There is no obvious cause of this and the effect is not found in the ratio when deduced from a different set of data (the dashed line in the figure).

(ii) All of the particle to anti-particle ratios decrease with decreasing x. The decrease is slowest for π^+/π^-. The ratios decrease to a value between 1 and 3 at $x = o$.

(iii) The particle to pion ratios tend to a value between 0.1 and 0.2 at $x = o$.

(iv) Those ratios involving protons display a strong x - dependence, reflecting the leading particle nature of the proton.

(v) The ratios π^+/π^-, $p/\bar{p}$, p/π^+ and k^+/π^+ level off to and essentially constant value for $x \lesssim 0.07$.

(vi) The separation between I.S.R. results and those at

24 GeV generally decreases with increasing x.

From the longitudinal momentum spectra of Antinucci et al (1973) (Fig. 7.23) particle ratios have been obtained simply by drawing a best line (by eye) through the data. These ratios are plotted as the dashed lines of Figs. 7.21 and 7.22. The agreement is surprisingly good; the indications are that the high data points in the region $x = 0.2 - 0.3$ of the k^+/k^- ratio are in error.

Having now considered the spectra of those particles produced most profusely in an interaction the absolute numbers of these particles will be considered.

7.3.5 Multiplicity

The true multiplicity (n, the number of particles in the final state) of a reaction is a difficult quantity to measure since, in particular, it requires the detection of neutral particles (mainly π^0 and n). The charged multiplicity, n_{ch}, is the number of charged particles in the final state and it is this quantity which is most often measured. Theoretical models tend to give predictions in terms of the true multiplicity and if comparisons are made with the experimentally measured charged multiplicity a considerable smoothing effect takes place (see, for example Morrison (1972)).

As mentioned above n_{ch} is the more commonly measured quantity and a brief list of some of the available data for p-p interactions, those of particular importance to the muon measurements, is given in Table 7.1 and plotted in Fig. 7.24 (where no error bars are shown, then the error is about the same size as the symbol). The quantity $\langle n_{ch} \rangle$ is the mean charged

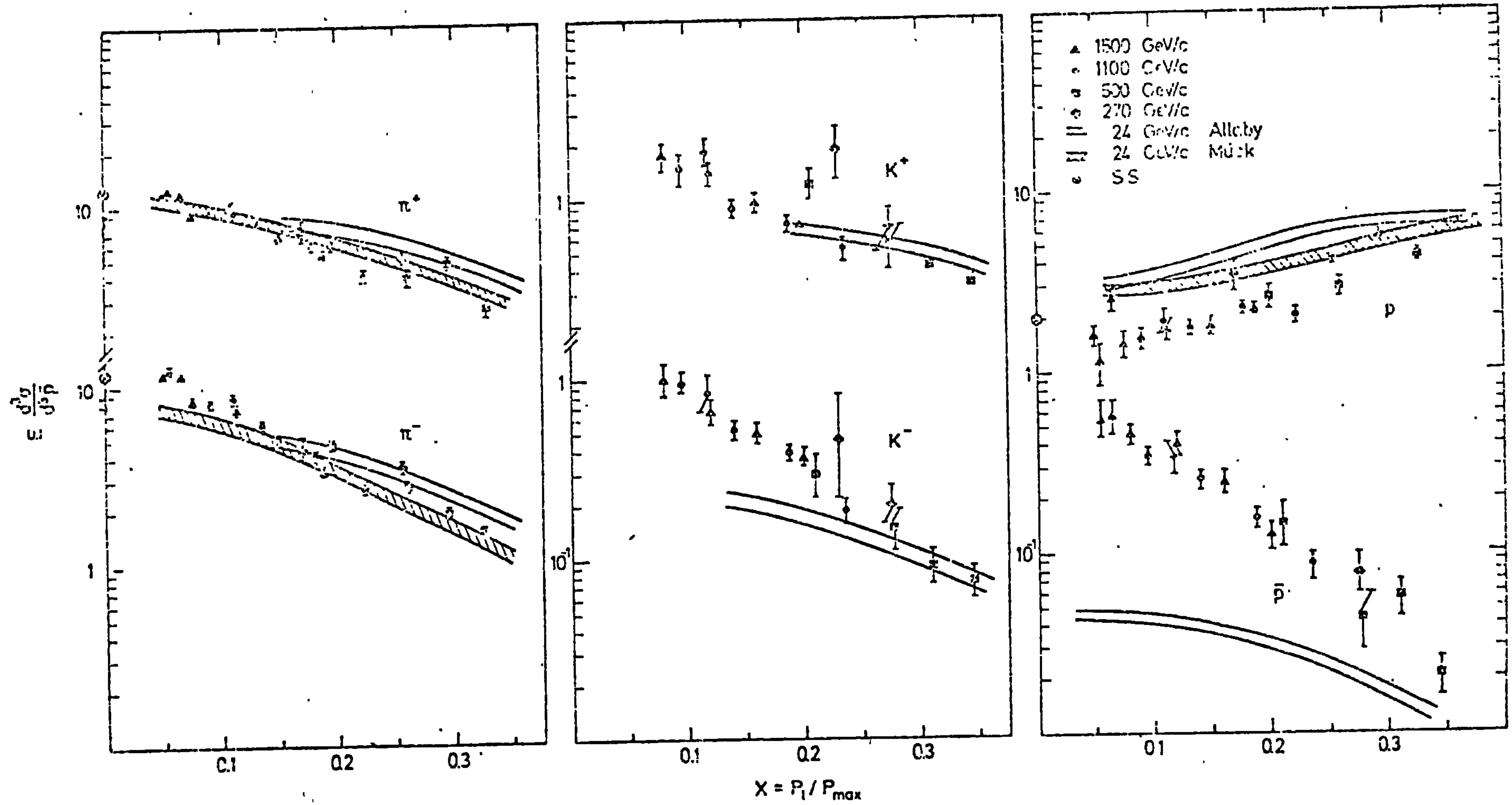

FIGURE: 7.23. PARTICLE LONGITUDINAL MOMENTUM SPECTRA ($P_T = 0.4$ GeV/c)

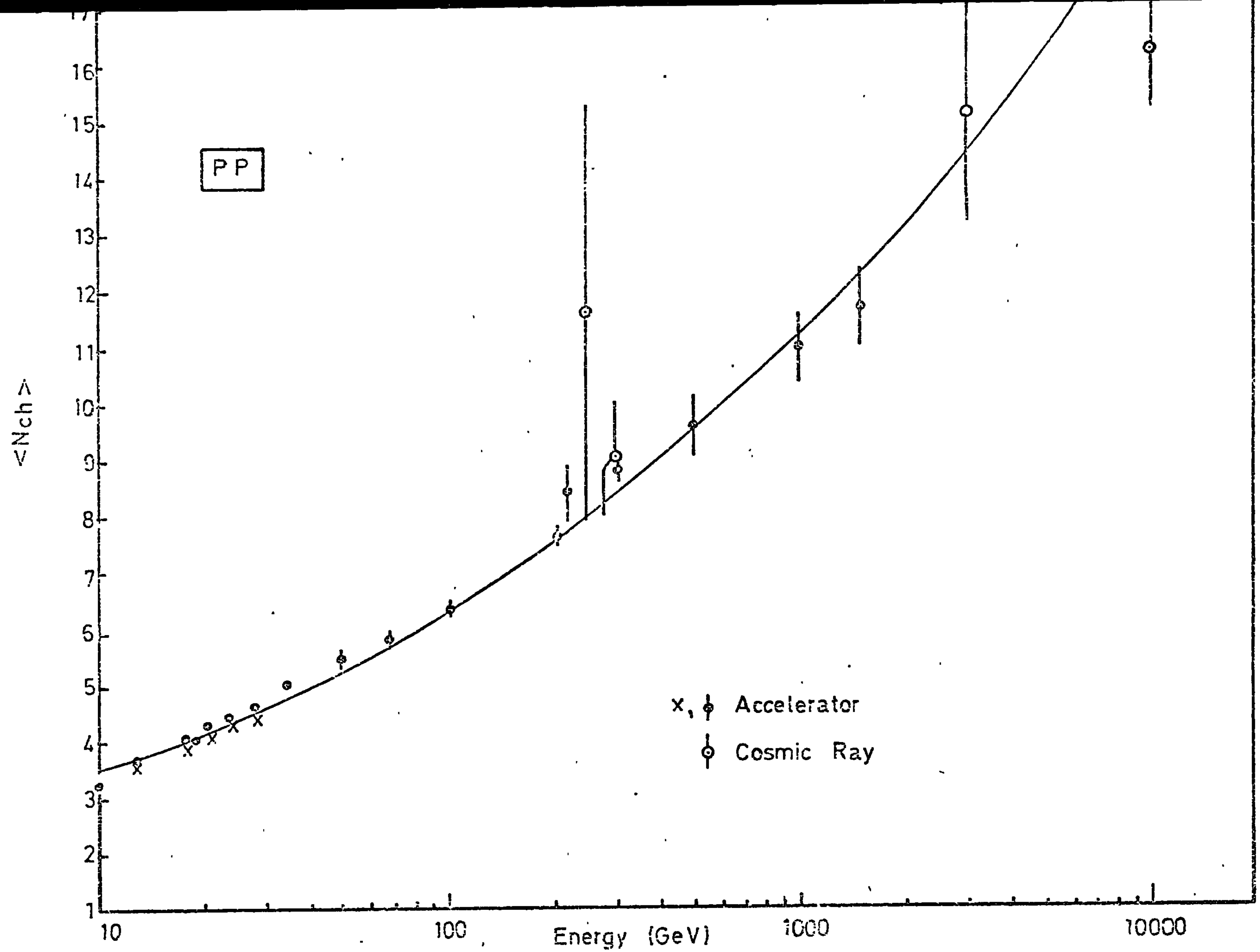

FIGURE: 7·24. PP MULTIPLICITY

multiplicity and includes any leading baryons.

A number of comments on the quality of some of the data points must be made. The experiment of Smith et al (1969) collected results only for interactions producing 4 or more prongs and corrections have been made to include inelastic 2-prong events. These corrections have been made, independently, by at least three different authors. The points plotted are those due to Jacob (1972) and to Czyzewski and Ribicki (1972). Below each of Jacob's estimates in Table 7.1 are given two other estimates - those of Czyzewski and Ribicki (1972) and of Malholtra and Ganguli (1972) respectively.

A number of estimates of $< n_{ch} >$ from the I.S.R. have been made. The latest results are those of Antinucci et al (1973) and these have smaller statistical errors than any previous estimates. The results of the authors are based upon empirical fits made to the variation of the invariant cross section as a function of secondary particle energy. This method has been adopted because there are no results available which cover the complete solid angle around an intersection. The technique used has been to express the invariant cross section (f) as a factorizable function of P_t and y. The variation with P_t has been taken as a pure exponential function. The distribution in y has been taken as that applying to $P_t = 0.4$ GeV/c (which is about the mean value of P_t for all particles). After integration over y and P_t and then summing over the particles $\pi^{\pm}$, $k^{\pm}$ and $p^{\pm}$ the results given in the table were obtained. The errors include an allowance for the fact that the P_t dependence is unknown for $P_t < 0.1$ GeV/c and a continuation of the pure exponential has been assumed. The effect of higher-than-expected cross sections at large transverse momenta ($\gtrsim$ 1 GeV/c) is unimportant since the absolute value of the cross section is small compared to that at lower momenta.

Above the highest I.S.R. energy multiplicities derived from cosmic ray experiments must be used. Most of these experiments use the emulsion technique and, since it is p-p interactions that are under consideration, the problem is to select such collisions from the raw data. From the chemical composition of emulsions it follows that the majority of interactions are with heavy nucleii (Ag, Br). Interactions with light nucleii (C, N, O) or Hydrogen nucleii amount to about 25% and 5% of all interactions respectively. It is possible to enrich the sample of p-nucleon collisions by considering those interactions involving only a peripheral nucleon of a heavy nucleus. Exactly how to detect such a collision is uncertain; for example Malholtra (1963) suggests that to ensure such a collision the number of heavily ionising (N_h) tracks emitted from the struck nucleus should be ≤ 2. This means that excitation of the struck nucleus is small and the contribution by the products of any intra-nuclear cascading to the multiplicity should also be small. A more severe criterion ($N_h = 0$) is used by Lohrman and Teucher (1962); a less severe test ($N_h \leq 5$) is recommended by Miespowicz (1971). A qualitative measure of the effect of constraining N_h has been given by Malholtra and Ganguli (1972); they give $\langle N_{ch} \rangle =$ 15.1 ± 2.9, 15.8 ± 3.8, 17.3 ± 4.2 and 27.9 ± 4.2 for N_h = 0, 1, 2 and 3 to 5 respectively. These authors restricting their data survey to $N_h \leq 2$ and combining the results with those of Nozaki and Koshiba (1971) give the multiplicity at 10 TeV as 16.3 ± 1.1. Besides demanding $N_h \leq 2$ they also made an attempt to eliminate scanning bias by only considering experiments in which one of two scanning methods were used. The first method was 'along the track scanning' in which the singly charged fragments resulting from the break-up of an energetic multiply charged nucleus are followed through the emulsion until an interaction occurs. The second method was to look for the large dark spots in the emulsion associated with an electromagnetic cascade. The cascade was followed back to the original interaction and which was then examined. Other methods of scanning depend upon the detection of shower particles produced in the interaction and are hence biased against low multiplicity events. Neither of the above two methods is subject to this type of bias. The authors point out that although a fairly severe criterion was demanded there may still be a contribution from intranuclear cascading which leads to an overestimate of $\langle N_{ch} \rangle$. However since some of the data were collected by the electromagnetic cascade method those fluctuations in the cascades resulting in a high value of $n\pi^{o}$ (and hence low $n\pi^{\pm}$) would be preferentially detected and hence compensate to some extent the effect of the nuclear cascade. An indication that the resulting bias is small is obtained by calculating the quantity $\langle n_{ch} \rangle / D$ where D is the dispersion, given by $D = (n_{ch}^{2} - \langle n_{ch} \rangle^{2})^{\frac{1}{2}}$. This ratio decreases from about 2.3 at 10 GeV to about 2.1 in the region 50-200 GeV. The value of D obtained by the authors for their results was 2.0 which is in reasonable agreement with the trend. A further bias, not considered by the authors is that collisions with peripheral nucleons of heavy nucleii may be either p-p or p-n with roughly equal probability. The presence of p-n collisions reduces the value of $\langle n_{ch} \rangle$. It has been estimated (Malholtra (1963)) that about two-thirds of the data involve collisions with peripheral nucleons and assuming that half of these are with neutrons then the calculated multiplicity is low by about 0.3. This is much smaller than the statistical error already present and can be ignored. The value $\langle n_{ch} \rangle = 16.3 \pm 1.1$ represents the best estimate of the multiplicity that can be made with the available data.

The solid line shown in Fig. 7.24 is

$$\langle n_{ch} \rangle = 2 E_{Lab}^{\frac{1}{4}}$$

and is a good empirical fit to the results in the range 20-1000 GeV. At higher energies the trend seems to be to lower multiplicities than predicted by this line.

Having thus dealt with the average charged multiplicity the distribution of this quantity will now be described. The distributions in prong number from three experiments are sketched in Fig. 7.25(A) where the broadening of the distribution with increasing energy is apparent. The cross section for the production of a given number (n) of prongs, (the topologic cross section, σ_n) as a function of incident proton energy is shown in Fig. 7.26. With increasing energy the final state of the interaction increases in complexity as the cross sections for the production of large numbers of charged particles rises. At the same time the low multiplicity cross sections are starting to fall. Whether this fall continues is unknown; no data at I.S.R. energies has so far been produced. The rising high multiplicity cross sections and falling low multiplicity cross section together result in a slow increase of the total inelastic cross section and a broadening of the multiplicity distribution.

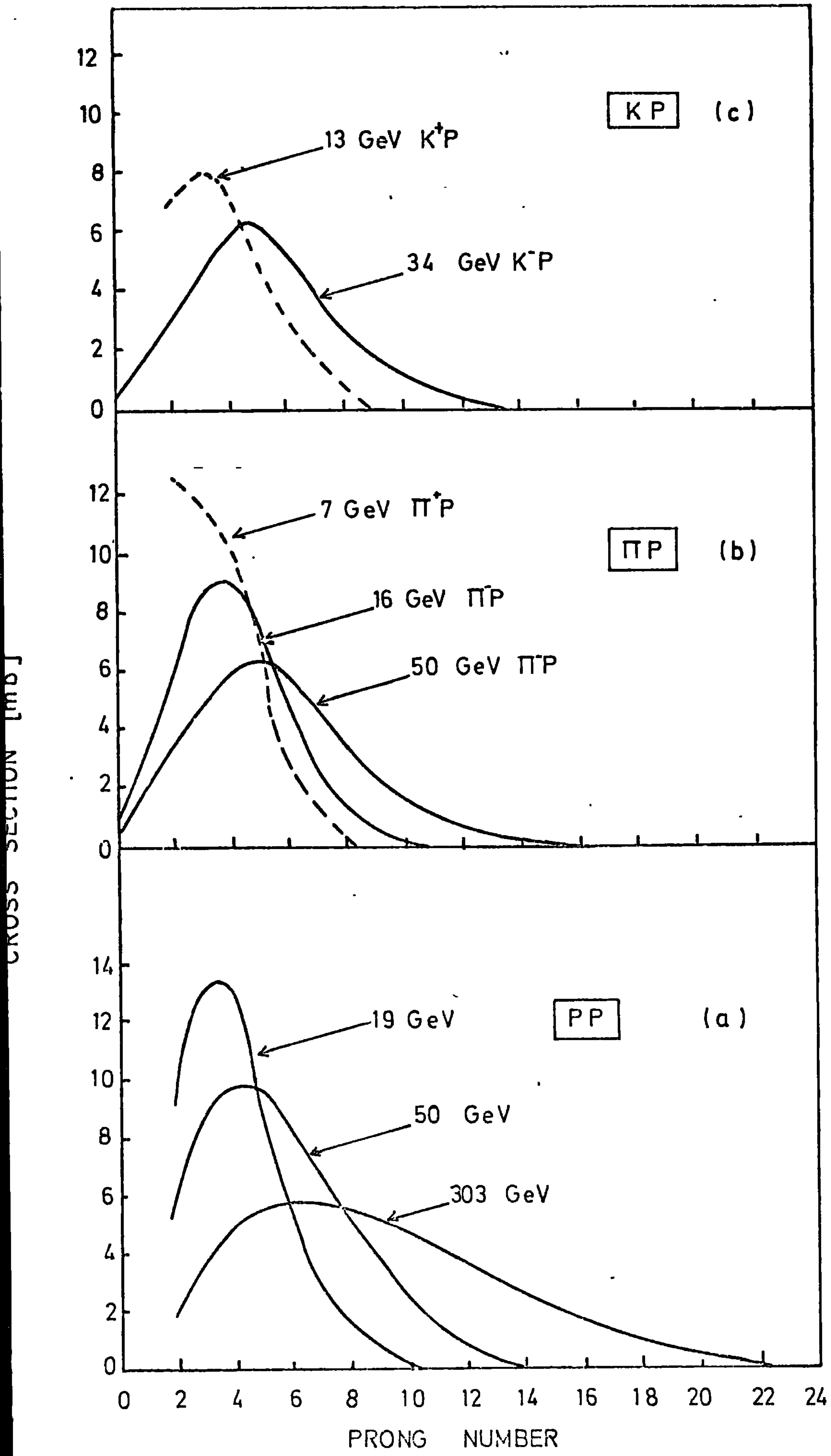
CROSS SECTION [mb]
KP (c)
13 GeV K⁺P
34 GeV K⁻P
ΠP (b)
7 GeV Π⁺P
16 GeV Π⁻P
50 GeV Π⁻P
PP (a)
19 GeV
50 GeV
303 GeV
0 2 4 6 8 10 12
0 2 4 6 8 10 12
0 2 4 6 8 10 12 14
0 2 4 6 8 10 12 14 16 18 20 22 24
PRONG NUMBER

FIGURE: 7.25.

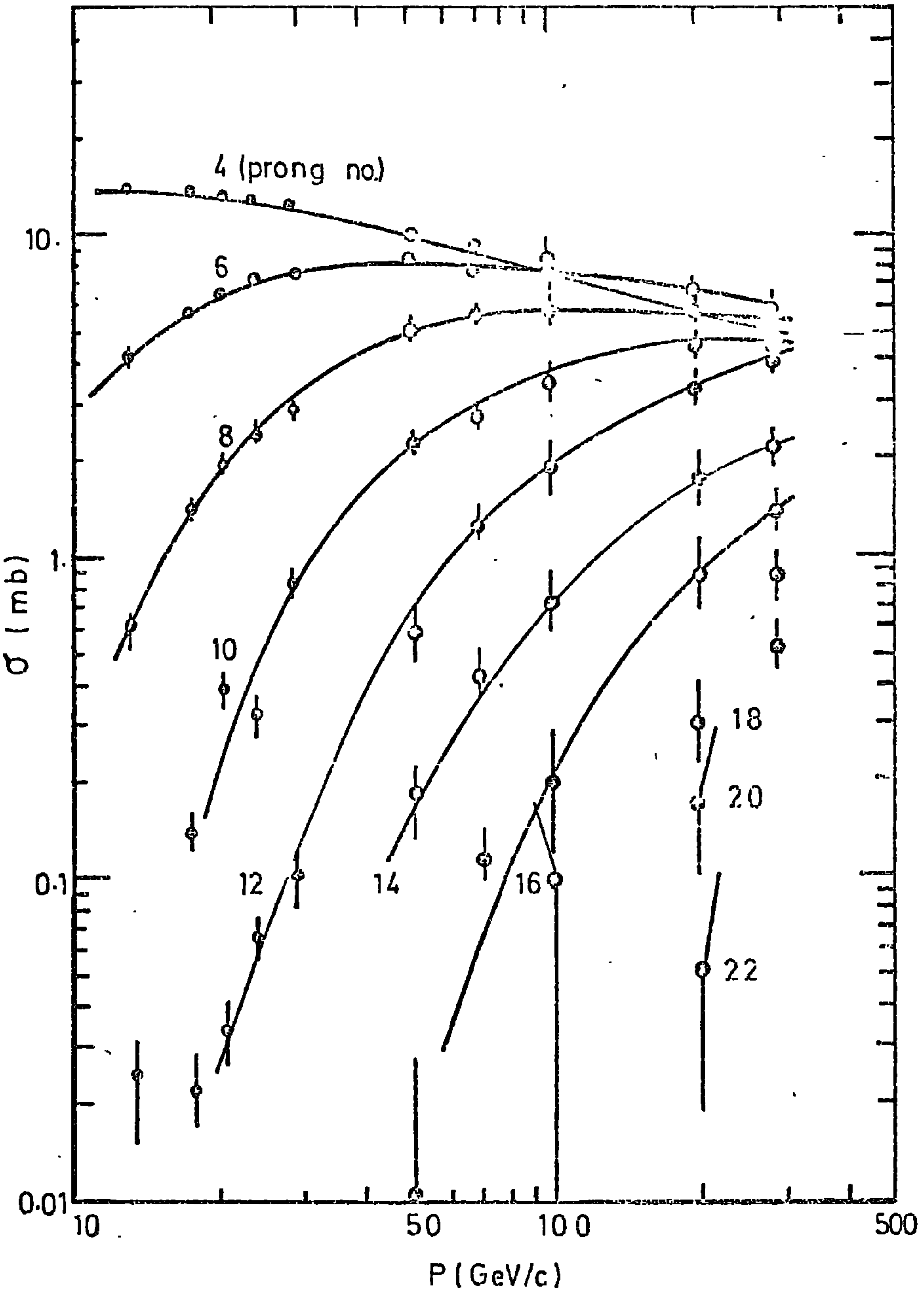

FIGURE 7·26. PP CHARGED PRONG CROSS SECTION

In the 10-30 GeV region a Poisson distribution has been found to give an approximate fit to the multiplicity variation but at higher energies this no longer applies (see for example Chapman et al (1972) at 102 GeV and Charlton et al (1972) at 205 GeV). At higher energies the multiplicity distribution becomes broader than the Poissonian; this effect is usually described by the use of the correlation coefficient f_2 defined by

$$f_2 = \langle n(n-1)\rangle - \langle n\rangle^2.$$

For a Poisson distribution $f_2 = 0$. Rather than consider the total charge distribution which would not be expected to be a perfectly Poissonian function because of constraints due to charge conservation it is usual to consider negative particles alone. The observed variation of f_2 computed for negative tracks only (and hence denoted f_2^-) is shown in Fig. 7.27. At about 80 GeV a Poisson distribution is a good fit, at lower energies the real distribution is narrower and at higher energies it is broader. The broadening is particularly interesting in view of the fact that if the pions were uncorrelated then the multiplicity distribution would be closely Poissonian (allowing for charge conservation restraints). The rise of f_2^- indicates important correlations among the secondaries.

A number of interesting trends have been observed in the charged multiplicity distributions of p-p collisions; two trends are briefly described below.

It has been found that the ratio $\langle n_{ch}\rangle/D$ as a function of energy approaches the value 2.0. This is shown in Fig. 7.28 where the values plotted are those of Ammosov et al (1973).

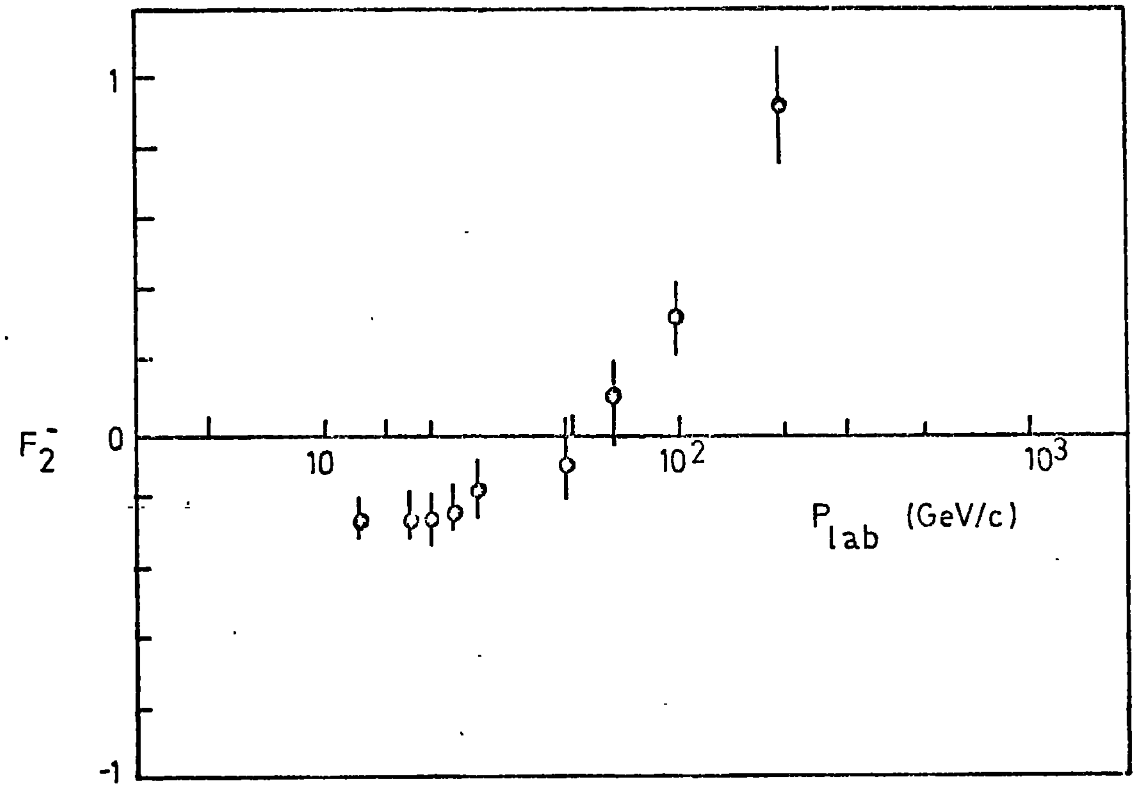

FIGURE. 7.27. F_2^- FOR PP REACTIONS

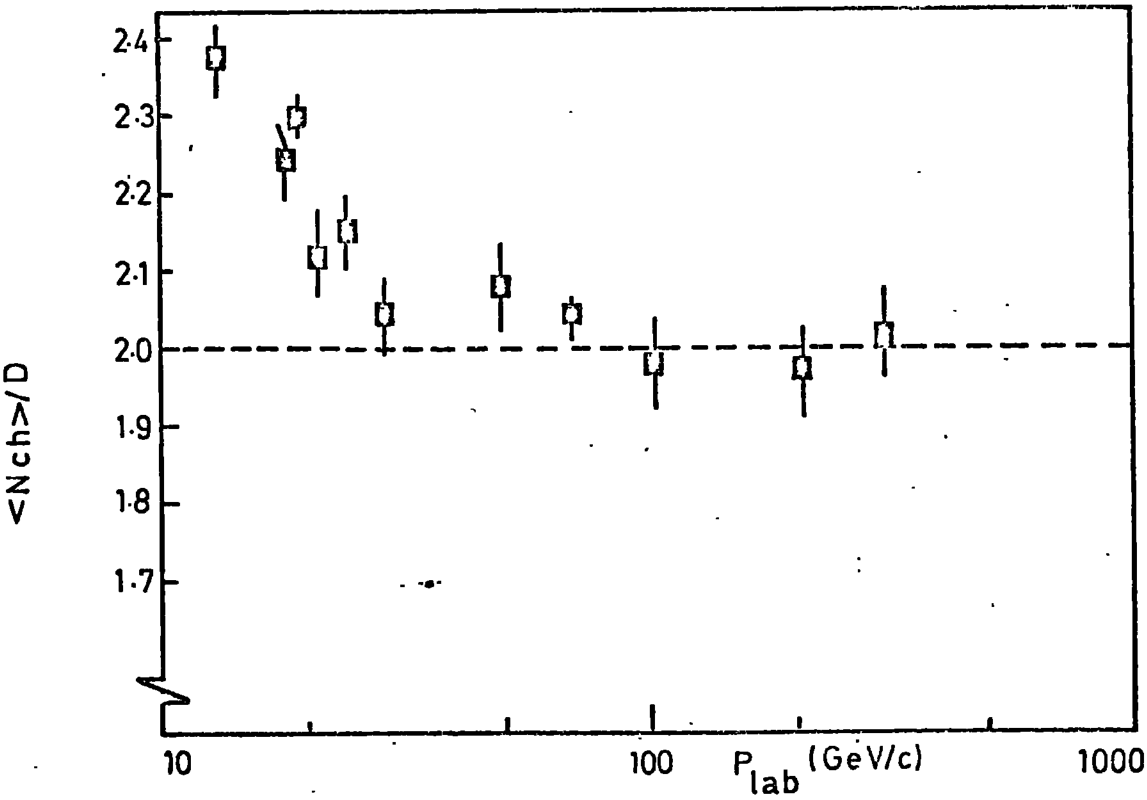

FIGURE. 7.28. <Nch>/D FOR PP REACTIONS

The fact that Malholtra and Ganguli (1972) obtained, from emulsion data, a value of $\langle n_{ch} \rangle / D$ of 2.0 is a good indicator of the freedom from bias of their data.

It has been suggested by Koba, Nielsen and Oleson (1972) that the topological cross sections expressed as fractions of the total inelastic cross section should reach an energy independent limit

i.e. $$\frac{\sigma_n}{\sigma_{inel}} \xrightarrow[s \to \infty]{} \frac{1}{\langle n_{ch} \rangle} \Psi\left(\frac{n}{\langle n_{ch} \rangle}\right)$$

where σ_{inel} is the total inelastic cross section, s is the centre of mass energy and Ψ is an energy independent function. Figure 7.29 is a plot of $\langle n_{ch} \rangle \ \sigma_n / \sigma_{inel}$ vs $n / \langle n_{ch} \rangle$ for incident proton energies $\geqslant$ 50 GeV. The solid line is a fit of Slattery (1972) and is given by

$$\Psi(Z = n / \langle n_{ch} \rangle) = (3.79Z + 33.7Z^2 - 6.64Z^5 + 0.32Z^7) \exp(-3.04Z)$$

The fact that the low energy data (inset) is quite well fitted by the curve is surprising since the prediction was based on asymptotic arguments.

This concludes the description of the multiplicities of proton induced reactions; a brief description of reactions induced by particles other than protons will now be given.

A summary of some of the available data on pion induced interactions is given in Table 7.2. The result at 60 GeV is from an emulsion experiment and is included because a strict limit ($N_h \leqslant 1$) was imposed on the dark tracks.

These data and some of Table 7.1 are plotted in Figue 7.30 (where no error bar

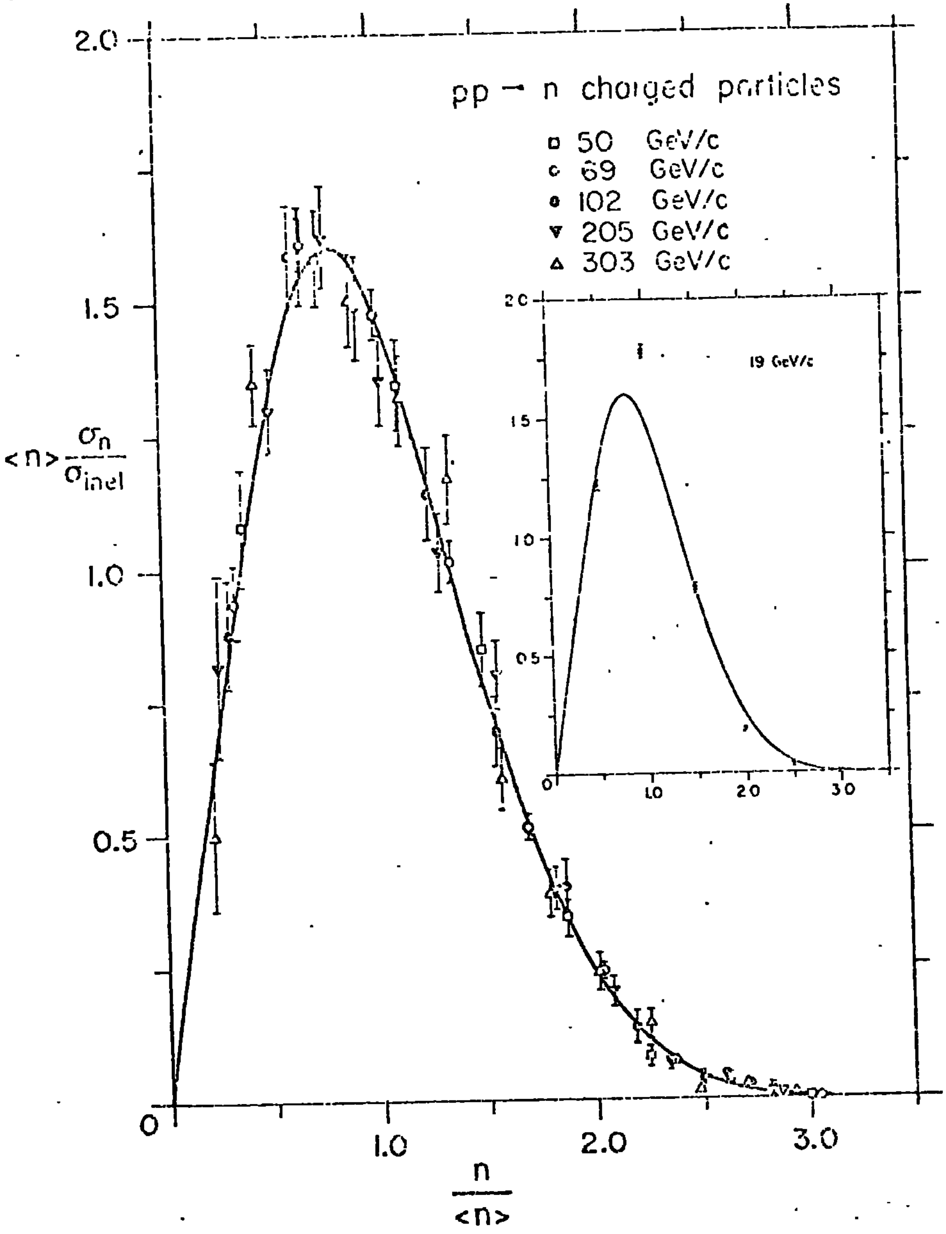
pp → n charged particles
□ 50 GeV/c
○ 69 GeV/c
● 102 GeV/c
▽ 205 GeV/c
△ 303 GeV/c
19 GeV/c
$<n>\frac{\sigma_n}{\sigma_{inel}}$
$\frac{n}{<n>}$
2.0
1.5
1.0
0.5
0
1.0
2.0
3.0

FIGURE: 7·29.

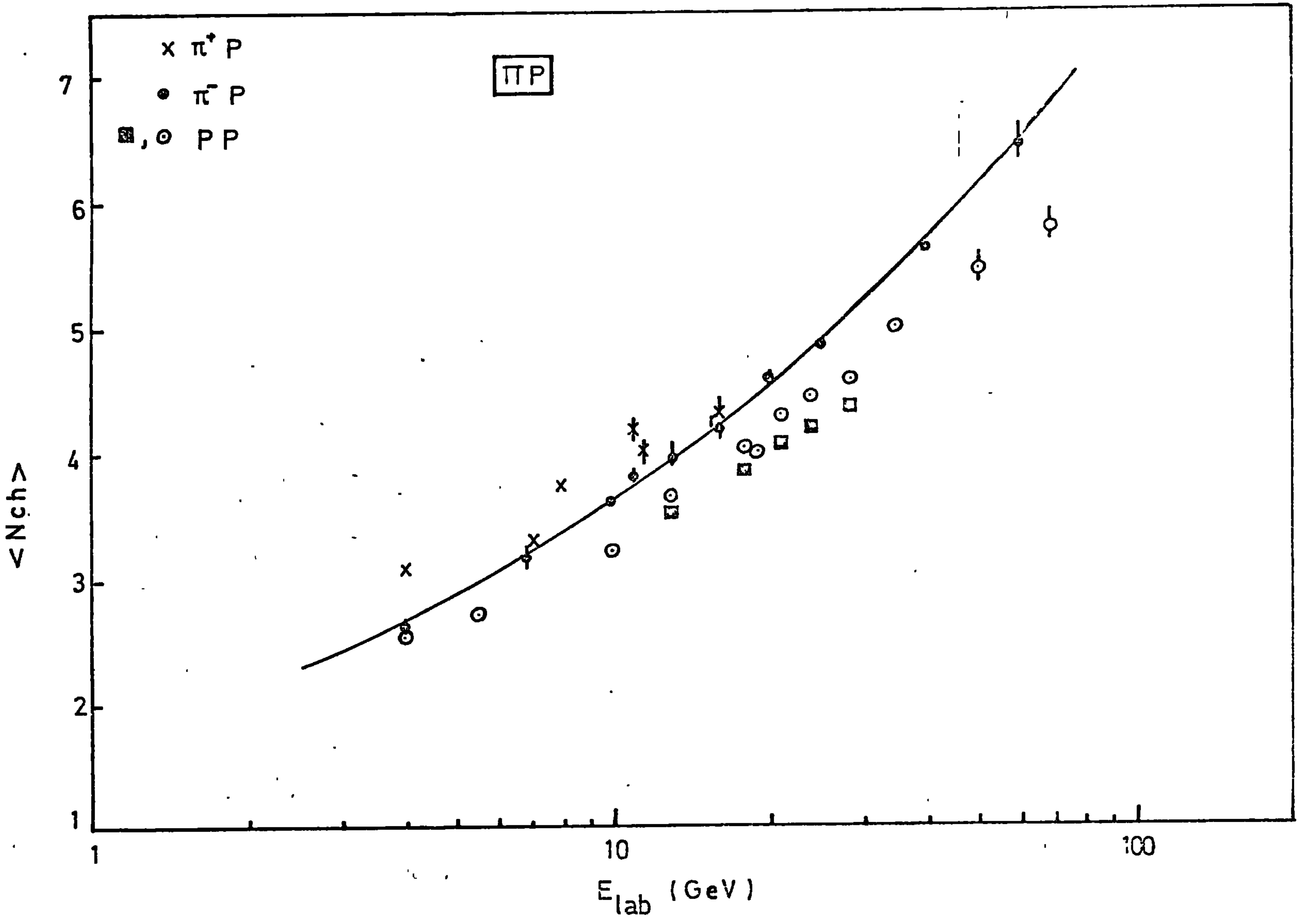

FIGURE:7·30.

is shown then the error is about the same size as the symbol).

It can be seen that the multiplicities of pion induced interactions are higher than those induced by protons. As already mentioned the p-p data in the range 13 - 28.5 GeV are two independent estimates based upon the same initial data. The difference between the πp and pp results seems to be increasing with increasing energy. The π^+ data of Fig. 7.30 is rather more scattered than that for π^- but the indications are that the values of $\langle n_{ch} \rangle$ associated with the former are higher than those with the latter. Concerning the topological cross-sections, the distributions are sketched in Fig. 7.25(B) for three primary energies. At the lower energies a Poisson distribution has been found to be a reasonable fit (Honecker et al (1969)) but at higher energies the fit is poor (Ammosov et al (1973)). The tendency for the deviation from a Poisson-like curve to pass through zero and to then increase with energy is displayed in $\pi^- p$ interactions as shown in Fig. 7.31 where the parameter f_2 has been calculated including both positive and negative particles. Results on $\pi^+ p$ collisions at higher energies than shown are not yet available. The quantity $\langle n_{ch} \rangle /D$ for $\pi^\pm p$ reactions is shown in Figs. 7.32a,b. The π^- data up to about 25 GeV seem fairly constant at around 2.25 but the last two points may indicate a falling value. The π^+ data are also fairly constant but the range of momenta is rather limited.

Turning now to kaon induced reactions a summary of the available multiplicity data has been given by Ammosov et al (1973) and is reproduced in Table 7.3. These results, along with some for pp collisions, are plotted in Fig. 7.33. Kaon induced reactions give slightly higher multiplicities.

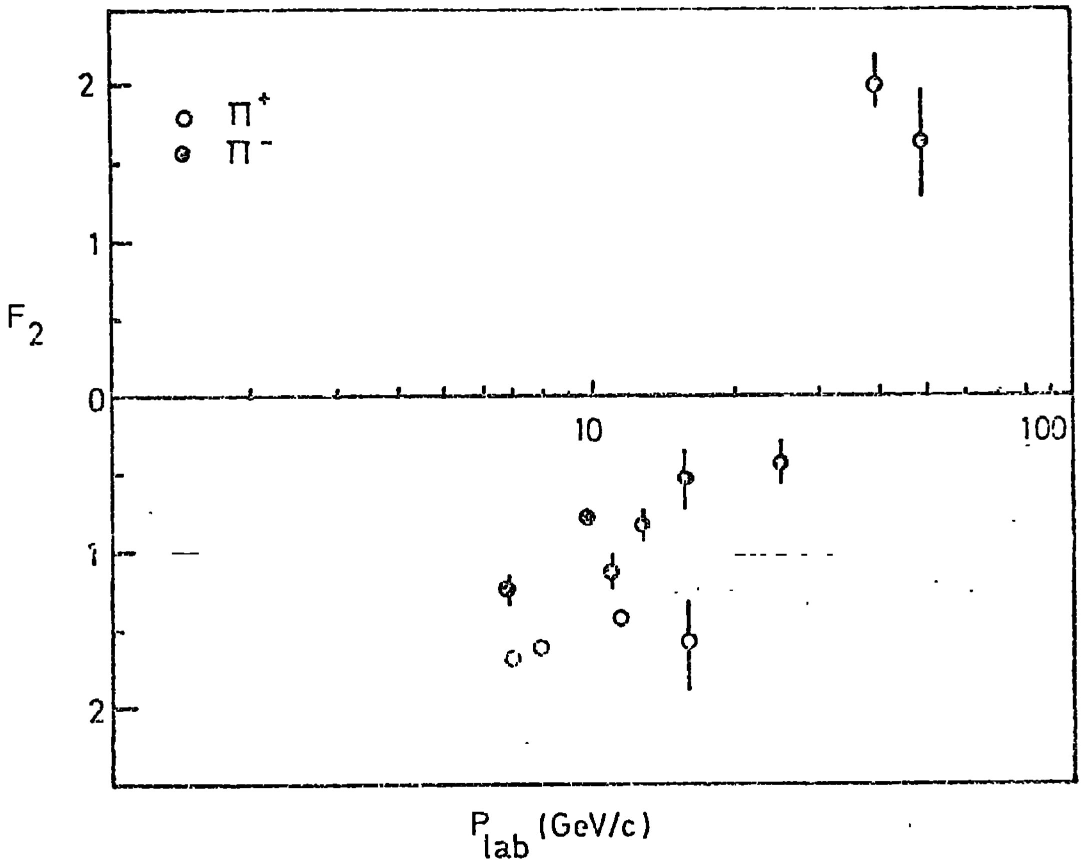

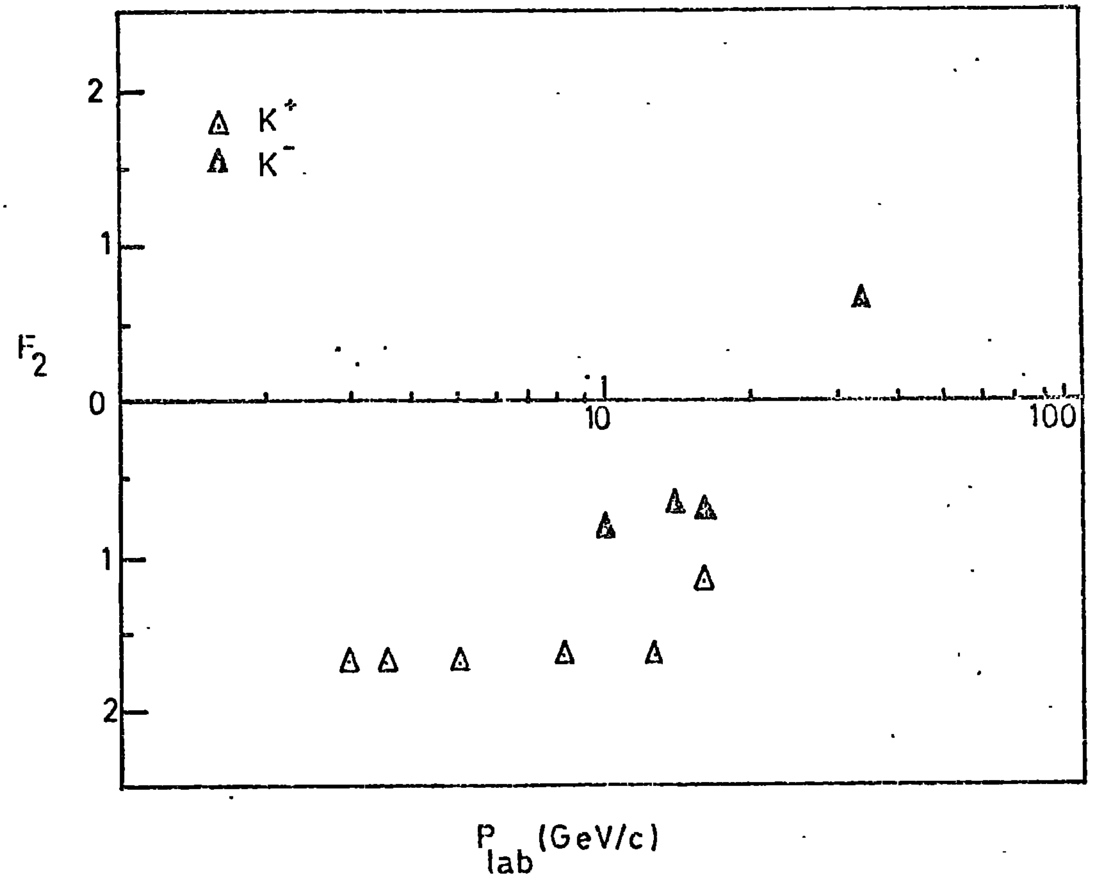

FIGURE 7·31. F_2 DISTRIBUTIONS FOR π, K

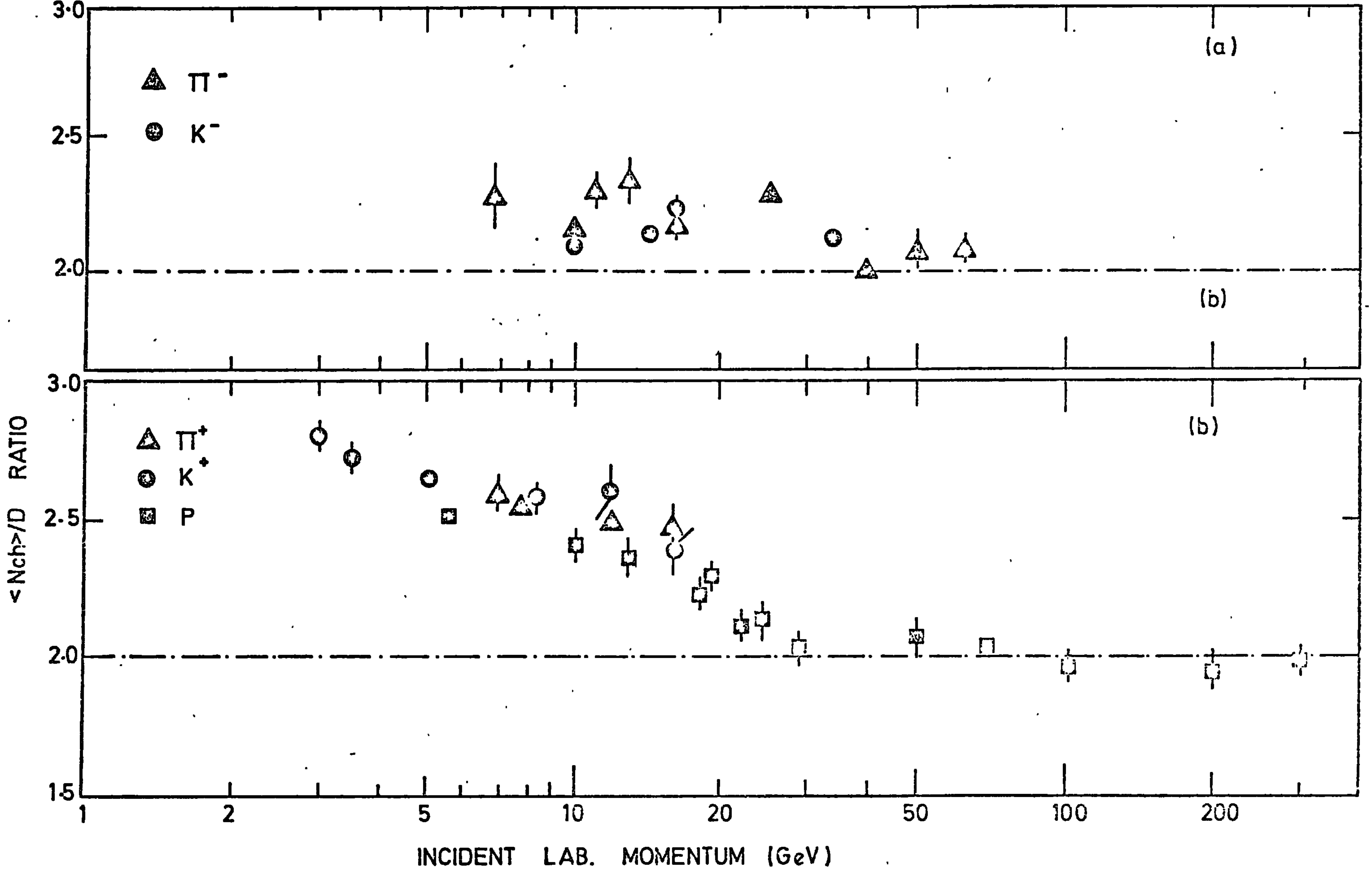

FIGURE: 7·32. <Nch>/D RATIO

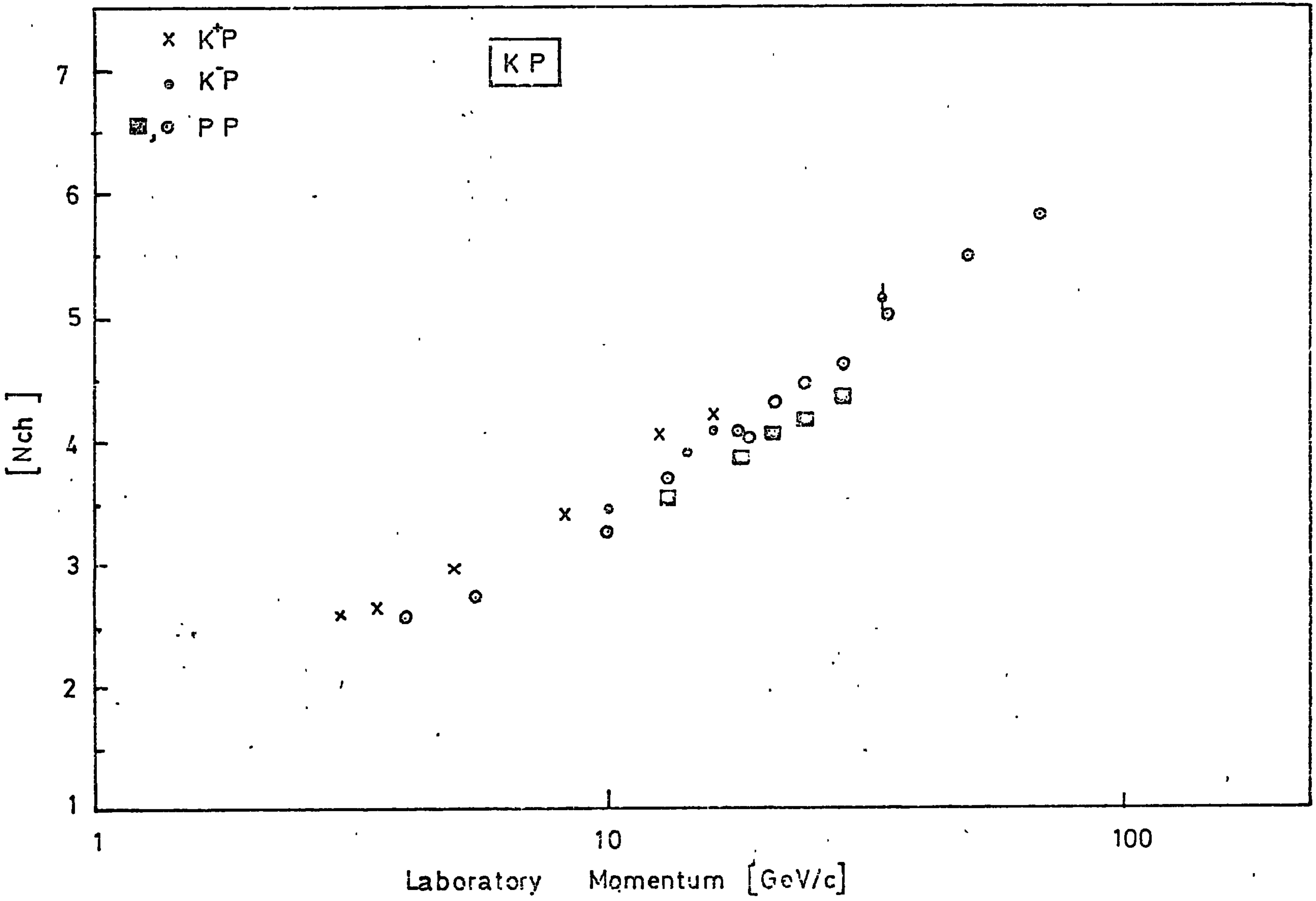

FIGURE: 7.33.

Typical topological cross section distributions are shown in Fig. 7.25(c). A Poisson distribution has been fitted to the lower energies but as before the fit is poor at higher energies. The values of f_2 for kaon induced reactions are shown in Fig. 7.31. The results are similar to those of pion induced reactions. The quantity $\langle n_{ch} \rangle /D$ is plotted in Fig. 7.32a,b. The k^-p data are fairly constant at about 2.15. The k^+p data show a fall with increasing momentum and, where comparison is possible the k^+p and π^+p data seem to be in agreement. In Fig. 7.32b the pp results are plotted for comparison.

7.3.6 Cross Sections

The p-p total cross section is, at conventional accelerator energies a well measured quantity. A brief survey of total (σ_t) and elastic (σ_e) cross sections has yielded the data of Tables 7.4, 7.5 and the graphs of Figs. 7.34 and 7.35. The results at the lowest energy are only a fraction of the available data but seem to be representative of the whole. The data gathered at N.A.L. are preliminary and their accuracy should soon be improved. Such an improvement is important since the cross section seems to reach a shallow minimum in the region between the finish of the J.I.N.R. results and the start of the I.S.R. results.

Considering σ_e, there is a lack of data in the 30-100 GeV region. The general trend of the data including the I.S.R. results which will be described later suggests a minimum in the 100-200 GeV range followed by a slow rise.

For both σ_t and σ_e the highest momentum conventional accelerator at 303 GeV/c agrees well with results at the lowest

KEY TO FIGURE 7.34

⌽ Galbraith et al (1965)

○ Belletini et al (1966)

▣ Denisov et al. (1971) (JINR)

○ (NAL) {
Chapman et al. (1972) - 102 GeV
Charlton et al (1972) - 205 GeV
Dao et al (1972) - 303 GeV.

ISR {
✕ Amaldi et al (1973a)
× Almendolia et al (1973)
⊗ Amaldi et al (1973)
⊠ Holder et al (1971)

KEY TO FIGURE 7.35

○ Almeida et al (1968)

⌽ Foley et al · (1963)

○ (NAL) {
Chapman et al (1972) - 102 GeV
Charlton · et al (1972) - 205 GeV
Dao et al (1972) - 303 GeV

⊡ Breitenloh et al (1963)

✕ Amaldi et al (1973a)

⊘ Amaldi et al (1973)

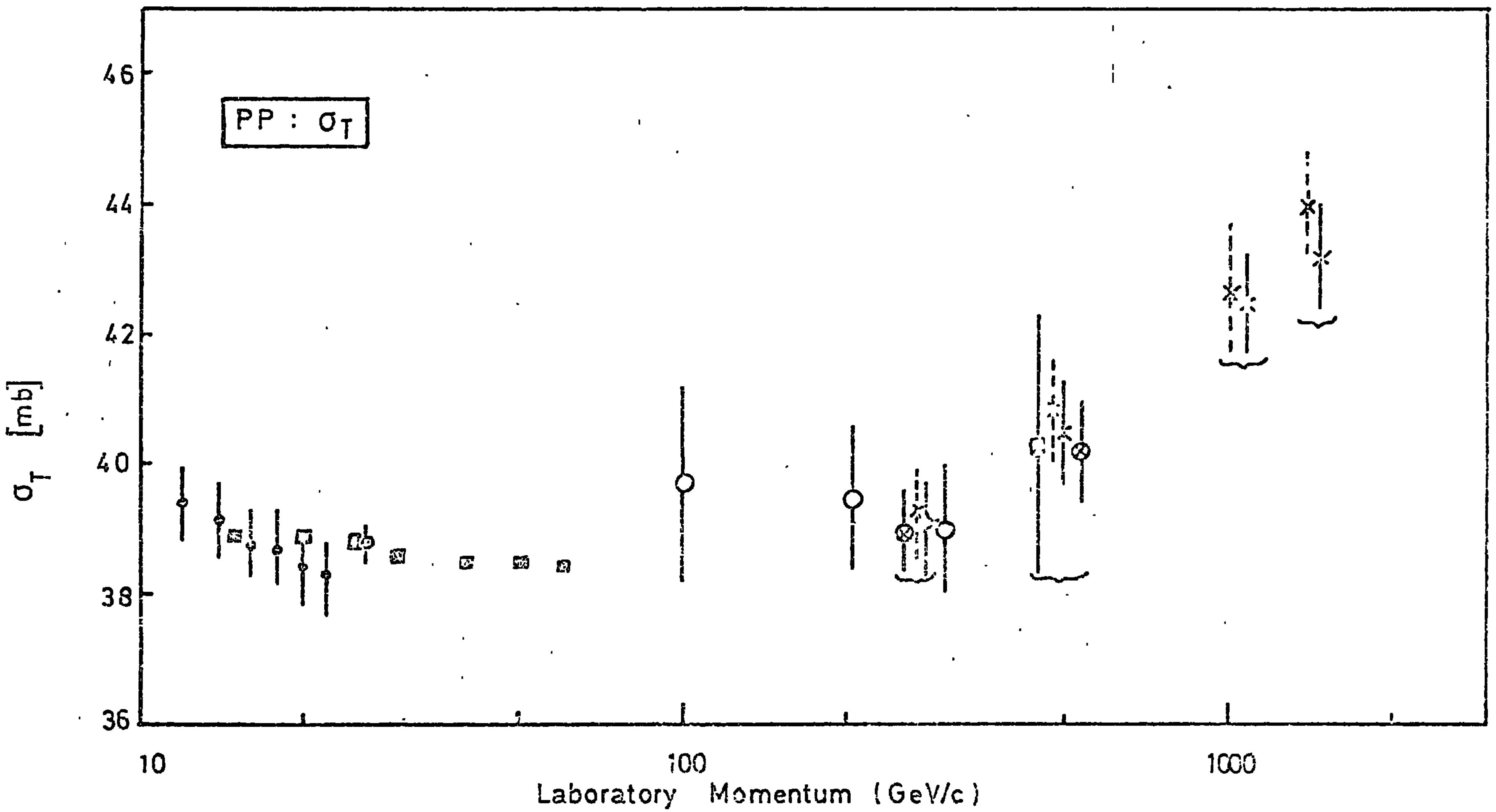

FIGURE: 7.34. TOTAL PP CROSS SECTION

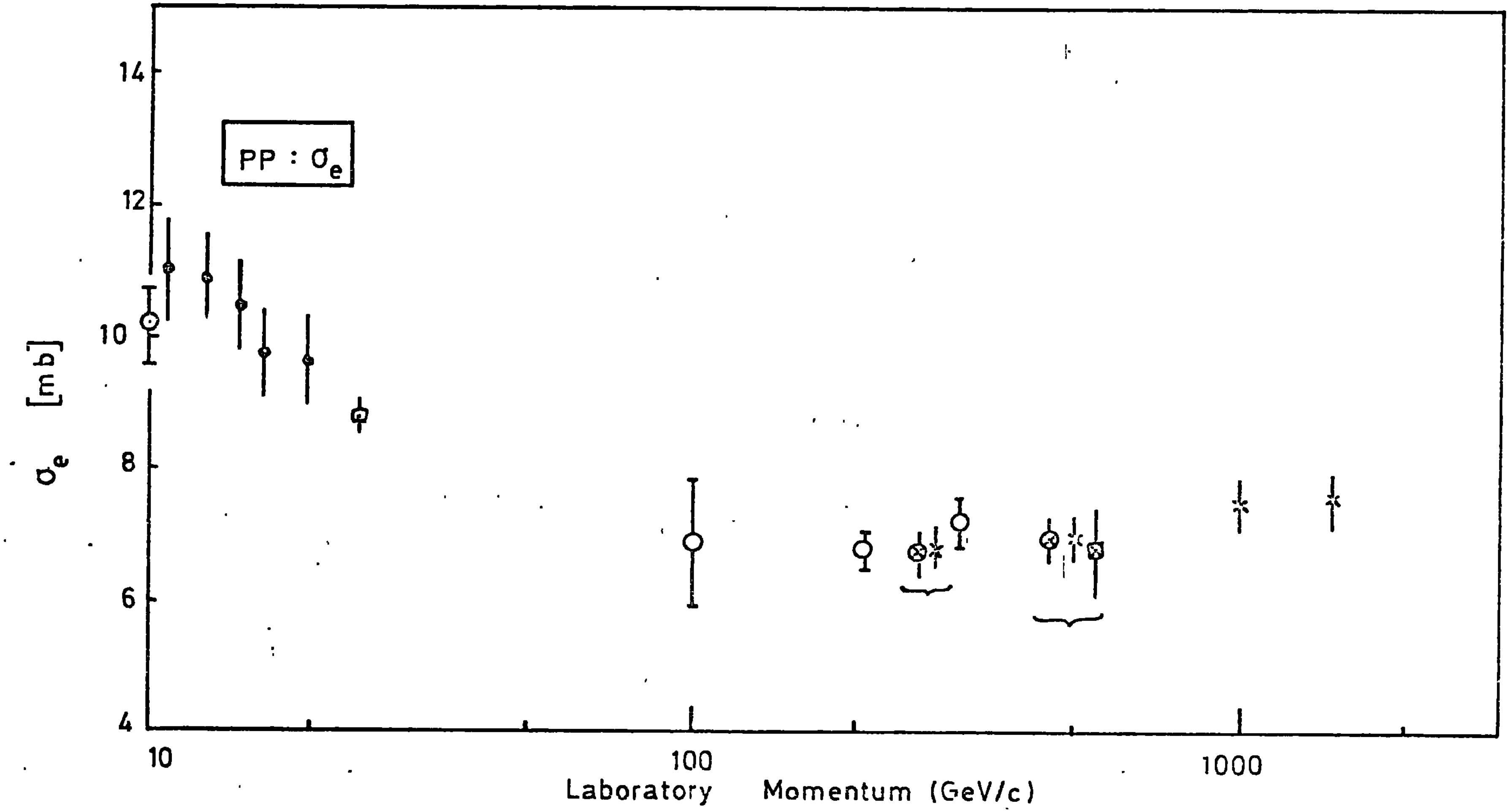

FIGURE: 7.35. ELASTIC PP CROSS SECTION

I.S.R. momentum ($\sim$290 GeV/c).

Recent measurements of σ_t and σ_e based upon work at the I.S.R. are those of Amendolia et al (1973) and Amaldi et al (1973a). After correcting for contributions from inelastic events and from Coulomb scattering the latter workers expressed the differential cross sections as functions of t, the 4-momentum transfer. Extrapolating back to t=o and using the relation $\sigma_t = \left[16\pi(d\sigma/dt)_{t=o}\right]^{\frac{1}{2}}$ led to the cross sections shown in Table 7.5. The quoted errors include estimates of systematic effects.

The experiment of Amendolia et al (1973) was based upon the equation $R_t = \sigma_t L$ where R_t is the total number of interactions and L is the luminosity and the results obtained by these workers are given in Table 7.5; the errors include estimates of systematic effects.

A further experiment has been reported by Amaldi et al (1973). This experiment was similar to that of Amaldi et al (1973a). The number of detected events as a function of the 4-momentum transfer is $N(t) \propto \left|fc + fn\right|^2$ where fc and fn are the Coulomb and nuclear scattering amplitudes respectively. Substituting for these parameters leads to

$$N(t) = k\left[(2\alpha/t)^2 G^4(t) - (\rho + \alpha\Phi)\,\frac{\alpha}{\pi}\,\sigma_t\,\frac{G^2(t)}{|t|}\,\exp\frac{(bt)}{(2)} + \frac{(\sigma_t)^2}{(4\pi)}\,(1+\rho^2)\,\exp(bt)\right]$$

where α is the fine structure constant

G is the proton electromagnetic form factor

$\alpha\Phi$ is given by $\alpha\Phi = \alpha \log_e (0.08/|t| - 0.577)$

ρ is the ratio of the real and imaginary parts of the forward scattering amplitude.

b is the slope parameter of the exponential dependence of the nuclear scattering cross section on t.

k is a normalization constant.

The above expression was fitted to the experimental data with d_t, ρ and k as free parameters. The value of b was taken from other I.S.R. experiments. The resulting values of σ_t are given in Table 7.5 where as usual the errors include estimates of systematic effects. Using the obtained normalization constant k and the assumed value of b the elastic cross section was also found. No results from this experiment are available at higher energies since particles must then be detected at angles too near to the beams.

From the table it can be seen that the results of this experiment are in good agreement with the other results described. This is a good indicator of the reliability of the results.

One other I.S.R. experiment has measured σ_t and σ_e - that of Holder et al (1971), this was at only one energy.

The I.S.R. results plotted in Fig. 7.34 and 7.35 show that in the laboratory energy range 290--1500 GeV the cross sections increase by about 10%. If a smooth line is drawn through the data points a shallow minimum is seen in the 100-200 GeV region.

Finally, considering neutrons the compilation of Benary et al (1970) shows that in the range 8 to about 30 GeV

σ_t (pp) = σ_t (pn) = σ_t (np). At higher energies there is no neutron data.

This completes the survey of experimental accelerator results on (mainly) p-p interactions. The energy range covered has included a significant part of that relevant to the charge ratio data reported in this work. Since the majority of particles produced in primary cosmic ray - atmospheric nucleii collisions are pions which then go on to interact with other nucleii the π -p cross sections are of interest. A short survey of the experimental data on total cross sections for interactions induced by particles other than protons is given below.

Tables 7.6 and 7.7 contain data for such interactions; they are plotted in Figs. 7.36 a-e.

The π^+ -p and k^- -p total cross sections show a monotonic decrease with momentum up to about 30 GeV/c and at higher momenta seem fairly constant. Denisov et al (1971) have fitted straight lines to their results for the π^- -p and k^- -p cross sections at energies greater than 30 GeV and find slopes of -0.004 ± 0.002 and -0.007 ± 0.003 respectively. The k^+ -p data exhibits a totally different behaviour; the cross section in the region 20-30 GeV seems rather constant but at higher momenta rises and shows no sign of flattening. At lower energies than those plotted the k^+ -p remains constant down to $\sim$ 3.5 GeV/c and then begins to exhibit structure due to resonance production. The cross sections $\pi^\pm$ -p and k^- -p at momenta less than 10 GeV/c carry on rising and at about 5 GeV/c start to display structure.

The $\bar{p}p$ cross section decreases with energy and seems

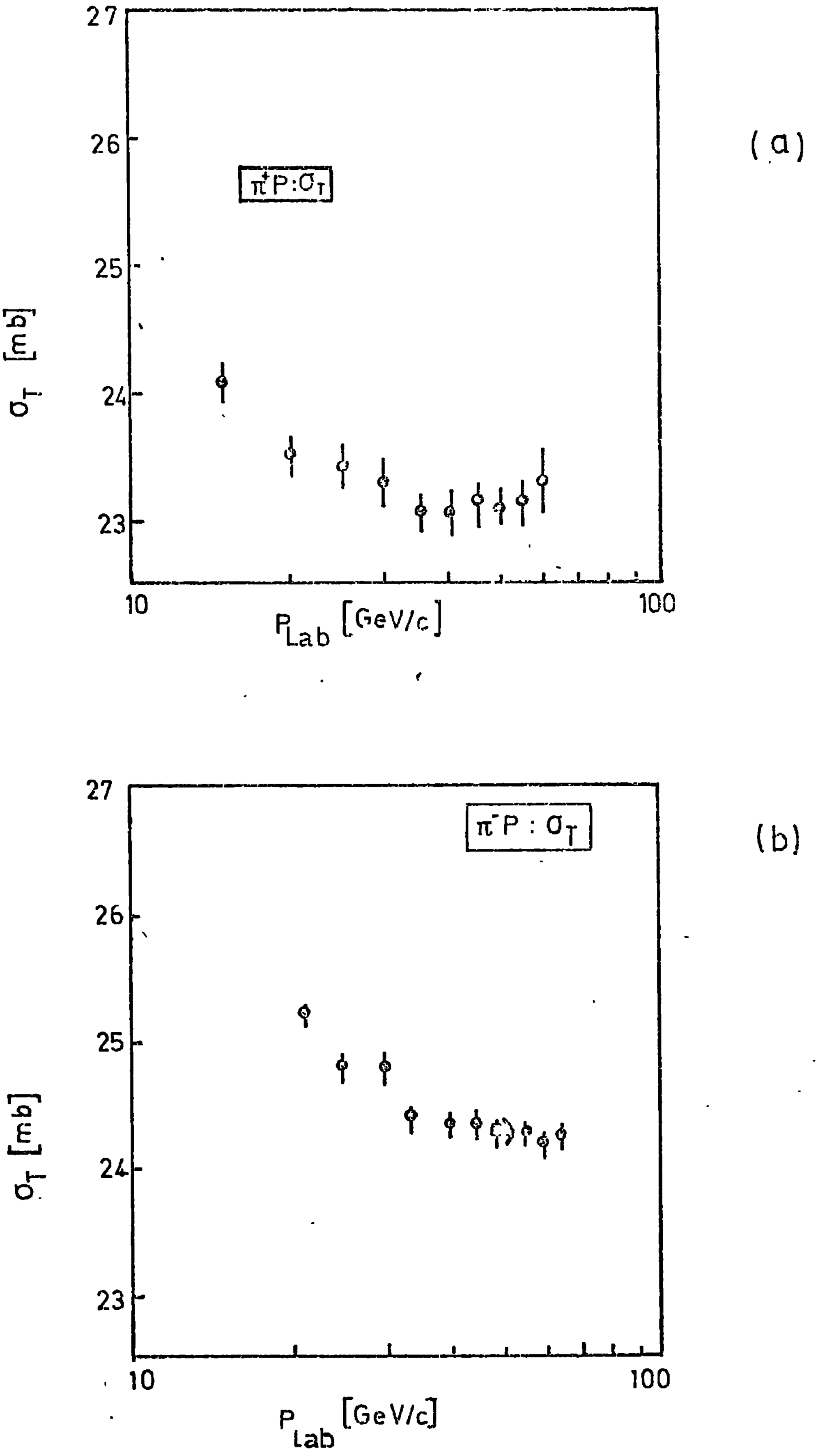

FIGURE: 7.36. TOTAL CROSS SECTIONS

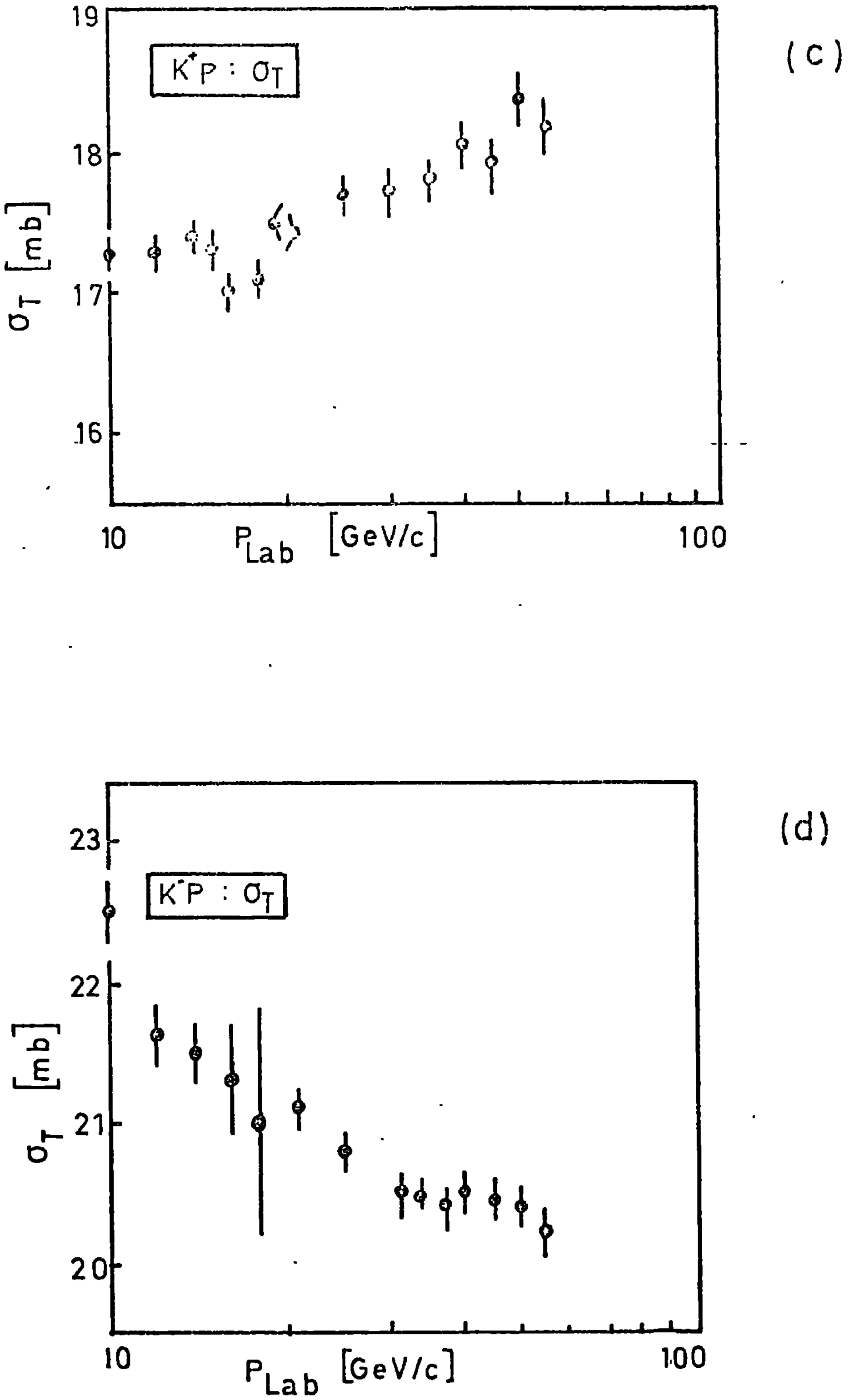

FIGURE: 7·36. TOTAL CROSS SECTIONS.

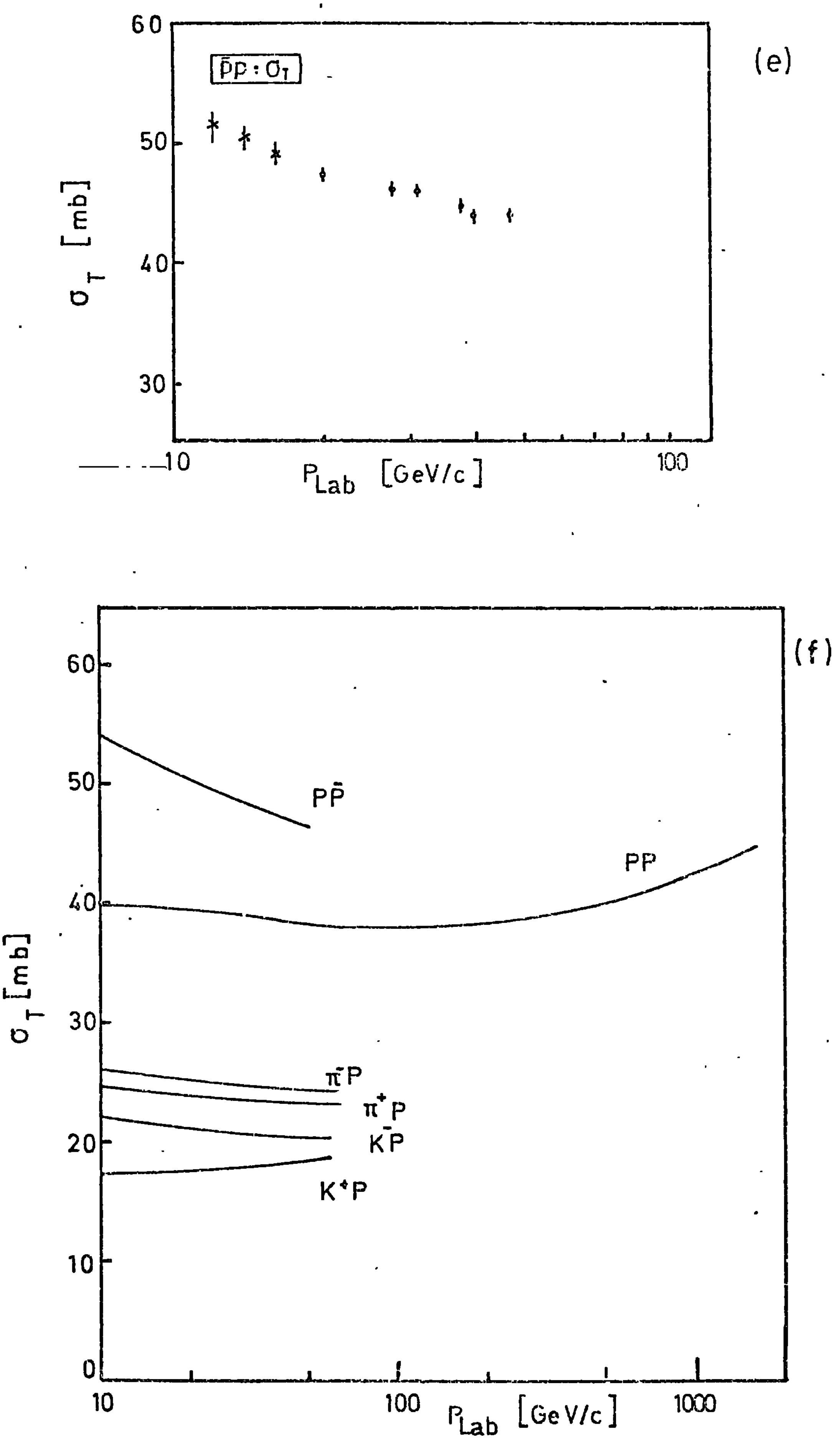

FIGURE: 7.36. TOTAL CROSS-SECTIONS

to be flattening. At lower energies than those shown it rises rapidly.

Finally in Fig. 7.36f all of the cross sections are plotted on a single graph. The curves have been obtained simply by drawing smooth lines through the data points.

At energies higher than those attainable by accelerators cross section measurements made in cosmic ray experiments must be used. These measurements have been made using two basic methods - one direct, the other indirect. The latter has provided the highest energy data and will be considered first.

The most recent attempts to derive cross sections by the indirect method have used data obtained by the B.A.S.J.E. group at Mt. Chacaltaya in Bolivia. This experiment, performed at an atmospheric depth of ~550 gms/cm^2 has been designed to detect surviving primary protons. The main detector is a calorimeter consisting of 60m^2 of scintillator shielded by ~400 gms/cm^2 of concrete. Above this are a number of smaller scintillators to act as shower detectors. Whenever a burst is detected in the calorimeter the pulse heights in the shower detectors are recorded. The most important events are those in which a burst, but no shower, is detected. These events are due to surviving primary protons; those protons having interacted in the atmosphere before penetrating the detector would be accompanied by a shower (as would any incident pions). From the burst size spectrum the energy spectrum of surviving protons has been calculated and integral spectra have been published for 10^{12} - 10^{14} eV (Murakami et al (1970), Kaneko et al (1971)). The relation between the primary integral spectrum and that observed at depth x is $I(>E, x) = I(>E, x=o) \exp(-x/L)$ where L is the interaction mean free path of protons in air and is inversely proportional to the inelastic cross section.

Two independent attempts to determine this last quantity have been made. Wdowczyk and Zujewska (1973) have corrected the data for inefficient shower detection. This is an important factor since it is energy dependent; the efficiency of detecting an accompanying shower is an increasing function of the proton energy. Consequently at low energies the surviving proton spectrum is overestimated but at higher energies the true spectrum is approached. The observed spectrum is thus too steep and the corrections reduce the slope. After applying their correction the authors find that the resulting spectrum is parallel to their best estimate of the primary spectrum. This latter was obtained by simply extrapolating the results of Ryan et al (1972) (which measured the spectrum up to 2.10^{12} eV). The fact that the spectra have the same shape is taken as evidence that L (and hence the inelastic cross section, σ_i) does not change over the energy range 2.10^{12} - 5.10^{13}.

The other interpretation of the data is that of Yodh, Yash Pal and Trefil (1972). These authors fit each point of the measured spectrum to an expression of the form given above and thus obtain values of σ_i, these are shown in Fig. 7.37. Despite the large errors there is some indication of an upward trend. In an attempt to obtain more information on this possible increase the authors have considered lower energy

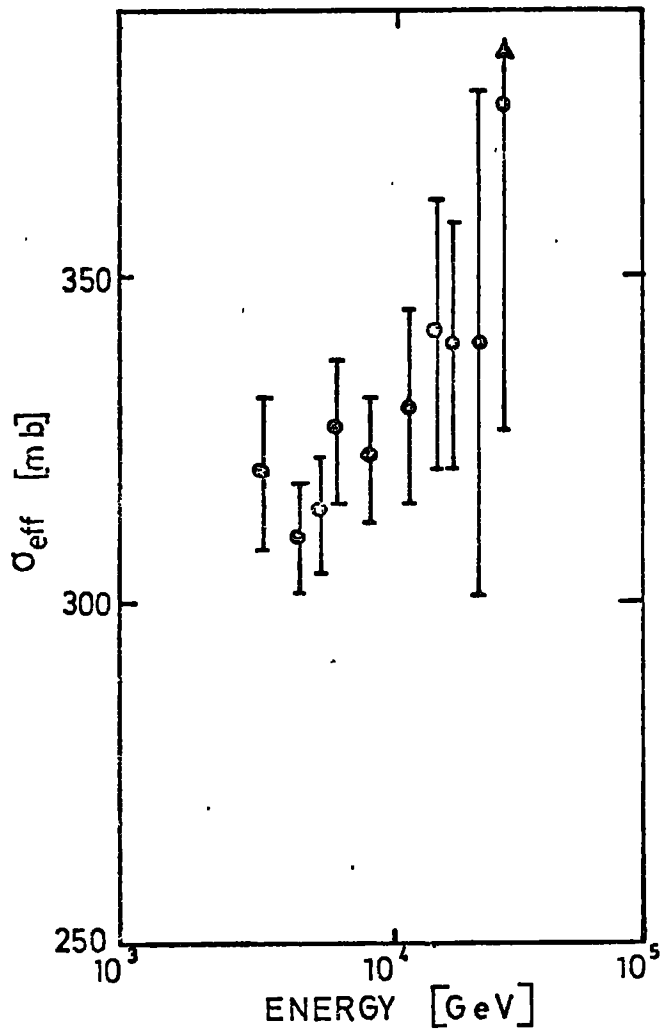

FIGURE: 7·37

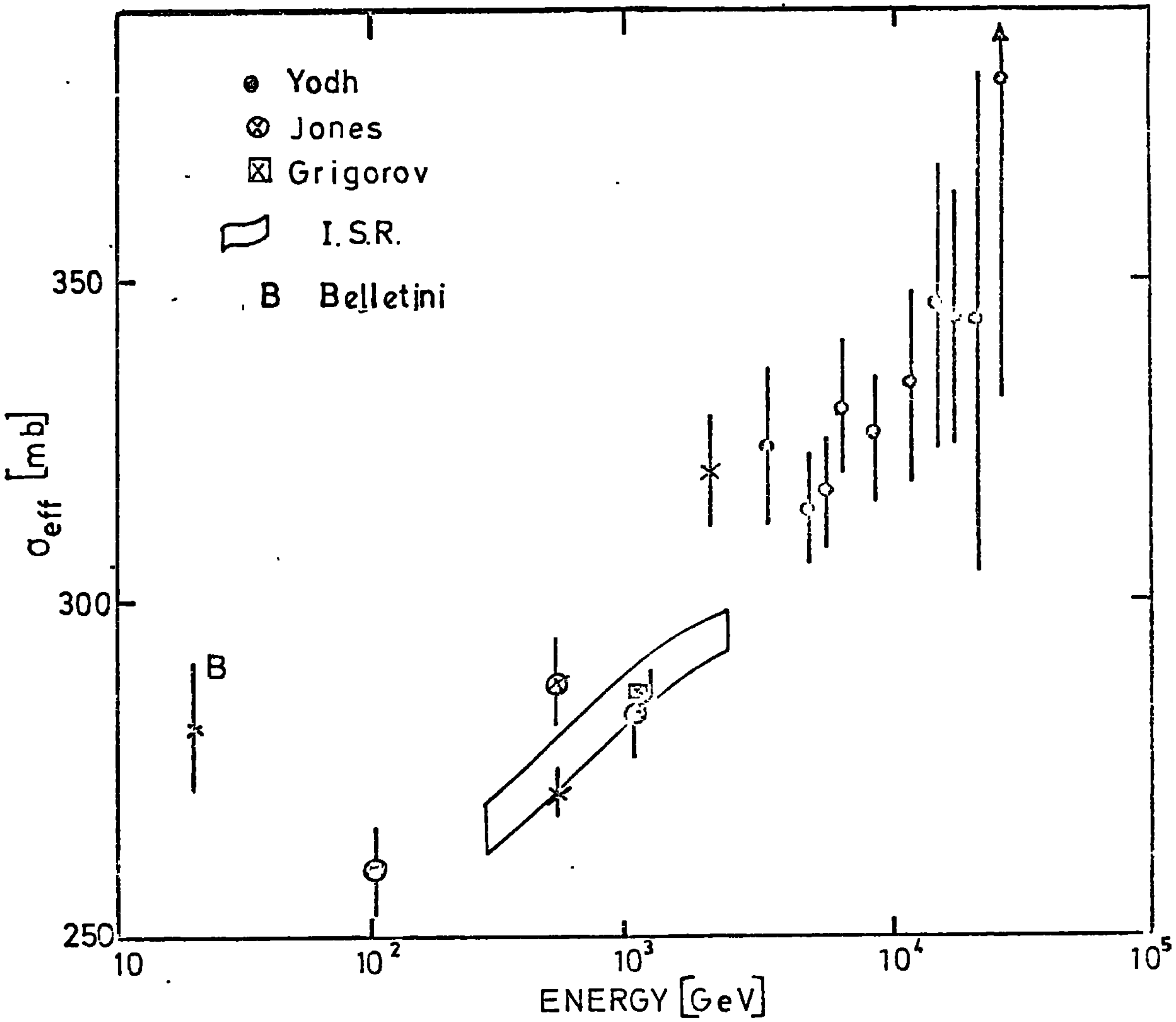

FIGURE: 7·38.

data and have applied their technique to results of Jones et al (1970) and Grigorov (1965). These results, along with the previous set are shown in Fig. 7.38. Also plotted are the results of Belletini et al (1966) who measured σ_i for a variety of elements from H to Pb; the plotted point is a value interpolated at A = 14. The I.S.R. data is that of Amuldi et al (1973) and Amendolia et al (1973). From this diagram there is evidence of a rise in σ_i in going from low energy ($\lesssim$ 1000 GeV) results to those of Chacaltaya. The conclusion of Yodh, Yash Pal and Trefil (1972) is that σ_i is rising rapidly.

The two interpretations are in a conflict which has yet to be resolved. Unfortunately the second technique of deriving cross sections - the direct method - is, as will be seen below, confined to energies $\lesssim$ 1000 GeV.

Some of the most recent measurements of the direct kind have been made by Jones et al (1971) and Akimov et al (1969). The data of the former are thought to be subject to severe bias (as indicated by the multiplicity results of the experiment) and will not be considered further. The experiment of Akimov et al (1969) was performed on an orbitting satellite. Results were obtained for the inelastic cross sections of p-c and p-p interactions; they are plotted in Fig. 7.39. To compare the p-c results with the previously described p-Air data they have both been plotted in Fig. 7.40 where the p-c results have been scaled up by a factor $(14/12)^{\frac{2}{3}}$. At the lowest energy the satellite results are significantly below the accelerator result of Belletini et al (1966). At higher energies there is evidence of an increasing cross section. In Fig. 7.39b the solid line is a line drawn by eye through the

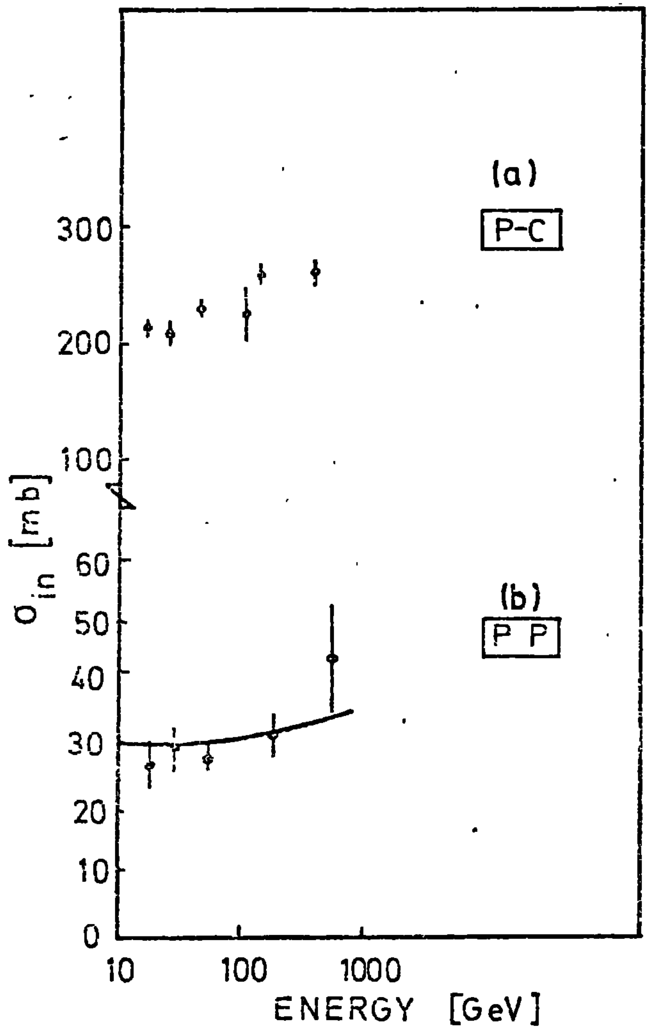

FIGURE:7.39.

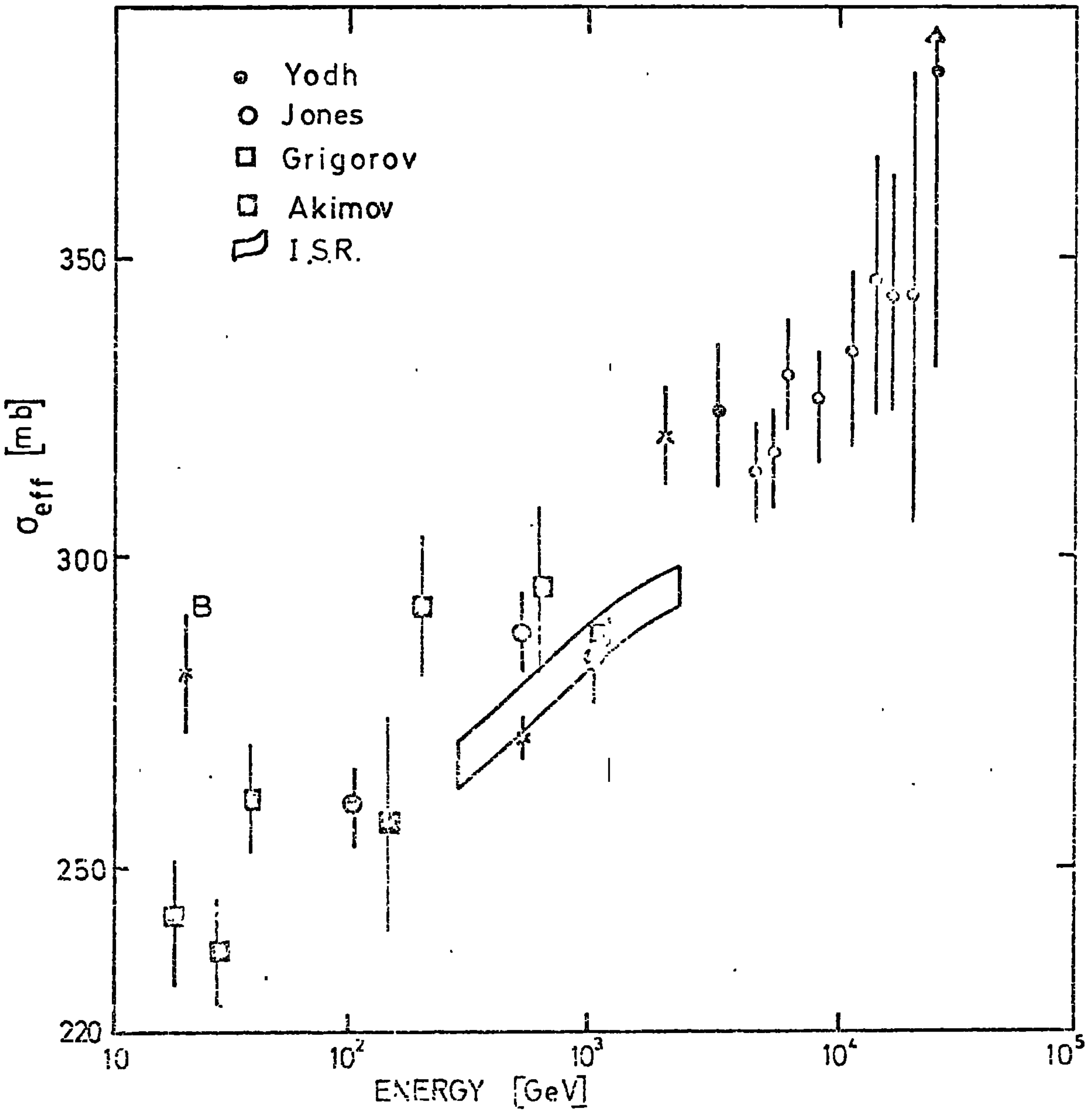

FIGURE:7.40.

available accelerator data; it can be seen that the experimental points of the satellite data are in reasonable agreement.

7.3.7 Inelasticity

It is known that in a collision with a nucleon or nucleus an incident particle usually gives up only a fraction (typically 0.3-0.5) although it may change its charge. This fraction is known as the inelasticity (k). The energies concerned here are laboratory energies; there are other definitions of inelasticity involving centre of mass energies but these will not be considered.

For N-N collisions k is often taken to be 0.5. This is a reasonable estimate as shown in Table 7.8 where the results of a few experiments have been listed. Some of these results quoted only the charged inelasticity; in these cases the value given was multiplied by 1.5 as suggested by Hayakawa (1969).

Of N-nucleus collisions, Feinberg (1972) states that k is not significantly different and this is indicated by the results in the table. However, some rather high values of k have been found by Nam et al (1971). In a cosmic ray experiment on N-nucleus collisions they measured k_γ - the fraction of incident laboratory energy given to γ production (taken to be equivalent to π^0 production) - to be 0.25 ± 0.02. This suggests $k = 0.75 \pm 0.06$ - rather high. This experiment involved mainly Pb nucleii but a similar value of k_γ has been found by Abdullaev et al (1971) for collisions with light nucleii.

Considering pion induced reactions a survey has yielded the rather meagre data of Table 7.8. That $k \neq 1$ for this type of collision is indicated by the momentum distribution of secondary particles produced in πp collisions. For example, in the data of Honecker et al (1969) ($\pi^- p$ collisions at 16 GeV/c) a leading particle effect can be seen in the π^- momentum distribution.

The distribution of k values in both N-N and N-nucleus experiments have been given by Feinberg (1972) and Hayakawa (1969). The statistics involved are poor because of the paucity of the data. An equation to fit the results of one experiment may be found in Lal et al (1965).

TABLE 7.1

p-p Multiplicity

Laboratory Energy (GeV)	$\langle n_{ch} \rangle$	Source	Comments
4	2.54 ± 0.03	Bodini et al (1968)	-
5.5	2.71 0.01	Alexander et al (1967)	-
10.0	3.22 0.06	Ameida et al (1968)	Quoted by Czyzowski and Ribicki (1972)
13	3.66 0.03 (3.54 0.03) (3.53 0.04)	Smith et al (1969)	Un-bracketed values are those of Jacob (1972). for other values see text.
18	4.05 0.03 (3.85 0.04) (3.91 0.04)		
21	4.30 0.04 (4.05 0.04) (4.17 0.05)		
24	4.45 0.04 (4.17 0.04) (4.30 0.04)		
28.5	4.60 0.04 (4.34 0.05) (4.56 0.04)		
19.0	4.02 0.02	Boggild et al (1971a)	-
35.0	5.01 0.07	-	Quoted by Jacob (1972)
50 69	5.47 0.17 5.81 0.13	- -	Quoted by Morrison (1972)
102	6.34 0.14	Chapman et al (1972)	-
205	7.65 0.17	Charlton et al (1972)	-
303	8.86 0.16	Dao et al (1972)	-
220 500 1000 1500	8.47 0.49 9.62 0.55 11.03 0.63 11.71 0.68	Antinucci et al (1973)	see text.

continued

TABLE 7.1 continued

Laboratory Energy (GeV)	< n_{ch} >	Source	Comments
250 3000	11.6 ± 3.7 15.2 2.0	Lohrman and Teucher (1962)	Emulsion N_h = o
300	9.0 1.0	Guseva et al (1962)	Li H target. No corrections.
10000	16.3 1.1	Malholtra and Ganguli (1972)	Emulsion N_h 2.

TABLE 7.2

$\pi^{\pm}p$ Multiplicity

Incident Particle	Laboratory Momentum (GeV/c)	$\langle n_{ch} \rangle$	$\langle n_{ch} \rangle /D$
π^-	4.0	2.63 ± 0.07	2.18 ± 0.13
	6.8	3.15 0.09	2.29 0.12
	10.0	3.61 0.03	2.19 0.03
	11	3.81 0.06	2.34 0.08
	13	3.99 0.10	2.24 0.09
	16	4.19 0.05	2.18 0.05
	20	4.60 0.05	2.40 0.05
	25	4.86 0.04	2.30 0.03
	40	5.62 0.04	2.02 0.03
	50	5.71 0.13	2.10 0.06
	60	6.46 0.16	2.11 0.10
π^+	4	3.08 ± 0.01	2.76 ± 0.03
	7	3.29 0.03	2.33 0.04
	8	3.74 0.01	2.59 0.02
	11	4.18 0.08	2.57 0.11
	11.5	4.00 0.11	2.47 0.09
	16	4.33 0.12	2.54 0.12

TABLE 7.3

$k^{\pm}p$ Multiplicity

Incident Particle	Laboratory Momentum (GeV/c)	$\langle n_{ch} \rangle$	$\langle n_{ch} \rangle /D$
k^-	10.0	3.44 ± 0.03	2.13 ± 0.03
	14.3	3.88 0.01	2.15 0.01
	16.0	4.06 0.04	2.21 0.03
	33.8	5.16 0.08	2.14 0.04
k^+	3.0	2.57 ± 0.03	2.81 ± 0.05
	3.5	2.62 0.02	2.71 0.04
	5.0	2.94 0.02	2.65 0.02
	8.2	3.38 0.03	2.56 0.03
	12.7	4.03 0.12	2.61 0.12
	16.0	4.17 0.09	2.40 0.09

TABLE 7.4

Cross Sections

Laboratory Momentum (GeV/c)	Cross Section (mb)		Source
	σ_t	σ_e	
10	39.9 ± 0.6		Galbraith et al (1965)
12	39.4 0.6		
14	39.1 0.6		
16	38.7 0.6		
18	38.7 0.6		
20	38.4 0.6		
22	38.3 0.6		
10.1	40.0 ± 0.3		Belletini et al (1965)
19.3	38.9 0.3		
26.4	38.8 0.3		
15	39.3 ± 0.1		Denisov et al (1971, 1971a)
20	39.1 0.1		
25	38.8 0.1		
30	38.6 0.1		
35	38.5 0.1		
40	38.5 0.1		
45	38.5 0.1		
50	38.5 0.1		
55	38.4 0.1		
60	38.4 0.1		
102	39.7 ± 1.5	6.9 ± 1.0	Chapman et al (1972)
205	39.5 ± 1.1	6.8 ± 0.3	Charlton et al (1972)
303	39.0 ± 1.0	7.2 ± 0.4	Dao et al (1972)
10.0	41.1 ± 1.7	10.2 ± 0.6	Almeida et al (1968)
10.8		11.0 ± 0.7	Foley et al (1963)
12.8		10.9 0.7	
14.8		10.5 0.7	
16.7		9.7 0.7	
19.6		9.6 0.7	
24.5	39.3 ± 0.8	8.8 ± 0.3	Breitenloh et al (1963)

TABLE 7.5

Cross Sections

Momentum (GeV/c)	C.M. Energy (GeV)	Equiv. Lab. Energy (GeV)	σ_t (mb)	σ_e (mb)	Source
11.8 x 11.8 15.4 x 15.4 22.6 x 22.6 26.6 x 26.6	23.5 30.6 44.9 52.8	290 500 1070 1480	39.10 ± 0.72 40.50 0.78 42.50 0.78 43.20 0.85	6.8 ± 0.36 7.0 0.36 7.5 0.42 7.6 0.42	Amaldi et al (1973a)
11.8 x 11.8 15.4 x 15.4 22.6 x 22.6 26.6 x 26.6	23.5 30.6 44.9 52.8	290 500 1070 1480	39.30 ± 0.79 40.85 0.82 42.57 0.86 42.98 0.84		Amendolia et al (1973)
11.8 x 11.8 15.4 x 15.4	23.5 30.6	290 500	38.9 ± 0.7 40.2 0.8	6.7 ± 0.3 6.9 0.4	Amaldi et al (1973)
15.4 x 15.4	30.6	500	40.3 ± 2.0	6.8 ± 0.6	Hodder et al (1971)

TABLE 7.6

Cross Sections

Laboratory Momentum (GeV/c)	Cross Sections in mb			Source
	$\pi^- p$	$k^- p$	$\bar{p}\,p$	
33.8		20.5 ± 0.1		Ammosov et al (1973)
50	24.3 ± 0.1			
21	25.2 ± 0.1	21.1 ± 0.1		Denisov et al (1971)
23			47.4 ± 0.4	
25	24.8 ± 0.1	20.8 0.1		
27.5			46.3 0.4	
30	24.8 0.1			
31			46.1 0.4	
32		20.5 0.1		
34	24.4 0.1			
38		20.4 0.1	44.7 0.4	
40	24.4 0.1	20.5 0.1	44.0 0.4	
45	24.4 0.1	20.5 0.1		
47.5			44.1 0.4	
50	24.3 0.1	20.4 0.1		
55	24.3 0.1	20.2 0.3		
60	24.2 0.1			
65	24.3 0.1			
10		22.5 ± 0.2		Galbraith et al (1965)
12		21.6 0.2	51.7 ± 0.8	
14		21.5 0.2	50.7 0.9	
16		21.3 0.2	49.2 0.8	
18		21.0 0.2		

TABLE 7.7

Cross Sections

Laboratory Momentum (GeV/c)	Cross Sections in mb.		Source
	π^+p	k^+p	
15	24.1 ± 0.2	17.3 ± 0.2	Gorin et al (1972)
20	23.5 0.1	17.4 0.2	
25	23.4 0.1	17.7 0.2	
30	23.3 0.1	17.7 0.2	
35	23.1 0.1	17.8 0.2	
40	23.1 0.1	~~18.1~~ 0.2	
45	23.1 0.1	17.9 0.2	
50	23.1 0.1	18.4 0.2	
55	23.1 0.1	18.2 0.2	
60	23.3 0.3		
10		17.3 ± 0.1	Galbraith et al (1965)
12		17.3 0.1	
14		17.4 0.1	
16		17.0 0.1	
18		17.1 0.1	
20		17.5 0.1	

TABLE 7.8

Inelasticity

Author	Laboratory Energy (GeV)	Projectile - Target Inelasticity				Comments
		N-N	π -N	N-Nucleus	π -Nucleus	
Hansen and Fretter (1960)	10-1000			0.56		Carbon target. Sea level cosmic ray expt hence projectiles are mixture of π and N. 41 events.
Barkow et al (1961)	~3500			0.50 ± 0.25	$\geqslant 0.6$	Emulsion method. High alt. cosmic ray expt.57 events.
Lohrman et al (1961)	~250	0.49 ± 0.12		0.47 ± 0.14		Emulsion method. Results given are for p-induced reactions; neutrons give same values (within errors) 52 events.
Dobrotin et al (1962)	> 100	0.43				Li H target. High altitude cosmic ray expt. 56 events.
Yash Pal et al (1963)	25			0.59 ± 0.07		Emulsion target in high (200 kg) magnetic field pulsed in synch. with bursts of protons from accelerat -or. 80 events.

continued

TABLE 7.8 continued-2

Koshiba et al (1963)	~ 3000	0.43	$0.75 {+0.24 \atop -0.15}$		0.45 ± 0.08	Emulsion target. High altitude (balloon) cosmic ray expt. Pion induced reactions found by track following.
Hildebrand and Silverberg (1963)	~ 3000			0.5 ± 0.1		As above.
Gerbowska et al (1964)	24			0.42 ± 0.05		Similar to Yash Pal,et al (1963) 145 events.
Hoffman et al (1965)	17				0.87 ± 0.04	Similar to Yash Pal et al (1963) except using an accelerator produced π^- beam. Events with $N_h > 8$ selected (reduces contribution from π-N collisions) 234 events.
Guseva et al (1962)	300	0.54 ± 0.05				Li H target. Result quoted by Hayakawa (1969).
Dobrotin et al (1962)	200	0.37 ± 0.02				Li H+ C target. Result quoted by Feinberg (1972) 52 events.
Feinberg (1972)	25-3000	(0.5 ± 0.15)		0.5 ± 0.15		Result of survey quoted by Feinberg (1972) for NN and NC interactions.

continued

TABLE 7.8 continued-3

Feinberg (1972)	28	0.4				Accelerator result (p-p) quoted by Feinberg (1972)
Boggild et al (1971a)	19	0.52				p-p accelerator result.

CHAPTER 8

INTERPRETATION OF THE MUON CHARGE RATIO

8.0 Introduction

In this chapter a rough estimation of the expected muon charge ratio, based upon high energy accelerator data, is made. The results of the calculations of other workers are discussed.

The main ingredients for the calculations are :-

(i) the relative fluxes of protons and neutrons in the primary cosmic ray beam,

(ii) details of particle production in high energy collisions and

(iii) the probability of these particles (mainly pions) decaying to muons.

8.1 The Primary Composition

The most significant part of the primary spectrum for the purposes of this work is the region 10^{11} - 10^{13} eV/nucleon. All components of the primary flux have been taken to have differential spectra of the same slope. This point is discussed further in 8.6.

Some detail as to the composition of the primary radiation is required since the usual approach to the treatment of primary cosmic ray $(z \geqslant 1)$ - 'air' nucleus collisions has been adopted i.e. that of treating the interaction as if it were between free nucleons. Thus the ratio of protons to neutrons in the primary flux must be known. Over the energy range of interest there is a reasonable amount of experimental data available.

The results of four surveys of the primary composition are shown in Part I of Table 8.1. The survey of Weber (1967) contains data only up to 1964; similarly the survey of Hayakawa (1969) extends only to 1962. From the table it can be seen that nucleii of $Z > 2$ contribute less than 1% to the total primary flux. However, the contribution of the overall proton : neutron ratio is not negligible because their average atomic weight is quite high (17).

The results of a recent survey on nucleii of $Z > 2$ by Shapiro and Silberberg (1970) are given in Part II of Table 8.1. The majority of more recent experimental data (for example, Buffington et al (1971), Garcia Munoz et al (1971) and Weber et al (1971) show no serious deviations from the given figures. A rather high H : M ratio (of ~ 0.8) has been reported by Choi and Kim (1971) for energies $\geqslant$ 1 GeV/nucleon. The results of several workers (Ryan et al (1971), Saito et al (1971) and Smith et al (1972)) indicate that for the energy range 20 - 1000 GeV/nucleon the relative proportions of L, M and H nucleii do not change significantly and that all three groups have differential spectra of slope 2.6 ± 0.1. More recent measurements, summarized by Ramaty et al (1973) indicate that the iron spectrum may be flatter than that of the other primary elements. This is considered further in Section 8.6.

Considering now the data on hydrogen and helium nucleii the result of Part I of the table gives $p/He = 17.1 \pm 1.0$. More recent experiments (Table 8.1, Part III) give a wide range of values for this ratio. The two sets of results of Ryan et al (1971, 1972) are inconsistent and in all that follows both have been ignored. Using the remaining data gives p/He = 13.1 ± 1.2. This figure is heavily weighted by the experiment of Anand et al (1967) whose measurements cover the lowest energy range but should still be free of any solar modulation effects (Part III of the table has been constructed only from data with energies $\geqslant$ 5 GeV/nucleon to attempt to minimise any biases due to these effects). If the result of Anand et al (1967) were ignored a higher ratio of 15.0 ± 2.7 is obtained. Using all of the data of Table 8.1 (excepting that of Ryan et al (1971, 1972)) yields a ratio p/He = 14.37 ± 1.0 which leads to a proton to neutron ratio of (89.1 ± 7.2) : (10.9 ∓ 7.2).

To take into account the effect of nucleii of $Z > 2$ the ratio G = abundance of nucleii of $Z > 2$/abundance of He nucleii, has been calculated from Table 7.1. The numerator was taken from Part II of the table while the denominator is the mean found from Part I of the table. In the numerator the results of Shapiro and Silberberg (1970) alone were used rather than including the survey data. This was because the latter may be, as suggested by Waddington (1960) and Shapiro and Silberberg (1970), subject to poor charge resolution. This would be particularly important for the L nucleii because of their much lower abundance than their neighbours (He and C). There is some indication of an effect in the fact that the survey data on L nucleii (Table 7.1, Part I) are all higher than that of Part II of the table (Shapiro and Silberberg (1970) have attempted to correct for poor charge resolution). The calculated value of G is 0.11 ± 0.04.

To estimate the mean atomic weight of nucleii of $Z > 2$

the relative abundances of the various elements as tabulated by Meyer (1969) and Cartwright et al (1971) have been used. Both yield similar results, the mean being $\langle A \rangle = 16.8$. Assuming this nucleus to be charge symmetric (i.e. to contain, on average, equal numbers of protons and neutrons) the contribution relative to the He flux and thence to the total primary flux has been calculated and the resulting proton to neutron ratio becomes $(85.7 \pm 7.2) : (14.3 \mp 7.2)$.

So far, the isotopic component of the H and He fluxes has not been considered but it is known that primary deuterium (d) and tritium (He^3) are present. Experimental data on these components is scarce, has large errors and is confined to the low energy regions. The results of Meyer (1969) and Tamai et al (1971) give consistent values of the quantity Γ_{He} ($= He^3/(He^3 + He^4)$) of $\sim (0.1 \pm 0.04)$ in the energy range 0.1 - 0.2 GeV/nucleon. Measurements on d by Fan et al (1971), Meyer et al (1967) and Biswas et al (1971) indicate the value of Γ_H (= d/p) to be $\lesssim$ 5% at energies of $\sim$ 0.1 GeV/nucleon; the ratio is thought to fall with increasing energy. Using the above figures the proton to neutron ratio was modified to $\sim (84 : 16)$ - the change is small compared to the errors which already exist in the quantity and since the result applies only to low energies it has been decided to neglect the modification.

The presence of anti-nucleons in the primary flux has also been neglected. Indeed it is not certain whether there are any such particles present and experiments have only been able to give upper limits to their flux. These limits are $\sim$ 0.25% of the flux of the true particles.

Thus the final proton to neutron ratio is $(85.7 \pm 7.2) : (14.3 \pm 7.2)$.

This is in quite good agreement with the commonly accepted value of 89 : 11 and in order to facilitate comparisons with other workers this latter has been adopted throughout unless otherwise stated.

8.2 High Energy Collisions

The available experimental results have been summarised in a previous chapter. Any additional details required specifically for the estimation of the charge ratio are described in section 8.4.

8.3 Pion Decay Probabilities

In order to calculate the muon flux arising from the decay of pions produced in collisions at various atmospheric depths the probabilities of the pions decaying before reaching sea level must be known.

The probability of decay is given by :-

$$D_{\pi} = \int_{x = x_o}^{x = SL} \left(\frac{B_{\pi}}{E_{\pi}(x + x_o)} \right) \cdot \left(\frac{x + x_o}{x_o} \right)^{-B/E} (\exp(-x)) \, dx \qquad \ldots . \; 8.1$$

where :

in the first term which represents the probability of decay in an element of depth dx, x_o is the depth of the pion-producing collision (measured in terms of the pion interaction length λ_i (taken as 80 gms cms^{-2})); E_{π} is the pion energy; $B_{\pi} = M_{\pi} C^2 h_o / c \tau_{\pi}$ where $M_{\pi} C^2$ is the pion rest mass, τ_π is the pion lifetime and h_o is the scale height of the atmosphere (which is a function of atmospheric depth but is usually considered a constant and in this case is initially assumed to be 6.5 km); the second term is the survival probability of the pion (Rossi (1952));

the third term represents the loss of pions due to interactions with air nucleii.

The above expression has been evaluated numerically for various pion energies and production depths (x_o); the result for E_π = 10 GeV is shown as the dash-dot line in Fig. 8.1.

To avoid the assumption of a constant h_o the regions of the atmosphere below and above the tropopause have been considered separately. These regions are $x \geqslant x_t$ and $x < x_t$ respectively, where x_t is the height of the tropopause. Over most of the second region the temperature may be assumed constant and the relation between density and depth is $\rho(x_1) = \rho_t . x_1/x_t$ where ρ_t is the air density at the tropopause (taken to be $3.7.10^{-4}$ gms cm^{-3}). For $x \geqslant x_t$ the temperature increases with increasing depth and the relation between density and depth is $\rho(x_1) = \rho_o (x_1/x_s)^{1-\Gamma Ra/g}$ where ρ_o is the air density at sea level (x_s) (taken to be $1.235\ 10^{-4}$ gms cm^{-3} at depth 1033.6 gms cm^{-2}); Γ is the atmospheric lapse rate (taken to be 6.5°C/km); Ra and g are the gas constant and gravitational acceleration respectively. The mean height of the tropopause was obtained from Meteorological Office data for the period 1951-55 (the latest available). The data were for the upper air stations at Lerwick (60°N) and Crawley (51°N); the interpolated

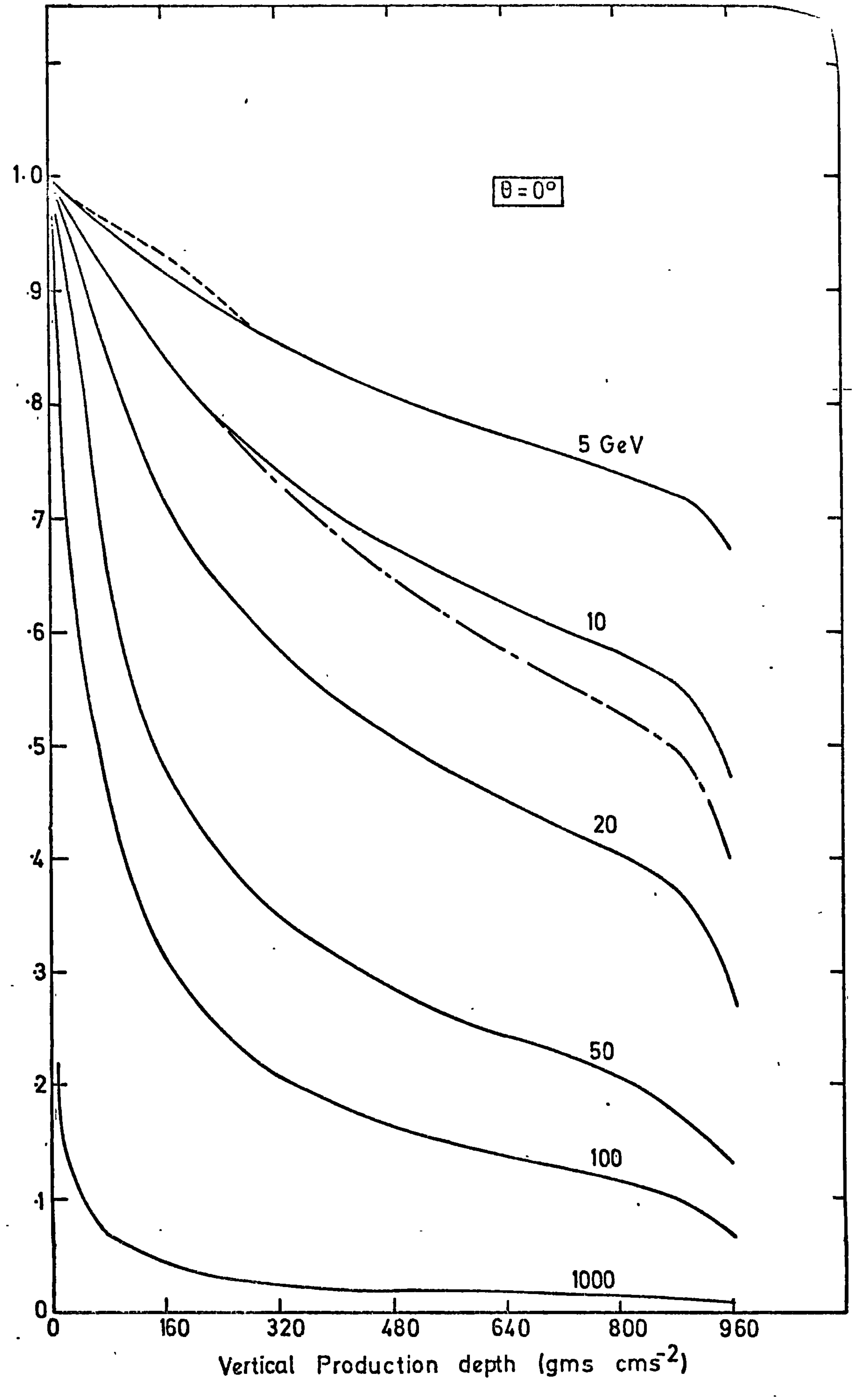

FIGURE. 8·1. PION DECAY PROBABILITIES.

value for Durham (55°N) was 248 gms cm^{-2}. This value is the mean over a whole year; seasonal effects are small - the change in x_t between the Winter and Summer months is ~2%, the tropopause being deepest during Winter. From the above, the density of air is

$$\rho(x_1) = 1.492 \times 10^{-6} \times x_1 \text{ gms cm}^{-3}, \quad x_1 < 248 \text{ gms cm}^{-2}$$

$$\rho(x_1) = 4.477 \times 10^{-6} \times (x_1^{0.821}) \text{ gms cm}^{-3}, \quad x_1 \geqslant 248 \text{ gms cm}^{-2}$$

These expressions were inserted into eqn. 8.1 and D_π evaluated, again numerically. The results are shown in Fig. 8.1. Since the expression for $\rho(x_1)$ has a discontinuity at the tropopause some effect on the resulting values of D_π could be expected and is shown by the dotted line for E_π = 5 GeV. The solid lines show the result of smoothing out (by eye) this feature; the discrepancy between the smoothed and unsmoothed values is a maximum of ~2½% at E_π = 5 GeV and decreases with increasing energy.

8.4 Interpretation of the Muon Charge Ratio

To obtain the basic details of the muon charge ratios predicted by the various ingredients so far discussed a simplified treatment has been used. The method adopted has been to consider primary cosmic ray initiated interactions at a number of depths in the atmosphere and to sum up the contributions of these interactions to the positive and negative muon beams observed at sea level. The main characteristics of nucleon interactions involved in these calculations are those of the charge ratios of the produced pions and kaons and the inelasticity of the interaction.

8.4(a) Estimation of the Pion Charge Ratio

The charge ratio of pions (the ratio of positive to negative particles) has been derived from ISR data as follows. The scaling hypothesis (in this case for pions) may be expressed as :

$$\frac{d^2\sigma}{dP_L\ dP_t} = \frac{f(x,\ P_t)}{E_\pi}$$

where the symbols have their usual meaning. The number of pions with energy in the range dE_π produced by incident primaries with energy in the range dEp is given by

$$N(Ep).dEp\ .\ \left[\int_0^\infty \frac{f(x\ ,\ Pt)}{E}\ dPt\right].\ dE_\pi$$

where N(Ep) represents the primary differential spectrum. The total number of such pions generated by all possible primaries is

$$dn_\pi = \int_{Ep\ =\ E_\pi}^\infty N(Ep)\ .\ \left[\int_0^\infty \frac{f(x\ ,\ Pt)}{E}\ dPt\right].\ dE\ .\ dEp$$

Hence

$$\frac{dn_\pi}{dE_\pi} = N_o \int_{E_\pi}^\infty Ep^{-\gamma}\ \left[\int_0^\infty \frac{f(x,Pt)}{E}\right] dEp,$$

by taking the differential spectrum $N(Ep) = N_o\ Ep^{-\gamma}$. In terms of x this becomes

$$\frac{dn_\pi}{dE_\pi} = N_o\ E_\pi^{\ -\gamma} \int_{x=0}^1 x^{\gamma-2}\ \left[\int_0^\infty f(x,Pt)dPt\right] dx$$

Since ratios rather than absolute values of numbers are to be considered N_o is put equal to unity and only pions with P_t = 0.4 GeV/c are considered; the above expression then becomes

$$\left(\frac{dn_\pi}{dE_\pi}\right)_{0.4} = E_\pi^{-\gamma} \int_0^1 x^{\gamma-2} f(x,0.4)\, dx.$$

Using the expressions for f(x,Pt) given by Damgaard and Hansen (1972 and chapter 7) the expression inside the integral has been plotted in Fig. 8.2 for π^+ and π^-. Using $\gamma = 2.6$ the median values of the positive and negative particle distributions are 0.245 and 0.215 respectively. The ratio of the areas under the curves is 1.72 and this is the pion charge ratio. Also shown in the figure are the distributions for $\gamma = 2.8$; in this case the respective median x values are 0.275 and 0.235 and the charge ratio is 1.79. For $\gamma = 2.7$ the charge ratio is 1.755.

The median values given above are interesting. Because of the rapid fall of the function (f(x Pt) with increasing x (as shown in Chapter 7) the above medians are large i.e. they are well outside the region of x in which the majority of particles lie. A useful physical interpretation of this effect has been given by Fraser et al (1972). The majority of pions produced in an interaction are low energy ('pionization') particles (with $x \lesssim 0.05$) and it might be expected that the dominant source of pions with energy E_π would be in this region. This small value of x ($x \sim E_\pi/Ep$) suggests that the primary energies making the greatest contributions to the pion production would be given by $Ep \gg 20E_\pi$. However, because of the steeply falling primary spectrum the contribution from these high energy primaries is somewhat suppressed. Lower energy primaries become of importance and as a consequence the effective value of x moves out to larger values.

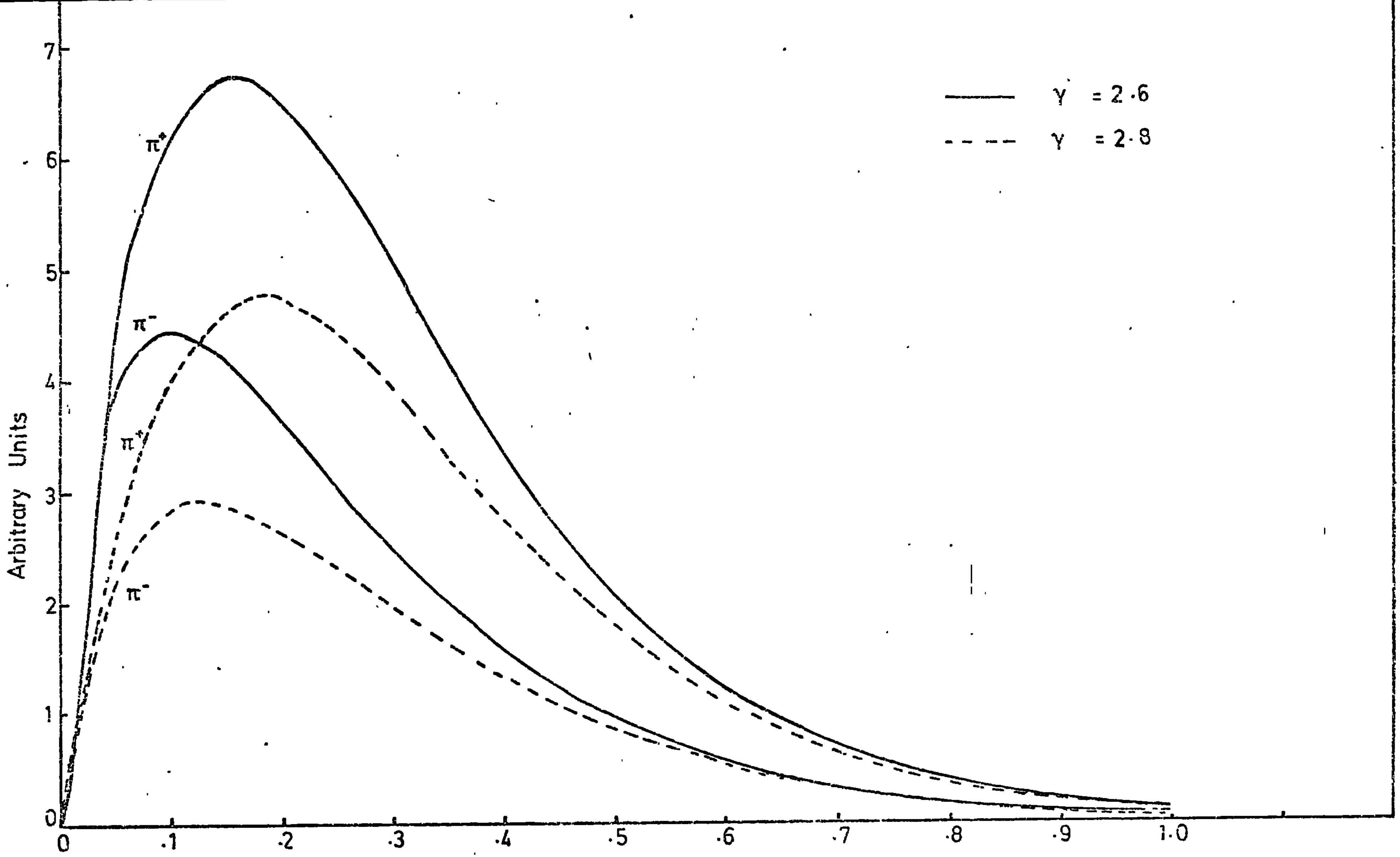

FIGURE: 8·2. WEIGHTED FUNCTIONS

It is important to note that pions with $x \gtrsim 0.2$ are produced with a multiplicity that is essentially independent of energy. This is illustrated in Fig. 8.3 where the production spectra for primary energies of 10^2 and 10^4 GeV are given. It can be seen that the increase in multiplicity associated with the increase in primary energy is mainly (in this case 90% of it) in the region $x < 0.05$.

8.4(b) Estimation of the Kaon Charge Ratio

Turning now to the kaon contribution to the muon charge ratio the results of Osborne (1966) have been modified. This author gives, in graphical form, the relative contributions of pions and the various decay modes of kaons to the vertical muon sea-level spectrum. These results, shown as dashed lines in Fig. 8.5 were calculated using the ratio (k/π) all = 0.4 where the subscript means that all three charge states of both particles have been considered. To 'update' this estimate the results from an ISR experiment (Bertin et al (1972a,b)) have been used. From the results of this experiment, which apply to laboratory energies in the range 200 to 1000 GeV, the following ratios (at $x = 0.2$) may be obtained

$$k^+/k^- = 2.0 \pm 0.6 \quad \pi^+/\pi^- = 1.63 \pm 0.3 \text{ and } k^+/\pi^+ = 0.11 \pm 0.02$$

Assuming that for neutral particle production

$\pi^o = (\pi^+ + \pi^-)/2$ and $k^o + \overline{k}^o = k^+ + k^-$, then the new ratio is : $(k/\pi)_{all} = 0.14 \pm 0.03$. The kaon contribution is thus much smaller and the original curves have been corrected simply by scaling them down. The solid lines of Fig. 8.5 show the results.

To determine the kaon contribution to the positive and

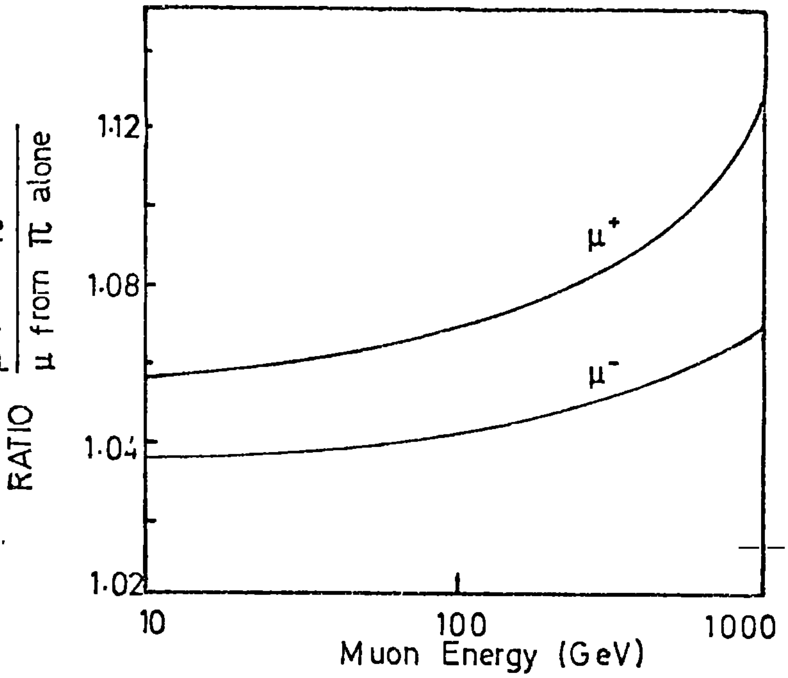

FIGURE: 8·4 EFFECT OF K's ON μ^+, μ^-

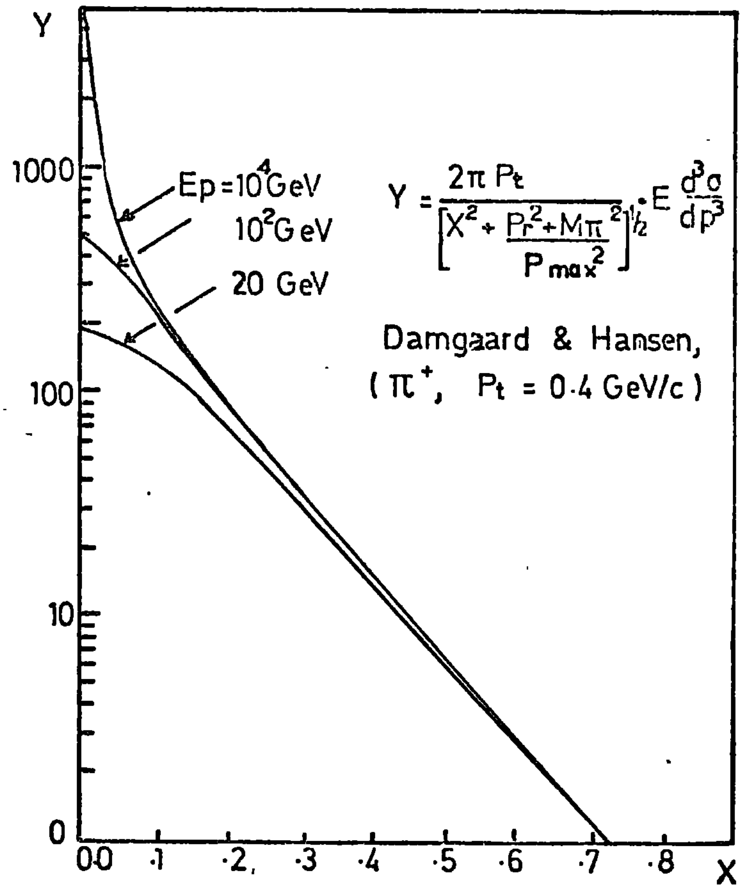

FIGURE: 8·3. EFFECT OF INCREASING ENERGIES ON π^+ PRODUCTION

FIGURE RELATIVE CONTRIBUTION OF π's AND K's TO THE VERTICAL SEA LEVEL MUON BEAM.

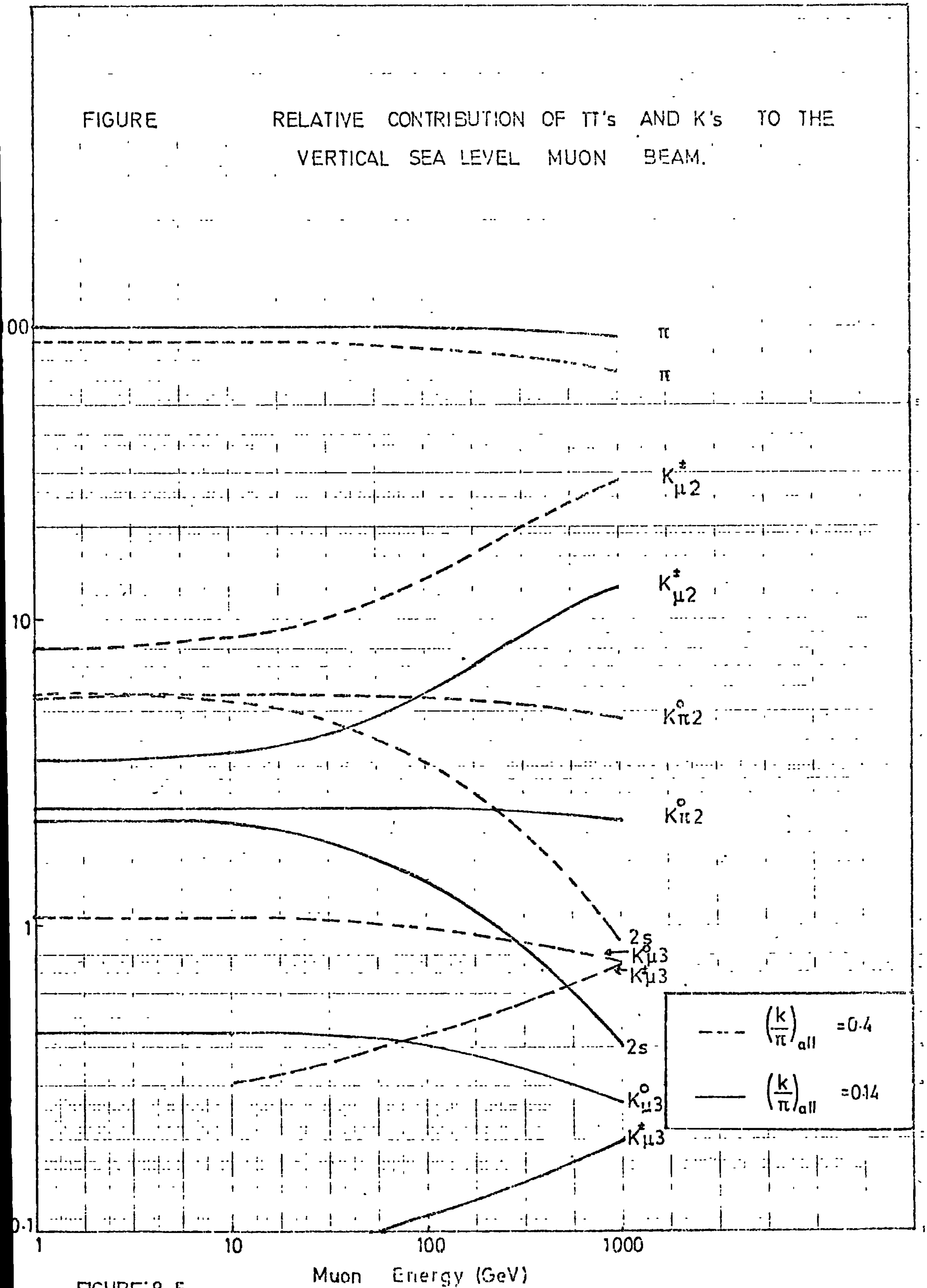

FIGURE. 8·5.

negative muon fluxes each kaon decay mode has been considered separately. The modes $k^{\pm}_{\mu 2}$ and $k^{\pm}_{\mu 3}$ were taken to give a k^{+}/k^{-} ratio of 2.0; the modes $k^{o}_{\pi 2}$ and $k^{o}_{\mu 3}$ were considered to give k^{+}/k^{-} ratios of 1.0. The two stage decay modes, other than $k^{o}_{\pi 2}$ were taken to give a kaon charge ratio of 2.0 since they are dominated by the $k^{\pm}_{\pi 2}$ mode. For a given muon energy the increases in the numbers of positive and negative muons relative to the pion contribution were obtained by summing the contributions of the various kaon decay modes. These results are shown in Fig. 8.4. The steeply rising curves indicate the increasing contribution of the (directly producing) $k^{\pm}\mu 2$ mode; the contribution of the other directly producing mode also increases but is negligible in absolute value.

8.4(c) The Inelasticity

The inelasticity usually assumed for nucleon-nucleon collisions is around 0.5; calculations by Wdowczyk and Wolfendale (A.W. Wolfendale, private communication) indicate that 0.45 may be a better estimate and this is the value which has been adopted. The relation between muon sea level energy ($E\mu$) and the energies of the primary particles producing the muons (Ep) has been taken to have a median value of $E\mu/Ep = 0.1$ (Gaisser (1973)). This effective x value of 0.1 for the muons is closer to the central region of particle production than found for pions as described above (where the median values were around 0.25). At this lower x value the assumption of constant multiplicity is not seriously affected. (Much more recent results - those of Erlykin et al (1974) - indicate that $E\mu/Ep = 0.14$ is a rather better estimate;

however, this result was not available for inclusion in this work on the muon charge ratio).

8.4(d) Calculation of the Muon Charge Ratio

The collision between primary cosmic ray particles and 'air' nucleii has been treated as one between independent nucleons. This is a conventional assumption and will be mentioned later. All collisions are considered to produce a constant number (ns) of pions each of energy (0.1/0.76) x Ep where Ep is the energy of the incident primary nucleon. The pion charge ratio is taken to be 1.755 (assuming for the moment that $\gamma = 2.7$).

Consider pions with energy in the range dE produced in collisions with primary particles of energy in the range dEp then the differential number of pions (i.e. the number of pions per unit energy) produced in the collision is : ns (Ep/E_π), where the bracketed term is a cell width correction factor. Pions of the required energy are also produced in the second collision of a primary particle with energy

$Ep_2 = {}^{Ep}/_{\beta}$ where β is the elasticity of the reaction and is given by $\beta = 1 - \eta$ where η is the inelasticity. In a similar way pions of the required energy are produced in the third collision of a primary of energy (Ep/β^2) and so on. By weighting the numbers of pions produced with the incident differential primary spectrum (of slope $-\gamma$) the total number of pions produced (N_π) is

$$N_\pi = {}^{ns}/_{E} \left[Ep^{-\gamma+1} + (Ep/\beta)^{-\gamma+1} + (Ep/\beta)^{-\gamma+2} + \ldots\ldots \right]$$

i.e. $N_\pi \propto \left[1 + \beta^{-1} + \beta^{2(\ -1)} + \ldots\ldots \right]$

The assumed value of n is 0.45, hence $B = 0.55$ and the above expression becomes :

$$N_\pi \propto \left[1 + 0.384 + 0.148 + 0.057 + \ldots\right] \quad \text{for } \gamma = 2.6$$
$$N_\pi \propto \left[1 + 0.362 + 0.131 + 0.047 + \ldots\right] \quad \text{for } \gamma = 2.7$$
$$N_\pi \propto \left[1 + 0.341 + 0.116 + 0.040 + \ldots\right] \quad \text{for } \gamma = 2.8$$

The terms inside the brackets are weighting terms and represent the contributions of the 1st, 2nd, 3rd etc. interactions of primary particles. These terms must be modified to allow for the fact that the decay probabilities of the pions and the survival probabilities of their daughter muons have been neglected. These corrections were calculated for a particular pion energy initially by considering the 1st, 2nd, 3rd etc. interactions to occur at fixed atmospheric depths of 80, 160, 240 etc. gms cm^{-2}. The pion decay probability was obtained from the results described previously; the pion was then assumed to move its characteristic decay distance before muon production occurred and the relevant muon survival probability was taken from the results of Osborne (1966). The product of the two probabilities was used as a correcting factor to be applied to the weightings given above. In an attempt to refine the calculations the assumption of interactions at fixed atmospheric depths was discarded and the distribution of depths considered. For a given order interaction the atmosphere was divided into a number of steps and the resulting correcting factors at each step were weighted using the relevant (Poisson) distribution. Modifying the weighting terms previously obtained with these new correcting factors gave curves as shown in Fig. 8.6 which applies for $\gamma = 2.7$. For almost all pion energies considered the muon

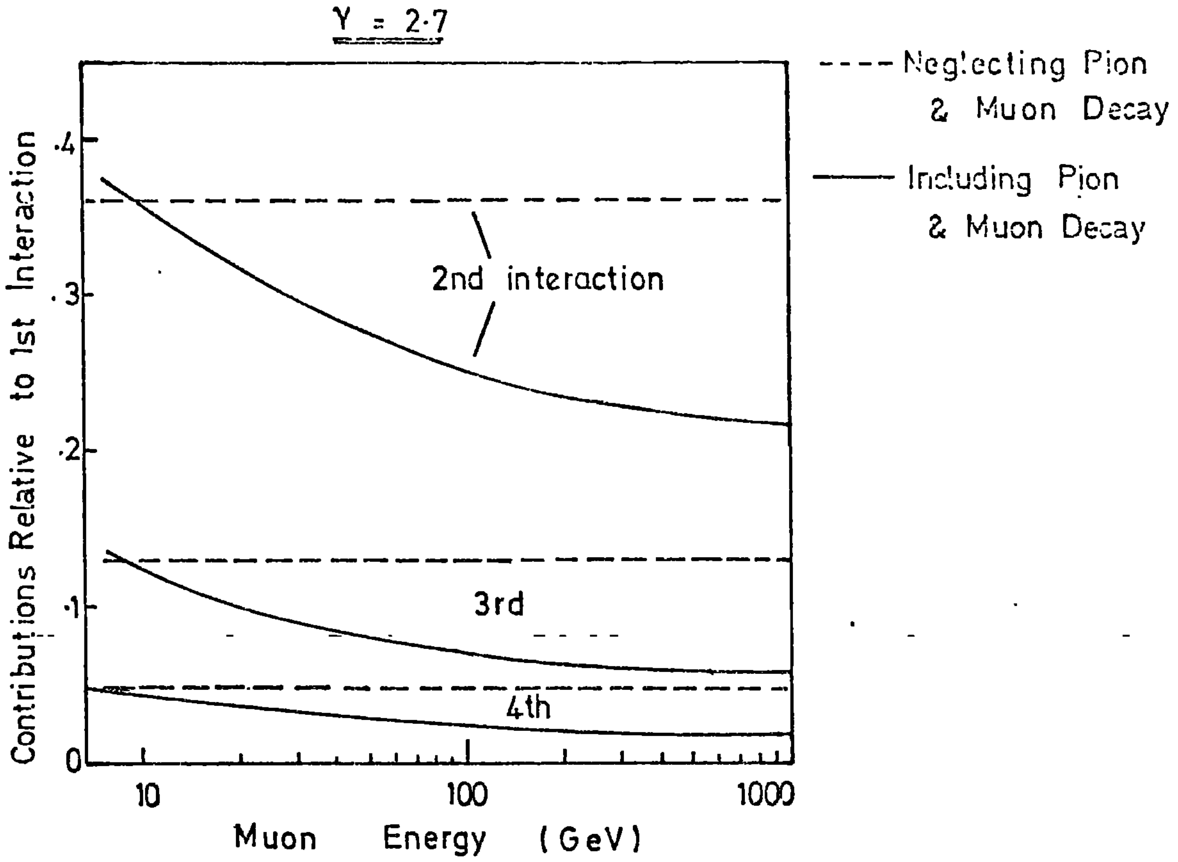
Y = 2·7
---- Neglecting Pion & Muon Decay
—— Including Pion & Muon Decay
Contributions Relative to 1st Interaction
·4
·3
·2
·1
0
2nd interaction
3rd
4th
10
100
1000
Muon Energy (GeV)

FIGURE: 8·6.

survival probabilities are all close to unity and the pion decay effects predominate. Since the probability of this decay decreases with increasing depth the effect of the correcting factors is to emphasise the importance of the first interaction. This is illustrated in Fig. 8.6 where the contributions of interactions other than the first are shown. For all energies the values are normalized such that the contribution of the first interaction is 1.0. The energies plotted are muon energies which are assumed to be given by the unique relation of (0.76 x pion energy). The enhancement of the first interaction is clearly shown; for example at a muon energy of 100 GeV the contribution of the second interaction is some 25% of the first whereas by ignoring decay effects (the dashed line) the figure was 36.2%.

Having thus derived the relative weights of the 1st, 2nd, 3rd etc. interactions the muon charge ratio at energy $E\mu$ has been obtained by summing separately the numbers of positive and negative muons from these interactions. As already mentioned n_s muons are assumed to be produced in each collision; n_s is an arbitrary, but constant, number. Muons of the required energy are produced in the first collision of a primary particle of energy E_1 ($= E\mu/0.1$). For a primary proton striking a target proton the number n_s is divided up between positive and negative particles in such a way as to give a charge ratio of 1.755 (again taking γ to be 2.7). This is also taken to be true when the target is a neutron. This assumption is in agreement with the scaling hypothesis since the considered x value (0.1) is large and the particles in this region of x are mainly projectile fragments and hence have a predominance of positive charge.

A theoretical basis for this assumption of the equivalence of pp and pn collisions has been provided by Cahn and Einhorn (1971). These authors, using the concepts of charge conjugation invariance and isospin invariance along with the work of Mueller (1970), have shown that pion spectra produced by incident protons may be expected to be independent of the target particle. The same authors also show that in the case of an incident neutron the produced pion spectra are the inverses of those for an incident proton. By inverse is meant that the spectra of positive and negative pions produced by a primary neutron are the same as the spectra of negative and positive particles respectively which are produced in a proton initiated reaction. Accordingly, in the present calculations the n_s-particles produced in neutron initiated reactions have been split in such a way as to give a charge ratio of 0.570 (= 1/1.755).

To determine the nature of the fast nucleon emerging from a collision an approximate result quoted by Morrison (1972) has been used. This author gives the measured proton spectrum emerging from a 24 GeV pp collision and an approximate neutron spectrum. At an x value of 0.45 the proton to neutron ratio is 1.35 with the probability (P_e) of the emergent particle being a proton of $P_e{}' = 0.575$; this is related to the probability of charge exchange (P_x) by $P_x = 1 - P_e = 0.425$. This value of P_x has been used for all types of collision - pp, pn, np, nn.

Thus for a given mixture of protons and neutrons in the primary cosmic ray beam the numbers of positive and negative pions produced in collisions may be determined.

If a second order collision is considered (involving a primary particle of energy $E_2 = E_1/\beta$) then the nature of this incident particle is determined not only by the relative numbers of protons and neutrons in the primary beam but also by the probability of charge exchange in its first collision. By considering these two variables along with the above described rules for finding the pion charge ratio the numbers of positive and negative pions may be determined.

In a similar fashion the pion numbers produced in third and fourth order collisions have been found.

The positive and negative pions from each order of interaction are weighted as previously described and then summed. Because of the weighting the resulting values are the effective (not the absolute) numbers of positive and negative muons and their ratio is the muon charge ratio due to pion production alone.

To include the effect of kaons the numbers of positive and negative particles generated above have been increased by the factor appropriate to the muon energy as shown in Fig. 8.4. Implicit in this procedure is the assumption that the k^+/k^- and $(k/\pi)_{all}$ ratios are independent of the nature (neutron or proton) of the incident particle. Since the predominance of k^+ production is due to associated production this seems a reasonable assumption. A further brief discussion is given later.

8.4(e) Results of Calculations and Discussion

The results of the above procedures are shown as the solid lines in Fig. 8.7 for three values of γ . The lack of

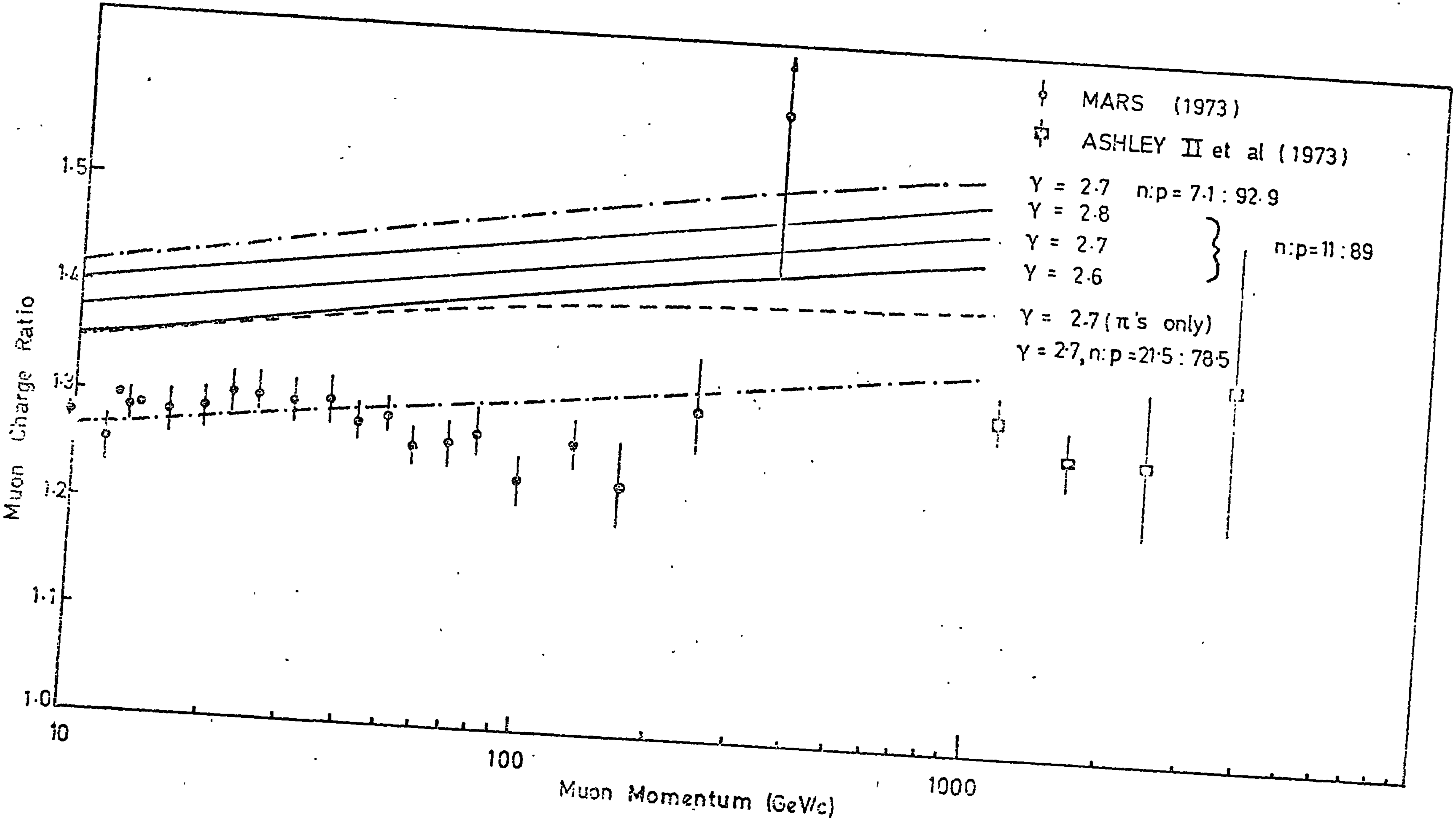
MARS (1973)
ASHLEY II et al (1973)
γ = 2·7 n:p = 7·1 : 92·9
γ = 2·8
γ = 2·7
γ = 2·6
n:p=11:89
γ = 2·7 (π's only)
γ = 2·7, n:p = 21·5 : 78·5
Muon Charge Ratio
1·0
1·1
1·2
1·3
1·4
1·5
10
100
1000
Muon Momentum (GeV/c)

FIGURE: 8·7

agreement with the experimental data is rather obvious.

As mentioned previously, four interactions have been considered. If only 2 or only 3 interactions had been used then the calculated ratios would have been higher by about 0.05 and 0.01 respectively. If more than four interactions are used the charge ratio is depressed by about 0.004; in view of the large discrepancy between observation and calculation this amount is negligible. A more important source of error is the neglect of pion induced collisions. These have the effect of diluting the charge excess. Only a rough estimate of these effects has been made. Assuming pion interactions to be responsible for about 10% of the observed sea level muon flux (Turver, private communication) the consequent reduction in the charge ratio has been estimated at ~2% which is rather small compared to the existing discrepancy but does go some way towards reducing that discrepancy.

Also shown in Fig. 8.7 are the results obtained by considering pion production alone (the dashed line for $\gamma = 2.7$). The contribution from pions can be seen to flatten out for $E_\mu \gtrsim 100$ GeV but still rises slowly. The results when kaons are included show almost no change of slope over the entire energy range.

Since a number of the ingredients of the calculations are not well known the effect of varying these parameters will be demonstrated. From Fig. 8.7 it can be seen that changing the slope of the primary differential spectrum is fairly small compared to the existing discrepancy.

The figure also shows the effect of changing the neutron to proton (n : p) ratio in the primary beam. The one standard deviation limits of this variable were derived in a previous section which gave n : p = (14.3 ± 7.2) : (85.7 ∓ 7.2). At $E\mu$ = 10 GeV the dependence of the muon charge ratio ($R\mu$) and charge excess ($\delta\mu$) on the primary proton excess ((n - p)/(n + p)) is illustrated in Fig. 8.8; it is seen that $\delta\mu$ is directly proportional to the primary excess. It is also seen that to obtain agreement with the observed ratio an n : p ratio of around 20 : 80 is required.

The result of varying Pe is shown in Fig. 8.9.

Using γ = 2.7 and varying the pion charge ratio for $E\mu$ = 10 GeV gives the curves of Fig. 8.10. It is seen that the calculated muon excess is linearly related to the input pion charge excess. To obtain a value of $R\mu$ of 1.285 at $E\mu$ = 10 GeV the required input pion charge ratio (R_π) is 1.535. The muon charge ratio (including the effect of kaons) as a function of energy for several input values of R_π (including R_π = 1.535) is given in Fig. 8.11. It is significant that even using R_π = 1.535 the calculated values of $R\mu$ seem to increase with energy rather more rapidly than indicated by experiment.

Considering the kaon contribution, the result of varying the k^+/k^- ratio is shown in Fig. 8.12. At $E\mu$ = 10 GeV the input kaon charge excess and $\delta\mu$ are linearly related. These curves refer to $(k/\pi)_{all}$ = 0.14. Varying the latter while keeping k^+/k^- = 2.0 gives the results of Fig. 8.13 where the 'kaon excess' is defined by $((k - \pi)/(k + \pi))$. The value of $R\mu$ as a function of $E\mu$ for a number of values of $(k/\pi)_{all}$ is shown in Figure 8.14.

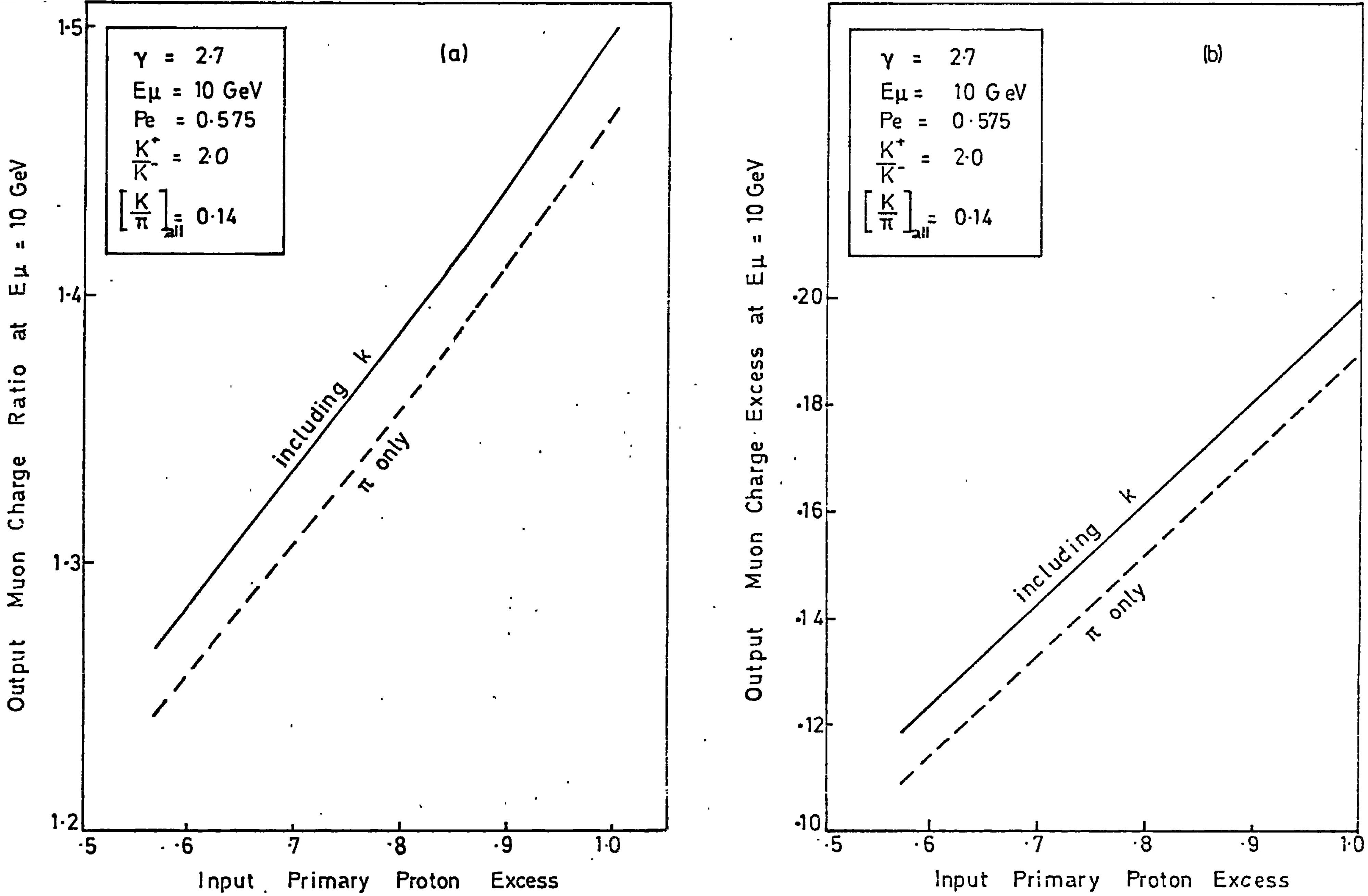
(a)
γ = 2·7
Eμ = 10 GeV
Pe = 0·575
K⁺/K⁻ = 2·0
[K/π]all = 0·14
including k
π only
Output Muon Charge Ratio at Eμ = 10 GeV
1·5
1·4
1·3
1·2
·5
·6
·7
·8
·9
1·0
Input Primary Proton Excess
(b)
γ = 2·7
Eμ = 10 GeV
Pe = 0·575
K⁺/K⁻ = 2·0
[K/π]all = 0·14
including k
π only
Output Muon Charge Excess at Eμ = 10 GeV
·20
·18
·16
·14
·12
·10
·5
·6
·7
·8
·9
1·0
Input Primary Proton Excess

FIGURE: 8·8

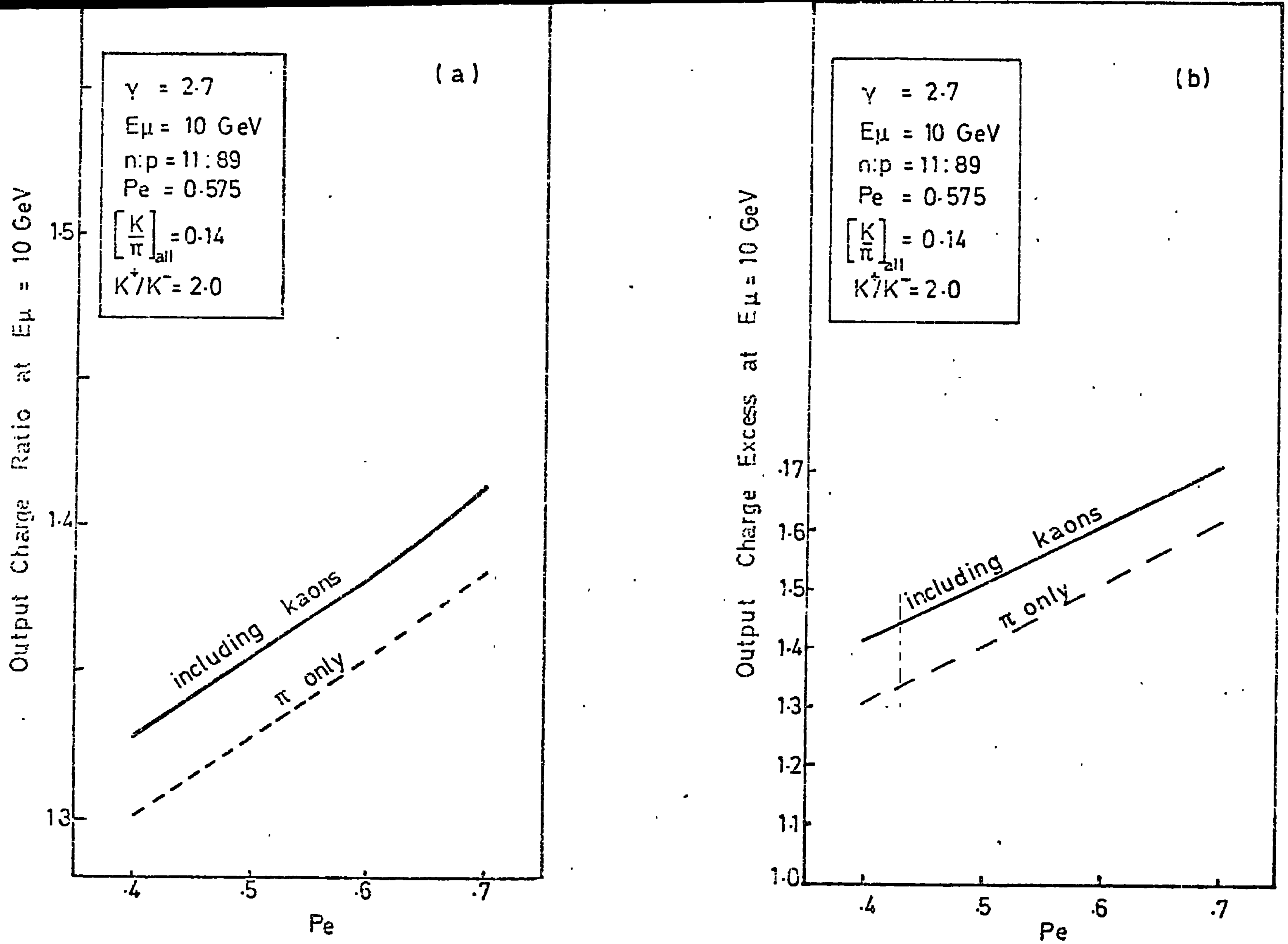
(a)
γ = 2·7
Eμ = 10 GeV
n:p = 11:89
Pe = 0·575
[K/π]all = 0·14
K⁺/K⁻ = 2·0
Output Charge Ratio at Eμ = 10 GeV
1·5
1·4
1·3
including kaons
π only
·4
·5
·6
·7
Pe
(b)
γ = 2·7
Eμ = 10 GeV
n:p = 11:89
Pe = 0·575
[K/π]all = 0·14
K⁺/K⁻ = 2·0
Output Charge Excess at Eμ = 10 GeV
·17
1·6
1·5
1·4
1·3
1·2
1·1
1·0
including kaons
π only
·4
·5
·6
·7
Pe

FIGURE:8·9.

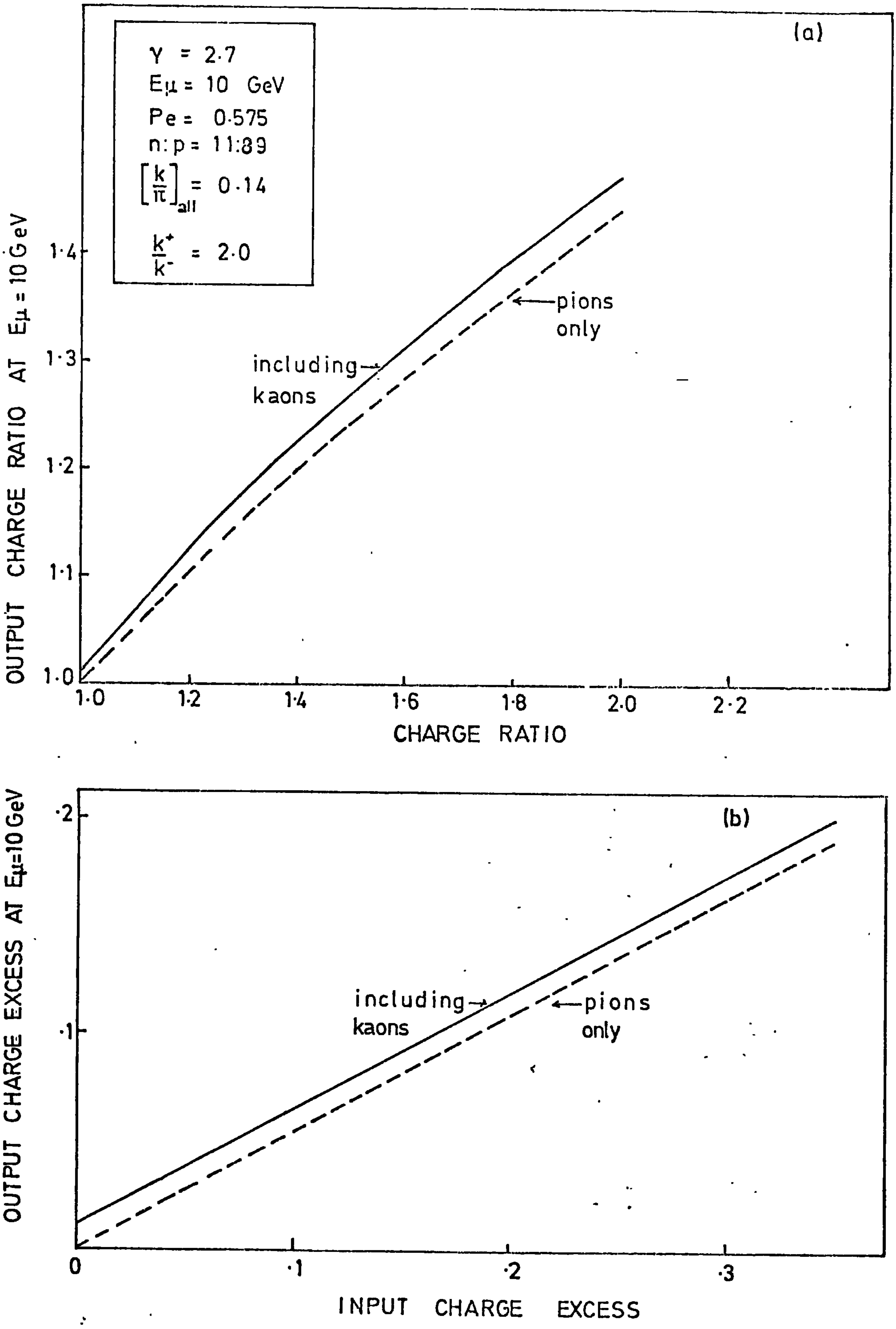
(a)
γ = 2·7
Eμ = 10 GeV
Pe = 0·575
n:p = 11:89
[k/π]all = 0·14
k+/k- = 2·0
including kaons
pions only
OUTPUT CHARGE RATIO AT Eμ = 10 GeV
1·0
1·1
1·2
1·3
1·4
CHARGE RATIO
1·0
1·2
1·4
1·6
1·8
2·0
2·2
(b)
including kaons
pions only
OUTPUT CHARGE EXCESS AT Eμ=10 GeV
·1
·2
INPUT CHARGE EXCESS
0
·1
·2
·3

FIGURE: 8·10.

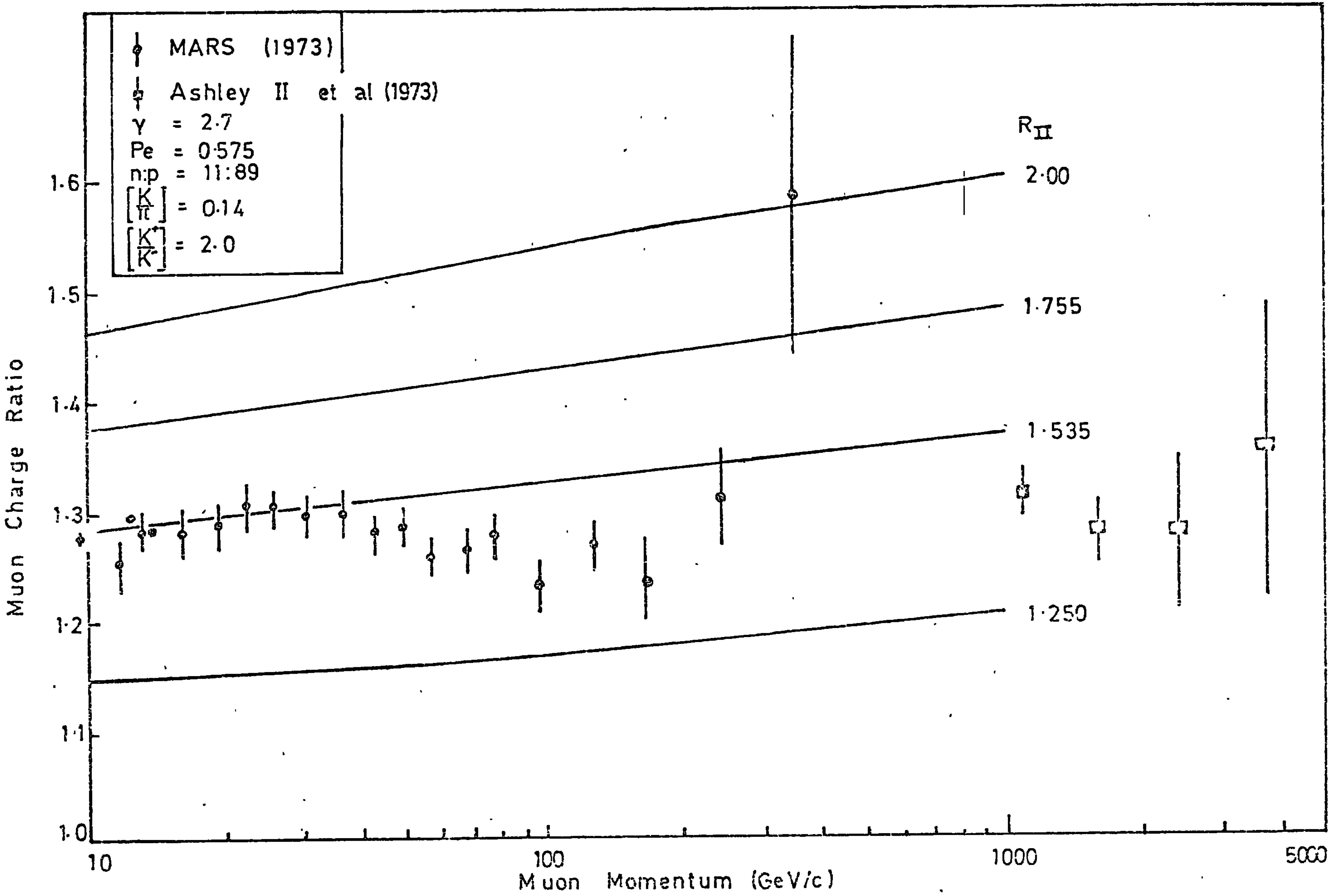
MARS (1973)
Ashley II et al (1973)
γ = 2·7
Pe = 0·575
n:p = 11:89
[K/π] = 0·14
[K⁺/K⁻] = 2·0
R_{II}
2·00
1·755
1·535
1·250
Muon Charge Ratio
1·6
1·5
1·4
1·3
1·2
1·1
1·0
10
100
1000
5000
Muon Momentum (GeV/c)

FIGURE:8·11.

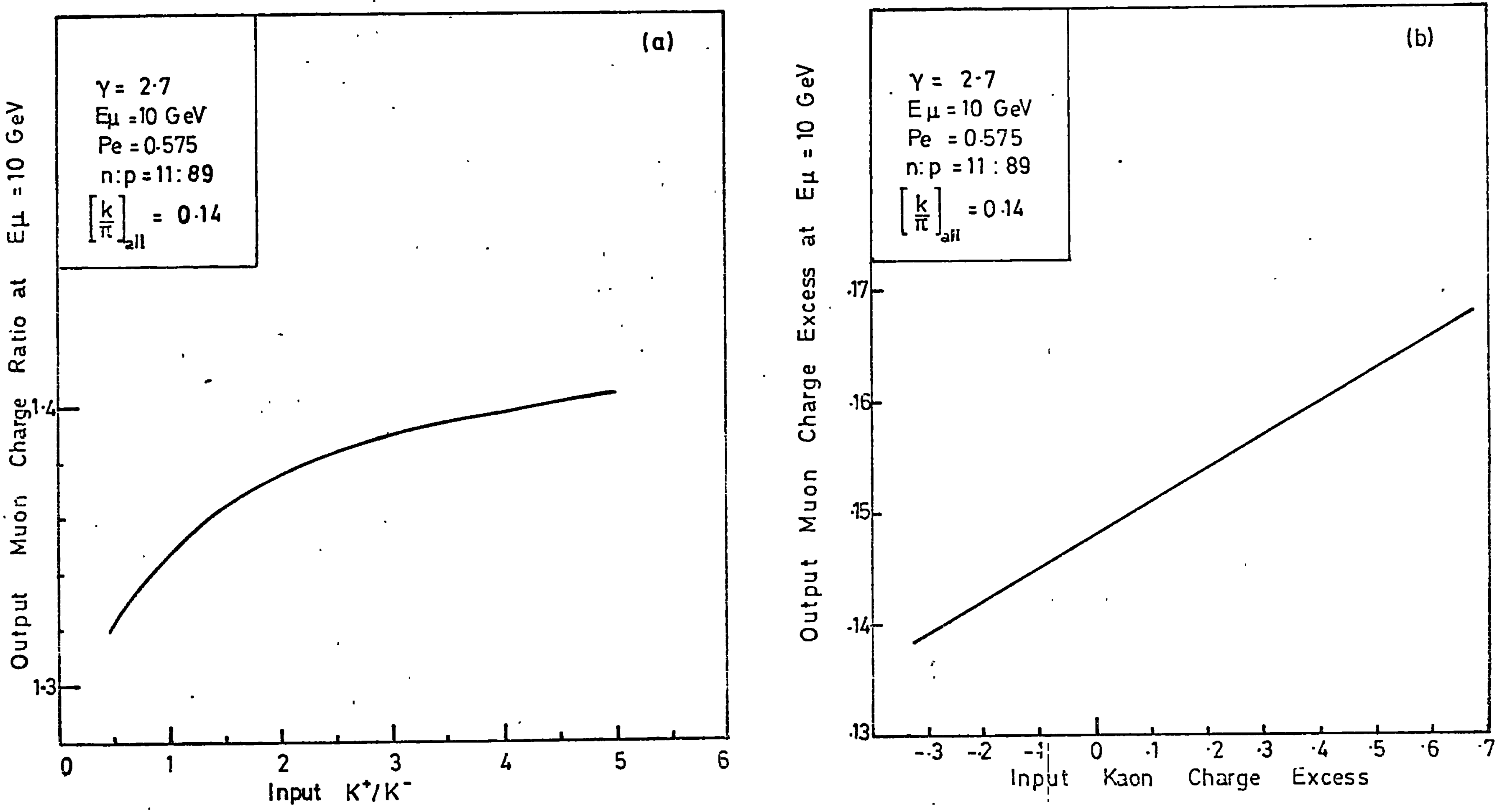
(a)
γ = 2·7
Eμ = 10 GeV
Pe = 0·575
n:p = 11:89
$\left[\frac{k}{\pi}\right]_{all}$ = 0·14
Output Muon Charge Ratio at Eμ = 10 GeV
1·3
1·4
0
1
2
3
4
5
6
Input K⁺/K⁻
(b)
γ = 2·7
Eμ = 10 GeV
Pe = 0·575
n:p = 11 : 89
$\left[\frac{k}{\pi}\right]_{all}$ = 0·14
Output Muon Charge Excess at Eμ = 10 GeV
·13
·14
·15
·16
·17
-·3
-·2
-·1
0
·1
·2
·3
·4
·5
·6
·7
Input Kaon Charge Excess

FIGURE: 8·12.

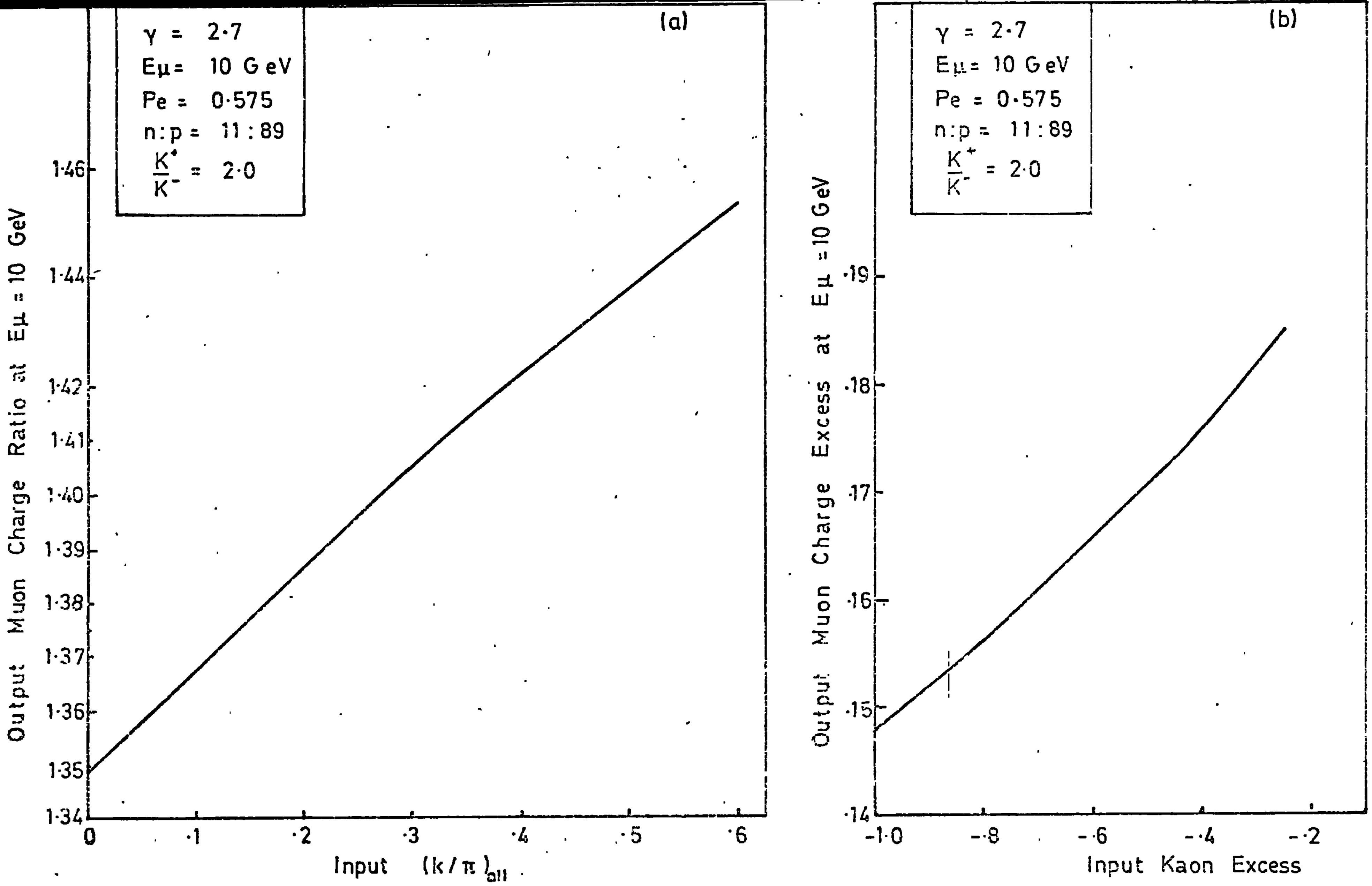
(a)
γ = 2·7
Eμ = 10 GeV
Pe = 0·575
n:p = 11:89
K⁺/K⁻ = 2·0
Output Muon Charge Ratio at Eμ = 10 GeV
1·34
1·35
1·36
1·37
1·38
1·39
1·40
1·41
1·42
1·44
1·46
0
·1
·2
·3
·4
·5
·6
Input (k/π)all
(b)
γ = 2·7
Eμ = 10 GeV
Pe = 0·575
n:p = 11:89
K⁺/K⁻ = 2·0
Output Muon Charge Excess at Eμ = 10 GeV
·14
·15
·16
·17
·18
·19
-1·0
-·8
-·6
-·4
-·2
Input Kaon Excess

FIGURE: 8·13.

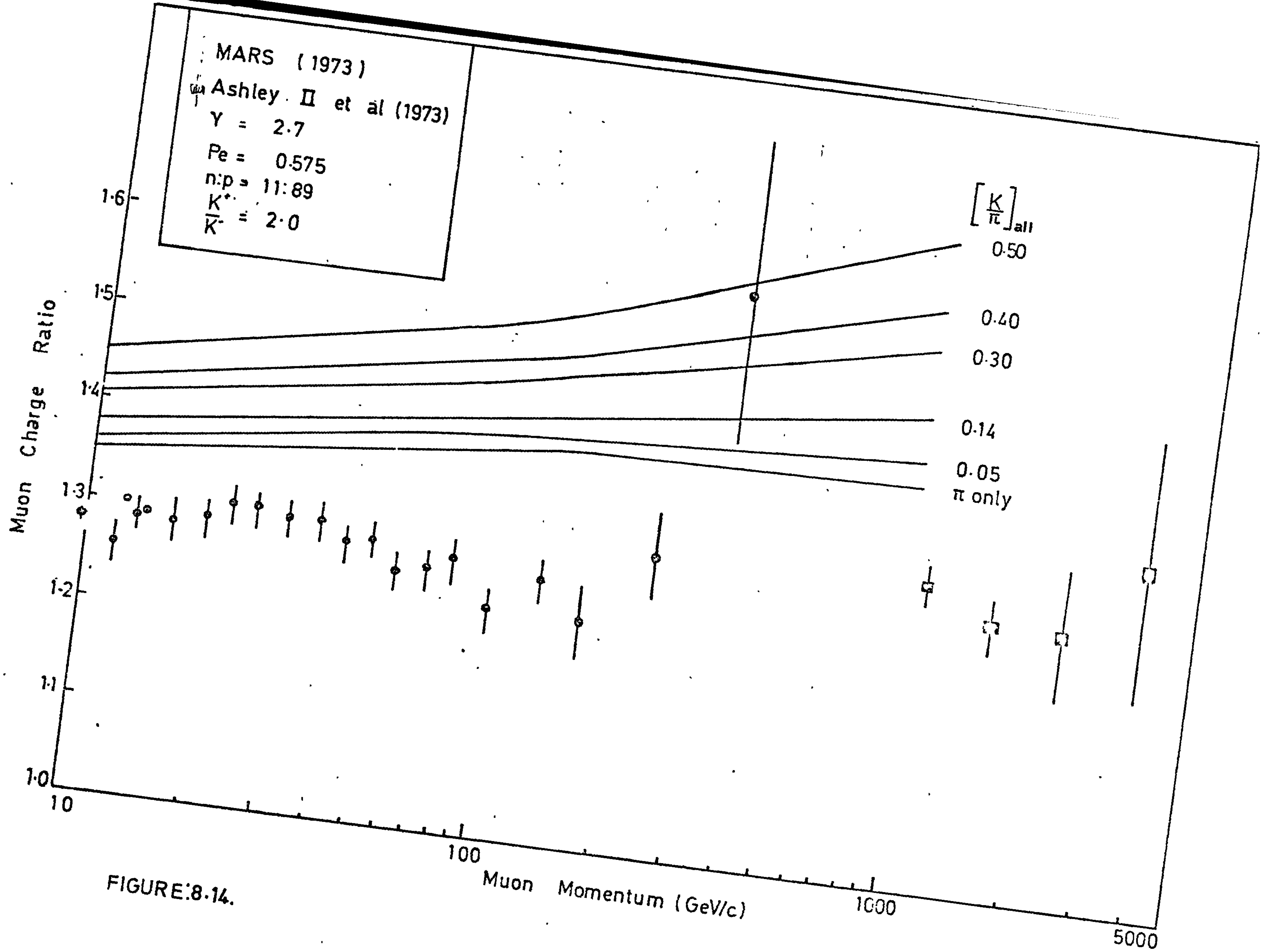
MARS (1973)
Ashley II et al (1973)
Y = 2·7
Pe = 0·575
n:p = 11:89
$\frac{K^+}{K^-}$ = 2·0
$\left[\frac{K}{\pi}\right]_{all}$
0·50
0·40
0·30
0·14
0·05
π only
Muon Charge Ratio
1·0
1·1
1·2
1·3
1·4
1·5
1·6
Muon Momentum (GeV/c)
10
100
1000
5000

FIGURE:8·14.

So for both the k^+/k^- and $(k/\pi)_{all}$ ratios have been considered energy independent. A brief survey of k^+/k^- data has indicated that it falls from ~ 2 at primary energies of about 20 GeV to around 1.3 - 1.4 at primary energies $\gtrsim$ 100 GeV. These ratios however are those obtained by integration over all x and Pt values and as such are inappropriate to this work where specific values of these variables (0.2 and 0.4 GeV/c respectively) are considered. Some calculations with the falling k^+/k^- ratio have however been performed (Hume et al (1973)). Compared with a constant k^+/k^- ratio of 2.0 the value of $R\mu$ is reduced by 0.02 and 0.03 at $E\mu$ = 100 and 1000 GeV respectively. The same falling ratio was used in the results of Ayre et al (1973) (where unfortunately, it is incorrectly stated that the constant value of 2.0 was used). The published data from the ISR do not as yet give comprehensive and accurate kaon data and as a consequence in the present work no energy variations of k^+/k or $(k/\pi)_{all}$ have been considered.

As mentioned previously the predominance of k^+ production over that of k^- has been assumed to be due to associated production. An alternative possibility is that kaon production is analagous to pion production in that the charge ratio produced in nn and np collisions are the inverses of those produced in pp and pn collisions. Using this last possibility values of $R\mu$ have been calculated. Using $\gamma = 2.7$, n : p = 11 : 89, Pe = 0.574 and R_π = 1.755 the results are that at $E\mu$ = 10,100 and 1000 GeV the values of $R\mu$, compared to those obtained assuming associated production, are reduced by 0.007, 0.008 and 0.017 respectively. These figures are small compared to the existing discrepancy.

The possibility that a collision between a primary nucleon and an air nucleus is not even approximately equivalent to that between completely free nucleons is well recognised. Since the physics of the intra-nuclear cascade is not at all well known all theoretical attempts to calculate the effects of such a phenomenon are subject to a large degree of uncertainty. This situation is made even more difficult by the lack of experimental data on nucleon-nucleus interactions. What evidence that there is available is conflicting. The conclusion of Subramanian, Lal and Vyas (1972) and of Subramanian (1972) is that in the forward direction the pion spectrum produced in nucleon-nucleus collisions is independent of the target. This conclusion is not consistent with the experimental results of Allaby (1970) who find a significant difference between the pion charge ratios produced in p - p and p - Al interactions. Resolution of this conflict will probably have to await the results of a high energy p - nucleus experiment at, for example, Batavia. An attempt has recently been made by Morrison and Elbert (1973)to calculate the expected muon charge ratio using the meagre amount of p - nucleus data that is available.

These authors obtained the inclusive distributions of particles produced in p - air nucleus collisions by interpolating between the 19 GeV p - Be and p - Al data of Allaby et al (1970). These data were taken for a large number of x and Pt values but only for $x > 0.3$. The interpolated data was fitted with the functional representation used by Boggild et al (1971) to describe their 19 GeV p - p results. Although the use of a p - p equation to represent p - nucleus data may introduce some error into the 'unexplored' region of $x < 0.3$, this technique could be expected to give some idea of the consequence of the intra-nuclear cascade. Morrison and Elbert found the effective pion charge ratio (for $\gamma = 2.7$) to be 1.461. This is markedly below the equivalent value used in this work (1.755 for the same value of γ). Other parameters which were found by similar methods were $k^+/k = 2.818$, $(k/\pi)_{all} = 11.7\%$ and $\beta = 0.42$.

In calculating the muon charge ratio the authors used a neutron to proton ratio of 9.5 : 90.5 in the primary radiation and a value of 0.565 for Pe; they also assumed the kaon contribution in n - nucleus collisions to be the inverse of that in p - nucleus collisions. The results of Morrison and Elbert are shown as the curves marked ME in Fig. 8.15. For momenta > 1000 GeV/c the solid line is in quite good agreement with the results of Ashley II et al (1973) although the errors of the latter are rather large. It should be mentioned that the results of Ashley II et al (1973) come from the underground experiment of the Utah group in which inclined muons are measured; the energies at which the ratios are plotted are those at production. A comparison with the mainly vertical results of M.A.R.S. is valid since the production energies here are only ~ 2 GeV higher than the energy at which the points are plotted. In the range 90 - 300 GeV/c the solid line (ME) passes through the M.A.R.S. data. Between 90 and 50 GeV/c the M.A.R.S. results are higher than the calculation. The trend of the data below 50 GeV/c disagrees with the data. Extrapolating the prediction to 10 GeV/c indicates a charge ratio of ~ 1.18 whereas the M.A.R.S. result and the result of a survey of other experiments in the

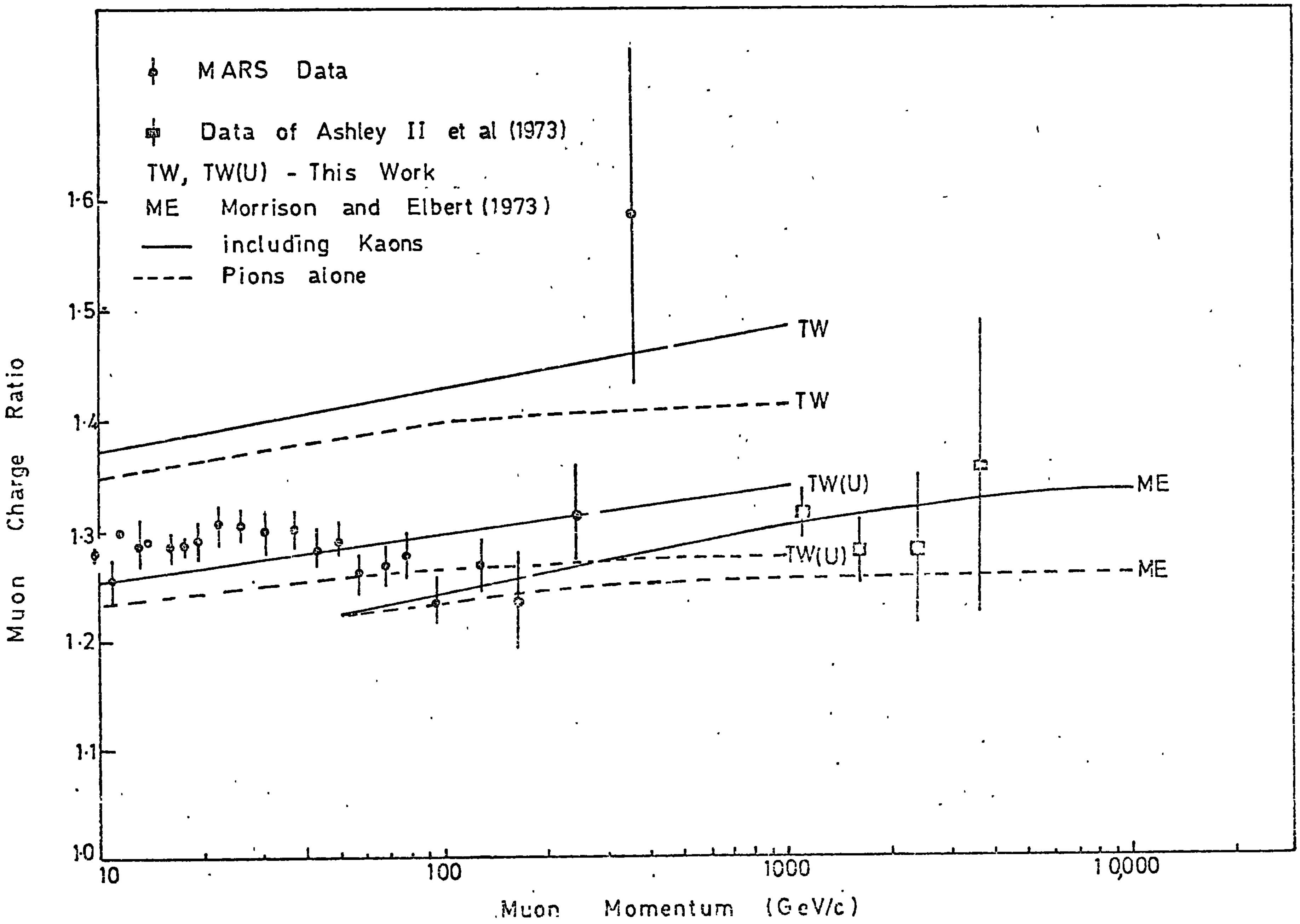
MARS Data
Data of Ashley II et al (1973)
TW, TW(U) - This Work
ME Morrison and Elbert (1973)
including Kaons
Pions alone
TW
TW
TW(U)
TW(U)
ME
ME
Muon Charge Ratio
1·6
1·5
1·4
1·3
1·2
1·1
1·0
10
100
1000
10,000
Muon Momentum (GeV/c)

FIGURE: 8·15.

near vertical direction are 1.285 and 1.264 respectively. Thus the calculation agrees quite well with observation at high energy ($\gtrsim$ 100 GeV) but at low energies ($\lesssim$ 90 GeV) the discrepancy increases.

To facilitate comparison between the present work and that of Morrison and Elbert (1973) the method of the present work has been used utilising the same parameters as those of Morrison and Elbert. The results of this process are shown by the curves marked TW(U) - the dashed curve represents the pions only contribution. The curves marked TW are the original results (γ = 2.7, Fig. 8.7). At energies $\lesssim$ 90 GeV the solid line TW(U) is closer to the data that the calculations of Morrison and Elbert (ME). At energies between 90 and 200 GeV the solid line TW(U) contradicts the observed fall of the M.A.R.S. data. Because the present calculation refer only to muons of energy $\leqslant$ 1000 GeV direct comparison with the results of Ashley II et al (1973) is not possible but simply extrapolating the line indicates too high a value.

Considering the contribution of pions the dashed lines TW, TW(U) and ME all show the contribution flattening with increasing muon energy. Physically this is due to the increasing contribution to the muon charge ratio of the particles produced in the first interaction; this is illustrated in Fig. 8.6. The charge ratio due to pions only thus approaches a limit which is determined mainly by the first interaction. The rate at which this limit is approached is rather different for the two curves TW(U) and ME. The latter reach the limit at ~ 1000 GeV whereas the former curve indicates a contribution that is still rising, albeit slowly. Over the range 50 - 1000 GeV the contributions shown by ME and TW(U) rise by 2.8% and 1.4% respectively. The relatively slow rise obtained in the present work is partly due to the previously described method used to adjust the weighting factors for pion and muon decay. Initially, interactions were considered to occur at fixed depths of 80, 160 etc gms cms^{-2}; the result of this was to produce a change in the pions-only charge ratio of 0.7% of the muon energy range 50 - 1000 GeV. Correcting the weights by dividing the atmosphere into steps, as already described, has yielded the above result of 1.4%. Further calculations using smaller atmospheric steps have given a figure of 1.7%. Consideration of smaller steps, though unlikely to account for all of the remaining discrepancy of 1.7% should go some way towards it. A better method of adjusting the weights would be to treat the problem analytically.

The curves TW(U) and ME are the results of calculations based upon the same input data. There are differences in the results based upon pions alone (a difference of ~0.02 at $E\mu$ = 500 GeV) and in the results including kaons (a difference of ~0.04 at $E\mu$ = 500 GeV). The basic causes of these differences remain unknown.

8.5 The Results of Previous Workers

The results of Morrison and Elbert (1973) are those with which the present work may be compared in greatest detail and this has been done at the end of the previous section. Some comparison is also possible with other works, the earliest of which is that of Mackeown and Wolfendale (1966).

These authors identify the major factors influencing the muon charge excess as :

(i) the properties of the primary radiation

(ii) the parameters which characterise the propagation (in the atmosphere) of the primary and secondary components and

(iii) the nuclear physics involved in primary nucleon-air nucleus collisions.

They then derive an expression for the charge excess (δ) in which the dependence upon the above three factors is written as the product of three separable variables

$$\delta(E\mu) = \delta_o . \delta_1 (E\mu) . D (E\mu) \quad \text{where}$$

δ_o is the charge excess in the primary nucleon beam, D ($E\mu$) is the so called dilution factor representing the contribution to the flux of muons from the first collision relative to the total flux at the energy Eu,

δ_1 ($E\mu$) is the charge excess of muons produced in a collision between a primary proton and an air nucleus.

The variation of D with $E\mu$ is shown as the curve marked MW in Fig. 8.16. A useful feature of the above representation is the possibility of varying the details of one of the factors while keeping the remaining two constant; the sensitivity of to such variations is thus conveniently obtained. In deriving their representation the authors made a number of simplifying assumptions the most important of which are, firstly, that the charge excess produced in a neutron-nucleus collision is the inverse of that produced in a proton-nucleus collision and secondly, that the probability of charge exchange in such

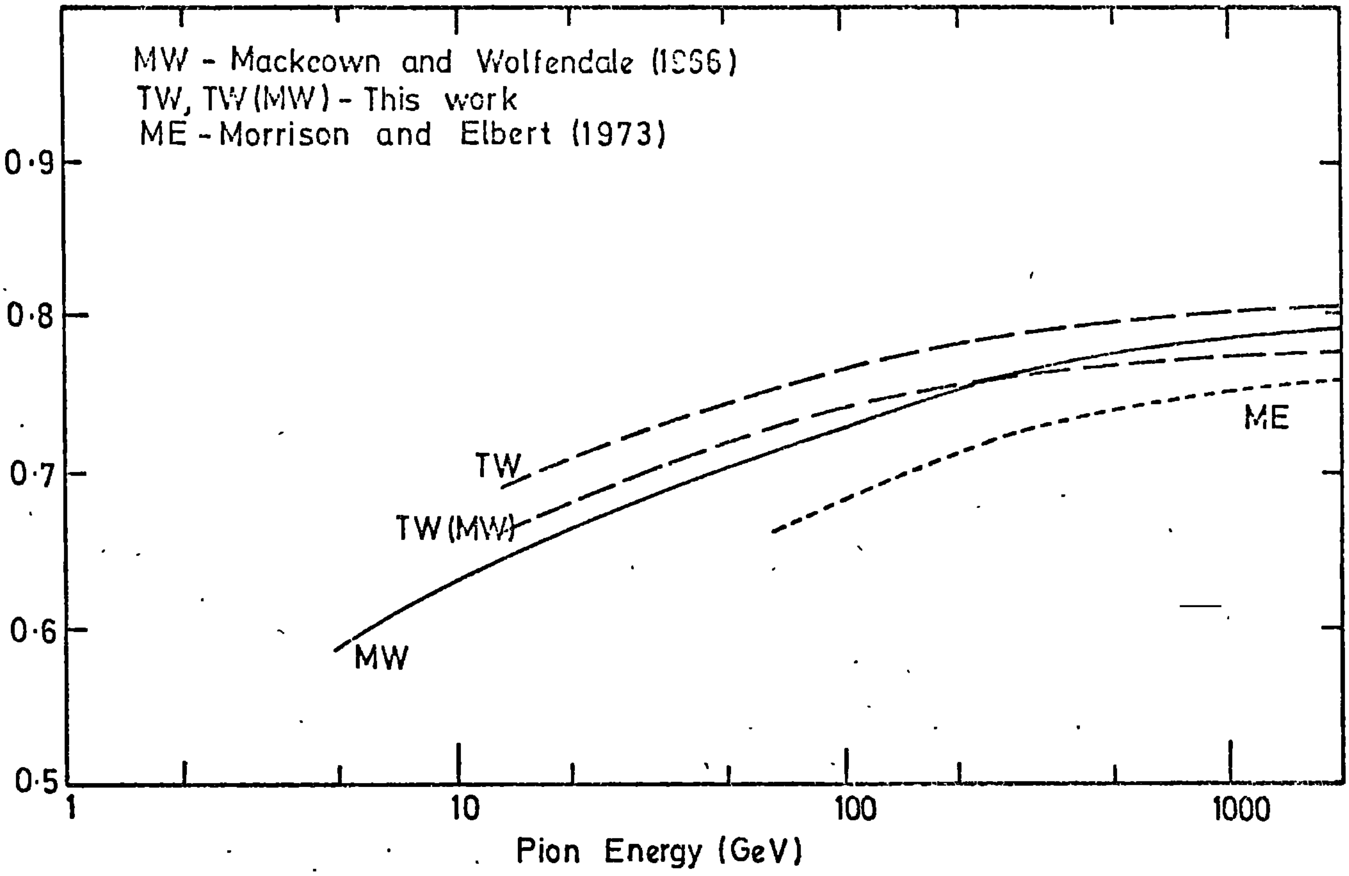

FIGURE: 8·16. DILUTION FACTORS

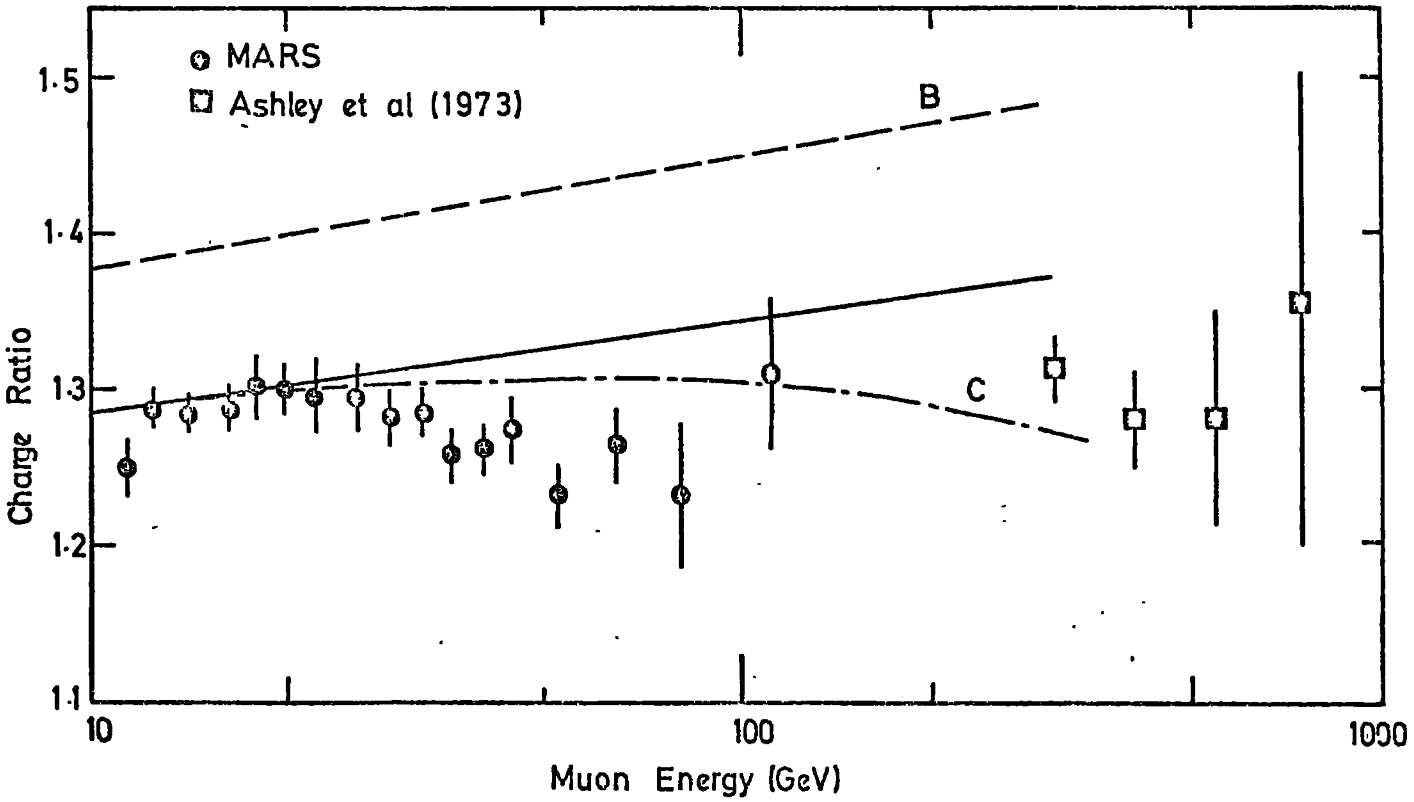

FIGURE: 8·17. CHARGE RATIO AFTER INTRODUCTION OF f.

interaction is 0.5 (i.e. Pe = 0.5). It is important to note that up to this stage of their calculations the authors have not considered kaons.

From the results of the present work the effective values of D have been found and are plotted as the curve TW in Fig. 8.16. This curve has the following input parameters : $\gamma = 2.7$, $R_\pi = 1.755$, n : p = 11 : 89 and $P_e = 0.575$. It can be seen that the curve TW has a similar shape to that calculated by the original authors (and re-calculated by the present author) but is somewhat flatter. Utilising the same values of Pe and the neutron to proton ratio as the original authors the calculations described in previous sections have been repeated and have yielded the values of D shown by the curve TW (MW) in Fig. 8.16. This again is rather flatter than the original curve (MW). The line ME represents the effective values of D derived from the results of Morrison and Elbert (1973) who used n : p = 9.5 : 90.5 and $P_e = 0.565$. This is almost parallel to the original curve and this may be an indication of some deficiency in the present method of calculation which yields the curves TW and TW(MW).

Using the value of Pe = 0.5 and then by considering the conservation of isotopic spin Mackeown and Wolfendale (1966) were able to predict values of δ_1 and taking $\delta_o = 0.74$ they were then able to derive $\delta(E\mu)$. The result was a low charge ratio varying from 1.07 at Eµ = 10 GeV to 1.02 at Eµ = 1000 GeV. This lack of agreement was assumed to be due to errors in the estimation of δ_1 and the authors went on to consider more complex nuclear interaction models based parly on low energy accelerator data. Any further comparisons with the present work which utilises high energy data is thus rather unprofitable.

The remaining works with which comparison may be made give less specific predictions than any so far considered. These works all have the common feature that they are based upon nucleon-nucleon collisions and they all predict charge ratios higher than observed. The main details of these works along with the present work and that of Morrison and Elbert (1973) are listed in Table 8.2.

Frazer et al (1972) describe the atmospheric propagation of primary nucleons, pions, muons and kaons by diffusion equations. They give solutions for the sea level muon flux and charge ratio for $E_{\mu} \gg 100$ GeV. The expression for the latter involves the effective pion charge ratio (R_{π}) which the authors find, from low energy accelerator data, to be in the range 1.8 - 2.25; they use 2.02 as a mean value to obtain a muon charge ratio (neglecting kaons) of 1.56. The above quoted range of values of R_{π} was for p-p interactions and because the main contribution to R_{π} comes from the projectile fragmentation region the fact that the true target is a nucleus, rather than a nucleon, is believed to be unimportant.

Replacing the original value of R_{π} (2.02) with that of the present work (1.755) reduces the predicted ratio to 1.43 which is still significantly higher than most of the data at high energy. Using $R_{\pi} = 1.461$ (the value of Morrison and Elbert (1973)) results in a predicted ratio of 1.275 which is in good agreement with the most accurate data at $E_{\mu} > 1000$ GeV.

In the calculations the effects of kaons and charge exchange in pion induced interactions were both ignored but the authors state that the contributions tend to cancel each other. Thus their value of 1.56 can be only slightly modified when those factors are considered. The authors suggest that a possible contribution to the discrepancy with observation may be the non-scaling of the low energy data.

The calculations of Garrafo, Pignotti and Zgrablich (1973) are based upon the solution of diffusion equations for the fluxes of nucleons, pions and muons. Using ISR data they find R_π to be 1.702 and thence predict an almost energy independent muon charge ratio of 1.53. This figure is based upon nucleon-nucleon collisions and the authors say they expect some modification to be expected because of multiple inelastic scattering inside the nucleus. An attempt is made to calculate the required correction by solving diffusion equations for particles passing through a nucleus. The charge ratio becomes 1.38 after this correction. This figure is rather high since kaons have not been considered.

The final work with which comparison may be made is that of Yekutielli (1972). This author also derives analytic solutions to the diffusion equations. He considers two slightly different primary spectra and derives his values of R_π from low energy experimental results on p-p collisions. The calculated values of the muon charge ratio are high at ~ 1.6. An attempt is made, using the observed muon charge ratio (taken to be 1.25) to determine the required values of the input parameters. The resulting values of R_π and Pe are shown in the table. The value of R_π has had to be severely reduced; the 'best-fit' value of Pe is high.

8.6 Discussion

The results of the work detailed in this chapter have, in common with the majority of other works described, predicted charge ratios higher than observed. The exception is the work of Morrison and Elbert (1973) who obtain good agreement at energies of about 100 GeV but with an increasing discrepancy at lower energies. Between these two classes of results the most significant difference is in the adopted values of R_π, the input pion charge ratio. In the first group the value of R_π ranges from 1.755 to 2.06 (for $\gamma = 2.7$) while in the second, the value is 1.461. By normalizing his calculations to the observed data Yekutielli (1972) found he needed a value of 1.5; in the present work a value of $R_\pi = 1.54$ is required to agree with data at 10 GeV. The reasons for the discordant values of R_π are largely unknown. Among the more obvious of the simpler possibilities are

(a) the lack of correction for the effects of the intra-nuclear cascade,

(b) the possibility that nuclear cascading effects are unimportant but that p-p and p-n collisions are not equivalent,

(c) changes in the primary composition such that the neutron component increases with increasing energy (as in Daniel et al (1973)), and finally,

(d) an overestimate of the value of R_π due to inadequate experimental data.

The first two possibilities are similar in that the presence of the nucleus does have an effect whereas in (c) and (d) no effect is allowed. As already mentioned, data on N-nucleus collisions is sparse but the results of Allaby et al (1970) at 19 GeV do suggest that the nucleus has some effect. The authors show the pion charge ratio for p-nucleus collisions to be significantly lower than for p-p collisions. At $x = 0.31$ (the smallest value used in the experiment) and for a transverse momentum of 420 MeV/c their results show R_π = 2.14, 1.71 and 1.71 for p-p, p-Be and p-Al interactions respectively. Experimental errors in the ratios are typically ± 0.08. The results of Eichten et al (1972) at 24 GeV extend to lower x values but do not include p-p interactions; their result for p-Al collisions at P_t = 0.4 GeV/c is R_π = 1.46 ± 0.06.

Some attempt at allowing for (b) above has been made in the present work by assuming that in a fraction f of p-n collisions the pion charge ratio is determined by the proton and in $(1-f)$ by the neutron. This is a violation of the ideas of limiting fragmentation. The value of R_π for p-p and p-n collisions remains unchanged at 1.755 and 1/1.755 respectively. The value of γ has been taken as 2.7 and the value of f has been determined which, using the methods of section 8.4, gives rise to the mean observed muon charge ratio. The result is shown in Fig. 8.17 as the solid line and shows a much better agreement with the data particularly below 50 GeV than the original calculations (shown by the dashed line B). The appropriate f value was 0.77. The value of R_π of the first proton induced collision, derived from these calculations is 1.54; this agrees with the value found simply by measuring the dependence of R_μ on R_π as described in section 8.4(c).

This is not surprising since the two methods are largely equivalent. The value of 1.54 compares not too badly with the result of Eichten et al (1972). In view of the approximate nature of the calculations and the fact that the fit is not good for energies $\gtrsim$ 50 GeV some discrepancy is reasonable. Thus the indication is that the behaviour exhibited in p - light nucleus collisions continues up to energies of at least 100 GeV (since the mean value of the muon charge ratio is heavily biased by the large amount of data at muon energies around 10 GeV). As already mentioned, an alternative explanation for the disparity between observation and calculation lies not in a simple difference between p-n and p-p interactions but in a more complex mechanism for p - light nucleus collisions than has been assumed.

Turning now to the third possibility, there is some experimental evidence favouring a flatter energy spectrum for primary iron nucleii than for the other components of the primary beam, at least up to energies of around 10^{12} eV/nucleon. Recent measurements with balloon borne detectors (Juliusson et al (1972), Ormes and Balasubrahmanyan (1973), Smith et al (1973), Balasubrahmanyan and Ormes (1973), Ormes and Weber (1965)) have indicated that the iron spectrum is significantly less steep than that of the other primary elements. From the summary of Ramaty et al (1973) the slope of the iron spectrum appears to be about -2.1. Figure 8.18 shows the data; the full lines cover regions over which measurements have been made and the dashed lines are extrapolations. Using these spectra the effect on the muon charge ratio - due to the increasing neutron to proton ratio with increasing

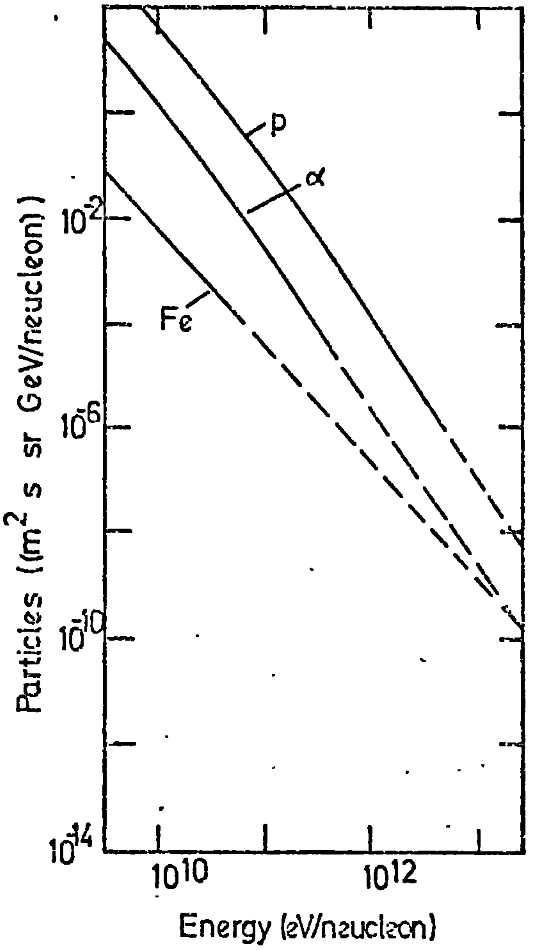

FIGURE: 8.18. PRIMARY SPECTRA

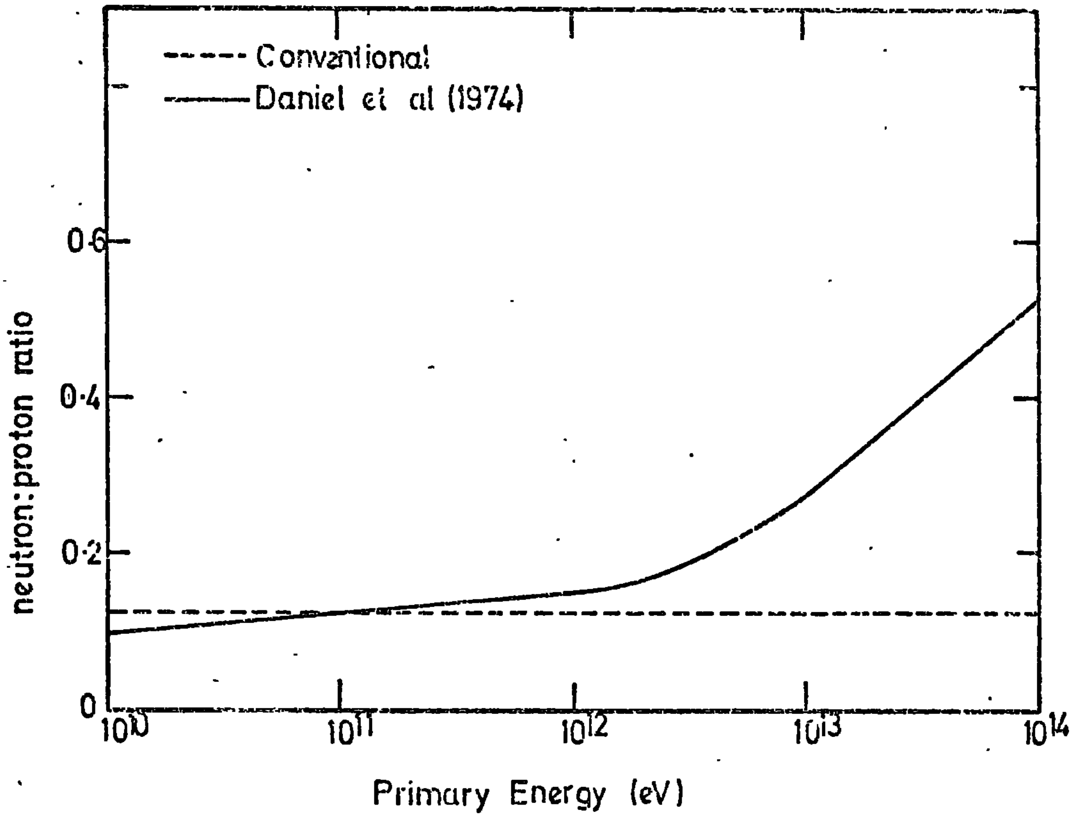

FIGURE: 8.19 n:p VARIATION

primary energy - has been calculated. The variation of the neutron to proton ratio is shown in Fig. 8.19, the dashed line shows the ratio previously used. The resultant charge ratio is shown as the line c in Fig. 8.17. This has been calculated in the manner described above i.e. by using the factor f and normalizing to the mean observed charge ratio. The appropriate f value is not significantly different from that found previously since at a primary energy of 10^{11} eV (taken to correspond to $E_\mu \approx 10$ GeV) the new value of the neutron to proton ratio is barely different from the old. The agreement with the data is better than any other curve but is still not good above about 50 GeV where prediction generally exceeds observation. Above 200 GeV the measured ratios are clearly higher than those predicted for the flatter iron spectrum. Taken at its face value this would indicate that the iron intensity starts to fall more rapidly above a primary energy of 2×10^{12} eV/nucleon.

Considering finally the overestimation of the input pion charge ratio, such a possibility is suggested by the very recent work of Erlykin et al (1974). These authors, using more precise ISR data than was available for the present work find R_π to be 1.54 ± 0.15 and predict a muon charge ratio of 1.40 at $E_\mu = 500$ GeV (compared to 1.47 from the present work). A detailed study of the work of these authors has not been made but their predictions seem to be in good agreement with data below 100 GeV while at higher energies the charge ratio is rather overestimated. In comparing their results with other workers, these authors attribute the lack of agreement to

(i) differences in the input data and/or

(ii) different models for propagation in the atmosphere having unequal degrees of accuracy.

The effect of differences in the input values of η and Pe and the effect of (ii) have been estimated by studying the dilution factors D obtained by the various workers. It is concluded that D is known to about ± 5%. Since $dR/R \sim 0.3 \times d\delta/\delta$ then $dR/R \sim 1.7\%$ i.e. an error of about 0.02 in R. This figure is small compared to the existing discrepancies and the major cause lies in the high values of R_π which have generally been used.

8.7 Conclusion

The results reported in this chapter have been disappointing in that the estimated muon charge ratio is much higher than is observed experimentally (a result found by several other workers). The crudest simplification made in the method of the calculation - the neglect of pion induced interactions - is unlikely to account for the discrepancy and the basic reason for the failure remains unknown.

Amongst the possible causes of the failure, as discussed in the previous section, that of a breakdown of limiting fragmentation is doubtful. Scaling is, according to ISR experiments, valid (at least for pions) up to energies of around 2000 GeV. The possibilities of intra-nuclear cascading effects and of the overestimation of R_π seem to be the most reasonable. The former derives some support from the low energy ($\sim$20 GeV) results described previously while the work of Erlykin et al (1974) gives support to the latter. (They argue that more recent results on f(x) for π^- production give higher values than had been hitherto adopted and thus their R_{π} is lower). Consideration of changes in the primary spectrum seems rather premature and these should await the resolution of the nuclear-physical aspects of the problem.

It has been seen that even when a value of R_{π} is used which gives agreement with the measured muon charge ratio at 10 GeV the resulting variation of the ratio with energy is still unacceptable beyond about 50 GeV. The authors view is that this is probably due to errors in the estimation of the contribution of kaons; data from the ISR on kaon production are less comprehensive than for pions. However, some argue (e.g. Erlykin et al 1974) that the reason for the discrepancy is probably an increase in the contribution of heavy nucleii at higher primary energies.

Thus the situation is rather unsatisfactory. Extended data from the ISR on pion and kaon production may go some way to solving the problem. Even more desirable is data on the production of these particles in high energy p - light nucleus collisions. Such data may be forthcoming shortly from the Batavia machine.

TABLE 8.1

Part	Date	Author	Energy eV/nucleon	Ratio P/He	Composition Normalized to M Nucleii				
					P	α	L	M	H
I	1958	see Hayakawa	$\geqslant 2.5\ 10^{9}$	14.7 ± 1.5	221	15.4	0.33	1	0.33
	1960	Waddington	$> 2.4\ 10^{11}$	17.0 ± 1.8	268	15.8	0.34	1	0.46
	1969	Hayakawa	$\gtrsim 10^{11}$	20.0 ± 2.1	303	15.2	0.27	1	0.33
	1967	Webber	$3.10^{9} - 10^{14}$	17.6 ± 1.2	267	15.2	0.31	1	0.31
II	1970	Shapiro and Silberberg	$10^{9} - 10^{10}$			15.4	0.23	1	0.39
III	1967	Anand	$5.10^{9} - 1.5\,10^{10}$	12.6 ± 0.6					
	1969	Pinkau	$10^{10} - 5.10^{10}$	19.0 ± 7.3					
	1971	Grigorov	$5.10^{10} - 10^{12}$	$20 \pm \sim 2$					
	1971	Ryan	$6.10^{10} - 4\,10^{11}$	10					
	1972	Ryan	$6.10^{10} - 4\,10^{11}$	26.1 ± 3.0					
	1972	Smith	$2.10^{10} - 10^{11}$	12.0 ± 1.5					

TABLE 8.2

Author	N N or N-Nuc.	Neutron initiated reactions give inver-se products of proton initiated reactions			Input Charge Ratios		Pe	Primary Spectrum		Results		Comments
		π's	N's	K's	π's	k's		n : p	γ	Rμ	Eμ	
FRAZER (1972)	N N	Yes	Yes	-	2.02	-	-	13 : 87	2.7	1.56	≫100	Effects of kaon production on pion interaction ignored
GARRAFFO (1973)	N-N (N-Nuc)	Yes	Yes	-	1.70 (1.70)	-	0.66	13 : 87	2.7	independent	1.58 (1.38)	kaons neglected
YEKUTIELI (1972)	N N	Yes	Yes	-	2.16 2.06	-	-	11 : 89 14.5:85.5	2.6 2.7	> 150	1.63 1.56	kaons neglected
	N-Nuc	Yes	Yes	-	1.50 1.50	-	0.87	11 : 89 14.5:85.5	2.6 2.7	> 150	1.25 1.25	Input parameters adjusted to give Rμ = 1.25
MORRISON (1973)	N-Nuc	Yes	Yes	Yes	1.561	2.818	0.565	9.5:90.5	2.7	500	1.285	
THIS WORK	N-N	Yes	Yes	Yes/No	1.755	2.0	0.575	11 : 89	2.7	500	1.468	

APPENDIX 1

ESTIMATIONS OF CHARGE RATIOS, CHARGE EXCESSES AND THEIR ERRORS

If N+ and N- are the numbers of positive and negative muons respectively, each with an error α_+ and α_- respectively, then the resultant error in the charge ratio (αR) has been calculated from the relation

$$\alpha_R^2 = \left(\frac{\partial R}{\partial N+}\right)^2 \alpha_+^2 + \left(\frac{\partial R}{\partial N-}\right)^2 \alpha_-^2 \qquad \ldots \text{(A1)}$$

The usual method of determining αR is to assume the values of $\alpha \pm$ to be $(N^{\pm})^{\frac{1}{2}}$ and to insert these values into the above equation to obtain $\alpha R = R\ (1/N+ \ + \ 1/N-)^{\frac{1}{2}}$.

Consider a sample of N events of which r are in and S are out, of a certain class. Let the probability of an event being in the class be t. Now consider the variable $(^r/N)$.

The mean value of this variable (which is given by mean value = $E\ (^r/N)$ where E denotes expectation) can be shown to be

mean = t.

The variance of the variable (given by $E\left[(^r/N - (E(^r/N))^2\right]$) can be shown to be

variance = t(1-t)/N)

Thus, the best estimate of t, available from the data is

$$t = {}^{r}/N \pm (t(1-t)/N)^{\frac{1}{2}} \qquad \ldots \text{(A2)}$$

An identical expression has been derived by Coxell (1959) in relation to measuring flash tube efficiencies.

Consider now the case where N represents a sample of muons, t is the probability of the muon carrying a positive charge, N+ and N- are the observed numbers of positive and negative muons ($N_+ + N_- = N$) and correspond to r and s respectively. Then from (A2) t is given by

$$t = N_+/N \pm (N_+ N_-/N^3)^{\frac{1}{2}}$$

The total number of positive muons is Nt, i.e.

$$\text{total number} = N_+ \pm (N_+ N_-/N)^{\frac{1}{2}}$$

Thus the error in N+ is $(N_+ N_-/N)^{\frac{1}{2}}$ and not $(N_+)^{\frac{1}{2}}$ as previously used. A similar procedure yields an identical value for the error in N-.

The charge ratio is given by

$$R = \frac{N_+ \pm (N_+ N_-/N)^{\frac{1}{2}}}{N_- \pm (N_+ N_-/N)^{\frac{1}{2}}} \qquad \ldots \text{(A3)}$$

The errors on the numbers of charged particles are equal and symmetrical. This arises because N+ and N- are related via the sample size N. This relation prohibits the direct use of (A1) on (A3). Re-writing eqn (A3) as $R = N/N_- - 1.0$ and applying (A1) yields

$$\alpha_R = R\sqrt{{}^{1}/N_+ + {}^{1}/N_-}$$

which is identical to the previously assumed value.

Considering now the charge excess

$$\delta = (N+ - N-)/(N_+ + N-) \qquad \ldots \text{(A4)}$$

The usual procedure of taking $\alpha_\pm = (N^\pm)^{\frac{1}{2}}$ and applying (A1) gives

$$\alpha_\delta = (^2/N^2)\,(N-\,N+^2 + N-^2\,N+)^{\frac{1}{2}}$$

Following the same procedure as for R yields an expression for α_δ which is identical to the above.

To summarise

$$R = {}^{N+}/N- \pm R\,(^1/N+ + {}^1/N-)^{\frac{1}{2}}$$

$$\delta = (N+ - N-)/(N+ + N-) \pm (^2/N2)\,(N-\,N+^2 + N-^2\,N+)^{\frac{1}{2}}$$

Attention will now be given to the subject of obtaining the best estimates of the charge ratios and excesses, given data for positive and negative field directions. Let I+ and I- be the rates of positive and negative particles (then the true charge ratio $R_T = I+/I-$); let t+, t- be the times of data collection with positive and negative magnetic fields respectively; let $A+^+$ and $A+^-$ be the acceptances of positive and negative particles with a positive magnetic field and $A-^+$, $A-^-$ be the analagous quantities for a negative magnetic field.

If the data for both field directions were summed, then the estimate of the charge ratio would be

$$R_1 = (I+\,t+\,A+^+ + I+\,t-\,A-^+)/(I-\,t+\,A+^- + I-\,t-\,A-^-)$$

i.e. $R_1 = R_T\,(t+\,A+^+ + t-\,A-^+)/(t+\,A+^- + t-\,A-^-)$

or $R_1 = R_T(N+^+ + N-^+)/(N-^+ + N-^-)$ say where the numbers of positive and negative particles collected with positive and negative magnetic fields are denoted $N+^+$,

$N+^{-}$, $N-^{+}$, $N-^{-}$ respectively. Since data were collected with unequal values of t+ and t− then R_1 is a biased estimate of R_T. In the data reported in this work t+ and t− differed by 1.8% in the worst case (series 8).

If the charge ratios measured with positive and negative field directions are denoted R+ and R− respectively then

$$R+ = R_T\, A+^{+}/A+^{-} \quad \text{and} \quad R- = R_T\, A-^{+}/A-^{-}.$$

To a good degree of approximation $A+^{+} = A-^{-}$ and $A+^{-} = A-^{+}$. Thus the quantity R_2 given by

$$R_2 = (R+\; R-)^{\frac{1}{2}}$$

is an unbiased estimate of the charge ratio,

Consider now the charge excess; let $\delta+$ and $\delta-$ be the excesses measured with positive and negative magnetic fields, then

$$\delta+ = (N+^{+} - N+^{-})/(N+^{+} + N+^{-}) \quad \text{and}$$
$$\delta- = (N-^{+} - N-^{-})/(N-^{+} + N-^{-})$$

If $\delta 1$ is the estimate of the true excess δT obtained by summing the data for both field directions :-

$$\delta 1 = (N+^{+} + N-^{+} - N+^{-} - N-^{-})/(N+^{+} + N-^{+} + N+^{-} + N-^{-})$$

i.e. $\delta 1 = (I+ - I-)/(I+ + I-)$

thus $\delta 1$ is an unbiased estimate of δ_T.

APPENDIX 2

R.U.D.I. BOARD DESCRIPTIONS

As seen from the overall block diagram in Chapter 3, R.U.D.I. is composed of 20 sections labelled A-T. These sections are built on 19 circuit boards, sections I and J sharing a board.

The order in which the boards are mounted in the instrument is, facing R.U.D.I. and reading from left to right :

A B C D E F I/J G H M N K L O P Q R S T.

Logic diagrams and very brief descriptions of each section are given in this Appendix. The currents given in brackets are those taken by the logic circuitry (from the 6v. power supply) when the board is in isolation from all others and all inputs are floating.

Board A (120 mA)

The functions of this board are :-

(i) to shape the clock and initial reset pulses.

(ii) to generate the arithmetic pulse, the display pulse, the PHA store pulse and the DM160 'stored' pulse. The delay of 750 µs. in the arithmetic and display pulse circuits is arbitrary and can be reduced if needed to a value $\gtrsim$ 40 µs.

Board B (185 mA)

This board determines :-

(i) the arrival order of the discharged cells from the shift registers A, B, C and

(ii) whether or not at least 1 bit has arrived from each shift register.

The board requires 3 inputs (one from each shift register) and for (i) there are 9 outputs, namely

A first, second or last
B ditto
C ditto

while for (ii) there are 3 outputs.

(i) There are 9 flip-flops on the board and they are arranged as shown below :

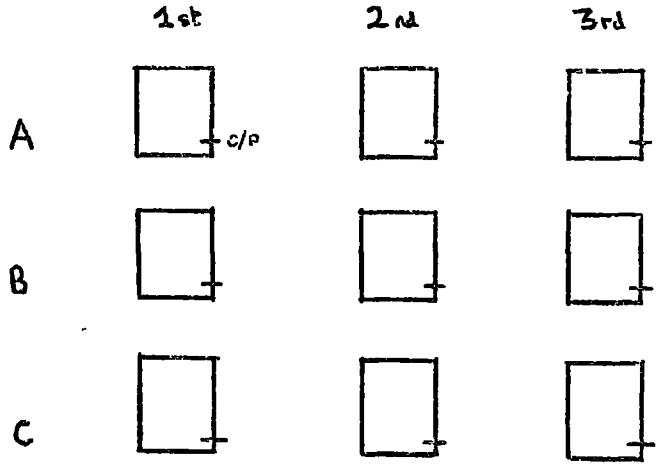

After reset, all flip-flop outputs are logical 1 and clock pulses may enter the left-hand column. A negative going edge from one or more of the shift registers sets a flip-flop in this column to logical 0 and after a delay (T_D) of 0.3 us closes G1 and opens G4 (see logic diagram of board B) thus steering clock pulses to the centre column. The next negative edge from the shift registers sets a flip-flop in the centre column to logical 0, closes G2 and opens G5. A third negative edge sets a flip-flop in the right hand column to logical 0 and shuts G3. From the diagram it can be seen that the width of the clock pulse must be less then the value of T_D.

(ii) The outputs of the 3 flip-flops associated with level A are gated and in the reset state the gate output is logical 0. When any one, any two or all 3 flip-flops change state this output goes to logical 1 indicating at least 1 discharged cell in the level. Similarly for levels B,C.

Board C (100 mA)

The functions of this board are :-

(i) to determine that either no cells or only 1 cell has been discharged in each shift register.

(ii) to define a 'satisfactory' event

(i) After reset, each flip-flop output is a logical 1 and the first discharged cell from, say, level A alters the state of flip-flop no. 1 only; a second discharged cell alter flip-flops 2 and 3. Further discharged cells have no effect on flip-flop 3. The outputs of the third flip-flops associated with each level A, B, C are fed to a gate. If either no cells or only 1 cell has been discharged at each level then these 3 inputs to the gate are all at logical 1.

(ii) If at least one cell has been discharged at each level then the inputs 1a, 1j, 1k (which come from board B) are all at logical 1. Under these conditions the remaining input to the gate, the inverted arithmetic pulse, is transmitted and becomes the satisfactory event pulse indicating one and only one discharged cell in each level.

Board D (65 mA)

This board determines :-

(i) the add or subtract instruction and

(ii) the muon sign, assuming a positive magnetic field.

The 9 inputs are the arrival orders from board B.

(i) The rule derived in Chapter 3 was :

if B is first or last - add

if B is second - subtract.

The logic circuitry required to obey this rule is quite simple and is shown in the diagram.

(ii) Except for arrival orders A, B, C and C, B, A the particle sign may be deduced from the rules given in Chapter 3 and again the logic diagram is straightforward.

For the arrival orders A, B, C, C, B, A the sign is indeterminate and must be given as (+ or -). Two outputs of this type are produced, one associated with arrival A, B, C and the other with order C, B, A. This ambiguity of sign is resolved on board E.

Board E (50 mA)

The functions of this board are :-

(i) to test the add/subtract instruction for ambiguity and

(ii) to give an unambiguous indication of the muon sign again assuming a positive magnetic field.

(i) (a) In the case of ambiguity of sign the add/subtract instruction should be subtract. This instruction is combined with each of the 2 outputs indicating the ambiguity. From the logic diagram it can be seen that the output of this combination is a logical 1 only if : the subtract instruction is present (a logical 1) and one of the ambiguity inputs is also a logical 1.

(b) If the particle sign is not ambiguous the add/subtract instruction should be add and combining this with the μ^+ and μ^- outputs from board D, as shown in the diagram, gives an output of logical 1 only if : the add instruction is a logical 1 and one of the muon sign inputs is a logical 1.

(c) Parts (a) and (b) are combined in such a way that the resulting output is a logical 1 only if their associated outputs are different.

(ii) As explained in chapter 3 the ambiguity of sign may be resolved by considering the 'carry 1' output of the binary adder. This is achieved as shown in the diagram.

<u>Board F</u> (145 mA)

This board generates the logic levels controlling the scalers A,B and B,C. In the reset condition the 2 outputs of the board are at logical 0.

Board I/J (130 mA)

The functions of section I are :-

(i) to determine the apparent arrival direction. The required inputs are the arrival orders from only the upper two shift registers (a total of 6 inputs).

(ii) to modify the result of (i) according to whether the left or right hand side of the spectrograph was triggered.

(iii) to ensure that the finally indicated arrival direction is unambiguous i.e. only one of the East or West outputs is a logical 1.

The functions of section J are :-

(i) to incorporate the true magnetic field direction into the determination of muon sign. Three inputs (from outside R.U.D.I.) are required to define the true field direction as +, - or zero. In the case of zero magnetic field the logic generates the same answer as a positive field.

(ii) to ensure that the finally indicated muon sign is unambiguous i.e. only one of the μ^+, μ^- outputs is a logical 1.

Board G (245 mA)

This board contains the scalers A,B and B,C. The logic circuitry of the scalers is standard (it may be found in the appropriate technical handbook) and only a rather schematic diagram is shown in this Appendix.

Board H (335 mA)

This board contains the binary adder which again is a standard circuit (Mullard Handbook - Integrated Logic Circuit Applications, page 101). The add/subtract decision made on board D is combined with the system of gates on the inputs to the adder, as shown in the diagram, to decide whether the operation performed is (AB + BC) or (AB + BC) (where + denotes the logical AND operation). The output of the binary adder is displayed on the front panel of R.U.D.I.

Board M (70 mA)

The purpose of this board is to reduce the output of board H to a number between 0 and 23, inclusive. Any number from board H which ≥ 23 is converted to 23.

Board N (120 mA)

This board converts the binary output of board M to binary coded decimal (BCD). The logic circuit is straightforward.

Board K (45 mA)

The function of this board is to determine which class of apparent zenith angle, East/West apparent arrival direction and sign that a triggering event is to be allocated. Since there are 4 classes of apparent zenith angle this board generates 16 outputs. The class of apparent zenith angle is found by considering the output of scaler AB. The circuit again is straightforward.

Board L (105 mA)

Using the output of board K, this board generates a code number depending upon the class to which the triggering event has been assigned. The output is in BCD.

Board O (275 mA)

This board contains a BCD adder which adds the reduced deflection of the particle (from board H via board M) to its code number (from board L). This gives the BCD form of the required address in the PHA. The circuitry of the adder is standard.

Board P (135 mA)

This board converts the BCD output of board O to decimal form. This is the decimal form of the PHA address.

Board Q (290 mA)

The functions of this board are :-

(i) to store the output of board P for display (via boards R,S) and

(ii) to display the muon sign produced by board E.

The board may be reset using the micro-switch on the front panel (this results in a blank display in the units position of the P.H.A. address).

Boards R,S

The circuits on these boards are used to drive the numerical indicator tube display. The inputs to the boards arethe decimal form of the P.H.A. address from board Q.

Board T

The purpose of the circuitry on this board is :-

(i) to convert the logical voltage levels of R.U.D.I. to those used by the P.H.A. These levels are :-

R.U.D.I. Logic			P.H.A. Logic
1	:	+ 6v	-6v or more negative
0	:	0v	+0.5v or more positive

The required inputs (10 of them) are the BCD form of the P.H.A. address from board O.

(ii) to generate, from the store pulse of board A, a store pulse acceptable to the P.H.A. The requirements of the latter are that its amplitude should be +7 - +10v, rise time $< 0.5\mu s$ and width $> 15\ \mu s$.

Other Information

1. When in operation R.U.D.I. draws 2.35A from the 6v power supply.

2. The rear panel connections are :-

Label	Connection
C	Level C
B	Level B
A	Level A
R	RHS trigger mode
L	LHS trigger mode
BN	Negative magnetic field
BP	Positive magnetic field
BO	Zero magnetic field
Clock	Clock input
PHA	PHA store pulse output

3. The power supply connections are :-

Socket	Label	Connection
Lower (Yellow)	A	+ 170v
	B	- 8.2v
	C	+ 6v
	D	+ 15.5v
	E	Common
	F	- (15.5v)
Upper	A	+ 40v
	B	- (40v)
	C	f + } 1v a.c.
	D	f -
	E	+ } feedback on 6v supply
	F	-

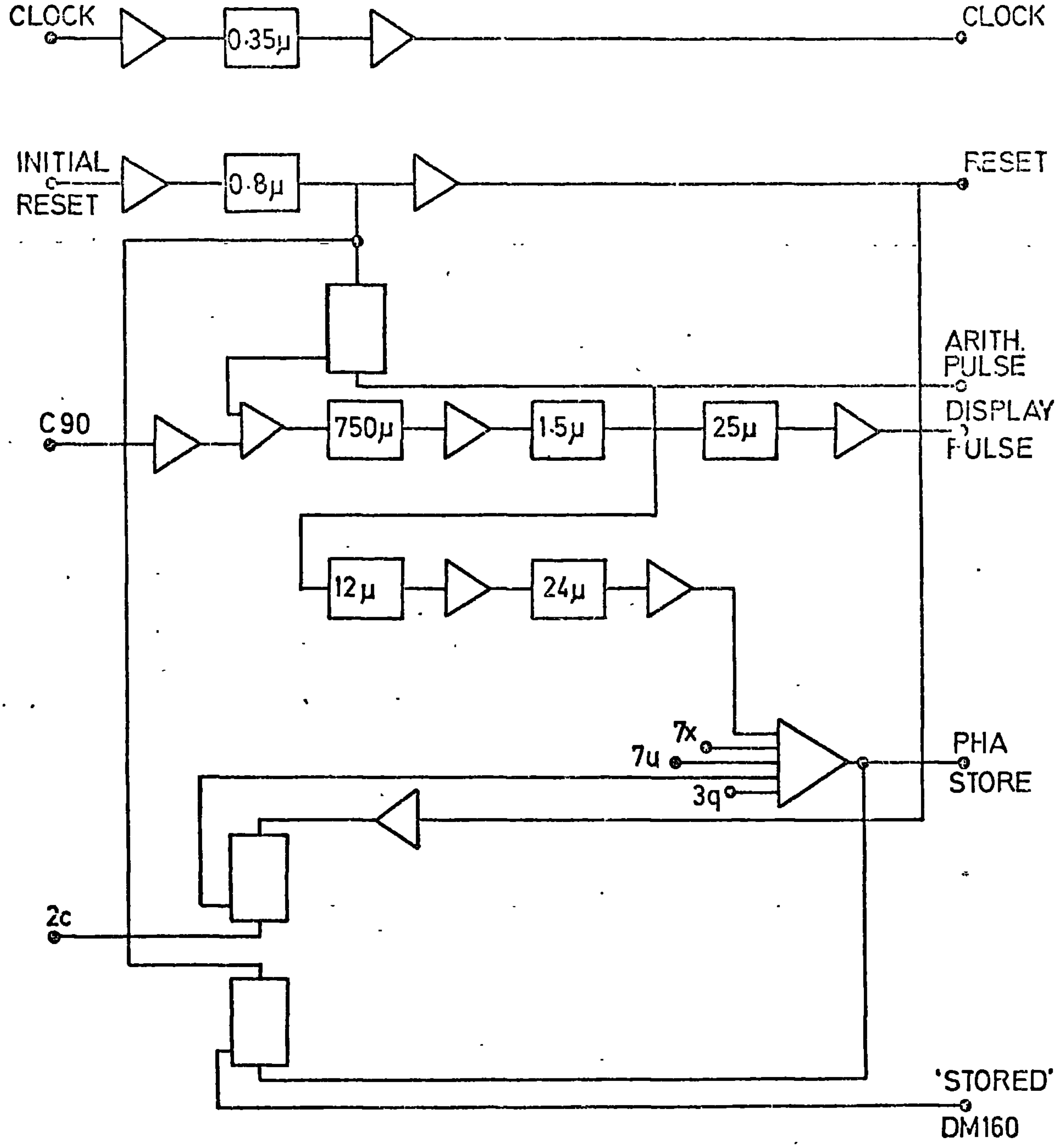
CLOCK
0·35μ
CLOCK
INITIAL RESET
0·8μ
RESET
ARITH. PULSE
C90
750μ
1·5μ
25μ
DISPLAY PULSE
12μ
24μ
7x
7u
3q
PHA STORE
2c
'STORED'
DM160

BOARD A

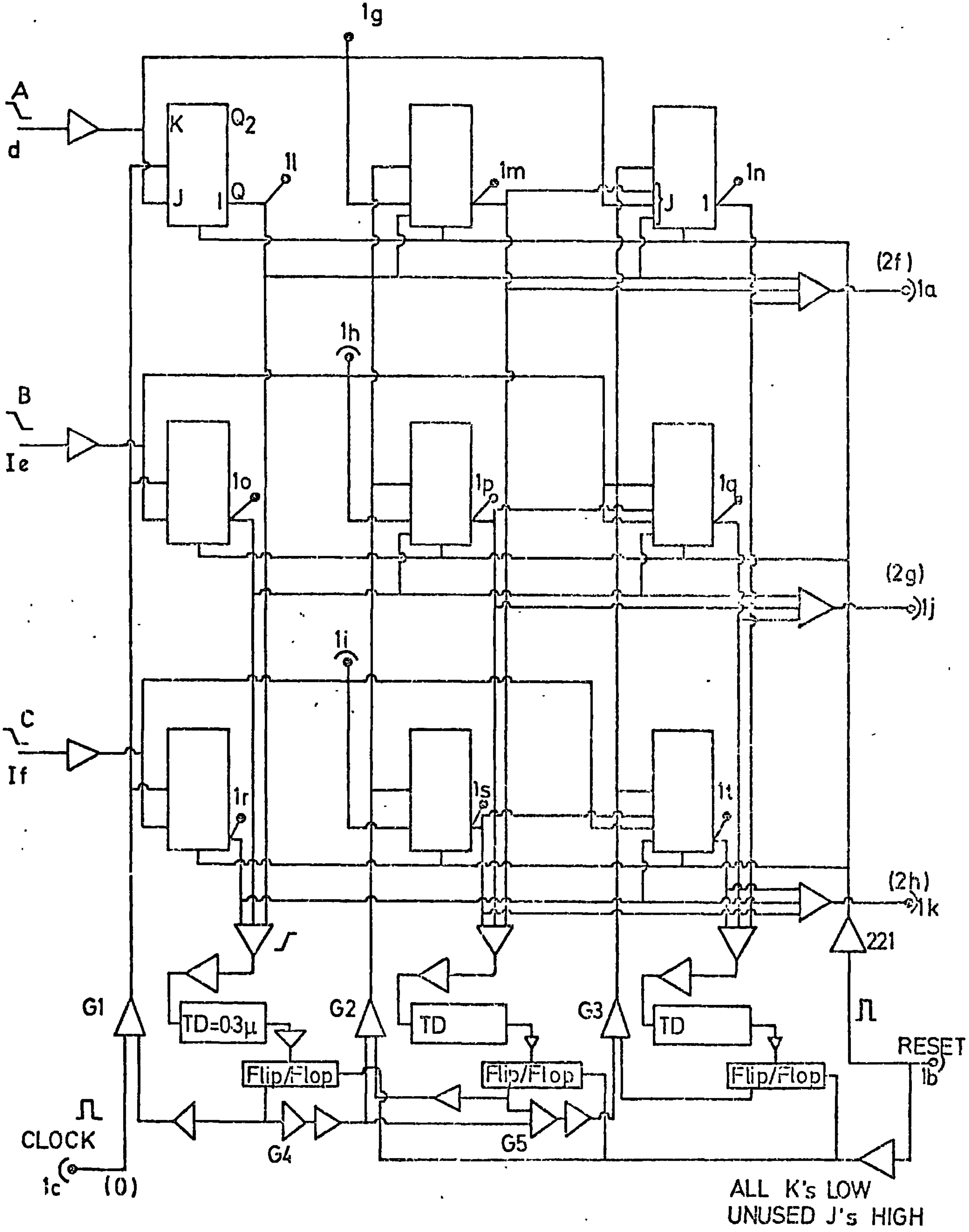

ALL K's LOW
UNUSED J's HIGH

BOARD B.

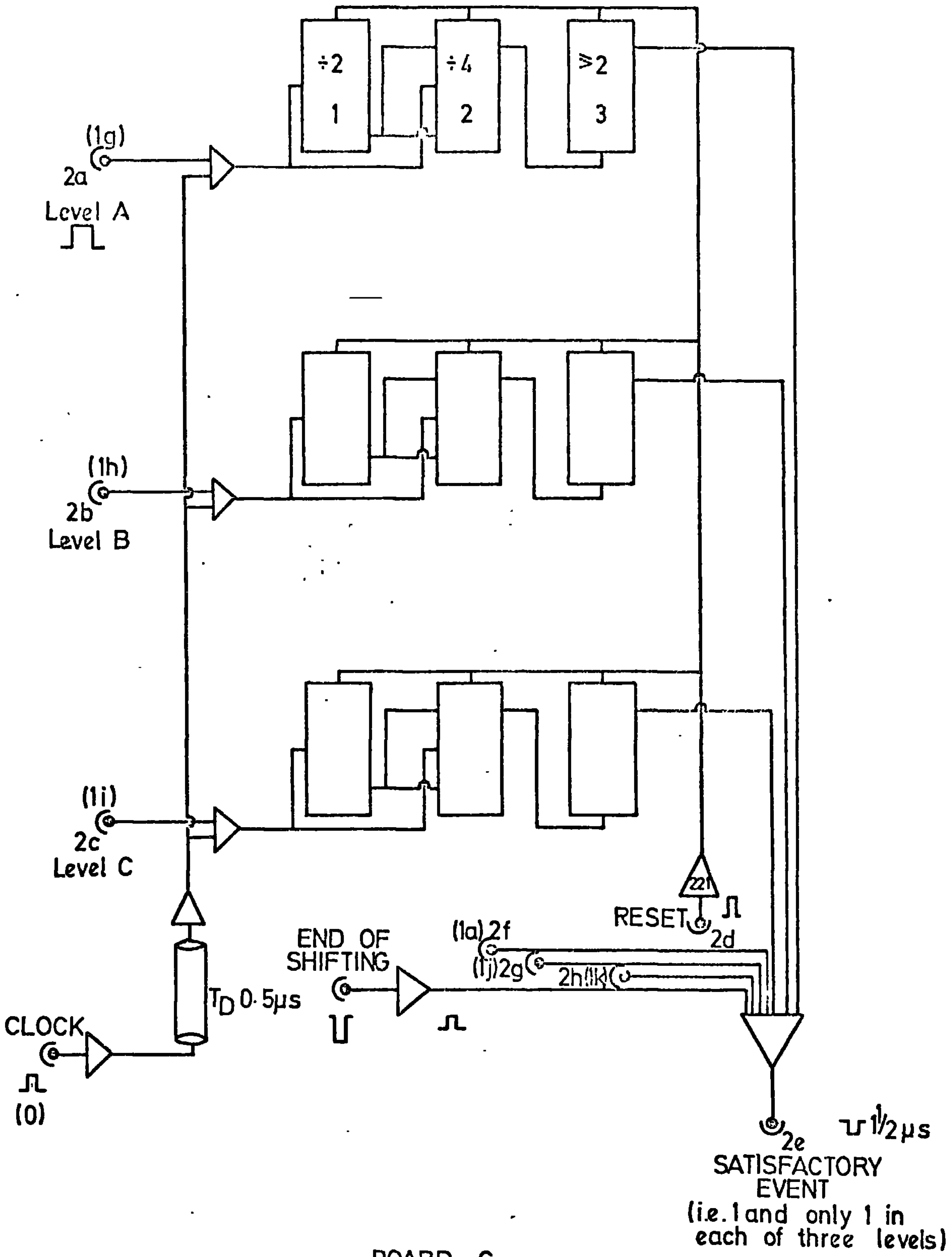
÷2
1
÷4
2
≥2
3
(1g)
2a
Level A
(1h)
2b
Level B
(1i)
2c
Level C
T_D 0·5μs
CLOCK
(0)
END OF SHIFTING
(1a) 2f
(1j) 2g
2h (1k)
221
RESET
2d
2e
1½ μs
SATISFACTORY EVENT
(i.e. 1 and only 1 in each of three levels)

BOARD C

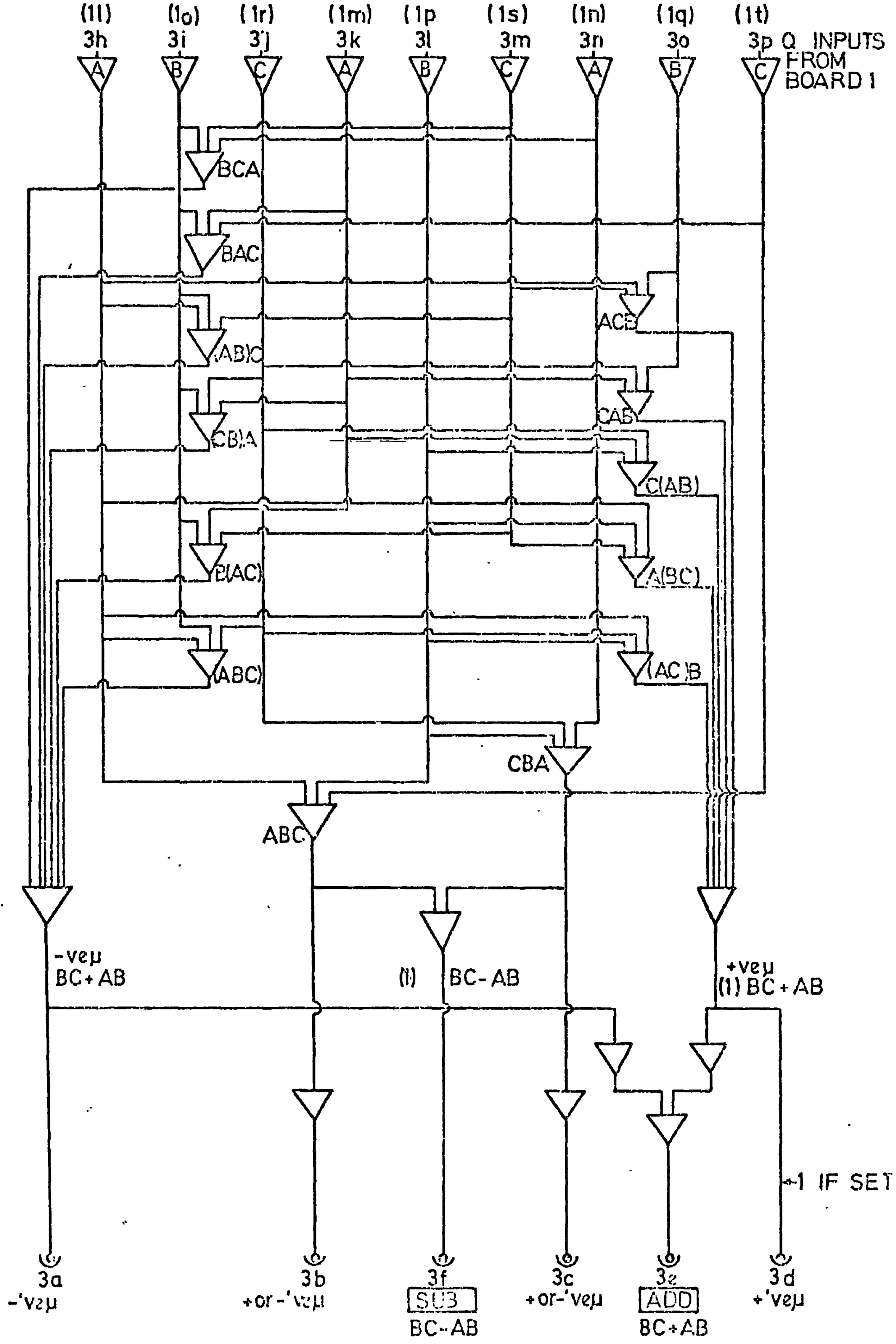
(1l)
3h
(1o)
3i
(1r)
3j
(1m)
3k
(1p
3l
(1s)
3m
(1n)
3n
(1q)
3o
(1t)
3p
Q INPUTS FROM BOARD 1
A
B
C
A
B
C
A
B
C
BCA
BAC
ACB
(AB)C
CAB
(CB)A
C(AB)
B(AC)
A(BC)
(ABC)
(AC)B
CBA
ABC
-veμ
BC+AB
(1)
BC-AB
+veμ
(1) BC+AB
←1 IF SET
3a
-'veμ
3b
+or-'veμ
3f
SUB
BC-AB
3c
+or-'veμ
3e
ADD
BC+AB
3d
+'veμ

BOARD D

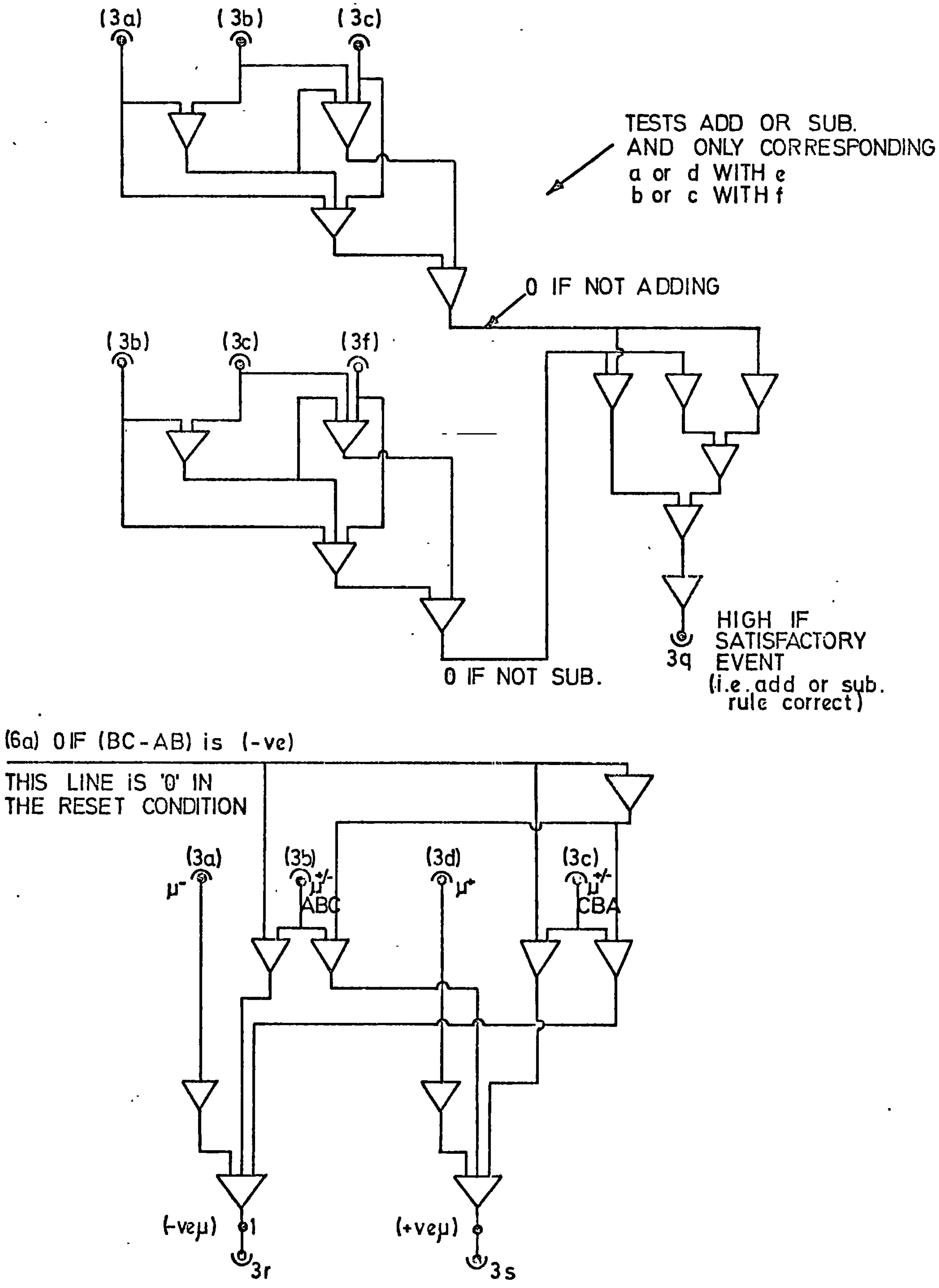
(3a)
(3b)
(3c)
TESTS ADD OR SUB.
AND ONLY CORRESPONDING
a or d WITH e
b or c WITH f
0 IF NOT ADDING
(3b)
(3c)
(3f)
0 IF NOT SUB.
3q
HIGH IF
SATISFACTORY
EVENT
(i.e. add or sub.
rule correct)
(6a) 0 IF (BC-AB) is (-ve)
THIS LINE IS '0' IN
THE RESET CONDITION
(3a)
μ-
(3b)
μ+/-
ABC
(3d)
μ+
(3c)
μ+/-
CBA
(-veμ)
1
3r
(+veμ)
3s

BOARD E

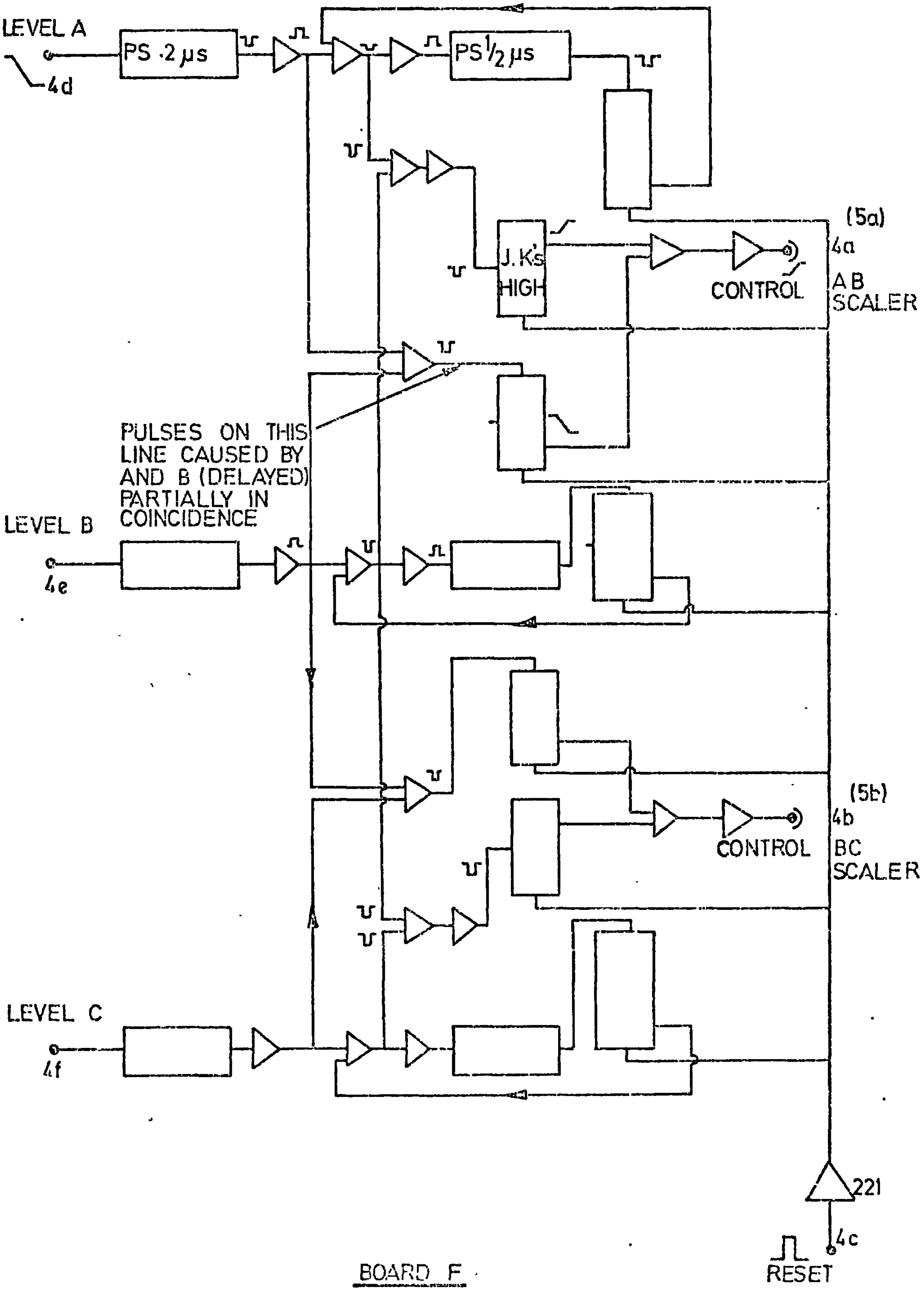
LEVEL A
4d
PS ·2 μs
PS 1/2 μs
J. K's HIGH
(5a)
4a
CONTROL
A B SCALER
PULSES ON THIS LINE CAUSED BY AND B (DELAYED) PARTIALLY IN COINCIDENCE
LEVEL B
4e
(5b)
4b
CONTROL
BC SCALER
LEVEL C
4f
221
4c
RESET

BOARD F

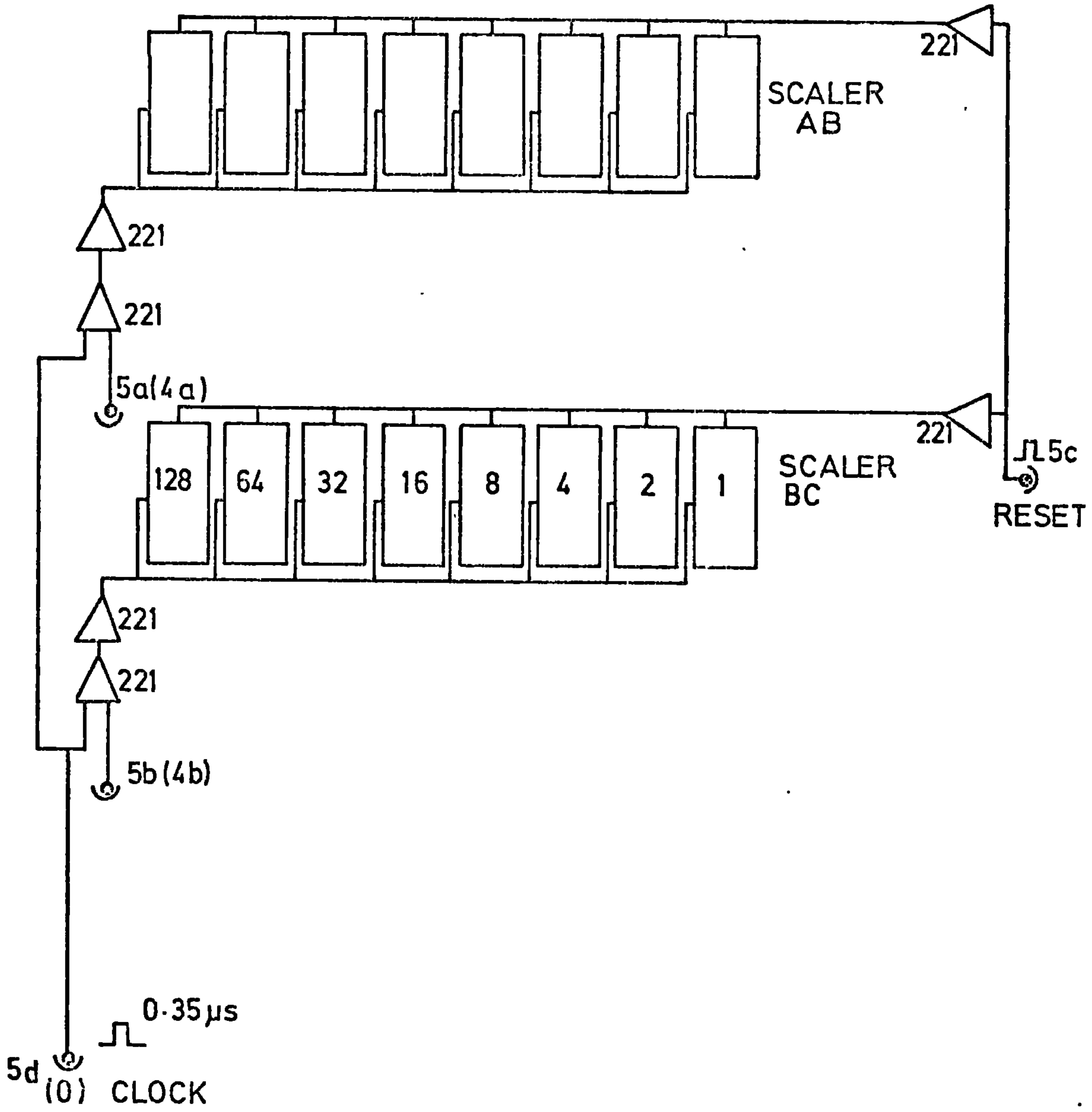
221
SCALER AB
221
221
5a(4a)
221
128
64
32
16
8
4
2
1
SCALER BC
5c
RESET
221
221
5b (4b)
0·35 μs
5d (0) CLOCK

BOARD G

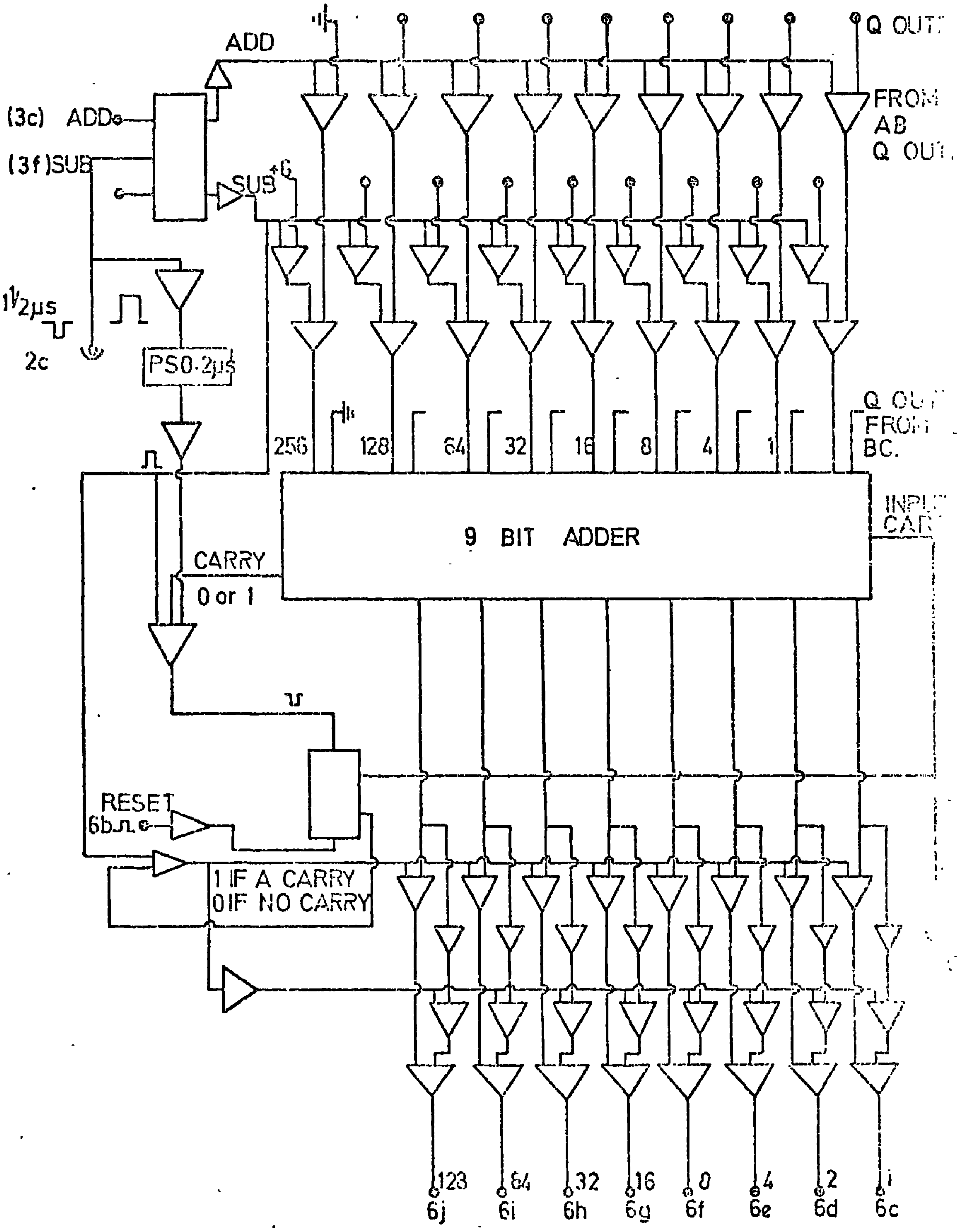
Q OUT
ADD
FROM
AB
Q OUT
(3c) ADD
(3f) SUB
SUB
+6
1½μs
2c
PS0·2μs
256
128
64
32
16
8
4
1
Q OUT
FROM
BC.
9 BIT ADDER
INPUT
CARRY
CARRY
0 or 1
RESET
6b
1 IF A CARRY
0 IF NO CARRY
128
6j
64
6i
32
6h
16
6g
8
6f
4
6e
2
6d
1
6c

BOARD H

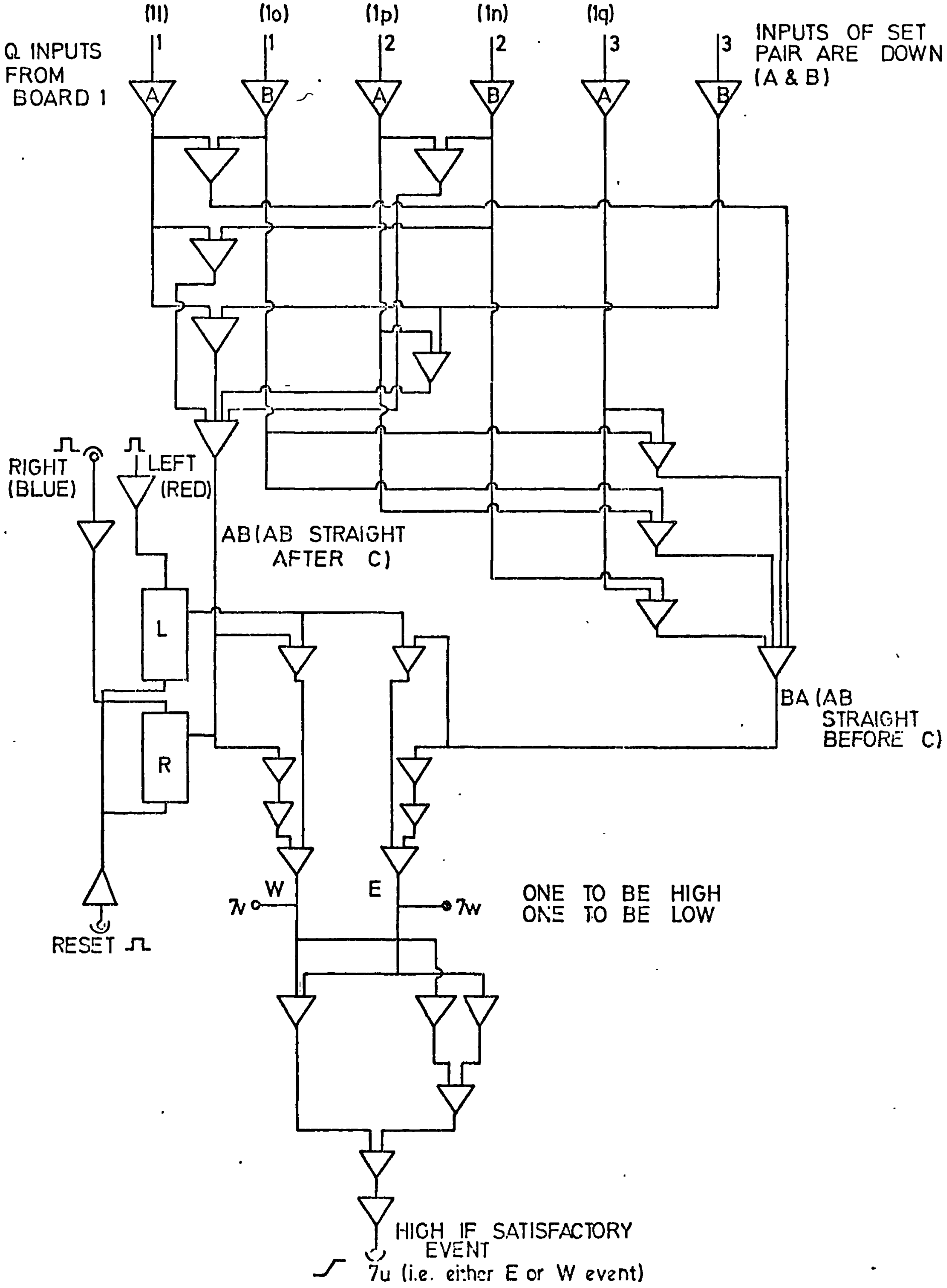
(1l)
(1o)
(1p)
(1n)
(1q)
Q INPUTS FROM BOARD 1
1
1
2
2
3
3
INPUTS OF SET PAIR ARE DOWN (A & B)
A
B
A
B
A
B
RIGHT (BLUE)
LEFT (RED)
AB (AB STRAIGHT AFTER C)
L
R
BA (AB STRAIGHT BEFORE C)
W
E
7v
7w
ONE TO BE HIGH
ONE TO BE LOW
RESET
HIGH IF SATISFACTORY EVENT
7u (i.e. either E or W event)

BOARD I

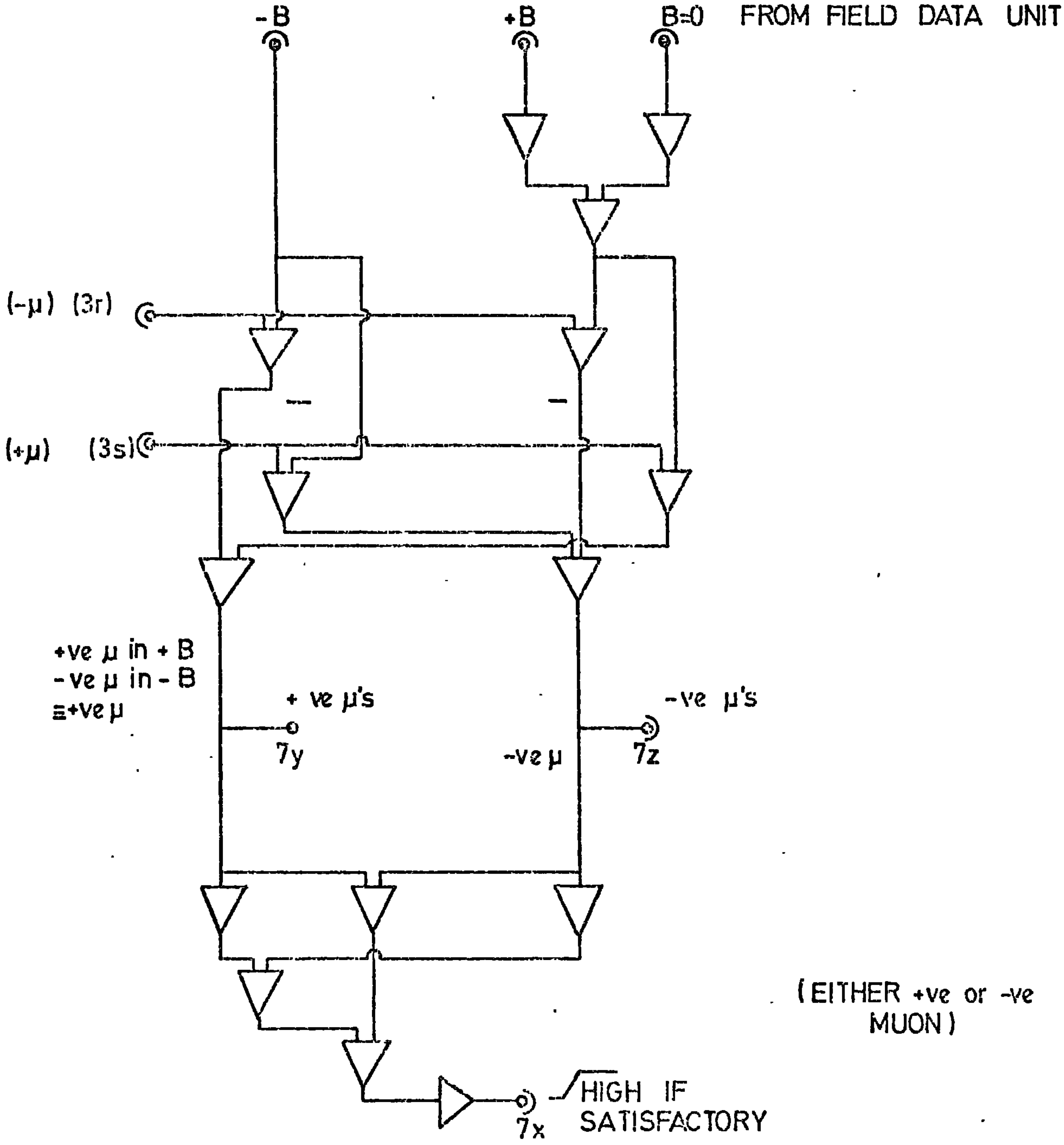
-B
+B
B=0
FROM FIELD DATA UNIT
(-μ) (3r)
(+μ) (3s)
+ve μ in + B
-ve μ in - B
≡+ve μ
+ ve μ's
7y
-ve μ's
-ve μ
7z
(EITHER +ve or -ve
MUON)
7x
HIGH IF
SATISFACTORY

BOARD J

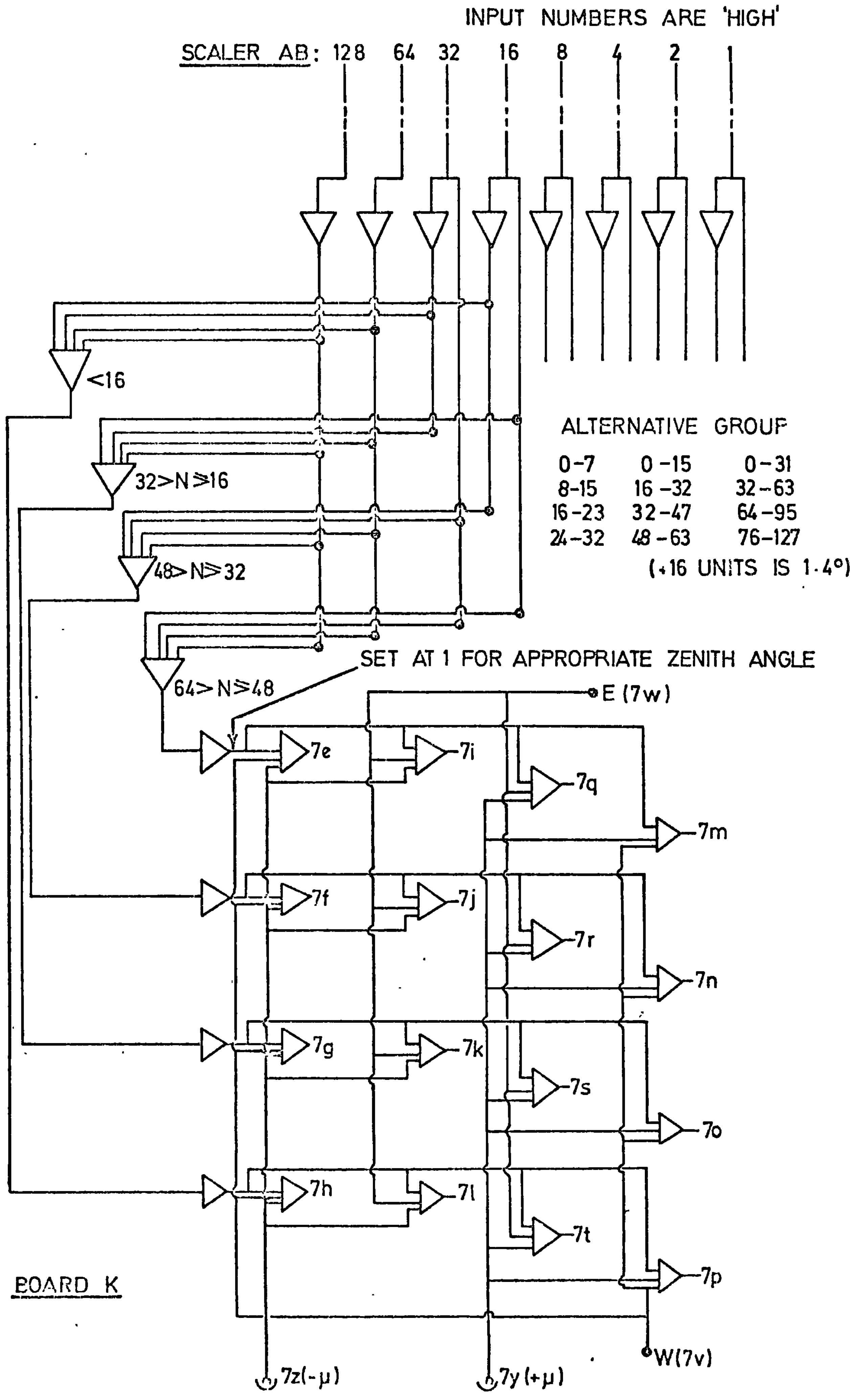

ALTERNATIVE GROUP

0-7	0-15	0-31
8-15	16-32	32-63
16-23	32-47	64-95
24-32	48-63	76-127

(+16 UNITS IS 1·4°)

BOARD K

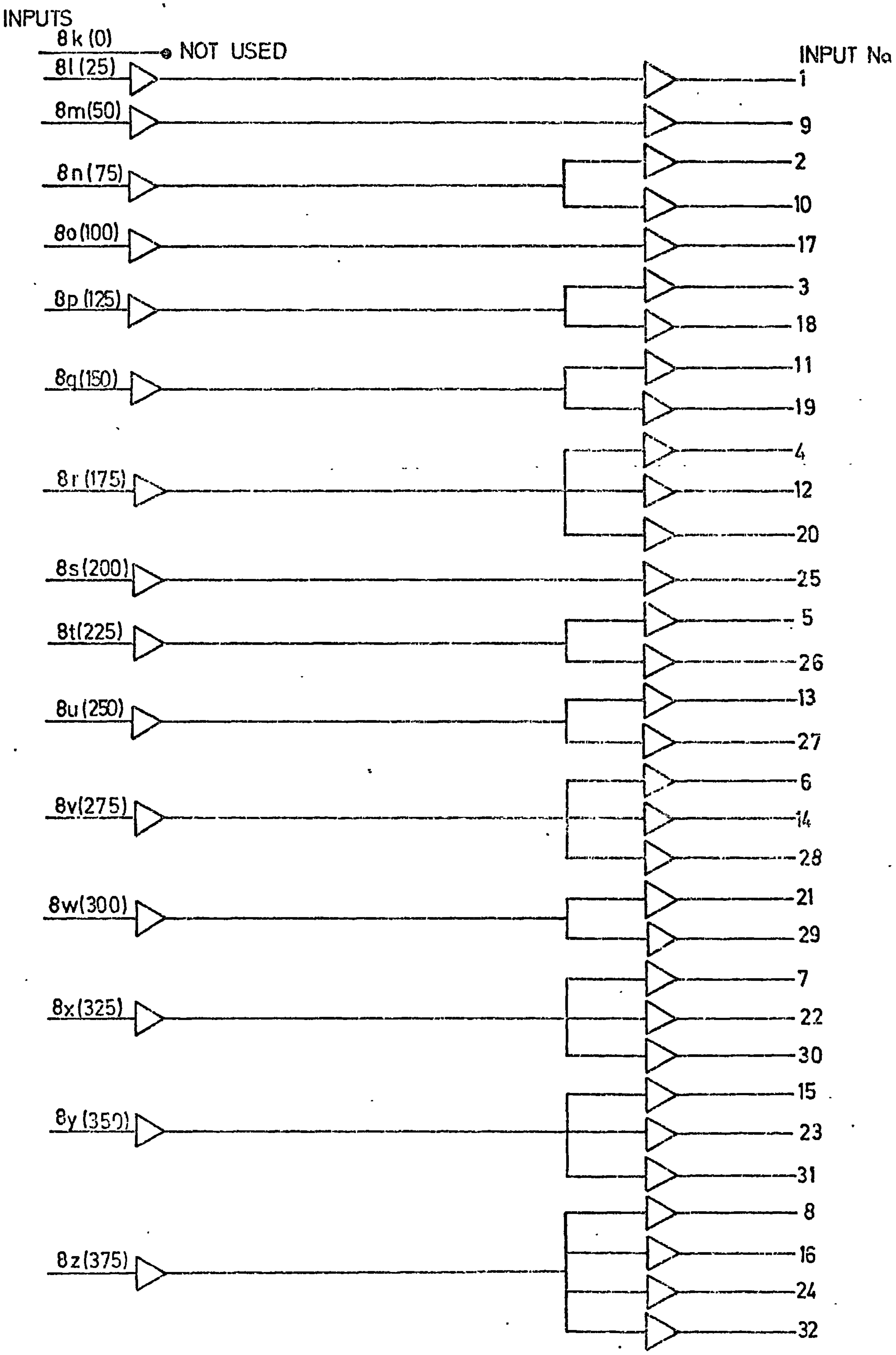

BOARD L

(sheet 1 of 2)

These nos. are the I/P's to 4 8-fold gates on next page.

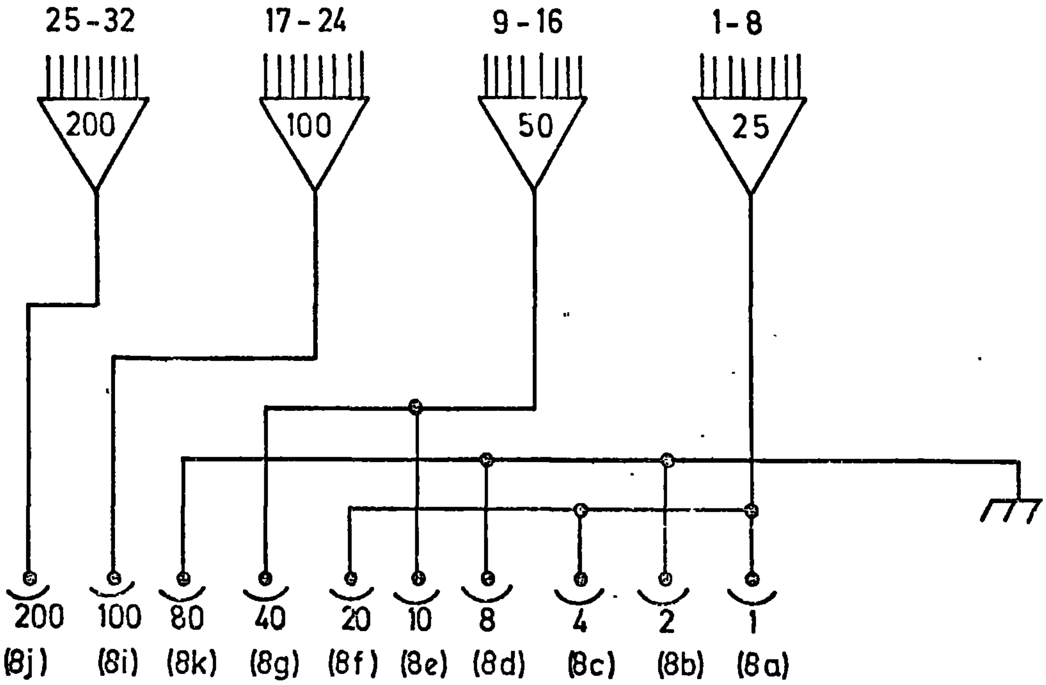

OUTPUT

BOARD L

(sheet 2 of 2)

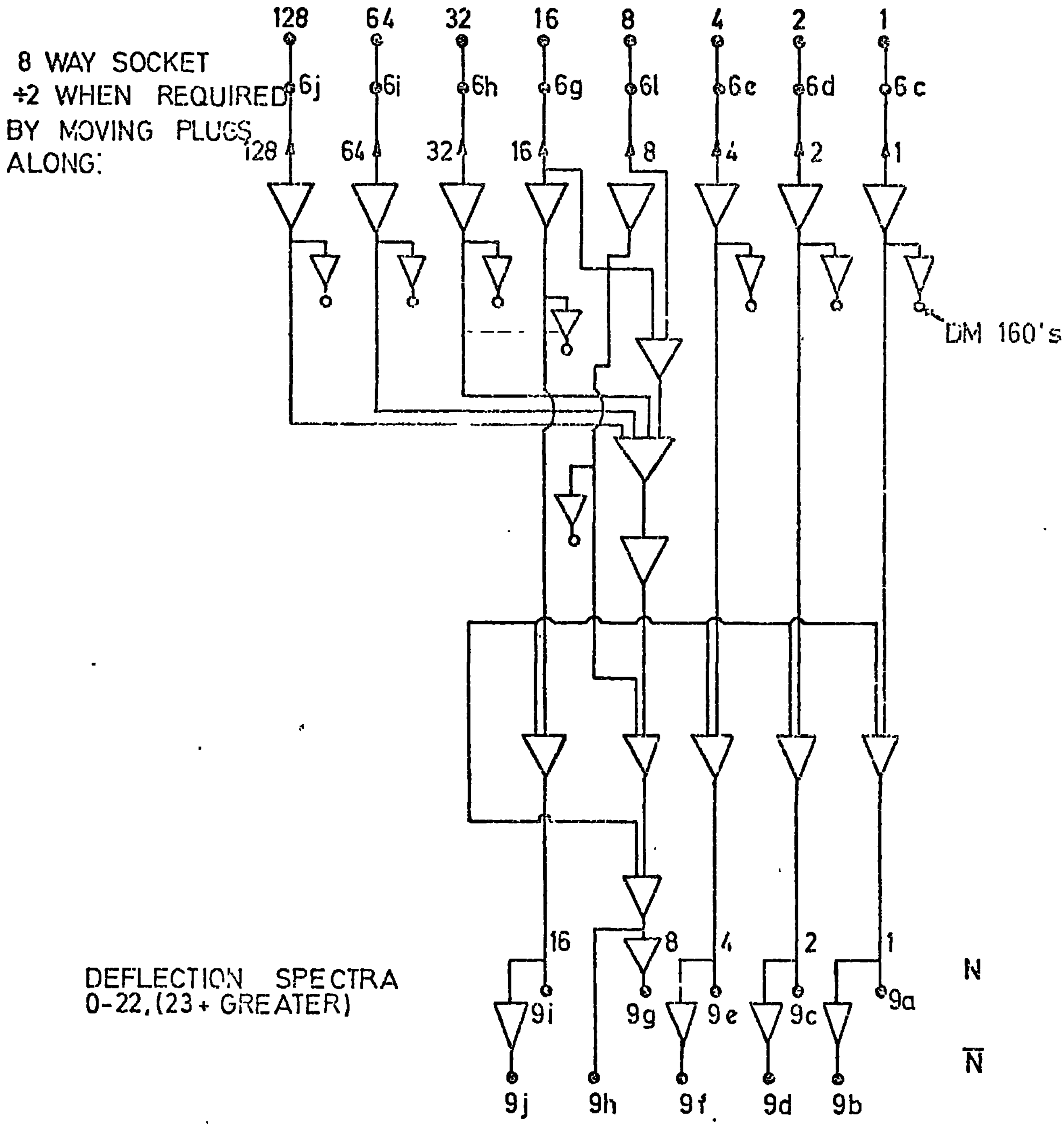
128
64
32
16
8
4
2
1
8 WAY SOCKET
÷2 WHEN REQUIRED
BY MOVING PLUGS
ALONG:
6j
6i
6h
6g
6f
6e
6d
6c
128
64
32
16
8
4
2
1
DM 160's
16
8
4
2
1
N
DEFLECTION SPECTRA
0-22, (23 + GREATER)
9i
9g
9e
9c
9a
N̄
9j
9h
9f
9d
9b

BOARD M

LETTERS REPRESENT THE FOLLOWING INPUTS

a	b	c	d	e	f	g	h	i	j
1	$\overline{1}$	2	$\overline{2}$	4	$\overline{4}$	8	$\overline{8}$	16	$\overline{16}$

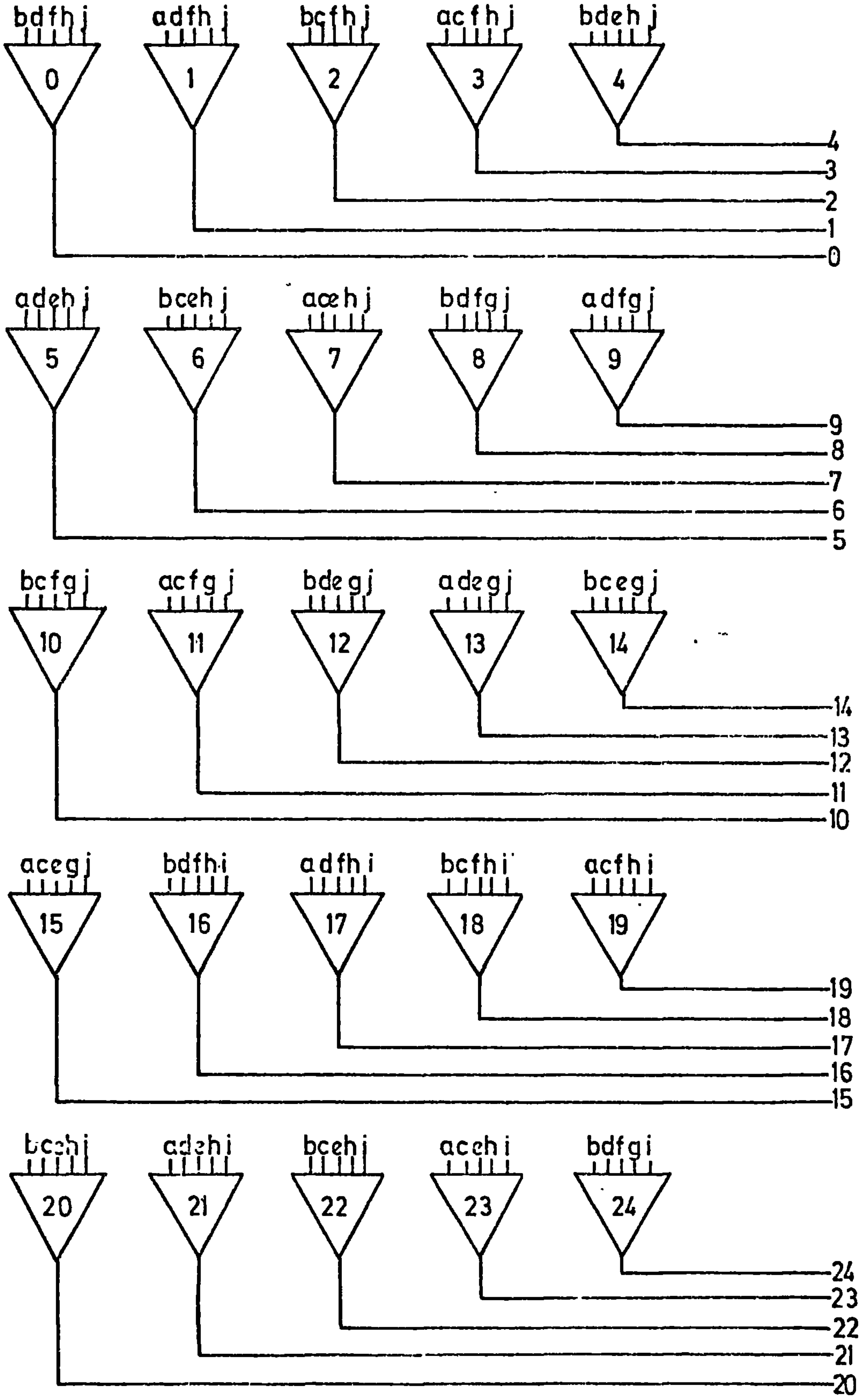

BOARD N

(sheet 1 of 2)

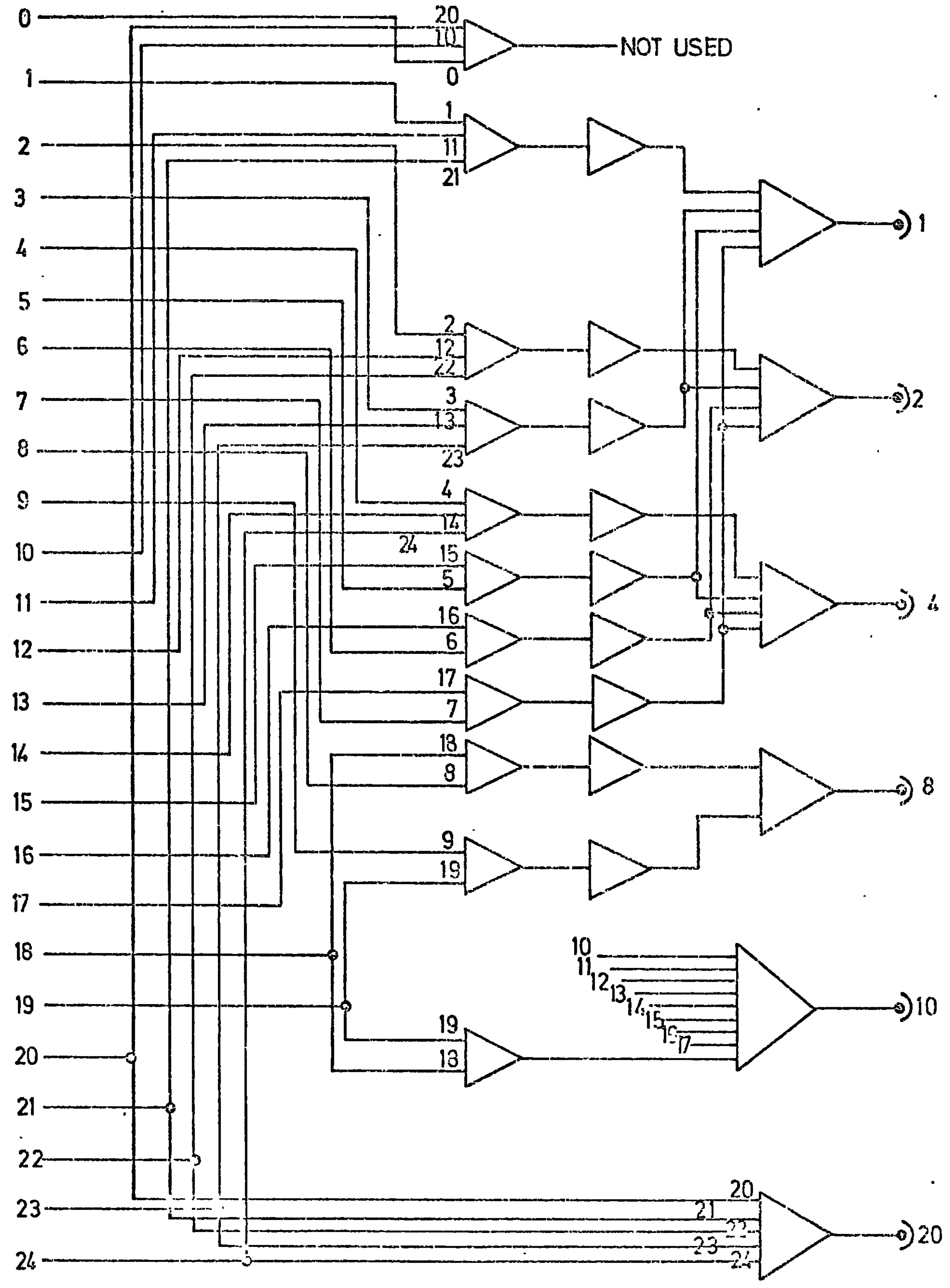

BOARD H
(sheet 2 of 2)

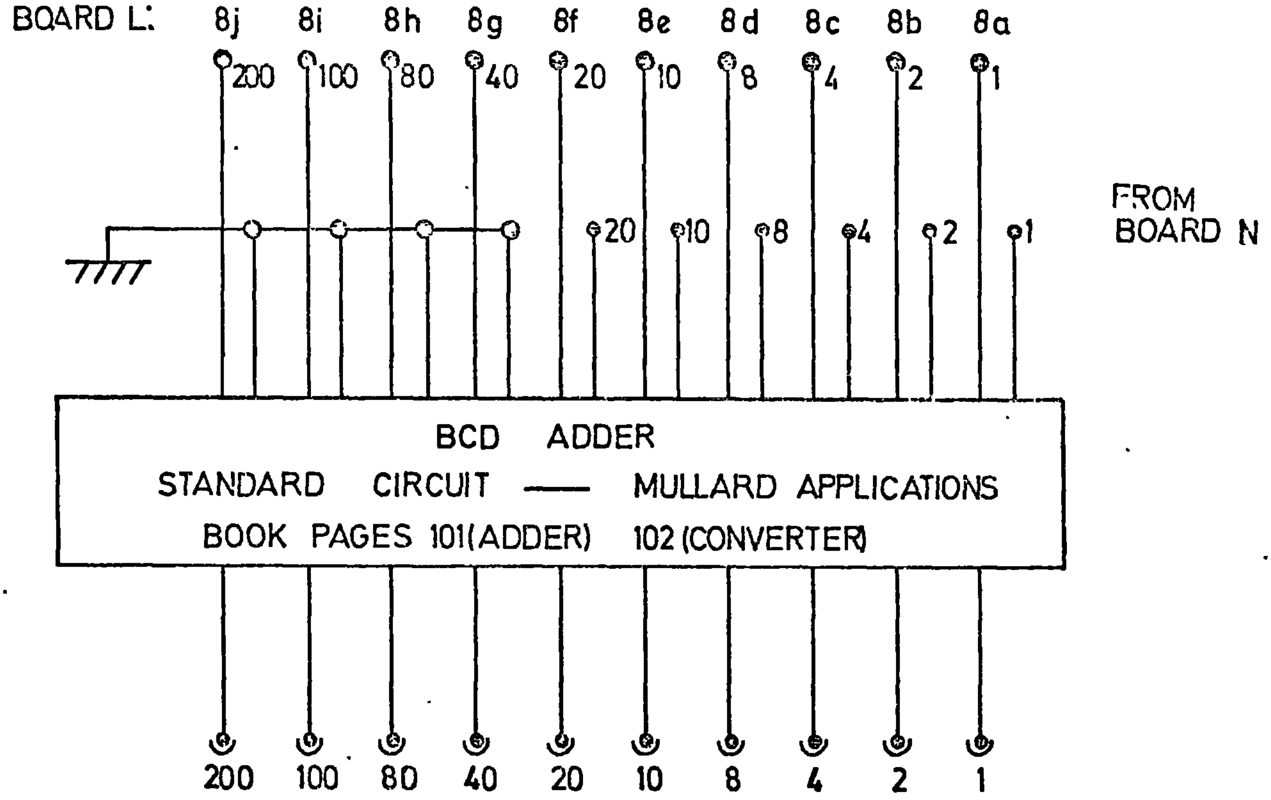
BOARD L:
8j
8i
8h
8g
8f
8e
8d
8c
8b
8a
200
100
80
40
20
10
8
4
2
1
FROM BOARD N
20
10
8
4
2
1
BCD ADDER
STANDARD CIRCUIT —— MULLARD APPLICATIONS
BOOK PAGES 101(ADDER) 102 (CONVERTER)
200
100
80
40
20
10
8
4
2
1

BOARD O

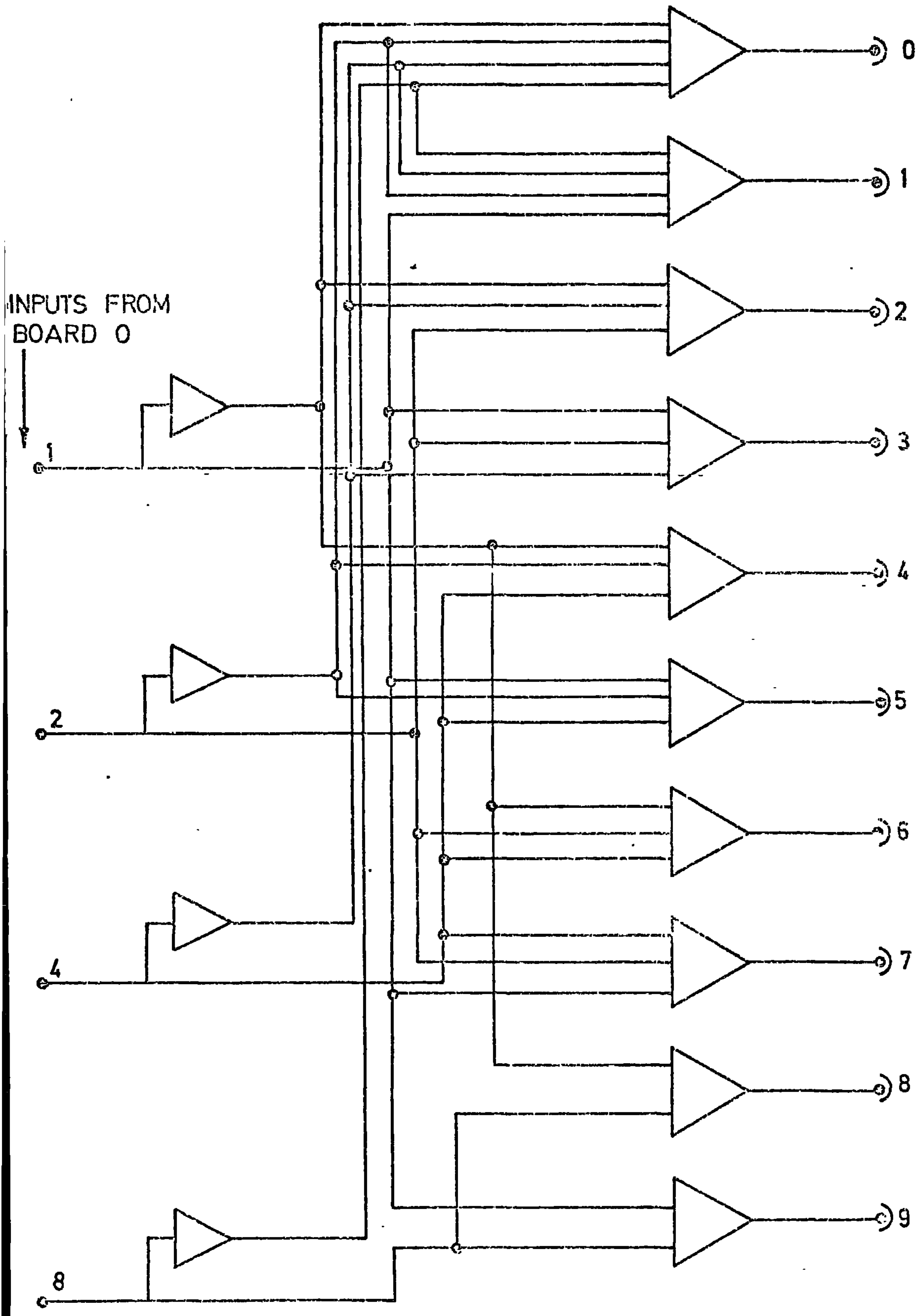

BOARD P
(sheet 1 of 2)

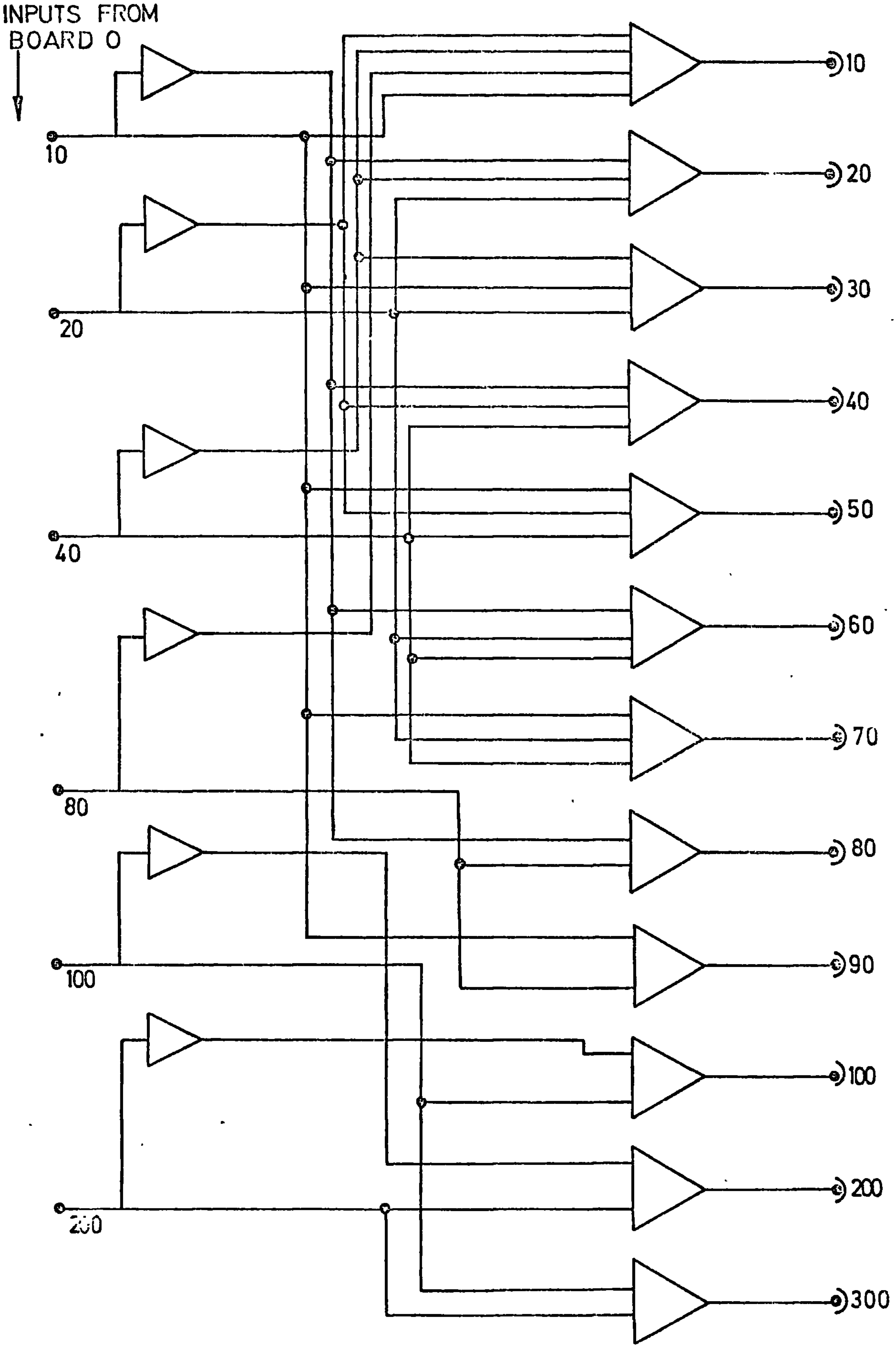

BOARD P
(sheet 2 of 2)

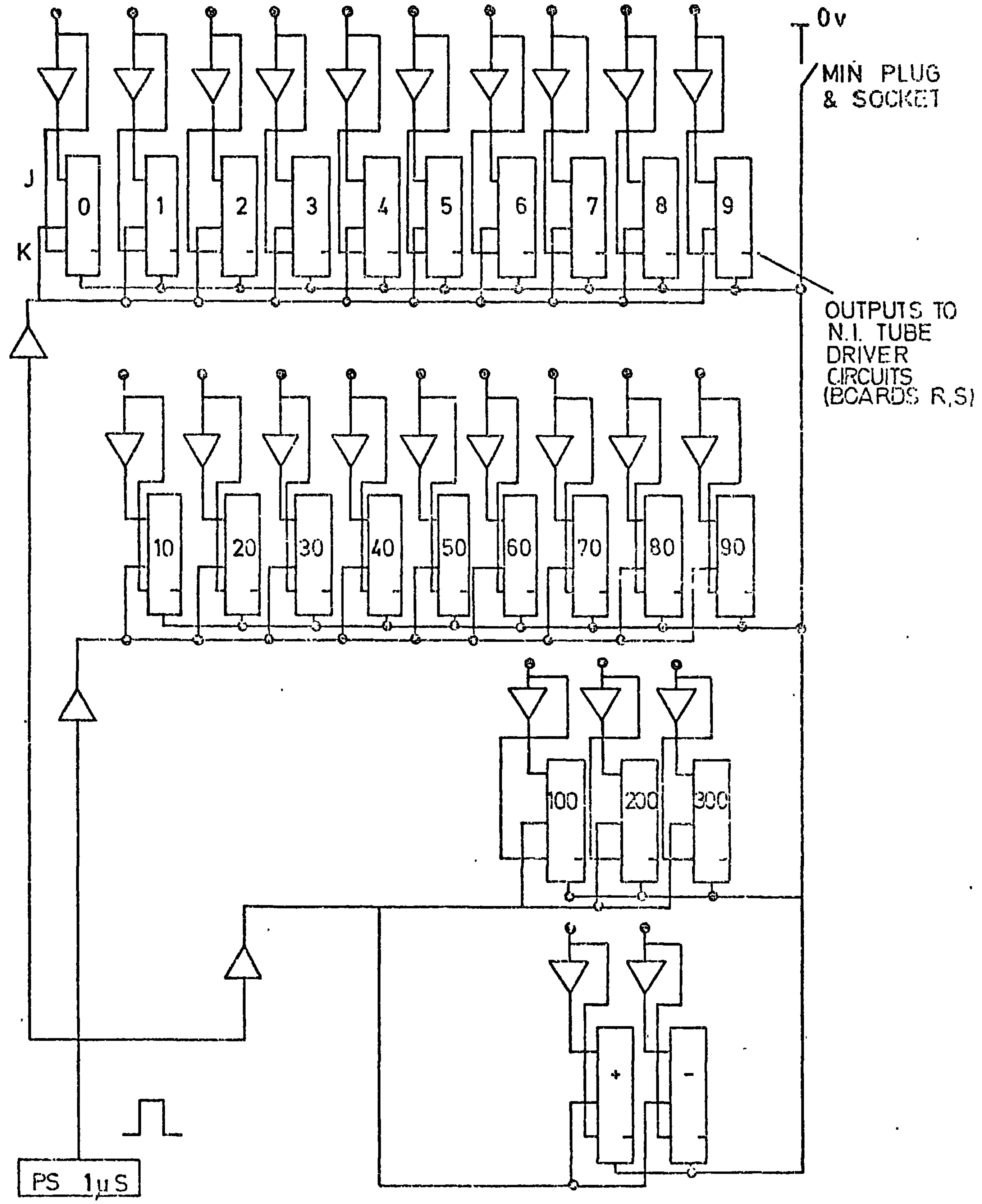

BOARD Q

(sheet 1 of 2)

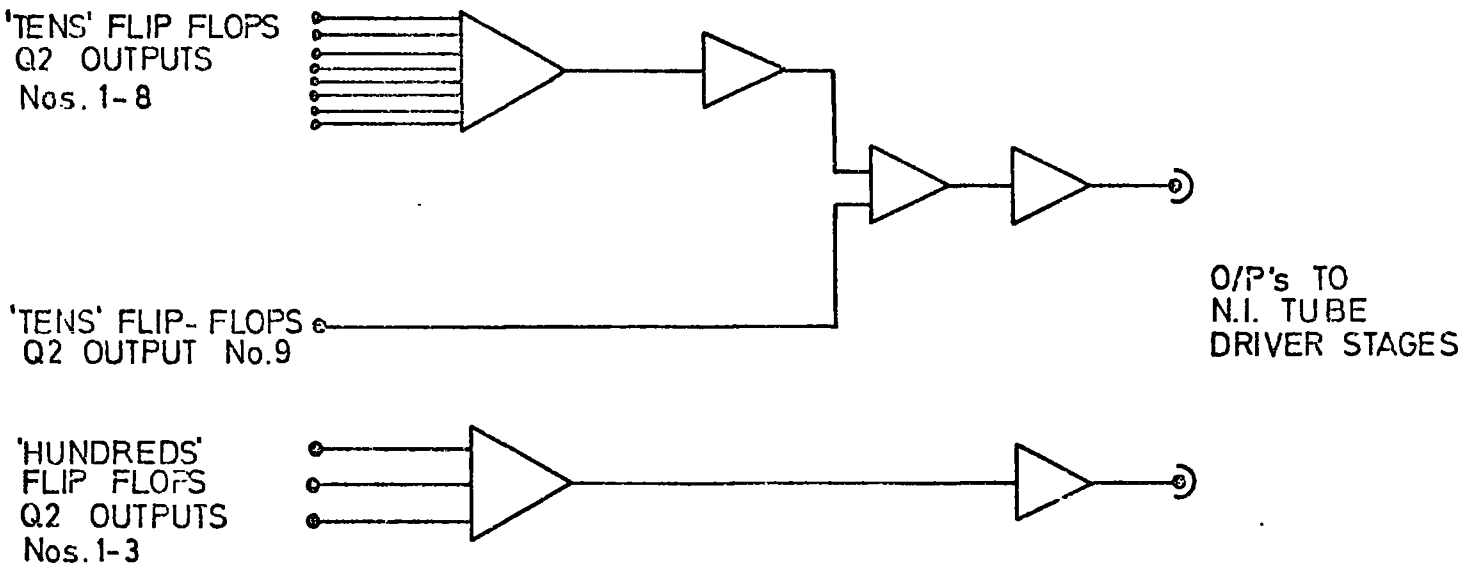

N.B. This is not done for the 'units' part of the memory ∴ upon RESET, the 'TENS' and 'HUNDREDS' of the N.I. Tube Display, each read 0 while the 'units' N.I. Tube goes dead.

BOARD Q
(sheet 2 of 2)

N.I. TUBE DRIVER CIRCUITS

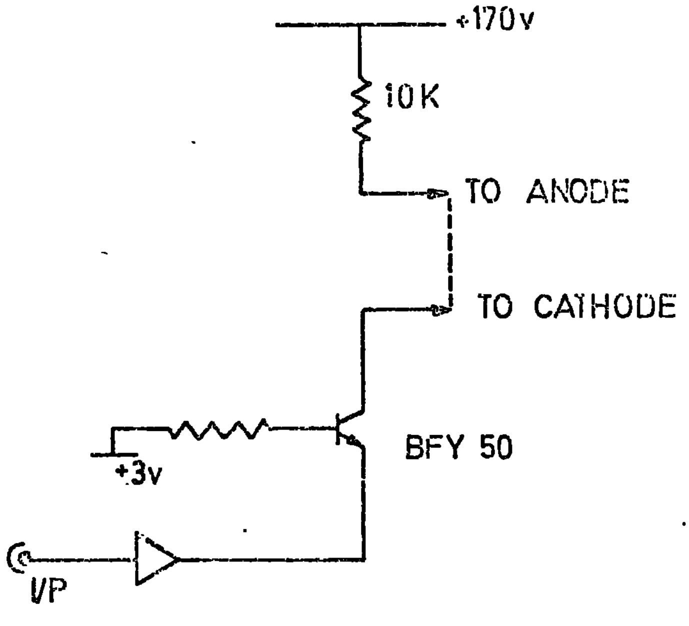

BOARDS R,S EACH CONTAIN 12 OF THESE CIRCUITS

BOARDS R, S.

LOGIC CHANGE CIRCUIT

[BOARD T CONTAINS 10 OF THESE CIRCUITS]

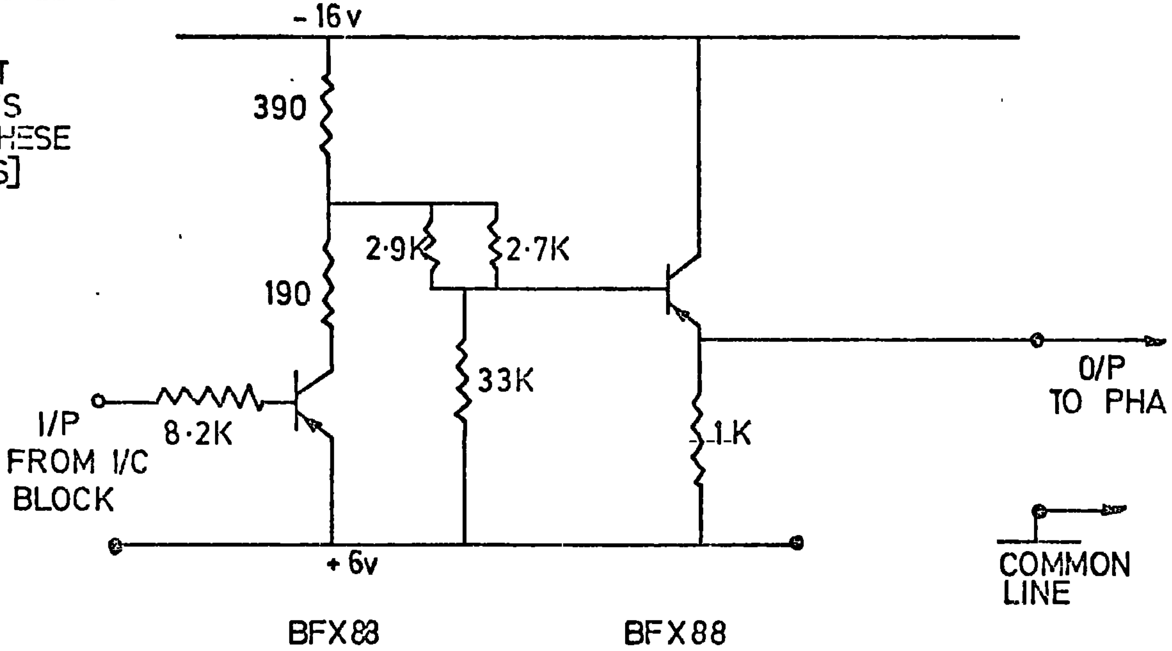

STORE PULSE CIRCUIT

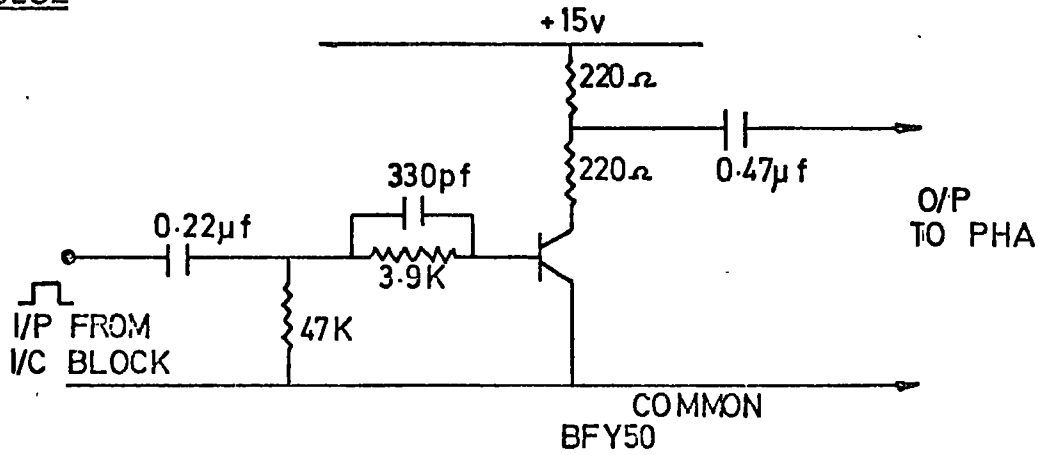

BOARD T

APPENDIX 3

THE R.U.D.I. TEST INSTRUMENT

This device was constructed in order that R.U.D.I. could be tested on a convenient, routine basis. The logic diagram of the circuit is shown in this Appendix.

The circuit is based upon three 8-bit binary counters which count clock pulses. The clock pulses are applied at one of two inputs on the rear panel of the instrument depending upon the source - the 330 Ω biasing resistor is necessary if a pulse generator is used but is not necessary if the pulses are logic pulses. The clock pulses are gated into the binary counters by triggering monostables with the TEST push button (which also triggers a pulse which simulates the C90 pulse). The real and inverse outputs of each counter element are fed, via 2-way switches, to an 8-fold coincidence gate. By suitable selection of switch positions a pulse may be obtained through the gate when a counter has reached some number between 1 and 255. By using different switch selections for each of the 3 counters, 3 time-separated pulses are produced and are used to simulate the arrival of pulses from the shift registers A, B and C. From the switch positions the deflection which should be indicated by R.U.D.I. is calculable and can be compared with that observed.

The facility also exists for simulating the discharge of 2 cells at a given level. This is done by placing the SINGLE/DOUBLE switch in the DOUBLE position. The circuitry involved is shown in the diagram.

The magnetic field direction and triggered side of the spectrograph are set by the appropriate switches.

The procedure for testing is :-

1. Remove from the rear panel of R.U.D.I. the real A, B, C and C90 inputs and replace them with the simulated inputs of the test instrument. Connect the clock pulses to the test instrument.
2. Set up the required switch positions, magnetic field direction and triggered side.
3. Reset.
4. Test.

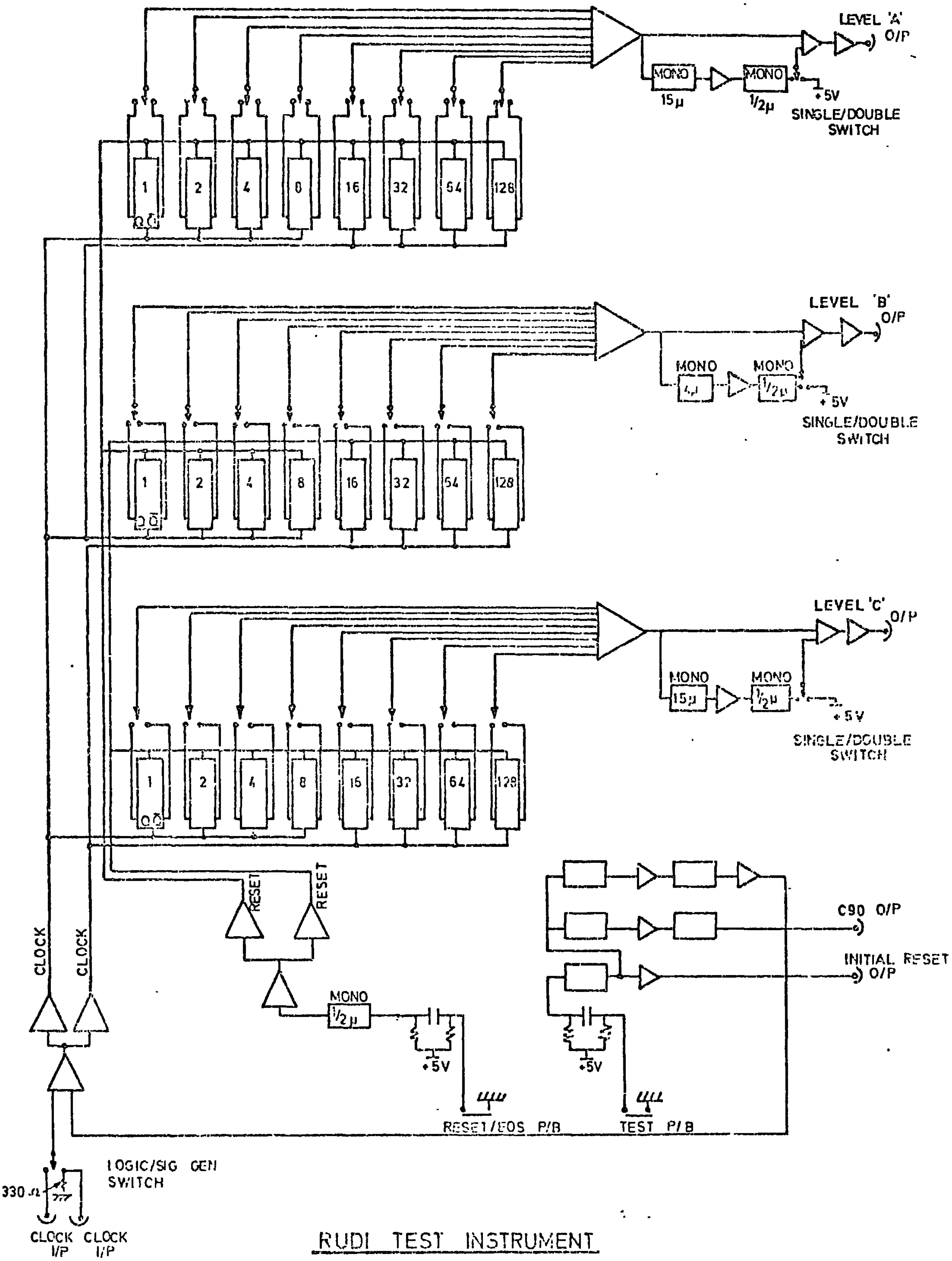

RUDI TEST INSTRUMENT

APPENDIX 4

THE R.U.D.I. CELL MONITOR

This instrument was constructed in order that, for a given level

a) the distribution of discharged cells could be found and

b) the distribution of number of discharged cells could be found.

The logic diagram is given in this Appendix.

The circuit is designed to control a digital counter; it generates pulses to start and stop counting and also the train of pulses which is to be counted.

a) Counting is started by the three-fold coincidence pulse of the spectrograph and stopped, with switch 1 in position b by the first discharged cell from the relevant level or, failing this latter a pulse some 170 μs after the starting pulse. The pulse train which is counted is the clock (switch 2 in position b). When stopped by a discharged cell the indicated count gives a measure of the position of that cell.

b) Counting is started as above but in this case the pulse train counted is the bursts of 10 Mc/s pulses gated by each discharged cell coming from the level which is being monitored. Switches 1 and 2 are in positions a for this application. Switch 1 ensures that a stop pulse is transmitted to the counter once there is no possibility of any more discharged cells being indicated (since the time required to empty the shift register of the monitored level is $\sim 150\ \mu s$).

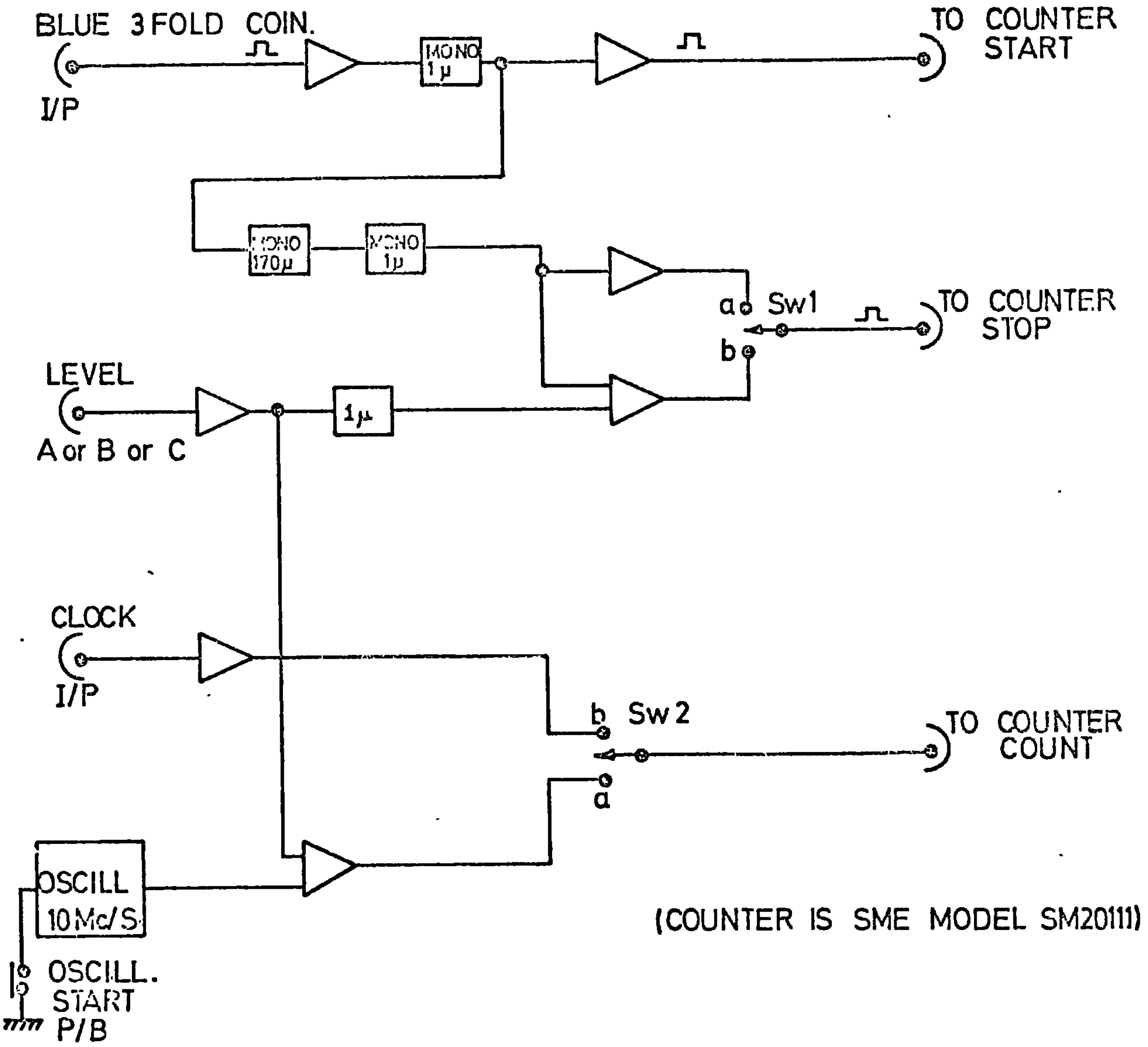

(COUNTER IS SME MODEL SM20111)

RUDI CELL MONITOR

REFERENCES

Abdullaev, A.M. et al, 1971, PICCR Hobart, 6, 2273-76.

Akimov, V.V. et al, 1969, PICCR Budapest, 3, 211-14.

Albrow, M.G. et al, 1972, Phys. Letts., 42B, 279-82.

Albrow, M.G. et al, 1973, Nucl. Phys., B51, 388-96.

Alexander, D.,1970, Ph.D. Thesis, University of Durham.

Alexander, G. et al, 1967, Phys. Rev., 154, 1284-1304.

Allaby, J.V. et al, 1970, CERN Report 70-12.

Allaby, J.V. et al, 1972, Proc. of Fourth Int. Conf. on High Energy Collisions, Oxford, 2, 85-116.

Allkofer, O.C. et al, 1969, PICCR Budapest, 4, 13-18.

Allkofer, O.C., Carstensen, K. and Dau, W.D., 1971, PICCR Hobart, 3, 1314-18.

Allkofer, O.C. et al, 1971, PICCR Hobart, 3, 1319-24.

Almeida, S.P. et al, 1968, Phys. Rev., 174, 1638-61.

Alper, B. et al, 1973, Presented at the Int. Conf. on New Results from Expts. on High Energy Collisions, Nashville.

Amaldi, U. et al, 1973a, Phys. Letts., 43B, 231-36.

Amaldi, U. et al, 1973, Phys. Letts., 44B, 112-18.

Amendolia, S.R. et al, 1973, Phys. Letts., 44B, 119-24

Amosov, V.V. et al, 1973, CERN Report D. Ph. II/PHYS 73-5 (submitted to Nucl. Phys.).

Anand, K.C. et al, 1967, PICCR Calgary, 3, S652-S654.

Antinucci, M. et al, 1973, Lett. Al. Nuovo Cimento, 6, 121-128.

Appleton, I.C., Hogue, M.T. and Rastin, B.C., 1971, Nucl. Phys., 26, 365-369.

Ashley II, G.K., Keuffel, J.W. and Larson, M.O., 1973, PICCR Denver, 3, 1828-32.

Ashton, F. and Wolfendale, A.W., 1963, Proc. Phys. Soc., 81, 593-603.

Aurela, M., Mackeown, P.K. and Wolfendale, A.W., 1966, Proc. Phys. Soc., 89, 401-408.

Ayre, C.A. et al, 1971, PICCR Hobart, 4, 1309-13.

Ayre, C.A. et al, 1971a, PICCR Hobart, 4, 1364-68.

Ayre, C.A. et al, 1971b, PICCR Hobart, 4, 1458-62.

Ayre, C.A. et al, 1972, J. Phys. A, 5, L53-L56.

Ayre, C.A. et al, 1972a, Nucl. Inst. and Meths., 102, 19-28.

Ayre, C.A. et al, 1972b, Nucl. Inst. and Meths., 102, 29-34.

Ayre, C.A. et al, 1973a, PICCR Denver, 3, 1822-27.

Ayre, C.A. et al, 1973b, PICCR Denver, 3, 1754-63.

Bacon, D.F. and Nash, W.F., 1965, Nucl. Inst. and Meths, 37, 43-48.

Balasubrahmanyan, V.K. and Ormes, J.F., 1973, Astrophys. J, 180, 4, 731-33.

Banner, M. et al, 1972, Phys. Letts., 41B, 547-51.

Barkow, A.G. et al, 1961, Phys. Rev. 122, 617-25.

Bassi, P. et al, 1949, Nuovo Cimento, 6, 509-10.

Bellettini, G. et al, 1965, Phys. Letts., 14, 164-68.

Bellettini, G. et al, 1966, Nucl. Phys., 79, 609-24.

Bellettini, G. et al, 1973, Phys. Letts., 45B, 69-72.

Benary, O., Price, L.R. and Alexander, G., 1970, Report UCRL 30000 NN. Compilation of NN and ND Interactions.

Benecke, J., 1971, Nuovo Cimento, 2A, 615-31.

Benecke, J., Chou, T.T. and Yang, C.N., 1969, Phys. Rev., 188, 2159-69.

Bertin, A. et al, 1972, Phys. Letts., 38B, 260-64.

Bertin, A. et al, 1972a, Phys. Letts. 41B, 201-204.

Biswas, N.N. et al, 1971, Phys. Rev. Letts., 26, 1589-92.

Blackett, P.M.S., 1937, Proc. Roy. Soc., A159, 1-18.

Bodini, L. et al, 1968, Nuovo Cimento, 58A, 475-81.

Boggild, H., Hansen, K.H. and Suk, M., 1971, Nucl. Phys., B27, 1-27.

Boggild, H. et al, 1971, Nucl. Phys., B27, 285-99.

Breitenloh, P. et al, 1963, Phys. Letts., 7, 73-75.

Brode, R.B., 1949, Nuovo Cimento, 6, 465-74.

Buffington, A., Smith, L.H. and Smoot, G., 1971, PICCR Hobart, 1, 147-54.

Burnett, T.H. et al, 1973, Pre-print, Univ. of California. (Submitted to Phys. Rev. Letts.).

Cahn, R.N. and Einhorn, M.B., 1971, Phys. Rev. D., 3337-44.

Cartwright, B.G., Garcia-Munoz, M. and Simpson, J.A., 1971, PICCR Hobart, 1, 209-14.

Chapman, J.W. et al, 1972, Phys. Rev. Letts., 29, 1686-88.

Charlton, G. et al, 1972, Phys. Rev. Letts., 29, 515-18.

Cheng, H. and Wu, T.T., 1969, Phys. Rev. Letts., 23, 1311-13.

Choi, K.A. and Kim, C.O., 1971, PICCR Hobart, 235-40.

Chou, T.T. and Yang, C.N., 1970, Phys. Rev. Letts., 25, 1072-74.

Coates, R.B., 1967, Ph.D. Thesis, University of Durham.

Conversi, M., 1949, Phys. Rev., 76, 311-13.

Coxell, H., 1961, Ph.D. Thesis, University of Durham.

Czyzewski, O. and Rybicki, K., 1972, Nucl. Phys., B47, 633-41.

Damgaard, G. and Hansen, H., 1972, University of Copenhagen Report, 'An Estimate of the Multiplicity of Charged Particles Produced at the I.S.R.'

Daniel, B.J. et al, 1974, J. Phys. A., 7, L20-L24.

Dao, F.T. et al, 1972, Phys. Rev. Letts., 29, 1627-30.

Denisov, S.P. et al, 1971, Phys. Letts., 36B, 528-32.

Denisov, S.P. et al, 1971a, Phys. Letts., 36B, 415-21.

Dobrotin, N.A. et al, 1962, Nucl. Phys., 35, 152-64.

Eichten, T. et al, 1972, Nucl. Phys., B44, 333-43.

Erlykin, A.D., Ng, L.K., and Wolfendale, A.W., 1974, University of Durham Internal Reports (i) Interpretation of Cosmic Ray Muon Data in the Light of Results from the I.S.R. Experiments and (ii) Relationship of the Spectrum of Sea-Level Muons to that of Primary Cosmic Rays.

Fan, C.Y., Gloeckler, G. and Simpson, J.A., 1966, Phys. Rev. Letts., 17, 329-33.

Feinberg, E.L., 1972, Phys. Letts. C, 5C, 237-350.

Feynman, R.P., 1969a, Phys. Rev. Letts., 23, 1415-17.

Feynman, R.P., 1969b, 'High Energy Collisions' (Ed: Yang) (Gordon and Breach), 237-58.

Filosofo, I., Pohl, E. and Pohl-Ruling, V., 1954, Nuovo Cimento, 12, 809-12.

Flint, R.W. and Nash, W.F., 1971, PICCR Hobart, 4, 1346-52.

Foley, K.J. et al, 1963, Phys. Rev. Letts., 11, 425-29.

Fowler, G.N. and Wolfendale, A.W., 1961, Handbuch Der Physik (Springer : Berlin), 46/1, 272-315.

Fraser, W.R. et al, 1972, Phys. Rev. D, 5, 1653-57.

Gaisser, T.K., 1973, Preprint, Bartol Research Foundation of the Franklin Institute, Swarthmore, Pennsylvania.

Galbraith, W. et al, 1965, Phys. Rev., 138B, 913-20.

Garcia-Munoz, M., Mason, G.M. and Simpson, J.A., 1971, PICCR Hobart, 1, 209-14.

Garraffo, Z., Pignotti, A. and Zgrablich, G., 1973, Nucl. Phys., B53, 419-28.

Gellert, R. 1972, Ph.D. Thesis, Lawrence Brookhaven Laboratory.

Gerbowska, K. et al, 1964, Nucl. Phys., 60, 654-65.

Gorin, Yu. P. et al, 1972, Sov. J. Nucl. Phys., 14, 560-64.

Greisen, K., 1965, PICCR London, 2, 609-15.

Grigorov, N.L. et al, 1965, PICCR London, 2, 860-62.

Grigorov, N.L. et al, 1971, PICCR Hobart, 1, 170-72.

Grupen, C. et al, 1972, J. Phys. A, 5, 1713-15.

Guseva et al, 1962, Quoted by Feinberg (1972).

Hansen, L.F. and Fretter, W.B., 1960, Phys. Rev., 118, 812-24.

Hayakawa, S., 1969, 'Cosmic Ray Physics' (Wiley Interscience).

Hayman, P.J. and Wolfendale, A.W., 1972, Proc. Phys. Soc., 80, 710-28.

Hess, V.F. 1912, Physik Zeitschr., 13, 1804-91.

Higgs, B.J., 1973, Ph.D. Thesis, Yale University.

Hildebrand, B. and Silberberg, R., 1963, Supp. Al Nuovo Cimento, 1, 1118-42.

Hoffman, L. et al, 1965, Nucl. Phys., 66, 657-68.

Holder, M. et al, 1971, Phys. Letts., 35B, 361-64.

Holmes, J.E.R., Owen, B.G. and Rodgers, A.L., 1961, Proc-Phys. Soc., 78, 505-15.

Honecker, R. et al, 1969, Nucl. Phys. B13, 571-86.

Horn, D., 1972, Phys. Letts. C, 4C, 1-66.

Hughes, D.J., 1940, Phys. Rev., 57, 592-97.

Hume, C.J. et al, 1973, J. Phys. A., 6, L53-L56.

Jacob, M., 1972, CERN Report, TH-1570.

Jones, H., 1939, Rev. Mod. Phys., 11, 235-38.

Jones, L.W. et al, 1970, Phys. Rev. Letts., 25, 1679-81.

Jones, L.W. et al, 1971, PICCR Hobart, 3, 1194-99.

Juliusson, E., Meyer, P. and Muller, D., 1972, Phys. Rev. Letts., 29, 445-48.

Kamiya, Y., Kawaguchi, S. and Iida, S., 1971, PICCR Hobart, 4, 1354-58.

Kaneko, J. et al, 1970, Proc. of the Sixth Interamerican Seminar on Cosmic Rays.

Kasha, H., Hawkins, C.J.B. and Stefanski, R.J. 1967, PICCR Calgary, S306-S308.

Kawaguchi, S. et al, 1965, PICCR London, 2, 941-43.

Kelly, G.N. et al, 1968, Can. J. Phys. 46, 5309-5312.

Koba, Z., Nielsen, H.B. and Olesen, P., 1972, Nucl. Phys. B40, 317-34.

Koshiba, M. et al, 1963, Supp. Al Nuovo Cimento, 1, 1091-1117.

Lal, S. et al, 1965, Phys. Letts., 14, 332-34.

Lillethun, E. 1972, Proc. of the Fourth Int. Conf. on High Energy Collisions, Oxford, 2, 197-213.

Lillethun, A., 1973, University of Bergen, Scientific/Technical Report 53.

Lipkin, H.J., 1973, Phys. Letts. C, 8C, 173-268.

Lohrman, E., Teucher, M.W. and Schein, M., 1961, Phys. Rev., 122, 672-86.

Lohrman, E. and Teucher, M.W., 1962, Nuovo Cimento, 10, 957-63.

Lovati, A. et al, 1954, Nuovo Cimento, 12, 526-37.

Mackeown, P.K. et al, 1965, PICCR London, 2, 937-40.

Mackeown, P.K. and Wolfendale, A.W., 1966, Proc. Phys. Soc., 89, 553-65.

Malholtra, P.K. 1963, Nucl. Phys., 46, 559-71.

Malholtra, P.K. and Ganguli, S.N., 1972, Phys. Letts., 42B, 83-87.

Meyer, J.P., Hagge, D.E. and McDonald, F.B., 1967, PICCR Calgary, 3, S503-S508.

Meyer, J.P., 1969, Ann. Rev. Astron. and Astrophys.

Michejda, L., 1971, Nucl. Phys., B35, 287-316.

Miesowicz, M., 1971, Prog. in Elem. Particle and Cosmic Ray Physics, Vol. X, 103-70.

Morony, J.R. and Parry, J.K., 1954, Aust. J. Phys., 7, 423-38.

Morrison, D.R.O., 1972, CERN Report PHYS-72-19.

Morrison, J.L. and Elbert, J.W., 1973, PICCR Denver, 3, 1833-36.

Muck, H.J. et al, 1972a, Phys. Letts., 39B, 303-306.

Muck, H.J. et al, 1972b, Proc. of Fourth Int. Conf. on High Energy Collisions, Oxford, 2, 117-139.

Mueller, A.H., 1970, Phys. Rev. D., 2, 2963-68.

Murakami, K. et al, 1971, PICCR Hobart, 3, 1235-38.

Nam, R.A. et al, 1971, PICCR Hobart, 6, 2259-72.

Nandi, B.C. and Sinha, M.S., 1972, Nucl. Phys. B40, 289-97.

Nereson, N., 1948, Phys. Rev. 73, 565-69.

Nozaki, T. and Koshiba, M., 1971, J. Phys. Soc. Japan, 30, 1-32.

Ormes, J.F., Webber, W.R. and von Rosenvinge, T., 1965, PICCR London, 1, 407-11.

Ormes, J.F. Balasubrahmanyan, V.K. and Arens, J.F., 1973, PICCR Denver, 1, 157-62.

Osborne, J.L., 1966, Ph.D. Thesis, University of Durham.

Owen, B.G. and Wilson, J.G., 1955, Proc. Phys. Soc., A68, 409-18.

Pine, J., Davisson, R.J. and Greisen, K., 1959, Nuovo Cimento, 14, 1181-1204.

Pinkau, K., Pollvogt, U. and Schmidt, W.K.H., 1969, PICCR Budapest, 1, 291-96.

Ramaty, R., Balasubrahmanyan, V.K. and Ormes, J.F., 1973, Science, 180, 731-2.

Ratner, L.G. et al, 1971, Phys. Rev. Letts., 27, 68-71.

Ratner, L.G. et al, 1971a, Proc. of the Rochester Conference on High Energy Physics.

Regener, F., 1951, Phys. Rev., 84, 161-63.

Reinse, F., 1967, Proc. Roy. Soc., A301, 125-35.

Rossi, B., 1952, 'High Energy Particles' (Prentice-Hall).

Ryan, M.J. Balasubrahmanyan, V.K. and Ormes J.F., 1971, PICCR Hobart, 1, 173-183.

Ryan, M.J., Ormes, J.F. and Balasubrahmanyan V.K., 1972, Phys. Rev. Letts., 28, 985-88 (and erratum, Phys. Rev. Letts., 28, 1497-98.)

Said, S.S., 1966, Ph.D. Thesis, University of Durham.

Saito, T., 1971, PICCR Hobart, 1, 259.

Sens, J.C., 1972, Proc. of the Fourth Int. Conf. on High Energy Collisions, Oxford, 1, 1-27.

Shapiro, M.M. and Silberberg R., 1970, Ann. Rev. Nucl. Sci., 324-92.

Slattery, P., 1972, Phys. Rev. Letts., 29, 1624-27.

Smith, D.B., Sprafka, R.J. and Anderson, J.A., 1969, Phys. Rev. Letts., 23, 1064-1067.

Smith, L. et al, 1972, Space Sciences Laboratory Report, Series 13, Issue 69, Univ. of California.

Smith, L. et al, 1973, Astrophys. J., 180, 987.

Tamai, E., Narita, N. and Saki, T., 1971, PICCR Hobart, 1, 156-61.

Tebb, R.G.P., Nash, W.F. and Deacon, C.A., 1971, PICCR Hobart, 1340-45.

Waddington, C.J., 1960, Prog. Nucl. Phys., 1-46.

Wdowczyk, J. and Zujewska, E., 1973, J. Phys. A, 6, L9-L11.

Webber, W.R., 1967, Handbuch Der Physik, 46/2, 181-264.

Webber, W.R., Damle, S.V. and Kish, J.M., 1971, PICCR Hobart 1, 229-34.

Whalley, M.R., 1974, Ph.D. Thesis, University of Durham.

Yang, C.N., 1969, 'High Energy Collisions' (Ed:Yang) (Gordon and Breach), 509-18.

Yash Pal, Ray, A.K. and Rengarajan, T.N., 1963, Nuovo Cimento, 23, 1177-89.

Yash Pal and Peters, B., 1964, Mat.-Fys. Medd. Dan. Vid. Selsk., 33, 1-55.

Yekutieli, G., 1972, Nucl. Phys., B47, 621-32.

Yodh, G.B., Yash Pal and Trefil, J.S., 1972, Phys. Rev. Letts., 1005-8.

(PICCR = Proceedings of the International Conference on Cosmic Rays)

ACKNOWLEDGEMENTS

The author wishes to thank Professor G.D. Rochester, F.R.S., for the provision of facilities for this work and for his interest in the experiment.

To his supervisor, Dr. M.G. Thompson, and to Professor A.W. Wolfendale the author wishes to express his sincere appreciation of their help, advice and guidance; also for their patience.

Past and present members of the M.A.R.S. group, in particular Dr. C.A. Ayre, Mr. J.M. Baxendale, Mr. B.J. Daniel, Mr. J.S. Hansen, Dr. M.A. Hamdan, Dr. B.C. Nandi, Dr. S.C. Wells and Dr. M.R. Whalley, are thanked for their help, both in discussion and in the running of the experiment.

Members of the technical staff of the Physics Department who have been active in this work are thanked. Particular thanks are due to Mr. K. Tindale for his help and advice on a wide range of topics and to Mr. P. Armstrong for his skilful manufacture of spark gaps. Special thanks are extended to Mrs. Audrey Gregory for her rapid and efficient drawing of diagrams; also to Mrs. P. Russell and Mrs. S. Swinburn for their contributions.

The author is grateful to Mrs. E.L. Greening and Mrs. L. Harris for their conscientious typing of this thesis.

To Miss Shirley H. Moss, for her support, help and encouragement the author is indebted.

Finally, the Science Research Council is thanked for providing a Research Studentship.